Paleoceanographic and paleoclimate evolution of the Northwest Pacific Ocean from the late Miocene to present

Dissertation

zur Erlangung des Doktorgrades
der Mathematisch-Naturwissenschaftlichen Fakultät
der Christian-Albrechts-Universität zu Kiel

vorgelegt von

Ann-Sophie Jonas

Kiel, 2021

Erster Gutachter / First referee:	Prof. Dr. Lorenz Schwark
Zweite Gutachterin / Second referee:	Prof. Dr. Denise K. Kulhanek
Datum der mündlichen Prüfung:	14.01.2022

To my family: Cristopher, Luise and Linnéa.

“*It seems to me that the natural world is the greatest source of excitement; the greatest source of visual beauty; the greatest source of intellectual interest. It is the greatest source of so much in life that makes life worth living.”*

- Sir David Attenborough -

List of Content

List of Content I
List of Figures VII
List of Tables XXI
List of abbreviations XXIII

Abstract XXX

Zusammenfassung (German abstract) XXXIII

Publications XXXVII

Chapter 1
1. Introduction 1
1.1. Oceanic circulation 3
1.1.1. The Kuroshio Current 4
1.1.2. The Oyashio Current 6
1.1.3. The Kuroshio-Oyashio Interfrontal Zone 7
1.2. Atmospheric circulation 9
1.2.1. The East Asian summer and winter monsoons 10
1.2.2. The westerly jet stream 14
1.3. Lipid biomarkers as proxies for paleoclimate, paleoceanographic and paleoenvironmental conditions 17
1.3.1. Marine biomarkers: sea surface and subsurface temperature proxies 17
1.3.2. Terrigenous biomarkers 26

Chapter 2
Study sites 33
2.1. Tectonic evolution of the study area in the NW Pacific 33
2.2. IODP Expedition 333 Site C0011 35
2.2.1. Lithology description and age model 35
2.3. IODP Expedition 350 Site U1437 38
2.3.1. Lithology description and age model 38

Chapter 3

Objectives and outline of this thesis 43

Chapter 4

Late Quaternary water temperature variations of the Northwest Pacific based on the lipid paleothermometers TEX^{H}_{86}, $U^{K'}_{37}$ and LDI 47

Abstract 47

Highlights 48

Key words 48

4.1. Introduction 48

4.1.1. Paleoceanography of the NW Pacific 50

4.2. Materials and methods 55

4.2.1. Sampling of sediments 55

4.2.2. Lipid extraction and fractionation 56

4.3. Results 58

4.3.1. Sea surface temperature reconstruction 58

4.3.2. Fractional abundance of C_{32} 1,15-diol 60

4.3.3. BIT index 60

4.4. Discussion 62

4.4.1. Effect of habitat and thermocline depth on the TEX^{H}_{86}, $U^{K'}_{37}$ and LDI 62

4.4.2. Effect of seasonality on the TEX^{H}_{86}, $U^{K'}_{37}$ and LDI 65

4.4.3. Paleoceanographic evolution of the Kuroshio Current 67

4.5. Conclusion 72

4.6. Acknowledgements 72

4.7. Appendix A Supporting information 74

Chapter 5

Southward displacement of the glacial westerly jet driven by Arctic amplification 79

Abstract 79

5.1. Introduction 80

5.2. Glacial-interglacial oceanographic changes across the MBE 82

5.3. Glacial-interglacial changes in the path of the westerly jet stream 83

5.4. Acknowledgements 88

Supplementary Materials 89
Materials and Methods 89
Sample material and age model 89
Lipid biomarker analysis 90
X-ray fluorescence 91
Spectral analysis 91
Supplementary Text 91
Complementary dust flux records 91
Changes in EASM strength across the MBE 92
Changes in marine primary productivity at Site U1437 94
Time series analysis on the Ba/Al paleoproductivity record 96
North Pacific sea surface temperature records of the past 1 Ma 97

Chapter 6

An 8-million-years history of paleoceanographic and paleoclimatic changes in the Northwest Pacific Ocean at IODP Sites C0011 and U1437 101
Abstract 101
6.1. Introduction 102
6.1.1. Regional oceanography 104
6.2. Materials and methods 105
6.2.1. Sediment samples and age model 105
6.2.2. Lipid biomarker analysis 107
6.3. Results and discussion 109
6.3.1. Unsaturated ketones and the $U^{K'}_{37}$ 109
6.3.2. Glycerol dialkyl glycerol tetraethers and the TEX^{H}_{86} 110
6.3.3. Late Miocene to present oceanographic evolution of the Northwest Pacific Ocean 110
6.3.4. Pliocene to present SST evolution and implications for past positions of the KC 113
6.3.5. Short-lived late Miocene subsurface cooling 115
6.3.6. Changes in continental climate conditions from the late Miocene to present 116
6.4. Conclusions 123
6.5. Acknowledgements 124
6.6. Appendix A Supporting information 125

Chapter 7

Validating the applicability of the novel RI-OH-proxy for paleotemperature reconstruction over the last 1 Ma at IODP Site U1437, NW Pacific Ocean 139

Abstract 139

7.1. Introduction 140

7.2. Materials and methods 141

7.3. Results and discussion 142

7.4. Conclusions 146

7.5. Acknowledgements 146

7.6. Appendix: Supporting information 147

Chapter 8

Impact of climate change on the magnetic mineral assemblage in marine sediments from Izu rear arc, NW Pacific Ocean, over the last 1 Ma 153

Abstract 153

8.1. Introduction 154

8.2. Geological setting 155

8.3. Material and methods 157

8.3.1. Rock magnetic measurements 157

8.3.2. Bulk-geochemical analyses 158

8.3.3. Time series analysis 159

8.4. Age model 160

8.5. Results 162

8.5.1. Magnetic mineral concentration 162

8.5.2. Magnetic mineralogy 163

8.5.3. Grain size of the magnetic minerals 168

8.5.4. Time series analysis 169

8.6. Discussion 169

8.6.1. Magnetic signal and global climate change 170

8.6.2. Paleoproductivity and water mass properties 176

8.6.3. Effect of magnetic diagenesis 179

8.6.4. Origin of the magnetic minerals 180

8.7. Conclusions 182

8.8. Acknowledgements 183

8.9. Appendix A. Supplementary data 184

Chapter 9

Summary and outlook to future work 199

Future work 203

Appendix Chapter 10

Magnetic mineral diagenesis in a high temperature and deep methanic zone in Izu rear arc marine sediments, Northwest Pacific Ocean 209

Abstract 210

Key points 210

10.1. Introduction 211

10.2. Materials and Methods 213

10.2.1. Studied samples 213

10.2.2. Rock magnetic measurements 213

10.2.3. Geochemical Analyses 215

10.2.4. DNA-Based Microbial Community Analysis 215

10.3. Results 216

10.3.1. Magnetic Mineral Contents 216

10.3.2. Grain Size of the Magnetic Minerals 217

10.3.3. Magnetic Mineralogy 218

10.3.4. Bulk Solid Phase Analysis 222

10.3.5. Microbiological Analyses 223

10.4. Discussion 225

10.4.1. Dissolution and Authigenic Magnetic Mineral Formation 225

10.4.2. Role of Methane and Porosity 227

10.4.3. Possible Mechanisms Responsible for Magnetic Mineral Alteration 229

10.5. Conclusions 232

10.6. Acknowledgments 233

Supporting Information 234

References 251

Personal contribution to multiple-author publications 289

List of publications 291

Acknowledgements 294

Affidavit 295

List of Figures

Figure 1.1 | False-color sea surface temperature map of the North Pacific Ocean as measured on June 1, 2003 by the AMSR-E (Advanced Microwave Scanning Radiometer for EOS (Earth Observing System)). Black arrows indicate surface currents: KC = Kuroshio Current, KE = Kuroshio Extension, NPC = North Pacific Current, CC = California Current, NEC = North Equatorial Current forming the North Pacific Subtropical Gyre, and the OC = Oyashio Current, SAC = Subarctic Current, AC = Alaska Current, AS = Alaskan Stream, EKC = East Kamchatka Current forming the Subarctic Gyre and its subgyres, the Western Subarctic Gyre and the Alaska Gyre. TwC = Tsushima Warm Current; MC = Mindanao Current; NECC = North Equatorial Countercurrent; SEC = South Equatorial Current; PC = Peru Current. Image is from https://earthobservatory.nasa.gov/images/3513/global-sea-surface-temperature-from-amsr-e. ……...3

Figure 1.2 | Bathymetric map of the northern Philippine Sea and the three different stable meander path modes of the Kuroshio Current south of Japan downstream of its exit from the ECS through the Tokara Strait. LM = large meander path, nSM = nearshore short meander path, and oSM = offshore short meander path. ECS = East China Sea. Locations of IODP Sites C0011 and U1437 are indicated by yellow stars. ……..5

Figure 1.3 | Satellite image taken on May 26, 2019 showing a phytoplankton bloom off of northeastern Japan. The advection of nutrient-rich waters from the Subarctic Pacific via the Oyashio Current supports marine primary productivity. NASA Earth Observatory image by Joshua Stevens, using MODIS data from NASA EOSDIS/LANCE and GIBS/ Worldview. Source: https://visibleearth.nasa.gov/images/ 145135/bloom-in-the-parent-stream/145137w. ……...7

Figure 1.4 | A well-defined large eddy formed in the KC/OC interfrontal zone off the east coast of Japan. The SeaWiFS image was taken on May 22, 1999 and is from NASA's Visible Earth Web Site (http://visibleearth.nasa.gov/), provided by the SeaWiFS Project, NASA Goddard Space Flight Center, and ORBIMAGE. ……..….8

Figure 1.5 | Map of the East Asian continent and adjacent Northwest Pacific Ocean showing major features of the atmospheric circulation for the summer (upper map) and winter (lower map) months, including the East Asian (EASM) and Indian (ISM) summer monsoons and the East Asian winter monsoon (EAWM). Limits for the summer monsoons and the EAWM are given by light orange and purple lines, respectively. The summertime and wintertime positions of the westerly jet stream (WJS) are indicated by the red and blue arrow, respectively. Source regions of eolian dust are displayed in orange (deserts) and yellow (loess deposits) colors. Atmospheric pressure systems are indicated by white eclipses: NPH = North Pacific High, AsL = Asian Low, SH = Siberian High, AL = Aleutian Low. The Kuroshio (KC) and Oyashio (OC) Currents are indicated by pink and light blue arrows, respectively. Yellow stars indicate locations of Sites C0011 and U1437. Abbreviations: HTP = Himalayan-Tibetan Plateau, CLP = Chinese Loess Plateau, TakD = Taklimakan Desert, GD = Gobi Desert, TD = Tengger Desert, OD = Ordos Desert. ..……...9

Figure 1.6 | Dust blown from East Asia over the Korean peninsula and the Japan Sea. The true-color satellite image was taken on April 1, 2002, by the Moderate-resolution Imaging Spectroradiometer (MODIS) aboard NASA's Terra satellite. Source: https://visibleearth.nasa.gov/images/58069/dust-over-korea-and-the-sea-of-japan. …..10

Figure 1.7 | Seasonal changes of the westerly jet axis at 200 hPa over Asia for January (a) and June (b). Figures on the left side show the total occurrence counts (shading, from 6-hourly ERA-40 fields) and the interannual variability of the jet latitude (blue box plots, from ERA-40 monthly mean horizontal wind). The figures on the right display the meridional distribution of the occurrence counts between 80-90 °E over (within the area marked by the dark green boxes on the left figures). The bold solid line and gray shading on the right figures display the mean and one standard deviation of interannual variability based on occurrence counts from the 6-hourly ERA-40 fields). The bold and thin dashed lines in the same figures represent the mean and one standard deviation of interannual variability based on occurrence counts from the 6-hourly CHRM fields. Figures modiefied after Schiemann et al. (2009). …….15

Figure 1.8 | Schematic overview of the concept of water temperature reconstruction using the $U^{K'}_{37}$, LDI, RI-OH (based on organisms dwelling at the sea surface) and TEX^{H}_{86} (subsurface) paleotemperature proxies. The respective compounds are synthesized by their source organisms at their preferred habitat depth and hence preserve the ambient water temperature signal at that depth. ……..……..19

Figure 1.9 | Structural formula of the di- and triunsaturated ketones (heptatriaconta-15E,22E-dien-2-one and heptatriaconta-8E,15E,22E-trien-2-one). ……...21

Figure 1.10 | Long-chain diols used for the calculation of the long-chain diol index and the C_{32}-1,15 diol. ……..22

Figure 1.11 | Isoprenoid GDGTs used for the calculation of the TEX_{86} (GDGT-1, GDGT-2, GDGT-3, and the crenarchaeol isomer) and the regular crenarchaeol with their associated mass-to-charge ratios (*m/z*). ……..……..24

Figure 1.12 | Structures of OH-GDGT-1 and OH-GDGT-2 both of which are used for the calculation of the RI-OH index. …….……..26

Figure 1.13 | Dominant west-to-east transport mechanisms of terrestrial organic matter from the Asian continent to the Northwest Pacific Ocean and its marginal seas. Adapted from and modified after Eglinton and Eglinton (2008). Pictured are also the compound structures of a selected long-chain *n*-alkane and *n*-alcohol, and nonacosan-*10*-ol. ……..28

Figure 1.14 | Structural formula of nonacosan-*10*-ol. ……..29

Figure 1.15 | Structures of brGDGTs-I, -II, and -II relevant for the calculation of the BIT index. …….30

Figure 2.1 | Bathymetric map of the northern Shikoku Basin including characteristic features. Convergent plate margins are indicated by red barbed lines. The inset map shows the major tectonic plates around Japan and their convergent plate margins. The blue rectangle represents the section of the bathymetric map. PhSP = Philippine Sea Plate, EP = Eurasian Plate, PacP = Pacific Plate, NAP = North American Plate. The white arrows give the direction and rate of subduction of the Philippine Sea Plate beneath the Eurasian Plate and the subduction direction and rate of the Pacific Plate beneath the Philippine Sea Plate. The dotted orange line displays the Sofugan Tectonic Line (STL) that separates the Izu arc from the Bonin arc. Orange solid lines give the locations of active rifts in the Izu arc to the west of the active volcanic front (VF, purple line). AR = Aogashima Rift; MR = Myojin Rift; SR = Sumisu Rift. Study site locations are given by yellow stars. ……..….34

Figure 2.2 | Age model of Site C0011 based on magnetic reversal events (blue curve for IODP Expedition 333 Holes C/D; red curve for Expedition 322 Hole B), volcanic marker events and nannofossil datums, including averaged sedimentation rates. The bars on the right give the lithostratigraphic units of the Shikoku facies as identified onboard in C0011 Holes C/D and B. Identified ash layers with onland equivalents are given as red bars. Modified after Expedition 333 Scientists (2012). ……36

Figure 2.3 | Bathymetric map of the northern Shikoku Basin with the paleogeographic track and the present location (yellow star) of IODP Site C0011. Orange colors display middle (dark orange) and late Miocene (light orange) positions of the site, the yellow circle gives its Pliocene position at ~4 Ma and the purple circle its position at ~2 Ma (Pleistocene). White arrows give the direction and convergence rate at which the Philippine Sea Plate moved north(north-)westward (Kimura et al., 2005). The paleo-positions of Site C0011 were taken from Expedition 322 Scientists (2010) and were calculated based on estimated plate convergence rates and magnetic stripes in the Shikoku Basin. The path of the KC with its offshore short meander configuration is indicated by the pink line. ……..…..37

Figure 2.4 | Age model of Site U1437 based on magnetic reversal events, nannofossil datums, and $\delta^{18}O$ stratigraphy from planktonic foraminiferal tests as given in Kars et al. (2017) (0-120 mbsf) and Tamura et al. (2015b) (~120-1303 mbsf). The bars on the right give the seven different lithostratigraphic units as identified onboard in U1437 Holes B, D and E (Tamura et al., 2015b). Orange colors represent higher relative contents of tuffaceous mud and mudstones, purple colors represent higher relative contents of volcaniclastics. ……..…...…….39

Figure 2.5 | Bathymetric map of the Shikoku Basin with the paleogeographic track of Site U1437 from the early Miocene (red) to its present location (yellow star). Orange colors display middle (dark orange) and late Miocene (light orange) positions of the site, yellow circles give the Pliocene positions and the purple circles the site´s position during the Pleistocene. The paleo-positions of Site U1437 were calculated and kindly provided by Robert J. Musgrave (personal communication). The path of the KC with its large meander configuration is indicated by the pink line. …….……...……..41

Figure 4.1 | Bathymetric map of the Northwest Pacific showing the flow path of the two major western boundary currents: the Kuroshio Current (red) and the Oyashio Current (blue) and their interfrontal zone (shaded area) including a detailed bathymetric map of the Nankai Trough area with both the short and large meander path configurations of the KC being displayed. The yellow star marks Site C0011, which was drilled during IODP Expedition 333. ……...51

Figure 4.2 | Oceanographic scenarios of the NW Pacific during warm phases (a) and cold phases (b). During warm phases, the heat export from the WPWP via the KC is strong and the KC takes the short meander SE of Japan and passes Site C0011 (scenario 1). In warm phase scenario 2, the KC is less strong, which favors the formation of the large meander. In both scenarios, the KC/OC interfrontal zone is located up north. During cold phases (b), the KC is weak and displaced southward, allowing for a southward shift of the KC/OC interfrontal zone and a direct influence of cold OC waters at Site C0011 (scenario 3). Associated fluctuations in the depth of the thermocline result in larger (a) or smaller (b) offsets in habitat depth of Thaumarchaeota, haptophytes and eustigmatophytes. ……54

Figure 4.3 | (*overleaf*) Reference curves of a) North Greenland Ice Core Project (NGRIP) $\delta^{18}O$ data (Andersen et al., 2004) as well as b) June insolation at 30 °N (Berger and Loutre, 1991), the $\delta^{18}O$ record of benthic foraminifera (c), and $\delta^{18}O$-SST record (d) from Site MD01-2421 off central Japan by Oba et al. (2006) in comparison with Site C0011 reconstructed water temperature records as 3-point averages (e: $U^{K'}_{37}$, f: LDI, g: TEX^{H}_{86}), ΔT values for the different lipid paleothermometers (h: $U^{K'}_{37}$-TEX^{H}_{86}, i: LDI-TEX^{H}_{86}, j: LDI-$U^{K'}_{37}$), the BIT index (k), and fractional abundance of the C_{32} 1,15-diol (l) over the last 145 ka. MIS 2, 4 and 6 are displayed as gray bars. Cold periods, such as the YD, the LGM and HEs (Heinrich et al., 1988; Rasmussen et al., 2003; Rashid et al., 2003) are shown in light blue, while the Bølling-Allerød (BA) warm period is indicated in orange. ΔT values are displayed as black lines with periods where $\Delta T < 0$ shaded in gray. Dashed lines indicate intervals with no available sample material. (For interpretation of the references to color in this figure legend, the reader is referred to the web version of this article.). ……...61

Figure 4.4 | a) Annual mean and seasonal water temperature profiles for the uppermost 200 m of the water column in a 1° grid at 32-33 °N and 136-137 °E for January-February-March (JFM), April-May-June (AMJ), July-August-September (JAS), October-November-December (OND) and b) monthly temperature variations for different water depths (0, 30, 50, 75, 100, 150, 200 m). Proxy-inferred water temperatures for the core-top sample are displayed as dashed gray lines. The temperature data was obtained from the Japan Oceanographic Data Center (http://www.jodc.go.jp/jdoss_stat/stat-infor-sca_e.htm). ..64

Figure 4.5 | Comparison of the different proxy-based water temperatures for warm MIS 1 (Holocene), 3 and 5 (a-c) and cold MIS 2, 4 and 6 (d-f). The dashed gray lines indicate the 1:1 correlation for the different lipid-derived temperatures. …….65

Figure 5.1 | Summertime and wintertime atmospheric circulation over East Asia and the NW Pacific. Yellow star represents IODP Site U1437. The arrows display atmospheric and oceanic current systems: EAWM, East Asian winter monsoon; EASM, East Asian summer monsoon; ISM, Indian summer monsoon; KC, warm Kuroshio Current; OC, cold Oyashio Current. The positions of the atmospheric pressure systems are indicated: AsL = Asian Low, NPH = North Pacific High, SH = Siberian High, AL = Aleutian Low, CLP = Chinese Loess Plateau. Map modified after Yancheva et al. (2007). Black solid lines give isobars with the mean sea level pressure given in hPa. Blue shaded areas are regions with water depths <120 m, which would be exposed during glacial sea level lowstand. ……..81

Figure 5.2 | Site U1437 paleoenvironment and paleoclimate proxies in comparison with previously published records. a: Summer insolation at 65 °N (Laskar et al., 2004), b: eccentricity (Laskar et al., 2004), c: global $\delta^{18}O$ record of benthic foraminifera (Lisiecki and Raymo, 2005), d: Site U1437 $\delta^{18}O$ record of planktonic foraminifera *N. dutertrei* (Kars et al., 2017), e: $U^{K'}_{37}$ sea surface temperature (SST) record of Site U1437 (this study), f: TEX^{H}_{86} water temperature record of Site U1437 (this study), g: concentrations of nonacosan-*10*-ol (this study), h: summed concentrations of long-chain *n*-alkanes (red) and *n*-alcohols (green) (this study), i: Southern Ocean dust mass accumulation rates (Martínez-Garcia et al., 2011), j: relative sea level curve (Rohling et al., 2014). MBE = Mid-Brunhes Event (orange vertical bar). Gray vertical bars denote glacial marine isotope stages. ……..84

Figure 5.3 | Concentrations or mass accumulation rates of *n*C_{27}-*n*C_{33}-alkanes over the past 1 Ma. Records from the NW Pacific (this study), North Atlantic (Naafs et al., 2012b) and Southern Ocean (Martínez-Garcia et al., 2011) all show elevated glacial MARs prior to the MBE, whereas only the sites from the North Atlantic and Southern Ocean continue to receive elevated glacial dust inputs after that. Gray vertical bars denote glacial marine isotope stages. ……...…..85

Figure 5.4 | Pre-MBE and post-MBE scenarios of atmospheric and oceanographic circulation in East Asia and the NW Pacific. The left picture shows the pre-MBE scenario with the EAWM (blue arrow) over Site U1437, an EASM (orange arrow) whose front is located further south and the main WJS axis (purple arrow) located north of the Himalayan-Tibetan Plateau. The right picture displays the post-MBE scenario with a southward displaced glacial WJS and stronger EAWM both resulting from amplified cooling in the Arctic region (blue vertical arrow). During post-MBE interglacial periods a stronger EASM associated with a northward shift of the ITCZ migrated further north (see Supplementary Materials). The Siberian High pressure (light blue area) in the post-MBE Scenario is after Hao et al. (2012). The basemap is from the NASA Eclipse Website (https://eclipse.gsfc.nasa.gov/transit/TV2004/Earth-Ingress1a.JPG). ……87

Figure 5.S1 | Site U1437 Al/Ca record in 10-point average (purple) as potential indicator for Asian dust input in comparison with the benthic $\delta^{18}O$ curve by Lisiecki and Raymo (2005) and the concentration of long-chain *n*-alkanes. Gray vertical bars denote glacial marine isotope stages. …….92

Figure 5.S2 | Site U1437 Ba/Al record as indicator for marine primary productivity in comparison with the benthic $\delta^{18}O$ curve by Lisiecki and Raymo (2005). The blue curve gives the smoothing spline applied to the Ba/Al dataset. Gray vertical bars denote glacial marine isotope stages. …….95

Figure 5.S3 | Multi taper method analysis of the Ba/Al record over the past 1 Ma. Note that low frequencies were removed by low frequency band-pass filtering (LF bpf). …….96

Figure 5.S4 | Running periodogram of the detrended Ba/Al record (Ba/Al_{res}) over the past 1 Ma. ……..97

Figure 5.S5 | A compilation of $U^{K'}_{37}$-reconstructed sea surface temperature records over the past 1 Ma in the Pacific Ocean (this study; Lawrence et al., 2006; Martínez-Garcia et al., 2010; Li et al., 2011; LaRiviere et al., 2012). Gray vertical bars denote glacial marine isotope stages. …….98

Figure 5.S6 | Map showing the locations of $U^{K'}_{37}$-based sea surface temperature records compiled in Figure 5.S5. Black arrows indicate major ocean surface currents in the North Pacific. Abbreviations for ocean currents are as follows: KC = Kuroshio Current; KE = Kuroshio Extension; OC = Oyashio Current; AC = Alaska Current; NPC = North Pacific Current; CC = California Current; NEC = North Equatorial Current; NECC = North Equatorial Counter Current; PC = Peru Current; SEC = South Equatorial Current; MC = Mindanao Current; TwC = Tsushima Warm Current. The false-color sea surface temperature base map of the North Pacific Ocean is from https://earthobservatory.nasa.gov/images/3513/global-sea-surface-temperature-from-amsr-e. ……..…….99

Figure 6.1 | Oceanographic regime in the North Pacific Ocean with all sites investigated (yellow stars; IODP Sites C0011 and U1437) and referenced (ODP Sites 806, 846, 883/884, 1010, 1021 and 1208) in this study. The false-color sea surface temperature base map is from https://earthobservatory.nasa.gov/images/3513/global-sea-surface-temperature-from-amsr-e. Abbreviations for ocean currents are as follows: KC = Kuroshio Current; KE = Kuroshio Extension; OC = Oyashio Current; OE = Oyashio Extension; EKC = East Kamtchatka Current; SAC = Subarctic Current; AS = Alaskan Stream; AC = Alaska Current; NPC = North Pacific Current; CC = California Current; NEC = North Equatorial Current; NECC = North Equatorial Counter Current; PC = Peru Current; SEC = South Equatorial Current; MC = Mindanao Current; TwC = Tsushima Warm Current. ……...104

Figure 6.2 | Bathymetric map of the northern Shikoku Basin showing the current locations of Sites C0011 and U1437 and their backtracked positions back to the middle Miocene. Past positions of Site C0011 are indicated by diamonds and those of Site U1437 by circles. Spacing between individual symbols is 2 Ma for Site C0011 and 1 Ma for Site U1437. Paleo positions of Site C0011 were calculated based on estimated plate convergence rates and magnetic stripes in the Shikoku Basin by Expedition 322 Scientists (2010). Past locations of Site U1437 were calculated and kindly provided by Robert J. Musgrave (*personal communication*). The symbols´ colors indicate different epochs: purple = Pleistocene, yellow = Pliocene, light orange = late Miocene, dark orange = middle Miocene. The path of the Kuroshio Current (KC) with its different meander configurations is indicated. ……..…..106

Figure 6.3 | Annual mean and seasonal temperature profiles throughout the uppermost 1000 m of the water column at Sites C0011 and U1437. The reconstructed temperatures of the respective core top sample are displayed by the vertical dashed lines (blue triangle: $U^{K'}_{37}$, red triangle: TEX^{H}_{86}). Temperature data was taken from the Japan Oceanographic Data Center (http://www.jodc.go.jp/jdoss_stat/stat-infor-sca_e.htm). ……..109

Figure 6.4 | Late Miocene to present water temperature records of Sites C0011 and U1437 in comparison with temperature records from North Pacific Site 883/884 (Herbert et al., 2016), Northeast Pacific Site 1021, subtropical NE Pacific Site 1010, Shatsky Rise Site 1208 (LaRiviere et al., 2012), as well as the tropical WPWP Site 806 (Zhang et al., 2014), eastern equatorial Pacific Site 846 (Lawrence et al., 2006; Herbert et al., 2016), and the global $\delta^{18}O$ stack by Lisiecki and Raymo (2005) (5.3-0 Ma; black) and Zachos et al. (2001) (8.2-5.3 Ma). Sites are ordered from north to south depending on their latitudinal position. For better identification of general temperature trends, curves are shown in 5-pt. (C0011, U1437, 806), 9-pt. (883/884, 1010, 1021, 1208), or 11-pt. average (846). ……..…….....112

Figure 6.5 | Temperature evolution at Sites C0011 and U1437 from the late early Pliocene to the Present (a), and over the past 150 ka (b). The global stack of benthic foraminiferal oxygen isotope values (Lisiecki and Raymo, 2005) is shown for reference. The small horizontal arrow in (a) represents the zoomed-in plot shown in (b). ……..114

Figure 6.6 | Late Miocene to present (Site C0011) and late early Pliocene to present (Site U1437) trends in relative changes in distribution of long-chain *n*-alkanes and *n*-alcohols. Data from both sites show systematic compositional variation from the late Miocene, late early Pliocene, respectively, to the Present. The wide variety in Pleistocene samples that is especially observed at Site C0011 is presumably due to the highly variable climate of this epoch with frequent glacial-interglacial cycles. The arrows in the ternary diagrams indicate – where feasible – the general temperature trend from the late Miocene, respectively late early Pliocene to the Pleistocene cold phases. ……..…..…..…118

Figure 6.7 | Sites C0011 and U1437 average chain length (ACL) records in comparison with the globally stacked benthic oxygen isotope records (Zachos et al., 2001; Lisiecki and Raymo, 2005) and atmospheric pCO_2 estimates from ice cores (Lüthi et al., 2008; dark blue solid line), boron isotopes (Hönisch et al., 2009 (filled diamonds); Bartoli et al., 2011 (open diamonds)), leaf stomata (black circles; Beerling and Royer, 2011; Stults et al., 2011), alkenones (Pagani et al., 1999 (blue shading); Seki et al., 2010 (green shading); Zhang et al., 2013b (purple shading and purple solid line with crosses)). MPWP = Mid-Pliocene Warm Period; NHG = Northern Hemisphere glaciation; MPT = Mid-Pleistocene Transition; MBE = Mid-Brunhes Event. ……..……..122

Figure 7.1 | Site U1437 RI-OH_{global}-SSTs (e), annual (f) and seasonal (g) RI-OH-SSTs in comparison with c) $U^{K'}_{37}$-SSTs and d) TEX^{H}_{86}-based water temperatures for the last 1 Ma. The a) global benthic (Lisiecki and Raymo, 2005) and b) Site U1437 planktonic foraminiferal $\delta^{18}O$ record of *Neogloboquadrina dutertrei* (Kars et al., 2017) are shown for reference. Colored triangles represent the respective temperature signal reconstructed from the core top-sample. Gray bars indicate cold marine isotope stages. ……143

Figure 7.2 | Correlation of the RI-OH, $U^{K'}_{37}$, and TEX^{H}_{86} paleothermometers. Dashed gray lines give the 1:1 correlation. ……145

Figure 8.1 | Location map and coordinates of Site U1437 drilled during IODP Expedition 350 (w.d. is water depth). Major rivers in Japan are indicated (T.r.: Tenryu river; F. r.: Fuji river). The map was generated with GeoMapApp (http://www.geomapapp.org) (Ryan et al., 2009). ……...156

Figure 8.2 | Multiproxy age model at Site U1437, constructed by combining magnetostratigraphic datums (black dots), calcareous nannofossil bioevents (green squares) and stable oxygen isotope ($\delta^{18}O$) data measured on planktonic foraminifera shells (orange squares) from Mleneck-Vautravers (2018). The lower part of the figures shows the isotopic data (orange curve) tuned to the orbitally calibrated LR04 reference stack of Lisiecki and Raymo (2005). The linear sedimentation rate (LSR) curve is expressed in m/Ma (blue curve). Glacial stages are in gray and the marine isotope stages (MIS) are shown. Green bars indicate the location of samples used for calcareous nannofossil analysis. ……....161

Figure 8.3 | Evolution of a) natural remanent magnetization (NRM) and anhysteretic remanent magnetization (ARM), b) magnetic susceptibility χ_{lf}, c) saturation isothermal remanent magnetization (SIRM), d) ARM/χ_{lf} and e) $S_{-0.3T}$ as a function of depth in meters below sea floor (mbsf) in Hole U1437B for the oriented samples. Core recovery and lithology from Tamura et al. (2015b) are also indicated. ……....164

Figure 8.4 | Representative rock magnetic results for a) hysteresis loops before (blue) and after (red) paramagnetic slope correction (saturation is assumed above 70 % of H_{max}=1T), b) FORC diagrams (SF is the smoothing factor), c) RT-SIRM on warming and cooling, and d) ZFC and FC. The rock magnetic measurements indicate (Ti-) magnetite as the dominant magnetic phase. ……165

Figure 8.5 | Evolution of the hysteresis properties as a function of depth in Hole U1437B. a) saturation magnetization (M_s), b) coercive field (B_c), c) remanent coercive field (B_{cr}), d) M_{rs}/M_s, e) B_{cr}/B_c. No major changes in the hysteresis properties are observed. ……166

Figure 8.6 | a) High-resolution FORC diagrams for samples presented in Fig. 8.4 showing a central ridge suggesting the presence of magnetofossils (biogenic magnetite), b) negative first derivative of the ZFC and FC curves (shown in Fig. 8.4) showing a double Verwey transition temperature indicating the presence of both biogenic and detrital magnetite. ……...167

Figure 8.7 | Time series analysis on Natural Gamma Ray (NGR) data averaged every 5 points (from Tamura et al., 2015b), magnetic susceptibility χ_{lf} and saturation remanent magnetization M_{rs} (this study, measured on non-oriented samples). Note the dominance of the 100-ka eccentricity cycle in all data sets. A 180° phase shift is observed between NGR and χ_{lf}. The cyclicity is less obvious during the Mid-Pleistocene Transition (MPT), likely as a result of lower core recovery. ……..……170

Figure 8.8 | Evolution of selected parameters as a function of time. $\delta^{18}O$ data are from Lisiecki and Raymo (2005) (gray). Carbonate measurements are from Tamura et al. (2015b). $S_{-0.3T}$, SIRM (measured on cube samples) and χ_{lf} (non-corrected values in blue, corrected values by carbonate content in orange) are from this study. Sea level fluctuations are from Rohling et al. (2014). Natural Gamma Ray (NGR) counts are averaged every 5 data points (data from Tamura et al. (2015b)). Orbital parameters (insolation, precession, obliquity and eccentricity) are from Laskar et al. (2004). Marine isotope stages (MIS) and magnetic chrons are indicated and glacial stages are shaded in gray. ……..171

Figure 8.9 | a) $S_{-0.3T}$, b) L-ratio and c) HIRM values as a function of time. Glacial stages are shaded in blue. ……..173

Figure 8.10 | Detailed rock magnetic study for two selected glacial/interglacial transitions. (Ti)-magnetite content as a function of depth for the a) MIS 16/15 and b) MIS 6/5 transitions, c) δ_{FC} *vs*. δ_{ZFC}, and d) (Ti)-magnetite content *vs*. $IRM_{1T}/IRM_{0.4T}$ (proxy for coercivity) measured on the same aliquot for the MIS 16/15 and MIS 6/5 specimens. Squares and diamonds represent the analyzed specimens for the MIS 6/5 and MIS 16/15 transitions, respectively. (Ti-)magnetite content is higher during the interglacials. Particles are coarser and of higher coercivity during the glacials. ……174

Figure 8.11 | Variations of selected geochemical parameters for MIS 6/5 and MIS 16/15 glacial-interglacial transitions. LR04 $\delta^{18}O$ are reported by Lisiecki and Raymo (2005). TOC: total organic carbon; $CaCO_3$: carbonate content; TN: total nitrogen; TS: total sulfur. TOC/TN ratios are provided on a molar basis. ……177

Figure 8.12 | K_2O *vs*. CaO plot (wt%) from XRF measurements. Three possible endmembers are indicated: Japan, Izu arc front and marine carbonate. Average elemental compositions of Izu rear arc (gray zone) and Chinese loess (after acid leaching and loss of ignition) (Chen et al., 2001) are also reported. Note that shipboard data are not corrected for their carbonate content. ……181

Figure 8.S1 | Evolution as a function of depth of a) the magnetic susceptibility χ_{lf} before (gray) and after (orange) correction by the carbonate content. b) $\chi_{fd\%}$ and $\chi_{F1\text{-}F3}$ used for checking the frequency dependence of the susceptibility (proxies for nanoparticles). Note that the magnetic susceptibility χ_{lf} before and after correction by the carbonate content show the same pattern than the fluctuations of χ_{lf} are not a result of a dilution effect by the carbonate matrix. ……...190

Figure 8.S2 | L-ratio *vs*. HIRM. L-ratio is independent of HIRM, indicating that the HIRM changes as a function of depth/age are mainly controlled by fluctuations in the concentration of high coercivity minerals. ……190

Figure 8.S3 | Examples of hysteresis loops before (blue) and after (red) paramagnetic slope correction (saturation is assumed above 70% of H_{max} = 1T). Samples show saturation at ~500-600 mT suggesting a dominant low coercivity phase, and probable mixture with a higher coercivity phase. ……191

Figure 8.S4 | IRM acquisition curve up to 4 T for samples shown on Figure 8.4. Saturation is reached by ~500-600 mT. ……192

Figure 8.S5 | Examples of FORC diagrams showing typical PSD-sized low coercivity magnetic grains. ……192

Figure 8.S6 | Examples of SIRM cycles at low temperature (RT-SIRM, ZFC and FC). The Verwey transition of magnetite at ~120 K (e.g., Muxworthy and McClelland, 2000) is easily recognized on all curves. The RT-SIRM is not fully recovered when warming back to room temperature suggesting coarse-grained (Ti-)magnetite. ……..193

Figure 8.S7 | Day plot (Day et al., 1977). All the samples are in the pseudo-single domain (PSD) field. Mixing curves for SD+MD assemblage from Dunlop (2002) are reported. ……...194

Figure 8.S8 | SEM observations. Scanning Electron Microscope (SEM) observations were carried out on 2 selected samples with a JEOL JSM-6500F microscope equipped with an energy dispersive X-ray spectrometer (EDS) at the CMCR. Py: pyrite, Mg: magnetite/titano-magnetite. ……..194

Figure 8.S9 | Evolution of geochemical and selected rock magnetic data in the first 120 meters of Hole U1437B that includes early diagenetic processes. a) sulfate (mM) and b) methane (ppm) content, c) Total Organic Carbon (TOC) defined as TOC = TC - $CaCO_3$, d) remanent magnetization (NRM and ARM), e) magnetic susceptibility χ_{lf} , f) $S_{-0.3T}$, g) Total Carbon (TC) and h) carbonate content $CaCO_3$. The sulfate-methane transition zone (SMTZ) identified onboard (27-83 mbsf) is reported (Tamura et al., 2015a). Data shown in a, b, c, g and h are from (Tamura et al., 2015a), data shown in d, e and f are from this study. ……..…195

Figure 8.S10 | Evolution of rock magnetic proxies for magnetic mineral concentration (NRM, SIRM and χ_{lf}) as a function of time. Interglacial stages are shaded in yellow. The values for χ_{lf} come from all oriented and non-oriented samples. NRM and SIRM are from cube samples. ……196

Figure 8.S11 | Comparison of magnetic mineral concentration and hardness proxies (M_s and B_c, respectively) with TOC and TS for two glacial/interglacial transitions (MIS 6/5 and MIS 16/15). Note the increase of TS and the lower M_s value in the glacials. ……..197

Figure 8.S12 | XRF data. Evolution of SiO_2 (wt%), CaO (wt%), Al_2O_3 (wt%), Ti/Al and log (Ti/Ca). Shipboard data are from Tamura et al. (2015b). MIS stages are reported in italic. ……...197

Figure 10.1 | Down-core variations of rock magnetic parameters in Hole U1437D. (a) Natural remanent magnetization (NRM), (b) anhysteretic remanent magnetization (ARM), (c) low-frequency magnetic susceptibility χ_{lf}, (d) high-field magnetic susceptibility χ_{hfield}, and (e) saturation isothermal remanent magnetization (SIRM) as a function of depth. Four magnetic zones are identified based on changes in the rock magnetic properties. Zones 1 and 3 correspond to higher rock magnetic parameter values; zones 2 and 4 correspond to lower values. Core recovery and lithology are indicated (from Tamura et al., 2015a). Evolved volcaniclastics are unaltered volcanic grains and clasts inferred to be intermediate and silicic in composition compared to basalt and basaltic andesite. mbsf = meters below sea floor. ……..217

Figure 10.2 | Down-core variations of coercivity proxies in the studied interval at Site U1437. (a) $S_{-0.3T}$, (b) B_c, (c) B_{cr}, (d) D_{JH}, and (e) M_{rs}/χ_{lf}. The magnetic zones (1 to 4) are indicated. Note the $S_{-0.3T}$ decrease in zones 2 and 4 and higher D_{JH} values in zones 1 and 3. The upper part of zone 2 has lower coercivity values and represents a transition zone. Core recovery and lithology are indicated (from Tamura et al., 2015). mbsf = meters below sea floor. ……..…218

Figure 10.3 | Low temperature magnetic measurements for representative samples from the different magnetic zones. (a) RT-SIRM cycle, ZFC, and FC curves. RT-SIRM cycling indicates an incompletely recovered Verwey transition at ~110-120 K, which suggests the presence of coarse-grained (titano)-magnetite. LT-SIRM results have an additional magnetic phase with a transition at ~32-34 K (first derivative of ZFC in inset) for samples from zones 1 and 3; (b) $LT\text{-}SIRM_{FC}/LT\text{-}SIRM_{ZFC}$ as a function of depth (note the higher values for zones 1 and 3); (c) δ_{FC} versus δ_{ZFC} with a 1:1 distribution. mbsf = meters below sea floor; RT-SIRM = room temperature saturation isothermal remanent magnetization; LT-SIRM = low temperature saturation isothermal remanent magnetization; ZFC = zero-field-cooled; FC = field-cooled. ……220

Figure 10.4 | Down-core variations of (a) methane (shipboard data), (b) total carbon (TC), (c) total inorganic carbon (TIC), (d) total organic carbon (TOC), (e) total sulfur (TS), and (f) $CaCO_3$ in the 770-1,010-mbsf depth interval. Note the increase in $CaCO_3$ content in zone 2, which may have altered the magnetic mineral concentration by dilution. Reported shipboard data, core recovery, and lithology are from Tamura et al. (2015a). The magnetic zones identified in this study are indicated. mbsf = meters below sea floor. ….……223

Figure 10.5 | Microbiological analyses for Site U1437. (a) Depth profile of 16S rRNA gene abundance determined by digital polymerase chain reaction and (b) archaeal community composition at class level. The inset is a zoom-in view of low relative 16S rRNA abundance for samples at depths between 472 and 1,380 mbsf, which includes the target stratigraphic interval of this study (~775-1,002 mbsf). mbsf = meters below sea floor; rRNA = ribosomal RNA. ……..……224

Figure 10.6 | Down-core variations of methane (CH_4) and porosity (ϕ) in the studied stratigraphic interval (data from Tamura et al., 2015a) with corresponding magnetic zones and magnetic mineral assemblages. mbsf = meters below sea floor; SP = superparamagnetic. ……...228

Figure 10.S1 | Location map of IODP Expedition 350 Site U1437 (modified from Tamura et al., 2015a). ……236

Figure 10.S2 | Selected shipboard gas and geochemical data for Site U1437 (Tamura et al., 2015). a) Methane, b) sulfate, c) dissolved iron (Fe), d) dissolved manganese (Mn), e) calcium carbonate ($CaCO_3$), f) total organic carbon (TOC). The red box indicates the depth interval studied in this manuscript. The gray zone is the interval in which no pore water could be obtained. ……237

Figure 10.S3 | Selected shipboard physical properties data for Site U1437 (Tamura et al., 2015a). a) Magnetic susceptibility (Instrumental Unit, IU), b) colorimetric parameter L*, c) colorimetric parameter a*. The red box indicates the depth interval studied in this manuscript. ……237

Figure 10.S4 | Down-core variations of magnetic grain size proxies in the studied interval. a) ARM/χ_{lf}, b) ARM/SIRM and c) χ_{fd} (%). The magnetic zones (1 to 4) are indicated. Note the slight increase of ARM/SIRM in zone 2. Core recovery and lithology are indicated (from Tamura et al., 2015). ……238

Figure 10.S5 | Selected hysteresis loops (not corrected in blue and high-field slope-corrected in red) and FORC diagrams for representative samples from the different magnetic zones. The magnetic mineralogy inferred from the FORC diagrams is vortex state low coercivity (titano)-magnetite. ……..……239

Figure 10.S6 | Day diagram (Day et al., 1977) showing the magnetic state of samples. ……240

Figure 10.S7 | a) Thermomagnetic curves for representative samples from the four magnetic zones. Tmg: titanomagnetite, Mg: magnetite; b) repeated heating-cooling cycles in the range 300-370°C for three samples showing reversible cycles. ……241

Figure 10.S8 | Scanning electron microscope (SEM) observations of samples from zones 1 and 2 showing the occurrence of coarse-grained titanomagnetite (Tmg), pyrite (Py) and small iron sulfide grains. ……242

Figure 10.S9 | Down-core variations of shipboard magnetic susceptibility (Tamura et al., 2015a) and selected elements and element ratios for 820-870 mbsf depth interval which covers zone 1 and the top of zone 2. Fe/S spikes are due to localized low concentration of S. The upper part of zone 2 (~855-863 mbsf) compares better to zone 1 and is called transition zone. Black lines are 10-pt average curves. Core recovery and lithology are indicated (from Tamura et al., 2015a). ……..…..242

Figure 10.S10 | Abundance of archaea and bacteria in subsurface sediments at Site U1437. Average and standard deviation are indicated. The depth interval in gray corresponds to the interval studied in the main text (775-1002 mbsf). ……..243

List of Tables

Table 4.A1 | Water temperature data (TEX^{H}_{86}, $U^{K'}_{37}$, and LDI), BIT values and fractional abundances of C_{32} 1.15-diols. ……..……74

Table 6.A1 | Water temperature data (TEX^{H}_{86} and $U^{K'}_{37}$) from Site C0011. ……..….125

Table 6.A2 | Water temperature data (TEX^{H}_{86} and $U^{K'}_{37}$) from Site U1437. ……...…132

Table 7.A1 | RI-OH SST data. ……147

Table 8.S1 | Core interval and average depth (in meters below sea floor, mbsf) of the calcareous nannofossil bioevents as identified in this study. The core interval and average depth of bioevents and magnetochron boundaries (underlined) identified by the Shipboard Scientific Party (Tamura et al., 2015a) are reported for comparison. The reference ages for each bioevent and magnetochron are from Gradstein et al. (2012). ……..……186

Table 8.S2 | Age control points at IODP Site U1437 employed in the age model construction. A: planktonic foraminifera $\delta^{18}O$ event as calibrated through AnalySeries software; B: calcareous nannofossil datum, i.e. cross-over of *Gephyrocapsa caribbeanica* and *Emiliania huxleyi*; C: magnetostratigraphic boundary. Reference ages for nannofossil bioevent and magnetochrons are from Gradstein et al. (2012). $\delta^{18}O$ data are from Mleneck-Vautravers (2018). ……186

Table 8.S3 | Normalized XRF measurements for 20 selected samples. XRF measurements on the standard sample JA-1 (far right) were triplicated. Data for JA-1 are average of three measurements. The raw XRF data (top) were obtained at the same time and under the same conditions as the results for JA-1. $CaCO_3$ was estimated using coulometry. Raw CaO* was reduced accordingly ($Ca^* = Ca_{XRFmeasured} - Ca_{coulometry}$)
$CaO^* = CaO_{XRFmeasured} - [CaCO_{3coulometry} \times 56/100]$ where 56/100 is the stoechiometric factor for Ca in $CaCO_3$
The XRF data sum to 100 in order to give results on an anhydrous, carbonate-free basis. Normalized data are used in Figure 8.11 (main text). ……..……188

Table 10.S1 | Average and standard deviation of selected rock magnetic properties for the different magnetic zones. Zone 1 = 775-846 mbsf, zone 2 = 855-936 mbsf, zone 3 = 936-949 mbsf, zone 4 = 949-1002 mbsf. N is the total number of samples analyzed per magnetic zone. ……..…..……244

Table 10.S2 | Mean RT-SIRM and LT-SIRM for samples measured at low temperature. RT-SIRM: room temperature saturation isothermal remanent magnetization; LT-SIRM: low temperature saturation isothermal remanent magnetization: ZFC: zero field cooled; FC: field cooled. N is the total number of samples analyzed per magnetic zone. … ……244

Table 10.S3 | Bulk-geochemical parameters of samples shown on Figure 10.4. TC: total carbon, TIC: total inorganic carbon, TOC: total organic carbon, TS: total sulfur, TN: total nitrogen, $CaCO_3$: calcium carbonate. …… ……244

Dataset 10.S1 | Rock magnetic parameters shown on Figures 10.1 and 10.2. χ_{lf} (x 10^{-8} m^3/kg), NRM (Am^2/kg), ARM (Am^2/kg), SIRM (Am^2/kg), $S_{-0.3T}$, χ_{hfield} (x 10^{-8} m^3/kg), M_s (Am^2/kg), M_{rs} (Am^2/kg), B_c (T), B_{cr} (T), D_{JH}, M_{rs}/χ_{lf} (kA/m). ……245

List of abbreviations

$\delta^{13}C$	Stable carbon isotope ratio
$\delta^{18}O$	Stable oxygen isotope ratio
δD	Stable hydrogen isotope ratio, deuterium/hydrogen ratio
AA	Arctic amplification
AABW	Antarctic Bottom Water
AAIW	Antarctic Intermediate Water
AC	Alaska Current
ACL	Average chain length
AF	Alternating field
AG	Alaska Gyre
AL	Aleutian Low
Al/Ca	Aluminium/calcium ratio
Al_2O_3	Aluminium oxide
AMJ	April - May - June
AMOC	Atlantic Meridional Overturning Circulation
AMSR-E	Advanced Microwave Scanning Radiometer
AOM	Anaerobic oxidation of methane
APCI	Atmospheric Pressure Chemical Ionization
ARM	Anhysteretic remanent
AS	Alaskan Stream
AsL	Asian Low
B	Base
BA	Bølling-Allerød
Ba/Al	Barium/aluminium ratio
B_c	Coercivity
B_{cr}	Remanent coercivity
BIT	Branched and isoprenoid tetraether index
bpf	Band-pass filtering
brGDGT	Branched glycerol dialkyl glycerol tetraethers
BSTFA	N,O-bis(trimethylsilyl)trifluoroacetamide
Ca_{coulo}	Coulometry-based Ca content
$Ca_{XRFmeasured}$	Ca content measured by x-ray fluorescence
$CaCO_3$	Calcium carbonate

CaO	Calcium oxide
CAS	Central American Seaway
CBT	Cyclization ratio of branched tetraethers
CC	California Current
CH_4	Methane
CLP	Chinese Loess Plateau
CMCR	Center for Advanced Marine Core Research
CO_2	Carbon dioxide
CPI	Carbon preference index
CSF-A	Core depth below sea floor. This scaling method allows an overlap at cored interval and section boundaries.
CSF-B	Core depth below sea floor. This scaling method applies a compression algorithm if the recovery exceeds 100 %.
CTD	Conductivity Temperature Depth
DC	Direct current
DCM	Dichloromethane
DFG	Deutsche Forschungsgemeinschaft, German Research Foundation
DJF	December - January - February
DNA	Deoxyribonucleic acid
EASM	East Asian summer monsoon
EAWM	East Asian winter monsoon
ECS	East China Sea
EKC	East Kamchatka Current
ENSO	El Niño-Southern Oscillation
EOS	Earth Observing System
EPS	Energy-dispersive X-ray spectroscopy
F	Fractional abundance
FC	Field Cooled
$FeCO_3$	Siderite
Fe/S	Iron/sulfur ratio
FeS_2	Pyrite
$Fe_{1-x}S$	Pyrrhotite; x = 0-0,125
Fe_3S_4	Ferrimagnetic greigite
Fe_7S_8	Monoclinic pyrrhotite
FORC	First Order Reversal Curves
F. r.	Fuji river

GC	Gas chromatography
GC/FID	Gas chromatograph coupled to a flame ionization detector
G - I	Glacial - interglacial
GC/MS	Gas chromatograph coupled to a mass spectrometer
GD	Gobi Desert
GDGTs	Glycerol dialkyl glycerol tetraethers
H_2O	Water
HCO^{3-}	Hydrogen carbonate/ Bicarbonate
HE	Heinrich Event
HIRM	Hard (high-coercivity) isothermal remanent magnetization
HPLC	High Performance Liquid Chromatography
HS^-	Hydrogen sulfide
HTP	Himalayan-Tibetan Plateau
ICP-AES	Inductively coupled plasma-atomic emission spectroscopy
ISM	Indian summer monsoon
IODP	Integrated Ocean Drilling Program (until 2013), now International Ocean Discovery Program
IRD	Ice-rafted debris
IRM	Isothermal remanent magnetization
isoGDGT	Isoprenoid glycerol dialkyl glycerol tetraethers
ITCZ	Intertropical convergence zone
IU	Instrumental unit
JAS	July - August - September
JFM	January - February - March
JJA	June - July - August
K_2O	Potassium oxide
KC	Kuroshio Current
KE	Kuroshio Extension
LCDs	Long-chain diols
LDI	Long-chain diol index
LF	Low frequency
LGM	Last glacial maximum
LM	Large meander
LR04	Orbitally calibrated reference stack by Lisiecki and Raymo (2005): an average of 57 globally distributed benthic foraminiferal oxygen isotope curves spanning the last 5.3 million years

LSR	Linear sedimentation rate
LT-SIRM	Low-temperature saturation isothermal remanent magnetization
M^+	Molecular ion
MAM	March - April - May
MBE	Mid-Brunhes Event
mbsf	Meters below seafloor
mbsl	Meters below sea level
MBT	Methylation of branched tetraethers
MC	Mindanao Current
MD	Multidomain
MeOH	Methanol
Mg	Magnetite
Mg/Ca	Magnesium/calcium ratio
MIS	Marine isotope stage
$MnCO_3$	Rhodochrosite
MPMS	Magnetic Properties Measurements System
MPT	Mid-Pleistocene Transition
MPWP	Mid-Pliocene warm period
M_{rs}	Saturation remanent magnetization
M_s	Saturation magnetization
MS	Mass Spectrometry
M_{SD}	Saturation remanence for soft single-domain magnetite
MTM	Multi-taper method
m/z	Mass-to-charge ratio
NADW	North Atlantic Deep Water
NAP	North American Plate
n-	normal
NE	Northeast
NEC	North Equatorial Current
NECC	North Equatorial Counter Current
NGR	Natural Gamma Ray
NGRIP	North Greenland Ice Core Project
NHG	Northern Hemisphere glaciation
NHSI	Northern Hemisphere summer insolation
NPH	North Pacific High

NPIW	North Pacific Intermediate Water
NRM	Natural remanent magnetization
nSM	Nearshore short meander
NW	Northwest
OC	Oyashio Current
OD	Ordos Desert
ODP	Ocean Drilling Program
OE	Oyashio Extension
OH-GDGTs	Hydroxylated GDGTs
OND	October - November - December
oSM	Offshore short meander
PC	Peru Current
pCO_2	Partial pressure of carbon dioxide
PCR	Polymerase chain reaction
PhSP	Philippine Sea Plate
ppmv	Parts per million by volume
PSD	Pseudo-single domain
PTFE	Polytetrafluoroethylene
Py	Pyrite
RI-OH	Ring index of hydroxylated GDGTs
rRNA	Ribosomal ribonucleic acid
RT	Room temperature
RT-SIRM	Room temperature saturation isothermal remanent magnetization
R/V	Research vessel
S	Sulfur
$S_{-0.3T}$	(=[(IRM$_{-0.3T}$)/SIRM)+1]/2); Bloemendal et al., 1992), an indication of the relative contribution of high (e.g, hematite, goethite, ferromagnetic iron sulfides) and low (e.g. magnetite, maghemite) coercivity minerals to the remanence
SAC	Subarctic Current
S/Cl	Sulfur/chlorine ratio
SCS	South China Sea
SD	Single-domain
SEC	South Equatorial Current
SEM	Scanning electron microscope
SF	Smoothing factor
SH	Siberian High

SIM	Single ion monitoring
SiO_2	Silica
SIR	Selected ion recording
SIRM	Saturation isothermal remanent magnetization
SMTZ	Sulfate-methane transition zone
SO_4^{2-}	Sulfate
SON	September - October - November
SP	Superparamagnetic
SST	Sea surface temperature
Sv	Sverdrup; 1 Sv = 10^6 m^3/s
T	Top
TakD	Taklimakan Desert
Tc	Top common
TC	Total carbon
TD	Tengger Desert
Td´	diatom temperature; ratio of cold- and warm-water diatoms from the open ocean as a proxy for sea surface temperature reconstruction
TEX_{86}	Tetraether index based on glycerol dialkyl glycerol tetraethers consisting of 86 carbon atoms
TEX^H_{86}	Tetraether index based on glycerol dialkyl glycerol tetraethers consisting of 86 carbon atoms in the modification for high temperatures (>15 °C) after Kim et al. (2010)
Ti/Al	Titanium/aluminium ratio
TIC	Total inorganic carbon
Ti/Ca	Titanium/calcium ratio
TLE	Total lipid extracts
Tmg	Titanomagnetite
TN	Total nitrogen
T_N	Néel temperature
TOC	Total organic carbon
TP	Tibetan Plateau
T. r.	Tenryu river
TS	Total sulfur
T_V	Verwey transition temperature
TwC	Tsushima Warm Current
UK	United Kingdom

$U^{K'}_{37}$	Unsaturated ketone index based on the ratio of di- and triunsaturated C_{37}-ketones
V/Al	Vanadium/aluminium ratio
VSM	Vibrating Sample Magnetometer
w. d.	Water depth
WJS	Westerly jet stream
WPWP	Western Pacific Warm Pool
WSAG	Western Subarctic Gyre
χ_{hf}	High frequency magnetic susceptibility
χ_{hfield}	Magnetic susceptibility at high fields
χ_{lf}	Low field magnetic susceptibility
χ_{lfcorr}	Corrected low field magnetic susceptibility
XRF	X-ray fluorescence
YD	Younger Dryas
ZFC	Zero Field Cooled

Abstract

The reconstruction of the climate evolution of the Northwest Pacific Ocean and the adjacent East Asian continent in the geological past has gained increasing interest in recent years. The area is today the most densely populated region on Earth and has enormous economic power and potential. In order to better evaluate the potential impact of future atmospheric greenhouse gas concentrations, rising global temperatures, and rising sea levels, exact climate reconstructions for phases in the geological past, whose boundary conditions were similar to what is expected for the future, are of utmost importance. The most recent analogues include the Miocene and Mid-Pliocene Warm Period.

The mid-latitudes of the Northwest Pacific Ocean are characterized by the confluence of its two major western boundary currents, the warm and saline Kuroshio Current that is fed from the Western Pacific Warm Pool in the equatorial West Pacific, and the cold, less saline and nutrient-rich Oyashio Current coming from the Subarctic Pacific. The convergence zone of these two currents, the Kuroshio-Oyashio interfrontal zone, is subject to intense eddy formation resulting from the different physical properties of the merging water masses. The Kuroshio Current as part of the North Pacific Subtropical Gyre is the major meridional transport mechanism for tropical heat and moisture northward and hence exerts significant control on the climate evolution of the Northwest Pacific Ocean and adjacent East Asian continent. Furthermore, the region is governed by the presence of the world´s largest weather system, the Asian monsoon, and the climate in the area is characterized by large seasonal variations in terms of dust storms and precipitation. Especially the latter is of major importance for the agricultural and economical sector in East Asia.

Using an organic-geochemical biomarker approach, this PhD thesis aimed at characterizing both the long-term (from the late Miocene to present) and shorter-term (on glacial-interglacial timescales) climatic and oceanographic variability in the Northwest Pacific Ocean. The results were placed into the context of already existing climate records from the Pacific and other regions of the globe in order to identify regional parallels and differences. In this context, one focus was set on the climate evolution and its impact on the paleoceanographic regime with respect to changes in the strength and flow pattern and latitudinal position of the beforementioned oceanic currents in the Northwest Pacific. A second research question targeted the changes in the atmospheric circulation over the Asian continent associated with climate variation. Two sediment cores that were drilled during two different Integrated Ocean Drilling Program and International Ocean Discovery Program expeditions, respectively, were used as

sedimentary archives, which allowed a detailed and continuous paleoclimate reconstruction for the last 8 and 4 million years, respectively.

In order to investigate both the long- and short-term evolution of paleoclimate and the paleoenvironment in the oceanic realm and on land, biomarkers that originate from marine organisms and land plants were extracted from the marine sediments, analyzed and subsequently interpreted using geochemical techniques. In a first step, in order to get most precise information on latitudinal shifts and changes in the strength of the beforementioned ocean currents, the growth season- and habitat depth-dependent signal of the proxies used for the paleowater temperature reconstruction was characterized. The application of these paleothermometers is founded on the adaption of the cell membrane or storage lipid composition of the particular source organisms to ambient water temperatures, which varies depending on the season and water depth. In the framework of the detailed investigation of the paleoclimate evolution over the last two glacial-interglacial cycles of the past 145,000 years, elevated interglacial water temperatures both at the sea surface and subsurface indicated a stronger warm water mass export from the tropics to the northern mid-latitudes via the Kuroshio Current. Overall higher Holocene than Eemian temperatures implied a stronger Holocene transport via the Kuroshio compared to the preceding warm phase, which potentially had impact on the current´s meandering behavior south of Japan. During glacial phases, comparably lower water temperatures indicated a southward displacement of the major oceanic fronts, thereby enabling an elevated influence of colder (sub-)polar water masses of the Oyashio Current in the oceanic region south of Japan. In a further step, the paleoclimatic and paleoceanographic investigations were extended to all glacial and interglacial cycles of the past 1 million years. Thereby, a focus was placed on the characterization of glacial-interglacial climate variability and associated changes in the circulation both in the ocean and the atmosphere. A change in the oceanic but even more significantly in the atmospheric circulation became obvious across the Mid-Brunhes Event, a significant paleoclimate shift ~430,000 years ago, that was accompanied by increasing amplitude in glacial-interglacial climate variability. Warmer absolute water temperatures in the interglacials following the Mid-Brunhes Event were interpreted as a strengthening of Kuroshio transport, presumably associated with intensified North Pacific Subtropical Gyre circulation. Simultaneously, pulsed glacial dust fluxes from mainland Asia to the Northwest Pacific Ocean decreased abruptly, which is expressed in lower sedimentary concentrations of land plant-derived lipids. This was suggested to result from a displacement of the westerly jet stream from a position predominantly to the north of the Himalayan-Tibetan Plateau over the extensive arid regions of central and East Asia during glacials prior to the Mid-

Brunhes Event to a position to the south of the plateau in the aftermath of this event, thereby bypassing the major dust source areas in Asia. This displacement was attributed to enhanced Arctic amplification, an intensified sensitivity and therefore increased response of the Arctic climate to general climate variability, following the Mid-Brunhes Event, as has been described in previous studies.

A complementary study of rock magnetic and bulk geochemical properties as well as elemental composition was carried out to characterize the variability in the magnetic mineral assemblage in sediments from the past 1 million years and found also significant glacial-interglacial variability. This was expressed in 1) magnetic mineral concentrations that co-varied with glacial-interglacial cycles and 2) overall higher abundances of fine-grained eolian particles in glacial stages, which was attributed to a strengthened East Asian winter monsoon. Overall, the findings from this study confirmed a strong climatic impact on the sedimentary magnetic mineral assemblage.

Finally, the entire time interval from the late Miocene to present was studied with respect to its general long-term climate evolution. To date, the Northwest Pacific Ocean region remains understudied when it comes to climate reconstructions on geological timescales. Admittedly, the region is of major importance for the heat balance of the entire (North-)Pacific Ocean as it hosts the convergence region of the two western boundary currents of the North Pacific and hence the mixing of two water masses with clearly contrasting properties. Therefore, it is of utmost importance to close the regional gap of long-term climate reconstruction. This thesis showed that the climate evolution of the Northwest Pacific Ocean followed largely the general global climate evolution with its unidirectional cooling trend from the late Miocene onwards, especially after the intensification of Northern Hemisphere glaciation at ~2.7 Ma. The cooling trend in the Northwest Pacific was, however, like the one in the tropical West Pacific, extenuated compared to other regions of the North and Equatorial Pacific Ocean. This was attributed to the presence of the Kuroshio and its warm water mass transport from the Western Pacific Warm Pool northwards.

Zusammenfassung (German abstract)

Die Rekonstruktion der Klimaentwicklung im Nordwestpazifik und dem angrenzenden ostasiatischen Kontinent während der geologischen Vergangenheit ist in den letzten Jahren auf stetig zunehmendes Interesse gestoßen. Die Region stellt heute die am dichtesten besiedelte Gegend der Erde mit enormer wirtschaftlicher Macht und hohem ökonomischen Potential dar. Um den potentiellen Impakt zukünftiger atmosphärischer Treibhausgaskonzentrationen, steigender globaler Temperaturen und eines steigenden Meeresspiegels besser abschätzen zu können, sind genaue Rekonstruktionen des Klimas während Phasen, die sich durch Bedingungen auszeichnen, wie sie für die nahe Zukunft prognostiziert werden, von immenser Bedeutung. Zu diesen analogen Phasen zählen u.a. das Miozän und die Mittelpliozäne Warmphase.

Die mittleren Breiten des nordwestpazifischen Ozeans zeichnen sich durch das Aufeinandertreffen seiner beiden westlichen Ozeanrandströmungen, dem warmen und salinen Kuroshio-Strom, der aus dem Western Pacific Warm Pool im äquatorialen Westpazifik gespeist wird, und dem kalten, weniger salinen und nährstoffreichen Oyashio-Strom aus dem subarktischen Pazifik aus. In der Konvergenzzone der beiden Strömungen im offenen Pazifik östlich von Japan, der sogenannten Kuroshio-Oyashio Interfrontalzone, kommt es, bedingt durch die unterschiedlichen physikalischen Eigenschaften der beiden Wassermassen, zu intensiver Eddybildung. Der Kuroshio-Strom als Teil der Nordpazifischen Subtropischen Gyre ist maßgeblich für den meridionalen Wärmetransport von den Tropen nordwärts verantwortlich und hat dadurch einen signifikanten Einfluss auf die Klimaentwicklung des Nordwestpazifiks und des angrenzenden ostasiatischen Kontinents. Die Region zeichnet sich zudem durch die Präsenz des größten atmosphärischen Wettersystems der Erde, dem asiatischen Monsun, aus und das dortige Klima ist durch starke saisonale Schwankungen im Hinblick auf Staubstürme und Niederschläge gekennzeichnet. Insbesondere letztere sind von großer Bedeutung für den (land-)wirtschaftlichen Sektor in Ostasien.

Unter Verwendung organisch-geochemischer Biomarker zielte die vorliegende Doktorarbeit darauf ab, sowohl langfristige (vom späten Miozän bis heute) als auch kurzfristigere (auf glazial-interglazialen Zeitskalen) Veränderungen des Klimas und des Strömungssgeschehens im Nordwestpazifik zu charakterisieren und diese in den Kontext bereits existierender Klimarecords sowohl aus dem zirkumpazifischen Raum als auch auf globaler Basis zu stellen, um so regionale Parallelen und Unterschiede zu identifizieren. Dabei wurde die Veränderung des Klimas zum einen in Bezug auf die Auswirkungen in der Paläozeanographie, ergo im

Hinblick auf vergangene Veränderungen in der Stärke und dem Verlauf der zuvor genannten Ozeanströmungen im Nordwestpazifik beleuchtet und zum anderen wurden potentiell assoziierte Veränderungen in der atmosphärischen Zirkulation über dem ostasiatischen Kontinent und dem Nordwestpazifik betrachtet. Zwei Bohrkerne, die während unterschiedlicher Expeditionen des Integrated Ocean Drilling Program bzw. International Ocean Discovery Program im Nordwestpazifik südlich von Japan gewonnen wurden, dienten hierbei als sedimentäre Archive, welche eine detaillierte und kontinuierliche Rekonstruktion der Paläoklimaentwicklung der letzten 8 bzw. 4 Millionen Jahre erlaubten.

Ein Schwerpunkt der Doktorarbeit lag bei der Untersuchung der langfristigen Klimaentwicklung und Paläoumweltbedingungen im Ozean und an Land über den Zeitraum vom späten Miozän bis heute. Dazu wurden u.a. Biomarker, die vornehmlich von marinen Organismen oder Landpflanzen stammen, aus den Sedimenten extrahiert und mit geochemischen Methoden analysiert und ausgewertet. Um möglichst genaue Aussagen über die latitudinalen Verlagerungen und Veränderungen in der Strömungsintensität der Ozeanströmungen treffen zu können, wurde zunächst das saisonale sowie wassertiefenabhängige Signal der Proxies charakterisiert, welche für die Rekonstruktion von Wassertemperaturen im Rahmen dieser Arbeit herangezogen wurden. Diese erwähnten Paläothermometer basieren auf der Anpassung der Zellmembran- oder Speicherlipidzusammensetzung der jeweiligen Produzenten an die Umgebungstemperatur, welche als Funktion von Wassertiefe und Jahreszeit variabel ist. Im Rahmen der detaillierten Untersuchung der Klimaentwicklung über die letzten beiden Glazial-Interglazialzyklen der letzten 145,000 Jahre deuteten einerseits erhöhte Wassertemperaturen sowohl an der Meeresoberfläche als auch in etwas größerer Tiefe während der Interglazialphasen auf einen stärkeren Export warmer Wassermassen aus den Tropen nordwärts über den Kuroshio hin. Dabei indizierten insgesamt höhere Temperaturen während des Holozäns im Vergleich zur vorherigen Warmzeit, dem Eem, einen stärkeren holozänen Warmwassertransport des Kuroshio, welches vermutlich Auswirkungen auf das Mäanderverhalten des Kuroshio südlich von Japan hatte. Während Glazialphasen, andererseits, deuteten vergleichsweise niedrige Wassertemperaturen auf eine südwärtige Verlagerungen der ozeanischen Fronten hin, was einen erhöhten Einfluss (sub-)polarer Wassermassen des Oyashio südlich von Japan zur Folge hatte.

In einem weiteren Schritt wurden die Klima- und paläozeanographischen Untersuchungen auf sämtliche Glazial-Interglazialzyklen der letzten 1 Millionen Jahre ausgeweitet. Dabei wurde der Fokus auf die Charakterisierung glazial-interglazialer Klimaschwankungen und assoziierter

Veränderungen im Strömungsgeschehen sowohl im Ozean als auch in der Atmosphäre gelegt. Hierbei zeigte sich im Hinblick auf das Strömungsgeschehen im Nordwestpazifik eine Verstärkung des Exports warmer Wassermassen über den Kuroshio, vermutlich bedingt durch eine stärkere Zirkulation der Nordpazifischen Subtropischen Gyre, in den Interglazialphasen nach dem Mid-Brunhes Event, einem signifikanten Shift im Klimageschehen vor ~430,000 Jahren, welches mit einer zunehmenden Amplitude in den Glazial-Interglazialzyklen einherging. Parallel dazu brachen die glazialen Staubeinträge aus Asien in den Nordwestpazifik ein, was sich in niedrigeren Konzentrationen von Landpflanzenlipiden in den untersuchten Sedimenten äußerte. Interpretiert wurde dies als eine Verlagerung des Westwind-Jetstreams von einer Position vornehmlich im Norden des Himalaya-tibetischen Plateaus über den ausgedehnten ariden Gebieten Zentral- und Ostasiens während der Glazialphasen vor dem Mid-Brunhes Ereignis zu einer Position südlich des Himalayas, wodurch die Staubliefergebiete nicht mehr im Pfad des Jetstreams lagen. Zurückgeführt wurde diese Verlagerung auf eine intensivierte Arktische Verstärkung, d.h. eine verstärkte Sensitivität und dadurch bedingte stärkere Reaktion des arktischen Klimas auf generelle Klimaschwankungen, wie es für die Zeit nach dem Mid-Brunhes Event bereits in der Literatur beschrieben wurde.

Eine komplementäre Studie basierend auf der Untersuchung gesteinsmagnetischer Eigenschaften, bulkgeochemischer Parameter und elementarer Zusammensetzungen zur Charakterisierung von Veränderungen in den sedimentären magnetischen Mineralvergesellschaftungen der letzten 1 Millionen Jahre wies ebenfalls deutliche glazial-interglaziale Unterschiede auf. Dies äußerte sich unter anderem in Veränderungen der sedimentären Konzentration an magnetischen Mineralen, welche die glazial-interglaziale Variabilität nachbildete, und zeigte somit den starken Einfluss von globalen Klimaschwankungen auf die sedimentäre Zusammensetzung. Glazialphasen zeichneten sich zudem durch einen höheren Anteil an feinen äolischen Partikeln aus, was auf eine stärkere Aktivität des Ostasiatischen Wintermonsuns zurückgeführt wurde.

Abschließend wurde der gesamte Zeitraum vom späten Miozän bis heute betrachtet und im Hinblick auf generelle Klimaentwicklungen untersucht. Bis dato stellt der Nordwestpazifik ein weißes Blatt dar, was Klimarekonstruktionen auf geologischen Zeitskalen angeht. Durch die Konvergenz der beiden dominanten westlichen Ozeanrandströmungen und der einhergehenden Vermischung zweier sehr unterschiedlicher Wassermassen, insbesondere im Hinblick auf deren Temperaturen, in der Region, ist diese aber von großer Bedeutung für die Wärmebilanz des gesamten (Nord-)pazifischen Ozeans. Aus diesem Grund ist es von größtem Interesse, die existierende räumliche Lücke in der langfristigen Klimarekonstruktion zu schließen. Hierbei

zeigte sich, dass die Klimaentwicklung im Nordwestpazifik im Großen und Ganzen der generellen globalen Klimaentwicklung mit ihrem unidirektionalen Abkühlungstrend, insbesondere nach der Intensivierung der Nordhemisphärenvereisung ab ~2.7 Ma vor heute, folgte. Dieser Abkühlungstrend war im Nordwestpazifik aber – genau wie im tropischen Westpazifik – schwächer ausgeprägt als in anderen Regionen des Nordpazifiks und des äquatorialen Ostpazifiks. Dies war vermutlich bedingt durch den Einfluss des Kuroshios und seinem Transport warmer Wassermassen aus dem Westpazifischen Warm Pool nordwärts.

Publications

The following manuscripts are in preparation for publication, in review or are published articles in scientific journals:

Jonas, A.-S., L. Schwark, and T. Bauersachs (2017), Late Quaternary water temperature variations of the Northwest Pacific based on the lipid paleothermometers TEX^{H}_{86}, $U^{K'}_{37}$ and LDI. Published in *Deep-Sea Research Part I* 125, 81-93, https://doi.org/10.1016/j.dsr.2017.04.018.

Jonas, A.-S., M. Kars, T. Bauersachs, W. Rübsam, and L. Schwark, Southward displacement of the glacial westerly jet driven by Arctic amplification. In review at *Paleoceanography and Paleoclimatology.*

Jonas, A.-S., T. Bauersachs, and L. Schwark, An 8-million-years history of paleoceanographic and paleoclimate changes in the Northwest Pacific Ocean at IODP Sites C0011 and U1437. *In preparation for publication.*

Jonas, A.-S., L. Schwark, and T. Bauersachs, Validating the applicability of the novel RI-OH-index for paleotemperature reconstruction over the last 1 Ma at IODP Site U1437, NW Pacific Ocean. *In preparation for publication.*

Kars, M., R. J. Musgrave, K. Kodama, **A.-S. Jonas,** M. Bordiga, W. Ruebsam, M. J. Mleneck-Vautravers, and T. Bauersachs (2017), Impact of climate change on the magnetic mineral assemblage in marine sediments from Izu rear arc, NW Pacific Ocean, over the last 1 Ma. Published in *Palaeogeography, Palaeoclimatology, Palaeoecology* 480, 53-69, doi:10.1016/j.palaeo.2017.05.016.

The following publication is part of the Appendix of this thesis:

Kars, M., R. J. Musgrave, T. Hoshino, T., **A.-S. Jonas,** T. Bauersachs, F. Inagaki, F., and K. Kodama (2018), Magnetic mineral diagenesis in a high temperature and deep methanic zone in Izu rear arc marine sediments, Northwest Pacific Ocean. Published in: *Journal of Geophysical Research: Solid Earth* 123, 8331-8348. https://doi.org/10.1029/2018JB015861.

DANGER
PROPELLER
KEEP CLEAR
JOIDES RESOLUTION

Chapter 1

1. Introduction

Ocean currents represent important means for the distribution of heat, salt and nutrients throughout the world´s oceans and are thereby exerting a major control on the evolution of both the regional and global climate. As a prominent example, the Gulf Stream, the major western boundary current in the North Atlantic Ocean, and its northern extension, the North Atlantic Drift, advect (sub-)tropical heat from the Gulf of Mexico to northern and western Europe. Without the influence of the Gulf Stream, the climate in these regions would be significantly colder, which, in turn, would impact the vegetation pattern and thereby also the agricultural sector. The warm and saline Kuroshio Current (KC) is the analogue to the Gulf Stream in the North Pacific Ocean, where it transports heat and moisture from the Western Pacific Warm Pool (WPWP) in the tropical Pacific to northern mid-latitudes, thereby exerting a major control on the climate evolution of the Northwest (NW) Pacific Ocean and the adjacent East Asian continent.

The distribution of heat throughout the oceans significantly impacts the formation of pressure cells and hence wind systems in the overlying atmosphere. Thereby, contrasting temperatures between different oceanic regions as well as the oceans and continents drive the pattern and strength of atmospheric circulation. The winds redistribute water that is evaporated over the ocean, and through the amount of subsequent precipitation significantly impact the continental environmental setting. For example, evaporated water over the tropical western Pacific and Indian Oceans is transported northward by summer monsoonal winds that form as a consequence of the development of high-pressure systems over the ocean and low pressures over continental Asia during summer. Associated subsequent rainfall over Southeast Asia is a crucial factor for the flourishing of the regional economy and agriculture. The Asian monsoon with its subcomponents, the East Asian and Indian monsoons, is the world´s largest weather system and affects almost half of the world´s population as its seasonal variabilities result in large fluctuations in terms of precipitation and dust flux in the region. Dust fluxes from the continent to the ocean significantly fuel marine primary productivity and hence fish growth via the input of nutrients. Knowledge of how the climate and environment in this region responded to past changes in the global climate system is hence fundamental to predict how the livelihood

in the region will evolve under rising temperatures, sea levels and atmospheric greenhouse gas levels.

Unfortunately, compared to other oceanic regions, the NW Pacific Ocean remains to date understudied when it comes to the reconstruction of its paleoceanographic and paleoclimatic evolution over timescales extending beyond the last glacial-interglacial cycle. During the past two decades, a few long-term water temperature records covering the time interval from the middle to late Miocene to the present day have become available from the Pacific Ocean. These records, however, mostly concentrated on the tropical Pacific Ocean including the WPWP (Li et al., 2011; Zhang et al., 2014), the eastern equatorial Pacific (Dekens et al., 2007; Zhang et al., 2014) including the cold tongue (Liu and Herbert, 2004; Lawrence et al., 2006), the eastern North Pacific margin (LaRiviere et al., 2012; Herbert et al., 2016) and the Subarctic Pacific Ocean (Martínez-Garcia et al., 2010; Herbert et al., 2016). The mid-latitudinal NW Pacific, unfortunately, is to date underrepresented and the only long-term record available is from Ocean Drilling Program (ODP) Site 1208 located in the open NW Pacific on Shatsky Rise (LaRiviere et al., 2012). Like most of the other beforementioned long-term records from the North Pacific Ocean, the record from this site lacks sufficient temporal resolution to deconvolve shorter-term paleoclimatic and paleoceanographic changes in the region on the glacial-interglacial scale. The detailed reconstruction of glacial-interglacial ocean temperature variation from the mid-Pleistocene to present is hence one of the main research questions that will be addressed in this PhD thesis.

For the study of the past development of strength and pathways of ocean currents and atmospheric circulation, a large variety of proxies exist, among them lipid biomarkers. Marine sediment cores are ideal archives to study both changes in the (pale-)oceanographic regime as well as the overall climate evolution and related changes on land. Drilling in the mid-latitudinal NW Pacific Ocean south of Japan during several International Ocean Discovery Program (IODP, formerly Integrated Ocean Drilling Program) expeditions yielded continuous deep-sea sediment successions that span back to the late Miocene. This allows the detailed study of paleoceanographic changes related to the major currents in the area, the Kuroshio and Oyashio western boundary currents, as well as the paleoclimate evolution in the NW Pacific Ocean and East Asia, including crucial components such as the East Asian monsoons and the westerly jet stream (WJS). In this thesis, several organic biomarkers and other proxies were studied in sedimentary archives drilled at IODP Expedition Sites C0011 and U1437. The sites are presently located under the influence of the KC, the East Asian winter and summer monsoons and the WJS, downwind of the arid Asian interior. Their positions between the tropical and

Subarctic Pacific as well as between the East Asian continent and the NW Pacific Ocean and its marginal seas make the sites ideal archives for studying varying influences of different water masses and changes in atmospheric circulation over time. The following subchapters of the Introduction section will 1) present oceanographic and atmospheric components that play crucial roles in the (paleo-)climate evolution in the NW Pacific Ocean and adjacent East Asian continent and 2) introduce the lipid-based proxies used in this thesis.

1.1. Oceanic circulation

At present, the surface circulation of the NW Pacific Ocean is governed by the interplay of its two major western boundary currents, the subtropical warm, saline and nutrient-poor Kuroshio Current and its northern counterpart, the subpolar cold, less saline and nutrient-rich Oyashio Current (OC) (Fig. 1.1). The relative latitudinal positions and strengths of the two currents have been proposed to directly impact the regional climate over the Japanese islands and part of the East Asian continent (Thompson, 1981). Hence, the mid-latitudinal region of the NW Pacific off Japan, including the KC and OC and their interfrontal mixing zone, is a key area for understanding the present and past climate variability of the East Asian continent and Japan.

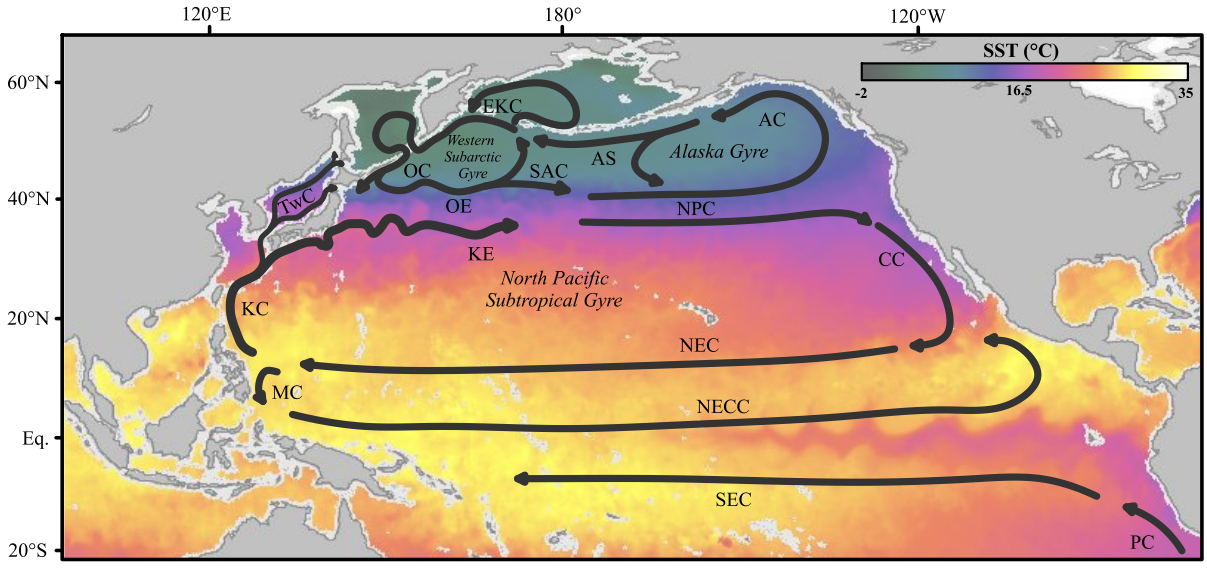

Figure 1.1 | False-color sea surface temperature map of the North Pacific Ocean as measured on June 1, 2003 by the AMSR-E (Advanced Microwave Scanning Radiometer for EOS (Earth Observing System)). Black arrows indicate surface currents: KC = Kuroshio Current, KE = Kuroshio Extension, NPC = North Pacific Current, CC = California Current, NEC = North Equatorial Current forming the North Pacific Subtropical Gyre, and the OC = Oyashio Current, SAC = Subarctic Current, AC = Alaska Current, AS = Alaskan Stream, EKC = East Kamchatka Current forming the Subarctic Gyre and its subgyres, the Western Subarctic Gyre and the Alaska Gyre. TwC = Tsushima Warm Current; MC = Mindanao Current; NECC = North Equatorial Countercurrent; SEC = South Equatorial Current; PC = Peru Current. Image is from https://earthobservatory.nasa.gov/images/3513/global-sea-surface-temperature-from-amsr-e.

1.1.1. The Kuroshio Current

The name "Kuroshio" means – translated from Japanese – black (= kuro) stream (= shio) and refers to its dark water color, which is a result of low bioproductivity and hence low abundances of organic matter and other detritus in the surface waters (Qiu, 2001). The KC is part of the wind-driven, clockwise circulating North Pacific Subtropical Gyre (Fig. 1.1) and advects tropical moisture and heat from the WPWP northward, thereby exerting major influence on the regional climate of the NW Pacific Ocean and the adjacent East Asian continent.

The KC is formed at 12-13 °N east of the Philippines, where the westward-flowing North Equatorial Current (NEC) splits into the KC and the southward-heading Mindanao Current (MC) (Qiu, 2001). With a width of less than 100 km and a maximum depth of ~1 km, the KC stretches over a total length of ~3000 km from the tropics to northern mid-latitudes (Barkley, 1970). Under prevailing northeasterly monsoonal winds in winter, the KC occasionally passes the Luzon Strait and enters into the northern South China Sea (SCS) between Luzon and Taiwan, where it forms a loop current that can reach as far as 117 °W (Qiu, 2001). During the summer months with prevailing southwesterly monsoonal winds, the KC passes the Luzon Strait without intrusion (Qiu, 2001). From there on, it continues its flow northward through the East Taiwan Channel into the East China Sea (ECS), where it follows the edge of the continental shelf in the Okinawa Trough (Gallagher et al., 2015). Just before leaving the ECS through the Tokara Strait, a subordinate branch of the KC, renamed the Tsushima Warm Current (TwC), heads off and continues its flow into the Japan Sea through the Tsushima Strait between the Korean peninsula and Japan. After having passed the Tokara Strait, the KC shows a bimodal stationary flow pattern south of Japan with either a short meander (SM) or a large meander (LM) path, the latter reaching as far south as 30 °N (Kawabe, 1985, 1995) (Fig. 1.2). The former can be further subdivided into a nearshore (nSM) and an offshore meander (oSM) path (Kawabe, 1985, 1995). The different meander states usually persist from one year to a decade (Kawabe, 1995). The formation of the respective meander paths depends mostly on changes in current velocity and volume transport of the KC south of Japan and its position when exiting the ECS through the Tokara Strait, with the short (large) meander predominantly being formed when both velocity and volume transport are high (low) (Tsujino et al., 2013; Usui et al., 2013) and the KC remaining in a southern (northern) position in the Tokara Strait (Kawabe, 1995) (Fig. 1.2). Superimposed on these annual to decadal variations in KC strength, its transport also shows seasonal variations with a maximum in spring and a minimum in fall (Qiu, 2001).

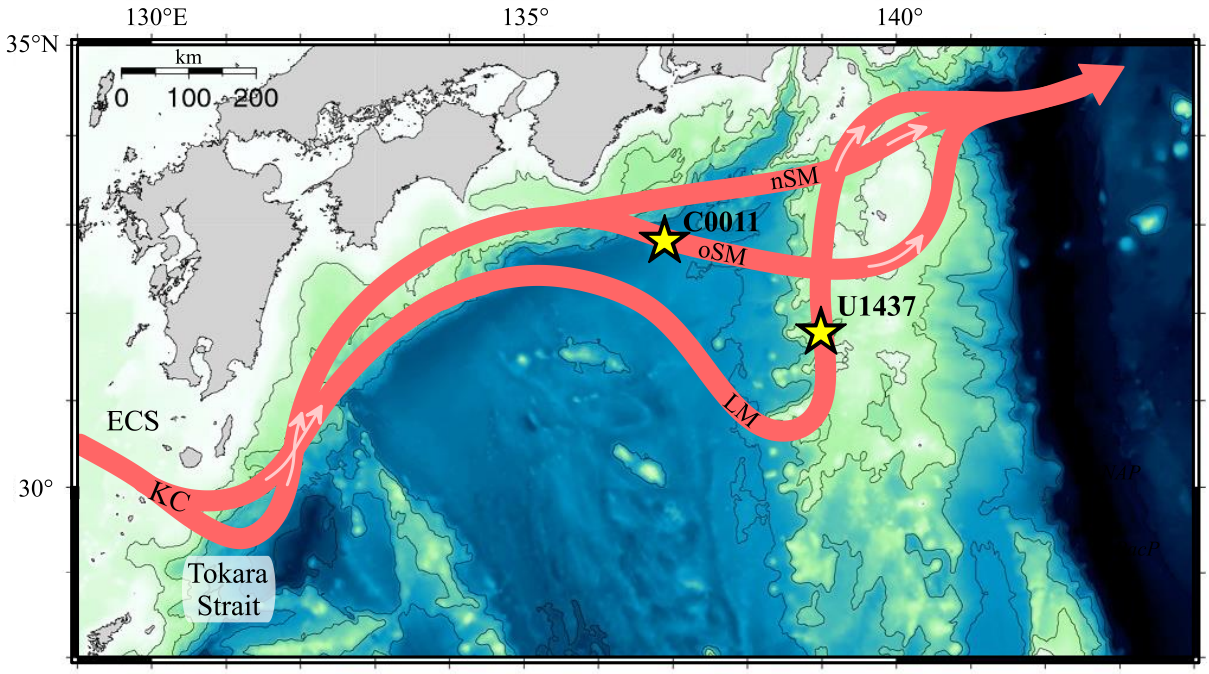

Figure 1.2 | Bathymetric map of the northern Philippine Sea and the three different stable meander path modes of the Kuroshio Current south of Japan downstream of its exit from the ECS through the Tokara Strait. LM = large meander path, nSM = nearshore short meander path, and oSM = offshore short meander path. ECS = East China Sea. Locations of IODP Sites C0011 and U1437 are indicated by yellow stars.

Meander path variations of the KC exhibit a significant impact on the surface pressure field and the development of low-pressure systems (Tsujino et al., 2013; and references therein). Under a prevailing large meander path, shifts in extratropical cyclone tracks and decreased air temperature related to a southward shift of the sea surface temperature front can even trigger snowfall events in coastal parts of southern Japan (Nakamura et al., 2012).

After passing over the northern Izu-Bonin ridge at ~34 °N (large meander or nearshore short meander path) or between 32 to 33 °N south of Hachijo Island (offshore short meander path) (Fig. 1.2), the KC leaves the coast of Japan at ~35 °N, 140 °E. It is then deflected eastward and enters the open North Pacific Ocean, where it is renamed the Kuroshio Extension (KE). The KE is characterized by a strong sea surface height gradient (Wu et al., 2018) and large-amplitude meanders (Qiu, 2002). Studies of the zonally averaged (141-150 °E) axis position and transport of the KE between 1992 and 1998 showed a maximum northward extension and transport during summer and fall (Tatebe and Yasuda, 2001). At present, the KE is the area of largest heat loss from the ocean to the overlying atmosphere in the NW Pacific Ocean and one of the largest globally (Qiu et al., 2004). This observation underlines the importance of the KC and KE as key roles in both regional and global climate evolution.

1.1.2. The Oyashio Current

The Oyashio Current is the renamed East Kamchatka Current (EKC) and forms within the Sea of Okhotsk, where the polar waters of the EKC are modified through sea ice formation and mixture with Okhotsk Sea waters (Qiu, 2001). After its exit from the marginal Sea of Okhotsk through the Bussol Strait, the OC flows southwestward along the coast of the Kuril Islands. As the northern counterpart of the KC and as part of the wind-driven counterclockwise circulating Western Subarctic Gyre, a subgyre of the Subarctic Gyre in the North Pacific, it transports cold waters from the Subarctic Pacific to the south. The OC has significant impact on the climate of the adjacent continental areas: owing to the presence of its cold waters, the tree line is shifted south by ~10° in latitude in Kamchatka and parts of the Russian Far East compared to the same latitude in inland Siberia (Pfadenhauer and Klötzli, 2020). Southeast of Japan´s northernmost island, Hokkaido, at about 43 °N, 145 °E, the OC splits into a southward heading branch strictly following the coastline of Honshu and an offshore path, the Oyashio Extension (OE), that is deflected eastward and rejoins the Subarctic Gyre (Yasuda, 2003). The OE is also referred to as the Subarctic Current as it transports waters of subarctic origin southward (Qiu, 2001). The OC´s nutrient-rich characteristics sourced from upwelling of deep waters in the Subarctic Pacific Ocean and Bering Sea led to the OC´s Japanese name as parent (= oya) stream (= shio) (Qiu, 2001). The advection of nutrients from Arctic waters and the coasts of Kamchatka and Siberia fuels phytoplankton blooms (Fig. 1.3) and hence fish growth in the region east of Japan, thereby providing important fishing grounds for local fisheries (Sakurai, 2007; Wu et al. 2018). Major blooms usually occur during early spring as the surface waters have been enriched with nutrients such as iron and silica blown in by Asian dust storms and volcanic ashes from Kamchatka in the preceding winter, while those storms in combination with reduced sunlight have kept marine primary productivity at a minimum during that time.
The coastal branch of the OC occasionally intrudes into intermediate layers (below ~200 mbsl) of the water column south of Japan (Yang et al., 1993), where it can be identified by low salinity (<34.1 ‰) and abnormally high dissolved oxygen levels (>3.0 ml/l) (Yang et al., 1993). The occurrence of polar and subpolar microfossil assemblages at more southerly latitudes of the NW Pacific during the last glacial period (Moore et al., 1980) and the southward migration of planktonic foraminiferal assemblages ~140-150 ka ago (Thompson, 1981) document the southward displacement of the KC, a concomitant advance of colder subpolar OC waters to ~33-35 °N, and an associated decline in sea surface temperatures by 4-6 °C during the last glacial and preceding glacial period (Thompson, 1981).

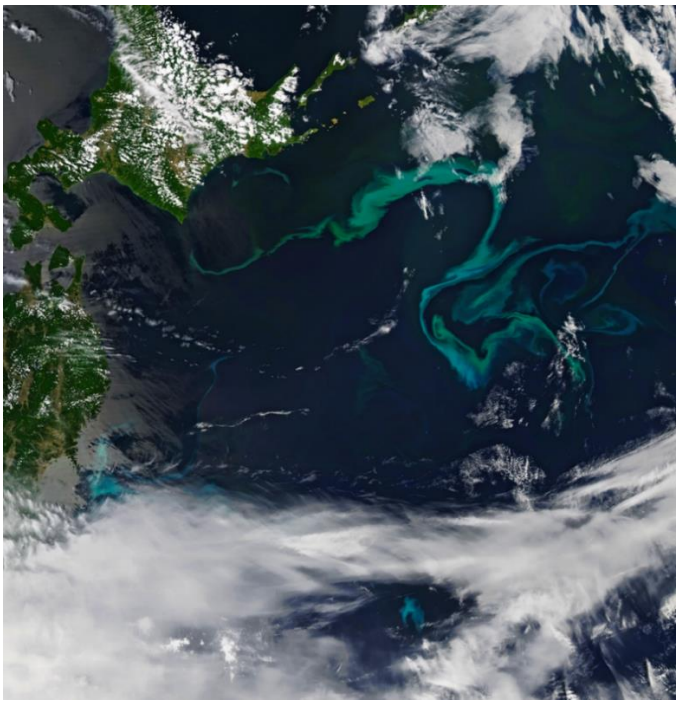

Figure 1.3 | Satellite image taken on May 26, 2019 showing a phytoplankton bloom off of northeastern Japan. The advection of nutrient-rich waters from the Subarctic Pacific via the Oyashio Current supports marine primary productivity. NASA Earth Observatory image by Joshua Stevens, using MODIS data from NASA EOSDIS/LANCE and GIBS/ Worldview. Source: https://visibleearth.nasa.gov/images/145135/bloom-in-the-parent-stream/145137w.

Like the KC, the OC exhibits large seasonal variations in terms of its volume transport and current velocity: it intensifies in early winter and reaches its maximum strength in late winter to spring associated with changes in the Aleutian Low and the latitudinal position and strength of the westerly jet stream (Qiu, 2001; Isoguchi and Kawamura, 2006). During this time, it reaches from the sea surface to the ocean floor along the continental slope southeast of Hokkaido (Qiu, 2001). In the summer and early fall, the OC´s current strength is reduced; its volume transport is only 10 to 20 % of its winter maximum (3-4 Sv *vs*. 20-30 Sv) and its flow is confined to the upper 2000 mbsl (Qiu, 2001).

1.1.3. The Kuroshio-Oyashio Interfrontal Zone

At present, the KC and OC converge at ~36 °N, 145 °E off the coast of Sanriku, Japan, and form an interfrontal mixing zone between their offshore extensions, the KE and OE. Hence, this zone is also often referred to as the Kuroshio-Oyashio extension region (e.g., Itoh and Yasuda, 2009) and is characterized by intense mesoscale eddy formation (Fig. 1.4) and complex upwelling of North Pacific Intermediate Water (NPIW) (Yasuda, 2003). Phytoplankton growing in the admixed nutrient-rich waters of the OC usually concentrate along the eddies´ boundaries, which oftentimes makes them clearly visible from above (Fig. 1.4). East of ~180°, the differentiation between the KE and the OE water masses is no longer clear and they form the broad North Pacific Current (Fig. 1.1) (Qiu, 2001), which forms the northern component of the North Pacific Subtropical Gyre and the southern component of the Subarctic Gyre.

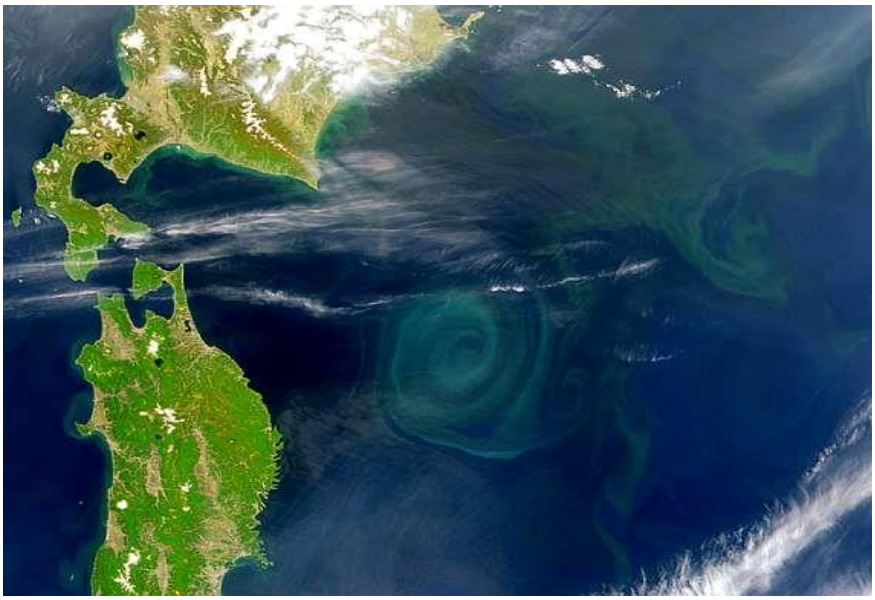

Figure 1.4 | A well-defined large eddy formed in the KC/OC interfrontal zone off the east coast of Japan. The SeaWiFS image was taken on May 22, 1999 and is from NASA's Visible Earth Web Site, (http://visibleearth.nasa.gov/), provided by the SeaWiFS Project, NASA Goddard Space Flight Center, and ORBIMAGE.

1.2. Atmospheric circulation

The atmospheric circulation over the East Asian continent and the NW Pacific Ocean is governed by the Asian monsoon and the westerly jet circulation (Fig. 1.5). Together, they depict major mechanisms for the transport and distribution of precipitation and eolian dust in the region. Dust deposited in the North Pacific Ocean primarily originates from the Taklimakan and Gobi deserts (Yu et al., 2019) and can easily be mobilized by dry winter monsoonal and/or westerly winds.

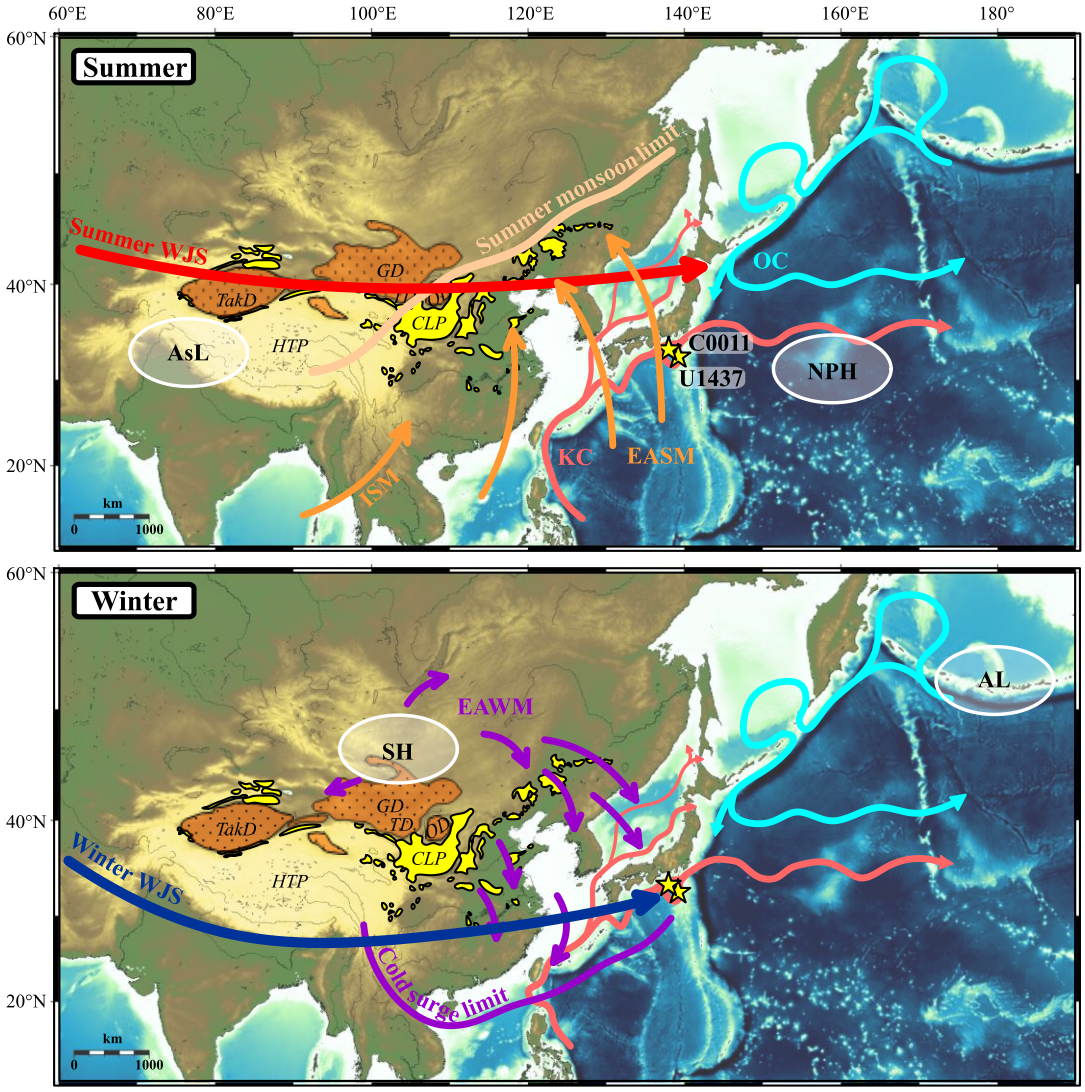

Figure 1.5 | Map of the East Asian continent and adjacent Northwest Pacific Ocean showing major features of the atmospheric circulation for the summer (upper map) and winter (lower map) months, including the East Asian (EASM) and Indian (ISM) summer monsoons and the East Asian winter monsoon (EAWM). Limits for the summer monsoons and the EAWM are given by light orange and purple lines, respectively. The summertime and wintertime positions of the westerly jet stream (WJS) are indicated by the red and blue arrow, respectively. Source regions of eolian dust are displayed in orange (deserts) and yellow (loess deposits) colors. Atmospheric pressure systems are indicated by white eclipses: NPH = North Pacific High, AsL = Asian Low, SH = Siberian High, AL = Aleutian Low. The Kuroshio (KC) and Oyashio (OC) Currents are indicated by pink and light blue arrows, respectively. Yellow stars indicate locations of Sites C0011 and U1437. Abbreviations: HTP = Himalayan-Tibetan Plateau, CLP = Chinese Loess Plateau, TakD = Taklimakan Desert, GD = Gobi Desert, TD = Tengger Desert, OD = Ordos Desert.

The lower-tropospheric winter monsoonal winds and the high-level WJS transport the eolian dust from the arid Asian interior eastward to the regions downwind such as the Chinese Loess Plateau (CLP) (Hao et al., 2012), the Japan Sea (Nagashima et al., 2007, 2011), the Northwest Pacific (Rea and Leinen, 1988), North Pacific (Nie et al., 2018; Abell et al., 2021), and tropical western Pacific Ocean (Xu et al., 2015; and references therein) (Fig. 1.6). Both the Asian monsoon and the WJS exhibit strong seasonal variations and therewith impact the local agriculture and (paleo-) environmental evolution.

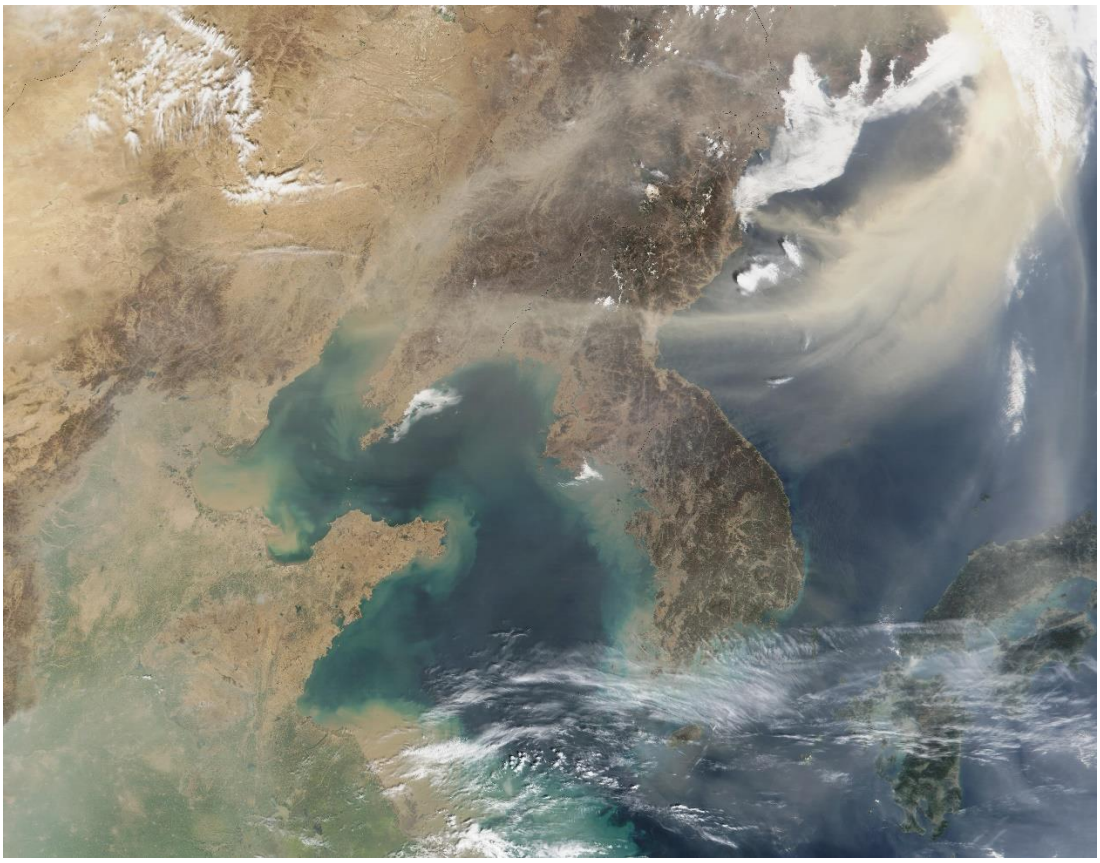

Figure 1.6 | Dust blown from East Asia over the Korean peninsula and the Japan Sea. The true-color satellite image was taken on April 1, 2002, by the Moderate-resolution Imaging Spectroradiometer (MODIS) aboard NASA's Terra satellite. Source: https://visibleearth.nasa.gov/images/58069/dust-over-korea-and-the-sea-of-japan.

1.2.1. The East Asian summer and winter monsoons

1.2.1.1. The present East Asian monsoon

The Asian monsoon is the Earth´s largest weather system affecting almost half of the world´s population. One of its subsystems, the East Asian Monsoon, is particularly interesting as it covers several climatic zones from the Tropics to the Subarctic. Knowledge of how this system responds to climate dynamics is fundamental as the region under the influence of the monsoons is one of major importance for global economy. The term monsoon in general refers

to a strong seasonality in wind and precipitation patterns, typically with onshore winds bringing elevated rainfall during the summer months and offshore winds with significantly less rainfall during the winter (Wang et al., 2019a).

The East Asian monsoon circulation with its two components, the warm and wet East Asian summer monsoon (EASM) and the dry and cold East Asian winter monsoon (EAWM), is driven by pressure gradients associated with atmospheric pressure systems that develop in summer and winter, respectively. These pressure gradients derive from the heat contrast between the Pacific Ocean and its marginal seas and the Asian continent, resulting in large seasonal variations in terms of precipitation and dust fluxes over these areas. This also has severe impact on the oceanography of the East Asian marginal seas and NW Pacific Ocean via changes in nutrient inputs, salinity, upwelling and deep-water ventilation (Tada et al., 2016; and references therein). The EAWM is controlled by the strength of the cold-core Siberian High (SH) and the warm-core Aleutian Low (AL) during the winter months and is characterized by strong cold and dry northwesterly winds in the lower troposphere (Wu and Wang, 2002). These low-level winds are the predominant transport mechanism of eolian dust from the arid Asian interior to the CLP (Hao et al., 2012). Furthermore, the outbreak and frequency of dust storms in East Asia in spring was found to positively correlate with the strength of the EAWM in the preceding winter (Wu et al., 2010).

The second subsystem of the East Asian monsoon, the EASM, is controlled by the development of the North Pacific High (NPH) over the North Pacific and the Asian Low (AsL) over southern Asia in spring and summer. Its southerly winds bring large amounts of moisture from the tropical Pacific Ocean to the East Asian continent, resulting in 80-85 % of the annual rainfall in the region during this season (Clift et al., 2020). For the environment and the local agriculture, the seasonal rainfall is vital, but torrential rainfall and strong typhoons may cause severe damage through flooding and mudslides (Clift et al., 2020). The high precipitation during the summer months is closely linked to the seasonal latitudinal migration of the intertropical convergence zone (ITCZ), which moves into China in boreal summer (Jo et al., 2014), and the position of the westerly jet axis (Sampe and Xie, 2010; Wei et al., 2017) (Fig. 1.5). Throughout the summer, the EASM rain belt, or Meiyu/Baiu rain belt referring to the rainy season in China/Japan, a zonally elongated rain band spanning between 30-40 °N from China over Japan to the NW Pacific Ocean, migrates northward in close association with the northward migration of the WJS axis and finally disappears by the end of the summer (Sampe and Xie, 2010; Nagashima et al., 2011).

1.2.1.2. The East Asian monsoon in the geological past

Both climate and topographic changes related to the uplift of the Himalayan-Tibetan Plateau (HTP) exert significant influence on the Asian monsoon on geological timescales, and these changes by themselves impact the region´s climatic evolution and topography, the latter mostly through the amounts of (paleo-)precipitation and associated erosion on the HTP (Clift et al., 2020). Uplift of the HTP resulting from the collision of the northward-drifting Indian subcontinent with the Eurasian Plate started in the early Eocene ~55 Ma ago (Clift et al., 2020) and has continued up to the Present, with phases of enhanced uplift in the late Eocene (40-35 Ma), late Oligocene to early Miocene (25-20 Ma), and middle to late Miocene (15-10 Ma) (Tada et al., 2016). This resulted in increased aridification of the Asian interior as it was progressively shielded from incoming moisture from the tropical Indian Ocean via the Indian monsoon (Sun and An, 2005). The East Asian and Indian monsoons exist at least since the Eocene (Licht et al., 2014) and intensified in the late Miocene in concordance with the aforementioned phased uplift of the HTP (An et al., 2001; Tada et al., 2016). Evidence exists that the monsoon-like regime was confined to the Tropics and Subtropics prior to the early Miocene, and extended further north afterwards, transforming the zonal Asian climate pattern to a monsoon-dominated one (e.g., Guo et al., 2008). The establishment of a modern-like East Asian monsoon circulation with its distinct seasonality in wind and rainfall by the early Miocene was attributed to combined effects of topographic uplift and long-term global cooling (Zhang et al., 2018). Uplift in Siberia and Mongolia since 10 Ma may have additionally affected the EAWM (Clift et al., 2020). Accumulation of wind-blown sediments in the present-day region of the CLP, which was attributed to increased aridification and intensified winter monsoonal winds, started by ~8 Ma and increased by an order of magnitude in the mid-Pliocene (Zheng et al., 2016).

Owing to its hydrological nature, variations in the past EASM strength are comparatively easier to reconstruct and various archives exist that allow a detailed study of past EASM behavior, including cave records, lakes, peat, and loess-paleosol sequences (Hu et al., 2012; and references therein). Direct phytolith-based records of vegetation changes in East Asia revealed a marked shift in the floral community in the Pliocene with a decrease in grasses adapted to warmer and humid climates and a concomitant increase in cool- and dry-climate adapted grasses (Wang et al., 2019b). The authors attributed this and the synchronous decline in mean annual precipitation to a reduction of monsoonal rainfall in the region associated with global cooling, under which the ITCZ and the associated monsoonal rain belt may have been shifted equatorward (Wang et al., 2019b). Similarly, a reduction in grain size in fluvial-lacustrine sequences in central China was interpreted as evidence for decreased hydrodynamic strength

and hence also points towards reduced rainfall in the mid-Pliocene (Wang et al., 2020). Over the course of the middle and late Pleistocene, the EASM seems to have regained some strength as indicated by increased speleothem growth in Korea (Jo et al., 2014) and changes in sediment provenance in the ECS (Beny et al., 2018) associated with increased rainfall and fluvial run-off due to a northward shift of the ITCZ.

Past variability of EAWM strength is more difficult to address as there are only very few proxies and limited archives that record changes in windiness. Proxies used for the reconstruction of past changes in EAWM strength include grain size variations in eolian deposits (e.g., Sun et al., 2011; Hao et al., 2012) and changes in oceanic productivity associated with fertilization of the ocean via dust inputs and wind-driven upwelling (e.g., Sadatzki et al., 2015). Especially the latter, however, may be strongly impacted by other mechanisms, including the advection of nutrients via ocean currents. Furthermore, due to low sedimentation rates and dating difficulties, reconstruction of EAWM strength variability on the millennial or sub-millennial scale may be limited (Hu et al., 2012).

Pollen-based reconstruction of winter temperature conditions as a function of EAWM strength from the late Pliocene to present showed a stepwise enhancement of the EAWM at 2.8 and 1.6 Ma and is consistent with changes in quartz grain sizes on the CLP (Xin et al., 2020). As these stepwise intensifications of the EAWM are in line with the initiation and intensification of Northern Hemisphere glaciation (NHG), changes in global ice volume and climate cooling were suggested to be important controlling factors on EAWM strength (Xin et al., 2020).

Another complicating factor for the reconstruction of past EAWM strength from both continental and marine archives is the presence of both the EAWM and WJS at similar latitudes over East Asia and the adjacent NW Pacific Ocean since – as mentioned previously – both of these winds have a strong potential for transporting dust downwind. The study of glacial-interglacial changes in dust fluxes to the NW Pacific Ocean south of Japan over the course of the last 1 Ma is subject of Chapter 5 of this thesis, in which this matter will be discussed in detail.

Factors that have been shown to exert a control on variations in the (paleo-)monsoon system besides topographic changes and long-term cooling, especially on shorter (glacial-interglacial) timescales, comprise insolation-driven climate changes in high latitudes, including the expansion of Northern Hemisphere ice sheets (Ding et al., 1995), and the occurrence of perennial sea ice (Meng et al., 2021), growth of the Antarctic ice sheet (Zhang et al., 2018), Antarctic climate variation (Chen et al., 2016), changes in Atlantic Meridional Overturning

Circulation (AMOC) (Sun et al., 2011), and to a lesser extent El Niño-Southern Oscillation (ENSO)-related convection in the western equatorial Pacific (Zhang et al., 1996).

1.2.2. The westerly jet stream

1.2.2.1. The present westerly jet stream over East Asia and the NW Pacific Ocean

The westerly jet streams are meandering narrow bands of airflow directed from west to east located in the upper troposphere of the mid-latitudes in both hemispheres. In each hemisphere, the polar and subtropical WJS develop between the Polar cell and Ferrel cell and the Ferrel cell and the Hadley cell, respectively. If not stated otherwise, the abbreviation WJS refers to the subtropical westerly jet stream in this thesis, as it is the one affecting the study region of the mid-latitudinal to subtropical regions of East Asia and the North Pacific Ocean. The latitudinal position and intensity of the WJS have a strong modulating effect on both regional and global climate evolution (Zhou et al., 2020). The westerly jet´s position and strength are often controlled by a so-called tug-of-war between climate forcing from polar regions (Arctic amplification and stratospheric cooling in Antarctica, respectively) and the tropics (through warming in the upper troposphere) (Coumou et al., 2018; Chen et al., 2020). Owing to the topographical complexity, the WJS circulation over the Asian continent shows a distinct bimodal seasonal flow pattern enabled by the topographic barrier of the HTP (Fig. 1.7): during the winter months, the WJS is located to the south of the HTP, jumps to the north of the plateau in the following spring where it stays throughout the summer, and gradually recedes to its southern pathway in fall (Schiemann et al., 2009).

It has previously been shown that a strong relationship exists between the subtropical Asian WJS and the summer rainfall mediated by the EASM and the Indian summer monsoon (ISM) over central and East Asia (e.g., Schiemann et al., 2009; Sampe and Xie, 2010; Wei et al., 2017; Herzschuh et al., 2019). A shift of the WJS´s axis to the north of the HTP in early May typically precedes the onset of the EASM over the SCS (Schiemann et al., 2009).

Like the EAWM, the WJS is a major transport mechanism for eolian dust from the East Asian continent. Dust derived from continental Asia can be transported over long distances by the WJS and has been found in Japan Sea (Nagashima et al., 2007, 2011), Northwest (Rea and Leinen, 1988), and North Pacific Ocean sediments (e.g., Nie et al., 2018; Abell et al., 2021), the tropical western Pacific (Xu et al., 2015; and references therein), as well as the North American continent (Sassen, 2002), the North Atlantic Ocean (Garrison et al., 2003), and even in the French Alps (Grousset et al., 2003). A modelling study by Uno et al. (2009) even

suggested that Asian dust can be transported one full circuit around the globe via the WJS before it descends and is deposited.

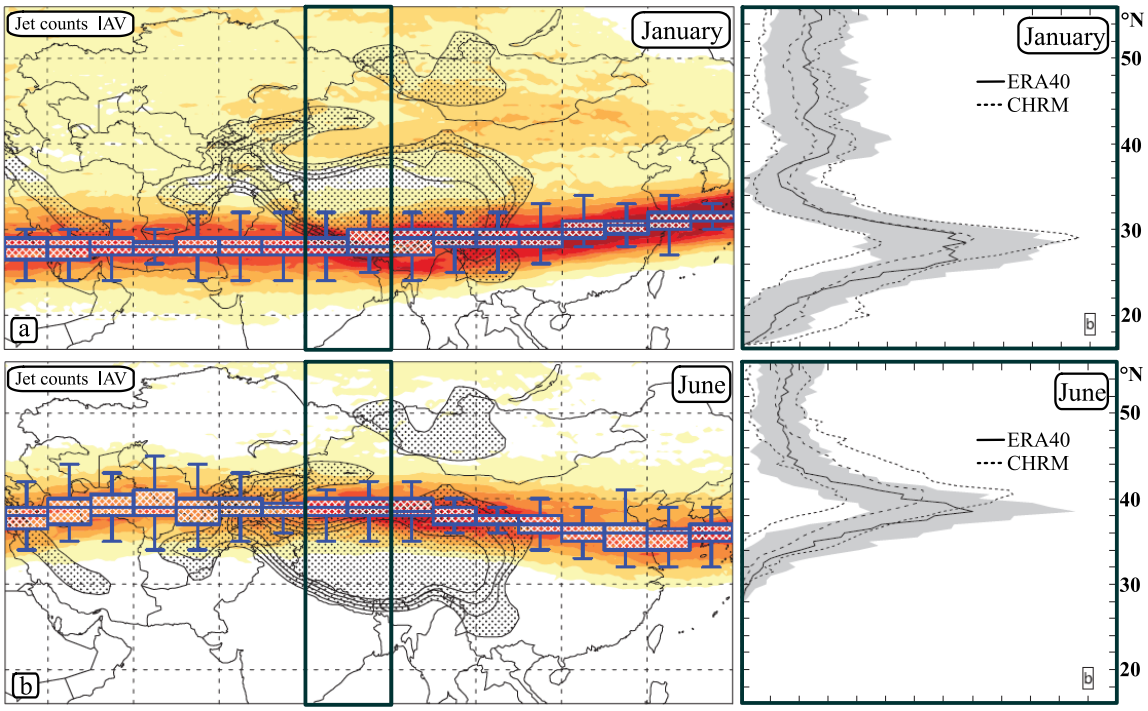

Figure 1.7 | Seasonal changes of the westerly jet axis at 200 hPa over Asia for January (a) and June (b). Figures on the left side show the total occurrence counts (shading, from 6-hourly ERA-40 fields) and the interannual variability of the jet latitude (blue box plots, from ERA-40 monthly mean horizontal wind). The figures on the right display the meridional distribution of the occurrence counts between 80-90 °E over (within the area marked by the dark green boxes on the left figures). The bold solid line and gray shading on the right figures display the mean and one standard deviation of interannual variability based on occurrence counts from the 6-hourly ERA-40 fields). The bold and thin dashed lines in the same figures represent the mean and one standard deviation of interannual variability based on occurrence counts from the 6-hourly CHRM fields. Figures modified after Schiemann et al. (2009).

1.2.2.2. The westerly jet stream in the geological past

Studies of past changes in the latitudinal position of the WJS over East Asia mostly only focussed on the last glacial period (Nagashima et al., 2007, 2011) or the Holocene (Herzschuh et al., 2019; Zhou et al., 2020); information on variations of the WJS further back in time, however, is sparse. Changes in the westerly jet path over East Asia on millennial timescales were previously found to exhibit the same cyclicity as Dansgaard-Oeschger cycles in the North Atlantic Ocean (Nagashima et al., 2011). The authors attributed stadial-interstadial changes in the dust source of eolian sediments from the Japan Sea to latitudinal changes in the position of the westerly jet axis. A dominance of dust originating from Mongolian deserts during stadials let the authors conclude that the WJS was shifted to the south of the HTP during these periods, thereby enabling the observed dominance of EAWM-transported dust (Nagashima et al., 2011) in Japan Sea sediments. The co-dominance of EAWM-transported Mongolian Gobi- and

Taklimakan Desert-sourced dust during interstadials was attributed to a position of the WJS to the north of the HTP over the arid regions of the Asian interior (Nagashima et al., 2007, 2011). In general, a strengthening of the westerly wind circulation was found to be closely related to the uplift of the HTP, and the northeastward expansion of the HTP during the late Miocene is thought to have strengthened the westerly wind speeds to an extent that eolian dust could be effectively transported to the North Pacific Ocean (Nie et al., 2018; and references therein). Only very recently, two studies investigated changes in the westerly jet strength and axis over Asia and the North Pacific Ocean during specific time intervals in the geological past: (1) over the past 3.6 Ma (Fang et al., 2020), (2) and from the Pliocene period between ~4.6-2.5 Ma (Abell et al., 2021). The former study revealed that loess has been accumulated continuously at the southern margin of the Taklimakan Desert at least since 3.6 Ma, thereby indicating that arid climate conditions and strong westerlies in mid-latitude Asia existed at least since that time. The same authors also found stepwise drying of the region and a strengthening of the zonal westerlies coeval with global ice volume variability, the latter being driven by changes in orbital forcing both in the time and frequency domain (e.g., a shift from a 41-ka cyclicity to a 100-ka cyclicity during the Mid-Pleistocene Transition (MPT)) (Fang et al., 2020). The most recent study by Abell et al. (2021) reconstructed changes in the latitudinal position of the westerly jet belt during the Pliocene, including the Mid-Pliocene Warm Period (MPWP) (3.29-2.97 Ma ago). During the Pliocene, atmospheric carbon dioxide levels (CO_2) were at ~350-450 ppmv and temperatures by 2-4 °C warmer than during the subsequent Pleistocene and pre-industrial times (Abell et al., 2021). The authors found that the zonal westerlies were weaker and located more poleward during the warm Pliocene as compared to glacial periods after the intensification of NHG ~2.7 Ma ago. Intensified NHG and continued ice sheet expansion was accompanied by significant increases in dust fluxes to the mid-latitudinal North Pacific Ocean and exceeded the dust fluxes to the Subarctic Pacific (Abell et al., 2021). Subsequently, variations in dust flux and paleoproductivity mostly followed glacial-interglacial cycles of the late Pliocene and early Pleistocene which let the authors conclude that the reconstructed shifts in the westerly jet axis resulted primarily from variations in Plio-Pleistocene thermal gradients and ice volume (Abell et al., 2021).

In order to take a more detailed look on glacial-interglacial variations in dust inputs presumably related to the WJS and East Asian monsoon circulation, Chapter 5 will investigate and discuss in detail the glacial-interglacial history of the latitudinal position of the WJS throughout the past 1 Ma and will examine the impact of changes in Arctic climate on the WJS over geological timescales.

1.3. Lipid biomarkers as proxies for paleoclimate, paleoceanographic and paleoenvironmental conditions

Molecular fossils or biomarkers are environmentally persistent and geologically stable organic compounds that are indicative for their biological precursor and hence their biological source organism(s), conditions prevailing during their synthesis, or alteration processes leading to their formation (e.g., Simoneit, 2004). They usually consist of carbon and hydrogen, and to subordinate amounts may also include nitrogen, oxygen, sulfur and other elements (e.g., Eglinton and Eglinton, 2008; and references therein).

Lipid biomarkers found in marine sediments mostly originate from marine and/or terrestrial sources. In these sediments, they have either been preserved in their initial form or have been modified upon deposition, diagenesis and catagenesis through the loss of functional groups, and/or structural reorganization (Simoneit, 2004).

In the open marine realm, only ~1 % of the organic matter that is being produced in the sunlit surface ocean escapes remineralization, recycling and degradation during its vertical transit and reaches the deep-sea ocean floor where it is preserved within the sediments (Seibold and Berger, 1996; Middelburg, 2019). Those biomarkers that end up in the sediments are valuable recorders of their biological source, conditions prevailing during their synthesis as well as diagenetic and postdepositional processes and states (Simoneit, 2004) and can inform on past changes in e.g., paleoclimate, the paleoenvironment, and/or the oceanographic regime (Eglinton and Eglinton, 2008). For example, the reconstruction of past water temperature is founded on the structural adaption of the membrane or storage lipid composition of marine organisms to ambient growth temperature (e.g., Eglinton and Eglinton, 2008).

Lipids of terrigenous origin are brought into the marine realm via eolian and/or fluvial transport. The study of the lipid biomarker inventory of marine sediments therefore enables the investigation of past changes both in the marine and terrestrial environment and can inform on changes in transport mechanisms to the sediments.

The following subchapters will provide some background information on the molecular proxies that were used in the framework of this thesis, including their potential biological sources, characteristics and applicability.

1.3.1. Marine biomarkers: sea surface and subsurface temperature proxies

In this study, some of the lipid biomarkers are used to reconstruct the water temperature evolution at the sea surface and subsurface of the ocean and thus allow inferring changes in

ocean current strength and pathways. These lipid biomarkers are hereafter referred to as lipid paleothermometers. Unlike some of the other proxies commonly used for paleo water temperature reconstructions (e.g., oxygen isotopes ($\delta^{18}O$) and Mg/Ca in the shells of marine calcareous organisms), the lipid paleothermometers are mostly unaffected by changes in ice volume, sea water chemistry or salinity. For the reconstruction of past sea surface and subsurface water temperatures, the unsaturated ketone index ($U^{K'}_{37}$) (Brassell et al., 1986; in its modification by Prahl and Wakeham, 1987), long-chain diol index (LDI) (Rampen et al., 2012) and tetraether index based on glycerol dialkyl glycerol tetraethers (GDGTs) consisting of 86 carbon atoms (TEX_{86}) (Schouten et al., 2002), respectively, have proven as reliable and useful tools. Another index, the RI-OH index based on hydroxylated GDGTs, has been proposed very recently as an additional proxy for the reconstruction of sea surface temperatures (SSTs) (Lü et al., 2015). All the four of these lipid paleothermometers make use of the adaption of the cell membrane or storage lipid composition of their source organisms to changes in growth temperature, that is ambient water temperature, in order to adjust their membrane fluidity, for example (Inglis and Tierney, 2020).

The lipids used for the different paleothermometers are synthesized by their respective source organisms at their preferred habitat depth (Fig. 1.8). As the structure of these lipids depends largely on growth temperature, the lipids preserve the ambient water temperature signal at the water depth the source organisms dwell in. For example, photosynthetic algae such as haptophytes are dependent on sunlight and therefore dwell exclusively in the sunlit surface layer of the ocean. Hence, their lipid composition is assumed to record the temperature signal at the sea surface (e.g., Prahl and Wakeham, 1987; Rampen et al., 2012). After the decease of the source organisms, the organic matter – if not dissolved, remineralized or recycled within the water column – sinks down to the seafloor (e.g., as marine snow aggregates or packaged onto fecal pellets; e.g., Inglis and Tierney, 2020), and the lipids are embedded in the sediments (Fig. 1.8) where they preserve the temperature signal at the time of their synthesis. Extraction and subsequent laboratory analysis of the sediments enables the reconstruction of the temperature signal at a specific time and the study of a whole set of samples from a sedimentary record allows the reconstruction of water temperature evolution over time.

Additional to habitat depth, the temperature signal recorded by the proxies also depends on the growth season of the respective source organisms as the thermal structure of the oceanic water column is subject to seasonal change throughout the year. Alkenone-synthesizing haptophyte algae, for example, have been shown to bloom during the spring and early summer months off Japan, resulting in maximum alkenone fluxes to the seafloor during these times (Sawada et al.,

1998). In other regions, however, the alkenone-based water temperatures seem to be more representative of the early fall (Castañeda et al., 2010), summer (Ternois et al., 2000; Rodrigo-Gámiz et al., 2015) or the annual mean temperature (e.g., Lopes dos Santos et al., 2013). Therefore, also regional differences when reconstructing water temperatures have to be considered.

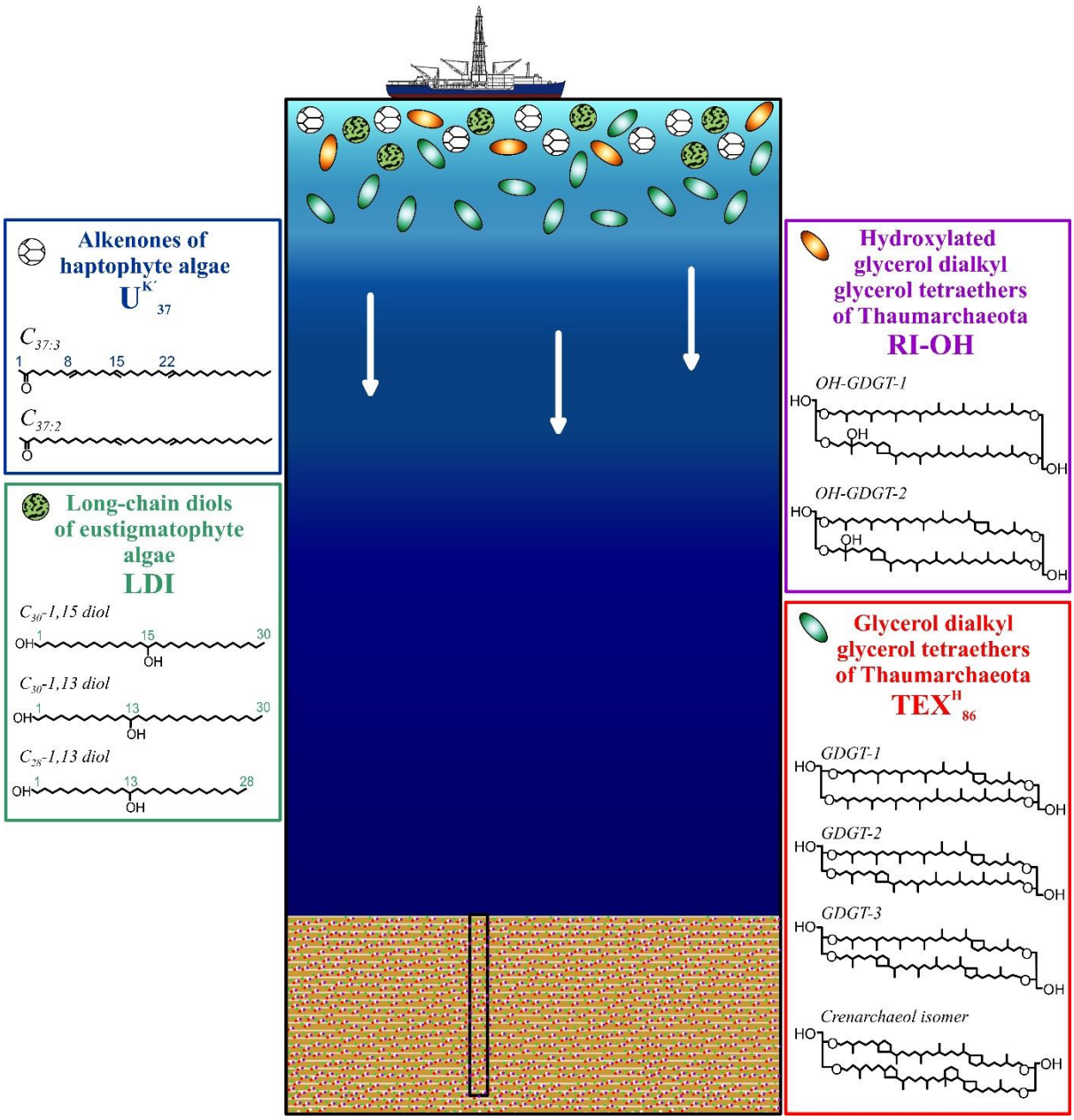

Figure 1.8 | Schematic overview of the concept of water temperature reconstruction using the $U^{K'}_{37}$, LDI, RI-OH (based on organisms dwelling at the sea surface) and TEX^{H}_{86} (subsurface) paleotemperature proxies. The respective compounds are synthesized by their source organisms at their preferred habitat depth and hence preserve the ambient water temperature signal at that depth.

The impact of growth season and preferred habitat depth of the source organisms on the $U^{K'}_{37}$, LDI, and TEX^{H}_{86} temperature signal at IODP Site C0011 is elaborated in detail in Chapter 4. This Chapter also discusses other factors that potentially impact the proxies´ signals.

1.3.1.1. Long-chain alkenones

Long-chain alkenones are long-chain unsaturated ketones that are biosynthesized by haptophyte algae and are commonly used for reconstructing SSTs. They have been identified in sedimentary records dating back to the early Aptian (Brassell et al., 2004), but their distributions in sediments from the Cretaceous (Brassell et al., 2004) and Danian (Yamamoto et al., 1996) differ significantly from those in younger sediments (Brassell, 2014; and references therein). It has been hypothesized that the alkenones with a higher degree of unsaturation, which are crucial for SST reconstruction via the $U^{K'}_{37}$ paleothermometer, may have been an evolutionary adaption to Cenozoic cooling (Brassell, 2014; Inglis and Tierney, 2020), therefore prohibiting the proxy´s application in older sediments. At present, the cosmopolitan haptophyte algae species *Emiliania huxleyi* (Volkman et al., 1980a, b) and *Gephyrocapsa oceanica* (Conte et al., 1995; Volkman et al., 1995; Sawada et al., 1996) of the family Noëlaerhabdaceae constitute the dominant alkenone producers in the oceans. Furthermore, non-calcifying haptophytes of the family Isochrysidaceae, *Chrysotila lamellosa* (formerly *Ruttnera lamellosa*) and *Tisochrysis lutea* (formerly *Isochrysis galbana*) have been reported to synthesize alkenones (Nakamura et al., 2015; and references therein), but are restricted to coastal areas and thus have been considered as insignificant contributors to the alkenone inventory in the open marine realm (e.g., Nakamura et al., 2015).

E. huxleyi and *G. oceanica* first appeared at 0.29 Ma (Thierstein et al., 1977; Raffi et al., 2006) and approximately 1.85 Ma before present (Pujos-Lamy, 1977), respectively. Even though the haptophyte source species of alkenones prior to the first occurrence of the modern alkenone producers is to date unknown, existing long-term records of SST evolution (e.g., Lawrence et al., 2006; LaRiviere et al., 2012; Zhang et al., 2014; Herbert et al., 2016) showed that alkenones are still applicable for SST reconstruction in sediments predating 1.85 Ma. Marlowe et al. (1990) suggested that the genus *Reticulofenestra* of the family Noëlaerhabdaceae is the most probable candidate for alkenone production during the Cenozoic. Similarly, Brassell (2014) showed that *Reticulofenestra* was an important producer of alkenones during the Eocene and Oligocene. In addition, he suggested that members of the genera *Cyclicargolithus* and *Dictyococcites* (both from the family Noëlaerhabdaceae) may also have produced alkenones.

The degree of unsaturation (that is the number of double bonds within the ketone chain) varies as a function of growth temperature and various calibrations exist to transfer the ratio of di- and triunsaturated ketones (heptatriaconta-15E,22E-dien-2-one ($C_{37:2}$) and heptatriaconta-8E,15E,22E-trien-2-one ($C_{37:3}$), respectively) (Fig. 1.9), the unsaturated ketone index ($U^{K'}_{37}$; Brassell et al., 1986; in the modification by Prahl and Wakeham, 1987), into sea surface

temperatures (Prahl and Wakeham, 1987; Sikes and Volkman, 1993; Volkman et al., 1995; Sawada et al., 1996; Müller et al., 1998; Conte et al., 2006).

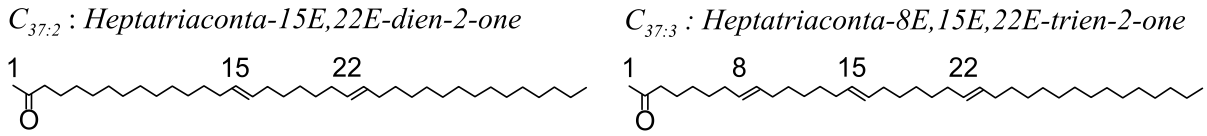

Figure 1.9 | Structural formula of the di- and triunsaturated ketones (heptatriaconta-15E,22E-dien-2-one and heptatriaconta-8E,15E,22E-trien-2-one).

Both *E. huxleyi* and *G. oceanica* are primary producers and therefore dwell exclusively in the photic zone and the $U^{K'}_{37}$ showed the best fit with *in situ* temperatures from 0-10 m water depth (Müller et al., 1998). In the NW Pacific off Japan, sediment trap studies by Sawada et al. (1998) demonstrated that alkenones were largely synthesized in the surface mixed layer (0-30 m) of the water column above the seasonal thermocline and the chlorophyll maximum. Due to the absence of alkatrienones ($C_{37:3}$) in sediments deposited where ocean temperatures exceeded ~28°C, the applicability of the $U^{K'}_{37}$ is oftentimes limited in (paleo-)tropical settings or warmhouse climates (Brassell, 2014).

1.3.1.2. Long-chain diols

Another tool for the reconstruction of SSTs is the long-chain diol index (LDI) which is based on the fractional abundances of long-chain diols (LCDs) (Fig. 1.10) in marine sediments (Rampen et al., 2012). The LDI is calculated as the ratio of the fractional abundance of the C_{30} 1,15-diol over the sum of the fractional abundances of the C_{28} and C_{30} 1,13- and the C_{30} 1,15-diols, with increasing fractional abundances of C_{30} 1,15-diols observed with increasing temperature. The LCDs relevant for the calculation of the LDI are thought to be mainly synthesized by eukaryotic algae belonging to the Eustigmatophyceae (Volkman et al., 1992; Rampen et al., 2014). Other LCDs, such as saturated C_{28}, C_{30}, and C_{32} 1,14-diols, for example, have been identified in the diatom species *Apedinella radians* (Rampen et al., 2011) and *Proboscia* diatoms (Sinninghe Damsté et al., 2003). The latter also produce minor amounts of 1,13-diols (Rampen et al., 2007), which biases the LDI towards colder temperatures (Lattaud et al., 2018). The LDI showed a strong positive correlation ($R^2 = 0.97$) with late summer and early fall temperatures of the 0-30 m layer of the water column in globally distributed marine surface sediments and some minor correlation with salinity and nutrient availability, of which the latter may also be indirectly influenced by temperature (Rampen et al., 2012).

The LDI has to date been successfully used for SST reconstruction in various ocean regions worldwide (e.g., Naafs et al., 2012a; Rodrigo-Gámiz et al., 2015; de Bar et al., 2016; Kotthoff et al., 2017; Jonas et al., 2017; Lattaud et al., 2018), but has been shown to not accurately reflect measured temperatures in coastal settings (De Bar et al., 2016; Lattaud et al., 2017) which was attributed to elevated freshwater inputs. Apart from growth temperature and freshwater inputs, another factor potentially impacting the LDI is oxic degradation as described by Rodrigo-Gámiz et al. (2016). An incubation study with the LCD-synthesizing alga *Nannochloropsis oculata* however showed no substantial impact of prolonged oxygen exposure on the LDI (Reiche et al., 2018).

Similar observations with the LDI corresponding best to late summer SSTs as reported in the initial study by Rampen et al. (2012) have also been made in multi-proxy studies from the Southern Ocean (Lopes dos Santos et al., 2013), in the Alboran Sea (Rodrigo-Gámiz et al., 2014), and the Northwest Pacific Ocean south of Japan (this study, Chapter 4; published in Jonas et al., 2017). In the Sea of Okhotsk, the LDI seemed to represent summer SSTs during glacial periods, but was correlated to fall SSTs during interglacials (Lattaud et al., 2018). A recent study investigating the applicability of various lipid paleothermometers in sediments from the Bass River core showed that the LDI could be used for temperature reconstructions at least back to the Eocene (De Bar et al., 2019). Several LCDs were present in older sediments dating back to the Late Cretaceous, however, due to the absence of 1,13-diols, the calculation of LDI was not feasible (De Bar et al., 2019).

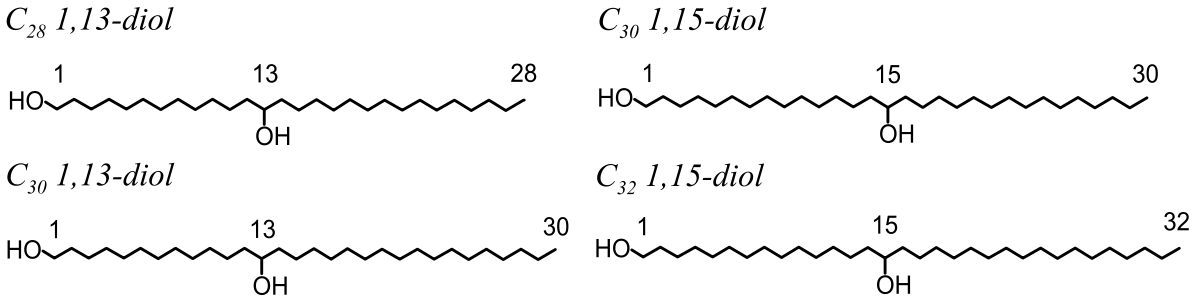

Figure 1.10 | Long-chain diols used for the calculation of the long-chain diol index and the C_{32}-1,15 diol.

The abundance of the C_{32} 1,15-diol relative to those of the other LCDs was proposed as a tracer for riverine input into marine settings as it was found to dominate the LCD distribution in proximity to river mouths (Lattaud et al., 2017) and can be used to determine the influence of non-marine LCD sources on the calculation of LDI-SSTs (De Bar et al. 2016). It has initially been suggested that the C_{32} 1,15-diol is produced *in situ* in rivers (De Bar et al., 2016), but consecutive research showed that non-marine LCDs are predominantly produced by

eustigmatophyte algae in slowly flowing water bodies like lakes and ponds, from which rivers will subsequently transport the LCDs to the river mouth and finally the marine environment (Lattaud et al., 2021; and references therein).

1.3.1.3. Isoprenoid glycerol dialkyl glycerol tetraethers

Glycerol dialkyl glycerol tetraethers and archaeols are uniquely synthesized by several phylogenetic groups of archaea (e.g., Schouten et al., 2013), which typically form a lipid monolayer in their cell membrane. Isoprenoid GDGTs (isoGDGTs) are specific membrane lipid constituents consisting of two C_{40} biphytane chains, which are connected to a terminal glycerol group via ether bonds, and a varying number of rings (Fig. 1.11). Ammonia-oxidizing Thaumarchaeota, a phylum of mesophilic archaea, are considered to be the dominant producers of isoGDGTs in marine environments (e.g., De Rosa and Gambacorta, 1988; Schouten et al., 2013; and references therein), where they inhabit the surface ocean and mesopelagic zone (Inglis and Tierney, 2020; and references therein) and make up to 20-30 % of marine picoplankton (Karner et al., 2001). The number of cyclopentane rings in isoGDGTs has been shown to increase with growth temperature, which led Schouten et al. (2002) to introduce the TEX_{86} (tetraether index based on GDGTs consisting of 86 carbon atoms), which was later recalibrated and modified for high (>15 °C; $TEX^{\mathbf{H}}_{86}$) and low (<15 °C; $TEX^{\mathbf{L}}_{86}$) temperature settings (Kim et al., 2010). Fig. 1.11 shows the different isoGDGTs (GDGT-1, GDGT-2 and GDGT-3) and the crenarchaeol isomer used for the TEX_{86} calculation. Crenarchaeol is an isoGDGT with four cyclopentane moieties and one additional cyclohexane moiety and has been suggested to be an adaption to colder, non-hyperthermophilic environments (Sinninghe Damsté et al., 2002; Inglis and Tierney, 2020). Its later eluting isomer was initially thought to be a regioisomer of crenarchaeol (Sinninghe Damsté et al., 2002), but recent studies suggest that it may rather be an isomer in which the cyclopentane moiety next to the cyclohexane moiety has the uncommon *cis* stereochemistry (Inglis and Tierney, 2020; and references therein).

IsoGDGTs occur ubiquitously, abundantly, and are relatively resistant to degradation (Inglis and Tierney, 2020) and can hence, despite their low thermal stability (Schouten et al., 2004; O´Brien et al., 2017), persist for hundreds of millions of years if environmental and post-depositional conditions are favorable. Apart from its wide applicability in a variety of settings, the TEX_{86} provides hence a useful tool for paleotemperature reconstructions in a) high-temperature settings and b) past warmhouse climates such as the Cretaceous or the Paleocene and Eocene, in which the application of the $U^{K'}_{37}$ is prohibited. To date, the oldest existing TEX_{86} records were generated for the late Pliensbachian to early Toarcian (Ruebsam et al.,

2020) and Sinemurarian to Pliensbachian stages (Robinson et al., 2017), both in the early Jurassic.

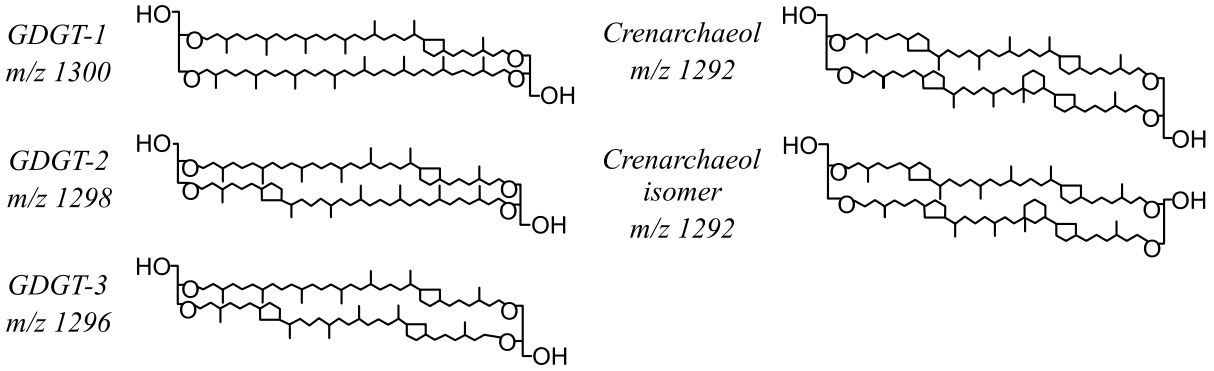

Figure 1.11 | Isoprenoid GDGTs used for the calculation of the TEX_{86} (GDGT-1, GDGT-2, GDGT-3, and the crenarchaeol isomer) and the regular crenarchaeol with their associated mass-to-charge ratios (*m/z*).

More recently, some organic-geochemical and microbiological studies indicated that the TEX_{86} may more accurately reflect subsurface water temperatures instead of SSTs (e.g., Huguet et al., 2007; Lopes dos Santos et al., 2010; Rommerskirchen et al., 2011; Kim et al., 2012; Yamamoto et al., 2012; Lo et al., 2018) and several studies found that TEX_{86} temperatures fit best with *in situ* temperatures at the depth of the thermocline in some oceanic settings (Lopes dos Santos et al., 2010; Nakanishi et al., 2012a, b; Yamamoto et al., 2012; Jonas et al., 2017). In addition, Kim et al. (2015, 2016) as well as Elling et al. (2015) found evidence that the presence of different archaeal populations within or below the surface mixed layer of the water column may alter the temperature signal preserved in the marine sediments. Similarly, Zhu et al. (2016) showed that the relationships of the TEX_{86} calculated from the distribution of intact polar lipid GDGTs (the biological precursor of the more stable core lipids) and temperature differed significantly between epipelagic waters and those found below. Of the four different groups of marine planktonic archaea, Marine Group (MG) I Thaumarchaeota (Brochier-Armanet et al., 2008), and MG II Euryarchaeota (DeLong et al., 1992), are the dominant ones. While chemolithotrophic nitrifying Thaumarchaeota dwell predominantly in greater depths of the open ocean, in coastal seas and estuaries (Ma et al., 2020; and references therein), the presumably heterotrophic Euryarchaeota thrive mostly in the photic zone (Ma et al., 2020; and references therein). Euryarchaeotal MG III and MG IV, which occur throughout the entire water column, or, for the latter, predominantly in the deep ocean, are less abundant (Ma et al., 2020). In the NW Pacific Ocean, MG II archaea have recently been shown to add significantly to the archaeal tetraether lipid pool (Ma et al., 2020) and the authors suggested that caution must be taken as this may potentially impact the TEX_{86}. Nonetheless, the same authors also showed that TEX_{86} based on core lipid distributions correlates well with *in situ* temperatures in waters

<100 m but not at greater depth. In general, the TEX_{86} can still be used for SST reconstruction even if GDGTs are produced at greater depth within the mixed layer since subsurface temperatures and those at the sea surface usually highly correlate (Inglis and Tierney, 2020; and references therein). Only in those settings with a shallow thermocline where subsurface temperatures may be decoupled from SST, the TEX_{86} is better treated as a thermocline temperature proxy (Wuchter et al., 2005; Inglis and Tierney, 2020).

Other factors potentially affecting the TEX_{86} include the metabolic state (Elling et al., 2014), the ammonia oxidation rate (Hurley et al., 2016) and the production season of GDGTs (Grauel et al., 2013; Lopes dos Santos et al., 2013), as Thaumarchaeota blooms occur when phytoplanktonic productivity is low (Pitcher et al., 2011). Furthermore, temperature reconstruction via the TEX_{86} may yield erroneous results at sites receiving larger inputs of soil organic matter (Weijers et al., 2006a). Downward sinking of GDGTs through the water column (Yamamoto et al., 2012), changes in redox conditions and oxic degradation (Schouten et al., 2004) and grazing (Huguet et al., 2006), in contrast, were found to have no to only little impact on the TEX_{86}.

1.3.1.4. Hydroxylated glycerol dialkyl glycerol tetraethers

More recently, a novel type of GDGTs, the hydroxylated GDGTs (OH-GDGTs) containing zero to two cyclopentane rings and up to two additional OH-groups bound to a tertiary carbon atom in one of the biphytanyl chains, was found and identified in marine sediments and a culture of the methanogen *Methanothermococcus thermolithotrophicus* (Liu et al., 2012). OH-GDGTs occur ubiquitously in globally distributed sediments (Liu et al., 2012; Huguet et al., 2013; Fietz et al., 2013; Lü et al., 2015). Like isoGDGTs, OH-GDGTs are thought to derive from Thaumarcheota, in which they have been observed in cultured populations of Group 1.1a (Pitcher et al., 2011; Liu et al., 2012; Elling et al., 2014, 2015). The occurrence of OH-GDGTs in globally distributed marine sediments from different environmental settings as reported by Liu et al. (2012) indicates that they may present a promising new tool for paleoenvironmental reconstructions. The ring-index of hydroxylated GDGTs (RI-OH; Lü et al., 2015) is based on the weighted average of OH-GDGTs 1 and 2 (Fig. 1.12) and exhibited a strong positive linear correlation with annual ($R^2 = 0.81$) and seasonal SSTs (spring: $R^2 = 0.78$, summer: $R^2 = 0.87$, autumn: $R^2 = 0.86$, winter: $R^2 = 0.77$) in the ECS and SCS (Lü et al., 2015). A study of the seasonal distribution of core OH-GDGTs in the Yangtze River estuary showed that they were mainly produced *in situ* in summer by marine planktonic archaea as

concentrations of OH-GDGTs were higher in the estuary than in the lower reaches of the Yangtze River (Lü et al., 2019).

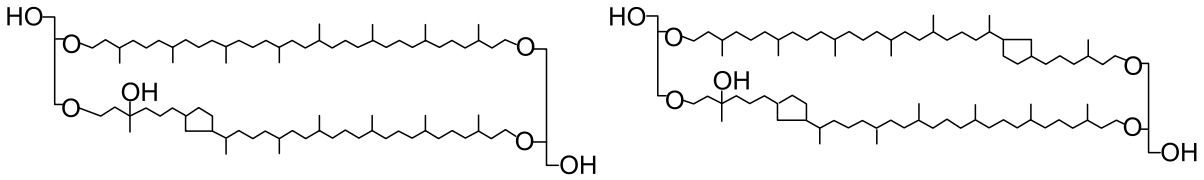

OH-GDGT-1 *OH-GDGT-2*

Figure 1.12 | Structures of OH-GDGT-1 and OH-GDGT-2 both of which are used for the calculation of the RI-OH index.

Furthermore, OH-GDGTs were, in comparison to isoGDGTs, more abundant at the sea surface, indicating that the producers of OH-GDGTs predominantly dwell in the surface layer of the ocean, whereas the isoGDGT synthesizers are more diverse and also inhabit subsurface layers (Lü et al., 2019). This makes the RI-OH a promising new proxy for SST reconstructions. Besides, the RI-OH may provide a useful addition to the toolbox of biomarkers for SST reconstructions in settings where the application of the TEX_{86} is compromised due to enhanced inputs of soil organic matter (Davtian et al., 2019).

1.3.2. Terrigenous biomarkers

Terrestrially sourced biomarkers found in marine sediments are brought to the marine realm via eolian and/or fluvial transport (Fig. 1.13). They include wax lipids of land plants and branched GDGTs, that potentially derive from anaerobic bacteria thriving in soils and peat (e.g., Weijers et al., 2007). The occurrence and abundance of these lipids in marine sediments can inform on past changes in atmospheric circulation, changes in the floral community and vegetation pattern on the continent, as well as fluvial run-off and hence precipitation.

1.3.2.1. Long-chain n-alkyl lipids

Long-chain normal (*n*-) alkyl lipids consisting of 24-36 carbon atoms are major components of epicuticular leaf waxes of land plants and as they are resistant to biodegradation, water insoluble and chemically inert (Meyers, 2003), they are environmentally persistent and can endure long-distance fluvial and eolian transport. Therefore, they are widely used biomarkers that can help to infer information on changes in continental vegetation related to changes in past climate and paleoenvironmental conditions. In general, depending on their chain length, *n*-alkyl lipids can be used to identify the source of organic matter found in marine

sediments. For example, short-chain *n*-alcohols, *n*-alkanes, and *n*-fatty acids occur in marine algae and photosynthetic bacteria (e.g., Meyers, 2003), whereas their long-chain homologues are characteristic for organic matter derived from land plants (e.g., Eglinton and Eglinton, 2008). As part of their epicuticular leaf waxes, they help forming a protective barrier between the plant itself and its surrounding environment. They prevent the plants from desiccation and allow controlling the water balance by regulating the rates of evapotranspiration, amongst other things. Under water stress conditions (due to high temperature and/or aridity), for example, plants were found to synthesize alkanes of higher chain length to provide a more efficient wax coating (Calvo et al., 2004; and references therein).

The leaf wax compounds enter the plants' environment in and on leaf fragments, adsorbed on mineral surfaces, and as aerosols formed by wind abrasion and vegetation fires (Eglinton and Eglinton, 2008). Long-chain *n*-alkanes and *n*-alcohols are major constituents of wax lipids of land plants and can easily be abraded by wind, especially dust storms, or rain (Eglinton and Eglinton, 2008), the former making them common organic compounds in eolian dust (Schefuß et al., 2003a). Studies of terrestrial lipid biomarker concentrations, including *n*-alkanes and *n*-alcohols, in surface sediments along a longitudinal transect from the western to central North Pacific Ocean showed decreasing concentrations with further distance from the continent (Kawamura, 1995), which the author attributed to long-range atmospheric transport from Asia to the open Pacific Ocean, mostly mediated by the WJS. Similarly, studies of lipid biomarkers in aerosols and comparison with data from oceanic sediment trap samples from remote marine settings in the North Pacific Ocean revealed that terrestrial organic matter associated with eolian dust significantly contributes to the total organic carbon pool in deep-sea sediments (Gagosian and Peltzer, 1986).

After dry and/or wet deposition and subsequent settling through the water column, the terrestrial lipids can be preserved in marine sediments, from which they can be readily extracted using organic geochemical techniques. The extractable wax lipids have a huge potential for the reconstruction of paleovegetation and associated prevailing paleoenvironmental conditions, which is why they have been commonly used for such research questions (e.g., Schwark et al., 2002; Rommerskirchen et al., 2003, 2006; Vogts et al., 2009, 2012; Stolpnikova et al., 2020). The following Figure 1.13 illustrates the major transport mechanisms of terrestrial derived lipids from East Asia to the North Pacific Ocean and its western marginal seas.

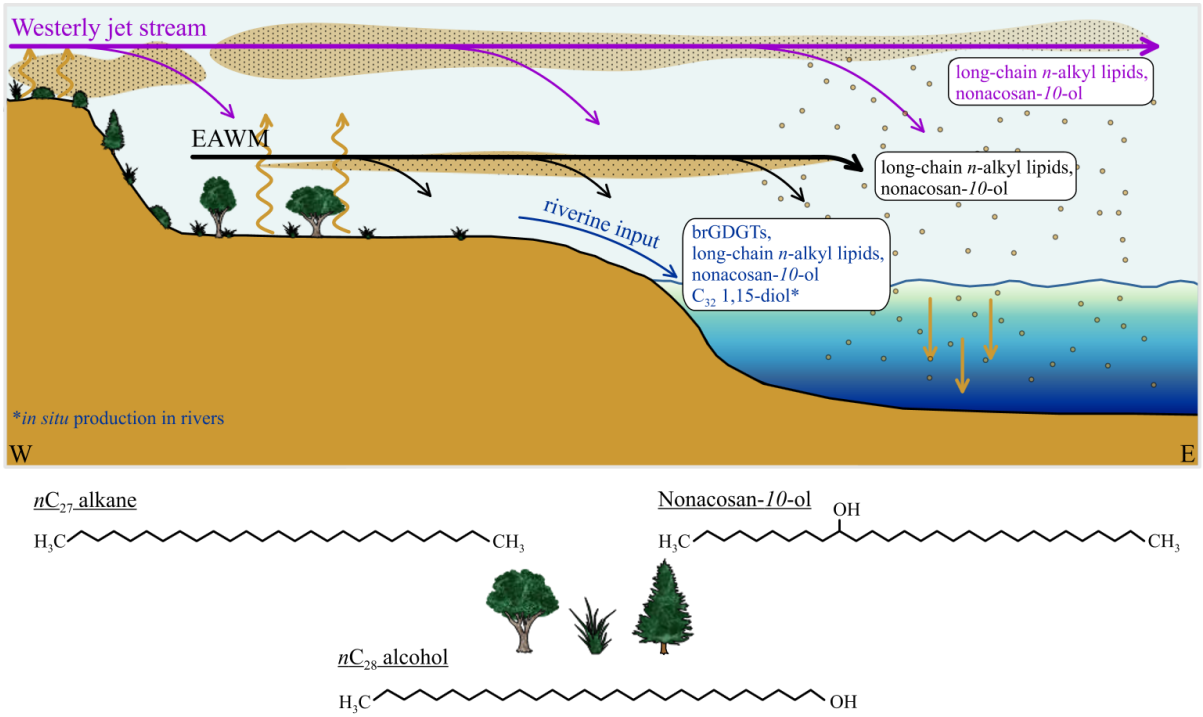

Figure 1.13 | Dominant west-to-east transport mechanisms of terrestrial organic matter from the Asian continent to the Northwest Pacific Ocean and its marginal seas. Adapted from and modified after Eglinton and Eglinton (2008). Pictured are also the molecular structures of a selected long-chain *n*-alkane and *n*-alcohol, and nonacosan-*10*-ol.

In the following, long-chain *n*-alkanes and *n*-alcohols will be presented in further detail as they were used in this study to track changes in dust fluxes from the Asian continent and Japan over time.

1.3.2.1.1. Long-chain n-alkanes

N-alkanes ($CH_3(CH_2)_nCH_3$) show a natural odd-over-even predominance as they are formed via enzymatic decarboxylation of their precursors, even-numbered *n*-fatty acids (Eglinton and Eglinton, 2008). Land plants typically synthesize a range of long-chain *n*-alkanes (*n*C23-*n*C35, with *n*C27, *n*C29 and *n*C31 generally dominating (Killops and Killops, 2005)), which, due to their hydrophobic properties, serve as a protective barrier that save the plants from dehydration (Jetter et al., 2006). Their straight-chain nature lacking any functional groups makes them particularly stable and resistant to degradation, allowing them to persist in fossil records for tens of millions of years (Bush and McInerney, 2013; and references therein). The relative abundances of and ratios calculated from the different homologues as well as the average chain length (ACL) of long-chain *n*-alkanes can be used to infer information on paleoecosystems and paleoenvironmental changes, such as aridity (e.g., Rommerskirchen et al., 2003; Schefuß et al., 2003b; Castañeda et al., 2009), growth temperature (e.g., Gagosian and

Peltzer, 1986; Tipple and Pagani, 2013), or the relative abundances of C_3 and C_4 plants (e.g., Rommerskirchen et al., 2006; Vogts et al., 2009; 2012). Angiosperms typically produce significantly more *n*-alkanes than gymnosperms (Bush and McInerney, 2013).

1.3.2.1.2. Long-chain n-alcohols

N-Alcohols ($CH_3(CH_2)_nCH_2OH$) are a product of enzymatic reduction of their precursor *n*-fatty acids and are thus also predominantly even-numbered. Like *n*-alkanes, they are relatively resistant against degradation but are overall less stable than the former. Land plants typically synthesize even-chain nC_{22}-nC_{32} alcohols as part of their protective wax layer, with nC_{24}-ols to nC_{28}-ols usually dominating (Killops and Killops, 2005). Similar to long-chain *n*-alkanes, different chain lengths of long-chain *n*-alcohols were proposed to be indicative for specific growth conditions and/or plant groups. For example, the nC_{26}-ol was found to be the dominant homologue in plants persuing the C_3-pathway in humid climates, whereas nC_{28}-ols are commonly found in trees of humid climates and the nC_{30} homologue was dominant in trees and shrubs of arid climates (e.g., Rommerskirchen et al., 2003, 2006; Vogts et al., 2009). C_4 grasses predominantly synthesize C_{32}-ol, which is largely absent in C_3 grasses (Rommerskirchen et al., 2006).

1.3.2.2. Nonacosan-10-ol

The secondary alcohol nonacosan-*10*-ol ($C_{29}H_{60}O$) (Fig. 1.14) is a biomarker for the gymnosperms *Pinus* and *Picea* (Jetter et al., 2006). In these boreal conifers, nonacosan-*10*-ol is a main component of the epicuticular waxes forming tubular crystals on the conifer needles (Matas et al., 2003). In GC/MS sample runs of derivatized total lipid extracts, nonacosan-*10*-ol can be identified by its specific trimethylsilyl derivative mass fragments m/z 229 and 369.

Nonacosan-10-ol

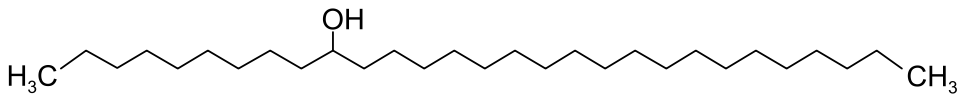

Figure 1.14 | Structural formula of nonacosan-*10*-ol.

1.3.2.3. Branched GDGTs

Branched glycerol dialkyl glycerol tetraethers (brGDGTs) are predominantly found in soils and peat, but it has also been suggested that they can be produced *in situ* in lakes (e.g., Sinninghe Damsté et al., 2009) and marine sediments (Peterse et al., 2009; Fietz et al., 2012).

However, their biological producer has not been identified yet. Some minor amounts of brGDGT-I have been found in cultured strains of *Acidobacteria* (Schouten et al., 2013). Elevated abundances of brGDGTs in the anoxic part of soils were taken as evidence that they were synthesized by anaerobic soil-thriving bacteria (Weijers et al., 2006b). BrGDGTs feature characteristics of both bacteria (an alkyl chain with a basic structure of 13, 16-dimethyloctacosane as membrane lipids) and archaea (cyclopentane rings). The opposite stereochemistry of their glycerol moiety compared to archaeal isoGDGTs as identified by Weijers et al. (2006b) is a distinctive evolutionary differentiator between membrane lipids of bacteria and archaea (Koga et al., 1998). Even though the biological sources of brGDGTs are yet unknown, several proxies based on their distribution exist to infer information on mean annual air temperature (methylation of branched tetraethers-cyclization of branched tetraethers; MBT´-CBT; Weijers et al. 2007; Peterse et al., 2012), soil pH (CBT, Weijers et al., 2007) or for tracking soil organic matter inputs into sediments (branched and isoprenoid tetraether index, BIT; Hopmans et al., 2004). Hopmans et al. (2004) proposed the BIT index which is based on the relative abundances of brGDGTs-I, -II, and -III (Fig. 1.15) and crenarchaeol (Fig. 1.11) as a proxy for the quantification of terrestrial-derived organic matter. Crenarchaeol was initially thought to be a characteristic membrane lipid of non-thermophilic archaea and specifically Thaumarchaeota abundantly occurring in marine and lacustrine environments (e.g., DeLong et al., 1998; Sinninghe Damsté et al., 2002). However, it has been identified later on also in cultured thermophilic Thaumarchaeota (De la Torre et al., 2008) and terrestrial hot springs (Pearson et al., 2008), therefore obscuring its physiological role (Inglis and Tierney, 2020).

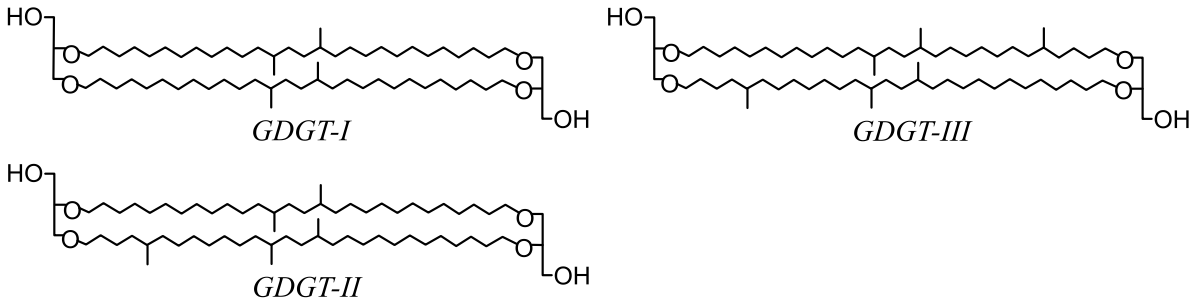

Figure 1.15 | Structures of brGDGTs-I, -II, and -III relevant for the calculation of the BIT index.

As brGDGTs are found in dust only in negligibly small amounts and are commonly elevated in river-suspended particulate matter and river sediments, it has been suggested that the BIT is representative of riverine transport (Schouten et al., 2013; and references therein). BIT index values of 1 are found in soils and peat and BIT values approaching 1 represent high fluvial inputs of soil organic matter, whereas values close to 0 represent an open marine setting

receiving negligible inputs of terrestrial-derived soil organic matter. A value of 0.3 has been proposed as a threshold for the reliable application of the TEX_{86} for reconstructing water temperatures (Weijers et al., 2006a), as higher inputs of terrestrial-derived GDGTs may potentially affect and hence compromise TEX_{86}-based temperature reconstructions (Weijers et al., 2006a; Schouten et al. 2013).

NIC

Chapter 2

Study sites

In order to provide some background information on the regional setting of the study area, this chapter will start off with a brief introduction to the tectonic evolution of the Shikoku Basin and the Izu-Bonin arc. The description of the study sites will include an overview of their present and past locations, depositional setting and lithology as well as their age models.

The data generated during this doctoral project is based on deep-sea sedimentary sequences drilled at two sites in the northern Shikoku Basin and the Izu-Bonin rear arc during International Ocean Discovery Program (IODP; formerly Integrated Ocean Drilling Program) Expeditions 333 and 350, respectively. Expedition 333 "NanTroSEIZE Stage 2: Subduction Inputs 2 and Heat Flow" took place in December 2010/ January 2011 and drilled at Site C0011 in the Nankai Trough area south of Japan. The recovered sediments span a time interval from the late Miocene to the present day. IODP Expedition 350 "Izu-Bonin-Mariana Rear Arc: the missing half of the subduction factory" drilled at Site U1437 in the Izu-Bonin rear arc in April and May 2014. Sediments from Site U1437 that were studied for this project cover the last ~4 Ma. One of the main objectives of the doctoral project was to reconstruct the long-term paleoceanographic and paleoclimatic evolution of the Northwest Pacific Ocean and adjacent East Asian continent, with emphasis on the subtropical Kuroshio Current and its northern counterpart, the subpolar Oyashio Current, and their impact on East Asian climate.

2.1. Tectonic evolution of the study area in the NW Pacific

At present, the Japanese islands are situated on four different plates: the Eurasian Plate, the North American Plate, the Philippine Sea Plate, and the Pacific Plate (see inset map in Fig. 2.1). Subduction of the Pacific Plate beneath the Philippine Sea Plate and associated igneous activity were initiated during the Eocene at ~52 Ma and ultimately resulted in the formation of the intraoceanic Izu-Bonin-Mariana arc system (Tamura et al., 2015a). The first mature arc, the Kyushu-Palau arc, formed during the Eocene and Oligocene (Tamura et al. 2015a). The lithosphere of the Shikoku Basin, a back-arc basin in the northern part of the Philippine Sea Plate, was formed by back-arc spreading and rifting in the eastern part of the plate between 25 and 15 Ma (Okino et al., 1994). This back-arc spreading and rifting and associated opening of

the Shikoku Basin resulted in the isolation of the Kyushu-Palau arc from the paleo-Izu-Bonin arc and formed the Kyushu-Palau ridge, a remnant arc, which today forms the western boundary of the Shikoku Basin. Even though the precise reason for the termination of major spreading in the Shikoku Basin at 15 Ma is to date unknown, a potential cause may be the beginning subduction of the northern Philippine Sea Plate including the Shikoku Basin spreading ridge beneath SW Japan by that time (Kimura et al., 2005). Late-stage rifting in the Shikoku Basin may have continued until 10 to 7 Ma (Ike et al., 2008; and references therein). The Shikoku Basin is confined by the convergent plate boundary of the Nankai Trough in the north, the Izu-Bonin arc in the east, the Kyushu-Palau ridge in the west and passes over into the Parece Vela Basin, another inactive back-arc basin, in the south (Fig. 2.1).

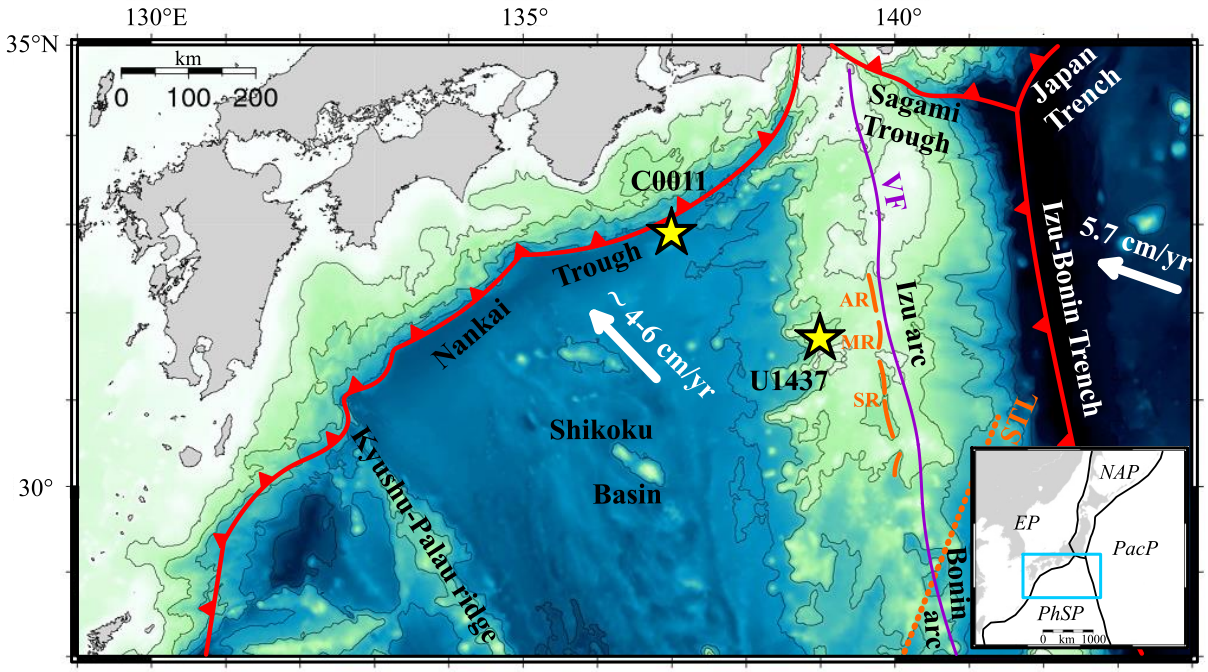

Figure 2.1 | Bathymetric map of the northern Shikoku Basin including characteristic features. Convergent plate margins are indicated by red barbed lines. The inset map shows the major tectonic plates around Japan and their convergent plate margins. The blue rectangle represents the section of the bathymetric map. PhSP = Philippine Sea Plate, EP = Eurasian Plate, PacP = Pacific Plate, NAP = North American Plate. The white arrows give the direction and rate of subduction of the Philippine Sea Plate beneath the Eurasian Plate and the subduction direction and rate of the Pacific Plate beneath the Philippine Sea Plate. The dotted orange line displays the Sofugan Tectonic Line (STL) that separates the Izu arc from the Bonin arc. Orange solid lines give the locations of active rifts in the Izu arc to the west of the active volcanic front (VF, purple line). AR = Aogashima Rift; MR = Myojin Rift; SR = Sumisu Rift. Study site locations are given by yellow stars.

As mentioned before, subduction of the Philippine Sea Plate beneath the Eurasian Plate began in the middle Miocene around 15 Ma. Following a relatively stagnant phase between 14-9 Ma, subduction of the Philippine Sea Plate picked up after 8 Ma and resulted in widespread volcanic activity in southern Kyushu and by 6 Ma also in southwest Japan (Taira, 2001). The subduction of the Philippine Sea Plate at the Nankai Trough created a frontal accretionary prism to the SW

Japan forearc, the Nankai accretionary prism (Taira, 2001; and references therein), which comprises large amounts of deformed trench sediments (Ike et al., 2008).

2.2. IODP Expedition 333 Site C0011

Site C0011 was drilled during IODP Expedition 333 ("NanTroSEIZE Stage 2: Subduction Inputs 2 and Heat Flow") in 2010/2011 in the Nankai Trough area southeast of Japan. The Nankai Trough is a subduction zone located south of Honshu, where the Philippine Sea Plate is subducted at its northern edge beneath the Eurasian Plate at rates of presently 4-6 cm/year (Henry et al., 2010). As a result of high sediment fluxes from the Japanese continental margin, the Nankai Trough is filled with sediments. Site C0011 is located at 32°49.7436´ N, 136°52.9250´ E in a water depth of 4050 mbsl on the northwestern flank of a prominent bathymetric high in the Shikoku basin, the Kashinosaki Knoll (Ike et al., 2008), ~150 km southeast off the coast of Japan (Fig. 2.1).

2.2.1. Lithology description and age model

The sediment samples used for this study were obtained from Site C0011 Holes C and D. The total length of the recovered sediment succession from these two holes is 377 m. The lithology consists of silty clay and clayey silt and clays interbedded with more or less prominent thin layers of tephra and volcaniclastic sands, tuffaceous sandstones and heterolithic gravels (Expedition 333 Scientists, 2012). Holes C and D were divided into two lithostratigraphic units, the Upper and Lower Shikoku Basin facies. The uppermost 347.82 meters below seafloor (mbsf) represent Shikoku Basin facies Unit I, which is subdivided into Unit I A (0-251.52 mbsf) and heavily bioturbated Unit I B (251.52-347.82 mbsf). Subunit I A consists of soft hemipelagic clays and silts that are interbedded with abundant thin volcanic ash layers, whereas the dominant lithology in Subunit I B is a heavily bioturbated mudstone. The boundary between Units I A and B is characterized by an abrupt appearance of abundantly burrowed and moderately consolidated mudstone and was dated to ~5.32 Ma (Expedition 333 Scientists, 2012). The deposition of both subunits was dominated by hemipelagic settling (Expedition 333 Scientists, 2012). Shikoku Basin facies Unit II (347.82-377 mbsf) comprises coarse-grained tuffaceous sandstones and heterolithic sands and gravels. The base of Unit II was not drilled during Expedition 333, but previous drilling at Hole C0011 B during IODP Expedition 322 showed that it extends down to ~479 mbsf (Expedition 322 Scientists, 2010). The depositional

environment of Unit II was supposedly dominated by sediment transports within a sandy turbidite system (Expedition 333 Scientists, 2012).

The shipboard age model at Site C0011 is based on biostratigraphy, magnetic reversal events as well as the identification of volcanic marker events with radiometrically dated onland equivalents (Fig. 2.2).

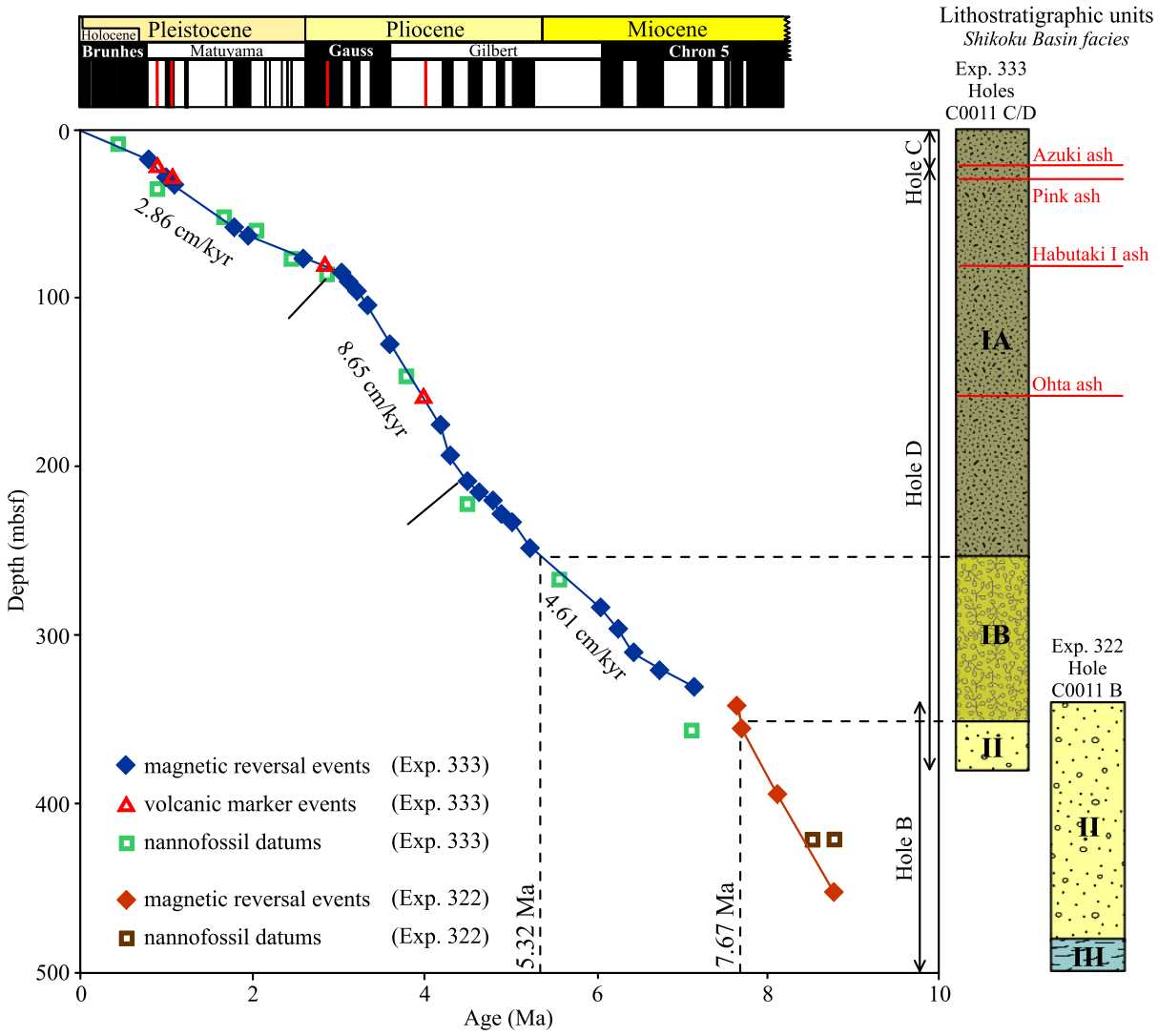

Figure 2.2 | Age model of Site C0011 based on magnetic reversal events (blue curve for IODP Expedition 333 Holes C/D; red curve for Expedition 322 Hole B), volcanic marker events and nannofossil datums, including averaged sedimentation rates. The bars on the right give the lithostratigraphic units of the Shikoku Basin facies as identified onboard in C0011 Holes C/D and B. Identified ash layers with onland equivalents are given as red bars. Modified after Expedition 333 Scientists (2012).

Four tephra layers with radiometrically dated onland equivalents were identified within the sedimentary succession drilled at Site C0011 Holes C and D (Expedition 333 Scientists, 2012) and hence provided useful age tie points (referred to as volcanic marker events in Fig. 2.2): the Azuki ash at 21.18 mbsf (0.85 Ma; Hayashida et al., 1996), the Pink ash at 31.3 mbsf (1.05 Ma; Hayashida et al., 1996), the Habutaki I ash at 80.56 mbsf (2.8-2.9 Ma; Nagahashi and Satoguchi, 2007), and the Ohta ash at 157.26 mbsf (4.0 Ma; Satoguchi et al., 2005).

The average sedimentation rate at Site C0011 Holes C and D is 4.63 cm/ka. Below ~208 mbsf, the sedimentation rate is at 4.61 cm/ka and increases to 8.65 cm/ka in the interval from ~208 to ~90 mbsf. At ~90 mbsf, the sedimentation rate decreases significantly again to 2.86 cm/ka and remains on this level throughout the uppermost ~90 mbsf (corresponding to the last ~3 Ma) (Expedition 333 Scientists, 2012). Based on the shipboard age model, the boundaries between Shikoku Basin facies Subunit I A and I B are at 5.32 Ma and at 7.67 Ma between Units I and II (Expedition 333 Scientists, 2012), respectively.

Expedition 322 Scientists (2010) reconstructed the past positions of Site C0011 based on estimated plate convergence rates and magnetic stripes in the Shikoku Basin. Based on these reconstructions, Site C0011 was located ~350 km southeast of its present position during the middle Miocene (~12 Ma) (Expedition 322 Scientists, 2010). Between 12 and 4 Ma, the site moved ~72 km north-northwestward at a rate of 0.9 cm/year (Fig. 2.3).

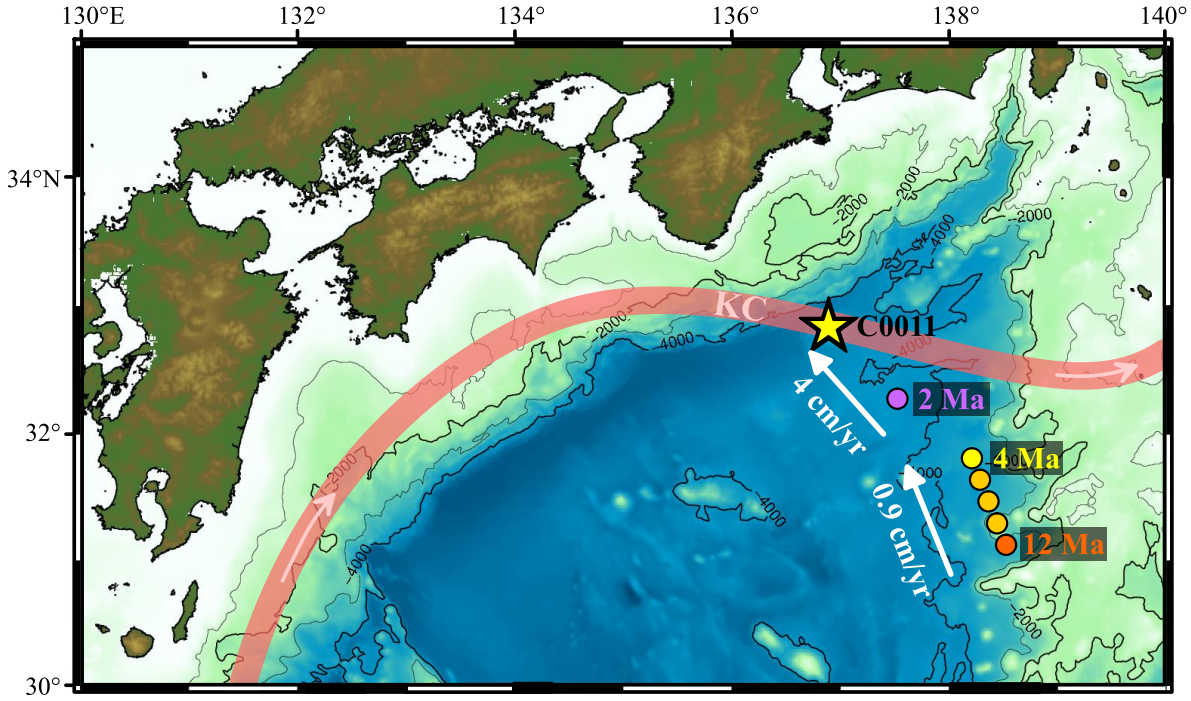

Figure 2.3 | Bathymetric map of the northern Shikoku Basin with the paleogeographic track and the present location (yellow star) of IODP Site C0011. Orange colors display middle (dark orange) and late Miocene (light orange) positions of the site, the yellow circle gives its Pliocene position at ~4 Ma and the purple circle its position at ~2 Ma (Pleistocene). White arrows give the direction and convergence rate at which the Philippine Sea Plate moved north(north-)westward (Kimura et al., 2005). The paleo-positions of Site C0011 were taken from Expedition 322 Scientists (2010) and were calculated based on estimated plate convergence rates and magnetic stripes in the Shikoku Basin. The path of the KC with its offshore short meander configuration is indicated by the pink line.

After that, from 4 Ma to present, Site C0011 continued to move another ~160 km northwestward at an accelerated motion rate of 4 cm/year. The described change in the site´s path parallels a reorientation of the back-arc spreading center in the late Miocene, which is also recorded by a

change in trending of magnetic anomalies from NNW-SSW to NW-SE in the northern Shikoku Basin (Okino et al., 1994; Ike et al., 2008).

The past locations of Site C0011 are far south from the nearshore and offshore short meander paths of the modern KC (Fig. 1.2), which may have reached the Pacific coast of Japan by 3 Ma the latest (see Chapter 6 for the detailed history of the KC). At present, Site C0011 is located beneath the KC short meander provided that the latter is prevailing.

2.3. IODP Expedition 350 Site U1437

Site U1437 was drilled during IODP Expedition 350 ("Izu-Bonin-Mariana Rear Arc: The missing half of the subduction factory") in spring 2014 in the Izu rear arc, ~330 km west of the axis of the Izu-Bonin Trench (Expedition 350 Scientists, 2014). The site lies in a volcano-bounded basin between the Manji and Enpo rear arc seamount chains to the west of an extensional zone with active rifting, which comprises – from north to south – the Aogashima, Myojin, and Sumisu rifts (Fig. 2.1). Site U1437 is located at 31°47.3911′ N, 139°01.5788′ E in a water depth of 2116 mbsl and was drilled to 1806.5 mbsf (Expedition 350 Scientists, 2014). At present, sites C0011 and U1437 are ~233 km apart.

2.3.1. Lithology description and age model

Consecutive drilling in Holes B, D and E recovered a stratigraphic succession that was distinguished onboard into seven different lithostratigraphic units. These units consist mainly of tuffaceous mud and mudstones with intercalated volcaniclastic layers in the uppermost 1300 m (lithostratigraphic units I-V) and gradually change to dominantly volcaniclastic layers below that depth (units VI-VII) (Expedition 350 Scientists, 2014) (Fig. 2.4). The different units were distinguished from one another based on the proportion and characteristics of the volcaniclastic layers relative to the tuffaceous mud and mudstone (Expedition 350 Scientists, 2014). Shipboard biostratigraphy and magnetic reversal event identification assigned an age range of late Miocene (8.771 Ma) to Holocene to the uppermost 1303 m of the sedimentary succession recovered from Site U1437 (Expedition 350 Scientists, 2014).

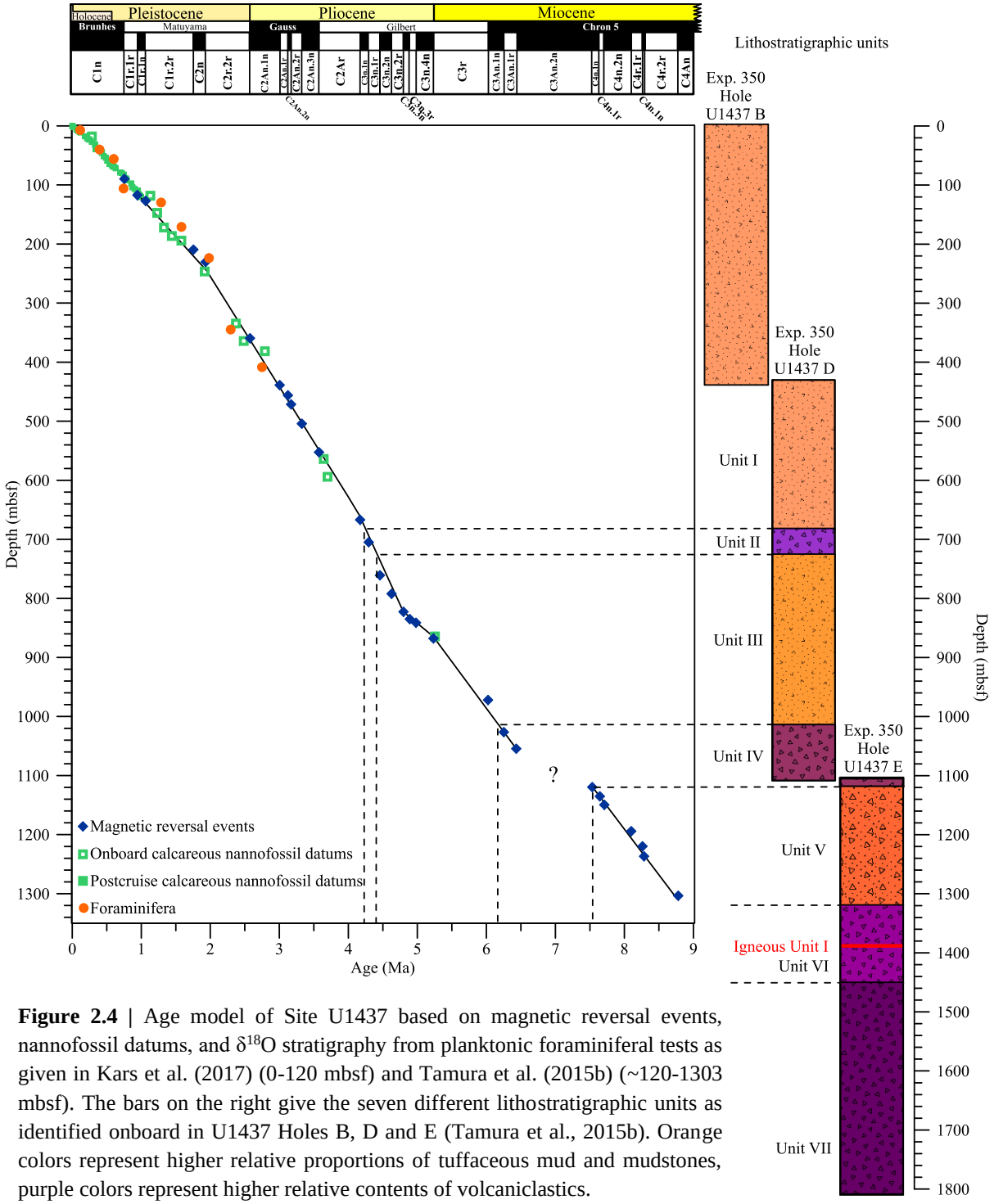

Figure 2.4 | Age model of Site U1437 based on magnetic reversal events, nannofossil datums, and $\delta^{18}O$ stratigraphy from planktonic foraminiferal tests as given in Kars et al. (2017) (0-120 mbsf) and Tamura et al. (2015b) (~120-1303 mbsf). The bars on the right give the seven different lithostratigraphic units as identified onboard in U1437 Holes B, D and E (Tamura et al., 2015b). Orange colors represent higher relative proportions of tuffaceous mud and mudstones, purple colors represent higher relative contents of volcaniclastics.

Lithostratigraphic Unit I (0-682.1 mbsf) spans the uppermost 4.3 Ma and consists mainly of mud or mudstone with >25% dispersed ash, referred to as tuffaceous mud and tuffaceous mudstone (Expedition 350 Scientists, 2014), respectively. Subsequent lithostratigraphic Unit II (682.1-726.5 mbsf) has much more abundant tephra layers and much less tuffaceous mudstone, and the tephra layers are coarser (lapilli-size) than in Unit I and subsequent Unit III. Unit III (726.5-1017.8 mbsf) consists of tuffaceous mudstone and less abundant tuff layers.

Lithostratigraphic Unit IV (1017.8-1120.1 mbsf) is composed of coarse-grained tuff and polymictic lapilli tuff and lapillistone layers with minor tuffaceous mudstone intervals. Underlying Unit V (1120.1-1320.0 mbsf) is distinguished from the surrounding units mostly based on its intervals of monomictic, reversely graded lapilli tuff which contrast with the polymictic, dominantly lithic lapilli tuff layers of the overlying and underlying lithostratigraphic units. Unit VI from 1320.0 to 1456.8 mbsf is dominated by thick beds of lapilli tuff and lapillistone with lesser tuff and minor tuffaceous mudstone intervals and is characterized by abundant polymictic lithic and pumice lapilli tuffs. A ~1 m thick single rhyolitic-dacitic intrusion, the only igneous unit observed at Site U1437, lies within lithostratigraphic Unit VI at 1388.9-1390.1 mbsf. The top of the lowermost lithostratigraphic Unit VII is at 1456.8 mbsf and its base was not recovered during drilling down to 1806.5 mbsf in Hole E. Unit VII is dominated by thick bedded, nongraded, nonstratified, poorly sorted, coarse-grained angular andesitic lapilli tuff.

Paleogeographic positions of Site U1437 from the early Miocene (20 Ma) to present were calculated and kindly provided by fellow cruise participant Robert J. Musgrave (personal communication) and are displayed in Fig. 2.5.

From the early Miocene (20 Ma) to the early Pliocene (5 Ma), Site U1437 moved ~1030 km northeastward, and another ~155 km west-northwestward from 5 Ma onwards to its present location. The initial northeastward movement of the site´s position resulted from a clockwise rotation of the Philippine Sea Plate by 90° around the Euler pole at 23 °N, 162 °E between 50 and 15 Ma (Kimura et al., 2005; Yamazaki et al., 2010) and continued spreading and rifting in the Shikoku Basin, which commenced in the late Oligocene (Okino et al., 1994). The site´s westnorthwestward movement after 5 Ma is potentially associated with intra-arc rifting which started in the Pliocene (Expedition 350 Scientists, 2014). Today, active rifting in the extensional zone between the *en echelon*-aligned rear arc seamount chains and the active volcanic front occurs – from north to south – ~10-15 km to the west of the volcanic front at the Aogashima, Myojin, and Sumisu rifts (Expedition 350 Scientists, 2014).

At present, Site U1437 is located beneath the KC large meander when the latter is present.

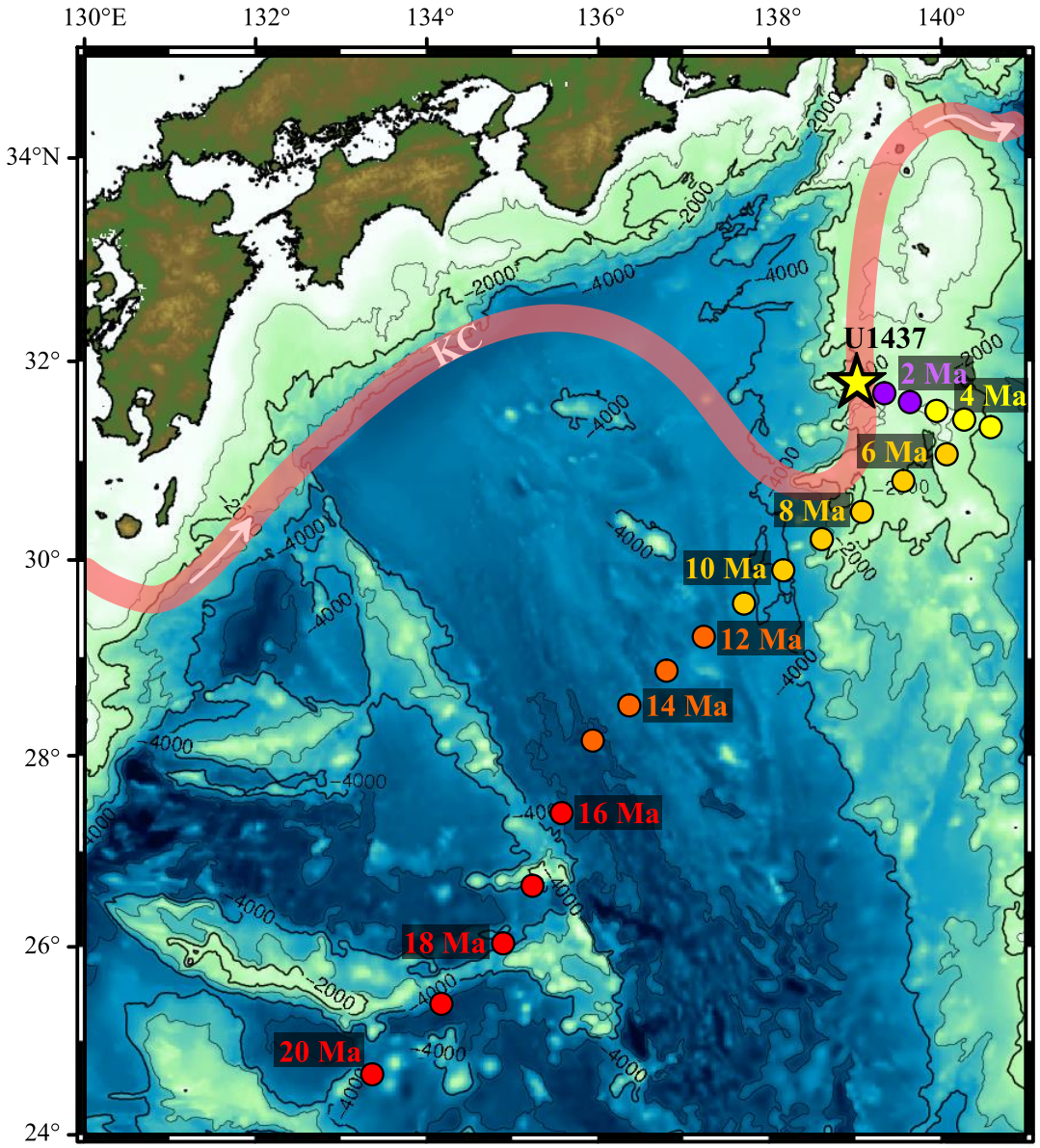

Figure 2.5 | Bathymetric map of the Shikoku Basin with the paleogeographic track of Site U1437 from the early Miocene (red) to its present location (yellow star). Orange circles display middle (dark orange) and late Miocene (light orange) positions of the site, yellow circles give the Pliocene positions and the purple circles show the site´s position during the Pleistocene. The paleo-positions of Site U1437 were calculated and kindly provided by Robert J. Musgrave (personal communication). The path of the KC with its large meander configuration is indicated by the pink line.

Chapter 3

Objectives and outline of this thesis

This PhD thesis was funded by the German Research Foundation (DFG) through project grants BA 3841/4-1 and BA 3841/6-1 awarded to Dr. Thorsten Bauersachs as well as grants SCHW 554/27-1, 2 given to Prof. Dr. Lorenz Schwark. These projects targeted the detailed investigation of paleoclimatic and paleoceanographic evolution in the NW Pacific Ocean and on the adjacent East Asian continent both on geological (late Miocene to present) and on shorter (glacial-interglacial) timescales. Thereby, a major objective of this thesis work was to close the existing regional gap of long-term paleotemperature reconstruction in the NW Pacific Ocean as the region provides a crucial link between the tropical and the Subarctic Pacific Ocean through the convergence of the North Pacific´s two major western boundary currents, the Kuroshio and Oyashio currents.

Chapter 1 provides background information on the major features of the oceanic and atmospheric circulation in and over the North(west) Pacific Ocean and East Asian continent, respectively. This chapter also introduces the lipid biomarkers that are used in the framework of this doctoral project.

Chapter 2 describes the two study sites that are used as sedimentary archives to meet the beforementioned scientific objectives.

In **Chapter 4**, the water temperature evolution of the NW Pacific Ocean at IODP Site C0011 is studied over the last two glacial-interglacial cycles. For this, water temperatures are reconstructed using the $U^{K'}_{37}$, LDI and TEX^{H}_{86} paleothermometers and resulting temperature signals from the different proxies are evaluated in terms of production season and habitat depth of their respective source organisms. Three different paleoceanographic scenarios that are characterized by variations in the current strength of the KC and OC and their latitudinal positions are developed and – based on the proxy-based water temperature variations over time – evaluated and discussed in order to reconstruct changes in the paleoceanographic configuration in the NW Pacific Ocean over the past 145 ka.

In **Chapter 5**, a multi-proxy approach is used at Site U1437 in order to characterize changes in the atmospheric and, secondarily, the paleoceanographic circulation over the East

Asian continent as well as over and in the Northwest Pacific Ocean over the course of the past 1 Ma. The atmospheric circulation over these regions is governed by the East Asian winter and summer monsoons and the westerly jet stream and changes in these wind systems result in large seasonal variations in terms of dust flux and rainfall, which has large impact on the local economy and agriculture.

Chapter 6 studies the long-term paleoclimate evolution of the NW Pacific Ocean and adjacent East Asian continent from late Miocene times to the Present using sediments from Site U1437. In this study, a special emphasis is placed on integrating the biomarker-based water temperature records from the study sites south of Japan with existing long-term water temperature records from the entire North and equatorial Pacific Ocean. Furthermore, associated changes in continental vegetation are examined using relative abundances of land plant-derived wax lipids.

In **Chapter 7**, the application of a relatively novel proxy for SST reconstruction, the RI-OH index (Lü et al., 2015) is tested in sediments from IODP Site U1437 spanning the last 1 Ma.

Chapter 8 contains a rock magnetic study that was conducted on sediments from the past 1 Ma at Site U1437 and investigates the paleoenvironmental changes in the NW Pacific Ocean and adjacent Asian continent associated with changes in the East Asian monsoon regime on glacial-interglacial timescales.

Chapter 9 summarizes the findings of this thesis and provides an outlook to proposed future studies that may help answer open questions that arose through the studies in the framework of this thesis.

In **Appendix Chapter 10**, a study of magnetic mineral diagenesis in a high temperature and deep methanic zone at Site U1437 is presented. Magnetic mineral alteration and dissolution in relation to geochemical processes and microbial activity under varying methane concentrations in deeply buried sediments are discussed. For this, samples from the depth interval of 775-1002 mbsf are studied for their rock magnetic properties, mineralogy and geochemical properties and the findings are integrated with data generated onboard R/V *JOIDES Resolution* during Expedition 350.

Chapter 4

Late Quaternary water temperature variations of the Northwest Pacific based on the lipid paleothermometers TEX^{H}_{86}, $U^{K'}_{37}$ and LDI

Ann-Sophie Jonas[1], Lorenz Schwark[1,2], and Thorsten Bauersachs[1]

[1] Department of Organic Geochemistry, Institute of Geosciences, Christian-Albrechts-University, Ludewig-Meyn-Straße 10, 24118 Kiel, Germany.

[2] Department of Chemistry, WA-OIGC, Curtin University, GPO Box U1987, Perth, WA 6845, Australia.

Published in *Deep-Sea Research Part I* 125 (2017), 81-93,
doi:10.1016/j.dsr.2017.04.018.

Abstract

The Kuroshio Current (KC) and Oyashio Current (OC) are the two major western boundary currents of the Pacific Ocean and their interplay exerts a major control on the climate evolution of the northwestern Pacific region as well as East Asia. Although millennial scale variations in the strength and flow pattern of the KC are well documented, only little is known on the long-term evolution of this ocean current and its role in affecting regional and global climate over geological time scales. Here, we present surface and thermocline temperature records covering the last two glacial-interglacial cycles of IODP (Integrated Ocean Drilling Program) Site C0011, SE of Japan, using the lipid paleothermometers TEX^{H}_{86} (tetraether index of tetraethers consisting of 86 carbon atoms), $U^{K'}_{37}$ (unsaturated ketone index) and LDI (long-chain diol index). Lower average water temperatures (20.1-20.7 °C in TEX^{H}_{86}, 21.6-22.0 °C in $U^{K'}_{37}$, and 20.7-21.9 °C in LDI) during marine isotope stages (MIS) 2 and 6 are considered to indicate a reduction in warm water mass export from the Western Pacific Warm Pool (WPWP) to northern mid-latitudes via the KC due to decreased subtropical gyre circulation in the North Pacific. A synchronous southward displacement of the KC/OC interfrontal zone resulted in an overall stronger influence of colder and more polar waters at Site C0011. MIS 1, 3 and 5 are

characterized by generally higher water temperatures (21.7-22.1 °C in TEX^{H}_{86}, 23.2-24.3 °C in $U^{K'}_{37}$, and 23.1-24.3 °C in LDI), likely reflecting an increased northward transport of subtropical waters to the study site. Higher Holocene than Eemian water temperatures are attributed to a stronger KC and the formation of its short meander south of Japan, whereas a less strong KC during the Eemian likely favored the formation of the large meander path. Better correlations between the different lipid paleothermometers during cold MIS are considered to indicate more similar production seasons and habitat depths of the biological proxy sources with the latter factor likely driven by thermocline shoaling.

Highlights

- Lipid-based reconstruction of paleo water temperatures offshore Japan
- Water temperature variations reflect changes in the KC over the last 145 ka
- Offsets in proxy temperatures relate to different production seasons and habitats
- Reduced offsets in production season and habitat depth occur during cold MIS

Key words

Kuroshio Current; Oyashio Current; Sea surface temperatures; Thermocline shoaling; Lipid paleothermometers; IODP Expedition 333; Site C0011

4.1. Introduction

The reconstruction of water temperatures is important for understanding changes in the oceanographic regime (e.g., changes in ocean current strength and flow paths) and their impact on past climate evolution. Various inorganic and organic proxies exist that allow studying changes in surface and thermocline temperatures. Such proxies include e.g. stable oxygen isotopes ($\delta^{18}O$) (Erez and Luz, 1983) and Mg/Ca ratios (Nürnberg et al., 1996) of calcareous nannoplankton and foraminifera as well as the study of microfossil assemblages such as diatoms, radiolarians (Chinzei et al., 1987; Chiyonobu et al., 2012) and planktonic foraminifera (e.g., Thompson, 1981; Kucera et al., 2005). Organic temperature proxies constitute a complementary means to study variations in water temperature over time. One of the most commonly employed lipid paleothermometers is the $U^{K'}_{37}$ (unsaturated ketone index; Prahl and Wakeham, 1987), which is based on the relative distribution of long-chain alkenones derived from haptophyte algae such as *Emiliania huxleyi* or *Gephyrocapsa oceanica* (Volkman et al.,

1980a, b; Marlowe et al., 1984). Since its introduction, the $U^{K'}_{37}$ has been employed to reconstruct sea surface temperature (SST) variations in numerous oceanographic settings, including the Atlantic Ocean (e.g., Kim et al., 2004), the Pacific Ocean (e.g., Sawada and Handa, 1998; LaRiviere et al., 2012; Zhang et al., 2014) and the Mediterranean Sea (Castañeda et al., 2010; Rodrigo-Gámiz et al., 2014). However, the $U^{K'}_{37}$ is not only impacted by temperature, but also by light and nutrient limitation (Versteegh et al., 2001; Herbert, 2003), salinity changes (Schulz et al., 2000), and diagenesis such as selective degradation under oxic conditions (Hoefs et al., 1998; Gong and Hollander, 1999; Huguet et al., 2009). Recently, Rosell-Melé and Prahl (2013) found that the $U^{K'}_{37}$ in marine sediments reflects the annual mean SSTs in a variety of settings regardless of the haptophyte bloom season and highest alkenone fluxes to depth. Off central Japan, however, studies of alkenone distributions in sediment traps revealed that reconstructed SSTs based on $U^{K'}_{37}$ values paralleled actual SSTs and that the maximum alkenone export to depth occurred after the spring bloom (Sawada et al., 1998). This suggests that the $U^{K'}_{37}$ signal preserved in the sediments of the NW Pacific reflects the SST during bloom season. Overall variations in $U^{K'}_{37}$ are thus a result of changes both in the timing of the spring bloom and its blooming intensity relative to the production throughout the rest of the year.

Another commonly used lipid paleothermometer is the TEX_{86} (tetraether index of tetraethers consisting of 86 carbon atoms), which is based on a significant correlation between the distribution of isoprenoid GDGTs of marine Thaumarchaeota and mean annual SST (Schouten et al., 2002). The TEX_{86} has been applied in many oceanic settings, including the tropical and NE Pacific Ocean (e.g., Huguet et al., 2007; Zhang et al., 2014), the Sea of Okhotsk (Harada et al., 2012), the South China Sea (Zhang et al., 2013a), the Southern Ocean (Lopes dos Santos et al., 2013), the Mediterranean Sea (Castañeda et al., 2010; Kim et al., 2015) and the Iceland Basin (Rodrigo-Gámiz et al., 2015). Some organic-geochemical and microbiological studies indicate that the TEX_{86} may more accurately reflect subsurface water temperatures instead of SSTs or a mixed temperature signal of the water column (e.g., Huguet et al., 2007; Lopes dos Santos et al., 2010; Rommerskirchen et al., 2011; Kim et al., 2012; Yamamoto et al., 2012) as maximum cell numbers of pelagic Thaumarchaeota occur in water depths up to 1000 m in the global oceans (Karner et al., 2001; Herndl et al., 2005). In addition, Kim et al. (2015, 2016) as well as Elling et al. (2015) found evidence that the presence of different archaeal populations within or below the surface mixed layer may alter the temperature signal preserved in sedimentary sequences. Similarly, Zhu et al. (2016) showed that the relationships of the TEX_{86} calculated from the distribution of intact polar lipid GDGTs (the biological precursor of the

more stable core lipids) and temperature differed significantly between epipelagic waters and those found below. Nonetheless, the same authors also showed that TEX_{86} based on core lipid distributions correlates well with *in situ* temperatures in waters <100 m but not at greater depth. Furthermore, the metabolic state (Elling et al., 2014), the ammonia oxidation rate (Hurley et al., 2016) and the production season of GDGTs (Grauel et al., 2013; Lopes dos Santos et al., 2013) may affect the TEX_{86} and it may yield erroneous results at sites receiving larger inputs of soil organic matter (Weijers et al., 2006a).

In addition to the $U^{K'}_{37}$ and the TEX_{86}, the LDI (long-chain diol index) represents a promising novel tool for the reconstruction of water temperatures in marine systems (Rampen et al., 2012). This proxy is based on the sedimentary distribution of long-chain diols (LCDs), which are generally thought to be synthesized by eustigmatophyte algae (Volkman et al., 1992; Rampen et al., 2014). The LDI shows strong positive correlation with late summer water temperatures from the uppermost 30 m of the water column in globally distributed marine core-top sediments (Rampen et al., 2012). Similar observations have been made in multi-proxy studies from the Southern Ocean (Lopes dos Santos et al., 2013) and in the Alboran Sea (Rodrigo-Gámiz et al., 2014). Although this proxy has been applied only to a limited number of marine sediments yet, comparison of reconstructed SSTs with those of other lipid paleothermometers over time indicate overall similar trends, although usually somewhat higher compared to $U^{K'}_{37}$- and TEX_{86}-based temperatures (Lopes dos Santos et al., 2013; Rodrigo-Gámiz et al., 2014; Becker et al., 2015). Similar impacts by environmental factors as for the $U^{K'}_{37}$ are also expected for the LDI, which showed minor correlations with salinity and nutrient availability (Rampen et al., 2012) and has also been shown to be affected by oxic degradation (Rodrigo-Gámiz et al., 2016). However, the effects of changing environmental parameters such as nutrient concentrations on lipid biosynthesis of LCDs and thus on the LDI are only poorly constrained at present and need more comprehensive studies in the future.

4.1.1. Paleoceanography of the NW Pacific

The NW Pacific has been subject of several paleoceanographic studies, which targeted the reconstruction of variations in the current strengths and flow paths of the two major western boundary currents of the NW Pacific (Fig. 4.1), the Kuroshio Current (KC) and the Oyashio Current (OC) (e.g., Chinzei et al., 1987; Sawada and Handa, 1998; Harada et al., 2004; Oba et al., 2006; Sagawa et al., 2006; Minoshima et al., 2007; Koizumi and Yamamoto, 2010; Matsuzaki et al., 2014; Yasudomi et al., 2014). The KC forms east of the Philippines, where the westward flowing North Equatorial Current (NEC) splits into the northward flowing KC

and the southward flowing Mindanao Current (Qiu, 2001), transporting warm, saline and oligotrophic water masses from the Western Pacific Warm Pool (WPWP) to northern mid-latitudes (Sawada and Handa, 1998). The KC has a total length of ~3000 km and a width of less than 100 km with a maximum depth of ca. 1 km (Barkley, 1970).

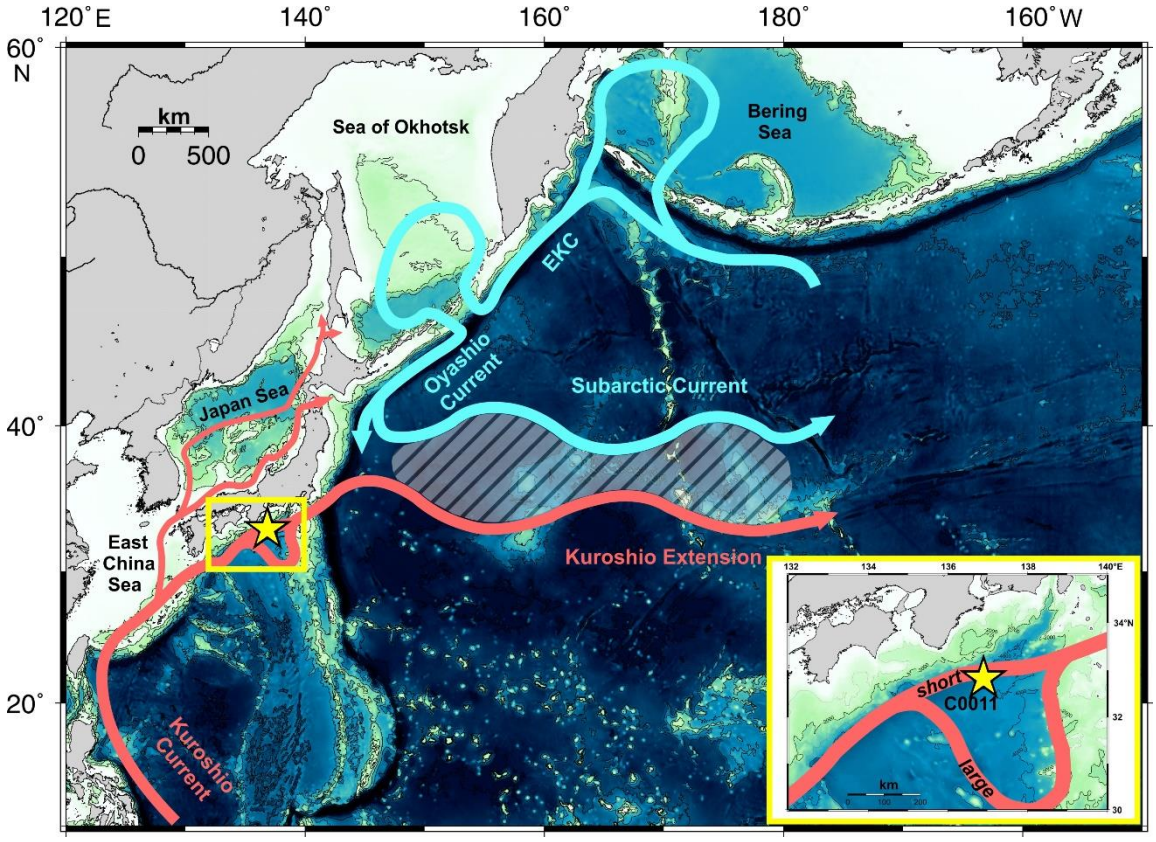

Figure 4.1 | Bathymetric map of the Northwest Pacific showing the flow path of the two major western boundary currents: the Kuroshio Current (red) and the Oyashio Current (blue) and their interfrontal zone (shaded area) including a detailed bathymetric map of the Nankai Trough area with both the short and large meander path configurations of the KC being displayed. The yellow star marks Site C0011, which was drilled during IODP Expedition 333.

Studies of the zonally averaged (141-150 °E) axis position and surface transport of the Kuroshio Extension (KE), the offshore prolongation of the KC in the N Pacific (Fig. 4.1), between 1992 and 1998 showed a maximum northward extension and transport during summer and fall (Tatebe and Yasuda, 2001). The KE is the area with the largest heat loss from the ocean to the atmosphere in the NW Pacific and one of the biggest globally (Qiu et al., 2004). Hence, variations in the strength and meridional transport of heat and moisture via the KC strongly affect the overlying atmosphere and are both considered to play a key role in the climate evolution of the NW Pacific including the Japanese islands and the East Asian continent (Sawada and Handa, 1998). Millennial-scale latitudinal fluctuations in the flow path of the KC as part of the wind-driven subtropical gyre are thought to result from variation in trade wind

intensity, which is directly influenced by the strength of the subtropical high-pressure over the North Pacific Ocean (Sawada and Handa, 1998). The strengthening of this high-pressure results in a stronger North Pacific Subtropical Gyre circulation and in turn in a more efficient heat transport from the WPWP to northern mid-latitudes via the KC. Superimposed on these millennial-scale variations, changes in the current velocity and volume transport of the KC lead to shorter-term (annual to decadal) aperiodic variations in the meander path of the KC southeast of Japan (Kawabe, 1995, 2005; Sawada and Handa, 1998; Qiu, 2001). Previous studies suggest that an enhanced volume transport of the KC fosters the formation of the short KC meander SE of Japan (Yasuda et al., 1985; Tsujino et al., 2013; Usui et al., 2013), which then passes Site C0011 (Fig. 4.1). The presence of the short meander results in SSTs that are often considerably higher than in areas further south. The large meander, on the other hand, has been suggested to preferentially form when volume transport and current velocity of the KC are low. During phases of the KC large meander, warm KC surface waters are found further offshore, leading to the establishment of a large cold surface water mass off central Japan (Sawada and Handa, 1998). The transport strength of the KC also shows seasonal variations with a weak maximum in summer and a weak minimum during winter, resulting from interaction with bottom topography and eddy activity (Kagimoto and Yamagata, 1997).

The Oyashio Current is the second large western boundary current of the North Pacific Ocean and merges with the KC at ~36 °N and ~145 °E (Fig. 4.1), where they form an interfrontal mixing zone. The cold, less saline and nutrient-rich OC is the southernmost extension of the subpolar East Kamchatka Current (EKC) and forms in the Sea of Okhotsk, where the polar waters of the EKC are modified due to sea ice formation and the mixture with Okhotsk Sea waters (Qiu, 2001). The OC splits southeast of Hokkaido (at about 43°N and 145°E) into a southward heading path (Fig. 4.1) that strictly follows the coastline of Honshu (Yasuda et al., 1996; Yasuda, 2003; Qiu, 2001) and an offshore path, that heads eastward and rejoins the Western Subarctic Gyre (Yasuda, 2003). During periods of global cooling, the OC migrates to more southerly latitudes in response to changes in the Okhotsk High and Aleutian Low as indicated by cold SST anomalies east of Japan (Ogi et al., 2004) and intrudes into the intermediate layer of the subtropical KC waters off the east coast of Japan (Yang et al., 1993; Oba et al., 2006; Yasudomi et al., 2014). Besides these long-term variations, OC intensities show large seasonal variations in terms of transport and velocity (Qiu, 2002) with an intensification in early winter and a maximum in winter-spring associated with a southward shift of the westerly jet axis (Isoguchi and Kawamura, 2006). During March and April, the OC coastal branch off Honshu extends to 38.8 °N, whereas it retreats to 41.2 °N in November

averaged over a ~40-year time interval from 1960 to 2001 (Yasuda, 2003). Winter mixing leads to an upwelling of nutrients to the sea surface causing an extensive spring bloom, which is mostly composed of diatoms (Yatsu et al., 2013).

The interfrontal mixing zone between the oceanic fronts of the KC and OC has a mixed signal in terms of temperature and salinity and is characterized by intense formation of mesoscale eddies (Shimizu et al., 2001) and a complex upwelling of North Pacific Intermediate Water (NPIW) (Yasuda, 2003), leading to a large primary productivity in this area (Koizumi and Yamamoto, 2010). In the past, the KC and OC and their interfrontal mixing zone were displaced north- or southward in response to global climate change (Chinzei et al., 1987; Harada et al., 2004; Oba et al., 2006; Koizumi and Yamamoto, 2010; Yasudomi et al., 2014), thereby exerting a significant control on the regional climate evolution of the NW Pacific and the East Asian region. For explaining the water temperature evolution at Site C0011 SE of Japan, different scenarios of changes in the oceanographic regime are conceivable (Fig. 4.2):

1) High export of warm surface water masses from the WPWP to northern mid-latitudes during times of a strong KC. Due to high current velocity and a large volume transport, the KC takes the short meander path SE of Japan and passes Site C0011 (Fig. 4.2). During this scenario, the KC/OC interfrontal mixing zone is located up north and water temperatures at Site C0011 are high (Fig. 4.2a).
2) The meridional heat transport via the KC is decreased; current velocity and volume transport are reduced, favoring the formation of the large meander. The interfrontal mixing zone is still located up north, but temperatures are lower due to the absence of warm KC waters and the formation of a cold surface water mass over Site C0011 (Fig. 4.2a).
3) The KC is weak and displaced southward as suggested by several studies (Kawahata and Ohshima, 2002; Yamamoto et al., 2004; Gallagher et al., 2015; and references therein). Concurrently, the KC/OC interfrontal mixing zone shifts southward. Due to the direct influence of cold waters from the polar OC, water temperatures at Site C0011 are at their minimum (Fig. 4.2b).

The paleoceanography of the KC and OC and their effect on the climate evolution of the NW Pacific Ocean since the last deglaciation has been studied intensively (e.g., Chinzei et al., 1987; Sawada and Handa, 1998; Harada et al., 2004; Oba et al., 2006; Sagawa et al., 2006; Minoshima et al., 2007; Koizumi and Yamamoto, 2010; Yamamoto et al., 2013; Yasudomi et al., 2014).

Yet, only little information on the variability of both ocean currents over longer time scales and their impact on the paleoclimatic evolution of the NW Pacific and adjacent continental areas is available (e.g., Thompson and Shackleton, 1980; Thompson, 1981; Oba et al., 2006; Matsuzaki et al., 2014; Yasudomi et al., 2014).

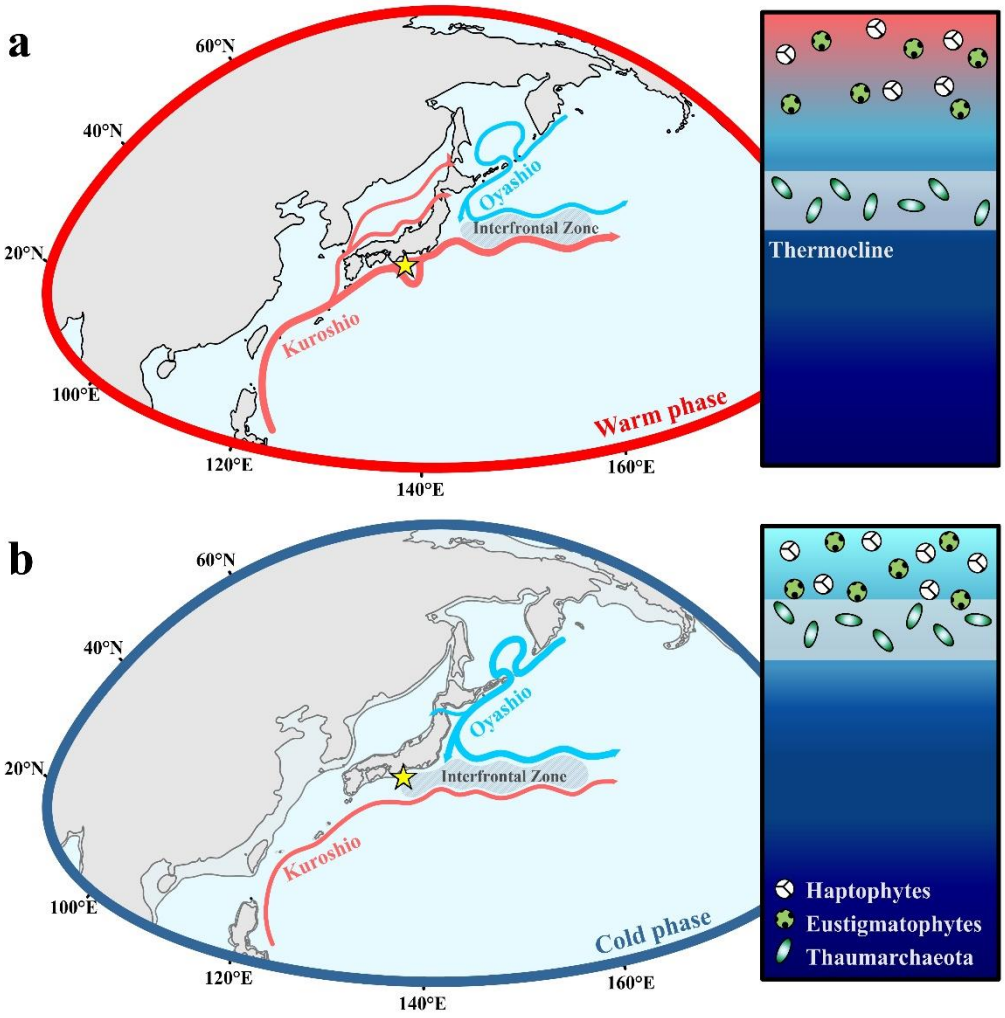

Figure 4.2 | Oceanographic scenarios of the NW Pacific during warm phases (a) and cold phases (b). During warm phases, the heat export from the WPWP via the KC is strong and the KC takes the short meander SE of Japan and passes Site C0011 (scenario 1). In warm phase scenario 2, the KC is less strong, which favors the formation of the large meander. In both scenarios, the KC/OC interfrontal zone is located up north. During cold phases (b), the KC is weak and displaced southward, allowing for a southward shift of the KC/OC interfrontal zone and a direct influence of cold OC waters at Site C0011 (scenario 3). Associated fluctuations in the depth of the thermocline result in larger (a) or smaller (b) offsets in habitat depth of Thaumarchaeota, haptophytes and eustigmatophytes.

In this study, we reconstructed surface ($U^{K'}_{37}$ and LDI) and thermocline (TEX^{H}_{86}) water temperature variations of the NW Pacific SE of Japan over the last two glacial-interglacial cycles (from ~145 ka to the present day) using the three lipid paleothermometers TEX^{H}_{86}, $U^{K'}_{37}$ and LDI, also with respect to climate events such as the Younger Dryas (YD) and the late Pleistocene Heinrich events (HEs). These have previously been identified in the NW Pacific

(Chinzei et al., 1987; Sagawa et al., 2006; Koizumi, 2008), the Okinawa Trough (Li et al, 2001; Shi et al., 2014) and the Sea of Okhotsk (Harada et al., 2004, 2012). HEs are periods of strong sea ice melting and deposition of ice-rafted debris (IRD). They have initially been described from sediments of the NE Atlantic Ocean and been shown to be insolation-driven occurring at each half-period of a precession cycle (Heinrich, 1988). IRD layers in the Sea of Okhotsk (Gorbarenko et al., 2010) and several IRD deposits on the Shirshov Ridge in the western Bering Sea (Levitan et al., 2013) occur synchronously with the North Atlantic HEs. In addition, the applied multi-proxy approach also aims at elucidating proxy-specific biases in the reconstruction of water temperatures due to seasonality and differences in the preferred habitat depth of the biological sources of the TEX^{H}_{86}, $U^{K'}_{37}$ and the LDI.

4.2. Materials and methods

4.2.1. Sampling of sediments

In this study, we investigated deep-sea sediments from Integrated Ocean Drilling Program (IODP) Expedition 333 Site C0011 (32° 49.7436´ N, 136° 52.9250´ E; see Fig. 4.1). The site is located at a water depth of 4050 m on the northwestern flank of the Kashinosaki Knoll, which is a bathymetric high situated in the Shikoku Basin (Ike et al., 2008). Onboard dating via biostratigraphy, the identification of magnetic reversal events and volcanic marker events indicates that the investigated sediment sequence covers a time period from 0 to 145 ka (Expedition 333 Scientists, 2012). Distinct events identified in our records, such as a warm temperature peak at ~14.4 ka and temperature minima corresponding to HEs coincide with SST peaks and minima in other records off central Japan (e.g., Oba et al., 2006; Sagawa et al., 2006), suggesting that the shipboard age model and assumed sedimentation rates allow an accurate dating of the studied sediment interval. The sediments consist mainly of hemipelagic mud and mudstones with mm- to cm-thick intercalations of volcanic ash and volcaniclastic sands (Expedition 333 Scientists, 2012). Samples were collected within 24 hours after core recovery and stored at -80 °C onboard the *R/V Chikyu*. A total of 102 samples were taken every 1 cm throughout the uppermost 27 cm and every 2 to 7 cm below that depth providing sufficient core recovery. Therefore, the temporal resolution is ~0.3 ka in the uppermost 27 cm and 1-3 ka in the lower part of the studied interval. All samples were shipped on dry ice to Christian-Albrechts-University, where they were kept frozen at -18 °C until further processing.

4.2.2. Lipid extraction and fractionation

Deep-sea sediments were lyophilized and homogenized using an agate mortar and pestle. 5-15 g of each sample were solvent-extracted with a Büchi Speed Extractor E-914 (Büchi, Switzerland) at elevated temperature (75 °C) and pressure (50 bar) with a solvent mixture of dichloromethane (DCM):methanol (MeOH) (93:7, v:v). Total lipid extracts (TLEs) were desulfurized overnight using activated copper turnings to remove elemental sulfur. In the following, they were evaporated to near dryness under vacuum, transferred to pre-weighed vials and dried under a gentle stream of N_2. An aliquot of each TLE (~1 mg) was separated into hydrocarbon, ketone (containing alkenones) and polar fractions (containing GDGTs) using a small Pasteur pipette filled with 3.5 cm of silica (SiO_2), which was overlain by 1.5 cm alumina oxide (Al_2O_3). Individual fractions were eluted subsequently with *n*-hexane/DCM (9:1, v:v), *n*-hexane:ethylacetate (7:3, v:v) and DCM:MeOH (1:1, v:v) as respective solvent mixtures.

4.2.2.1. Unsaturated alkenone analysis

Aliquots of the ketone fractions were subjected to gas chromatography coupled to mass spectrometry (GC/MS) and measured in a concentration of 2 mg/ml on a 7890A gas chromatograph (Agilent, Germany) equipped with a fused silica capillary column (DB-5; 30 m × 0.25 mm, Agilent, Germany). The oven temperature was programmed isothermally at 70 °C for 3 min, from 70 °C to 140 °C at 10 °C/min, from 140 °C to 325 °C at 3 °C/min, and held constant at 325 °C for 20 min. The GC was directly coupled to a 5975B mass spectrometer (Agilent, Germany), which was operated at an electron energy of 70 eV and an ion source temperature of 250 °C. Di- and triunsaturated alkenones, which on several occasions occurred in only low abundances in full scan mode, were quantified in single ion monitoring (SIM) mode at *m/z* 97 to increase intensity. The mass fragment at *m/z* 97 was used in SIM mode as it gave the best signal to noise ratio in full scan measurements on GC/MS. To test whether the use of *m/z* 97 for the analysis of $C_{37:3}$ and $C_{37:2}$ would affect the calculation of the $U^{K'}_{37}$, ten samples spanning the entire temperature range and showing significant differences in signal intensity were selected and measured on both GC/FID and GC/MS systems. $U^{K'}_{37}$ temperature values differed by some 0.1 to 1.3 °C for the same sample between both instrument set-ups, which is well within the range of the calibration error of ± 1.5 °C of the $U^{K'}_{37}$ (Müller et al., 1998). Therefore, the quantification of relative abundances of $C_{37:3}$ and $C_{37:2}$ alkenones using the *m/z* 97 ion was found suitable for the reconstruction of $U^{K'}_{37}$-inferred SSTs. Identification of the target compounds was achieved by direct comparison of alkenone distribution patterns in Nankai Trough deep-sea sediments with those in an axenic culture of *E. huxleyi*. The $U^{K'}_{37}$ was

calculated using the equation (1) given by Prahl and Wakeham (1987) and converted into SSTs using the global core-top calibration (2) of Müller et al. (1998), which covers a temperature range of 0 to 29 °C.

$U^{K'}_{37} = [C_{37:2}] / ([C_{37:2}] + [C_{37:3}])$ (1)

$SST = (U^{K'}_{37} - 0.044) / 0.033$ (2)

Replicate measurements of selected samples resulted in a standard deviation for the $U^{K'}_{37}$ of 0.02 or better, which is equivalent to ± 0.6 °C.

4.2.2.2. Long-chain diol analysis

For the analysis of LCDs, aliquots (~0.5 mg) of the TLE were dissolved in DCM at a concentration of 2 mg/ml and derivatized with N,O-bis(trimethylsilyl)trifluoroacetamide (BSTFA) and pyridine at 60 °C for 2 h. The GC/MS conditions and oven program were similar to the one described for the analysis of unsaturated alkenones with the exception that LCDs were detected and quantified using SIM of the masses *m/z* 313 (C_{28} 1,13- and C_{30} 1,15-diols) and *m/z* 341 (C_{30} 1,13- and C_{32} 1,15-diols), representing characteristic fragment ions of the target LCDs (Versteegh et al., 1997). The LDI was calculated using the fractional abundances (*F*) of LCDs and converted to SSTs using the equations (3, 4) given by Rampen et al. (2012):

$LDI = [FC_{30}\ 1,15\text{-diol}] / ([FC_{28}\ 1,13\text{-diol}] + [FC_{30}\ 1,13\text{-diol}] + [FC_{30}\ 1,15\text{-diol}])$ (3)

$SST = (LDI - 0.095) / 0.033$ (4)

The calibration covers a temperature range of -3 to 27 °C and has an error of ± 2.0 °C (Rampen et al., 2012). Replicate measurements of selected samples gave a standard deviation for the LDI of 0.029 or better, equivalent to ± 0.9 °C.

To determine the influence of non-marine LCD sources on the calculation of LDI-SSTs, fractional abundances of C_{32} 1,15-diols relative to the C_{28} 1,13-, C_{30} 1,13- and C_{30} 1,15-diols were investigated along the profile as described by De Bar et al. (2016).

4.2.2.3. Glycerol dialkyl glycerol tetraether (GDGT) analysis

Aliquots of the polar fractions were dissolved in *n*-hexane:2-propanol (99:1, v:v) at a concentration of 3 mg/ml before they were filtered through a polytetrafluoroethylene (PTFE) filter (45 µm mesh size). GDGTs were analyzed using high performance liquid chromatography coupled to mass spectrometry (HPLC/MS) using the method originally described by Hopmans et al. (2004) and the gradient profile of Liu et al. (2012). Briefly, GDGTs were separated using an Alliance 2690 HPLC (Waters, UK) equipped with a Prevail Cyano column (2.1 × 150 mm,

3 µm; Grace, US) maintained at a constant temperature of 30 °C. The flow rate was set to 0.2 ml/min. Solvents used were (A) hexane and (B) hexane: 2-propanol (90:10, v:v). Detection of isoprenoid and branched GDGTs (iso- and brGDGTs) was accomplished using a Quattro LC triple quadrupole mass spectrometer (Micromass, UK) equipped with an atmospheric pressure chemical ionization (APCI) interface operated in positive ion mode. Source conditions were identical to those reported in Heyng et al. (2015). GDGTs were detected by selected ion recording (SIR) of their $[M+H]^+$ ions (dwell time = 200 ms) as reported by Hopmans et al. (2000, 2004). TEX^H_{86} values were calculated and transferred into temperatures using the equations (5, 6) of Kim et al. (2010):

$$TEX^H_{86} = \log ([GDGT\text{-}2] + [GDGT\text{-}3] + [Cren´]) / ([GDGT\text{-}1] + [GDGT\text{-}2] + [GDGT\text{-}3] + [Cren´]) \quad (5)$$

$$T = 68.4 \times TEX^H_{86} + 38.6 \quad (6)$$

The latter equation is calibrated for a temperature range of -3 to 30 °C with a reported error of ± 2.5 °C (Kim et al., 2010). Duplicate analysis of every tenth sample yielded a standard deviation of 0.01 for the TEX^H_{86}, corresponding to a temperature variation of 0.7 °C or better.

In order to determine the influence of land-derived GDGTs on our TEX^H_{86}-based water temperature record, we studied the correlation between TEX^H_{86} and BIT (branched isoprenoid tetraether) index values as suggested by Schouten et al. (2013). For this, the BIT index was calculated following the equation (7) given by Hopmans et al. (2004):

$$BIT = ([GDGT\text{-}I] + [GDGT\text{-}II] + [GDGT\text{-}III]) / ([GDGT\text{-}I] + [GDGT\text{-}II] + [GDGT\text{-}III] + [Cren]) \quad (7)$$

Duplicate measurements of every tenth sample gave standard deviations of 0.005 or better for the BIT index.

4.3. Results

4.3.1. Sea surface temperature reconstruction

SSTs calculated from the $U^{K´}_{37}$ range between 20.4 °C at 14.8 ka and 26.2 °C at 60.5 ka (Fig. 4.3). TEX^H_{86}-inferred temperatures reach a minimum of 19.4 °C at 9.4 (early Holocene) and 136 ka (MIS 6) and are at maximum (25.2 °C) in the core-top sample. The highest SST inferred from the LDI (25.6 °C) is found at ~0.9 ka. Minimum LDI-SSTs of 18.5 °C occur during the last deglaciation between 12.9 and 13.4 ka as well as at 14.8 ka.

TEX^H_{86}-based water temperatures are 20.1 (± 0.4) °C during MIS 6 and are on average 2 °C lower than LDI- (21.9 ± 1.2 °C) and $U^{K´}_{37}$- (22.0 ± 0.6 °C) SSTs within this interval (Fig. 4.3).

All three proxies show a slight but constant temperature increase of 2-2.5 °C throughout subsequent MIS 5 with TEX^{H}_{86}-based temperatures (averaging 22.1 ± 1 °C during MIS 5) generally remaining below $U^{K'}_{37}$- and LDI-based SSTs (average SSTs of 23.4 ± 0.9 and 23.1 ± 0.9 °C, respectively). TEX^{H}_{86}- and LDI-inferred temperatures for the Eemian (the last interglacial phase MIS 5e) average 22.0 and 22.6 °C, respectively, and are up to ~3 °C lower than modern SSTs (Fig. 4.3). $U^{K'}_{37}$-based SSTs approximate 23.1 °C and are of similar magnitude as during the Holocene Thermal Maximum and the modern warm phase. MIS 4 shows a significant decline in temperatures to 21.3-22.1 °C in all three temperature proxies, which is most pronounced (ca. 3 °C) in the $U^{K'}_{37}$ and LDI records. However, average temperatures for TEX^{H}_{86} (23.1 ± 1 °C), $U^{K'}_{37}$ (24.1 ± 1.5 °C) and LDI (23.1 ± 1.5 °C) during MIS 4 are nearly on the same level as those from the preceding and subsequent cold MIS 5 and 3. At the transition from MIS 4 to MIS 3, the reconstructed water temperatures increase again by about 2 °C, after which they gradually decline to minimum values of ~20 °C (TEX^{H}_{86}) and ~22 °C ($U^{K'}_{37}$) in sediments deposited during HE 3. In general, MIS 3 is characterized by higher and more frequent fluctuations in water temperatures with several abrupt drops by ~1.5 to 3 °C coinciding with the timing of HEs. Average temperatures during MIS 3 are at 21.7 ± 1.4 °C (TEX^{H}_{86}), 24.3 ± 1.2 °C ($U^{K'}_{37}$), and 23.1 ± 1.3 °C (LDI). On the contrary, MIS 2 is characterized by minimum water temperatures, with lowest SSTs both in $U^{K'}_{37}$ and LDI observed during the last deglaciation. This minimum is only interrupted by a short-lived warming at ~14.4 ka in all three proxies, but after this punctuated rise in temperatures, they drop again rapidly. MIS 2 water temperatures average 20.7 ± 0.9 °C for TEX^{H}_{86} and 20.7 ± 2 °C for LDI, whereas they are with 21.6 ± 1.2 °C about 1 °C higher for $U^{K'}_{37}$. The early Holocene is characterized by an overall rapid increase in water temperature to values of 22.0-24.5 °C, although the onset of the warming and the absolute temperature rise vary slightly between the different lipid paleothermometers. The observed rise in temperature continues throughout the Holocene in the TEX^{H}_{86} record, while the LDI remains on a rather constant level with temperatures averaging at 24.6 °C and showing a slight warming only throughout the latest Holocene. The $U^{K'}_{37}$, on the contrary, shows decreasing temperatures with minima of 21.7 °C following peak SSTs of 24.5 °C at ~9 ka. Only the core-top sample has an elevated SST value of 23.5 °C, while TEX^{H}_{86} and LDI core-top temperatures are at 25.2 °C and 25.5 °C, respectively. Holocene (MIS 1) water temperatures average at 21.7 ± 1.6 °C (TEX^{H}_{86}), 23.2 ± 0.8 °C ($U^{K'}_{37}$), and 24.3 ± 1.3 °C (LDI).

4.3.2. Fractional abundance of C_{32} 1,15-diol

The abundance of the C_{32} 1,15-diol relative to C_{28} 1,13-, C_{30} 1,13- and C_{30} 1,15 diols generally varies from 0 to 0.16 (average 0.08 ± 0.04) (Fig. 4.3). An exception is found in sediments deposited at 62 ka, in which the relative abundance of the C_{32} 1,15-diol is with ~0.3 slightly higher.

4.3.3. BIT index

BIT values are generally low (<0.2) throughout the sequence and a significant correlation between BIT and TEX^{H}_{86} ($R^2 = 0.26$) is not observed. In certain intervals (e.g., 0.9 -3.3 ka, 54-71 ka and 88-91 ka), however, the BIT exceeds a value of 0.3 (Fig. 4.3), which has been suggested as a threshold for the reliable application of the TEX_{86} and its derivatives (Weijers et al., 2006a; Schouten et al. 2013).

Figure 4.3 | (*overleaf*) Reference curves of a) North Greenland Ice Core Project (NGRIP) $\delta^{18}O$ data (Andersen et al., 2004) as well as b) June insolation at 30 °N (Berger and Loutre, 1991), the $\delta^{18}O$ record of benthic foraminifera (c), and $\delta^{18}O$-SST record (d) from Site MD01-2421 off central Japan by Oba et al. (2006) in comparison with Site C0011 reconstructed water temperature records as 3-point averages (e: $U^{K'}_{37}$, f: LDI, g: TEX^{H}_{86}), ΔT values for the different lipid paleothermometers (h: $U^{K'}_{37}$-TEX^{H}_{86}, i: LDI-TEX^{H}_{86}, j: LDI-$U^{K'}_{37}$), the BIT index (k), and fractional abundance of the C_{32} 1,15-diol (l) over the last 145 ka. MIS 2, 4 and 6 are displayed as gray bars. Cold periods such as the YD, the LGM and HEs (Heinrich et al., 1988; Rasmussen et al., 2003; Rashid et al., 2003) are shown in light blue, while the Bølling-Allerød (BA) warm period is indicated in orange. ΔT values are displayed as black lines with periods where ΔT <0 shaded in gray. Dashed lines indicate intervals with no available sample material.

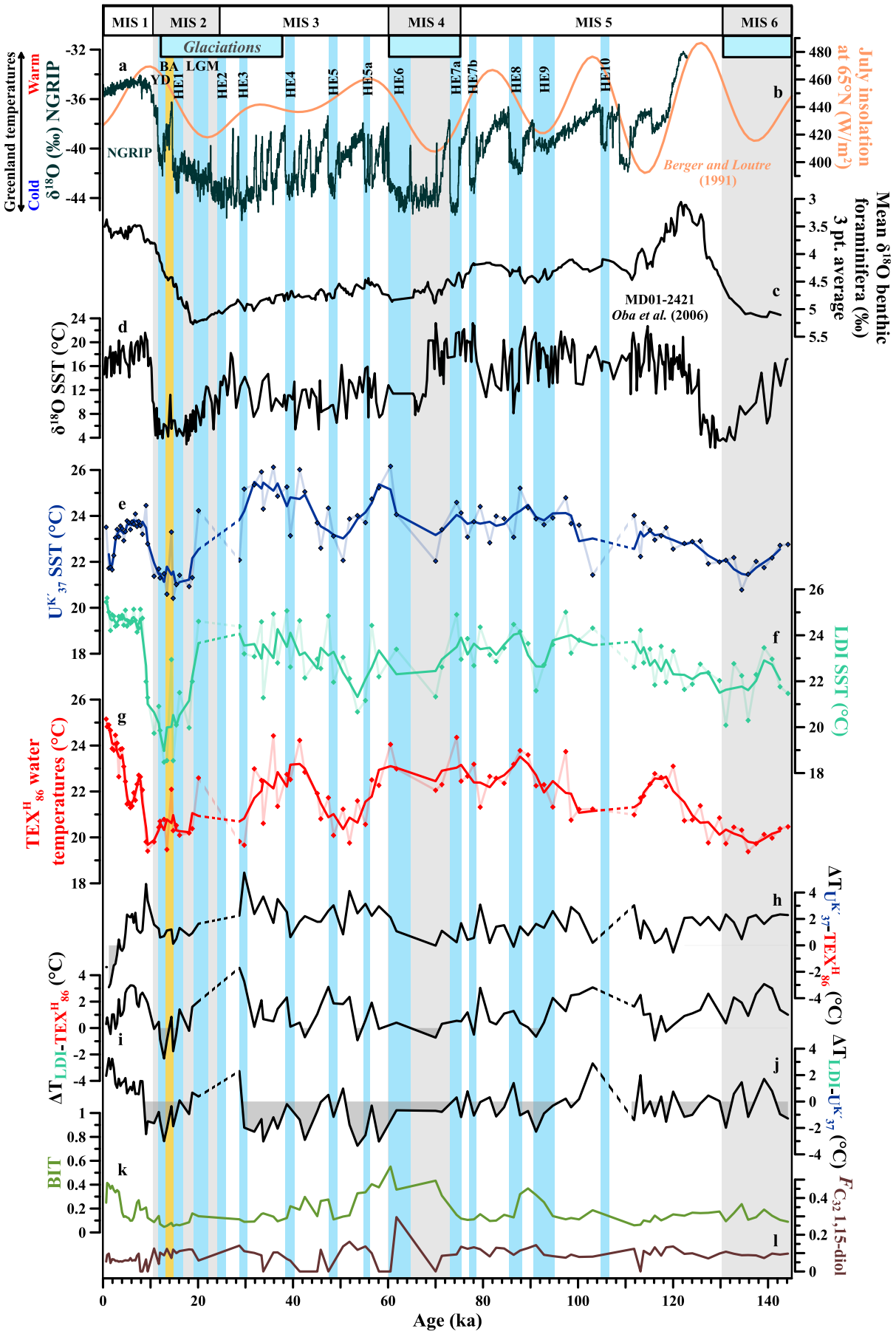
MIS 1
MIS 2
MIS 3
MIS 4
MIS 5
MIS 6
Glaciations
Greenland temperatures
Warm
Cold
a
BA
LGM
YD
HE1
HE2
HE3
HE4
HE5
HE5a
HE6
HE7a
HE7b
HE8
HE9
HE10
NGRIP
δ18O (‰) NGRIP
b
July insolation at 65°N (W/m2)
Berger and Loutre (1991)
c
MD01-2421
Oba et al. (2006)
Mean δ18O benthic foraminifera (‰)
3 pt. average
d
δ18O SST (°C)
e
UK'37 SST (°C)
f
LDI SST (°C)
g
TEXH86 water temperatures (°C)
h
ΔTUK'37-TEXH86 (°C)
i
ΔTLDI-TEXH86 (°C)
j
ΔTLDI-UK'37 (°C)
k
BIT
l
FC32 1,15-diol
Age (ka)

4.4. Discussion

The three lipid-based paleotemperature records obtained from Site C0011 show overall similar trends, although offsets regarding the magnitude and timing of absolute values are observed. Some of this variation may be explained by calibration errors, which are in the order of 1.5-2.5 °C (Müller et al., 1998; Kim et al., 2010; Rampen et al., 2012), but other factors such as selective degradation under oxic conditions (Hoefs et al., 1998; Gong and Hollander, 1999; Huguet et al., 2009; Rodrigo-Gámiz et al., 2016), light and nutrient limitation (Herbert, 2003; Rampen et al., 2012), salinity changes (Schulz et al., 2000; Rampen et al., 2012), and environmental boundary conditions that differently affect lipid synthesis (Elling et al., 2014, 2015) may also impact the lipid-based water temperature reconstructions. In addition, the TEX^{H}_{86} may yield erroneous results at sites receiving larger inputs of soil organic matter (Weijers et al., 2006a). BIT values exceeding a threshold of 0.3 during the later Holocene (e.g., 0.9-3.3 ka) and the late Pleistocene (e.g., 54-71 ka and 88-91 ka) mostly likely indicate increased riverine loading of soil organic matter to our study site. In particular for the late Holocene period, this might result from higher precipitation by a stronger summer monsoon (Zhao et al., 2013; Chen et al., 2015) in response to a northward migration of the intertropical convergence zone (ITCZ) as seen in increased growth rates of Korean speleothems (Jo et al., 2014). For most of the record, however, the generally low BIT values of <0.2 and an overall weak correlation between TEX^{H}_{86} and BIT ($R^2 = 0.26$) indicate that land-derived GDGTs are insignificant to the calculation of our TEX^{H}_{86}-derived water temperatures. The fractional abundance of C_{32} 1,15-diol relative to other LCDs was within the typical range of marine sediments and generally did not exceed a value of 0.2 (Versteegh et al., 1997; De Bar et al., 2016). This value has been proposed as a cut-off for the reliable reconstruction of LDI-SST with fractional abundances above 0.2 indicating an increased contribution of LCDs of non-marine sources and as a consequence erratic temperature reconstructions (De Bar et al., 2016). The overall low fractional abundances of the C_{32} 1,15-diol at Site C0011 (with the exception of the sediment deposited 62 ka ago) thus suggest that LCDs are primarily of marine origin and that other sources had a negligible effect on the calculation of LDI-SSTs.

4.4.1. Effect of habitat and thermocline depth on the TEX^{H}_{86}, $U^{K'}_{37}$ and LDI

The $U^{K'}_{37}$ and the LDI are proxies based on the lipid distribution pattern of photosynthetic eukaryotes and are therefore assumed to reflect photic zone temperatures (e.g., Prahl and Wakeham, 1987; Rampen et al., 2012). This is supported by sediment trap studies in

the NW Pacific off Japan showing that unsaturated alkenones are largely synthesized in the surface mixed layer of the water column (0-30 m) above the seasonal thermocline (30-80 m in September) and the chlorophyll maximum (60-80 m) (Sawada et al., 1998). Differences in LDI- and $U^{K'}_{37}$-calculated SSTs are thus most likely a result of different production seasons rather than of different habitat depths, which will be discussed in more detail in section 4.2. In contrast, the nature of the water temperature recorded by the TEX^{H}_{86} is currently under debate. Schouten et al. (2002) initially introduced the TEX_{86} as a proxy for the reconstruction of SSTs. However, maximum production and abundances of isoGDGTs in the East China Sea have been reported at a water depth of 50 to 100 m that coincides with the position of the thermocline (Nakanishi et al., 2012a, b), resulting in TEX^{H}_{86}-based water temperatures that are significantly lower than *in situ* SSTs. Similar findings with the TEX^{H}_{86} likely representing thermocline temperatures were reported from the continental shelf of NW Africa (Lopes dos Santos et al., 2010) and the western North Pacific (Yamamoto et al., 2012). The development of a strong seasonal thermocline has been reported for the KC and during summer it is located at 50-100 m water depth in the southern Okinawa Trough (Chern and Wang, 1994) and between 30 and 80 m off central Japan (Sawada et al., 1998). In turn, this implies that the generally by 1-2 °C lower TEX^{H}_{86}-based water temperatures in our study, compared to $U^{K'}_{37}$ and LDI-derived SSTs (Fig. 4.3), may result from the synthesis of isoGDGTs at greater water depths with lower temperatures. The TEX^{H}_{86} core-top temperature of 25.2 °C corresponds best to water temperatures at 30 m in July or between 0-50 m in October (Fig. 4.4), suggesting that the TEX^{H}_{86} in contrast to both other temperature proxies may indeed reflect deeper water temperatures at our site, potentially associated with the depth of the thermocline. Offshore south-eastern Australia, the TEX^{H}_{86} shows offsets with the $U^{K'}_{37}$ and LDI in the same order of magnitude as observed in this study, which was explained by differences in preferred habitat depths of the surface water-living eukaryotic algae and the deeper water-dwelling Thaumarchaeota (Lopes dos Santos et al., 2013). Microbiological studies support this perception as they show that Thaumarchaeota occur in epi- (<200 m), meso- (200-1000 m), and bathypelagic (>1000 m) water masses of the world's oceans (Karner et al., 2001) and increase in abundance below the photic zone (Herndl et al., 2005; Lincoln et al., 2014).

In the East China Sea, through which the KC is partly flowing, thaumarchaeal gene expressions increase with water depth and are highest immediately below the seasonal thermocline in autumn and summer (Hu et al., 2013). Variations between $U^{K'}_{37}$- as well as LDI-SSTs and reconstructed TEX^{H}_{86} temperatures can thus, among other factors, be related to differences in habitat depths of the biological proxy sources and therefore to the position of the thermocline.

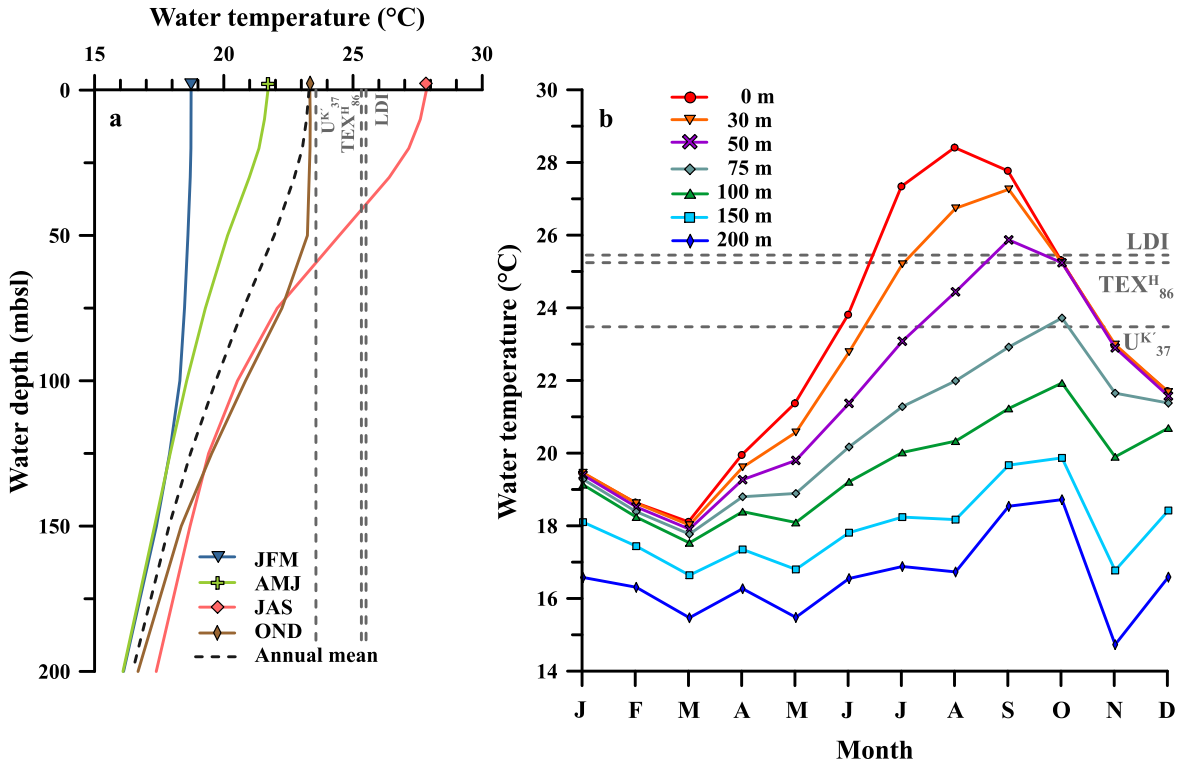

Figure 4.4 | a) Annual mean and seasonal water temperature profiles for the uppermost 200 m of the water column in a 1° grid at 32-33 °N and 136-137 °E for January-February-March (JFM), April-May-June (AMJ), July-August-September (JAS), October-November-December (OND) and b) monthly temperature variations for different water depths (0, 30, 50, 75, 100, 150, 200 m). Proxy-inferred water temperatures for the core-top sample are displayed as dashed gray lines. The temperature data was obtained from the Japan Oceanographic Data Center (http://www.jodc.go.jp/jdoss_stat/stat-infor-sca_e.htm).

The depth of the latter coincides with the water depth that seems to be represented by TEX^{H}_{86} temperatures. In this context, the absent or weak correlations between the TEX^{H}_{86} and the other two temperature proxies especially during the warm MIS 1, MIS 3 and MIS 5 (Fig. 4.5a-c) may indicate greater differences in habitat depths as a strengthened export of subtropical water masses from the WPWP to northern mid-latitudes via the KC results in a deepening of the thermocline (Shi et al., 2014). This may, in turn, result in a greater vertical separation of both pelagic Thaumarchaeota and eukaryotic algae (Fig. 4.2a). By contrast, we found a significant increase in correlation between all three lipid paleothermometers during cold MIS 2 and 4 (Fig. 4.5d-f). This better correlation likely indicates a weakening of the KC during cold phases as suggested by Kao et al. (2006a), resulting in less export of warm surface waters to our study site and therewith to a shoaling of the thermocline depth. This has previously been observed during cold events at Site CSH1 in the northern Okinawa Trough (Shi et al., 2014). In turn, the thermocline shoaling may have led to an upward migration of pelagic Thaumarchaeota closer to the sea surface, mitigating the difference in habitat depths between Thaumarchaeota and the phototrophic haptophytes and eustigmatophytes (Fig. 4.2b). A similar scenario with Thaumarchaeota oscillating between surface and subsurface water layers during cold and warm

phases has also been invoked to explain differences between TEX^{H}_{86}- as well as $U^{K'}_{37}$- and LDI-based water temperatures offshore south-eastern Australia (Lopes dos Santos et al., 2013). In contrast, the weak correlations between the three proxies during MIS 6 (Fig. 4.5) may result from changes in nutrient availability during transitions from warm to cold phases causing a larger scatter between the LDI and $U^{K'}_{37}$ as proposed by Rodrigo-Gámiz et al. (2014), but also from the low temperature difference of no more than 2 °C for the individual lipid paleothermometers in this interval (Fig. 4.3h-j), which is already close to their reported calibration errors.

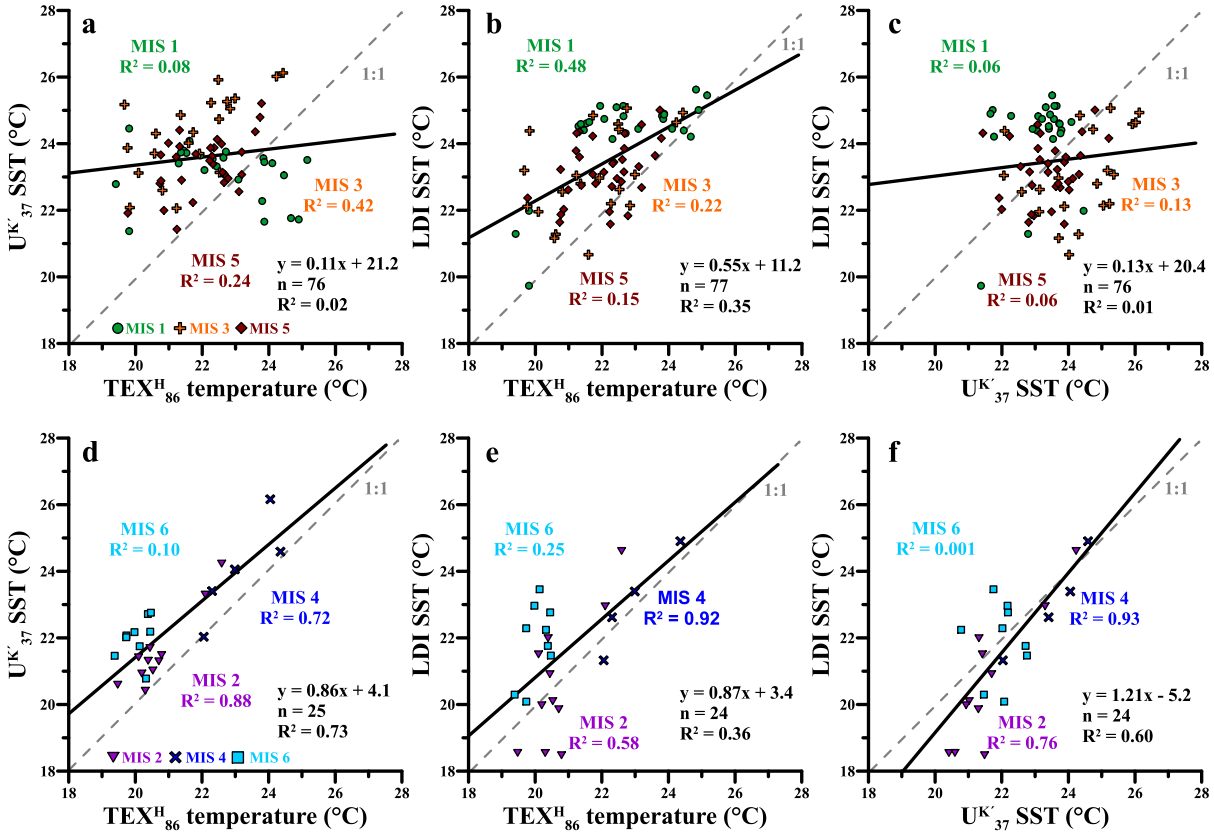

Figure 4.5 | Comparison of the different proxy-based water temperatures for warm MIS 1 (Holocene), 3 and 5 (a-c) and cold MIS 2, 4 and 6 (d-f). The dashed gray lines indicate the 1:1 correlation for the different lipid-derived temperatures.

4.4.2. Effect of seasonality on the TEX^{H}_{86}, $U^{K'}_{37}$ and LDI

Besides habitat depth, seasonality of production may affect the temperature signal that is reconstructed using lipid paleothermometers. Differences in the season of highest productivity of haptophytes and eustigmatophytes have been inferred to explain discrepancies between SSTs reconstructed from $U^{K'}_{37}$ and LDI offshore south-eastern Australia and in the Mediterranean Sea (Lopes dos Santos et al., 2013; Rodrigo-Gámiz et al., 2014). SSTs of the

modern KC range from 20 to 28 °C annually (Barkley, 1970) with an average of 23.3 °C (0 m) at Site C0011 (Japan Oceanographic Data Center; http://www.jodc.go.jp/index.html) as shown in Fig. 4.4. This is very similar to the core-top $U^{K'}_{37}$-based SST (~23.5 °C) at Site C0011 and elsewhere in this region of the NW Pacific (Sawada and Handa, 1998), but slightly lower than temperatures from the TEX^{H}_{86} (~25.2 °C) and LDI (~25.5 °C). In consequence, the latter two proxies either overestimate present-day SSTs or reflect a different season of production. The $U^{K'}_{37}$-inferred core-top SST fits best with both annual mean SST at 0 m and temperatures in June (23.8 °C) and November (23.0 °C) at 0-30 m (Fig. 4.4b). Off Japan blooms of haptophyte algae and maximum alkenone fluxes occur in spring and early summer (Sawada et al., 1998), indicating that $U^{K'}_{37}$-SSTs reflect early summer temperatures during warm phases at our study site. Such a seasonal bias of the $U^{K'}_{37}$ signal has also been observed in several other oceanic regions such as the Southern Ocean and the Mediterranean Sea (e.g., Castañeda et al., 2010; Lopes dos Santos et al., 2013; Rodrigo-Gámiz et al., 2014). The $U^{K'}_{37}$ does not indicate a significant decrease in SST during MIS 2 and 4, which suggests a delay in the production season of haptophytes during cold periods. Such a situation has also been invoked to explain an increase of $U^{K'}_{37}$-based SSTs during the LGM in the KC/OC mixed water region in the NW Pacific off Honshu (Minoshima et al., 2007) and in the Sea of Okhotsk (Harada et al., 2012), where the maximum productivity of haptophyte algae occurs in mid-summer due to prolonged periods of sea ice coverage. Other factors that may affect the $U^{K'}_{37}$ and lead to an overestimation of calculated temperatures during cold periods are selective degradation with a preferential removal of the triunsaturated alkenone (Hoefs et al., 1998) and/or the delayed sinking of alkenones synthesized during preceding warmer periods (Rodrigo-Gámiz et al., 2015; and references therein).

The core-top LDI-SST of 25.5 °C seems to reflect either July temperatures at 30 m or those at 0 m in June or October (Fig. 4.4). At present, very little is known about the distribution and seasonality of marine eustigmatophytes (i.e. the biological sources of LCDs). Analysis of globally distributed surface sediments suggests that the LDI records summer instead of annual mean SST (Rampen et al., 2012). Similarly, Lopes dos Santos et al. (2013) attributed higher SST values for the LDI as compared to $U^{K'}_{37}$- and TEX^{H}_{86}-based temperatures in the Southern Ocean to bloom-formation of eustigmatophytes during austral summer. This implies that the maximum productivity of eustigmatophytes at our site is during mid-summer, slightly later than that of haptophyte algae. Why LDI-SSTs then not always exceed $U^{K'}_{37}$-SSTs throughout the last 145 ka, however, remains elusive, but may result from changes in production season of haptophyte and eustigmatophyte algae associated with changing oceanographic conditions (see

scenarios presented in Fig. 4.2) or factors other than production season and habitat depth. For example, it may be that the LDI was affected by oxic degradation. Rodrigo-Gámiz et al. (2016) showed that C_{28} 1,13- and C_{30} 1,13-diols were generally better preserved than the C_{30} 1,15-diol under oxygen exposure, resulting in reconstructed SSTs that were up to 3 °C lower than actual SSTs. Nonetheless, the suggested offset in production season of haptophytes and eustigmatophytes may account for the absent correlations during warm MIS (Fig. 4.5c), whereas a more similar production season due to a delay and shift in haptophyte bloom formation to mid-summer during cold MIS may explain the significantly better correlations (Fig. 4.5f).

The reconstruction of TEX^{H}_{86}-based water temperatures might be confounded by the production season of isoGDGTs (Grauel et al., 2013; Lopes dos Santos et al., 2013), which varies significantly between oceanic regions. Herfort et al. (2007) reported that TEX_{86} values in the North Sea reflect winter SSTs, a result of increased growth of Thaumarchaeota associated with lower competition with eukaryotic algae at colder temperatures. In line with this observation is that TEX^{H}_{86}-based temperatures agree with coolest months SSTs reconstructed from foraminiferal assemblages offshore south-eastern Australia (Lopes dos Santos et al., 2013) and in the coastal South China Sea (Zhang et al., 2013a). The TEX^{H}_{86}-based water temperatures that were always below those of both other proxies prior to the mid-Holocene thus likely represent a wintertime signal at Site C0011. However, the relatively high temperature in our core-top sample is either due to production of isoGDGTs in July at 30 m water depth or in October between 0 and 50 m depths, coinciding with the depth of the seasonal thermocline at around 30-80 m. The TEX^{H}_{86}-based water temperatures for the mid- to late Holocene are generally higher than $U^{K'}_{37}$-SSTs and similar to those from the LDI (Fig. 4.3), invoking a shift in the production season of pelagic Thaumarchaeota to warmer months. A summer signal has also been reported for the TEX_{86} in offshore core-top samples from the Adriatic Sea (Leider et al, 2010). However, as discussed above, other factors such as changes in nutrient supply may also have an impact on the reconstructed TEX^{H}_{86} temperature signal (Elling et al., 2014; and references therein). Still, the unique shift in TEX^{H}_{86} production season during the Holocene compared to other warm phases has – to the best of our knowledge – not been described in any other oceanic region and needs further investigation in the future.

4.4.3. Paleoceanographic evolution of the Kuroshio Current

Our $U^{K'}_{37}$, TEX^{H}_{86} and LDI temperature records indicate long-term changes in water temperature evolution off central Japan and provide evidence for rapid cooling and warming

events in the NW Pacific region SE off Japan over the last 145 ka. These are related to (I) variations in the export of subtropical water masses from the WPWP through the KC, (II) changes in the flow path of the KC (scenarios 1 and 2), and (III) the latitudinal displacement of the KC/OC interfrontal mixing zone (scenario 3). During glacial times, when large parts of North America were covered by the Laurentide ice sheet, increased albedo led to a southward movement and weakening of the Northern Pacific subtropical high pressure (COHMAP members, 1988). This, in turn, slowed down the subtropical circulation in the Northern Pacific, which reduced the export of warm water masses from the WPWP to northern mid-latitudes. At the same time, a relative strengthening of the Okhotsk High initiated the migration of cold OC waters further southward (Oba et al., 2006; and references therein). The relative strengths of the high pressures and their impact on the latitudinal positions of the KC and OC displaced the interfrontal mixing zone of both ocean currents southward (Sagawa et al., 2006). This is evident in lower average temperatures (20.1-20.7 °C in TEX^{H}_{86}, 21.6-22.0 °C in $U^{K'}_{37}$, and 20.7-21.9 °C in LDI) during MIS 2 and 6 as well as short-term excursions to reduced water temperatures such as those observed during e.g. HEs (Fig. 4.3). The low sample resolution in MIS 4 does not allow for a detailed investigation of the temperature evolution, but consistent trends in temperature are apparent between the different lipid paleothermometers. In the following, the long-term paleoceanographic evolution of the late Pleistocene, the last deglaciation and Holocene period and short-term climate events will be discussed separately.

4.4.3.1. Late Pleistocene paleoceanographic evolution

The variability of the flow path of the KC during cold phases is controversially discussed with some authors arguing for a southward shift of the KC frontal zone by 3° to 10° in latitude (Kawahata and Ohshima, 2002; Yamamoto et al., 2004; Gallagher et al., 2015; and references therein). At Site C0011, a weakening of the KC and a simultaneous displacement of the KC/OC interfrontal zone by at least 6° allowing colder waters to reach south of our study site during cold MIS 2 and 6 is evident by a decrease in water temperatures by up to 6 °C (Fig. 4.3). This southward displacement of the KC (scenario 3; see introduction and Fig. 4.2 b) is also manifested in a drastic decrease in the abundance of warm water dwelling planktonic foraminifera of the *Pulleniatina* group in the northern and southern Okinawa Trough (Jian et al., 2000). It also agrees with changes in the terrestrial floral community with an expansion of tundra vegetation in northernmost Hokkaido and an extensive coverage of boreal and subalpine conifer forests in central and northern Honshu (Tsukada, 1983). All three temperature proxies show a decline in water temperatures during MIS 4, but average temperatures are still on the

same level or exceed those from the preceding and following warmer MIS 5 and 3, hence indicating that the influence of the KC was still strong and colder interfrontal zone waters were mostly absent from Site C0011, which may correspond to scenario 2 with the formation of the large meander. Similarly, Oba et al. (2006) and Yasudomi et al. (2014) found evidence that the Kuroshio front was still located north of 36 °N during the first half of MIS 4 and started retreating to southerly latitudes afterwards. The water temperature shifts of up to 6.5 °C at glacial-interglacial transitions at Site C0011 are in the same order of magnitude as inferred from alkenone measurements (Sawada and Handa, 1998). MIS 3 is characterized by higher and more frequent fluctuations in water temperatures than any other MIS in our records (Fig. 4.3). This may indicate that oceanographic conditions were overall less stable during this period and that the KC alternated more frequently between its short (scenario 1) and large (scenario 2) meander path configurations (Fig. 4.2).

During the Eemian (warm MIS 5e), diatoms (Koizumi and Sakamoto, 2010) and radiolarian assemblages (Yasudomi et al., 2014) indicate a stronger influence of the KC at 36 °N off central Japan with SSTs being up to ~5 °C higher than at present due to the subtropical KC waters replacing colder transitional waters from the interfrontal mixing zone (Yasudomi et al., 2014). At Site C0011, we observe a general warming during MIS 5 with water temperatures increasing by 3 °C in all three proxy records. For the Eemian, maximum water temperatures are at 23.5 °C both for the $U^{K'}_{37}$ and the LDI and at 23.1 °C for the TEX^{H}_{86}. However, compared to modern SSTs, water temperatures for the Eemian are significantly lower (by ca. 2.5 °C) except for the $U^{K'}_{37}$-SSTs, which are similar to late Holocene values. These comparatively low water temperatures during the Eemian may indicate the persistence of the KC large meander flowing south of Site C0011 (Fig. 4.1) as described in scenario 2 (see introduction and Fig. 4.2a). This meander path configuration may have triggered the establishment of cold surface waters along the coast of Japan and at our study site but additional studies at other core locations are necessary to unequivocally determine the KC meander path configuration during the Eemian.

4.4.3.2. Last deglaciation and the Holocene

Minimum water temperatures for all three lipid paleothermometers between 19-11 ka (Fig. 4.3) indicate a stronger influence of colder waters resulting from a southward shift of the subpolar OC and the KC/OC interfrontal zone waters. A similar shift has been reported for the time period following the LGM at several sites off central Japan (Thompson and Shackleton, 1980; Oba and Murayama, 2004). This also agrees well with findings made by COHMAP members (1988), who reported that the subtropical N Pacific high pressure was weaker and

displaced southward from 18-12 ka. The minimum in temperatures is interrupted by a short-lived warming of 2-4 °C at ~14.4 ka, which is considered to indicate the Bølling-Allerød (BA) interstadial that has also been observed in records taken offshore central Japan (Oba and Murayama, 2004; Oba et al., 2006; Sagawa et al., 2006). After the BA warm event, water temperatures significantly drop by 2.5-4.5 °C between 12.9 and 11.6 ka. The timing of the decrease in temperature is synchronous with the YD cold event that has also been recorded in sediments from the NW Pacific Ocean (Chinzei et al., 1987; Sagawa et al., 2006; Koizumi, 2008), the N Atlantic Ocean (Duplessy et al., 1981; Ruddiman and McIntyre, 1981) as well as in Greenland and Antarctic ice cores (e.g., Lorius et al., 1979; Dansgaard et al., 1982; Grootes et al., 1993; Andersen et al., 2004). The observed decline in water temperatures at our site is in the same order of magnitude as seen in a pollen-based temperature record from central Japan (Nakagawa et al., 2003), but lower than at sites further north in the confluence zone of the KC and OC off Tohoku (Oba et al., 2006; Sagawa et al., 2006; Koizumi, 2008). These differences are likely related to a more immediate impact of subpolar OC waters on these more northern sites. The YD was terminated by a shift to significantly warmer conditions at the Pleistocene-Holocene boundary (Dansgaard et al., 1989) as seen in a rapid increase in temperatures by up to 6.5 °C at Site C0011, starting after the transition from MIS 2 to the Holocene. The rapid oceanic warming during early MIS 1 is followed by a more gradual rise of LDI- and TEX^{H}_{86}-inferred water temperatures throughout the Holocene up to ~25 °C at the core-top. In contrast, the Holocene temperature trend for the $U^{K'}_{37}$-inferred SSTs shows a steep increase from 21.5 to 24.5 °C during the transition period from the YD to the early Holocene followed by a ~1.5 °C decline throughout the early to middle Holocene and a very abrupt temperature drop to 21.7 °C at around 4 ka. This is well in line with temperature records from the Japanese margin (Isono et al., 2009) and the Tohoku area with similar declines in $U^{K'}_{37}$-, *Td´*- (a diatom-based proxy for SST), Mg/Ca-, and δ^{18}O-SST records (Sagawa et al., 2006; Oba et al., 2006). A similar decrease in SST, inferred from planktonic foraminiferal assemblages, occurs at the Okinawa Trough at ~4 ka (Jian et al., 2000) and was interpreted to result from a weakened KC associated with stronger winter monsoonal winds and an associated shift of the main axis of the KC. The pronounced offsets between $U^{K'}_{37}$- as well as TEX^{H}_{86}- and LDI-derived temperatures during the Holocene (Fig. 4.3h-j) remain elusive at this point, but may be caused by a combination of environmental as well as physiological factors (including changes in nutrient availability and production season of haptophyte algae and/or variation of habitat depths). A return to higher temperatures in $U^{K'}_{37}$ and TEX^{H}_{86} in the core-top sample and consistently high proxy-based water temperatures from the surface sediments of Site C0011, however, indicate an overall

strengthening of the KC in the recent past, allowing for an increased meridional heat transport that significantly exceeds the strengthening during the Eemian warm period. The overall higher temperatures at Site C0011 during the last ~9 ka compared to the Eemian also suggest a stronger influence of the KC during the Holocene, implying an increased and more effective export of warm surface waters from the WPWP to northern mid-latitudes. This is also in line with higher Holocene $\delta^{18}O$ -SSTs compared to Eemian SSTs at a site of central Japan (Oba et al., 2006) (Fig. 4.3). Alternatively, it cannot be excluded at this point that elevated water temperatures during the Holocene may indicate the dominance of the KC short meander at our study site (scenario 1, Fig. 4.2a).

4.4.3.3. Short-term climate events

Repeatedly occurring short-lived declines in water temperatures throughout the lipid paleothermometer records at Site C0011 partly coincide with Heinrich Events as observed in NGRIP $\delta^{18}O$ records (Andersen et al., 2004) (Fig. 4.3). The abrupt shifts to more negative values in NGRIP $\delta^{18}O$ and colder temperatures in Greenland during HEs coincide with dryer conditions in East Asia as reported from Chinese speleothems in the Hulu and Sanbao caves (Wang et al., 2001, 2008), resulting from a southward shift of the ITCZ and a weaker SE Asian summer monsoon (Wang et al., 2008; Jo et al., 2014). At the same time, the intensification of the Aleutian Low caused a southward displacement of the westerly jet axis in harmony with an intensification of the winter monsoon (Nagashima et al., 2007) and a southward migration of the OC (Sagawa et al., 2006) as in scenario 3 (Fig. 4.2b). The latter likely led to the observed declines in water temperature at Site C0011. For example, the abrupt drops in water temperature by 0.6-2.1 °C during late MIS 5 likely correspond to HEs 7b, 8 and 9 and minimum temperatures at ~49 and ~56 ka coincide with HEs 5 and 5a. The timing of lowest water temperatures during HEs at Site C0011 is synchronous with a shoaling of the thermocline in the Okinawa Trough probably due to a reduced volume transport of the KC (Shi et al., 2014). Since a reduced volume transport fosters the formation of the KC large meander off central Japan, the observed declines in water temperature during HEs may also be linked to the predominance of the large meander path configuration of the KC (scenario 2; Fig. 4.2a), promoting the establishment of stable and cold surface water masses off central Japan. Again, more detailed paleoceanographic studies following a transect across the different meander pathways are needed to fully elucidate the spatiotemporal distribution of the KC over geological time.

4.5. Conclusion

The paleoceanographic and paleoclimate evolution of the NW Pacific Ocean was investigated over the last two glacial-interglacial cycles (~145 ka) using the lipid paleothermometers TEX^{H}_{86}, $U^{K'}_{37}$ and LDI. High water temperatures during MIS 1, 3 and 5 indicate a strengthening of the KC associated with an intensified North Pacific Subtropical Gyre circulation and thus a more effective meridional heat transport from the WPWP to northern mid-latitudes. In contrast, low water temperatures during MIS 2 and 6 as well as during short-term climate events indicate a southward migration of the KC/OC interfrontal mixing zone by at least 6° in latitude compared to its modern position and possibly a stronger influence of cold OC waters at Site C0011. Reconstructed water temperatures differ by up to 5.5 °C between the investigated lipid paleothermometers even within the same sample, suggesting, among other factors, differences in habitat depths and production season of haptophytes, eustigmatophytes and pelagic Thaumarchaeota at Site C0011. Significantly higher correlations between the three different proxies during cold phases (MIS 2, 4 and 6) may be related to a shift in production season to mid-summer for alkenone-producing haptophyte algae and the shoaling of the thermocline due to reduced meridional heat transport from the WPWP to northern mid-latitudes. In turn, this thermocline shoaling may have displaced maximum abundances of pelagic Thaumarchaeota to shallower water depths, thereby minimizing temperature offsets between the different lipid paleothermometers. In contrast, weaker correlations of the TEX^{H}_{86} and $U^{K'}_{37}$ as well as LDI during warm MIS 1, 3 and 5 may reflect a deepening of the thermocline due to a stronger transport of subtropical surface water masses from the WPWP via the KC, resulting in the vertical movement of isoGDGT-synthesizing Thaumarchaeota to greater water depths. Contrarily to previous findings, our data imply a stronger KC during the Holocene than during the Eemian warm period. South of Japan, this may have caused the formation of the short meander path during Holocene times, whereas a weakened warm water mass transport via the KC during the Eemian may have favored the formation of the KC large meander, therefore establishing colder surface water masses over our study site.

4.6. Acknowledgements

Sample material for this study was provided through the Integrated Ocean Drilling Program. We are grateful to Marta Rodrigo-Gámiz, Kevin W. Becker and other anonymous reviewers for their constructive comments on the manuscript. We thank Igor M. Belkin for

editorial handlings. This work was supported by the German Research Foundation (Grants BA 3841/4-1 and BA 3841/6-1 awarded to TB as well as grant SCHW 554/27-1 given to LS).

4.7. Appendix A Supporting information

Supplementary data associated with this article can be found in the online version at doi:10.1016/j.dsr.2017.04.018.

Table 4.A1 | Water temperature data (TEX^{H}_{86}, $U^{K'}_{37}$, and LDI), BIT values and fractional abundances of C_{32} 1.15-diols.

Sample	Absolute depth (m CSF-B)	Age (ka)	TEX^{H}_{86} T (°C)	$U^{K'}_{37}$ SST (°C)	LDI SST (°C)	BIT	*f*C_{32} 1.15-diols
C0011C - 1H - 1 W, 0.0 - 2.0 cm	0.02	0.7	25.2	23.5	25.5	0.25	0.05
C0011C - 1H - 1 W, 2.0 - 3.0 cm	0.03	0.9	24.8		25.6	0.42	0.09
C0011C - 1H - 1 W, 3.0 - 4.0 cm	0.04	1.2	24.9	21.7	25.0	0.40	0.10
C0011C - 1H - 1 W, 4.0 - 5.0 cm	0.05	1.6	24.7	21.8	24.2	0.37	0.05
C0011C - 1H - 1 W, 5.0 - 6.0 cm	0.06	1.9	23.9	21.7	24.9	0.39	0.07
C0011C - 1H - 1 W, 6.0 - 7.0 cm	0.07	2.3	23.8	22.3	24.8	0.36	0.07
C0011C - 1H - 1 W, 7.0 - 8.0 cm	0.08	2.6	24.5	23.0	24.4	0.34	0.06
C0011C - 1H - 1 W, 8.0 - 9.0 cm	0.09	3.0	24.1	23.4	24.4	0.35	0.06
C0011C - 1H - 1 W, 9.0 - 10.0 cm	0.10	3.3	22.6	23.1	24.8	0.34	0.05
C0011C - 1H - 1 W, 10.0 - 11.0 cm	0.11	3.7	23.8	23.6	24.7	0.26	0.06
C0011C - 1H - 1 W, 11.0 - 12.0 cm	0.12	4.0	23.9	23.4	24.9	0.17	0.05
C0011C - 1H - 1 W, 12.0 - 13.0 cm	0.13	4.4	23.1	22.9	24.4	0.13	0.06
C0011C - 1H - 1 W, 13.0 - 14.0 cm	0.14	4.7	22.4	23.3	25.1	0.14	0.06
C0011C - 1H - 1 W, 14.0 - 15.0 cm	0.15	5.1	21.5	23.8	24.4	0.13	0.06
C0011C - 1H - 1 W, 15.0 - 16.0 cm	0.16	5.4	21.5	23.7	24.6	0.12	0.06
C0011C - 1H - 1 W, 16.0 - 17.0 cm	0.17	5.8	21.3	23.4	24.5	0.10	0.07
C0011C - 1H - 1 W, 17.0 - 18.0 cm	0.18	6.1	21.4	23.7	24.6	0.10	0.06
C0011C - 1H - 1 W, 18.0 - 19.0 cm	0.19	6.5	21.9	23.6	25.1	0.13	0.06
C0011C - 1H - 1 W, 19.0 - 20.0 cm	0.20	6.8	21.6	24.1	24.6	0.19	0.06
C0011C - 1H - 1 W, 20.0 - 21.0 cm	0.21	7.2	22.3	23.5	24.1	0.25	0.09
C0011C - 1H - 1 W, 21.0 - 22.0 cm	0.22	7.5	22.7	23.8	24.3	0.27	0.10
C0011C - 1H - 1 W, 22.0 - 23.0 cm	0.23	7.9	22.6	23.6	25.1	0.19	0.00
C0011C - 1H - 1 W, 23.0 - 24.5 cm	0.24	8.3	22.1	23.2	24.7	0.19	0.00
C0011C - 1H - 1 W, 25.0 - 27.0 cm	0.26	9.1	19.8	24.5	22.0	0.21	0.07
C0011C - 1H - 1 W, 28.0 - 30.0 cm	0.27	9.4	19.4	22.8	21.3	0.12	0.00
C0011C - 1H - 1 W, 31.0 - 33.0 cm	0.31	10.8	19.8	21.4	19.7	0.09	0.13
C0011C - 1H - 1 W, 33.0 - 35.0 cm	0.34	11.7	20.4	21.7	20.9	0.14	0.04
C0011C - 1H - 1 W, 35.0 - 36.5 cm	0.34	12.0	20.7	21.3	19.9	0.07	0.10
C0011C - 1H - 1 W, 37.5 - 39.0 cm	0.37	12.8	20.8	21.5	18.5	0.05	0.09
C0011C - 1H - 1 W, 39.0 - 41.0 cm	0.38	13.4	19.5	20.6	18.5	0.06	0.12
C0011C - 1H - 1 W, 41.0 - 43.0 cm	0.41	14.4	22.1	23.3	22.9	0.08	0.07
C0011C - 1H - 1 W, 43.0 - 45.0 cm	0.42	14.8	20.3	20.4	18.5	0.05	0.12
C0011C - 1H - 1 W, 45.0 - 47.0 cm	0.44	15.4	20.5	21.0	20.1	0.06	0.10
C0011C - 1H - 1 W, 47.0 - 49.0 cm	0.46	16.1	20.1	21.4	21.5	0.06	0.11
C0011C - 1H - 1 W, 53.0 - 55.0 cm	0.52	18.1	20.2	20.9	20.0	0.09	0.12

Sample	Absolute depth (m CSF-B)	Age (ka)	TEX^{H}_{86} T (°C)	$U^{K'}_{37}$ SST (°C)	LDI SST (°C)	BIT	FC_{32} 1.15-diols
C0011C - 1H - 1 W, 55.0 - 57.0 cm	0.54	18.8	20.4	21.3	22.0	0.16	0.12
C0011C - 1H - 1 W, 58.0 - 60.0 cm	0.58	20.1	22.6	24.2	24.6	0.14	0.06
C0011C - 1H - 3 W, 0.0 - 2.0 cm	0.82	28.7	19.8	22.1	24.4	0.11	0.14
C0011C - 1H - 3 W, 4.0 - 6.0 cm	0.85	29.7	19.7	25.2	23.2	0.09	0.11
C0011C - 1H - 3 W, 8.5 - 10.5 cm	0.91	31.9	23.0	25.4	23.1	0.09	0.10
C0011C - 1H - 3 W, 13.0 - 15.0 cm	0.95	33.4	22.5	25.9	24.6	0.15	0.09
C0011C - 1H - 3 W, 16.0 - 18.0 cm	0.97	33.7	20.6	24.3	21.3	0.16	0.00
C0011C - 1H - 3 W, 20.5 - 22.5 cm	1.03	35.9	24.4	26.1	24.9	0.13	0.10
C0011C - 1H - 3 W, 25.0 - 27.0 cm	1.05	36.7	21.4	24.9	22.8	0.09	0.10
C0011C - 1H - 3 W, 29.0 - 31.0 cm	1.11	38.7	22.7	25.3	25.1	0.12	0.07
C0011C - 1H - 3 W, 33.0 - 35.0 cm	1.13	39.4	22.5	23.1	22.6	0.22	0.06
C0011C - 1H - 3 W, 37.0 - 39.0 cm	1.18	41.4	24.2	26.0	24.6	0.19	0.00
C0011C - 1H - 3 W, 42.0 - 44.0 cm	1.22	42.5	22.8	25.1	22.1	0.30	0.00
C0011C - 1H - 3 W, 48.0 - 50.0 cm	1.29	45.1	21.9	23.7	23.0	0.14	0.00
C0011C - 1H - 3 W, 52.0 - 54.0 cm	1.31	45.8	20.8	22.6	22.6	0.26	0.12
C0011C - 1H - 3 W, 55.0 - 57.0 cm	1.36	47.4	21.7	24.3	24.8	0.28	0.00
C0011C - 1H - 3 W, 60.0 - 62.0 cm	1.39	48.5	20.1	23.1	22.0	0.11	0.05
C0011C - 1H - 3 W, 65.0 - 67.0 cm	1.45	50.5	21.2	22.1	23.0	0.13	0.14
C0011C - 1H - 3 W, 70.0 - 72.0 cm	1.48	51.9	19.8	23.9	22.1	0.14	0.16
C0011C - 1H - 3 W, 75.0 - 77.0 cm	1.53	53.6	21.6	24.0	20.7	0.33	0.12
C0011C - 1H - 3 W, 80.0 - 82.0 cm	1.58	55.2	20.6	23.7	21.2	0.34	0.14
C0011C - 1H - 3 W, 83.0 - 85.0 cm	1.62	56.6	22.5	24.7	24.4	0.40	0.10
C0011C - 1H - 3 W, 88.5 - 90.5 cm	1.66	58.1	22.3	25.2	22.2	0.38	0.00
C0011C - 1H - 3 W, 94.0 - 96.0 cm	1.73	60.5	24.0	26.2		0.55	0.00
C0011C - 1H - 3 W, 98.5 - 100.5 cm	1.77	61.8	23.0	24.1	23.4	0.36	0.30
C0011C - 1H - 5 W, 0.0 - 2.0 cm	2.00	70.0	22.1	22.0	21.3	0.43	0.00
C0011C - 1H - 5 W, 5.0 - 7.0 cm	2.04	71.3	22.3	23.4	22.6	0.31	0.09
C0011C - 1H - 5 W, 12.5 - 14.5 cm	2.13	74.4	24.4	24.6	24.9	0.15	0.09
C0011C - 1H - 5 W, 17.0 - 19.0 cm	2.16	75.4	22.5	24.1	23.0	0.12	0.13
C0011C - 1H - 5 W, 20.0 - 22.0 cm	2.19	76.7	22.7	23.1	23.9	0.11	0.12
C0011C - 1H - 5 W, 25.0 - 27.0 cm	2.23	78.1	23.2	23.7	22.7	0.11	0.13
C0011C - 1H - 5 W, 29.0 - 31.0 cm	2.27	79.4	21.3	24.4	24.4	0.15	0.12
C0011C - 1H - 5 W, 34.0 - 36.0 cm	2.33	81.4	22.7	22.8	23.2	0.10	0.08
C0011C - 1H - 5 W, 39.0 - 41.0 cm	2.37	82.8	22.6	24.0	22.9	0.10	0.13
C0011C - 1H - 5 W, 44.0 - 46.0 cm	2.42	84.4	22.4	23.9	23.4	0.15	0.13
C0011C - 1H - 5 W, 49.0 - 51.0 cm	2.47	86.5	23.2	23.1	24.5	0.13	0.09
C0011C - 1H - 5 W, 54.0 - 56.0 cm	2.51	87.8	23.8	25.2	24.2	0.32	0.11
C0011C - 1H - 5 W, 59.0 - 61.0 cm	2.56	89.5	23.6	24.4	23.6	0.37	0.13
C0011C - 1H - 5 W, 64.0 - 66.0 cm	2.61	91.2	22.2	23.9	21.6	0.31	0.14
C0011C - 1H - 5 W, 69.0 - 71.0 cm	2.66	92.8	22.3	23.6	22.7	0.25	0.09
C0011C - 1H - 5 W, 74.5 - 76.5 cm	2.71	94.7	21.3	23.9	23.6	0.14	0.08

Sample	Absolute depth (m CSF-B)	Age (ka)	TEX^{H}_{86} T (°C)	$U^{K'}_{37}$ SST (°C)	LDI SST (°C)	BIT	FC_{32} 1.15-diols
C0011C - 1H - 5 W, 81.0 - 83.0 cm	2.79	97.4	23.7	24.8	25.0	0.11	0.08
C0011C - 1H - 5 W, 86.0 - 88.0 cm	2.82	98.5	20.8	23.7	23.2	0.12	0.09
C0011C - 1H - 5 W, 91.0 - 93.0 cm	2.87	100.2	21.2	23.6	23.8	0.11	0.08
C0011C - 1H - 5 W, 98.5 - 100.5 cm	2.95	103.1	21.2	21.4	24.3	0.19	0.08
C0011C - 1H - CC W, 0.0 - 2.0 cm	3.20	111.8	21.0	24.0	22.6	0.06	0.12
C0011C - 1H - CC W, 3.0 - 5.0 cm	3.24	113.1	21.7	22.2	24.2	0.06	0.00
C0011C - 1H - CC W, 6.0 - 8.0 cm	3.26	113.8	21.8	23.7	22.8	0.10	0.11
C0011C - 1H - CC W, 9.0 - 11.0 cm	3.29	115.2	22.3	23.4	23.4	0.09	0.09
C0011C - 1H - CC W, 13.0 - 15.0 cm	3.32	116.2	22.8	23.0	21.8	0.14	0.13
C0011C - 1H - CC W, 16.0 - 18.0 cm	3.36	117.5	22.6	23.1	23.5	0.10	0.09
C0011C - 1H - CC W, 20.0 - 22.0 cm	3.39	118.5	22.2	23.5	22.0	0.12	0.13
C0011C - 1H - CC W, 23.5 - 25.5 cm	3.43	120.0	23.1	22.6	23.3	0.15	0.14
C0011C - 2H - 1 W, 0.0 - 2.0 cm	3.50	122.4	20.7	22.8	21.6	0.14	0.10
C0011C - 2H - 1 W, 5.0 - 7.0 cm	3.55	124.1	20.8	22.9	21.9	0.17	0.10
C0011C - 2H - 1 W, 10.0 - 12.0 cm	3.60	125.7	21.4	22.9	22.7	0.16	0.09
C0011C - 2H - 1 W, 15.0 - 17.0 cm	3.64	127.4	19.8	21.9	22.4	0.16	0.07
C0011C - 2H - 1 W, 21.0 - 23.0 cm	3.71	129.8	20.9	22.0	22.0	0.18	0.10
C0011C - 2H - 1 W, 26.0 - 28.0 cm	3.75	131.1	19.7	22.1	20.1	0.09	0.11
C0011C - 2H - 1 W, 31.0 - 33.0 cm	3.80	132.8	20.4	22.2	22.8	0.16	0.10
C0011C - 2H - 1 W, 35.0 - 37.0 cm	3.85	134.5	20.3	20.8	22.2	0.24	0.09
C0011C - 2H - 1 W, 40.0 - 42.0 cm	3.88	135.8	19.4	21.5	20.3	0.11	0.09
C0011C - 2H - 1 W, 45.0 - 47.0 cm	3.93	137.5	19.7	22.0	22.3	0.13	0.09
C0011C - 2H - 1 W, 50.0 - 52.0 cm	3.98	139.2	20.1	21.7	23.5	0.19	0.07
C0011C - 2H - 1 W, 55.0 - 57.0 cm	4.03	140.8	20.0	22.2	23.0	0.14	0.10
C0011C - 2H - 1 W, 60.0 - 62.0 cm	4.08	142.5	20.4	22.7	21.8	0.11	0.09
C0011C - 2H - 1 W, 65.0 - 67.0 cm	4.12	144.2	20.5	22.8	21.5	0.09	0.10

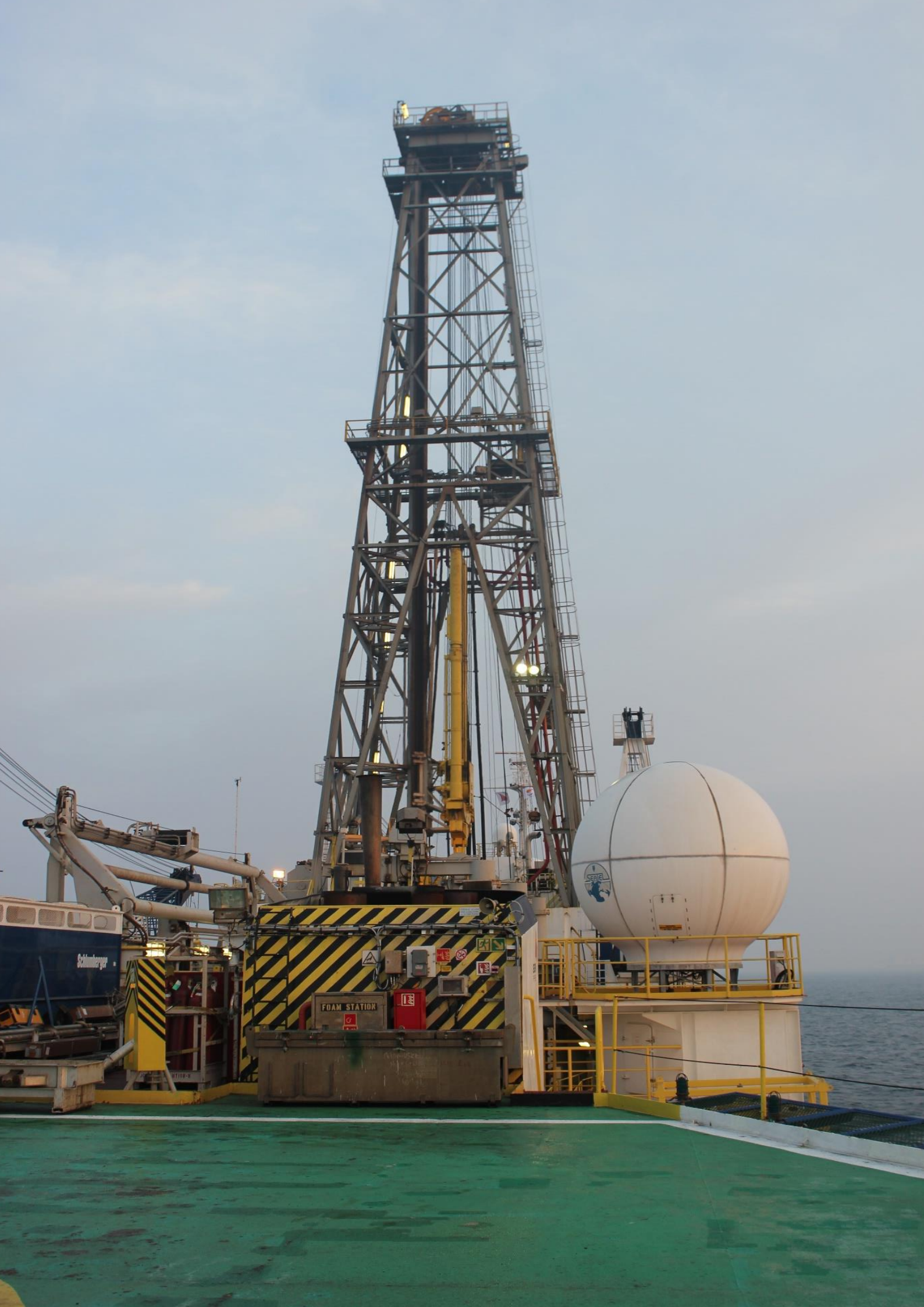
Schlumberger
FOAM STATION

Chapter 5

Southward displacement of the glacial westerly jet driven by Arctic amplification

Ann-Sophie Jonas[1], Myriam Kars[2], Thorsten Bauersachs[1], Wolfgang Ruebsam[1], and Lorenz Schwark[1,3]

[1] Department of Organic Geochemistry, Institute of Geosciences, Christian-Albrechts-University, Ludewig-Meyn-Straße 10, 24118 Kiel, Germany.

[2] Center for Advanced Marine Core Research, Kochi University, Nankoku, Japan

[3] WA-OIGC, Earth and Planetary Sciences, Curtin University, Perth, Australia

In review at *Paleoceanography and Paleoclimatology.*

Abstract

The westerly jet stream and East Asian monsoon are crucial components of climate evolution over East Asia, an area that is inhabited by almost half of the world´s population. Reconstruction of past changes in atmospheric circulation in this area is to date scarce, especially on longer timescales. Here, we reconstruct dust fluxes, marine productivity and water temperatures in the Northwest Pacific Ocean and evaluate changes both in the zonal westerlies and monsoonal winds over the past 1 Ma. We demonstrate substantial changes in wind patterns across the Mid-Brunhes Event (~430 ka ago), resulting in reduced dust fluxes to the Northwest Pacific in ensuing glacials. We propose that the westerly jet stream was permanently located south of the Himalayan-Tibetan Plateau through peak glacials, fostered by amplified Arctic cooling.

One sentence summary: Reduced dust fluxes to the North Pacific indicate southward shift of glacial westerly jet related to amplified Arctic cooling.

5.1. Introduction

The Quaternary is a period with major changes in Earth´s climate, including the build-up of stable Northern Hemisphere ice caps. The Mid-Pleistocene Transition (MPT; ~1.2-0.7 million years (Ma) ago) marks one of these substantial changes and was characterized by global cooling, intensification and lengthening of glacial phases from ~41 to ~100 thousand years (ka) (Lisiecki and Raymo, 2005), and abrupt ice sheet expansion and stabilization after ~900 ka (Polyak et al., 2013). Another significant transition in Quaternary climate is the Mid-Brunhes Event (MBE, at ~430 ka), roughly corresponding to the transition from glacial marine isotope stage (MIS) 12 to interglacial MIS 11, after which the amplitude in glacial-interglacial cycles increased significantly (Jansen et al., 1986; Yin and Berger, 2010). In the Arctic region, this was marked by a shift from mostly seasonal to perennial sea ice cover with thick sea ice and ice shelves during glacials (Polyak et al., 2013; Cronin et al., 2017). The MBE was characterized by minimum variation in insolation in the Northern Hemisphere likely forged by the 405 ka-eccentricity cycle and corresponding precession (Jansen et al., 1986; Barth et al., 2018). The mechanisms proposed as causes for the changes across the MBE include insolation-induced changes in Antarctic Bottom Water formation and Southern Ocean ventilation (Yin, 2013) and increased upwelling of respired carbon in the Southern Ocean resulting from a latitudinal shift of the westerly jet stream (WJS) in the Southern Hemisphere (Kemp et al., 2010). Post-MBE interglacials were characterized by higher temperatures and by ~40 ppmv higher atmospheric CO_2 levels compared to pre-MBE interglacials (Lisiecki and Raymo, 2005; Jouzel et al., 2007; Lüthi et al., 2008), by lower ice volume and corresponding higher sea levels (Lisiecki and Raymo, 2005). In eastern Siberia, MIS 11 coincided with the longest and most extensive period of permafrost thawing in the past 500 ka (Vaks et al., 2013). As permafrost soils store tremendous amounts of organic carbon, the release of such carbon as CO_2 and CH_4 to the atmosphere during this extended thawing period may have added to atmospheric warming.

The East Asian continent and Northwest (NW) Pacific Ocean experience large seasonal variations in terms of precipitation and dust fluxes related to the two East Asian monsoonal subsystems, the warm and wet East Asian summer monsoon (EASM) and the dry and cold East Asian winter monsoon (EAWM), as well as the latitudinal position of the WJS. The EAWM is controlled by the strength of the cold-core Siberian High and the warm-core Aleutian Low during winter months and is characterized by strong cold and dry low-level northwesterly winds (Wu and Wang, 2002). Glacial periods were usually characterized by the prevalence of a stronger EAWM associated with an expanded Siberian High that lasted longer and retreated

later than during interglacials (Ding et al., 1995, 2002) and a weakened EASM, whereas during interglacials the opposite was the case. This anti-phase relationship with a strong (weak) EAWM (EASM) during glacials and a weak (strong) EAWM (EASM) during interglacials existed since the mid-Pleistocene (Hao et al., 2012). Glacial-interglacial humidity/aridity variations related to the East Asian monsoon are superimposed on the late Pliocene to Pleistocene increase in aridity in the Asian interior associated with the development of Northern Hemisphere ice caps and the continued uplift of the Himalayan-Tibetan Plateau (HTP), with the latter efficiently blocking off the inflow of moisture from the Indian Ocean (Sun and An, 2005).

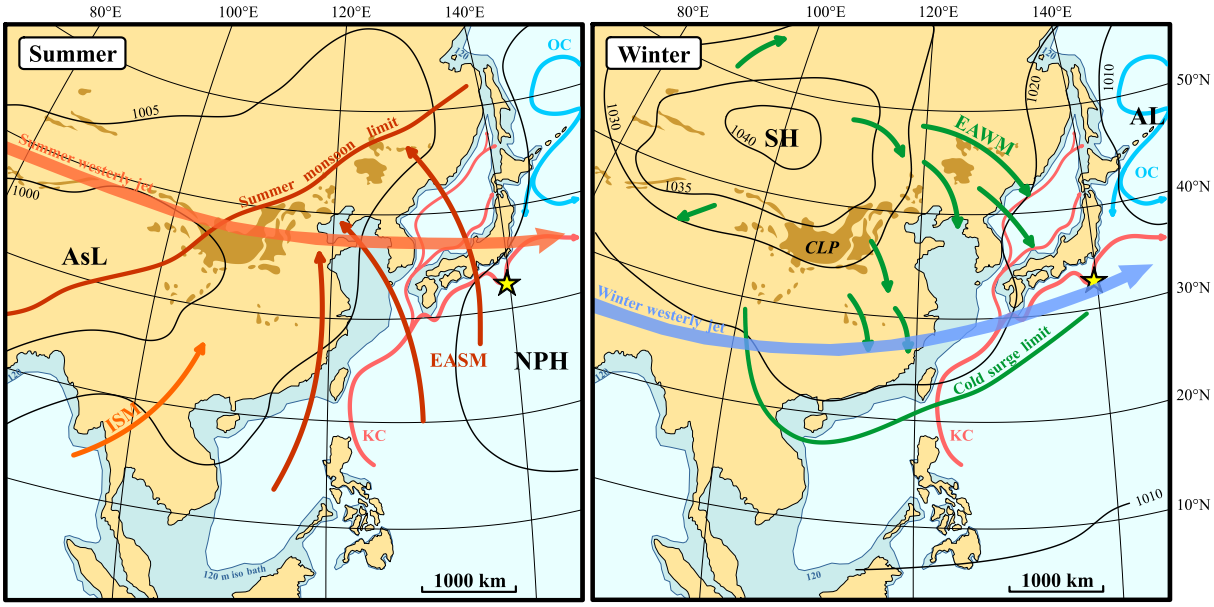

Figure 5.1 | Summertime and wintertime atmospheric circulation over East Asia and the NW Pacific. Yellow star represents IODP Site U1437. The arrows display atmospheric and oceanic current systems: EAWM, East Asian winter monsoon; EASM, East Asian summer monsoon; ISM, Indian summer monsoon; KC, warm Kuroshio Current; OC, cold Oyashio Current. The positions of the atmospheric pressure systems are indicated: AsL = Asian Low, NPH = North Pacific High, SH = Siberian High, AL = Aleutian Low, CLP = Chinese Loess Plateau. Map modified after Yancheva et al. (2007). Black solid lines give isobars with the mean sea level pressure given in hPa. Blue shaded areas are regions with water depths <120 m, which would be exposed during glacial sea level lowstand.

Dust deposited in the North Pacific Ocean primarily originates from the Taklimakan and Gobi deserts (Yu et al., 2019) and is transported eastward by the EAWM in the lower troposphere and the mid-latitude WJS at higher levels. The latter advects dust particles over long distances to the distant North Pacific Ocean (Abell et al., 2021), North American continent (Sassen, 2002) and occasionally the North Atlantic Ocean (Garrison et al., 2003). Over the East Asian continent, the WJS shows a bimodal seasonal flow pattern enabled by the topographic barrier of the HTP. During winter, its axis is predominantly located to the south of the HTP and shifts to the north of the plateau in spring, where it remains until fall (Schiemann et al., 2009).

Low-altitude winds of the EAWM are the predominant dust transport mechanism on the Chinese Loess Plateau (CLP) (Hao et al., 2012) and the elevated deposition of eolian dust particles in NW Pacific Ocean sediments during glacial stages was previously attributed to a stronger EAWM (Kars et al., 2017). At present, the contribution of eolian dust by the EAWM to the Japan Sea and the North Pacific Ocean is negligibly small and dust transport to these areas is linked more closely to the WJS (Nagashima et al., 2007). However, this may have been different in the geological past, when arid areas in the source region of dust transported by the EAWM, Siberia, were more expanded (Nagashima et al., 2007). Despite its currently small contribution to eolian deposition in the North Pacific sediments, the strength of the EAWM in winter was found to positively correlate with the outbreak and frequency of dust storm events in East Asia in the following spring (Wu et al., 2010), thereby controlling the amount of dust formation and mobilization both by the EAWM and WJS.

How the mid-latitudinal atmospheric circulation over the North Pacific has changed in the geological past is to date only poorly constrained. In order to elucidate previous changes in the location of the WJS and variations in the strength of the EAWM on glacial-interglacial timescales, we reconstructed water temperature variations, marine productivity and determined concentrations of land plant-derived lipids as a dust flux indicator in a continuous marine sediment record from the mid-latitudinal Northwest Pacific Ocean spanning the last 1 Ma. International Ocean Discovery Program (IODP) Site U1437 is located at 31°47.3911 ′N, 139°01.5788 ′E (2116 m water depth) under the influence of the WJS, the EAWM and EASM downwind of the major arid regions of the Asian interior, the Taklimakan and Gobi deserts as well as the CLP (Fig. 5.1). The site is expected to receive larger amounts of dust from the continent during cold periods, when aridity in Asia was increased and windiness enhanced (Sun and An, 2005; Fang et al., 2020). Additionally, the site is occasionally located beneath the large meander of the warm and saline Kuroshio Current (KC), which advects tropical moisture and warmth northward. During cold periods, the site supposedly experienced increasing influence of cold and less saline waters of the Oyashio Current (OC) from the Subarctic Pacific owing to a southward displacement of oceanic current fronts (e.g., Jonas et al., 2017). Sediment ages were assigned using the previously published age model by Kars et al. (2017).

5.2. Glacial-interglacial oceanographic changes across the MBE

Changes in water temperatures at the sea surface and subsurface have been reconstructed using the lipid paleothermometers $U^{K'}_{37}$ (unsaturated ketone index; in the modification by Prahl and Wakeham, 1987) and TEX^{H}_{86} (tetraether index based on glycerol

dialkyl glycerol tetraethers consisting of 86 carbon atoms; Schouten et al., 2002) (for details see the supplementary material). Records based on these two paleothermometers have previously been used to reconstruct the interplay of the two major western boundary currents of the North Pacific Ocean, the KC and OC, on glacial-interglacial timescales (Jonas et al., 2017). At Site U1437, both temperature proxies show an overall similar pattern reflecting the well-documented glacial-interglacial sawtooth pattern (Lisiecki and Raymo, 2005) of climate evolution over the past 1 Ma (Fig. 5.2). Interglacials are generally more pronounced in the $U^{K'}_{37}$ with overall SSTs higher by 2 °C, whereas glacials are better expressed in the TEX^{H}_{86} record. As the latter is interpreted to reflect subsurface water temperatures (Jonas et al., 2017), this may indicate an intrusion of cold OC waters into subsurface layers of the water column at Site U1437 during glacials.

Model-simulated surface air temperature differences between average post-MBE and pre-MBE interglacials showed that the former are up to 3.5 °C warmer during the winter and fall in high latitudes and up to 2.5 °C warmer in East Asia (Yin and Berger, 2010). In the paleowater temperature record at Site U1437, a similar shift in average temperatures across the MBE from cold to warm is present, only one order of magnitude smaller and within the calibration errors reported for the respective proxies: average post-MBE interglacials are ~0.2 °C warmer at the sea surface ($U^{K'}_{37}$: 25.1 ± 1.4 °C) and subsurface (TEX^{H}_{86}: 23.5 ± 1.7 °C) than pre-MBE interglacials ($U^{K'}_{37}$. 24.9 ± 1.4 °C, TEX^{H}_{86}: 23.3 ± 1.6 °C). Higher post-MBE interglacial water temperatures at Site U1437 indicate a fortified meridional warm water mass and moisture transport via the KC (Fig. 5.2). This is well in line with elevated precipitation amounts in Korea at the Meiyu/Baiu rain belt, which is associated with a strong North Pacific Subtropical High circulation and a strong EASM (Jo et al., 2014; Sun et al., 2011). Post-MBE glacials at Site U1437 are on average 0.2 °C and 0.4 °C colder than pre-MBE ($U^{K'}_{37}$: 23.2 ± 1.3 °C *vs*. 23.0 ± 1.1 °C post-MBE; TEX^{H}_{86}: 22.1 ± 1.7 °C *vs*. 21.7 ± 1.6 °C post-MBE), which is consistent with previous observations of larger amplitudes in glacial-interglacial cyclicity after the MBE (Yin and Berger, 2010).

5.3. Glacial-interglacial changes in the path of the westerly jet stream

Long-chain *n*-alkanes and *n*-alcohols are major constituents of wax lipids of land plants and can easily be abraded by wind, especially dust storms (Eglinton and Eglinton, 2008). Hence, they are common organic compounds in eolian dust (Schefuß et al., 2003a). A study of land plant-derived lipids in marine aerosols showed that *n*-alkane fluxes to the open North Pacific

Ocean were at maximum during winter and spring, which was attributed to strong westerly winds that typically occur in this region at that time of the year (Kawamura et al., 2003).

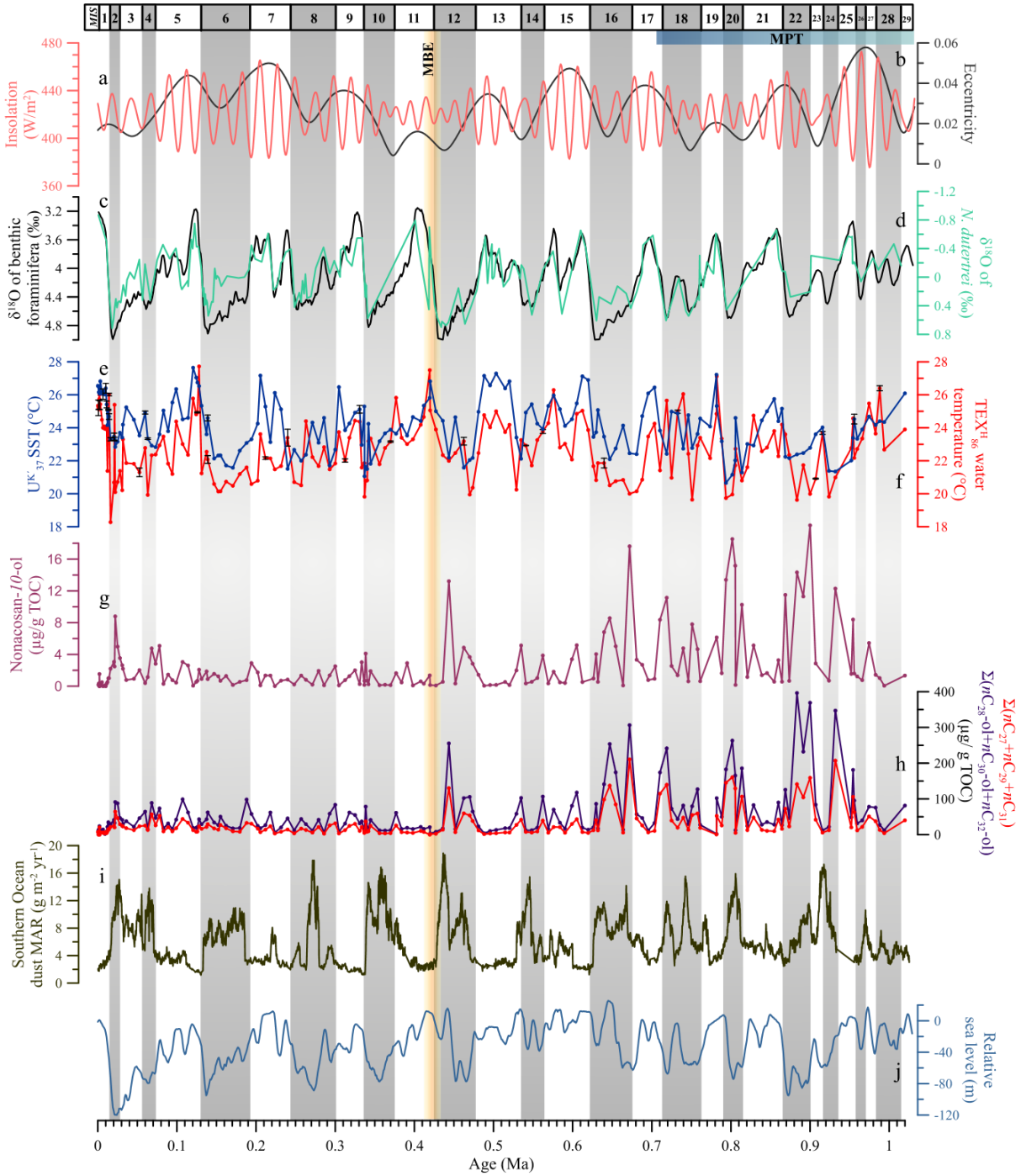

Figure 5.2 | Site U1437 paleoenvironment and paleoclimate proxies in comparison with previously published records. a: Summer insolation at 65 °N (Laskar et al., 2004), b: eccentricity (Laskar et al., 2004), c: global $\delta^{18}O$ record of benthic foraminifera (Lisiecki and Raymo, 2005), d: Site U1437 $\delta^{18}O$ record of planktonic foraminifera *N. dutertrei* (Kars et al., 2017), e: $U^{K'}_{37}$ sea surface temperature (SST) record of Site U1437 (this study), f: TEX^{H}_{86} water temperature record of Site U1437 (this study), g: concentrations of nonacosan-*10*-ol (this study), h: summed concentrations of long-chain *n*-alkanes (red) and *n*-alcohols (green) (this study), i: Southern Ocean dust mass accumulation rates (Martínez-Garcia et al., 2011), j: relative sea level curve (Rohling et al., 2014). MBE = Mid-Brunhes Event (orange vertical bar). Gray vertical bars denote glacial marine isotope stages.

Carbon preference index (CPI) values always >2 throughout the entire U1437 *n*-alkane record indicate that the *n*-alkanes are unaltered and can serve as paleoclimate indicators (Bush and McInerney, 2013). While water temperature variations at Site U1437 reflect dominantly the global glacial/interglacial climate evolution, sedimentary concentrations of land plant derived wax lipids show additional features (Fig. 5.2): pre-MBE concentrations of long-chain *n*-alkanes, *n*-alcohols, and nonacosan-*10*-ol, a biomarker for boreal conifer species *Pinus* and *Picea* (Jetter et al., 2006), overall strongly mimic the glacial-interglacial pattern of dust and *n*-alkane accumulation in the North Atlantic (Naafs et al., 2012b) and Southern Ocean (Martínez-Garcia et al., 2011) with elevated concentrations during glacials (Fig. 5.3). Like Site U1437, the Atlantic and Southern Ocean sites are located in the westerly wind belt and receive eolian sediments from North America or Patagonia, respectively.

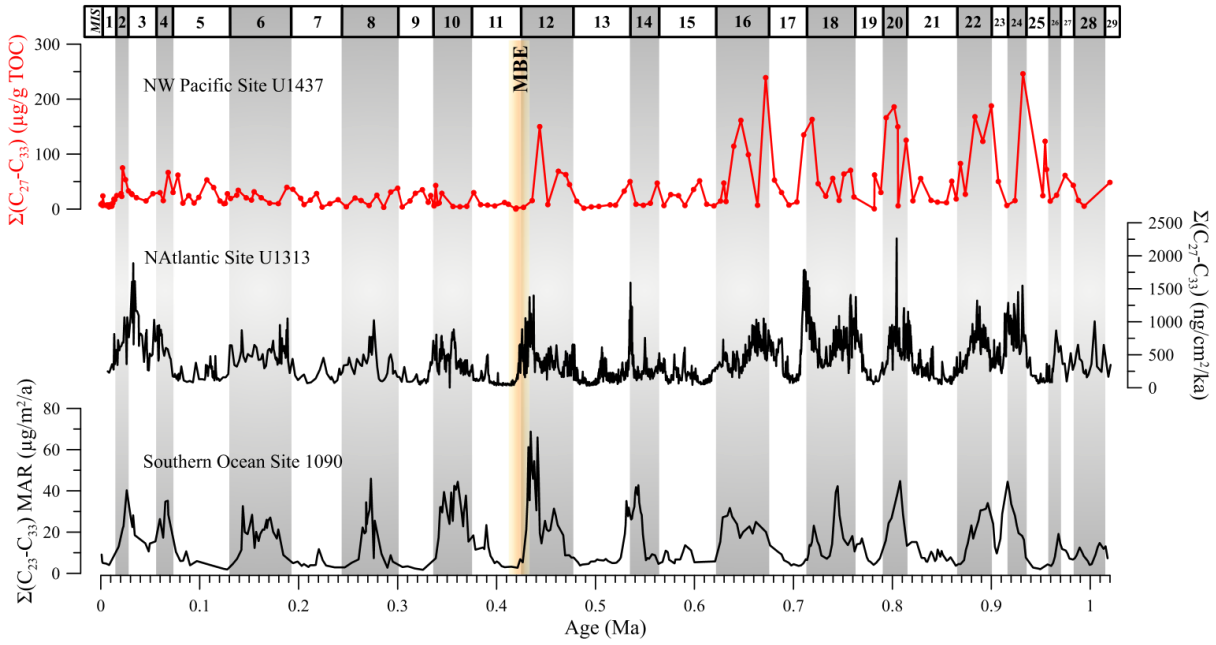

Figure 5.3 | Concentrations or mass accumulation rates of *n*C$_{27}$-*n*C$_{33}$-alkanes over the past 1 Ma. Records from the NW Pacific (this study), North Atlantic (Naafs et al., 2012b) and Southern Ocean (Martínez-Garcia et al., 2011) all show elevated glacial MARs prior to the MBE, whereas only the sites from the North Atlantic and Southern Ocean continue to receive elevated glacial dust inputs after that. Gray vertical bars denote glacial marine isotope stages.

Elevated glacial dust accumulation rates at all three sites may hence indicate changes in aridity of the dust source areas, or latitudinal movements of the WJS. While the two other sites continue to receive unwaveringly high amounts of dust in post-MBE glacials, *n*-alkane accumulation at Site U1437 declines abruptly and significantly after the MBE and shows minimal glacial-interglacial variability thereafter. This indicates that the dust flux to the NW Pacific at Site U1437 was decoupled from the global climate evolution and governed by a westerly wind pattern that is unique to this region.

Grain sizes of loess samples were previously used to reconstruct past variations in the strength of the EAWM or the WJS (Sun et al., 2011; Hao et al., 2012; Fang et al., 2020). Grain size records from the CLP indicate a weak EAWM when Northern Hemisphere summer insolation (NHSI) variability is at minimum (Hao et al., 2012). This occurs at 400 ka intervals (Hao et al., 2012) and happened last ~400 ka ago, which roughly corresponds to the marked changes in alkyl lipid accumulation in Site U1437 sediments (Fig. 5.2). Two atmospheric processes may be held responsible for the observed changes in alkyl lipid accumulation: first, the strength and frequency of dust storms which is mediated by the strength of the EAWM (Wu et al., 2010) may have significantly decreased as a result of a weakened EAWM, and/or second, the atmospheric carrier for eolian dust to the North Pacific, mainly the WJS, may have shifted its latitudinal position. The persisting absence of elevated *n*-alkyl lipid and nonacosan-*10*-ol accumulation in the glacials after the MBE (Fig. 5.2) furthermore indicates that a threshold was reached during this climate transition which allowed a consolidation of the changes in the atmospheric realm.

Insolation-driven climate changes in northern high latitudes, including the expansion of Northern Hemisphere ice sheets (Ding et al., 1995) and the occurrence of perennial sea ice (Meng et al., 2021), changes in Atlantic Meridional Overturning Circulation (AMOC) (Sun et al., 2011), and to a lesser extent El Niño-Southern Oscillation (ENSO)-related convection in the western equatorial Pacific (Zhang et al., 1996) were previously identified as controlling mechanisms for variations in the East Asian Monsoon system. Less pronounced NHSI minima around the MBE (Fig. 5.2) may have suppressed the snow accumulation and ice sheet build-up in the Arctic and thereby weakened the Siberian High and hence the EAWM circulation (Hao et al., 2012). Considering that the northern high latitudes respond much stronger to changes in global climate, a process called Arctic amplification (Cronin et al., 2017), and that the strength of the Siberian High, which controls the strength of the EAWM itself, is controlled by the extent of ice sheets in the Arctic region (Ding et al., 1995), even minimal variations in Arctic climate will severely impact the atmospheric circulation in the northern mid-latitudes. During post-MBE interglacial periods, the Arctic Ocean experienced a rise in bottom intermediate water temperatures and sea surface productivity as well as an extension of perennial sea ice (Cronin et al., 2017). These observations were attributed to enhanced Arctic amplification (Masson-Delmotte et al., 2006; Cronin et al., 2017; Coumou et al., 2018), whereby the interglacial (glacial) Arctic temperature rise (decline) exceeded the Northern Hemisphere average by a factor of 3-4 (Miller et al., 2010). Under presently rising greenhouse gas levels, amplified Arctic warming is accompanied by a significant reduction in boreal snow cover (Coumou et al., 2018),

sea-ice loss (Dai et al., 2019), and resulting changes in albedo and ocean-atmosphere heat and carbon dioxide exchange (Cronin et al., 2017). A decrease in sea ice associated with a release of oceanic heat to the atmosphere under amplified warming in the Arctic reduces the meridional temperature gradient (Zhou, 2017) and thereby weakens the interglacial winter monsoonal circulation. Indeed, a strong winter Arctic amplification was found to reduce dust event occurrences in spring (Liu et al., 2020).

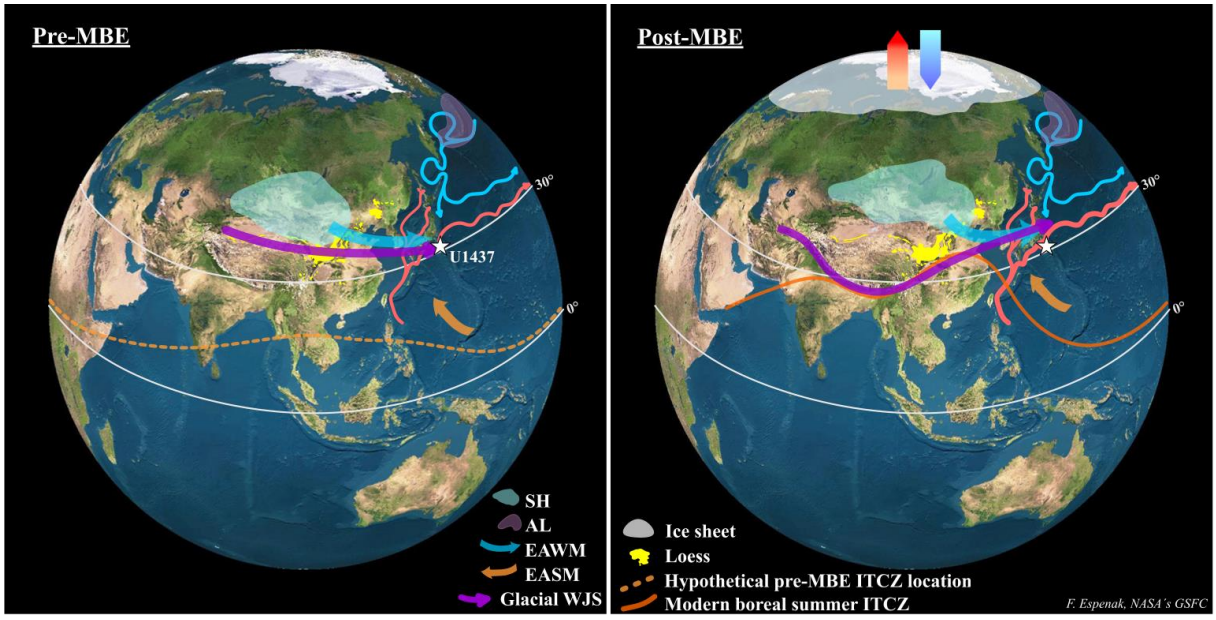

Figure 5.4 | Pre-MBE and post-MBE scenarios of atmospheric and oceanographic circulation in East Asia and the NW Pacific. The left picture shows the pre-MBE scenario with the EAWM (blue arrow) over Site U1437, an EASM (orange arrow) whose front is located further south and the main WJS axis (purple arrow) located north of the Himalayan-Tibetan Plateau. The right picture displays the post-MBE scenario with a southward displaced glacial WJS and stronger EAWM both resulting from amplified cooling in the Arctic region (blue vertical arrow). During post-MBE interglacial periods a stronger EASM associated with a northward shift of the ITCZ migrated further north (see Supplementary Materials). The Siberian High pressure (light blue area) in the post-MBE Scenario is after Hao et al. (2012). The basemap is from the NASA Eclipse Website (https://eclipse.gsfc.nasa.gov/transit/TV2004/Earth-Ingress1a.JPG).

At present, the response to amplified warming in the Arctic is most pronounced in the Kara and Barents Sea (Labe et al., 2020) which are the source areas for most (56 % and 25 %, respectively) of the cold air accumulating over Siberia (Tao and Chen, 1957). As a result, amplified warming over these areas will ultimately weaken the Siberian High. During glacial periods, however, amplified Arctic cooling and associated extensive ice sheets would strengthen the Siberian High and hence the EAWM, which is in line with observations made in grain size records from the CLP (Hao et al., 2012). In conclusion, the cessation in pulsed dust fluxes to NW Pacific Site U1437 is rather a result of latitudinal shift than strength of the EAWM.

A long-term grain size record from loess deposits at the southern margin of the Taklimakan Desert, a region unaffected by EAWM winds, showed a coarsening trend after ~500 ka, which was interpreted as an intensification of the zonal westerlies at this time (Fang et al., 2020). A good match of the Taklimakan loess record with dust records from the North Pacific was proposed to support the hypothesis of dust-borne iron fertilization and hence a rise in oceanic primary productivity under enhanced westerlies circulation (Fang et al., 2020). Indeed, the Site U1437 Ba/Al productivity record shows a slight increase in marine productivity at around 430 ka with average Ba/Al ratios rising from 0.47 ± 0.3 cps to 0.64 ± 0.4 cps (Supplementary information), which may result from dust inputs via stronger westerlies. This raises the question why an intensified WJS does not reflect in post-MBE glacial periods at Site U1437. Looking at the timing of maximum alkyl lipid abundances in pre-MBE glacials shows that in the majority of the cases, concentrations are at maximum during peak glacials as inferred from the stacked benthic $\delta^{18}O$ record (Fig. 5.2). Considering that amplified glacial cooling in the Arctic enhanced after the MBE (Cronin et al., 2017), we propose that the main axis of the WJS was predominantly displaced to the south of the HTP for an extended period of time during post-MBE peak glacials, thereby reducing the amount of dust and hence land plant-derived lipids transported to Site U1437 (Fig. 5.4). A position to the south of the HTP is at present frequently observed in wintertime and a prolonged perseverance at this position in the following spring results in decreased precipitation in central Asia (Schiemann et al., 2009). We therefore hypothesize that the supposed extended residence of the WJS south of the HTP during peak glacial periods after the MBE further contributed to the aridification of the Asian interior associated with global cooling.

5.4. Acknowledgements

The International Ocean Discovery Program is thanked for providing sample material and support for XRF scanning at KCC. Funding of this project was received through grants BA 3841/4-1 and BA 3841/6-1 awarded to TB as well as grants SCHW 554/27-1,2 given to LS.

Chapter 5

Supplementary Materials for

Southward displacement of the glacial westerly jet driven by Arctic amplification

A.-S. Jonas[1], M. Kars[2], T. Bauersachs[1], W. Ruebsam[1], and L. Schwark[1,3]

[1] Department of Organic Geochemistry, Institute of Geosciences, Christian-Albrechts-University, Ludewig-Meyn-Straße 10, 24118 Kiel, Germany.

[2] Center for Advanced Marine Core Research, Kochi University, Nankoku, Japan

[3] WA-OIGC, Earth and Planetary Sciences, Curtin University, Perth, Australia

The file includes:

Materials and Methods

Supplementary Text

Figs. 5.S1 to 5.S6

References

Materials and Methods

Sample material and age model

International Ocean Discovery Program (IODP) Expedition 350 Site U1437 was drilled in a volcano-bounded basin between the Manji and Enpo rear arc seamount chains ~330 km to the west of the Izu-Bonin Trench *(*Tamura et al., 2015b). Hole U1437 B is located at 31° 47.3911 ′N, 139° 01.5788 ′E in a water depth of 2116 mbsl. For this study, we investigated the uppermost 120 m of Hole B consisting mainly of tuffaceous mud and mudstones of lithostratigraphic Unit I (Tamura et al., 2015b). Ages were assigned using the age model of Kars et al. (2017) based on off- and onshore generated data from calcareous nannofossil biostratigraphy, magnetic reversal events and stable oxygen isotope ($\delta^{18}O$) measurements on tests from the planktonic foraminifer *N. dutertrei*.

Lipid biomarker analysis

For lipid biomarker analysis, ~15-25 g each of 174 lyophilized and homogenized sediment samples were solvent-extracted with a Büchi Speed Extractor E-914 (Büchi, Switzerland) at 75 °C, 50 bar using a solvent mixture of dichloromethane (DCM):methanol (MeOH) (93:7, v:v).

An aliquot of desulfurized total lipid extract (TLE) was dissolved in DCM at a concentration of 2 mg/ml and derivatized with N,O-bis(trimethylsilyl)trifluoroacetamide (BSTFA) and pyridine at 60 °C for 2 h. Prior to derivatization, 15 µl of a standard mixture of deuterated tetracosane and deuterated octadecanol (1:3) was added before samples were subjected to GC/MS analysis (as in Jonas et al., 2017) for identification and quantification of *n*-alkyl lipids. The carbon preference index (CPI) of *n*-alkanes (Bray and Evans, 1961) was calculated as follows:

$$CPI_{n\text{-alkanes}} = ½ \times ((\Sigma_{odd}\ (C_{25\text{-}33})/\ \Sigma_{even}\ (C_{24\text{-}32})) + (\Sigma_{odd}\ (C_{25\text{-}33})/\ \Sigma_{even}\ (C_{26\text{-}34}))).$$

Another TLE aliquot was separated into apolar, ketone (containing the alkenones) and polar fractions (containing glycerol dialkyl glycerol tetraethers, GDGTs) using a small Pasteur pipette filled with 3.5 cm of silica (SiO_2) overlain by 1.5 cm of aluminium dioxide (Al_2O_3). Individual fractions were eluted consecutively with *n*-hexane/DCM (9:1, v:v), *n*-hexane:ethylacetate (7:3, v:v) and DCM:MeOH (1:1, v:v) as respective solvent mixtures.

Aliquots of the ketone fractions were measured in a concentration of 2 mg/ml on an Agilent 7890A gas chromatograph coupled to an Agilent 5970B mass spectrometer (GC/MS). Alkenone analysis and identification were previously described in Jonas et al. (2017). Di- and tri-unsaturated alkenones ($C_{37:2}$ and $C_{37:3}$) were quantified in single ion monitoring (SIM) mode at *m/z* 97 to increase intensity as described in Jonas et al. (2017). The $U^{K'}_{37}$ was calculated using the equation by Prahl and Wakeham (1987):

$$U^{K'}_{37} = [C_{37:2}] / ([C_{37:2}] + [C_{37:3}])$$

and converted into SSTs using the global core-top calibration (Müller et al., 1998):

$$SST = (U^{K'}_{37} - 0.044) / 0.033$$

Replicate measurements of selected samples resulted in a standard deviation of 0.01 or better for the $U^{K'}_{37}$, which is equivalent to an analytical error of ± 0.3 °C.

Polar fractions were dissolved in *n*-hexane:2-propanol (99:1, v:v) at a concentration of 3 mg/ml and filtered through a polytetrafluoroethylene (PTFE) filter (45 µm mesh size). They were then subjected to high performance liquid chromatography coupled to mass spectrometry (HPLC/MS). A detailed description of instrument setup and settings can be found in Jonas et al. (2017).

TEX^{H}_{86} values were calculated using the following equation:

$$TEX^{H}_{86} = \log ([GDGT\text{-}2] + [GDGT\text{-}3] + [Cren´]) / ([GDGT\text{-}1] + [GDGT\text{-}2] + [GDGT\text{-}3] + [Cren´])$$

and subsequently converted into temperatures using the equation of Kim et al. (2010):

$$T = 68.4 \times TEX^{H}_{86} + 38.6$$

covering a temperature range of -3 to 30 °C at an uncertainty of ± 2.5 °C. Duplicate analysis of every tenth sample yielded a standard deviation of 0.007 for the TEX^{H}_{86}, corresponding to an analytical error of ± 0.5 °C or better.

X-ray fluorescence

The uppermost 120 m of Site U1437 Hole B (sections 350-U1437B-1H-1A to 17F-4A) were scanned for their elemental composition using the ITRAX micro-X-ray fluorescence (XRF) core scanner at Kochi Core Center, Japan. XRF spectra were generated every 2 cm with an exposure time of 60 sec. The X-ray beam was generated with a 3 kW Mo tube run at 30 kV and 55 mA.

Spectral analysis

Spectral analysis was performed on the Ba/Al dataset. Prior to analysis, the high-resolution Ba/Al data was linearly interpolated in order to achieve an even-scaled data series. Subsequently, long-term trends were removed from the data set by low-frequency band-pass filtering. The de-trended data set was subjected to spectral analysis using a multi-taper method (Thomson, 1982) as implemented in the KSPectra toolkit V3.4.1 (Ghil et al., 2002). Calculation of confidence levels followed the red-noise modelling method (Mann and Less, 1996). A running periodogram has been calculated by evolutionary spectral analysis (step: 0.0016; sliding window: 0.2) using the ACYCLE 2.3 Tool for Matlab (Li et al., 2019).

Supplementary Text

Complementary dust flux records

The Al/Ca ratio was calculated using the data generated from XRF measurements in order to identify changes in the detrital supply to the studied marine sediments. Some glacial-interglacial variability can be seen in the Al/Ca record prior to 700 ka (Fig. 5.S1), however, the pattern is not consistent with alkyl lipid concentrations: during some glacials, Al/Ca is elevated

as would be expected under enhanced glacial windiness and aridity. During others (e.g., MIS 16 and 20), when elevated alkyl lipid concentrations indicate enhanced dust flux, the Al/Ca remains on a low level. After ~530 ka, the data shows more short-term fluctuations and becomes highly variable. In conjunction with the wax lipid-based dust flux records, this indicates that eolian inputs to Site U1437 were only of minor importance during post-MBE times. The lack of covariance between Al/Ca and alkyl lipid concentrations is attributed to a mixed contribution by aquatic (via the Kuroshio) and eolian transport. Alkyl lipids are less subject to aquatic transport, whereas major and trace element fluxes are mediated by both transport mechanisms. Advection of land plant waxes to Site U1437 afforded eolian transport, exclusively.

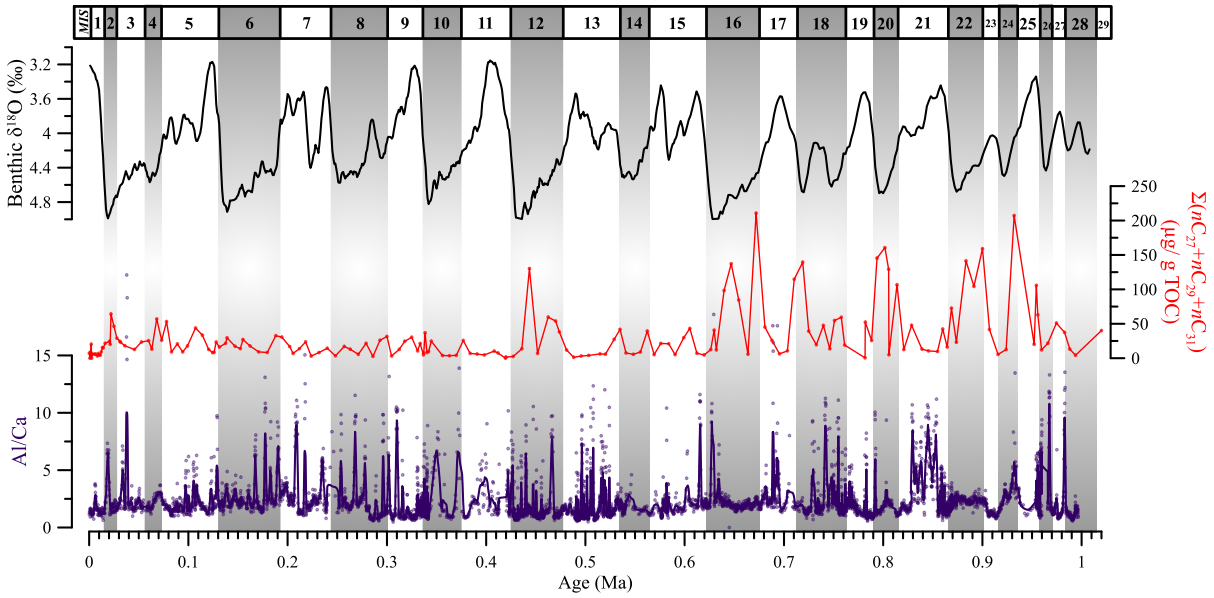

Figure 5.S1 | Site U1437 Al/Ca record in 10-point average (purple) as potential indicator for Asian dust input in comparison with the benthic $\delta^{18}O$ curve by Lisiecki and Raymo (2005) and the concentration of long-chain *n*-alkanes. Gray vertical bars denote glacial marine isotope stages.

Changes in EASM strength across the MBE

Enhanced warming in the tropical tropopause associated with increased tropical convection and latent heating is known to increase the upper-level poleward pressure gradient, thereby counteracting the reduction of atmospheric pressure gradients enforced by an increased Arctic warming during interglacial periods (Coumou et al., 2018; and references therein). This process was hence previously described as a "tug-of-war" between the tropics and the northern high latitudes (Coumou et al., 2018), with the increase in pressure gradients resulting from enhanced tropical warming strengthening mid-latitudinal zonal winds such as the WJS and shifting them poleward, and the decrease in pressure gradients due to amplified Arctic warming having the opposite effect (Coumou et al., 2018; and references therein). As described in the

main paper, grain size records from loess deposits on the southern margin of the Taklimakan Desert showed a coarsening trend associated with global cooling, which further increased after ~500 ka (Fang et al., 2020). The Taklimakan Desert is unaffected by the EAWM and the authors therefore argued that the observed coarsening resulted from an intensification of the zonal westerlies and a further increase of Inner Asian aridification at that time.

Our reconstruction of water temperatures south of Japan indicated a stronger warm water mass transport from the tropics northward via the KC in the interglacials following the MBE (see Chapter 5.2 of the main paper), presumably due to a stronger North Pacific Subtropical Gyre circulation associated with enhanced tropical convection. As described before, the latter would have strengthened the mid-latitudinal atmospheric circulation and shifted the zonal winds poleward (Coumou et al., 2018). The latitudinal migration of the summer monsoonal rain belt is closely tied to the position of the WJS (Schiemann et al., 2009; Sampe and Xie, 2010; Wei et al., 2017; Herzschuh et al., 2019) and based on the previously discussed teleconnective mechanisms, one would expect that under enhanced convective heating in the tropics and associated strengthening and poleward movement of the WJS, the summer monsoon will behave likewise. Indeed, there is increasing evidence that the EASM has strengthened throughout the past ~400 ka (Jo et al., 2014; Beny et al., 2018). In Korea, increased speleothem growth resulting from elevated precipitation during interglacial periods was attributed to a northward movement of the Meiyu/Baiu rain belt and the EASM front associated with a strong and persistent North Pacific Subtropical High pressure and an insolation-driven northward shift of the ITCZ, which moves into China and India in boreal summer (Jo et al., 2014) (Fig. 5.4). Magnetic susceptibility is a well-accepted proxy for the reconstruction of the EASM (Hao et al., 2012). The magnetic susceptibility record of Site U1437 shows a clear glacial-interglacial pattern with higher values during interglacials (Kars et al., 2017). Strikingly, the amplitude in the observed glacial/interglacial variation becomes higher after the MBE, mostly driven by overall higher absolute magnetic susceptibility values during interglacials (Kars et al., 2017). This is consistent with increased magnetic susceptibilities after ~500 ka on the CLP (Sun and An, 2005) and indicates a stronger EASM, likely associated with a further northward advancement of the ITCZ and also the WJS in boreal summer during post-MBE interglacials. Similar assumptions were recently made based on sediment provenance records in sediments from the northern East China Sea (Beny et al., 2018). Moreover, a stronger EASM during interglacials and associated elevated precipitation amounts would increase soil moisture and foster an intensive vegetation cover, thereby hampering dust formation and mobilization (Liu et al., 2020). This, in turn, would lead to decreased dust fluxes to the ocean and may be the

reason for the observed minimal accumulation of dust-transported land plant-derived lipids in marine sediments at Site U1437 during interglacial periods.

Changes in marine primary productivity at Site U1437

Marine primary productivity is driven by the availability of nutrients, either by advection via ocean currents, dust-borne inputs, or by remineralization and upwelling from greater depth. At present and under warm climate states, Site U1437 is located under the warm and oligotrophic Kuroshio Current, whereas it is expected to have experienced increasing influence of cold and more nutrient-rich waters from the Oyashio Current in cold periods as the respective currents were displaced to the south (Jonas et al., 2017). The KC is fed from the Western Pacific Warm Pool (WPWP) in the equatorial Pacific, an oceanic area, where nutrients are completely consumed as the biological pump is at its maximum efficiency (Jaccard et al., 2010). The OC is the southernmost extension of the Western Subarctic Gyre. The Subarctic Pacific is a high nutrient, low chlorophyll area and changes in productivity strongly depend on the availability of micronutrients such as iron (Jaccard et al., 2010). Another potential driver for organic primary productivity is iron fertilization mediated by dust-borne inputs. Changes in aridity of the Asian interior are thought to impact North Pacific primary productivity (Fang et al., 2020) and addition of iron via increased dust fluxes associated with increasing aridification in central Asia was proposed to have provided a positive feedback mechanism for global cooling since the late Pliocene via the drawdown of atmospheric CO_2 through its positive effect on primary productivity (Fang et al., 2020).

In order to infer changes in marine primary productivity, we generated a Ba/Al record based on data from XRF measurements. The Ba/Al ratio is a well-accepted proxy for paleoproductivity, but may be biased in some oceanic settings. In highly productive oceanic areas such as the Eastern equatorial upwelling systems of the Pacific and Atlantic Oceans or highly productive coastal seas, dissolution of biogenic barite through post-depositional microbial sulfate reduction and resulting sulfate depletion may occur under suboxic conditions and hence bias the sedimentary Ba/Al signal. At present, the western North Pacific is considered an ultraoligotrophic region (Martiny et al., 2019) with only very low nutrient availability in the ocean´s surface mixed layer. Under such limited nutrient availabilities and hence comparatively low productivity, post-depositional biogenic barite dissolution is not likely to occur.

The high-resolution Ba/Al record from Site U1437 shows no clear glacial-interglacial pattern from its base at 1 Ma to the end of the Mid-Pleistocene Transition at 0.7 Ma. During most of the ensuing glacial periods (including marine isotope stages (MIS) 16, 12, late MIS 10, early

MIS 6, 4 and 2), the Ba/Al ratio declines, thereby indicating a lower marine productivity as compared to interglacial periods (Fig. 5.S2). Similar observations were previously made in the Subarctic Pacific (Jaccard et al., 2010), where elevated interglacial Ba/Al was attributed to increased export production.

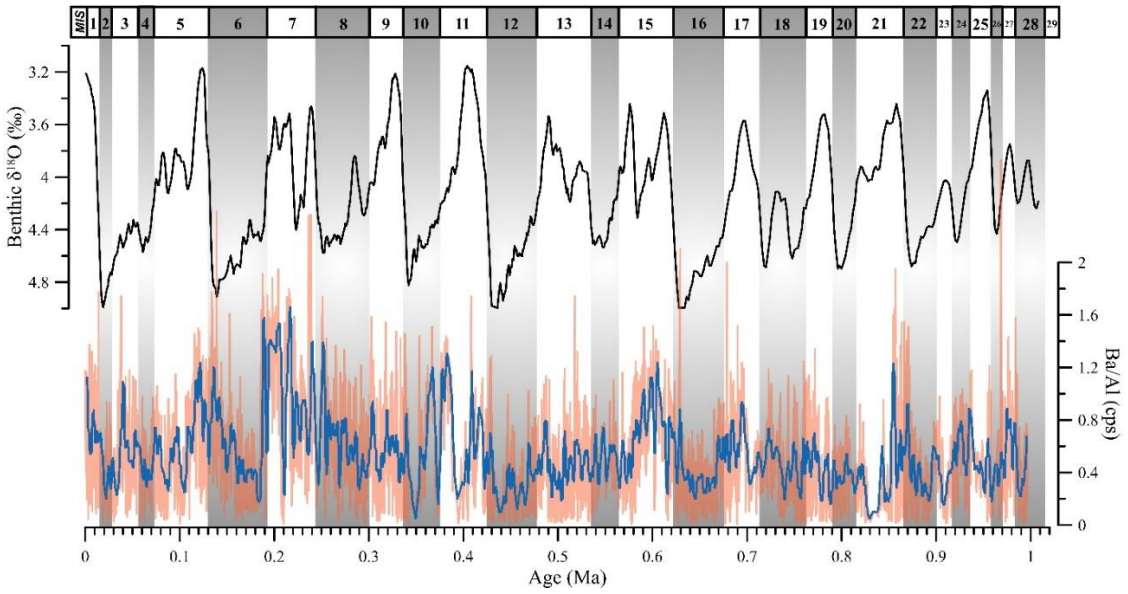

Figure 5.S2 | Site U1437 Ba/Al record as indicator for marine primary productivity in comparison with the benthic $\delta^{18}O$ curve by Lisiecki and Raymo (2005). The blue curve gives the smoothing spline applied to the Ba/Al dataset. Gray vertical bars denote glacial marine isotope stages.

If it is assumed that the Ba/Al ratio is reflecting changes in marine productivity related to eolian dust fluxes only, decreased productivity during glacial periods may provide further evidence for reduced dust fluxes to Site U1437 resulting from a latitudinal shift of the WJS as discussed in the main paper. Interestingly, two significant declines in Ba/Al occur during MIS 5 and coincide with stadials MIS 5b (peaking at 87 ka) and MIS 5d (peaking at 109 ka) (Lisiecki and Raymo, 2005). Following the assumption that the Ba/Al record reflects paleoproductivity changes related to dust inputs, this observation may indicate that dust fluxes were significantly reduced during these two stadial periods and that the WJS axis may also have been located to the south of the HTP for a prolonged period of time. A similar suggestion was made for stadials of the past 60 ka based on changes in sediment provenance in Japan Sea sediments (Nagashima et al., 2011). We cannot further constrain the interpretation of a southward displaced WJS during stadials 5b and 5d based on the wax lipid accumulation at Site U1437 during this time as it is generally low during interglacial periods. As mentioned before, also changes in nutrient availability governed by ocean currents have to be considered and the relative contribution of eolian *vs*. oceanic drivers is difficult to deconvolve. The interpretation of the Ba/Al is hence not as straightforward as the flux of terrestrial lipids to Site U1437. In conclusion, changes in

paleoproductivity at Site U1437 may result from latitudinal shifts in atmospheric systems, presumably the westerly jet as the main contributor of eolian dust from the arid Asian interior to the North Pacific Ocean (Fang et al., 2020), and/or from latitudinal shifts in ocean currents (KC *vs*. OC, oligotrophic *vs*. eutrophic).

Time series analysis on the Ba/Al paleoproductivity record

Time series analysis of the Site U1437 magnetic susceptibility record revealed a strong orbital forcing dominated by the 100 ka-eccentricity cycle, 40 ka-obliquity and 19-23 ka-precession periodicities (Kars et al., 2017). In order to check for periodicities in the Ba/Al record, the dataset was subjected to frequency analyses as described in the Material and Methods section. Milankovitch periodicities were identified in the Ba/Al data set with the 100 ka-eccentricity cycle being dominant throughout the whole record (Fig. 5.S3), and most pronounced after the MBE (Fig. 5.S4). Obliquity was of greater importance during the MPT and after the MBE. Precessional frequencies became more significant after the MBE (Fig. 5.S4).

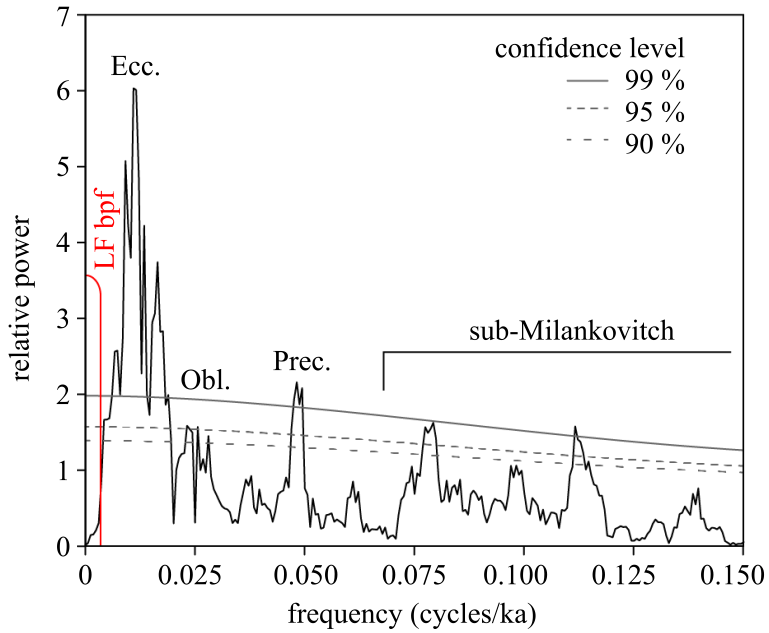

Figure 5.S3 | Multi taper method analysis of the Ba/Al record over the past 1 Ma. Note that low frequencies were removed by low frequency band-pass filtering (LF bpf).

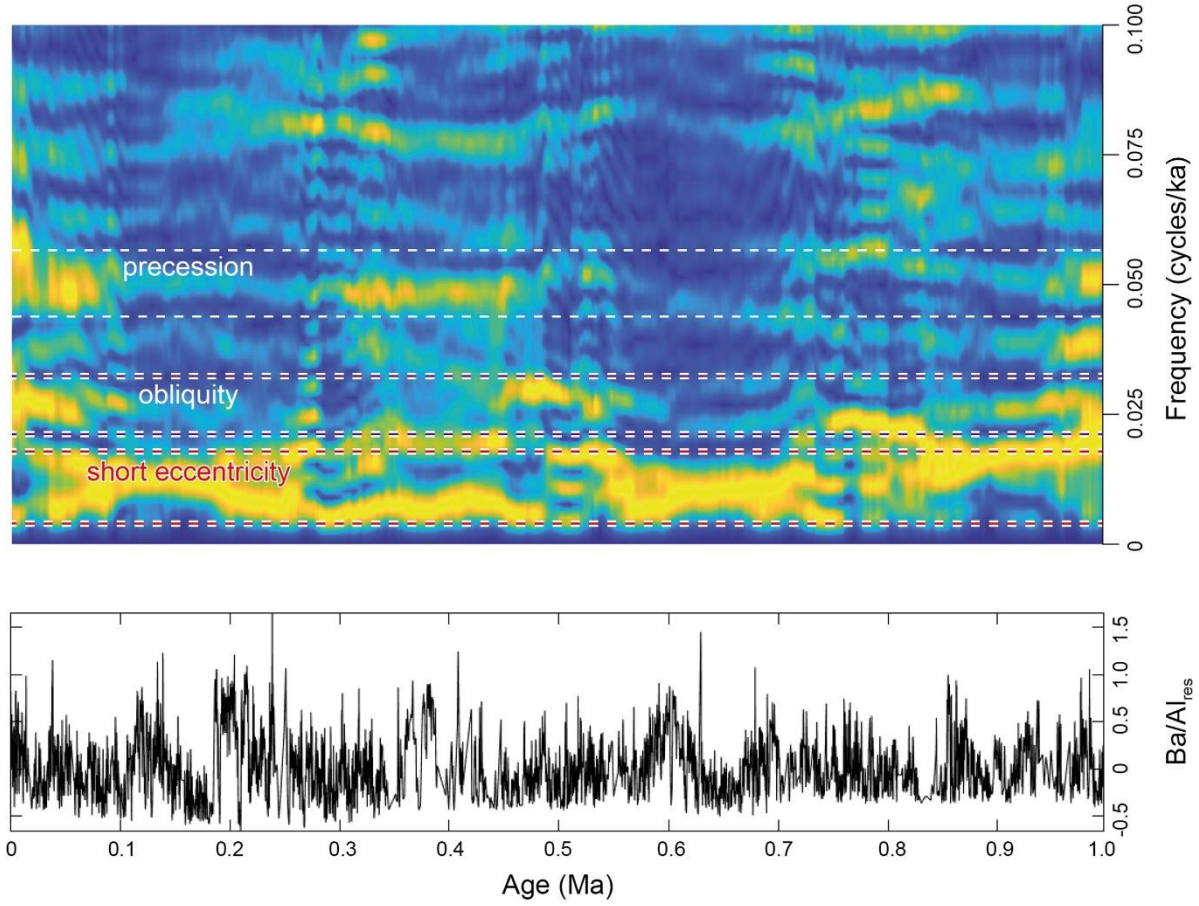

Figure 5.S4 | Running periodogram of the detrended Ba/Al record (Ba/Al_{res}) over the past 1 Ma.

North Pacific sea surface temperature records of the past 1 Ma

Fig. 5.S5 shows Site U1437 temperature records in comparison with other existing long-term $U^{K'}_{37}$-based SST records from the North Pacific Ocean (Fig. 5.S6). While the SST record from Subarctic Pacific Site 882 (Martínez-Garcia et al., 2010) seems to rather show gradual warming from 1 Ma to MIS 5, all other high-resolution sites (U1437, 1143 (Li et al., 2011), 846 (Lawrence et al., 2006)) reflect the typical glacial-interglacial sawtooth pattern as also observed in the global benthic foraminiferal $\delta^{18}O$ stack (Lisiecki and Raymo, 2005). The other existing records from the Northeast (NE) Pacific (LaRiviere et al., 2012), Shatsky Rise (LaRiviere et al., 2012) and the California upwelling in the subtropical NE Pacific (LaRiviere et al., 2012) lack sufficient temporal resolution for identifying both clear long-term trends as well as glacial-interglacial variations. Site U1437 records are well in line with records from the equatorial Pacific, even though the amplitude of glacial-interglacial temperature variations is larger at Site U1437 compared to the tropical sites, owing to its location at mid-latitudes in the NW Pacific with varying influences of tropical and subarctic water masses on glacial-interglacial timescales (KC *vs.* OC).

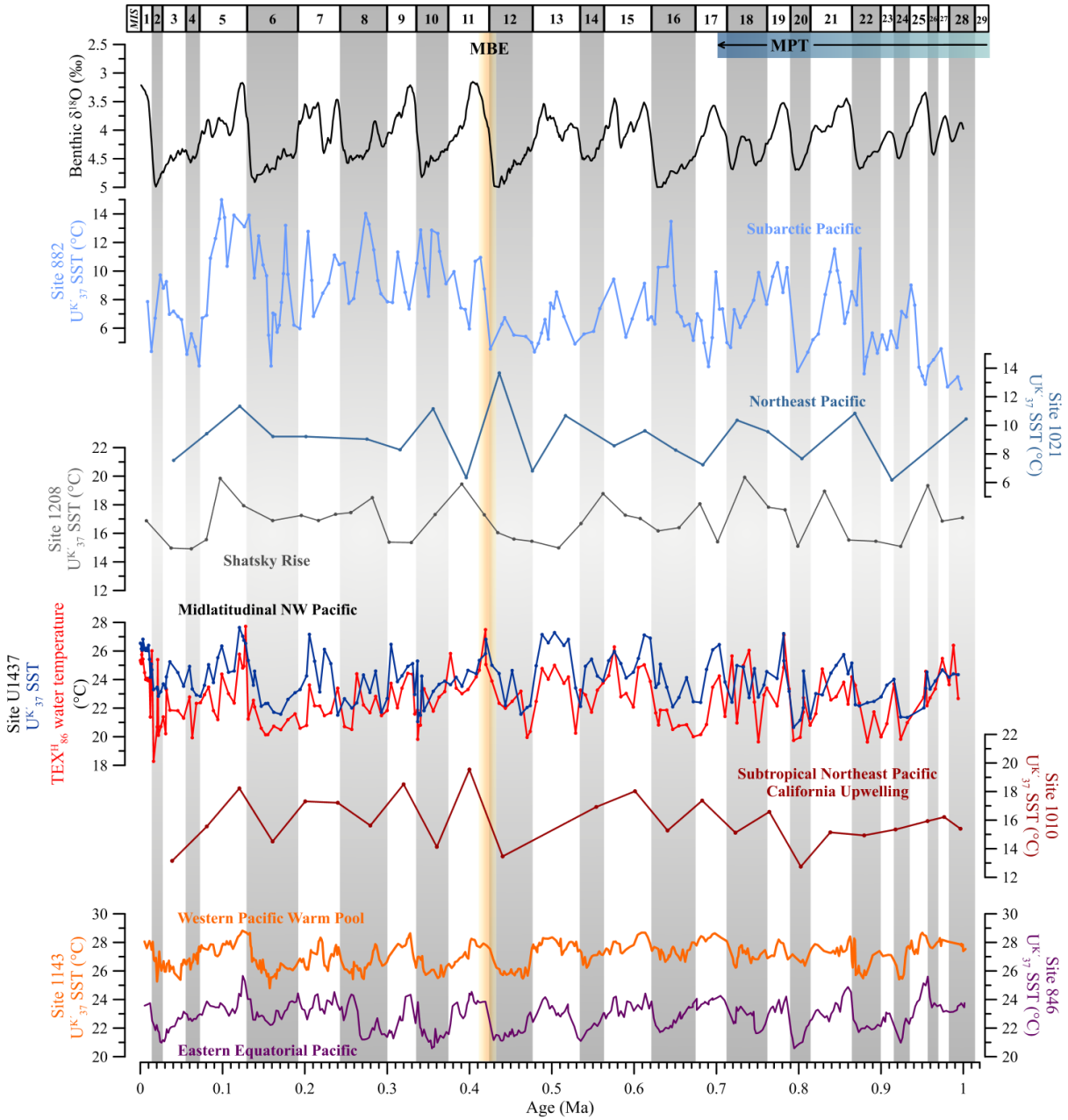

Figure 5.S5 | A compilation of $U^{K'}_{37}$-reconstructed sea surface temperature records over the past 1 Ma in the Pacific Ocean (this study; Lawrence et al., 2006; Martínez-Garcia et al., 2010; Li et al., 2011; LaRiviere et al., 2012). Gray vertical bars denote glacial marine isotope stages.

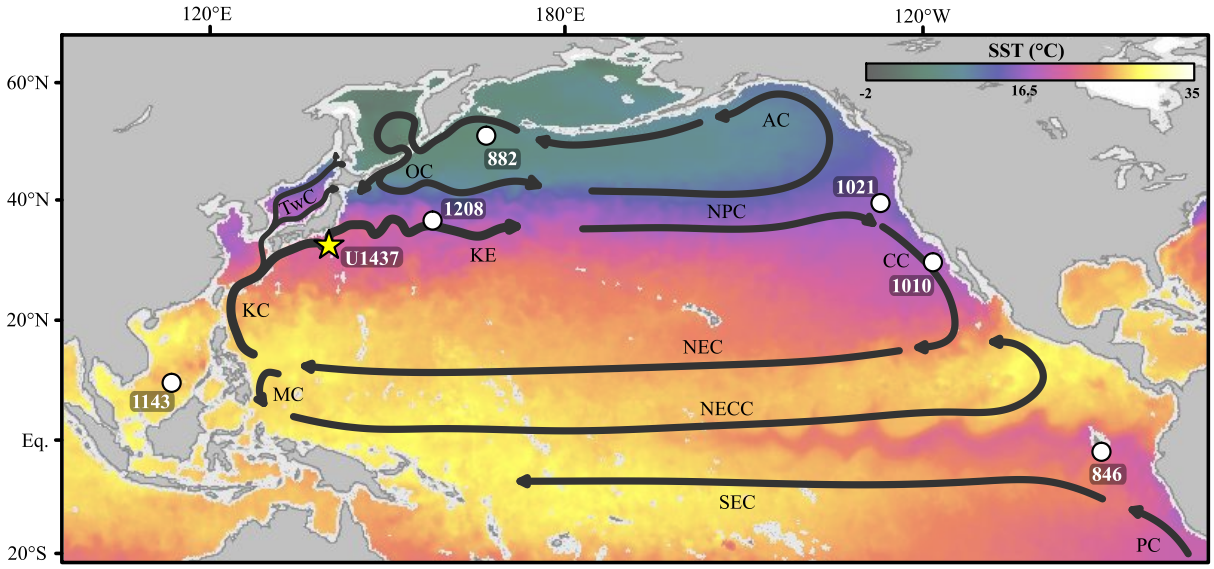

Figure 5.S6 | Map showing the locations of $U^{K'}_{37}$-based sea surface temperature records compiled in Figure 5.S5. Black arrows indicate major ocean surface currents in the North Pacific. Abbreviations for ocean currents are as follows: KC = Kuroshio Current; KE = Kuroshio Extension; OC = Oyashio Current; AC = Alaska Current; NPC = North Pacific Current; CC = California Current; NEC = North Equatorial Current; NECC = North Equatorial Counter Current; PC = Peru Current; SEC = South Equatorial Current; MC = Mindanao Current; TwC = Tsushima Warm Current. The false-color sea surface temperature base map of the North Pacific Ocean is from https://earthobservatory.nasa.gov/images/3513/global-sea-surface-temperature-from-amsr-e.

Chapter 6

An 8-million-years history of paleoceanographic and paleoclimatic changes in the Northwest Pacific Ocean at IODP Sites C0011 and U1437

Ann-Sophie Jonas[1], Thorsten Bauersachs[1], and Lorenz Schwark[1,2]

[1] Department of Organic Geochemistry, Institute of Geosciences, Christian-Albrechts-University, Ludewig-Meyn-Straße 10, 24118 Kiel, Germany.

[2] Department of Chemistry, WA-OIGC, Curtin University, GPO Box U1987, Perth, WA 6845, Australia.

In preparation for publication.

Abstract

The climate and ecosystem evolution of the East Asian continent and adjacent Northwest Pacific Ocean results from a complex coupling of ocean current and atmospheric circulation dynamics as well as tectonic processes including the uplift of the Himalayan-Tibetan Plateau. Here, we present long-term records of ocean temperatures from two sites in the Northwest Pacific Ocean south of Japan from the late Miocene and late early Pliocene to present, respectively, and leaf wax-inferred aridity estimates to track associated changes on land. With this study we achieve to close the existing regional gap of long-term temperature reconstruction in the North Pacific Ocean. We show that water temperatures cooled on average by ~1 °C from the late Miocene to the Pliocene and an additional ~2-3 °C to the Present. Synchronous changes in wax lipid composition indicate a concomitant increase in aridity in East Asia, presumably resulting from combined effects of general global cooling, tectonic uplift and associated changes in hydroclimate.

6.1. Introduction

From the late Miocene to present, planet Earth experienced a long-term cooling accompanied by a decline in atmospheric carbon dioxide levels (e.g., Zhang et al., 2013b) and the intensification of Northern Hemisphere glaciation at ~2.7 Ma, expressed by the establishment of stable ice sheets at northern high latitudes (Maslin et al., 1998). This was followed by the emergence into frequent glacial-interglacial cycles with a 41-kyr-, and after a transitioning period (the Mid-Pleistocene Transition from ~1.25-0.7 Ma), a 100-kyr- periodicity (Lisiecki and Raymo, 2005). Additionally, several major tectonic reorganizations occurred from the late Miocene onwards, including the closure of the Central American Seaway (CAS) (Lyle et al., 2008), further constriction of the Indonesian Seaway (Kuhnt et al., 2004), the opening of the Bering Strait (Gladenkov et al., 2002), and the continued uplift of the Himalayan-Tibetan Plateau (HTP) (An et al., 2001; Tada et al., 2016). In Asia, combined effects of global cooling and tectonic uplift led to a progressive aridification of the Asian interior and associated changes in the hydrographic regime, thereby promoting significant changes in the floral community including the expansion of C_4 plants (Shen et al., 2018).

Studies of the long-term climate evolution are crucial for the understanding of climate responses to coupled effects of changes in atmospheric CO_2 concentrations, regional tectonics and external forcing mechanisms such as incoming solar radiation (e.g., Brierley et al., 2009). Several records exist that track the long-term climate evolution of the northern Pacific Ocean from the late Miocene to present, however, these records concentrate on the equatorial western (Wara et al., 2005; Zhang et al., 2014) and eastern Pacific (Seki et al., 2012; Rouselle et al., 2013) including the cold tongue (Lawrence et al., 2006; Zhang et al., 2014), the eastern North Pacific margin (LaRiviere et al., 2012), and the Subarctic Pacific Ocean (Herbert et al., 2016). Unfortunately, these studies lack spatial coverage of the Northwest Pacific Ocean, an area that is important for the heat balance of the northern Pacific as it is a region that is governed by the confluence of warm and saline tropical waters advected by the Kuroshio Current (KC) and cold and fresher waters from the Subarctic Pacific transported by the Oyashio Current (OC). The only existing long-term temperature record is from ODP Site 1208 on Shatsky Rise located in the open North Pacific Ocean (LaRiviere et al., 2012). Furthermore, most of these deep-time temperature reconstructions rely either on the unsaturated ketone index ($U^{K'}_{37}$) or planktonic foraminiferal Mg/Ca ratios (Wara et al., 2005), both of which are limited in applicability in high temperature settings such as the tropical Western Pacific Warm Pool (WPWP) and during past warmhouse climates such as the late Miocene and Mid-Pliocene Warm Period (Brassell, 2014; O´Brien et al., 2014). The tetraether index of glycerol dialkyl glycerol tetraethers (GDGTs)

consisting of 86 carbon atoms (TEX_{86}; Schouten et al., 2002) serves as a lipid paleothermometers whose application is not compromised in high temperature settings and has been successfully applied to reconstruct western equatorial Pacific sea surface temperature (SST) evolution from the middle Miocene to present (Zhang et al., 2014).

Both modelling data (Brierley et al., 2009) and proxy-based studies (LaRiviere et al., 2012; Zhang et al., 2014) indicate reduced meridional temperature gradients during the late Miocene and early Pliocene, mostly due to greater warmth at high latitudes (Brierley et al., 2009; LaRiviere et al., 2012). Resulting from major constriction of the CAS by the early Pliocene, the tropical Pacific thermocline shoaled, thereby enabling a closer coupling of sea surface temperatures (SSTs) and overlying atmosphere evolution (LaRiviere et al., 2012). Meridional SST gradients reportedly increased between the tropical and mid-latitudinal Pacific Ocean and both Hadley and Walker circulations became stronger (LaRiviere et al., 2012).

From the late Miocene onwards, large continental areas underwent aridification associated with changes in the floral community (Herbert et al., 2016). This drying was especially significant in Asia, where the continued uplift of the HTP added to the aridification by efficiently blocking off incoming moisture from the tropical Indian Ocean via the Indian summer monsoon (ISM) (Sun and An, 2005). Today, the Asian interior is home to some of the largest deserts in the world, including the sandy Taklimakan Desert, which may have formed as early as in the late Oligocene - early Miocene (Zheng et al., 2015) or late Miocene (Sun et al., 2009), and the mostly rocky Gobi Desert, whose formation dates back to the late Pliocene (Lu et al., 2019).

The NW Pacific Ocean off Japan constitutes a crucial link between the tropical Pacific Ocean, including the WPWP, and the Subarctic Pacific, as the two major western boundary currents of the North Pacific converge in this region. Nonetheless, the region is to date largely understudied when it comes to the reconstruction of long-term paleoceanographic and paleoclimatic changes. In order to increase our understanding of how the regional climate and oceanographic setting of the Northwest Pacific evolved from the late Miocene to present, we studied the long-term paleoclimatic and paleoceanographic evolution at two sites south of Japan. With the resulting lipid paleothermometer-based records of ocean temperature changes, we achieve to close the existing regional gap and yield crucial information on how this specific region, in comparison with other regions of the North Pacific Ocean, responded to large-scale changes in global climate, tectonic setting and external forcing mechanisms. As the study sites in the NW Pacific Ocean are located downwind of the Asian continent, wax lipid-based estimates of changes in continental aridity from the same set of samples allow for a more complete understanding of associated changes on land.

6.1.1. Regional oceanography

The surface circulation of the equatorial; North and Subarctic Pacific Ocean is governed by the circulation of the North Pacific Subtropical and Subarctic Gyres (Fig. 6.1). As part of the clockwise circulating North Pacific Subtropical Gyre, the warm and saline Kuroshio Current, one of the two major western boundary currents in the North Pacific, advects heat and moisture from the WPWP in the tropical Pacific to northern mid-latitudes. East of Japan, the KC merges with the cold and less saline Oyashio Current, the second large western boundary current that is part of the Western Subarctic Gyre, and is deflected eastward forming the Kuroshio Extension (KE).

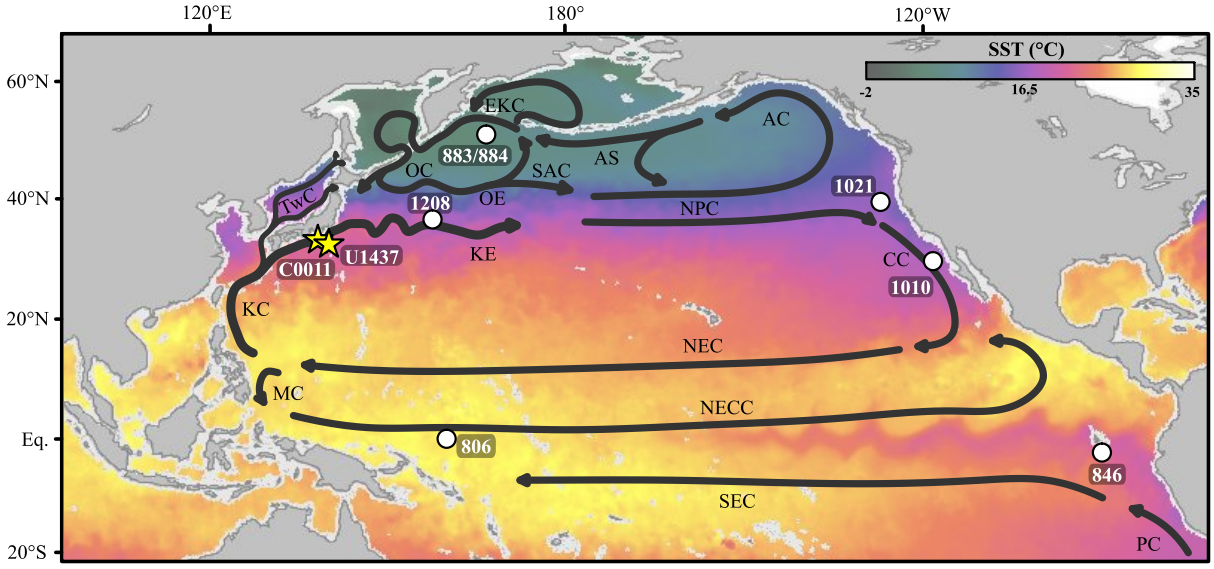

Figure 6.1 | Oceanographic regime in the North Pacific Ocean with all sites investigated (yellow stars; IODP Sites C0011 and U1437) and referenced (ODP Sites 806, 846, 883/884, 1010, 1021 and 1208) in this study. The false-color sea surface temperature base map is from https://earthobservatory.nasa.gov/images/3513/global-sea-surface-temperature-from-amsr-e. Abbreviations for ocean currents are as follows: KC = Kuroshio Current; KE = Kuroshio Extension; OC = Oyashio Current; OE = Oyashio Extension; EKC = East Kamtchatka Current; SAC = Subarctic Current; AS = Alaskan Stream; AC = Alaska Current; NPC = North Pacific Current; CC = California Current; NEC = North Equatorial Current; NECC = North Equatorial Counter Current; PC = Peru Current; SEC = South Equatorial Current; MC = Mindanao Current; TwC = Tsushima Warm Current.

South of Japan and following its exit from the East China Sea through the Tokara Strait, the KC shows a bimodal stationary flow pattern with a short and a large meander path. The latter can reach as far south as 30 °N (Kawabe, 1985) and currently is occasionally present above Site U1437 (Fig. 6.2). The short meander path can be further subdivided into a nearshore and an offshore meander path, of which the latter is located above Site C0011. The formation of the different meander states depends on changes in current velocity and volume transport as well as the current´s position upon its exit through the Tokara Strait (Tsujino et al., 2013; Usui et al., 2013).

The modern surface circulation of the Pacific Ocean, including the northward deflection of the warm current in the tropical equatorial Pacific that forms the KC, was established during the middle Miocene at ~13.9 Ma (Kuhnt et al., 2004). At that time, eustatic sea level fall resulting from a major expansion of the East Antarctic ice sheet significantly restricted the Indonesian Throughflow (Kuhnt et al., 2004). Tomida and Kitao (2002) and Tomida et al. (2013) attributed the presence of the tropical planktic gastropod *Janthina (Hartungia) typica* in the Neogene Miyazaki Group in Kyushu by ~5 Ma to the "arrival" of the KC at the Pacific coast of Japan at that time. Other studies suggested that the KC may finally have reached its present-day latitude south of Japan by ~3 Ma during the late Pliocene, when Indo-Pacific benthic foraminifera and gastropod species first occurred in strata in Japan (Tsuchi and Shuto, 1984; Shuto, 1990; Gallagher et al., 2009). This increase in strength and northward transport of warm water masses from the tropical Pacific to northern mid-latitudes via the KC was attributed to an increase in intensity of the North Pacific Subtropical Gyre circulation and an expansion of the WPWP during the Pliocene associated with the onset of Northern Hemisphere glaciation and the final closure of the CAS (Maier-Reimer et al., 1990; Sato et al., 2008).

6.2. Materials and methods

6.2.1. Sediment samples and age model

Two sets of sediment samples were taken from sediment cores drilled at International Ocean Discovery Program (formerly Integrated Ocean Drilling Program) (IODP) Expeditions 333 and 350 Sites C0011 (259 samples) and U1437 (247 samples), respectively, in the western North Pacific Ocean south of Japan.

Expedition 333 Site C0011 is located at 32° 49.7436 ′N, 136° 52.9250 ′E in a water depth of 4050 meters below sea level (mbsl) on the northwestern flank of a prominent bathymetric high, the Kashinosaki knoll, in the Nankai Trough area. The sequences drilled at the site comprise a 377 m thick sedimentary succession that spans the last ~8.2 Ma (late Miocene to present). The drilled lithologies consist of silty clay and clayey silt and clays interbedded with layers of tephra and volcaniclastic sands, tuffaceous sandstones and heterolithic gravels of various thicknesses (Expedition 333 Scientists, 2012). A detailed age model based on biostratigraphy, magnetic reversal events and volcanic marker events with radiometrically dated onland equivalents can be found in Expedition 333 Scientists (2012). The temporal sampling resolution for the past 9 ka is ~0.3 ka, between 9 and 150 ka ~2 ka, between 150 ka and 1 Ma 16 ka and from 1-8.2 Ma ~70 ka at Site C0011.

Expedition 350 Site U1437 was drilled at 31°47.3911 ′N, 139°01.5788 ′E in a water depth of 2116 mbsl in a volcano-bounded basin between the Manji and Enpo rear arc seamount chains west of the Izu Bonin arc. The uppermost ~606 mbsf of Site U1437 span the last ~3.9 Ma and consist of tuffaceous mud and mudstones intercalated with volcaniclastic layers (Tamura et al., 2015b). The age model of Site U1437 is based on shipboard biostratigraphy and magnetic reversal events (Tamura et al., 2015b) and was further refined for the uppermost 120 m of Site U1437 Hole B (corresponding to the last ~1 Ma) using magnetic reversal events, biostratigraphic datums and planktonic foraminiferal oxygen isotope data ($\delta^{18}O$) (Kars et al., 2017). The temporal sampling resolution for the past 1 Ma is ~6 ka, between 1 and 3 Ma ~30 ka, and from 3-3.9 Ma ~135 ka at Site U1437. Figure 6.2 shows the current locations of Sites C0011 and U1437 in the Philippine Sea and their backtracked positions from the middle Miocene to present.

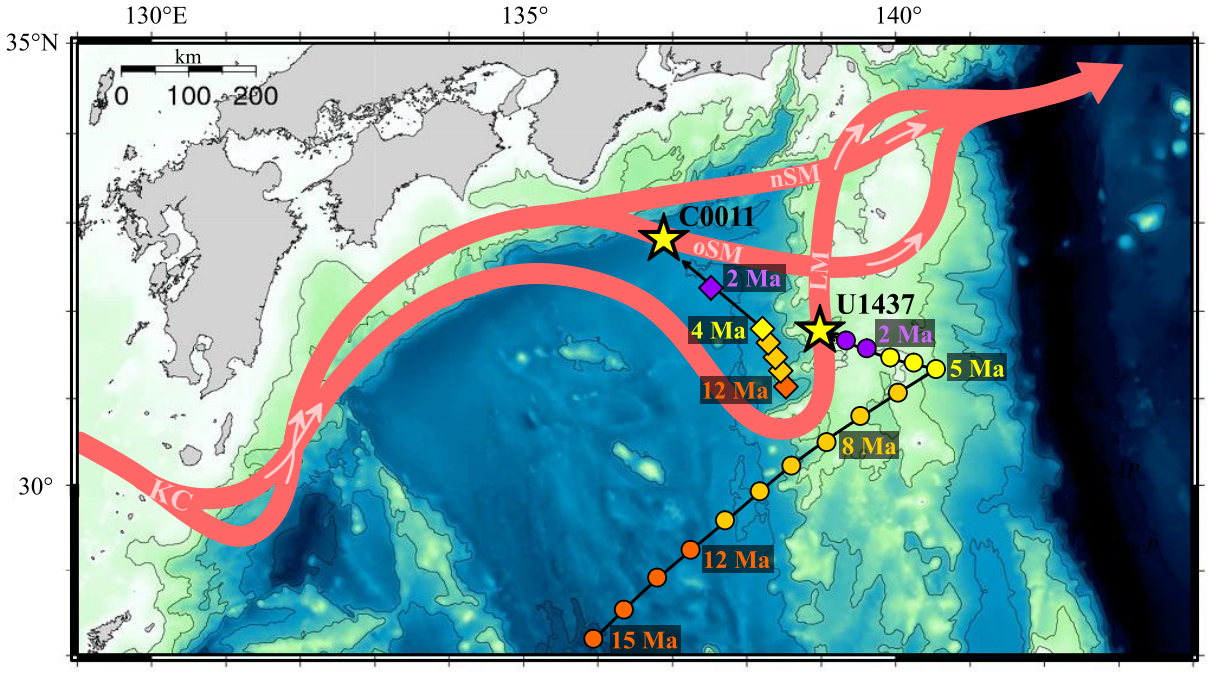

Figure 6.2 | Bathymetric map of the northern Shikoku Basin showing the current locations of Sites C0011 and U1437 and their backtracked positions back to the middle Miocene. Past positions of Site C0011 are indicated by diamonds and those of Site U1437 by circles. Spacing between individual symbols is 2 Ma for Site C0011 and 1 Ma for Site U1437. Paleo positions of Site C0011 were calculated based on estimated plate convergence rates and magnetic stripes in the Shikoku Basin by Expedition 322 Scientists (2010). Past locations of Site U1437 were calculated and kindly provided by Robert J. Musgrave (*personal communication*). The symbols´ colors indicate different epochs: purple = Pleistocene, yellow = Pliocene, light orange = late Miocene, dark orange = middle Miocene. The present-day path of the Kuroshio Current (KC) with its different meander configurations is indicated.

Differences in back trajectory positions of the two different sites despite their position on the same tectonic plate, the Philippine Sea Plate, arise from different tectonic settings: whereas Site C0011 is located in the northern Shikoku Basin and its northwestward path is controlled by the subduction rate and direction of the Philippine Sea Plate under the Eurasian Plate beneath Japan

and the orientation of the spreading center in the Shikoku Basin, Site U1437 is located on the Philippine Sea Plate´s edge in the Izu-Bonin arc system. Additional to spreading and rifting in the Shikoku Basin and subsuction of the Izu arc beneath Japan at its northern end, the site experienced intra-arc rifting since the Pliocene, which may explain the drastic change in the site´s track after 5 Ma.

For a detailed overview of tectonic processes involved in the past tracks of the two study sites, the reader is referred to Chapter 2 of this thesis.

6.2.2. Lipid biomarker analysis

For lipid biomarker analysis, 259 sediment samples from Site C0011 and 247 samples from Site U1437 were lyophilized and subsequently homogenized using an agate mortar and pestle. ~5-25 g of each sample were then solvent-extracted using a Büchi Speed Extractor (E-914) (Büchi, Switzerland) at 75 °C / 50 °bar with a solvent mixture of dichloromethane (DCM): methanol (MeOH) (93:7, v:v). The total lipid extracts (TLEs) were then desulfurized overnight using activated copper turnings to remove elemental sulfur. TLEs were subsequently evaporated to near dryness under vacuum, transferred to pre-weighed vials and dried under a gentle stream of N_2.

An aliquot of desulfurized TLE was dissolved in DCM at a concentration of 2 mg/ml and derivatized with N,O-bis(trimethylsilyl)trifluoroacetamide (BSTFA) and pyridine at 60 °C for 2 h. Prior to derivatization, 15 µl of a standard mixture of deuterated tetracosane and deuterated octadecanol (1:3) were added before samples were subjected to gas chromatograpy coupled with mass spectrometry (GC/MS) for identification and quantification of *n*-alkyl lipids. The 7890A gas chromatograph (Agilent, Germany) was equipped with a fused silica capillary column (DB-5; 30 m × 0.25 mm, Agilent, Germany) and its oven temperature was programmed as follows: 70 °C (3 min isothermal) to 140 °C at 10 °C/min, then to 325 °C at 3 °C/min, and held constant at 325 °C for 20 min. The 5975B mass spectrometer (Agilent, Germany) was operated at an electron energy of 70 eV and an ion source temperature of 250 °C. Target compounds including long-chain *n*-alkanes and *n*-alcohols were identified via characteristic mass spectra and peak areas were integrated using the GC/MS Chemstation Software (Agilent Technologies).

The concentration-weighted average chain length (ACL) of long-chain *n*-alkanes was calculated according to Bush and McInerney (2013) as follows:

$$ACL_{odd\ C27\text{-}C33} = (27 \times C_{27} + 29 \times C_{29} + 31 \times C_{31} + 33 \times C_{33}) / (C_{27} + C_{29} + C_{31} + C_{33})$$

A second aliquot of each TLE was separated into hydrocarbon, ketone (containing alkenones) and polar fractions (containing GDGTs) using a small Pasteur pipette filled with 3.5 cm of silica (SiO_2), which was overlain by 1.5 cm alumina oxide (Al_2O_3). In the following, individual fractions were eluted with *n*-hexane/DCM (9:1, v:v), *n*-hexane:ethylacetate (7:3, v:v), and DCM:MeOH (1:1, v:v) as respective solvent mixtures. Ketone fractions were re-dissolved in DCM (2 mg/ml) and measured on the GC/MS using the same settings as described above. Di- and triunsaturated alkenones were quantified in single ion monitoring (SIM) mode at *m/z* 97. A detailed description of the method refinement for alkenone analysis can be found in Jonas et al. (2017). The $U^{K'}_{37}$, a well-established proxy for sea surface temperature (SST) reconstruction, was calculated following the equation by Prahl and Wakeham (1987):

$$U^{K'}_{37} = [C_{37:2}] / ([C_{37:2}] + [C_{37:3}])$$

and was transferred into SSTs using the global core-top calibration by Müller et al. (1998):

$$SST = (U^{K'}_{37} - 0.044) / 0.033$$

covering a temperature range of 0-29°C.

Duplicate measurements of selected samples resulted in a standard deviation for the $U^{K'}_{37}$ of 0.02 or better at Site C0011, which is equivalent to ± 0.7 °C, and 0.01 or better at Site U1437 (equivalent to ± 0.3 °C).

For GDGT analysis, aliquots of polar fractions were re-dissolved in *n*-hexane:2-propanol (99:1, v:v; 3 mg/ml) and filtered through a polytetrafluoroethylene (PTFE) filter (45 µm mesh size). GDGTs were then analysed on a Waters Alliance 2690 high performance liquid chromatograph (HPLC) (Waters, UK) coupled to a Quattro LC triple quadrupole mass spectrometer (Micromass, UK) using the method described in Hopmans et al. (2004) with the gradient profile of Liu et al. (2012). The HPLC was equipped with a Prevail Cyano column (2.1 × 150 mm, 3 µm; Grace, US) maintained at a constant temperature of 30 °C. The flow rate was set to 0.2 ml/min. Solvents used were hexane and hexane:2-propanol (90:10, v:v). The MS was equipped with an atmospheric pressure chemical ionization (APCI) interface operated in positive ion mode. Source conditions were identical to those described in Heyng et al. (2015). GDGTs were detected by selected ion recording (SIR) of their $[M+H]^+$ ions (dwell time = 200 ms) according to Hopmans et al. (2000, 2004) and were integrated using the MassLynx software. TEX^H_{86} values were calculated and transferred into temperatures following the equations given in Kim et al. (2010):

$$TEX^H_{86} = \log ([GDGT\text{-}2] + [GDGT\text{-}3] + [Cren']) / ([GDGT\text{-}1] + [GDGT\text{-}2] + [GDGT\text{-}3] + [Cren'])$$

$$T = 68.4 \times TEX^H_{86} + 38.6$$

The latter calibration covers a temperature range of -3 to 30°C at an uncertainty of ± 2.5 °C (Kim et al., 2010). Duplicate analysis of every tenth sample yielded a standard deviation of 0.01 for the TEX^{H}_{86} at Site C0011, corresponding to a temperature variation of ± 0.6°C or better. At Site U1437, the standard deviation of TEX^{H}_{86} values was at 0.007 or better, which is equivalent to ± 0.5 °C.

6.3. Results and discussion

6.3.1. Unsaturated ketones and the $U^{K'}_{37}$

255 out of 259 samples at Site C0011 and 246 out of 247 samples at Site U1437 contained sufficient amounts of di- and triunsaturated alkenones to calculate $U^{K'}_{37}$ temperatures. At Site C0011, $U^{K'}_{37}$ values varied between 0.71 (at 0.147 Ma) and 0.98 (during the late Miocene at 6.47 Ma), corresponding to a temperature range of 20.3 to 28.4 °C. At Site U1437 the $U^{K'}_{37}$ ranged from 0.73 (20.7 °C at 0.794 Ma) to 0.97 (28.1 °C during the late Pliocene at 3.19 Ma and 2.65 Ma, and the early Pleistocene at 2.49 and 2.33 Ma).

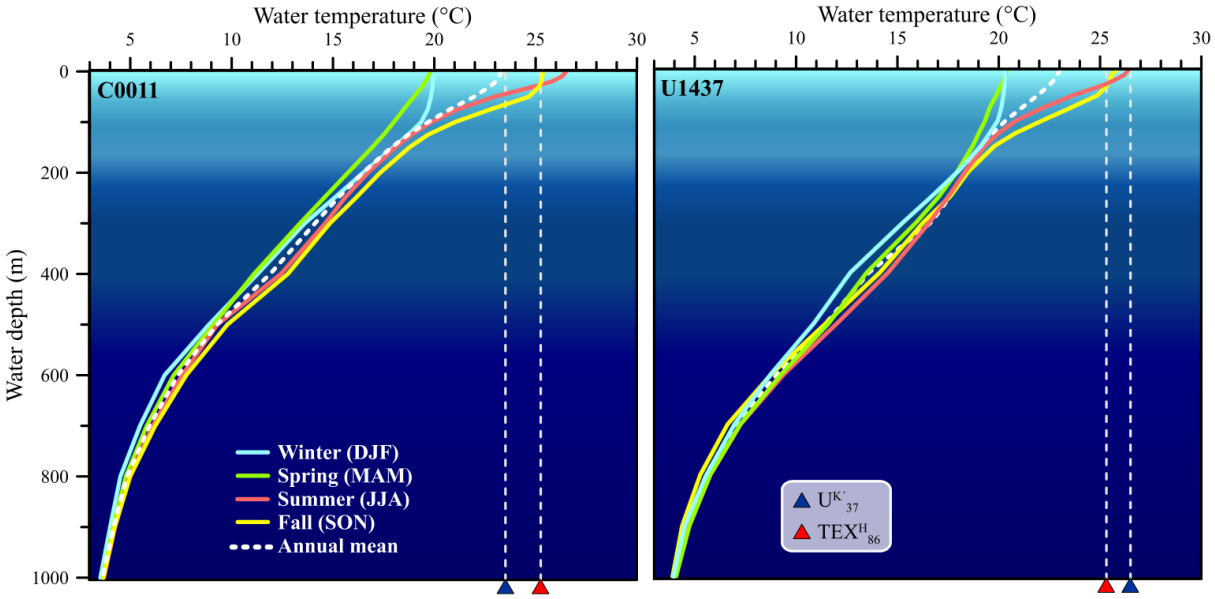

Figure 6.3 | Annual mean and seasonal temperature profiles throughout the uppermost 1000 m of the water column at Sites C0011 and U1437. The reconstructed temperatures of the respective core top sample are displayed by the vertical dashed lines (blue triangle: $U^{K'}_{37}$, red triangle: TEX^{H}_{86}). Temperature data was taken from the Japan Oceanographic Data Center (http://www.jodc.go.jp/jdoss_stat/stat-infor-sca_e.htm).

Based on comparison of the $U^{K'}_{37}$-based temperature of the core-top samples (23.5 °C at Site C0011 and 26.5 °C at Site U1437) with *in situ* water temperatures provided by the Japan Ocean Data Center (http://www.jodc.go.jp/jdoss_stat/stat-infor-sca_e.htm.) (Fig. 6.3) and considering the observations made in sediment trap studies in the NW Pacific off Japan showing that

unsaturated alkenones are largely synthesized in the surface mixed layer of the water column (0-30 m) and blooms occurring in spring and early summer (Sawada et al., 1998), the $U^{K'}_{37}$ seems to reflect early summer temperatures at the sea surface in the study area.

Given that the present latitudinal positions of the two sites differ only by 1° in latitude and that their locations are only ~230 km apart, a different production season is unlikely to account for the observed temperature difference by 3 °C in the core-top samples. This may rather either be due to the integrated time interval that is comprised in each core top sample (~0.66 ka at Site C0011 and ~0.3 ka at Site U1437) or may simply be the effect of varying positions of the KC meander path, with higher SSTs at Site U1437 than at C0011 indicating a predominance of the KC large meander path.

6.3.2. Glycerol dialkyl glycerol tetraethers and the TEX^{H}_{86}

258 out of 259 samples at Site C0011 and all 247 samples from Site U1437 contained sufficient amounts of GDGTs to calculate the TEX^{H}_{86}. At Site C0011, TEX^{H}_{86} values ranged from -0.28 (during the last deglaciation at 14.8 and 13.6 ka and the early Holocene at 9 ka) and -0.16 (during the late Miocene at 6.71 Ma), corresponding to a temperature range of 19.4 to 27.8 °C. At Site U1437 the TEX^{H}_{86} varied between -0.30 (18.3 °C at 16 ka) and -0.16 (27.7 °C during the Eemian warm period (MIS 5e) at 128 ka).

Based on comparison of TEX^{H}_{86}-based temperature of the core-top samples (25.2 °C at Site C0011 and 25.3 °C at Site U1437) with *in situ* water temperatures (Japan Ocean Data Center, http://www.jodc.go.jp/jdoss_stat/stat-infor-sca_e.htm), the TEX^{H}_{86} shows the best fit with measured temperatures at 30 mbsl in July or 0-50 mbsl in October at both sites, potentially associated with the depth of the seasonal thermocline (30-80 mbsl in September) (Sawada et al., 1998) as was suggested previously by Jonas et al. (2017).

6.3.3. Late Miocene to present oceanographic evolution of the Northwest Pacific Ocean

The $U^{K'}_{37}$ and TEX^{H}_{86} lipid paleothermometers showed overall similar trends in terms of temperature evolution from the late Miocene (Site C0011) and late early Pliocene (Site U1437) to present, respectively, and compare well with previously published records in terms of the observed long-term cooling trend. $U^{K'}_{37}$-based temperatures always exceeded those inferred from the TEX^{H}_{86} (Fig. 6.4). The only exemption is the Holocene interval at Site C0011, where TEX^{H}_{86}-based temperatures exceeded those of the $U^{K'}_{37}$ (Fig. 6.5). This was previously attributed to a potential shift in production season of marine Thaumarchaeota, the source

organisms of isoGDGTs (Jonas et al., 2017). Alkenone- and TEX^{H}_{86}-based water temperature records at Sites C0011 and U1437 show a similar unidirectional cooling trend from the late Miocene (C0011) and late early Pliocene (U1437) to present, respectively, as observed in the global $\delta^{18}O$ stack of benthic foraminifera (Zachos et al., 2001; Lisiecki and Raymo, 2005), and SST records from ODP Sites in the North Pacific (Martínez-Garcia et al., 2010; Herbert et al., 2016), on Shatsky Rise (LaRiviere et al., 2012), and in the tropical western (Zhang et al., 2014) and eastern equatorial Pacific (Lawrence et al., 2006) (Fig. 6.4). Alkenone-based records from the (western) tropical Pacific Ocean have to be treated with caution, as reconstructed SSTs occasionally reach the upper limit of the calibration range and may thus not capture temperatures above that limit. Hence, the TEX^{H}_{86}-based temperature record from WPWP Site 806 (Zhang et al., 2014) was used for comparison to avoid temperature limitations.

A striking difference occurs when comparing the slopes of temperature decline from the late Miocene to present from Site C0011 records with the global benthic $\delta^{18}O$ curve and the other paleotemperature records: from the late Miocene until the late Pliocene (~3 Ma), the slope of the temperature decline at Site C0011 compares well with that of $\delta^{18}O$ enrichment as seen in the stacked global benthic $\delta^{18}O$ trend (Fig. 6.4). Afterwards, however, the slope of temperature decline decreases significantly both in the $U^{K'}_{37}$ and TEX^{H}_{86} trends and does not comply with that of changes in $\delta^{18}O$. One possible explanation for the observed temperature trend may be a potential sampling bias, if the studied samples were predominantly picked from interglacial phases after 3 Ma. However, if we assign glacial and interglacial marine isotope stages to the samples based on the age model, this shows that samples derive equally from glacial and interglacial phases. Hence, a sampling bias is unlikely to account for the observed temperature trend in the records from Sites C0011 and U1437. We interpret the likely cause for the observed difference in slope after 3 Ma to derive from the aforementioned commencing influence of warm tropical waters related to a presence of the KC in the Philippine Sea south of Japan. Indeed, it was previously postulated based on the first occurrence of Indo-Pacific gastropod species in Japanese strata that the KC may not have reached its present latitudinal position south of Japan until ~3 Ma (Tsuchi and Shuto, 1984; Shuto, 1990; Gallagher et al., 2009). Further support for this assumption of the KC´s expansion to its present-day northern latitude by 3 Ma comes from the Site 806 temperature record (Zhang et al., 2014). The site is located in the western tropical Pacific Ocean in the heart of the WPWP, from which the KC is fed, and also shows a reduced temperature decline as compared to a site from the eastern equatorial Pacific Ocean (Lawrence et al., 2006).

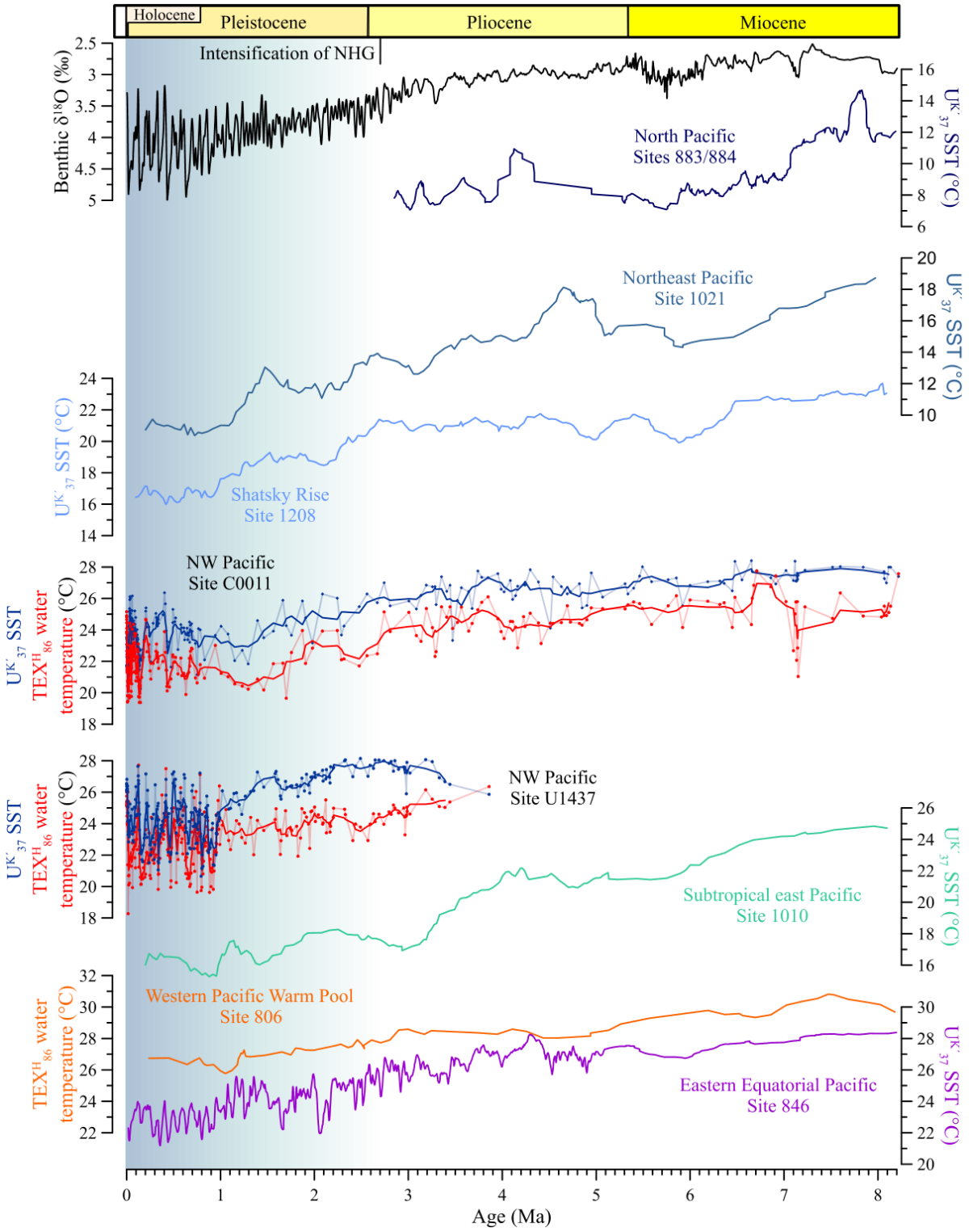

Figure 6.4 | Late Miocene to present water temperature records of Sites C0011 and U1437 in comparison with temperature records from North Pacific Site 883/884 (Herbert et al., 2016), Northeast Pacific Site 1021, subtropical NE Pacific Site 1010, Shatsky Rise Site 1208 (LaRiviere et al., 2012), as well as the tropical WPWP Site 806 (Zhang et al., 2014), eastern equatorial Pacific Site 846 (Lawrence et al., 2006; Herbert et al., 2016), and the global $\delta^{18}O$ stack by Lisiecki and Raymo (2005) (5.3-0 Ma; black) and Zachos et al. (2001) (8.2-5.3 Ma). Sites are ordered from north to south depending on their latitudinal position. For better identification of general temperature trends, curves are shown in 5-pt. (C0011, U1437, 806), 9-pt. (883/884, 1010, 1021, 1208), or 11-pt. average (846).

As part of the North Pacific Subtropical Gyre, whose circulation intensified following the final closure of the CAS (Maier-Reimer et al., 1990; Sato et al., 2008; LaRiviere et al., 2012), the KC has likely strengthened, thereby increasing meridional transport of tropical heat northward and reaching its present-day latitude in the Philippine Sea south of Japan. Hence, we attribute the extenuated temperature decline at the NW Pacific Sites C0011 (and U1437) after 3 Ma to the commencing influence of warm KC waters advected from the WPWP to northern mid-latitudes south of Japan.

Additional to the observed long-term temperature decline observed at the two study sites, the Site C0011 TEX^{H}_{86} record shows several short-lived temperature declines between 7.2 and 7 Ma. Potential causes for these cooling events will be discussed in the following subchapter 6.3.5.

6.3.4. Pliocene to present SST evolution and implications for past positions of the KC

Comparison of the SST records of Sites C0011 and U1437 can help to shed light on past changes in KC surface circulation south of Japan. Even though potential biases may occur due to different spacing and ages of samples at the two sites, it is still feasible to extract information on general intra- and inter-site-specific trends. $U^{K'}_{37}$-based SSTs at Site U1437 exceed those at Site C0011 for most of the time span from the late early Pliocene to present (Fig. 6.5). This becomes especially apparent between ~3.3 and ~0.7 Ma. $U^{K'}_{37}$-based SSTs at Site U1437 additionally show a rise in temperatures between ~4 and 3.3 Ma. Considering the past locations of the study sites (Fig. 6.2), this may result from the absence of the KC at latitudes north of ~31 °N prior to ~3.3 Ma, while the rise in SSTs towards 3.3 Ma and generally high SSTs between ~3.3 and 2 Ma may indicate the arrival and increasing influence of the KC at Site U1437. Site U1437 was always located further south than Site C0011 throughout the past 4 Ma (Fig. 6.2). Four Ma ago, Site C0011 was located slightly to the west of the present location of Site U1437 in the Shikoku Basin. If we assume that the KC was located to the south of ~31 °N prior to 3.3 Ma, then reached the past location of Site U1437 at ~3.3 Ma, migrated further north afterwards and eventually arrived at its present-day latitudinal position (Tsuchi and Shuto, 1984; Shuto, 1990; Gallagher et al., 2009), then Site C0011 was well out of the reach of warm KC waters at least until ~3.3 Ma. Even though the number of data points at Site C0011 is limited during this time interval, the sustained high $U^{K'}_{37}$-SSTs at Site U1437 between 3.3 to 2 Ma, which exceeded those at Site C0011, further indicate that Site U1437 remained under the influence of warm KC waters for an extended period of time. Intensification of Northern Hemisphere glaciation, which was accompanied by a general decline in temperatures all over

the globe after ~2.7 Ma presumably also led to the observed temperature declines at the two sites over the course of the late Pliocene and following Pleistocene (Fig. 6.5).

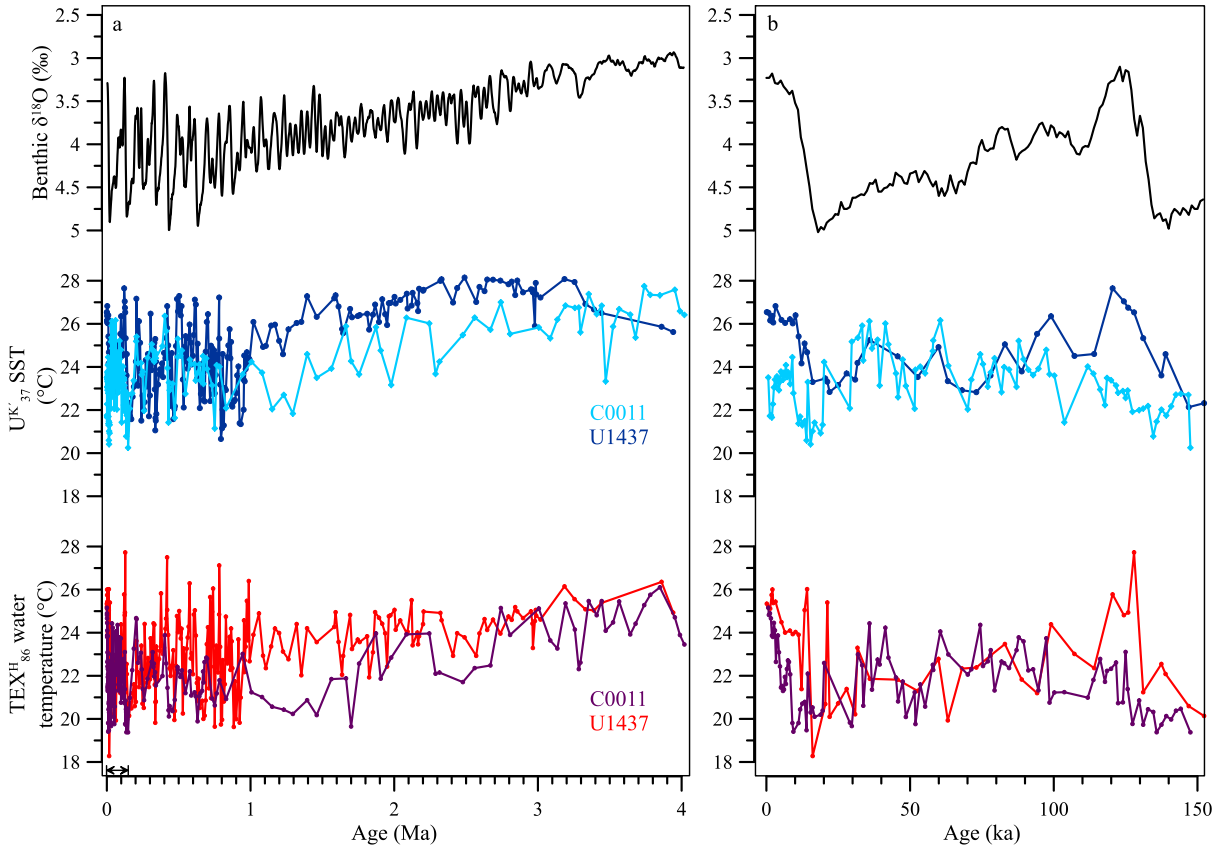

Figure 6.5 | Temperature evolution at Sites C0011 and U1437 from the late early Pliocene to the Present (a), and over the past 150 ka (b). The global stack of benthic foraminiferal oxygen isotope values (Lisiecki and Raymo, 2005) is shown for reference. The small horizontal arrow in (a) represents the zoomed-in plot shown in (b).

The generally lower SSTs at Site C0011 despite the site´s northward movement into the region of the warm KC and the current´s parallel northward migration may indicate that even though the KC reached the coast of Japan by ~3 Ma (Tsuchi and Shuto, 1984; Shuto, 1990; Gallagher et al., 2009), Site C0011 remained out of reach of the warm KC for most of the time. Given that the regional tectonic setting was established by 3 Ma and that a weak Tsushima Current, a subordinate branch of the KC, entered the Japan Sea from the East China Sea through the Tsushima Strait (Gallagher et al., 2015), it is feasible to assume that the bimodal flow behavior of the KC south of Japan was already in place by that time. Hence, we attribute the lower SSTs at Site C0011 to its past position out of the reach of both stable meander paths of the KC. It is only after ~0.7 Ma, that SSTs at Site C0011 occasionally exceeded those at Site U1437 (e.g., between 0.7 and 0.64 Ma; between ~0.25 and 0.15 Ma, and during several intervals of the past 150 ka (Fig. 6.5b)). On one hand, the observation of higher inter-sites temperature variation in part may be due to the generally higher sampling resolution at both sites after ~1 Ma. On the other hand, especially for the past 150 ka, when both sites were at or close to their present

location, this may reflect the alternating predominance of either the short (Site C0011) or large meander path (Site U1437) south of Japan. However, in order to further constrain past movements of the KC and its meanders from the late early Pliocene to present, an elevated sampling resolution and potentially samples from additional sites would be needed.

6.3.5. Short-lived late Miocene subsurface cooling

Short-lived cooling events with temperature drops by up to 4 °C were recorded in the TEX^{H}_{86} record at Site C0011 during the late Miocene between ~7.2 and 7 Ma (Fig. 6.4). Herbert et al. (2016) compiled various globally distributed alkenone-based SST records spanning the past 12 Ma and found circumglobal evidence for sustained late Miocene cooling between ~7 and 5.4 Ma with associated drying of large continental areas. This cooling furthermore coincided with transient glaciations in the Northern Hemisphere and increasing meridional temperature gradients and was attributed to a decline in atmospheric carbon dioxide levels at that time (Herbert et al., 2016). The short-term declines at Site C0011 are only apparent in the TEX^{H}_{86} record and are simultaneous with an enrichment in the global $\delta^{18}O$ curve by ~0.5 ‰ (Zachos et al., 2001) (Fig. 6.4). Considering that the TEX^{H}_{86} paleothermometer likely reflects subsurface temperatures at Site C0011, this may reflect the intrusion of colder water masses at that depth, while the sea surface still remained largely unaffected as indicated by mostly invariant $U^{K'}_{37}$ temperatures. Indeed, a southward migration of the OC is usually accompanied by an intrusion of its subpolar waters into the intermediate layer of the KC off the coast of Japan (Yang et al., 1993; Oba et al., 2006; Yasudomi et al., 2014). Even though this observation is based on hydrographic observations from the 1970s and 80s as well as paleoceanographic reconstructions for the past ~144 ka and the KC was supposedly still absent from the region in the late Miocene, a similar process with an intrusion of southward migrating subpolar waters into intermediate water layers during phases of cooling and ephemeral ice build-up may have been in place at that time. Given the timing of the observed TEX^{H}_{86}-based temperature declines, our observation may indicate that the equatorward migration and intrusion of subpolar waters into subsurface layers preceded similar events at the sea surface. Nonetheless, if based on a single study site this is highly speculative and a) additional data increasing the temporal resolution at Site C0011 and b) complementary data from other sites with sufficient resolution would be required to draw further conclusions on paleoceanographic changes in this particular time interval.

6.3.6. Changes in continental climate conditions from the late Miocene to present

The continental vegetation in East Asia results from a complex interplay of various factors, including both regional and global climate variation with associated changes in oceanic circulation (the KC for example advects tropical moisture and heat northward), atmospheric circulation (Asian monsoons and westerly jet stream (WJS), especially with respect to varying precipitation amounts), and tectonic processes (uplift of the HTP, thereby blocking off incoming moisture from the tropical Indian Ocean, which adds to the global-cooling induced aridification of the Asian interior). In order to increase our understanding of changes in the continental paleoclimatic and environmental conditions, we studied land plant-derived cuticular lipids at Sites C0011 and U1437. Land plants typically synthesize a range of long-chain *n*-alkanes and *n*-alcohols as part of their protective wax lipid layer (Meyers, 2003; Eglinton and Eglinton, 2008). Some previous work studying the provenance of terrestrial organic matter in aerosol samples on remote islands (Chiji-Jima island and Enewetak atoll) and deep-sea sediments in the North Pacific Ocean demonstrated that the lipids predominantly originated from soil erosion and direct wind abrasion from vegetation in Asia (Gagosian and Peltzer, 1986; Kawamura, 1995; Kawamura et al., 2003). Highest organic and inorganic aerosol concentrations on Enewetak were observed shortly after major dust storms in the arid Asian interior in April and May (Gagosian and Peltzer, 1986). On Chiji-Jima, elevated concentrations of wax lipids in aerosol samples occurred in winter and spring (Kawamura et al., 2003). Based on air mass trajectory analysis, the upper level WJS was identified as the major atmospheric transport mechanism (Gagosian and Peltzer, 1986; Kawamura et al., 2003), which is located north of the HTP and above the extensive elevated arid areas in central Asia from spring to summer (Schiemann et al., 2009).

At present, the main contributor to eolian deposition in sediments from the Japan Sea is the WJS, whereas dust transport via the East Asian winter monsoon (EAWM) was found to be only of minor importance (Nagashima et al., 2007). In context of these findings and those made previously in a detailed study of sedimentary concentrations of wax lipids during the past 1 Ma at Site U1437 and associated changes in atmospheric circulation (Jonas et al., *in review*; Chapter 5), we attribute variations in the land plant-derived lipid inventory at the study sites to be representative of climate- and ecosystem-related changes upwind and interpret the distribution of wax lipids to represent the environmental change along the path of the WJS, and only to a minor extent the EAWM.

The deep-sea sediments from both study sites contained abundant long-chain *n*-alkanes and *n*-alcohols, which allowed tracking floral changes on land. While absolute sedimentary

concentrations of the particular compounds largely depend on preservation within and transport efficiency to the sediments – including atmospheric transport (Jonas et al., *in review*; Chapter 5) – their relative abundances can be used to assess general changes and trends related to climate and associated factors. It has initially been suggested that changes in relative abundances of the long-chain isomers of *n*-alkanes can be used as source-diagnostic differentiators between graminoids (herbs and grasses) (nC_{31}), and woody plants (deciduous forest (nC_{29}), and pioneer forest (nC_{27}) vegetation) and hence for paleovegetation reconstruction (Schwark et al., 2002; Diefendorf et al., 2011, 2015). However, as Schwark et al. (2002) also noted, a plant´s *n*-alkane composition can be affected by factors other than its species alone, including, amongst others, elevation, exposure to wind stress, and extent of snow or ice cover. Later on, it was also demonstrated that the respective structural isomers are highly variable on the intra- and inter-plant group level, therefore hampering the applicability for paleovegetation reconstruction based on the isomers alone (Diefendorf et al., 2011, 2015; Bush and McInerney, 2013). Despite these limitations for paleovegetation reconstruction in terms of the vegetation type, it is still feasible to infer general information on long-term changes in growth conditions and the paleoenvironment in relation to aridity and/ or climate. Figure 6.6 illustrates late Miocene and late early Pliocene to present changes in relative abundances of the C_{27}, C_{29}, and C_{31} homologues of *n*-alkanes and the C_{28}-ol, C_{30}-ol, and C_{32}-ol homologues of *n*-alcohols at sites C0011 and U1437, respectively. Both *n*-alkanes and *n*-alcohols show a distinct time-dependent trend from the late Miocene and the late early Pliocene to the Holocene, respectively. The *n*-alkane distribution at Site C0011 shows an increase in nC_{31} from the late Miocene to the Holocene at the expense of nC_{27}, whereas nC_{29} relative abundances largely remain between ~35-40 %. Pleistocene samples cover a wide range in nC_{31} and nC_{27} abundances plotting all over the range of Miocene, Pliocene and Holocene values and contributing between ~31 % to ~47 % in nC_{31} and 18 % to 33 % in nC_{27} to the sum of long-chain *n*-alkanes (Fig. 6.6). The wide range in Pleistocene values can presumably be explained by the large variety of paleoclimatic and paleoenvironmental conditions (glacials and interglacials) covered by the epoch compared to the Miocene, Pliocene, and Holocene.

The *n*-alkane distribution at Site U1437 shows a similar time-dependent pattern: except for two Pleistocene outliers, Pliocene samples show the lowest abundances of nC_{31} and range generally between 29 % and 45 %. Comparable to Site C0011, nC_{29} abundances remain largely invariant and on the same level of ~35-40 % throughout the entire record. The majority of Pleistocene samples concentrates at values of 40-50 % in nC_{31} and 15-22 % in nC_{27}. The Holocene samples

plot intermediate between Plio- and Pleistocene samples and seem to show a slight enrichment in nC$_{29}$ (Fig. 6.6).

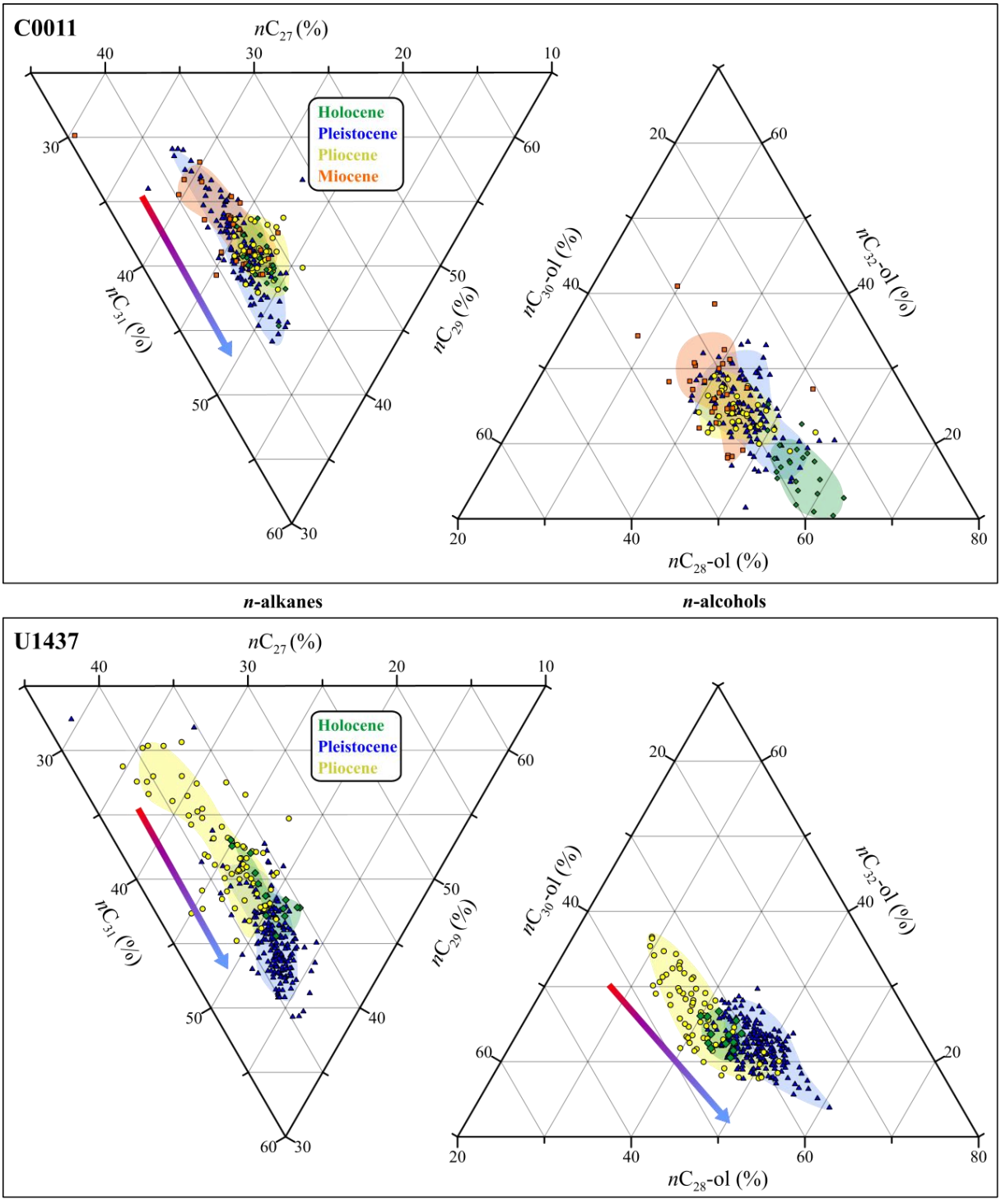

Figure 6.6 | Late Miocene to present (Site C0011) and late early Pliocene to present (Site U1437) trends in relative changes in distribution of long-chain *n*-alkanes and *n*-alcohols. Data from both sites show systematic compositional variation from the late Miocene and late early Pliocene to the Present, respectively. The wide variety in Pleistocene samples that is especially observed at Site C0011 is presumably due to the highly variable climate of this epoch with frequent glacial-interglacial cycles. The arrows in the ternary diagrams indicate – where feasible – the general temperature trend from the late Miocene and late early Pliocene, respectively, to the Pleistocene cold phases.

The *n*-alcohols show a continuous enrichment in nC_{28}-ol (ranging from 29 % to 62 %) at the expense of nC_{32}-ol (15-41 %) from the late Miocene to Holocene at Site C0011. Proportions of nC_{30}-ol mostly range between 24 % and 36 % and Holocene abundances seem to be slightly lower than those of the Pliocene and Miocene. The Holocene samples only show an overlap with a few Pleistocene samples and one Pliocene sample at Site C0011 (Fig. 6.6).

The samples at Site U1437 exhibit a generally similar trend as seen at Site C0011, with three differences: firstly, whereas at Site C0011 the Holocene samples constitute the endmember with the lowest values in nC_{32}-ol and the highest in nC_{28}-ol, the Holocene samples at Site U1437 plot intermediate between those from the Pliocene and Pleistocene. Secondly, Pliocene samples at Site U1437 show generally higher (lower) relative abundances in nC_{32}-ol (nC_{28}-ol) than those at Site C0011. Lastly, Pleistocene samples at Site U1437 are generally more depleted in nC_{30}-ol than the Pliocene and Holocene samples. Altogether, the distinction of different geological epochs is expressed more systematically in the distribution of long-chain *n*-alkanes and *n*-alcohols at Site U1437 compared to C0011.

Plants persuing the C_4 photosynthetic pathway (Hatch-Slack pathway) evolved as an adaption to warmer and more arid climate conditions, reduced atmospheric CO_2 concentrations, and higher light intensities (Gowik and Westhoff, 2011), equipping them with a physiological advantage over plants persuing the C_3 photosynthetic pathway (Benson-Calvin cycle) as the Hatch-Slack pathway conserves water and reduces photorespiration under high-temperature, low-precipitation conditions. Therefore, C_4 plants dominate grassland floras and biomass production in warm regions of the subtropics and tropics (Gowik and Westhoff, 2011), whereas C_3 grasses are more common in mid- to high-latitudinal regions. C_3 plants, on the other hand, are better adapted to colder and more humid conditions and higher atmospheric CO_2 levels. The expansion of C_4 grasslands started in the late Miocene, when atmospheric CO_2 levels declined below a threshold that favored C_3 photosynthesis (Cerling et al., 1997; Ehleringer et al., 1997). This drawdown in atmospheric CO_2 was suggested to have been associated with the continued uplift of the HTP, which exposed massive amounts of fresh silicate rocks to weathering (Ehleringer et al., 1997; and references therein). The change in the grassland community occurred earlier in tropical and subtropical regions as the threshold for C_3 photosynthesis is higher in warm temperature settings (Cerling et al., 1997). First evidence for C_4 vegetation in western China comes from characteristic carbon isotope signatures in fossil herbivorian tooth enamel and was dated to 8-6.5 Ma (Passey et al., 2009).

Previous studies of the *n*-alcohol composition in C_3 and C_4 grasses showed that nC_{26}-ol and nC_{28}-ol were dominant in C_3 grasses, whereas nC_{32}-ol was characteristic for C_4 grasses as this

homologue was largely absent in C_3 grasses (Rommerskirchen et al., 2006). The observed enrichment of *n*C_{28}-ols at the expense of *n*C_{32}-ols over time (Fig. 6.6) may hence be interpreted as a proliferation of C_3 grasses and a simultaneous gradual decrease of C_4 grasses. This is well in line with previous phytolith-based vegetation reconstructions (Wang et al., 2019b) and the stable carbon isotopic composition of herbivorian tooth enamel (Passey et al., 2009; Zhang et al., 2009), which evidenced that those C_4 grasses that are specifically adapted to warm and more humid climate conditions, including grasses of the subfamily Panicoideae, were the dominant grassland component during the late Miocene and early Pliocene in large parts of central China, including the CLP, and Inner Mongolia. Concomitant with global cooling and intensification of Northern Hemisphere glaciation, C_3 grasses of the subfamily Pooideae that constitute the cold and dry endmember of all grass subfamilies and presently inhabit the coldest and driest environments in China (Wang et al., 2019b) spread in the late Pliocene and became the dominant grassland component (Wang et al., 2019b). The simultaneous occurrence of *Paracamelus*, a mammal adapted to extremely dry climates, during the late Pliocene provides further evidence for the fundamental climatic and environmental changes (Wang et al., 2019b). Grasses are monocotyledonous plants and it was reported previously that the C_3/C_4 grass distribution is largely controlled by temperature, with relatively higher abundances of C_4 grasses under warmer conditions (Ehleringer et al., 1997; and references therein). While C_4 dicotyledonous plants are by far less abundant than C_4 monocotyledonous plants, their relative abundance with respect to C_3 dicotyledonous plants was found to be primarily controlled by aridity (Ehleringer et al., 1997; and references therein). Hence, the observed trends in the relative abundances of long-chain *n*-alcohols are assumed to reflect changes in the C_3/C_4 grassland community associated with temperature rather than aridity changes.

An additional tool for inferring paleoclimate and/or paleoenvironmental information using wax lipids of land plants is the calculation of the ACL. Thereby, variations in the ACL of land plant-derived long-chain *n*-alkyl lipids can help to identify climate-related changes in continental vegetation and hence the paleoenvironment over time.

Previous work used the ACL either as an indicator for growth season temperature (e.g., Gagosian and Peltzer, 1986; Tipple and Pagani, 2013), an estimate for the degree of aridity (e.g., Schefuß et al., 2003b; Peng et al., 2016), or changes in the floral community with respect to the plants´ photosynthetic pathways (C_3 *vs*. C_4) (Rommerskirchen et al., 2006; Vogts et al., 2009, 2012). For example, ACL values of *n*-alkanes in plants were found to increase with increasing growth temperature and high ACL values were therefore postulated to be representative of warm climates as land plants tend to synthesize longer *n*-alkane homologues

at elevated temperature to reduce evapotranspiration (Tipple and Pagani, 2013). Other studies, however, argued that the ACL is more suitable as a measure for aridity (e.g., Calvo et al., 2004; Peng et al., 2016) with higher values under increased aridity. Moreover, higher ACL values have been found in C_4 vegetation as compared to C_3 plants (e.g., Rommerskirchen et al., 2006; Vogts et al., 2009, 2012). However, as C_4 plants often but not exclusively thrive under more arid conditions (see e.g. Wang et al., 2019b) compared to C_3 plants, changes in the ACL are closely tied to the degree of aridity and it has been suggested that climate-related changes in ACL may outcompete those related to vegetation changes only, provided that the latter were not significant (Tipple and Pagani, 2013).

At Site C0011, ACL values range from 28.8 to 30.1 and average at 29.8. A similar variation was found at Site U1437, with ACL ranging between 28.7 to 30.3 (average of 29.9). The ACL records from both sites show a trend towards higher values from the late Miocene and Pliocene to present (Fig. 6.7), respectively. While Site U1437 ACL values show a clear and steady rise in ACL values by ~0.4 from ~4 Ma onwards until ~1 Ma, the rise in ACL values at Site C0011 – even though present – is not as pronounced. As global climate experienced general cooling on the same timescale, which, as discussed before, should result in decreasing ACL values, we argue that ACL values in this study are mostly representative of changes in continental aridity and not temperature. A similar conclusion was drawn by Peng et al. (2016), who attributed increasing ACLs from the Neogene to Quaternary to progressive aridification on the NE Tibetan Plateau. The same authors also ruled out changes in the floral community alone, as data from the Linxia Basin indicated that C_3 vegetation dominated the ecosystem and that the proportion of C_4 plants was negligibly small (Peng et al., 2016). The phytolith-based quantitative reconstruction of paleoprecipitation in central China revealed a rainfall reduction by ~50 % from the late Miocene to Pliocene (Wang et al., 2019b), which the authors attributed to a global-cooling controlled equatorward shift of the ITCZ (intertropical convergence zone) and associated Asian summer monsoonal rain belt.

If the observed changes in ACL were controlled by vegetational changes with respect to the plants´ photosynthetic pathways, then the increasing ACL trend would indicate a spread of C_4 vegetation, as would be generally expected under increasingly arid conditions. This however, would contradict the abovementioned findings by Wang et al. (2019b) and Peng et al. (2016), who found a dominance of C_3 plants in the dust source regions in East Asia, and also our own findings based on the long-chain *n*-alcohols. Also, as mentioned before, temperature was found to be the primary controlling factor in the C_3/C_4 distribution in monocotyledonous plants, including all grasses (Ehleringer et al., 1997). Therefore, the long-term cooling from the late

Miocene and Pliocene onwards, as also expressed in the water temperature records from Sites C0011 and U1437, respectively, may have been the primary controlling factor on the C_3/C_4 grass distribution. In conclusion, the changes in ACL-inferred aridity variations do not have to necessarily parallel the changes in the presumably temperature-controlled C_3/C_4 grass distribution as inferred from the abundances of the studied long-chain *n*-alcohols.

In order to gain more precise information on the changes in the floral community, additional studies will be needed. For example, these may include complementary compound-specific carbon isotope analysis on wax lipids as C_3 and C_4 plants exhibit different distinct $\delta^{13}C$ composition ranges owing to their respective photosynthetic pathway, which will allow for clearer identification of changes in the floral community with respect to C_3 and C_4 plants. Also, complementary studies of hydrogen isotopic signatures of the leaf waxes will allow to infer information on paleohydrological changes and may hence provide valuable and independent data on continental aridity/humidy changes.

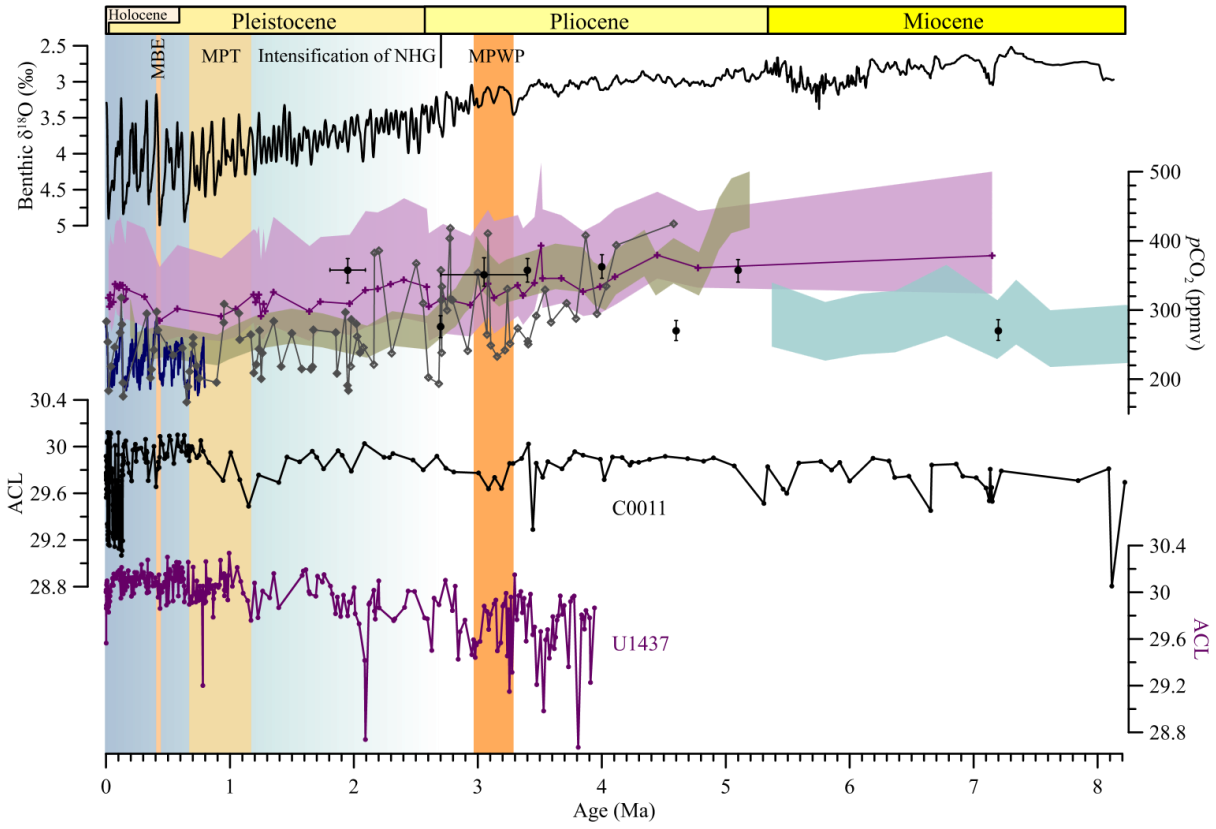

Figure 6.7 | Sites C0011 and U1437 average chain length (ACL) records in comparison with the globally stacked benthic oxygen isotope records (Zachos et al., 2001; Lisiecki and Raymo, 2005) and atmospheric pCO_2 estimates from ice cores (Lüthi et al., 2008; dark blue solid line), boron isotopes (Hönisch et al., 2009 (filled diamonds); Bartoli et al., 2011 (open diamonds)), leaf stomata (black circles; Beerling and Royer, 2011; Stults et al., 2011), alkenones (Pagani et al., 1999 (blue shading); Seki et al., 2010 (green shading); Zhang et al., 2013b (purple shading and purple solid line with crosses)). MPWP = Mid-Pliocene Warm Period; NHG = Northern Hemisphere glaciation; MPT = Mid-Pleistocene Transition; MBE = Mid-Brunhes Event.

Throughout the last 1 Ma, ACL values at both study sites are on a comparatively stable level of ~30 at Site U1437 and 29.7 at Site C0011, respectively, and show no glacial/interglacial variation at Site U1437, which has a sufficient temporal sample resolution to enable tracking these changes if present. During the last 150 ka, with a high temporal sample resolution at Site C0011, ACL values at the site show significant variation between 29.2 and 30.1. However, comparison of the ACL record from this time interval with variations in benthic $\delta^{18}O$ and atmospheric carbon dioxide levels as reconstructed from ice cores does not allow for the identification of temperature or pCO_2 dependency (Fig. 6.7). These observations suggest that even though changes in ACL allowed to track the general aridification trend from the late Miocene and more pronounced late Pliocene onwards, aridity changes on shorter timescales (e.g., on the glacial/interglacial level) were not significant enough to result in pronounced changes in the floral community and/or adaption to the changed boundary conditions. Only in the Holocene a slight decline in ACL is observed at Site U1437 and supports the assumption that variations in ACL are mostly driven by changes in aridity and not temperature, as this period is characterized by higher temperatures (favouring higher ACLs) and more humid conditions (favouring lower ACLs) than the preceding cold phase.

6.4. Conclusions

The multiproxy-based study of paleoceanographic and concomitant paleoenvironmental changes of the NW Pacific Ocean and adjacent East Asian continent revealed a long-term cooling by on average 4 °C from the late Miocene to present. On a circum-Pacific scale, oceanic cooling accelerated with the intensification of Northern Hemisphere glaciation in the late Pliocene. In the NW Pacific, this cooling seems to have been attenuated by intensified North Pacific Subtropical Gyre circulation and the presence of warm KC waters in the Philippine Sea south of Japan. With our records of long-term temperature evolution from the late Miocene and late early Pliocene to the Present, respectively, we achieved to close the regional gap that existed in this particular region of the Northwest Pacific Ocean. Concomitant variations in the inventory of land plant-derived wax lipids indicate that the long-term cooling was accompanied by progressive aridification of the Asian continent, presumably resulting from coupled global cooling and tectonic uplift of the HTP. The multiproxy approach in this study helps to increase our understanding of the coupling between the aforementioned mechanisms and elucidates their joint impact on the local ecosystem. In order to further investigate associated climate- and aridity-related changes in the floral community, additional compound-specific carbon and potentially hydrogen isotopic measurements on wax lipids would provide helpful and more

diagnostic information on changes in the floral community in East Asia from the late Miocene to present (distinction between C_3 *vs*. C_4 plants, identification of changes in moisture sources potentially related to the progressive uplift of the HTP).

6.5. Acknowledgements

Sample material for this study was provided through the Integrated Ocean Drilling Program (Expedition 333) and International Ocean Discovery Program (Expedition 350), respectively. This work was supported by the German Research Foundation (Grants BA 3841/4-1 and BA 3841/6-1 awarded to TB as well as grants SCHW 554/27-1,2 given to LS).

6.6. Appendix A Supporting information

Table 6.A1 | Water temperature data (TEX^{H}_{86} and $U^{K'}_{37}$) from Site C0011.

Sample	Absolute depth CSF-B (m)	Age (Ma)	TEX^{H}_{86}	TEX^{H}_{86} T (°C)	$U^{K'}_{37}$	$U^{K'}_{37}$ SST (°C)
C0011C - 1H - 1W, 0.0 - 2.0 cm	0.02	0.001	-0.20	25.2	0.82	23.5
C0011C - 1H - 1W, 2.0 - 3.0 cm	0.03	0.001	-0.20	24.8		
C0011C - 1H - 1W, 3.0 - 4.0 cm	0.04	0.001	-0.20	24.9	0.76	21.7
C0011C - 1H - 1W, 4.0 - 5.0 cm	0.05	0.002	-0.20	24.7	0.76	21.8
C0011C - 1H - 1W, 5.0 - 6.0 cm	0.06	0.002	-0.22	23.9	0.76	21.7
C0011C - 1H - 1W, 6.0 - 7.0 cm	0.07	0.002	-0.22	23.8	0.78	22.3
C0011C - 1H - 1W, 7.0 - 8.0 cm	0.08	0.003	-0.21	24.5	0.80	23.0
C0011C - 1H - 1W, 8.0 - 9.0 cm	0.09	0.003	-0.21	24.1	0.82	23.4
C0011C - 1H - 1W, 9.0 - 10.0 cm	0.10	0.003	-0.23	22.6	0.81	23.1
C0011C - 1H - 1W, 10.0 - 11.0 cm	0.11	0.004	-0.22	23.8	0.82	23.6
C0011C - 1H - 1W, 11.0 - 12.0 cm	0.12	0.004	-0.22	23.9	0.82	23.4
C0011C - 1H - 1W, 12.0 - 13.0 cm	0.13	0.004	-0.23	23.1	0.80	22.9
C0011C - 1H - 1W, 13.0 - 14.0 cm	0.14	0.005	-0.24	22.4	0.81	23.3
C0011C - 1H - 1W, 14.0 - 15.0 cm	0.15	0.005	-0.25	21.5	0.83	23.8
C0011C - 1H - 1W, 15.0 - 16.0 cm	0.16	0.005	-0.25	21.5	0.83	23.7
C0011C - 1H - 1W, 16.0 - 17.0 cm	0.17	0.006	-0.25	21.3	0.82	23.4
C0011C - 1H - 1W, 17.0 - 18.0 cm	0.18	0.006	-0.25	21.4	0.83	23.7
C0011C - 1H - 1W, 18.0 - 19.0 cm	0.19	0.006	-0.24	21.9	0.82	23.6
C0011C - 1H - 1W, 19.0 - 20.0 cm	0.20	0.007	-0.25	21.6	0.84	24.1
C0011C - 1H - 1W, 20.0 - 21.0 cm	0.21	0.007	-0.24	22.3	0.82	23.5
C0011C - 1H - 1W, 21.0 - 22.0 cm	0.22	0.008	-0.23	22.7	0.83	23.8
C0011C - 1H - 1W, 22.0 - 23.0 cm	0.23	0.008	-0.23	22.6	0.82	23.6
C0011C - 1H - 1W, 23.0 - 24.5 cm	0.24	0.008	-0.24	22.1	0.81	23.2
C0011C - 1H - 1W, 25.0 - 27.0 cm	0.26	0.009	-0.27	19.8	0.85	24.5
C0011C - 1H - 1W, 28.0 - 30.0 cm	0.27	0.009	-0.28	19.4	0.80	22.8
C0011C - 1H - 1W, 31.0 - 33.0 cm	0.32	0.011	-0.27	19.8	0.75	21.4
C0011C - 1H - 1W, 33.0 - 35.0 cm	0.34	0.012	-0.27	20.4	0.76	21.7
C0011C - 1H - 1W, 35.0 - 36.5 cm	0.36	0.013	-0.26	20.7	0.75	21.3
C0011C - 1H - 1W, 37.5 - 39.0 cm	0.38	0.013	-0.26	20.8	0.75	21.5
C0011C - 1H - 1W, 39.0 - 41.0 cm	0.40	0.014	-0.28	19.5	0.72	20.6
C0011C - 1H - 1W, 41.0 - 43.0 cm	0.41	0.014	-0.24	22.1	0.81	23.3
C0011C - 1H - 1W, 43.0 - 45.0 cm	0.44	0.015	-0.27	20.3	0.72	20.4
C0011C - 1H - 1W, 45.0 - 47.0 cm	0.46	0.016	-0.26	20.5	0.74	21.0
C0011C - 1H - 1W, 47.0 - 49.0 cm	0.48	0.017	-0.27	20.1	0.75	21.4
C0011C - 1H - 1W, 53.0 - 55.0 cm	0.54	0.019	-0.27	20.2	0.73	20.9
C0011C - 1H - 1W, 55.0 - 57.0 cm	0.56	0.020	-0.27	20.4	0.75	21.3
C0011C - 1H - 1W, 58.0 - 60.0 cm	0.58	0.020	-0.23	22.6	0.84	24.2
C0011C - 1H - 3W, 0.0 - 2.0 cm	0.83	0.029	-0.27	19.8	0.77	22.1
C0011C - 1H - 3W, 4.0 - 6.0 cm	0.85	0.030	-0.28	19.7	0.87	25.2

Sample	Absolute depth CSF-B (m)	Age (Ma)	TEX^{H}_{86}	TEX^{H}_{86} T (°C)	$U^{K'}_{37}$	$U^{K'}_{37}$ SST (°C)
C0011C - 1H - 3W, 8.5 - 10.5 cm	0.91	0.032	-0.23	23.0	0.88	25.4
C0011C - 1H - 3W, 13.0 - 15.0 cm	0.95	0.033	-0.24	22.5	0.90	25.9
C0011C - 1H - 3W, 16.0 - 18.0 cm	0.97	0.034	-0.26	20.6	0.85	24.3
C0011C - 1H - 3W, 20.5 - 22.5 cm	1.03	0.036	-0.21	24.4	0.91	26.1
C0011C - 1H - 3W, 25.0 - 27.0 cm	1.05	0.037	-0.25	21.4	0.86	24.9
C0011C - 1H - 3W, 29.0 - 31.0 cm	1.11	0.039	-0.23	22.7	0.88	25.3
C0011C - 1H - 3W, 33.0 - 35.0 cm	1.13	0.039	-0.24	22.5	0.81	23.1
C0011C - 1H - 3W, 37.0 - 39.0 cm	1.18	0.041	-0.21	24.2	0.90	26.0
C0011C - 1H - 3W, 42.0 - 44.0 cm	1.22	0.042	-0.23	22.8	0.87	25.1
C0011C - 1H - 3W, 48.0 - 50.0 cm	1.29	0.045	-0.24	21.9	0.83	23.7
C0011C - 1H - 3W, 52.0 - 54.0 cm	1.31	0.046	-0.26	20.8	0.79	22.6
C0011C - 1H - 3W, 55.0 - 57.0 cm	1.36	0.047	-0.25	21.7	0.85	24.3
C0011C - 1H - 3W, 60.0 - 62.0 cm	1.39	0.049	-0.27	20.1	0.81	23.1
C0011C - 1H - 3W, 65.0 - 67.0 cm	1.48	0.052	-0.25	21.2	0.77	22.1
C0011C - 1H - 3W, 70.0 - 72.0 cm	1.48	0.052	-0.28	19.8	0.83	23.9
C0011C - 1H - 3W, 75.0 - 77.0 cm	1.53	0.054	-0.25	21.6	0.84	24.0
C0011C - 1H - 3W, 80.0 - 82.0 cm	1.58	0.055	-0.26	20.6	0.83	23.7
C0011C - 1H - 3W, 83.0 - 85.0 cm	1.66	0.058	-0.24	22.5	0.86	24.7
C0011C - 1H - 3W, 88.5 - 90.5 cm	1.66	0.058	-0.24	22.3	0.88	25.2
C0011C - 1H - 3W, 94.0 - 96.0 cm	1.73	0.061	-0.21	24.0	0.91	26.2
C0011C - 1H - 3W, 98.5 - 100.5 cm	1.81	0.063	-0.23	23.0	0.84	24.1
C0011C - 1H - 5W, 0.0 - 2.0 cm	2.00	0.070	-0.24	22.1	0.77	22.0
C0011C - 1H - 5W, 5.0 - 7.0 cm	2.04	0.071	-0.24	22.3	0.82	23.4
C0011C - 1H - 5W, 12.5 - 14.5 cm	2.13	0.074	-0.21	24.4	0.86	24.6
C0011C - 1H - 5W, 17.0 - 19.0 cm	2.16	0.075	-0.24	22.5	0.84	24.1
C0011C - 1H - 5W, 20.0 - 22.0 cm	2.20	0.077	-0.23	22.7	0.81	23.1
C0011C - 1H - 5W, 25.0 - 27.0 cm	2.23	0.078	-0.23	23.2	0.83	23.7
C0011C - 1H - 5W, 29.0 - 31.0 cm	2.27	0.079	-0.25	21.3	0.85	24.4
C0011C - 1H - 5W, 34.0 - 36.0 cm	2.34	0.082	-0.23	22.7	0.80	22.8
C0011C - 1H - 5W, 39.0 - 41.0 cm	2.37	0.083	-0.23	22.6	0.84	24.0
C0011C - 1H - 5W, 44.0 - 46.0 cm	2.42	0.084	-0.24	22.4	0.83	23.9
C0011C - 1H - 5W, 49.0 - 51.0 cm	2.49	0.087	-0.23	23.2	0.81	23.1
C0011C - 1H - 5W, 54.0 - 56.0 cm	2.51	0.088	-0.22	23.8	0.88	25.2
C0011C - 1H - 5W, 59.0 - 61.0 cm	2.56	0.089	-0.22	23.6	0.85	24.4
C0011C - 1H - 5W, 64.0 - 66.0 cm	2.61	0.091	-0.24	22.2	0.83	23.9
C0011C - 1H - 5W, 69.0 - 71.0 cm	2.66	0.093	-0.24	22.3	0.82	23.6
C0011C - 1H - 5W, 74.5 - 76.5 cm	2.71	0.095	-0.25	21.3	0.83	23.9
C0011C - 1H - 5W, 81.0 - 83.0 cm	2.79	0.097	-0.22	23.7	0.86	24.8
C0011C - 1H - 5W, 86.0 - 88.0 cm	2.82	0.099	-0.26	20.8	0.82	23.7
C0011C - 1H - 5W, 91.0 - 93.0 cm	2.87	0.100	-0.25	21.2	0.82	23.6
C0011C - 1H - 5W, 98.5 - 100.5 cm	2.97	0.104	-0.25	21.2	0.75	21.4
C0011C - 1H - CC W, 0.0 - 2.0 cm	3.20	0.112	-0.26	21.0	0.84	24.0
C0011C - 1H - CC W, 3.0 - 5.0 cm	3.26	0.114	-0.25	21.8	0.83	23.7

Sample	Absolute depth CSF-B (m)	Age (Ma)	TEX^{H}_{86}	TEX^{H}_{86} T (°C)	$U^{K'}_{37}$	$U^{K'}_{37}$ SST (°C)
C0011C - 1H - CC W, 6.0 - 8.0 cm	3.32	0.116	-0.23	22.8	0.80	23.0
C0011C - 1H - CC W, 9.0 - 11.0 cm	3.37	0.118	-0.25	21.7	0.78	22.2
C0011C - 1H - CC W, 13.0 - 15.0 cm	3.39	0.119	-0.24	22.2	0.82	23.5
C0011C - 1H - CC W, 16.0 - 18.0 cm	3.43	0.120	-0.24	22.3	0.82	23.4
C0011C - 1H - CC W, 20.0 - 22.0 cm	3.48	0.122	-0.23	22.6	0.81	23.1
C0011C - 1H - CC W, 23.5 - 25.5 cm	3.50	0.122	-0.26	20.7	0.80	22.8
C0011C - 2H - 1W, 0.0 - 2.0 cm	3.55	0.124	-0.26	20.8	0.80	22.9
C0011C - 2H - 1W, 5.0 - 7.0 cm	3.58	0.125	-0.23	23.1	0.79	22.6
C0011C - 2H - 1W, 10.0 - 12.0 cm	3.60	0.126	-0.25	21.4	0.80	22.9
C0011C - 2H - 1W, 15.0 - 17.0 cm	3.64	0.127	-0.28	19.8	0.77	21.9
C0011C - 2H - 1W, 21.0 - 23.0 cm	3.71	0.130	-0.26	20.9	0.77	22.0
C0011C - 2H - 1W, 26.0 - 28.0 cm	3.75	0.131	-0.28	19.7	0.77	22.1
C0011C - 2H - 1W, 31.0 - 33.0 cm	3.80	0.133	-0.27	20.4	0.78	22.2
C0011C - 2H - 1W, 35.0 - 37.0 cm	3.85	0.135	-0.27	20.3	0.73	20.8
C0011C - 2H - 1W, 40.0 - 42.0 cm	3.88	0.136	-0.28	19.4	0.75	21.5
C0011C - 2H - 1W, 45.0 - 47.0 cm	3.93	0.137	-0.28	19.7	0.77	22.0
C0011C - 2H - 1W, 50.0 - 52.0 cm	3.98	0.139	-0.27	20.1	0.76	21.7
C0011C - 2H - 1W, 55.0 - 57.0 cm	4.03	0.141	-0.27	20.0	0.78	22.2
C0011C - 2H - 1W, 60.0 - 62.0 cm	4.08	0.143	-0.27	20.4	0.79	22.7
C0011C - 2H - 1W, 65.0 - 67.0 cm	4.12	0.144	-0.27	20.5	0.79	22.8
C0011C - 2H - 1W, 70.0 - 72.0 cm	4.20	0.147	-0.20		0.79	22.7
C0011C - 2H - 1W, 75.0 - 77.0 cm	4.22	0.148	-0.28	19.4	0.71	20.3
C0011C - 2H - 1W, 107.0 - 109.0 cm	4.57	0.160	-0.26	21.0	0.77	22.1
C0011C - 2H - 3W, 23.0 - 25.0 cm	5.05	0.177	-0.24	22.3	0.80	22.8
C0011C - 2H - 3W, 54.0 - 56.0 cm	5.36	0.187	-0.22	23.3	0.82	23.4
C0011C - 2H - 3W, 101.5 - 103.5 cm	5.83	0.204	-0.20	24.7	0.88	25.2
C0011C - 2H - 3W, 110.0 - 112.0 cm	5.92	0.207	-0.20	24.6	0.88	25.4
C0011C - 2H - 3W, 139.0 - 141.0 cm	6.21	0.217	-0.23	22.6	0.84	24.2
C0011C - 2H - 4W, 26.0 - 28.0 cm	6.58	0.237	-0.23	23.1	0.84	24.2
C0011C - 2H - 4W, 54.5 - 56.5 cm	6.87	0.243	-0.24	22.3	0.82	23.6
C0011C - 2H - 4W, 83.0 - 85.0 cm	7.15	0.250	-0.25	21.4	0.83	23.8
C0011C - 2H - 4W, 109.0 - 111.0 cm	7.41	0.259	-0.26	20.9	0.77	22.0
C0011C - 2H - 6W, 24.5 - 26.5 cm	7.81	0.283	-0.24	21.9	0.85	24.4
C0011C - 2H - 6W, 55.0 - 57.0 cm	8.11	0.313	-0.23	22.6	0.87	25.1
C0011C - 2H - 6W, 107.0 - 111.0 cm	8.63	0.319	-0.23	23.1	0.86	24.8
C0011C - 2H - 6W, 112.0 - 114.0 cm	8.68	0.323	-0.24	22.4	0.85	24.3
C0011C - 2H - 6W, 126.5 - 128.5 cm	8.83	0.328	-0.23	22.6	0.86	24.7
C0011C - 2H - 7W, 0.0 - 2.0 cm	9.16	0.330	-0.24	22.0	0.84	24.2
C0011C - 2H - 7W, 14.0 - 16.0 cm	9.30	0.336	-0.24	22.2	0.86	24.7
C0011C - 2H - 7W, 48.0 - 50.0 cm	9.64	0.341	-0.25	21.6	0.85	24.4
C0011C - 2H - 7W, 57.0 - 59.0 cm	9.73	0.387	-0.24	22.0	0.87	25.0
C0011C - 2H - 7W, 87.5 - 89.5 cm	10.03	0.404	-0.22	23.9	0.91	26.4
C0011C - 2H - 7W, 114.0 - 116.0 cm	10.30	0.413	-0.23	22.6	0.89	25.7

Sample	Absolute depth CSF-B (m)	Age (Ma)	TEX^{H}_{86}	TEX^{H}_{86} T (°C)	$U^{K'}_{37}$	$U^{K'}_{37}$ SST (°C)
C0011C - 2H - 9W, 30.0 - 32.0 cm	10.58	0.422	-0.25	21.4	0.83	23.9
C0011C - 2H - 9W, 45.0 - 47.0 cm	10.73	0.429	-0.27	20.4	0.75	21.4
C0011C - 2H - 9W, 59.0 - 61.0 cm	10.87	0.432	-0.27	20.1	0.81	23.3
C0011C - 2H - 9W, 87.5 - 89.5 cm	11.16	0.437	-0.26	20.6	0.80	22.9
C0011C - 2H - 9W, 116.0 - 118.0 cm	11.44	0.457	-0.27	20.4	0.81	23.2
C0011C - 2H - 11W, 47.0 - 49.0 cm	12.11	0.472	-0.26	20.9	0.76	21.6
C0011C - 3H - 1W, 8.0 - 10.0 cm	13.04	0.492	-0.24	22.4	0.85	24.5
C0011C - 3H - 1W, 36.0 - 38.0 cm	13.32	0.494	-0.24	22.3	0.88	25.3
C0011C - 3H - 1W, 90.0 - 92.0 cm	13.86	0.512	-0.24	21.9	0.85	24.5
C0011C - 3H - 1W, 97.0 - 99.0 cm	13.93	0.522	-0.24	22.3	0.86	24.8
C0011C - 3H - 2W, 8.0 - 10.0 cm	14.30	0.547	-0.25	21.2	0.79	22.7
C0011C - 3H - 2W, 48.0 - 50.0 cm	14.78	0.578	-0.24	22.2	0.85	24.3
C0011C - 3H - 2W, 90.0 - 92.0 cm	15.20	0.587	-0.26	21.1	0.84	24.1
C0011C - 3H - 2W, 118.0 - 123.0 cm	15.48	0.610	-0.25	21.2	0.84	24.1
C0011C - 3H - 3W, 8.0 - 10.0 cm	15.71	0.618	-0.26	21.0	0.82	23.4
C0011C - 3H - 3W, 48.0 - 50.0 cm	16.11	0.631	-0.27	19.9	0.83	23.7
C0011C - 3H - 3 W, 59.0 - 61.0 cm	16.22	0.644	-0.26	21.1	0.84	24.1
C0011C - 3H - 3W, 90.0 - 92.0 cm	16.53	0.651	-0.25	21.2	0.82	23.4
C0011C - 3H - 4W, 8.0 - 10.0 cm	16.90	0.663	-0.25	21.3	0.82	23.7
C0011C - 3H - 4W, 21.5 - 23.5 cm	17.04	0.670	-0.24	22.2	0.85	24.5
C0011C - 3H - 5W, 8.0 - 10.0 cm	17.14	0.672	-0.25	21.7	0.81	23.2
C0011C - 3H - 5W, 19.5 - 21.5 cm	17.26	0.679	-0.23	22.6	0.85	24.3
C0011C - 3H - 6W, 30.0 - 32.0 cm	17.59	0.692	-0.23	22.8	0.85	24.4
C0011C - 3H - 6W, 73.0 - 75.0 cm	18.02	0.698	-0.23	22.8	0.83	23.9
C0011C - 3H - 7W, 21.0 - 23.0 cm	18.90	0.733	-0.26	20.9	0.81	23.1
C0011C - 3H - 7W, 73.0 - 75.0 cm	19.42	0.751	-0.26	20.6	0.74	21.1
C0011C - 3H - 9W, 41.0 - 43.0 cm	20.53	0.765	-0.25	21.2	0.84	24.1
C0011C - 3H - 9W, 76.0 - 78.0 cm	20.88	0.784	-0.25	21.8	0.84	24.0
C0011D - 1H - 2W, 132.0 - 134.0 cm	23.74	0.830	-0.26	20.9	0.77	22.1
C0011D - 1H - 5W, 114.0 - 116.0 cm	26.60	0.945	-0.23	23.0	0.82	23.7
C0011D - 1H - 8W, 95.0 - 100.0 cm	28.78	1.006	-0.25	21.2	0.84	24.2
C0011D - 2H - 1W, 38.0 - 40.0 cm	30.89	1.080	-0.26	21.0	0.83	23.7
C0011D - 2H - 2W, 100.0 - 102.0 cm	32.91	1.151	-0.26	20.6	0.77	22.0
C0011D - 2H - 4W, 60.0 - 62.0 cm	35.22	1.232	-0.27	20.4	0.79	22.7
C0011D - 2H - 7W, 65.0 - 70.0 cm	36.91	1.295	-0.27	20.2	0.76	21.8
C0011D - 2H - 9W, 84.0 - 86.0 cm	39.76	1.394	-0.26	20.9	0.86	24.6
C0011D - 3H - 2W, 92.0 - 94.0 cm	42.35	1.461	-0.27	20.2	0.82	23.5
C0011D - 3H - 4W, 65.0 - 70.0 cm	44.70	1.563	-0.24	21.8	0.83	23.9
C0011D - 3H - 7W, 128.0 - 130.0 cm	47.61	1.665	-0.24	21.9	0.90	25.9
C0011D - 3H - CC W, 16.0 - 18.0 cm	49.20	1.700	-0.28	19.6	0.84	24.3
C0011D - 4H - 2W, 5.0 - 10.0 cm	50.21	1.755	-0.23	22.6	0.82	23.7
C0011D - 4H - 7W, 60.0 - 62.0 cm	53.56	1.873	-0.21	24.0	0.90	25.8
C0011D - 4H - 8W, 38.0 - 40.0 cm	54.52	1.906	-0.24	21.9	0.86	24.8

Sample	Absolute depth CSF-B (m)	Age (Ma)	TEX^{H}_{86}	TEX^{H}_{86} T (°C)	$U^{K'}_{37}$	$U^{K'}_{37}$ SST (°C)
C0011D - 5H - 1W, 110.0 - 115.0 cm	56.60	1.979	-0.23	22.8	0.81	23.2
C0011D - 5H - 4W, 10.0 - 12.0 cm	59.65	2.086	-0.21	23.9	0.91	26.3
C0011D - 5H - 8W, 58.0 - 60.0 cm	64.17	2.244	-0.21	24.0	0.90	26.0
C0011D - 6H - 1W, 40.0 - 45.0 cm	65.43	2.288	-0.24	22.1	0.83	23.7
C0011D - 6H - 1W, 122.0 - 127.0 cm	66.21	2.315	-0.24	22.2	0.84	24.2
C0011D - 6H - 6W, 50.0 - 52.0 cm	70.86	2.478	-0.25	21.7	0.88	25.5
C0011D - 6H - 8W, 15.0 - 17.0 cm	73.22	2.560	-0.24	22.4	0.91	26.3
C0011D - 7H - 3W, 110.0 - 115.0 cm	76.35	2.670	-0.24	22.5	0.89	25.7
C0011D - 7H - 7W, 70.0 - 72.0 cm	78.14	2.742	-0.20	25.1	0.94	27.0
C0011D - 8H - 1W, 135.0 - 140.0 cm	79.41	2.807	-0.21	23.9	0.89	25.5
C0011D - 9H - 5W, 55.0 - 60.0 cm	85.98	3.006	-0.20	25.1	0.90	25.8
C0011D - 9H - 7W, 11.0 - 13.0 cm	88.26	3.086	-0.22	23.6	0.88	25.3
C0011D - 10H - 2W, 10.0 - 15.0 cm	91.95	3.135	-0.22	23.3	0.91	26.2
C0011D - 10H - 3W, 77.0 - 79.0 cm	93.90	3.192	-0.19	25.4	0.93	26.8
C0011D - 10H - 6W, 22.0 - 24.0 cm	96.05	3.257	-0.21	24.1	0.93	26.7
C0011D - 11H - 2W, 52.0 - 56.0 cm	101.93	3.285	-0.24	22.3	0.93	26.8
C0011D - 11H - 3W, 13.0 - 15.0 cm	102.91	3.296	-0.23	22.6	0.89	25.6
C0011D - 11H - 8W, 71.0 - 73.0 cm	107.86	3.353	-0.19	25.5	0.95	27.4
C0011D - 12H - 3W, 50.0 - 55,0 cm	112.67	3.409	-0.20	24.8	0.92	26.5
C0011D - 12H - 6W, 130.0 - 132.0 cm	115.72	3.444	-0.19	25.5	0.93	26.8
C0011D - 12H - 8W, 90.0 - 92,0 cm	118.08	3.471	-0.21	24.1	0.81	23.3
C0011D - 13H - 6W, 110.0 - 115.0 cm	122.54	3.523	-0.21	24.5	0.90	25.9
C0011D - 14H - 1W, 135.0 - 137.0 cm	126.19	3.565	-0.19	25.4	0.92	26.7
C0011D - 14H - 3W, 120.0 - 125.0 cm	128.54	3.642	-0.21	23.9	0.92	26.4
C0011D - 15H - 2W, 120.0 - 125.0 cm	136.07	3.679	-0.21	24.4	0.88	25.4
C0011D - 15H - 7W, 95.0 - 97.0 cm	141.32	3.740	-0.19	25.3	0.96	27.8
C0011D - 16H - 3W, 40.0 - 45.0 cm	144.93	3.782	-0.19	25.8	0.95	27.3
C0011D - 17H - 1W, 80.0 - 85.0 cm	150.72	3.849	-0.18	26.1	0.95	27.3
C0011D - 18H - 2W, 105.0 - 110.0 cm	159.75	3.953	-0.20	24.7	0.95	27.6
C0011D - 18H - 7W, 23.0 - 25.0 cm	164.54	3.989	-0.22	23.9	0.92	26.6
C0011D - 19H - 1W, 115.0 - 120.0 cm	168.95	4.020	-0.22	23.5	0.92	26.4
C0011D - 19H - 4W, 110.0 - 112.0 cm	171.30	4.087	-0.21	24.5	0.94	27.1
C0011D - 20H - 3W, 100.0 - 105.0 cm	177.69	4.111	-0.21	24.5	0.90	25.9
C0011D - 20H - 5W, 70.0 - 72.0 cm	178.69	4.142	-0.21	24.2	0.91	26.2
C0011D - 21H - 1W, 120.0 - 125.0 cm	181.40	4.164	-0.23	22.9	0.93	26.8
C0011D - 21H - 5W, 90.0 - 92.0 cm	183.51	4.228	-0.20	24.8	0.93	26.9
C0011D - 22H - 1W, 118.0 - 120.0 cm	184.80	4.243	-0.21	24.2	0.93	26.9
C0011D - 23T - 3W, 73.0 - 75.0 cm	189.57	4.298	-0.20	25.1	0.96	27.8
C0011D - 24T - 2W, 70.0 - 75.0 cm	197.17	4.386	-0.21	24.4	0.94	27.0
C0011D - 25T - 1W, 50.0 - 52.0 cm	200.50	4.414	-0.23	23.1		
C0011D - 26X - 5W, 90.0 - 92.0 cm	208.10	4.512	-0.21	24.4	0.84	24.1
C0011D - 27X - 1W. 80.0 - 82.0 cm	210.62	4.541	-0.21	24.4	0.95	27.4
C0011D - 27X - 6W, 12.0 - 17.0 cm	214.39	4.629	-0.21	24.5	0.93	26.8

Sample	Absolute depth CSF-B (m)	Age (Ma)	TEX^{H}_{86}	TEX^{H}_{86} T (°C)	$U^{K'}_{37}$	$U^{K'}_{37}$ SST (°C)
C0011D - 28X - 2W, 105.0 - 110.0 cm	217.33	4.693	-0.19	25.5	0.91	26.3
C0011D - 28X - 3W, 132.0 - 134.0 cm	218.85	4.726	-0.21	24.5	0.92	26.4
C0011D - 29X - 3W, 96.0 - 101.0 cm	223.26	4.822	-0.21	24.4	0.93	26.9
C0011D - 29X - 5W, 110.0 - 112.0 cm	224.56	4.850	-0.21	24.3	0.88	25.4
C0011D - 30X - 2W, 50.0 - 55.0 cm	226.95	4.902	-0.20	24.6	0.89	25.6
C0011D - 30X - CC W, 10.0 - 12.0 cm	229.08	4.948	-0.19	25.4	0.96	27.6
C0011D - 31X - 1W, 10.0 - 15.0 cm	234.65	5.069	-0.19	25.4	0.90	26.1
C0011D - 32X - 5W, 124.0 - 126.0 cm	245.69	5.308	-0.19	25.3	0.93	26.9
C0011D - 33X - 1W, 56.0 - 61.0 cm	247.07	5.338	-0.19	25.6	0.91	26.3
C0011D - 33X - 4W, 74.0 - 76.0 cm	249.88	5.399	-0.19	25.8	0.92	26.7
C0011D - 34X - 2W, 49.0 - 54.0 cm	252.84	5.463	-0.19	25.7	0.95	27.4
C0011D - 34X - 3W, 106.0 - 108.0 cm	254.19	5.493	-0.19	25.4	0.97	28.0
C0011D - 34X - CC W, 33.0 - 35.0 cm	258.68	5.590	-0.21	24.3	0.94	27.1
C0011D - 36X - 1W, 84.0 - 88.0 cm	266.83	5.767	-0.19	25.5	0.94	27.2
C0011D - 36X - 4W, 90.0 - 92.0 cm	270.85	5.854	-0.18	26.2	0.95	27.3
C0011D - 36X - 7W, 130.0 - 135.0 cm	273.91	5.920	-0.21	24.2	0.89	25.5
C0011D - 37X - 2W, 85.0 - 87.0 cm	277.56	6.000	-0.19	25.9	0.93	26.8
C0011D - 38X - 4W, 52.0 - 57.0 cm	286.26	6.188	-0.19	25.8	0.94	27.1
C0011D - 39X - 1W, 17.0 - 22.0 cm	292.21	6.317	-0.19	25.6	0.94	27.1
C0011D - 39X - 2W, 97.0 - 102.0 cm	294.32	6.363	-0.19	25.7	0.93	27.0
C0011D - 39X - 6W, 92.0 - 94.0 cm	298.30	6.449	-0.21	24.2	0.92	26.5
C0011D - 39X - 8W, 91.0 - 93.0 cm	301.01	6.478	-0.18	26.1	0.98	28.4
C0011D - 40X - 6W, 102.0 - 107.0 cm	307.67	6.553	-0.20	25.2	0.94	27.2
C0011D - 40X - 8W, 120.0 - 122.0 cm	310.48	6.654	-0.21	24.3	0.98	28.4
C0011D - 41X - 1W, 121.0 - 126.0 cm	312.26	6.662	-0.18	26.0	0.96	27.7
C0011D - 41X - 6W, 79.0 - 82.0 cm	317.60	6.678	-0.17	26.8		
C0011D - 42X - 1W, 25.0 - 27.5 cm	320.26	6.710	-0.16	27.8	0.96	27.8
C0011D - 43X - 2W, 37.0 - 40.0 cm	330.96	6.860	-0.17	26.7	0.95	27.3
C0011D - 43X - 5W, 81.0 - 83.0 cm	333.94	6.913	-0.16	27.4	0.93	26.9
C0011D - 44X - 5W, 54.0 - 59.0 cm	338.04	7.022	-0.19	25.8	0.96	27.8
C0011D - 44X - 6W, 48.0 - 50.0 cm	338.44	7.100	-0.23	22.7	0.94	27.1
C0011D - 44X - 6W, 82.0 - 84.0 cm	338.78	7.118	-0.20	25.0	0.98	28.4
C0011D - 45X - 1W, 13.5 - 15.5 cm	339.65	7.126	-0.19	25.8	0.94	27.1
C0011D - 45X - 1W, 53.0 - 58.0 cm	340.03	7.135	-0.24	22.1	0.94	27.1
C0011D - 45X - 2W, 81.0 - 85.0 cm	341.74	7.142	-0.19	25.8	0.95	27.6
C0011D - 45X - 5W, 67.0 - 69.0 cm	344.42	7.146	-0.23	22.8	0.94	27.2
C0011D - 46X - 1W, 134.0 - 136.0 cm	345.85	7.151	-0.26	21.0	0.95	27.5
C0011D - 46X - 4W, 73.0 - 77.0 cm	347.81	7.224	-0.19	25.5	0.96	27.8
C0011D - 47X - 1W, 100.0 - 105.0 cm	350.30	7.517	-0.20	24.7	0.97	28.0
C0011B - 1R - 1W, 2.0 - 4.0 cm	340.00	7.600	-0.18	26.4	0.97	28.0
C0011D - 47X - 3W, 23.0 - 25.0 cm	351.50	7.844	-0.20	24.9	0.97	28.0
C0011D - 48X - 1W, 105.0 - 110.0 cm	355.41	8.038	-0.20	24.8		
C0011D - 48X - 4W, 36.0 - 38.0 cm	357.14	8.066	-0.20	24.9	0.96	27.7

Sample	Absolute depth CSF-B (m)	Age (Ma)	TEX^{H}_{86}	TEX^{H}_{86} T (°C)	$U^{K'}_{37}$	$U^{K'}_{37}$ SST (°C)
C0011B - 6R - 1W, 2.0 - 4.0 cm	384.03	8.068	-0.19	25.5	0.94	27.3
C0011D - 49X - 5W, 53.0 - 55.0 cm	364.75	8.091	-0.20	24.9	0.93	27.0
C0011D - 50X - 1W, 36.0 - 41.0 cm	365.41	8.115	-0.20	25.1	0.97	28.0
C0011D - 51X - 1W, 90.0 - 95.0 cm	370.95	8.135	-0.19	25.5	0.97	28.0
C0011D - 52X - 2W, 118.0 - 123.0 cm	377.63	8.220	-0.16	27.6	0.95	27.4

Table 6.A2 | Water temperature data (TEX^{H}_{86} and $U^{K'}_{37}$) from Site U1437.

Sample	Absolute depth CSF-A (m)	Age (Ma)	TEX^{H}_{86}	TEX^{H}_{86} T (°C)	$U^{K'}_{37}$	$U^{K'}_{37}$ SST (°C)
U1437B - 1H - 1W. 0.0 - 3.0 cm	0.02	0.000	-0.19	25.3	0.92	26.5
U1437B - 1H - 1W. 6.0 - 9.0 cm	0.08	0.001	-0.20	25.2	0.92	26.5
U1437B - 1H - 1W. 12.0 - 15.0 cm	0.14	0.001	-0.20	25.1	0.91	26.2
U1437B - 1H - 1W. 18.0 - 20.0 cm	0.19	0.002	-0.19	25.7	0.91	26.1
U1437B - 1H - 1W. 20.0 - 23.0 cm	0.22	0.002	-0.18	26.0	0.91	26.4
U1437B - 1H - 1W. 24.0 - 26.0 cm	0.25	0.002	-0.19	25.4	0.90	26.1
U1437B - 1H - 1W. 32.0 - 34.0 cm	0.33	0.003	-0.19	25.4	0.93	26.8
U1437B - 1H - 1W. 52.0 - 55.0 cm	0.54	0.005	-0.21	24.5	0.91	26.2
U1437B - 1H - 1W. 65.0 - 68.0 cm	0.67	0.007	-0.21	24.0	0.90	26.0
U1437B - 1H - 1W. 82.0 - 85.0 cm	0.84	0.008	-0.21	24.1	0.91	26.2
U1437B - 1H - 1W. 92.0 - 95.0 cm	0.94	0.009	-0.21	23.9	0.90	26.0
U1437B - 1H - 1W. 102.0 - 105.0 cm	1.04	0.010	-0.21	24.0	0.92	26.4
U1437B - 1H - 1W. 113.0 - 116.0 cm	1.15	0.011	-0.21	23.9	0.88	25.4
U1437B - 1H - 1W. 123.0 - 126.0 cm	1.25	0.012	-0.25	21.4	0.84	24.2
U1437B - 1H - 1W. 134.0 - 137.0 cm	1.36	0.013	-0.20	25.0	0.87	25.1
U1437B - 1H - 1W. 143.0 - 146.0 cm	1.45	0.014	-0.18	26.0	0.86	24.7
U1437B - 1H - 2W. 15.0 - 18.0 cm	1.64	0.016	-0.30	18.3	0.81	23.3
U1437B - 1H - 2W. 47.0 - 50.0 cm	1.96	0.021	-0.26	20.7	0.82	23.5
U1437B - 1H - 2W. 53.0 - 56.0 cm	2.02	0.021	-0.19	25.4	0.81	23.3
U1437B - 1H - 2W. 60.0 - 63.0 cm	2.09	0.022	-0.27	20.1	0.80	22.8
U1437B - 1H - 2W. 86.0 - 89.0 cm	2.35	0.025	-0.26	20.7	0.81	23.2
U1437B - 1H - 2W. 112.0 - 115.0 cm	2.61	0.028	-0.25	21.4	0.83	23.7
U1437B - 1H - 2W. 138.0 - 141.0 cm	2.87	0.031	-0.27	20.2	0.82	23.4
U1437B - 1H - 3W. 22.0 - 25.0 cm	2.94	0.032	-0.22	23.3	0.84	24.2
U1437B - 1H - 3W. 61.0 - 63.0 cm	3.32	0.036	-0.24	21.9	0.88	25.2
U1437B - 1H - 4W. 4.0 - 7.0 cm	4.17	0.046	-0.25	21.8	0.85	24.5
U1437B - 1H - 4W. 65.0 - 68.0 cm	4.78	0.053	-0.25	21.3	0.82	23.5
U1437B - 2H - 1W. 20.0 - 22.0 cm	5.41	0.060	-0.23	22.8	0.87	24.9
U1437B - 2H - 1W. 43.0 - 46.0 cm	5.66	0.063	-0.27	19.9	0.81	23.3
U1437B - 2H - 1W. 78.0 - 81.0 cm	6.01	0.068	-0.24	22.3	0.80	22.9
U1437B - 2H - 2W. 23.0 - 26.0 cm	6.36	0.073	-0.24	22.4	0.80	22.8
U1437B - 2H - 2W. 58.0 - 61.0 cm	6.71	0.078	-0.23	22.9	0.82	23.6
U1437B - 2H - 3W. 34.0 - 36.0 cm	7.21	0.083	-0.22	23.5	0.87	25.0
U1437B - 2H - 3W. 107.0 - 110.0 cm	7.93	0.089	-0.25	21.8	0.83	23.8
U1437B - 2H - 4W. 9.0 - 12.0 cm	8.49	0.094	-0.25	21.2	0.89	25.5
U1437B - 2H - 4W. 60.0 - 62.0 cm	8.97	0.099	-0.21	24.4	0.91	26.3
U1437B - 2H - 4W. 140.0 - 143.0 cm	9.79	0.107	-0.23	23.0	0.85	24.5
U1437B - 2H - 5W. 46.0 - 49.0 cm	10.35	0.114	-0.24	22.4	0.86	24.6
U1437B - 2H - 5W. 92.0 - 94.0 cm	10.79	0.120	-0.19	25.8	0.96	27.6
U1437B - 2H - 5W. 123.0 - 126.0 cm	11.12	0.124	-0.20	24.8	0.94	27.0
U1437B - 2H - 5W. 139.0 - 142.0 cm	11.28	0.126	-0.20	24.9	0.93	26.7

Sample	Absolute depth CSF-A (m)	Age (Ma)	TEX^{H}_{86}	TEX^{H}_{86} T (°C)	$U^{K'}_{37}$	$U^{K'}_{37}$ SST (°C)
U1437B - 2H - 6W, 11.0 - 14.0 cm	11.50	0.128	-0.16	27.7	0.92	26.5
U1437B - 2H - 6W, 45.0 - 48.0 cm	11.84	0.131	-0.25	21.2	0.88	25.3
U1437B - 2H - 6W, 113.0 - 116.0 cm	12.52	0.137	-0.23	22.5	0.82	23.6
U1437B - 2H - 6W, 130.0 - 132.0 cm	12.67	0.139	-0.24	22.1	0.86	24.6
U1437B - 2H - 7W, 66.0 - 69.0 cm	13.54	0.147	-0.26	20.6	0.77	22.1
U1437B - 2H - 8W, 20.0 - 23.0 cm	14.11	0.152	-0.27	20.1	0.78	22.3
U1437B - 2H - 8W, 50.0 - 52.0 cm	14.39	0.155	-0.27	20.1	0.78	22.3
U1437B - 3H - 1W, 47.0 - 50.0 cm	15.16	0.162	-0.26	20.7	0.76	21.7
U1437B - 3H - 1W, 140.0 - 142.0 cm	16.08	0.171	-0.26	20.5	0.76	21.6
U1437B - 3H - 2W, 80.0 - 8.0 cm	17.02	0.179	-0.25	21.2	0.79	22.6
U1437B - 3H - 3W, 28.0 - 30.0 cm	17.91	0.188	-0.25	21.6	0.81	23.1
U1437B - 3H - 3W, 88.0 - 91.0 cm	18.52	0.194	-0.26	20.6	0.81	23.3
U1437B - 3H - 4W, 22.0 - 25.0 cm	19.32	0.202	-0.26	20.8	0.84	24.3
U1437B - 3H - 4W, 58.0 - 60.0 cm	19.66	0.205	-0.22	23.6	0.94	27.2
U1437B - 3H - 4W, 124.0 - 127.0 cm	20.31	0.212	-0.24	22.2	0.88	25.3
U1437B - 3H - 5W, 37.0 - 40.0 cm	20.92	0.218	-0.24	22.1	0.81	23.1
U1437B - 3H - 5W, 92.0 - 94.0 cm	21.46	0.224	-0.25	21.5	0.91	26.1
U1437B - 3H - 6W, 19.0 - 22.0 cm	22.21	0.232	-0.25	21.7	0.87	25.1
U1437B - 3H - 6W, 100.0 - 102.0 cm	23.00	0.240	-0.22	23.4	0.75	21.5
U1437B - 3H - 6W, 109.0 - 112.0 cm	23.11	0.248	-0.26	20.7	0.79	22.7
U1437B - 3H - 7W, 12.0 - 15.0 cm	23.76	0.257	-0.26	20.5	0.77	22.0
U1437B - 4H - 1W, 15.0 - 18.0 cm	24.38	0.263	-0.21	24.4	0.78	22.4
U1437B - 4H - 1W, 102.0 - 105.0 cm	25.21	0.271	-0.24	22.2	0.85	24.3
U1437B - 4H - 2W, 30.0 - 33.0 cm	26.02	0.279	-0.25	21.7	0.81	23.1
U1437B - 4H - 2W, 102.0 - 105.0 cm	26.74	0.286	-0.23	22.8	0.86	24.6
U1437B - 4H - 3W, 30.0 - 33.0 cm	27.52	0.293	-0.25	21.5	0.76	21.7
U1437B - 4H - 3W, 108.0 - 111.0 cm	28.30	0.300	-0.25	21.8	0.79	22.7
U1437B - 4H - 4W, 10.0 - 12.0 cm	28.81	0.305	-0.22	23.7	0.92	26.5
U1437B - 4H - 4W, 84.0 - 87.0 cm	29.67	0.312	-0.24	22.0	0.83	23.9
U1437B - 4H - 5W, 6.0 - 9.0 cm	30.28	0.318	-0.22	23.4	0.84	24.3
U1437B - 4H - 5W, 84.0 - 87.0 cm	31.06	0.325	-0.21	24.4	0.87	24.9
U1437B - 4H - 6W, 50.0 - 5.0 cm	32.21	0.331	-0.21	24.4	0.87	25.1
U1437B - 5H - 1W, 17.0 - 20.0 cm	33.89	0.333	-0.25	21.6	0.80	23.0
U1437B - 5H - 2W, 84.0 - 86.0 cm	36.05	0.337	-0.24	21.9	0.88	25.3
U1437B - 5H - 2W, 99.0 - 102.0 cm	36.22	0.337	-0.27	19.8	0.74	21.1
U1437B - 5H - 3W, 42.0 - 45.0 cm	37.14	0.338	-0.26	20.8	0.76	21.6
U1437B - 5H - 4W, 11.0 - 14.0 cm	38.34	0.340	-0.26	20.8	0.75	21.5
U1437B - 5H - 4W, 120.0 - 122.0 cm	39.41	0.342	-0.23	23.2	0.84	24.2
U1437B - 5H - 4W, 129.0 - 132.0 cm	39.52	0.345	-0.22	23.4	0.76	21.8
U1437B - 5H - 5W, 22.0 - 25.0 cm	39.94	0.356	-0.25	21.8	0.81	23.2
U1437B - 5H - 5W, 48.0 - 51.0 cm	40.20	0.363	-0.23	22.8	0.82	23.7
U1437B - 5H - 5W, 74.0 - 77.0 cm	40.46	0.370	-0.23	23.2	0.83	23.9
U1437B - 5H - 5W, 100.0 - 103.0 cm	40.72	0.377	-0.19	25.8	0.82	23.6

Sample	Absolute depth CSF-A (m)	Age (Ma)	TEX^{H}_{86}	TEX^{H}_{86} T (°C)	$U^{K'}_{37}$	$U^{K'}_{37}$ SST (°C)
U1437B - 5H - 5W, 126.0 - 129.0 cm	40.98	0.384	-0.22	23.4	0.84	24.2
U1437B - 5H - 6W, 2.0 - 5.0 cm	41.24	0.391	-0.23	23.0	0.82	23.5
U1437B - 5H - 6W, 29.0 - 32.0 cm	41.51	0.398	-0.22	23.3	0.86	24.7
U1437B - 5H - 6W, 66.0 - 69.0 cm	41.88	0.408	-0.21	24.2	0.85	24.4
U1437B - 5H - 7W, 9.0 - 12.0 cm	42.13	0.412	-0.20	24.7	0.88	25.3
U1437B - 6H - 1W, 1.0 - 4.0 cm	43.23	0.419	-0.16	27.5	0.90	25.8
U1437B - 6H - 1W, 10.0 - 12.0 cm	43.31	0.420	-0.20	25.1	0.93	26.8
U1437B - 6H - 1W, 118.0 - 121.0 cm	44.40	0.427	-0.21	23.9	0.87	25.0
U1437B - 6H - 3W, 60.0 - 62.0 cm	46.70	0.436	-0.24	22.3	0.85	24.4
U1437B - 6H - 4W, 67.0 - 70.0 cm	48.39	0.444	-0.24	22.0	0.78	22.2
U1437B - 6H - 5W, 120.0 - 122.0 cm	50.18	0.452	-0.24	22.5	0.86	24.6
U1437B - 6H - 6W, 119.0 - 122.0 cm	51.91	0.462	-0.23	23.2	0.76	21.6
U1437B - 6H - 7W, 29.0 - 32.0 cm	52.51	0.470	-0.27	20.0	0.77	22.0
U1437B - 7H - 1W, 13.0 - 16.0 cm	52.80	0.474	-0.27	20.4	0.78	22.2
U1437B - 7H - 1W, 71.0 - 74.0 cm	53.38	0.481	-0.24	22.5	0.87	25.0
U1437B - 7H - 1W, 130.0 - 132.0 cm	53.96	0.488	-0.20	24.8	0.94	27.2
U1437B - 7H - 2W, 140.0 - 143.0 cm	55.62	0.496	-0.21	24.0	0.92	26.6
U1437B - 7H - 4W, 64.0 - 66.0 cm	57.42	0.503	-0.20	25.0	0.94	27.3
U1437B - 7H - 6W, 23.0 - 26.0 cm	59.85	0.515	-0.22	23.7	0.91	26.4
U1437B - 7H - 7W, 10.0 - 12.0 cm	60.88	0.520	-0.21	24.2	0.93	26.8
U1437B - 7H - CC, 31.0 - 34.0 cm	62.54	0.529	-0.27	20.2	0.82	23.4
U1437B - 8H - 1W, 146.0 - 149.0 cm	63.68	0.535	-0.22	23.3	0.77	22.1
U1437B - 8H - 2W, 110.0 - 112.0 cm	64.80	0.541	-0.23	22.9	0.87	24.9
U1437B - 8H - 2W, 134.0 - 137.0 cm	65.05	0.548	-0.25	21.7	0.88	25.4
U1437B - 8H - 3W, 6.0 - 9.0 cm	65.28	0.555	-0.22	23.3	0.84	24.2
U1437B - 8H - 3W, 28.0 - 31.0 cm	65.50	0.562	-0.22	23.8	0.83	23.9
U1437B - 8H - 3W, 50.0 - 53.0 cm	65.72	0.569	-0.21	24.3	0.88	25.3
U1437B - 8H - 3W, 72.0 - 75.0 cm	65.94	0.576	-0.18	26.3	0.90	26.0
U1437B - 8H - 5W, 24.0 - 26.0 cm	68.42	0.584	-0.23	22.8	0.87	25.1
U1437B - 8H - 5W, 57.0 - 60.0 cm	68.76	0.590	-0.23	23.0	0.84	24.1
U1437B - 8H - 5W, 97.0 - 100.0 cm	69.18	0.599	-0.24	22.1	0.85	24.5
U1437B - 8H - 5W, 128.0 - 131.0 cm	69.47	0.605	-0.20	24.8	0.88	25.5
U1437B - 8H - 6W, 12.0 - 15.0 cm	69.84	0.612	-0.20	25.0	0.94	27.1
U1437B - 8H - 6W, 90.0 - 93.0 cm	70.65	0.620	-0.22	23.9	0.93	26.9
U1437B - 8H - 7W, 47.0 - 50.0 cm	71.39	0.626	-0.25	21.7	0.82	23.4
U1437B - 9H - 1W, 5.0 - 8.0 cm	71.77	0.630	-0.26	20.8	0.83	23.7
U1437B - 9H - 1W, 30.0 - 32.0 cm	72.01	0.632	-0.24	21.9	0.87	25.1
U1437B - 9H - 1W, 116.0 - 119.0 cm	72.89	0.640	-0.24	21.9	0.82	23.5
U1437B - 9H - 2W, 49.0 - 52.0 cm	73.71	0.647	-0.26	20.5	0.77	22.1
U1437B - 9H - 2W, 134.0 - 137.0 cm	74.56	0.654	-0.26	20.8	0.79	22.7
U1437B - 9H - 3W, 90.0 - 92.0 cm	75.61	0.664	-0.26	20.8	0.84	24.1
U1437B - 9H - 4W, 32.0 - 35.0 cm	76.54	0.672	-0.27	20.0	0.78	22.5
U1437B - 9H - 4W, 132.0 - 135.0 cm	77.54	0.681	-0.27	20.1	0.78	22.4

Sample	Absolute depth CSF-A (m)	Age (Ma)	TEX^{H}_{86}	TEX^{H}_{86} T (°C)	$U^{K'}_{37}$	$U^{K'}_{37}$ SST (°C)
U1437B - 9H - 5W, 63.0 - 66.0 cm	78.35	0.688	-0.26	20.9	0.86	24.7
U1437B - 9H - 6W, 18.0 - 20.0 cm	79.19	0.695	-0.22	23.5	0.90	26.1
U1437B - 9H - 6W, 50.0 - 53.0 cm	79.53	0.704	-0.21	24.3	0.92	26.4
U1437B - 10H - 1W, 6.0 - 9.0 cm	79.78	0.710	-0.25	21.4	0.83	23.8
U1437B - 10H - 1W, 31.0 - 34.0 cm	80.03	0.719	-0.19	25.7	0.78	22.4
U1437B - 10H - 1W, 88.0 - 91.0 cm	80.60	0.725	-0.26	21.0	0.87	25.0
U1437B - 10H - 2W, 11.0 - 14.0 cm	81.33	0.733	-0.20	25.0	0.86	24.9
U1437B - 10H - 2W, 78.0 - 81.0 cm	82.00	0.740	-0.18	26.0	0.79	22.7
U1437B - 10H - 3W, 3.0 - 5.0 cm	82.61	0.746	-0.24	22.4	0.86	24.8
U1437B - 10H - 3W, 95.0 - 98.0 cm	83.54	0.751	-0.28	19.6	0.80	22.8
U1437B - 10H - 4W, 105.0 - 108.0 cm	85.27	0.758	-0.23	22.9	0.82	23.6
U1437B - 10H - 5W, 72.0 - 74.0 cm	86.14	0.761	-0.22	23.4	0.85	24.6
U1437B - 10H - CC, 1.0 - 3.0 cm	89.34	0.774	-0.24	22.2	0.84	24.1
U1437B - 11F - 1W, 80.0 - 82.0 cm	89.97	0.782	-0.20	24.8	0.94	27.2
U1437B - 11F - 1W, 84.0 - 87.0 cm	90.02	0.782	-0.17	27.1	0.88	25.3
U1437B - 11F - 2W, 54.0 - 57.0 cm	91.26	0.788	-0.22	23.3	0.81	23.2
U1437B - 11F - 3W, 8.0 - 11.0 cm	92.30	0.794	-0.28	19.7	0.73	20.7
U1437B - 11F - 3W, 80.0 - 83.0 cm	93.02	0.802	-0.27	20.0	0.74	21.2
U1437B - 11F - 4W, 15.0 - 18.0 cm	93.34	0.806	-0.25	21.7	0.77	22.0
U1437B - 11F - 4W, 19.0 - 21.0 cm	93.37	0.806	-0.23	22.7	0.86	24.6
U1437B - 12F - 1W, 17.0 - 20.0 cm	94.09	0.814	-0.26	20.8	0.75	21.3
U1437B - 12F - 1W, 77.0 - 80.0 cm	94.69	0.821	-0.25	21.6	0.80	23.0
U1437B - 12F - 1W, 146.0 - 149.0 cm	95.38	0.829	-0.20	24.7	0.80	22.9
U1437B - 12F - 2W, 88.0 - 91.0 cm	96.30	0.839	-0.23	22.6	0.85	24.5
U1437B - 12F - 3W, 22.0 - 25.0 cm	96.86	0.846	-0.23	22.8	0.87	25.0
U1437B - 12F - 3W, 104.0 - 106.0 cm	97.67	0.855	-0.22	23.8	0.89	25.7
U1437B - 13F - 1W, 15.0 - 18.0 cm	98.77	0.860	-0.24	22.3	0.85	24.4
U1437B - 13F - 2W, 48.0 - 50.0 cm	100.59	0.865	-0.21	24.2	0.87	25.2
U1437B - 14F - 1W, 20.0 - 23.0 cm	102.32	0.869	-0.22	23.6	0.78	22.2
U1437B - 14F - 2W, 80.0 - 82.0 cm	104.32	0.874	-0.24	22.3	0.78	22.2
U1437B - 14F - 3W, 7.0 - 10.0 cm	105.19	0.883	-0.28	19.6	0.78	22.4
U1437B - 14F - 3W, 72.0 - 75.0 cm	105.84	0.891	-0.25	21.7	0.79	22.5
U1437B - 14F - 4W, 22.0 - 25.0 cm	106.54	0.900	-0.27	20.0	0.80	22.8
U1437B - 15F - 1W, 37.0 - 40.0 cm	107.12	0.907	-0.26	20.9	0.82	23.6
U1437B - 15F - 1W, 120.0 - 122.0 cm	107.94	0.916	-0.22	23.7	0.84	24.0
U1437B - 15F - 2W, 40.0 - 43.0 cm	108.72	0.924	-0.27	19.8	0.75	21.4
U1437B - 15F - 2W, 116.0 - 119.0 cm	109.48	0.932	-0.26	21.0	0.75	21.3
U1437B - 15F - 3W, 42.0 - 45.0 cm	110.24	0.952	-0.23	22.8	0.77	22.0
U1437B - 15F - 3W, 62.0 - 65.0 cm	110.44	0.954	-0.21	24.6	0.82	23.4
U1437B - 15F - 4W, 44.0 - 46.0 cm	111.17	0.956	-0.24	22.2	0.85	24.5
U1437B - 16F - 2W, 75.0 - 78.0 cm	113.08	0.960	-0.23	22.7	0.81	23.3
U1437B - 17F - 1W, 10.0 - 12.0 cm	116.30	0.966	-0.22	23.3	0.83	23.9
U1437B - 17F - 1W, 142.0 - 145.0 cm	117.61	0.975	-0.19	25.5	0.86	24.7

Sample	Absolute depth CSF-A (m)	Age (Ma)	TEX^{H}_{86}	TEX^{H}_{86} T (°C)	$U^{K'}_{37}$	$U^{K'}_{37}$ SST (°C)
U1437B - 17F - 2W, 120.0 - 122.0 cm	118.71	0.983	-0.22	23.6	0.84	24.2
U1437B - 17F - 3W, 72.0 - 75.0 cm	119.94	0.988	-0.18	26.4	0.85	24.4
U1437B - 17F - 4W, 30.0 - 33.0 cm	120.43	0.994	-0.23	22.7	0.85	24.3
U1437B - 18F - 1W, 139.0 - 141.0 cm	122.24	1.020	-0.21	23.9	0.90	26.1
U1437B - 19F - 1W, 42.0 - 44.0 cm	126.01	1.059	-0.20	24.9		
U1437B - 19F - 3W, 97.0-99.0 cm	129.35	1.087	-0.23	22.9	0.87	24.9
U1437B - 20F - 2W, 19.0 - 21.0 cm	131.90	1.107	-0.24	22.4	0.87	25.0
U1437B - 21F - 2W, 38.0 - 40.0 cm	136.79	1.144	-0.22	23.4	0.90	25.9
U1437B - 22F - 2W, 130.0 - 132.0 cm	140.24	1.170	-0.21	24.2	0.90	26.0
U1437B - 24F - 1W, 33.0 - 35.0 cm	144.03	1.199	-0.21	24.0	0.88	25.2
U1437B - 25X - 2W, 40.0 - 42.0 cm	147.62	1.226	-0.23	23.1	0.86	24.6
U1437B - 25X - 4W, 99.0 - 101.0 cm	151.21	1.264	-0.23	22.8	0.89	25.7
U1437B - 26X - 1W, 8.0 - 10.0 cm	155.39	1.321	-0.21	24.4	0.90	26.0
U1437B - 26X - 2W, 96.0 - 98.0 cm	157.77	1.354	-0.24	22.0	0.91	26.1
U1437B - 26X - 4W, 88.0 - 90.0 cm	160.69	1.394	-0.21	24.2	0.94	27.3
U1437B - 27X - CC W, 60.0 - 62.0 cm	165.61	1.461	-0.22	23.6	0.91	26.3
U1437B - 28X - 1W, 10.0 - 12.0 cm	174.81	1.583	-0.21	24.3	0.94	27.2
U1437B - 28X - 2W, 25.0 - 27.0 cm	176.46	1.592	-0.20	24.9	0.95	27.3
U1437B - 28X - 4W, 90.0 - 92.0 cm	180.11	1.612	-0.22	23.6	0.93	26.8
U1437B - 29X - 1W, 10.0 - 12.0 cm	184.51	1.637	-0.24	22.0	0.89	25.8
U1437B - 29X - 1W, 140.0 - 142.0 cm	185.81	1.644	-0.23	22.9	0.89	25.6
U1437B - 30X - 1W, 30.0 - 32.0 cm	194.41	1.693	-0.20	24.8	0.92	26.7
U1437B - 30X - 2W, 120.0 - 122.0 cm	196.81	1.706	-0.22	23.2	0.91	26.3
U1437B - 31X - 1W, 4.0 - 6.0 cm	203.85	1.746	-0.22	23.7	0.91	26.4
U1437B - 31X - 2W, 98.0 - 100.0 cm	206.29	1.759	-0.22	23.6	0.92	26.4
U1437B - 32X - 1W, 14.0 - 16.0 cm	213.65	1.811	-0.22	23.8	0.92	26.5
U1437B - 32X - 2W, 30.0 - 32.0 cm	215.31	1.825	-0.24	21.9	0.89	25.7
U1437B - 32X - 4W, 46.0 - 48.0 cm	218.47	1.852	-0.23	23.1	0.92	26.4
U1437B - 32X - CC W, 24.0 - 26.0 cm	220.22	1.867	-0.20	25.0	0.93	26.9
U1437B - 33X - 1W, 18.0 - 20.0 cm	223.39	1.894	-0.20	24.7	0.90	26.1
U1437B - 33X - 3W, 34.0 - 36.0 cm	226.06	1.916	-0.21	24.4	0.94	27.1
U1437B - 33X - 4W, 126.0 - 128.0 cm	228.48	1.937	-0.21	24.0	0.92	26.4
U1437B - 33X - CC W, 24.0 - 26.0 cm	230.14	1.950	-0.24	22.4	0.90	25.9
U1437B - 34X - 1W, 14.0 - 16.0 cm	233.05	1.962	-0.20	24.8	0.93	27.0
U1437B - 34X - 2W, 138.0 - 140.0 cm	235.79	1.974	-0.20	24.8	0.93	27.0
U1437B - 35X - 1W, 14.0 - 16.0 cm	242.75	2.002	-0.20	25.1	0.94	27.2
U1437B - 35X - 2W, 62.0 - 64.0 cm	244.73	2.010	-0.21	24.1	0.93	26.9
U1437B - 36X - CC W, 19.0 - 21.0 cm	252.50	2.042	-0.21	24.6	0.94	27.1
U1437B - 37X - 2W, 10.0 - 12.0 cm	263.61	2.088	-0.21	24.0	0.95	27.4
U1437B - 37X - CC W, 20.0 - 22.0 cm	264.96	2.093	-0.21	24.0	0.93	26.7
U1437B - 38X - 1W, 8.0 - 10.0 cm	271.79	2.121	-0.19	25.5	0.93	26.8
U1437B - 38X - 2W, 52.0 - 54.0 cm	273.43	2.128	-0.22	23.4	0.95	27.4
U1437B - 39X - 1W, 8.0 - 10.0 cm	281.49	2.161	-0.21	24.0	0.93	27.0

Sample	Absolute depth CSF-A (m)	Age (Ma)	TEX^{H}_{86}	TEX^{H}_{86} T (°C)	$U^{K'}_{37}$	$U^{K'}_{37}$ SST (°C)
U1437B - 39X - 1W, 136.0 - 138.0 cm	282.77	2.166	-0.22	23.5	0.92	26.6
U1437B - 39X - 3W, 22.0 - 24.0 cm	284.43	2.173	-0.22	23.8	0.96	27.6
U1437B - 40X - 1W, 4.0 - 6.0 cm	291.15	2.200	-0.21	24.4	0.95	27.5
U1437B - 40X - CC W, 28.0 - 30.0 cm	292.11	2.204	-0.20	25.0	0.95	27.6
U1437B - 43X - 1W, 36.0 - 38.0 cm	320.57	2.321	-0.20	24.9	0.97	28.0
U1437B - 43X - CC W, 18.0 - 20.0 cm	322.61	2.329	-0.21	24.6	0.97	28.1
U1437B - 45X - 1W, 12.0 - 14.0 cm	339.73	2.409	-0.23	22.9	0.93	27.0
U1437B - 45X - 3W, 54.0 - 56.0 cm	343.15	2.438	-0.21	24.0	0.96	27.7
U1437B - 46X - CC W, 8.0 - 10.0 cm	349.39	2.490	-0.22	23.8	0.97	28.1
U1437B - 47X - 1W, 14.0 - 16.0 cm	359.15	2.570	-0.23	22.9	0.94	27.0
U1437B - 47X - 3W, 58.0 - 60.0 cm	362.59	2.593	-0.21	24.0	0.96	27.7
U1437B - 48X - 1W, 8.0 - 10.0 cm	368.79	2.628	-0.20	24.6	0.95	27.5
U1437B - 48X - CC W, 30.0 - 32.0 cm	372.04	2.647	-0.21	24.1	0.97	28.1
U1437B - 49X - 1W, 70.0 - 72.0 cm	379.11	2.687	-0.20	24.6	0.97	28.0
U1437B - 50X - CC W, 8.0 - 10.0 cm	388.19	2.739	-0.21	24.0	0.97	28.0
U1437B - 51X - 1W, 16.0 - 18.0 cm	397.97	2.795	-0.20	24.7	0.96	27.8
U1437B - 51X - 3W, 111.0 - 113.0 cm	401.92	2.817	-0.20	24.6	0.97	28.0
U1437B - 52X - 1W, 20.0 - 22.0 cm	406.21	2.842	-0.20	25.2	0.95	27.3
U1437B - 52X - 2W, 132.0 - 134.0 cm	408.83	2.857	-0.20	25.0	0.97	28.0
U1437B - 53X - CC W, 8.0 - 10.0 cm	415.79	2.896	-0.20	24.7	0.95	27.5
U1437B - 54X - 1W, 5.0 - 7.0 cm	425.46	2.952	-0.20	25.0	0.95	27.6
U1437D - 2R - 1W, 10.0 - 12.0 cm	427.31	2.962	-0.21	24.4	0.95	27.6
U1437B - 54X - 2W, 101.0 - 103.0 cm	427.82	2.965	-0.22	23.3	0.95	27.5
U1437D - 2R - 3W, 8.0 - 10.0 cm	430.29	2.979	-0.21	24.5	0.90	25.9
U1437B - 55X - 1W, 118.0 - 120.0 cm	431.29	2.985	-0.20	25.1	0.96	27.9
U1437D - 2R - CC W, 10.0 - 12.0 cm	431.91	2.988	-0.20	24.8	0.95	27.4
U1437D - 3R - 1W, 20.0 - 22.0 cm	437.11	3.018	-0.20	24.6	0.94	27.2
U1437D - 6R - 1W, 10.0 - 12.0 cm	466.11	3.185	-0.18	26.2	0.97	28.1
U1437D - 7R - 6W, 40.0 - 42.0 cm	483.43	3.255	-0.19	25.6	0.97	27.9
U1437D - 10R - 1W, 10.0 - 12.0 cm	504.91	3.330	-0.20	25.1	0.93	26.9
U1437D - 11R - 1W, 120.0 - 122.0 cm	515.71	3.390	-0.20	25.0	0.92	26.7
U1437D - 12R - 1W, 110.0 - 112.0 cm	525.31	3.443	-0.19	25.4	0.92	26.5
U1437D - 20R - 3W, 140.0 - 142.0 cm	606.22	3.860	-0.18	26.4	0.90	25.9
U1437D - 22R - 1W, 4.0 - 6.0 cm	621.25	3.942	-0.20	24.9	0.89	25.6

Chapter 7

Validating the applicability of the novel RI-OH-proxy for paleotemperature reconstruction over the last 1 Ma at IODP Site U1437, NW Pacific Ocean

Ann-Sophie Jonas[1], Thorsten Bauersachs[1], and Lorenz Schwark[1,2]

[1] Department of Organic Geochemistry, Institute of Geosciences, Christian-Albrechts-University, Ludewig-Meyn-Straße 10, 24118 Kiel, Germany.

[2] Department of Chemistry, WA-OIGC, Curtin University, GPO Box U1987, Perth, WA 6845, Australia.

In preparation for publication.

Abstract

Recently, a new proxy for reconstructing sea surface temperatures (SSTs), the RI-OH (ring index of hydroxylated glycerol dialkyl glycerol tetraethers (GDGTs)), was proposed and successfully applied to surface sediments from the East and South China Sea. Initial attempts to use the RI-OH for reconstructing paleo-SSTs have proven successful, but until now, the index has not been applied to sediments from beyond the last glacial-interglacial cycle. In order to test the applicability of the novel paleothermometer in mid-Pleistocene sediments, we studied deep-sea sediment samples from the Northwest Pacific Ocean spanning the last ~1 Ma for their OH-GDGT inventory. We show that OH-GDGTs were preserved in sufficient amounts throughout all glacial and interglacial cycles to calculate the RI-OH-index and the resulting paleo-SST record shows a good agreement with both $U^{K'}_{37}$ and TEX^{H}_{86} records from the same set of samples. We therefore conclude that the RI-OH can be used to reconstruct SSTs at least from the mid-Pleistocene onwards.

7.1. Introduction

Several proxies exist for the reconstruction of paleo water temperatures. Among them, organic paleothermometers including the unsaturated ketone index ($U^{K'}_{37}$) of haptophyte algae (Brassell et al., 1986), the TEX^{H}_{86} of marine Thaumarchaeota (Schouten et al., 2002; Kim et al., 2010), and the long-chain diol index (LDI) (presumably) of eustigmatophyte algae origin (Rampen et al., 2012) are commonly applied. Recently, Lü et al. (2015) proposed the ring index of hydroxylated glycerol dialkyl glycerol tetraethers (OH-GDGTs), the RI-OH, as a proxy for the reconstruction of sea surface temperatures (SSTs). The RI-OH index is based on the weighted average of OH-GDGTs 1 and 2 and shows a strong positive linear correlation with summer ($R^2 = 0.87$) and autumn SSTs ($R^2 = 0.86$), and slightly lower correlations with annual mean ($R^2 = 0.81$), spring ($R^2 = 0.78$) and winter ($R^2 = 0.77$) SSTs (Lü et al., 2015). OH-GDGTs were first identified by Liu et al. (2012) as GDGTs with up to two additional hydroxyl groups in one of their alkyl chains. They occur globally in marine sediments (Liu et al., 2012; Huguet et al., 2013; Fietz et al., 2013; Lü et al., 2015) and are – like isoprenoid (iso)GDGTs – thought to derive from Thaumarcheota, in which they have been observed in cultured representatives of ammonia-oxidizing Group 1.1a (Liu et al., 2012; Elling et al., 2015). The occurrence of OH-GDGTs in globally distributed marine sediments from various environmental settings (Liu et al., 2012) indicates that they may present a promising new tool for paleoenvironmental reconstructions and provide an additional mean to reconstruct past marine SSTs. The RI-OH index has been successfully applied to surface sediments from the Chinese Coastal Seas (Lü et al., 2015) and the South China Sea (Yang et al., 2017). The modification of the RI-OH for an application in polar waters, the RI-OH´ (Lü et al., 2015) has been shown to more accurately reflect the SST evolution in colder waters, in which the OH-GDGT-0 is the most abundant and OH-GDGT-2 mostly absent (Lü et al., 2015; Kremer et al., 2018). Some promising initial studies showed the applicability of the RI-OH and its derivative RI-OH´ in geological samples, resulting in continuous temperature records for the past 14 ka in the Beaufort Sea (Wu et al., 2020) and the past 160 ka in the western Mediterranean Sea (Davtian et al., 2019), off the Iberian margin (Davtian et al., 2021), and on the Yermak Plateau off Svalbard (Kremer et al., 2018), as well as two individual temperature data points from the Eocene and Oligocene period from the Bass River core (de Bar et al., 2019). It was also shown that the RI-OH´ more reliably than the RI-OH recorded the influence of (sub-) polar waters during cold periods in the mid-latitudinal North Atlantic off the Iberian margin (Davtian et al., 2021). Furthermore, the RI-OH may provide a useful addition to the toolbox of biomarkers for SST reconstructions in settings where the application of the TEX_{86} is compromised due to enhanced inputs of soil organic

matter (Davtian et al., 2019), as it seems to be largely unaffected by these (Lü et al., 2015). Apart from the initial paleo-SST studies based on the RI-OH by Davtian et al. (2019, 2021) and Kremer et al. (2018) in sediments from the last glacial cycle, its applicability in older sediments is still elusive. In this study, we reconstructed RI-OH-SSTs in sediments from the NW Pacific south of Japan covering the last 15 glacial-interglacial cycles from the mid-Pleistocene to present.

7.2. Materials and methods

A total of 174 deep-sea sediments from International Ocean Discovery Program (IODP) Expedition 350 Site U1437 spanning the last 1 Ma were studied for their OH-GDGT inventory. Site U1437 is located at 31° 47.3911´ N, 139° 01.5788´ E at a water depth of 2116 mbsl (meters below sea level) in the Izu-Bonin rear arc ~330 km west of the axis of the Izu-Bonin Trench and lies in a volcano-bounded basin between the Manji and Enpo rear arc seamount chains. Sediment ages were assigned using the previously published age model by Kars et al. (2017) which is based on nannofossil biostratigraphy, magnetic revearsal events and stable oxygen isotope ($\delta^{18}O$) stratigraphy. Lyophilized and homogenized sediments (5-25 g) were solvent-extracted using a Büchi Speed Extractor E-914 (Büchi, Switzerland) at 75 °C and 50 bar with a mixture of dichloromethane (DCM):methanol (MeOH) (93:7, v:v). Total lipid extracts (TLEs) were desulfurized overnight using activated copper turnings to remove elemental sulfur. An aliquot of each TLE was separated into apolar, ketone and polar fractions (containing OH-GDGTs) using a small Pasteur pipette filled with 3.5 cm of silica (SiO_2) overlain by 1.5 cm aluminium oxide (Al_2O_3). Fractions were eluted consecutively with *n*-hexane:DCM (9:1, v:v), *n*-hexane:ethylacetate (7:3, v:v) and DCM:MeOH (1:1, v:v) as respective solvents. For the analysis of OH-GDGTs, polar fractions were dissolved in *n*-hexane:2-propanol (99:1, v:v) and filtered through a polytetrafluoroethylene (PTFE) filter of 45 µm mesh size. Filtered polar fractions were then dissolved in the same solvent mixture at a concentration of 3 mg/ml and subjected to high performance liquid chromatography coupled to mass spectrometry (HPLC/MS). A detailed description of the HPLC/MS measurement protocol can be found in Jonas et al. (2017). The RI-OH was calculated and transferred into SSTs following the global, annual and seasonal calibrations by Lü et al. (2015). Duplicate measurements of every tenth sample yielded standard deviations of 0.02, corresponding to an analytical error of ±1.0°C or better. The resulting RI-OH-based SST records were then compared to those generated previously for the same set of samples using the $U^{K'}_{37}$ and TEX^{H}_{86} paleothermometers as reported elsewhere (Chapter 5; Jonas et al., *in review*). If not stated otherwise, RI-OH-SST

refers to SSTs calculated from the global calibration equation by Lü et al. (2015) in the following text. Measured *in situ* temperature data are from the Japan Oceanographic Data Center.

7.3. Results and discussion

172 of the 174 studied samples contained sufficient amounts of OH-GDGTs for the determination of RI-OH-SSTs. In order to check for a potential seasonal imprint on the water temperatures at Site U1437, the RI-OH-SSTs calculated from the global, annual and seasonal calibrations (see Introduction section) were compared with actual *in situ* SSTs at the site as inferred from the Japan Oceanographic Data Center (http://www.jodc.go.jp/jdoss_stat/stat-infor-sca_e.htm). Using the global calibration, the RI-OH-SST of the core-top sample is 23.6 °C, which is close to the annual mean SST of 23.03 °C at 0 m or the *in situ* temperature from 0-10 mbsl in June (23.63 °C) at Site U1437. Following the calculation of the annual mean RI-OH-SST, the core-top sample is at 21.9 °C, thereby slightly underestimating the actual annual mean SST. The calculated seasonal RI-OH-SSTs of the core-top sample are as follows: spring RI-OH-SST is 19.7 °C (20.4 °C; March-April-May (MAM)), 26.8 °C (26.4 °C; June-July-August (JJA)) during summer, 25.2 °C (25.8 °C; September-October-November (SON)) during autumn, and 17.3 °C (20.3 °C; December-January-February (DJF)) during winter, with the seasonal average *in situ* reference value from Site U1437 given in brackets for comparison. Hence, except for annual mean and winter RI-OH-SSTs, which seem to underestimate actual SSTs by ~1 °C and 3 °C, respectively, all other seasonal RI-OH-SSTs agree well with *in situ* seasonal SSTs.

In general, all RI-OH-SST records, although different in amplitude, show a similar glacial-interglacial sawtooth pattern as seen in Site U1437 $U^{K'}_{37}$- and TEX^{H}_{86}-temperature records (Chapter 5; Jonas et al., *in review*) and as reflected in both the global (Lisiecki and Raymo, 2005) and local foraminiferal oxygen isotope ($\delta^{18}O$) curve (Kars et al., 2017) (Fig. 7.1). Highest annual RI-OH-SSTs of up to 30.8 °C were reached during MIS 5, 11, and 19, with MIS 11 being warmest. This agrees well with maximum temperatures in both $U^{K'}_{37}$- and TEX^{H}_{86}-records. Lowest RI-OH-SSTs (19.2 °C) occurred during late MIS 6.

Comparison of existing $U^{K'}_{37}$- and TEX^{H}_{86} temperature records from Site U1437 with the global, annual and seasonal RI-OH-SST curves show the best fit of $U^{K'}_{37}$-SSTs with the $RI\text{-}OH_{global}$-SST curve, especially between 1 Ma and 430 ka, and an overall larger temperature amplitude in the RI-OH curve compared to the $U^{K'}_{37}$ afterwards. While $U^{K'}_{37}$-SSTs always exceed annual, spring and winter RI-OH-SSTs throughout the past 1 Ma, summer and fall RI-

OH-SSTs are usually higher than $U^{K'}_{37}$-SSTs. Fall RI-OH-SSTs are mostly well above $U^{K'}_{37}$-SSTs between 1 Ma and 140 ka and show a good fit afterwards. Core-top $U^{K'}_{37}$-SSTs (26.5 °C) agree best with the *in situ* temperature at the sea surface (0 mbsl) in JJA (26.4 °C), the integrated depth from 0-30 mbsl in July (26.5 °C), or the uppermost 75 mbsl in August (26.4 °C), indicating that the $U^{K'}_{37}$ is representative of summer temperatures.

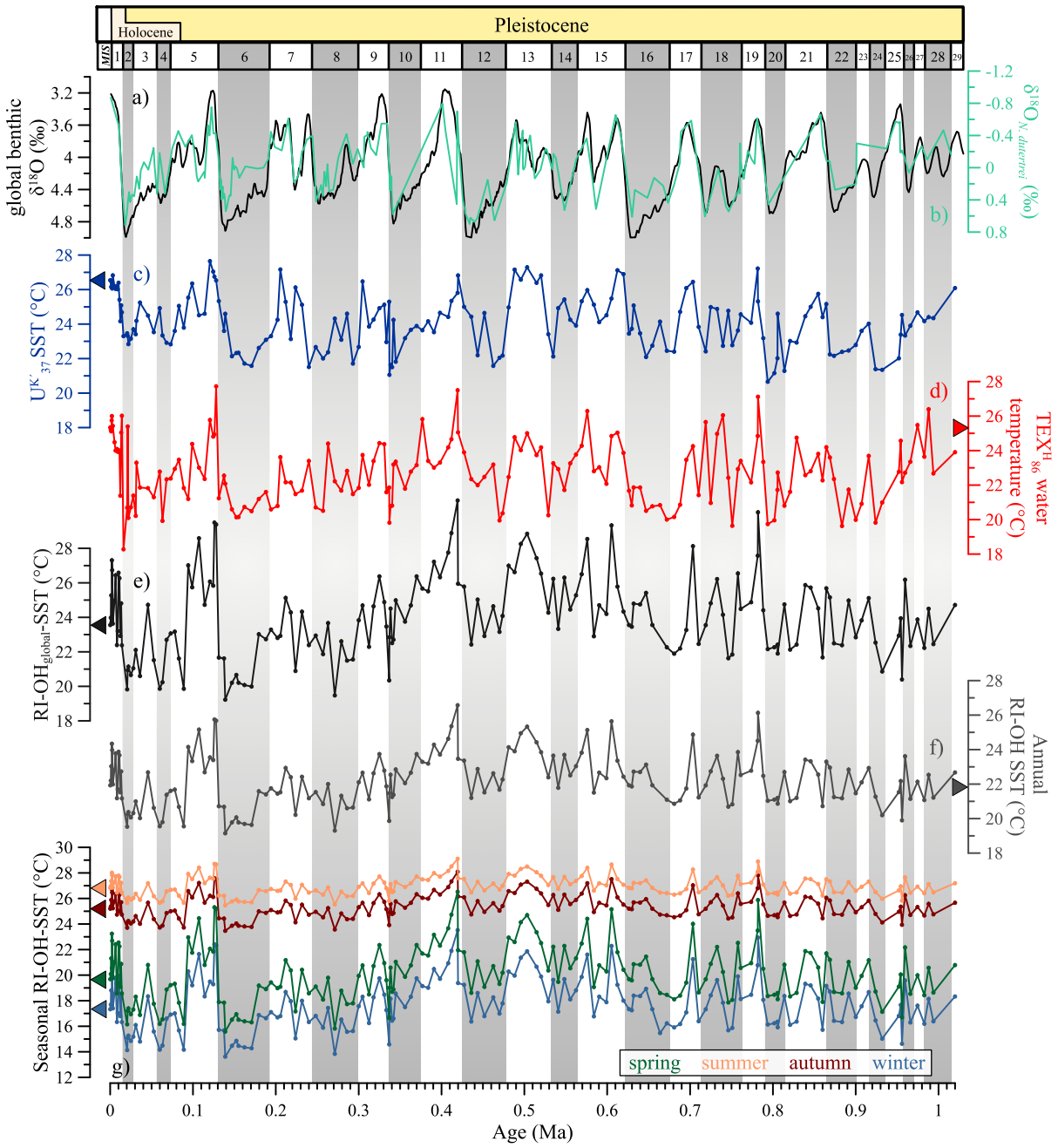

Figure 7.1 | Site U1437 $RI\text{-}OH_{global}$-SSTs (e), annual (f) and seasonal (g) RI-OH-SSTs in comparison with c) $U^{K'}_{37}$-SSTs and d) TEX^{H}_{86}-based water temperatures for the last 1 Ma. The a) global benthic (Lisiecki and Raymo, 2005) and b) Site U1437 planktonic foraminiferal $\delta^{18}O$ record of *Neogloboquadrina dutertrei* (Kars et al., 2017) are shown for reference. Colored triangles represent the respective temperature signal reconstructed from the core top-sample. Gray bars indicate cold marine isotope stages.

Comparison of the $U^{K'}_{37}$-SST record – which, as aforementioned, seems to be representative of summertime temperatures – with the summer RI-OH-SST curve, however, shows that RI-OH-SSTs usually exceed those of the $U^{K'}_{37}$ by 1-3 °C (interglacials) and 2-5 °C (glacials). This may indicate that even though the $U^{K'}_{37}$ seems to be representative of summer SSTs at present, the production season of haptophytes may have been shifted to a colder season previously.

The overall best fit of the TEX^{H}_{86}-temperature record in terms of absolute temperatures is found with the annual mean RI-OH-SSTs, while seasonal RI-OH SSTs are always well above (summer, fall) or below (winter, spring) TEX^{H}_{86} temperatures. $RI\text{-}OH_{global}$ shows the same little to no glacial-interglacial variation in the oldest part of the record (MIS 29-20), always exceeds TEX^{H}_{86} temperatures during all interglacials and most glacials between 790 and 375 ka (MIS 19-11), and shows a good fit with TEX^{H}_{86} temperatures from early MIS 10 onwards, except for some parts of MIS 5. The TEX^{H}_{86}-temperature of the core-top sample (25.3 °C) shows the best fit with average summer (JJA) and fall (SON) *in situ* temperatures at 30 mbsl. This is in line with previous findings that the TEX^{H}_{86} more accurately reflects subsurface temperatures in some oceanic settings (e.g., Lopes dos Santos et al., 2010; Yamamoto et al., 2012; Jonas et al., 2017). A study of the seasonal distribution of core OH-GDGTs in the Yangtze River estuary showed their *in situ* production by marine planktonic archaea predominantly in summer (Lü et al., 2019). Furthermore, a higher ratio of OH-GDGTs *vs*. isoGDGTs in the upper layer than in the bottom waters of the Yangtze River estuary, regardless of season, indicated that the OH-GDGT-producing organisms predominantly dwell in surface waters and that the RI-OH signal hence reflects the temperature evolution at the sea surface (Lü et al., 2019). IsoGDGT-producing organisms, in comparison, are more diverse and also inhabit subsurface layers (Lü et al., 2019) and the resulting TEX^{H}_{86} signal may hence be an integrated temperature signal of different water depths. Considering that the TEX^{H}_{86} reflects summer or fall temperatures at Site U1437, the TEX^{H}_{86} record is compared with summer and fall RI-OH-SSTs. Absolute summer and fall RI-OH-SSTs exceed TEX^{H}_{86} temperatures by up to ~7.5 °C and 6 °C, respectively, thereby further supporting the assumption that the TEX^{H}_{86} represents subsurface temperatures. The overleaf Figure 7.2 illustrates the correlation of the three paleothermometers. The overall low correlations presumably result from the differences in production seasons, habitat depths and other factors potentially influencing the resulting signals. The correlations of the paleothermometers were slightly better for interglacial phases as compared to glacial phases (R^2 of 0.34 *vs*. 0.11 for RI-OH *vs*. TEX^{H}_{86}; $R^2 = 0.20$ *vs*. <0.01 for RI-OH *vs*. $U^{K'}_{37}$; and 0.34 *vs*. 0.16 for $U^{K'}_{37}$ *vs*. TEX^{H}_{86}; see Fig. 7.2), indicating a more similar habitat depth and production season of the respective source organisms.

Despite the overall offsets and low correlations, all three paleothermometers manage to capture the general climate variations of the past 1 Ma very well and capture the sawtooth pattern of glacial-interglacial climate variability (Fig. 7.1).

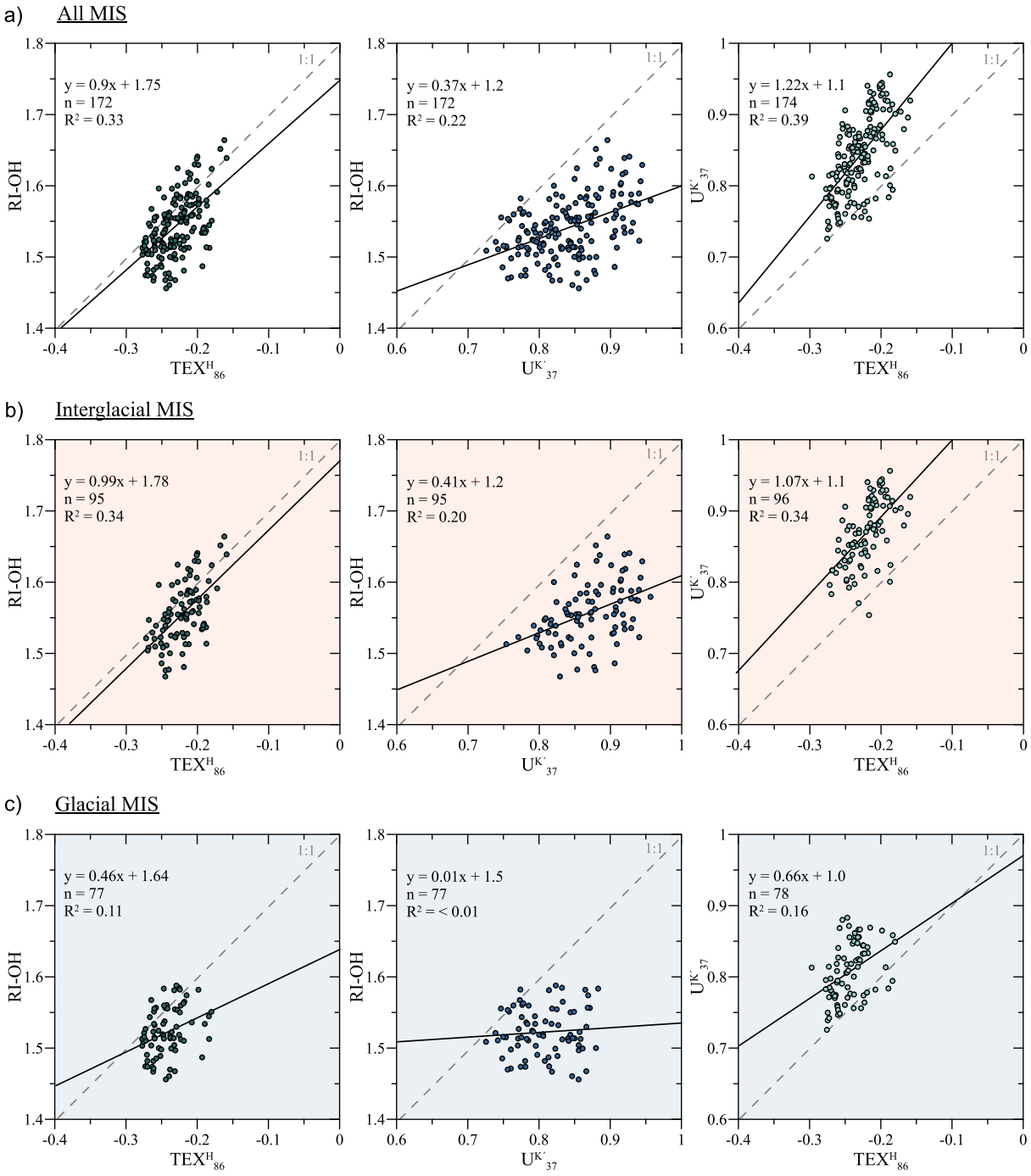

Figure 7.2 | Correlation of the RI-OH, U$^{K'}_{37}$, and TEX$^{H}_{86}$ paleothermometers for all (a), only interglacial (b), and only glacial (c) marine isotope stages (MIS). Dashed gray lines give the 1:1 correlation.

Altogether, our results from the past 1 Ma at Site U1437 confirm the applicability of the RI-OH as a proxy for SST reconstruction on geological timescales, as has been shown previously for the last glacial-interglacial cycle (Kremer et al., 2018; Davtian et al., 2019; 2021), and we successfully extend its range of application back to the mid-Pleistocene.

7.4. Conclusions

Our 1 Ma RI-OH record from the Northwest Pacific Ocean shows overall similar trends as seen in $U^{K'}_{37}$- and TEX^{H}_{86}-records, thus indicating that the RI-OH is a suitable complementary tool for water temperature reconstructions. Seasonal and annual mean RI-OH-SSTs from the core top sample agree well with *in situ* SSTs at U1437 (except for winter RI-OH-SSTs, which underestimate *in situ* SSTs by 3 °C). Using the global calibration for the RI-OH, the proxy shows the best fit with annual mean *in situ* temperatures at the sea surface. With this study, we extend the current range of application of the RI-OH for paleo-SST reconstruction from previously the late Pleistocene back to the middle Pleistocene.

7.5. Acknowledgements

Sample material for this study was provided through the International Ocean Discovery Program. This work was supported by the German Research Foundation (grants BA 3841/4-1 and BA 3841/6-1 awarded to TB as well as grants SCHW 554/27-1,2 given to LS).

7.6. Appendix: Supporting information

Table 7.A1 | RI-OH SST data.

Sample U1437B-	Absolute depth (m CSF-B)	Age (ka)	RI-OH	RI-OH SST_{global} (°C)	RI-OH SST_{annual} (°C)	RI-OH SST_{spring} (°C)	RI-OH SST_{summer} (°C)	RI-OH SST_{autumn} (°C)	RI-OH SST_{winter} (°C)
1H - 1W, 0.0 - 3.0 cm	0.02	0.1	1.53	23.6	21.9	19.7	26.8	25.2	17.3
1H - 1W, 6.0 - 9.0 cm	0.08	0.7	1.54	24.0	22.2	20.1	27.0	25.4	17.7
1H - 1W, 12.0 - 15.0 cm	0.14	1.3	1.56	25.3	23.0	21.3	27.4	25.9	18.8
1H - 1W, 18.0 - 20.0 cm	0.19	1.8	1.54	23.7	22.0	19.8	26.9	25.3	17.5
1H - 1W, 20.0 - 23.0 cm	0.22	2.1	1.60	27.3	24.3	23.2	28.0	26.7	20.5
1H - 1W, 24.0 - 26.0 cm	0.25	2.4	1.59	26.7	24.0	22.7	27.8	26.5	20.1
1H - 1W, 32.0 - 34.0 cm	0.33	3.2	1.54	23.6	22.0	19.8	26.8	25.2	17.4
1H - 1W, 52.0 - 55.0 cm	0.54	5.3	1.56	25.0	22.8	21.0	27.3	25.8	18.5
1H - 1W, 65.0 - 68.0 cm	0.67	6.5	1.59	26.4	23.8	22.4	27.7	26.4	19.8
1H - 1W, 82.0 - 85.0 cm	0.84	8.2	1.51	22.4	21.2	18.6	26.5	24.7	16.3
1H - 1W, 92.0 - 95.0 cm	0.94	9.2	1.53	23.2	21.7	19.3	26.7	25.1	17.0
1H - 1W, 102.0 - 105.0 cm	1.04	10.2	1.59	26.6	23.9	22.6	27.8	26.4	19.9
1H - 1W, 113.0 - 116.0 cm	1.15	11.2	1.58	26.3	23.7	22.3	27.7	26.3	19.7
1H - 1W, 123.0 - 126.0 cm	1.25	12.2	1.52	22.9	21.5	19.1	26.6	24.9	16.8
1H - 1W, 134.0 - 137.0 cm	1.36	13.3	1.56	24.8	22.7	20.9	27.2	25.7	18.4
1H - 1W, 143.0 - 146.0 cm	1.45	14.2	1.51	22.4	21.2	18.6	26.5	24.7	16.3
1H - 2W, 15.0 - 18.0 cm	1.64	16.1							
1H - 2W, 47.0 - 50.0 cm	1.96	20.5	1.47	19.8	19.5	16.1	25.6	23.7	14.1
1H - 2W, 53.0 - 56.0 cm	2.02	21.2	1.49	20.9	20.2	17.2	26.0	24.2	15.1
1H - 2W, 60.0 - 63.0 cm	2.09	22.0	1.49	21.1	20.4	17.4	26.1	24.2	15.3
1H - 2W, 86.0 - 89.0 cm	2.35	25.0	1.48	20.7	20.1	16.9	25.9	24.0	14.8
1H - 2W, 112.0 - 115.0 cm	2.61	27.9	1.49	21.0	20.3	17.3	26.0	24.2	15.2
1H - 2W, 138.0 - 141.0 cm	2.87	30.9	1.51	22.1	21.0	18.3	26.4	24.6	16.1
1H - 3W, 22.0 - 25.0 cm	2.94	31.7							
1H - 3W, 61.0 - 63.0 cm	3.32	36.0	1.48	20.6	20.0	16.9	25.9	24.0	14.8
1H - 4W, 4.0 - 7.0 cm	4.17	45.7	1.56	24.7	22.7	20.8	27.2	25.7	18.3
1H - 4W, 65.0 - 68.0 cm	4.78	52.7	1.50	21.5	20.6	17.8	26.2	24.4	15.6
2H - 1W, 20.0 - 22.0 cm	5.41	59.9	1.47	19.9	19.6	16.2	25.7	23.7	14.2
2H - 1W, 43.0 - 46.0 cm	5.66	63.1	1.47	20.2	19.8	16.5	25.8	23.9	14.5
2H - 1W. 78.0 - 81.0 cm	6.01	68.1	1.52	22.7	21.4	18.9	26.6	24.9	16.6
2H - 2W, 23.0 - 26.0 cm	6.36	73.1	1.53	23.1	21.6	19.2	26.7	25.0	16.9
2H - 2W, 58.0 - 61.0 cm	6.71	78.0	1.53	23.2	21.7	19.3	26.7	25.0	17.0
2H - 3W, 34.0 - 36.0 cm	7.21	83.0	1.50	21.6	20.7	17.8	26.2	24.4	15.7
2H - 3W, 107.0 - 110.0 cm	7.93	88.9	1.47	19.9	19.6	16.2	25.7	23.7	14.2
2H - 4W, 9.0 - 12.0 cm	8.49	94.2	1.60	27.0	24.1	23.0	27.9	26.6	20.3
2H - 4W, 60.0 - 62.0 cm	8.97	99.1	1.57	25.7	23.3	21.8	27.5	26.1	19.2
2H - 4W, 140.0 - 143.0 cm	9.79	107.2	1.62	28.6	25.2	24.4	28.4	27.2	21.6
2H - 5W, 46.0 - 49.0 cm	10.35	114.0	1.56	24.7	22.7	20.8	27.2	25.7	18.3
2H - 5W, 92.0 - 94.0 cm	10.79	120.5	1.58	26.1	23.5	22.1	27.6	26.2	19.5
2H - 5W, 123.0 - 126.0 cm	11.12	124.4	1.58	25.8	23.4	21.8	27.5	26.1	19.3

Sample U1437B-	Absolute depth (m CSF-B)	Age (ka)	RI-OH	RI-OH SST_{global} (°C)	RI-OH SST_{annual} (°C)	RI-OH SST_{spring} (°C)	RI-OH SST_{summer} (°C)	RI-OH SST_{autumn} (°C)	RI-OH SST_{winter} (°C)
2H - 5W, 139.0 - 142.0 cm	11.28	125.9	1.64	29.5	25.7	25.3	28.7	27.6	22.4
2H - 6W, 11.0 - 14.0 cm	11.50	127.9	1.64	29.4	25.7	25.2	28.7	27.5	22.3
2H - 6W, 45.0 - 48.0 cm	11.84	131.1	1.50	21.7	20.7	17.9	26.2	24.4	15.7
2H - 6W, 113.0 - 116.0 cm	12.52	137.5	1.50	21.6	20.7	17.8	26.2	24.4	15.7
2H - 6W, 130.0 - 132.0 cm	12.67	138.9	1.46	19.2	19.1	15.6	25.5	23.5	13.6
2H - 7W, 66.0 - 69.0 cm	13.54	147.0	1.47	20.2	19.8	16.5	25.8	23.9	14.5
2H - 8W, 20.0 - 23.0 cm	14.11	152.3	1.48	20.7	20.1	16.9	25.9	24.0	14.9
2H - 8W, 50.0 - 52.0 cm	14.39	154.9	1.47	20.2	19.8	16.5	25.8	23.9	14.5
3H - 1W, 47.0 - 50.0 cm	15.16	162.1	1.47	20.1	19.7	16.4	25.7	23.8	14.3
3H - 1W, 140.0 - 142.0 cm	16.08	170.7	1.47	20.0	19.6	16.3	25.7	23.8	14.3
3H - 2W, 80.0 - 8.0 cm	17.02	179.4	1.52	23.0	21.6	19.2	26.7	25.0	16.9
3H - 3W, 28.0 - 30.0 cm	17.91	188.0	1.52	22.7	21.4	18.9	26.6	24.9	16.6
3H - 3W, 88.0 - 91.0 cm	18.52	194.1	1.53	23.3	21.8	19.4	26.7	25.1	17.1
3H - 4W, 22.0 - 25.0 cm	19.32	202.0	1.52	22.8	21.4	19.0	26.6	24.9	16.7
3H - 4W, 58.0 - 60.0 cm	19.66	205.5	1.52	22.9	21.5	19.1	26.6	24.9	16.8
3H - 4W, 124.0 - 127.0 cm	20.31	211.9	1.56	25.1	22.9	21.2	27.3	25.8	18.7
3H - 5W, 37.0 - 40.0 cm	20.92	218.1	1.55	24.3	22.4	20.4	27.1	25.5	18.0
3H - 5W, 92.0 - 94.0 cm	21.46	223.7	1.49	20.9	20.2	17.2	26.0	24.1	15.0
3H - 6W, 19.0 - 22.0 cm	22.21	231.6	1.55	24.3	22.4	20.4	27.1	25.5	18.0
3H - 6W, 100.0 - 102.0 cm	23.00	239.9	1.51	22.4	21.2	18.6	26.5	24.7	16.3
3H - 6W, 109.0 - 112.0 cm	23.11	248.1	1.52	22.9	21.5	19.1	26.6	25.0	16.8
3H - 7W, 12.0 - 15.0 cm	23.76	257.0	1.50	21.9	20.8	18.1	26.3	24.5	15.9
4H - 1W, 15.0 - 18.0 cm	24.38	263.0	1.54	23.7	22.0	19.8	26.9	25.2	17.4
4H - 1W, 102.0 - 105.0 cm	25.21	271.2	1.46	19.5	19.3	15.8	25.5	23.6	13.8
4H - 2W, 30.0 - 33.0 cm	26.02	279.0	1.52	22.6	21.3	18.8	26.5	24.8	16.5
4H - 2W, 102.0 - 105.0 cm	26.74	285.9	1.50	21.5	20.6	17.7	26.2	24.4	15.6
4H - 3W, 30.0 - 33.0 cm	27.52	293.0	1.50	21.6	20.6	17.8	26.2	24.4	15.6
4H - 3W, 108.0 - 111.0 cm	28.30	300.0	1.54	23.8	22.1	19.9	26.9	25.3	17.6
4H - 4W, 10.0 - 12.0 cm	28.81	304.7	1.55	24.7	22.7	20.8	27.2	25.7	18.3
4H - 4W, 84.0 - 87.0 cm	29.67	312.4	1.51	22.3	21.1	18.5	26.4	24.7	16.2
4H - 5W, 6.0 - 9.0 cm	30.28	317.9	1.55	24.6	22.6	20.7	27.2	25.6	18.3
4H - 5W, 84.0 - 87.0 cm	31.06	325.0	1.58	26.4	23.7	22.4	27.7	26.3	19.7
4H - 6W, 50.0 - 5.0 cm	32.21	330.9	1.56	24.9	22.8	20.9	27.2	25.7	18.5
5H - 1W, 17.0 - 20.0 cm	33.89	333.5	1.53	23.5	21.9	19.6	26.8	25.2	17.3
5H - 2W, 84.0 - 86.0 cm	36.05	336.8	1.48	20.3	19.9	16.6	25.8	23.9	14.6
5H - 2W, 99.0 - 102.0 cm	36.22	337.1	1.52	22.8	21.5	19.0	26.6	24.9	16.7
5H - 3W, 42.0 - 45.0 cm	37.14	338.5	1.55	24.5	22.5	20.6	27.1	25.6	18.1
5H - 4W, 11.0 - 14.0 cm	38.34	340.3	1.52	22.5	21.3	18.7	26.5	24.8	16.4
5H - 4W, 120.0 - 122.0 cm	39.41	342.0	1.52	22.7	21.4	18.9	26.6	24.9	16.6
5H - 4W, 129.0 - 132.0 cm	39.52	344.7	1.56	25.0	22.8	21.0	27.3	25.8	18.6
5H - 5W, 22.0 - 25.0 cm	39.94	356.0	1.54	23.7	22.1	19.9	26.9	25.3	17.5
5H - 5W, 48.0 - 51.0 cm	40.20	362.9	1.55	24.7	22.7	20.8	27.2	25.7	18.3
5H - 5W, 74.0 - 77.0 cm	40.46	369.9	1.58	26.4	23.7	22.4	27.7	26.3	19.7
5H - 5W, 100.0 - 103.0 cm	40.72	376.9	1.57	25.7	23.3	21.7	27.5	26.0	19.1

Sample U1437B-	Absolute depth (m CSF-B)	Age (ka)	RI-OH	RI-OH SST_{global} (°C)	RI-OH SST_{annual} (°C)	RI-OH SST_{spring} (°C)	RI-OH SST_{summer} (°C)	RI-OH SST_{autumn} (°C)	RI-OH SST_{winter} (°C)
5H - 5W, 126.0 - 129.0 cm	40.98	383.9	1.57	25.5	23.2	21.5	27.4	26.0	19.0
5H - 6W, 2.0 - 5.0 cm	41.24	390.9	1.60	27.2	24.3	23.2	28.0	26.7	20.5
5H - 6W, 29.0 - 32.0 cm	41.51	398.1	1.58	26.3	23.7	22.3	27.7	26.3	19.7
5H - 6W, 66.0 - 69.0 cm	41.88	408.0	1.61	27.8	24.6	23.7	28.2	26.9	20.9
5H - 7W, 9.0 - 12.0 cm	42.13	411.9	1.63	28.9	25.4	24.7	28.5	27.3	21.9
6H - 1W, 1.0 - 4.0 cm	43.23	419.5	1.66	30.8	26.6	26.5	29.1	28.1	23.5
6H - 1W, 10.0 - 12.0 cm	43.31	420.0	1.58	25.9	23.5	21.9	27.6	26.2	19.4
6H - 1W, 118.0 - 121.0 cm	44.40	427.2	1.57	25.8	23.4	21.8	27.5	26.1	19.2
6H - 3W, 60.0 - 62.0 cm	46.70	436.0	1.51	22.4	21.2	18.6	26.5	24.7	16.4
6H - 4W, 67.0 - 70.0 cm	48.39	443.6	1.56	25.0	22.9	21.1	27.3	25.8	18.6
6H - 5W, 120.0 - 122.0 cm	50.18	451.8	1.52	22.9	21.5	19.1	26.6	24.9	16.8
6H - 6W, 119.0 - 122.0 cm	51.91	462.5	1.55	24.6	22.6	20.7	27.2	25.6	18.3
6H - 7W, 29.0 - 32.0 cm	52.51	470.0	1.53	23.2	21.7	19.3	26.7	25.0	17.0
7H - 1W, 13.0 - 16.0 cm	52.80	473.7	1.54	24.1	22.3	20.2	27.0	25.4	17.8
7H - 1W, 71.0 - 74.0 cm	53.38	481.0	1.60	27.0	24.1	22.9	27.9	26.6	20.3
7H - 1W, 130.0 - 132.0 cm	53.96	488.2	1.59	26.6	23.9	22.6	27.8	26.4	20.0
7H - 2W, 140.0 - 143.0 cm	55.62	495.7	1.62	28.3	24.9	24.1	28.3	27.1	21.4
7H - 4W, 64.0 - 66.0 cm	57.42	503.3	1.63	28.8	25.3	24.7	28.5	27.3	21.9
7H - 6W, 23.0 - 26.0 cm	59.85	514.7	1.60	27.4	24.4	23.4	28.0	26.8	20.7
7H - 7W, 10.0 - 12.0 cm	60.88	520.2	1.59	26.5	23.8	22.5	27.8	26.4	19.9
7H - CC, 31.0 - 34.0 cm	62.54	528.9	1.55	24.3	22.4	20.4	27.1	25.5	17.9
8H - 1W, 146.0 - 149.0 cm	63.68	534.9	1.58	26.2	23.6	22.2	27.7	26.3	19.6
8H - 2W, 110.0 - 112.0 cm	64.80	540.9	1.53	23.3	21.8	19.5	26.8	25.1	17.1
8H - 2W, 134.0 - 137.0 cm	65.05	548.3	1.58	26.3	23.7	22.3	27.7	26.3	19.7
8H - 3W, 6.0 - 9.0 cm	65.28	555.3	1.55	24.5	22.5	20.5	27.1	25.6	18.1
8H - 3W, 28.0 - 31.0 cm	65.50	562.3	1.56	25.3	23.0	21.3	27.4	25.9	18.8
8H - 3W, 50.0 - 53.0 cm	65.72	569.2	1.59	26.5	23.8	22.5	27.8	26.4	19.9
8H - 3W, 72.0 - 75.0 cm	65.94	576.0	1.62	28.5	25.1	24.4	28.4	27.2	21.6
8H - 5W, 24.0 - 26.0 cm	68.42	583.9	1.52	22.9	21.5	19.1	26.6	24.9	16.8
8H - 5W, 57.0 - 60.0 cm	68.76	590.3	1.55	24.7	22.7	20.8	27.2	25.7	18.3
8H - 5W, 97.0 - 100.0 cm	69.18	599.1	1.55	24.2	22.3	20.3	27.0	25.5	17.9
8H - 5W, 128.0 - 131.0 cm	69.47	605.2	1.64	29.3	25.6	25.2	28.6	27.5	22.3
8H - 6W, 12.0 - 15.0 cm	69.84	612.3	1.57	25.8	23.4	21.8	27.5	26.1	19.2
8H - 6W, 90.0 - 93.0 cm	70.65	619.6	1.55	24.3	22.4	20.4	27.1	25.5	18.0
8H - 7W, 47.0 - 50.0 cm	71.39	626.3	1.53	23.6	21.9	19.7	26.8	25.2	17.3
9H - 1W, 5.0 - 8.0 cm	71.77	629.7	1.53	23.5	21.9	19.6	26.8	25.2	17.2
9H - 1W, 30.0 - 32.0 cm	72.01	631.9	1.56	24.8	22.7	20.9	27.2	25.7	18.4
9H - 1W, 116.0 - 119.0 cm	72.89	639.7	1.56	24.7	22.7	20.8	27.2	25.7	18.4
9H - 2W, 49.0 - 52.0 cm	73.71	646.9	1.57	25.4	23.1	21.4	27.4	25.9	18.9
9H - 2W, 134.0 - 137.0 cm	74.56	654.4	1.53	23.6	21.9	19.7	26.8	25.2	17.3
9H - 3W, 90.0 - 92.0 cm	75.61	663.8	1.51	22.4	21.2	18.6	26.5	24.7	16.3
9H - 4W, 32.0 - 35.0 cm	76.54	672.0	1.51	22.3	21.1	18.5	26.4	24.7	16.2
9H - 4W, 132.0 - 135.0 cm	77.54	680.8	1.50	21.9	20.9	18.1	26.3	24.5	15.9
9H - 5W, 63.0 - 66.0 cm	78.35	688.0	1.51	22.2	21.1	18.4	26.4	24.7	16.2

Sample U1437B-	Absolute depth (m CSF-B)	Age (ka)	RI-OH	RI-OH SST_{global} (°C)	RI-OH SST_{annual} (°C)	RI-OH SST_{spring} (°C)	RI-OH SST_{summer} (°C)	RI-OH SST_{autumn} (°C)	RI-OH SST_{winter} (°C)
9H - 6W, 18.0 - 20.0 cm	79.19	695.5	1.53	23.3	21.7	19.4	26.7	25.1	17.1
9H - 6W, 50.0 - 53.0 cm	79.53	703.5	1.62	28.1	24.9	24.0	28.3	27.0	21.2
10H - 1W, 6.0 - 9.0 cm	79.78	710.4	1.51	22.5	21.2	18.6	26.5	24.8	16.4
10H - 1W, 31.0 - 34.0 cm	80.03	718.9	1.53	23.5	21.9	19.7	26.8	25.2	17.3
10H - 1W, 88.0 - 91.0 cm	80.60	725.0	1.56	24.8	22.7	20.9	27.2	25.7	18.4
10H - 2W, 11.0 - 14.0 cm	81.33	732.7	1.58	26.2	23.6	22.2	27.7	26.3	19.6
10H - 2W, 78.0 - 81.0 cm	82.00	739.7	1.54	24.1	22.3	20.2	27.0	25.4	17.8
10H - 3W, 3.0 - 5.0 cm	82.61	746.2	1.50	21.6	20.7	17.9	26.2	24.4	15.7
10H - 3W, 95.0 - 98.0 cm	83.54	751.0	1.50	21.8	20.8	18.1	26.3	24.5	15.9
10H - 4W, 105.0 - 108.0 cm	85.27	757.8	1.59	26.5	23.9	22.5	27.8	26.4	19.9
10H - 5W, 72.0 - 74.0 cm	86.14	761.2	1.55	24.5	22.5	20.6	27.1	25.6	18.1
10H - CC, 1.0 - 3.0 cm	89.34	773.7	1.56	24.9	22.8	20.9	27.2	25.7	18.5
11F - 1W, 80.0 - 82.0 cm	89.97	781.7	1.61	27.6	24.5	23.5	28.1	26.8	20.8
11F - 1W, 84.0 - 87.0 cm	90.02	782.0	1.65	30.1	26.1	25.9	28.9	27.8	22.9
11F - 2W, 54.0 - 57.0 cm	91.26	788.4	1.55	24.4	22.5	20.5	27.1	25.5	18.1
11F - 3W, 8.0 - 11.0 cm	92.30	793.8	1.51	22.2	21.0	18.4	26.4	24.6	16.1
11F - 3W, 80.0 - 83.0 cm	93.02	801.8	1.51	22.3	21.1	18.5	26.4	24.7	16.2
11F - 4W, 15.0 - 18.0 cm	93.34	805.5	1.51	22.4	21.2	18.6	26.5	24.7	16.4
11F - 4W, 19.0 - 21.0 cm	93.37	805.8	1.50	21.9	20.9	18.1	26.3	24.5	15.9
12F - 1W, 17.0 - 20.0 cm	94.09	814.0	1.56	24.8	22.7	20.8	27.2	25.7	18.4
12F - 1W, 77.0 - 80.0 cm	94.69	820.8	1.51	22.1	21.0	18.3	26.4	24.6	16.1
12F - 1W, 146.0 - 149.0 cm	95.38	828.6	1.51	22.4	21.2	18.6	26.5	24.7	16.4
12F - 2W, 88.0 - 91.0 cm	96.30	839.1	1.58	25.9	23.4	21.9	27.6	26.1	19.3
12F - 3W, 22.0 - 25.0 cm	96.86	845.5	1.57	25.7	23.3	21.7	27.5	26.1	19.2
12F - 3W, 104.0 - 106.0 cm	97.67	854.7	1.55	24.5	22.5	20.6	27.1	25.6	18.2
13F - 1W, 15.0 - 18.0 cm	98.77	860.0	1.50	21.7	20.7	17.9	26.2	24.4	15.7
13F - 2W, 48.0 - 50.0 cm	100.59	864.5	1.57	25.7	23.3	21.7	27.5	26.1	19.2
14F - 1W, 20.0 - 23.0 cm	102.32	868.8	1.56	25.2	23.0	21.2	27.3	25.8	18.7
14F - 2W, 80.0 - 82.0 cm	104.32	873.7	1.51	22.5	21.2	18.7	26.5	24.8	16.4
14F - 3W, 7.0 - 10.0 cm	105.19	883.4	1.51	22.4	21.2	18.6	26.5	24.7	16.3
14F - 3W, 72.0 - 75.0 cm	105.84	891.4	1.56	25.0	22.8	21.0	27.3	25.8	18.5
14F - 4W, 22.0 - 25.0 cm	106.54	900.0	1.52	22.8	21.5	19.0	26.6	24.9	16.7
15F - 1W, 37.0 - 40.0 cm	107.12	907.1	1.54	23.8	22.1	19.9	26.9	25.3	17.6
15F - 1W, 120.0 - 122.0 cm	107.94	915.7	1.56	25.1	22.9	21.2	27.3	25.8	18.7
15F - 2W, 40.0 - 43.0 cm	108.72	923.9	1.52	22.5	21.3	18.7	26.5	24.8	16.5
15F - 2W, 116.0 - 119.0 cm	109.48	931.9	1.49	20.9	20.2	17.1	26.0	24.1	15.0
15F - 3W, 42.0 - 45.0 cm	110.24	952.1	1.52	22.9	21.5	19.1	26.6	25.0	16.8
15F - 3W, 62.0 - 65.0 cm	110.44	954.3	1.54	23.9	22.2	20.1	26.9	25.4	17.7
15F - 4W, 44.0 - 46.0 cm	111.17	955.8	1.48	20.4	19.9	16.7	25.8	23.9	14.6
16F - 2W, 75.0 - 78.0 cm	113.08	959.6	1.58	26.2	23.6	22.2	27.7	26.2	19.6
17F - 1W, 10.0 - 12.0 cm	116.30	966.0	1.51	22.3	21.1	18.5	26.4	24.7	16.3
17F - 1W, 142.0 - 145.0 cm	117.61	974.6	1.54	23.9	22.1	20.0	26.9	25.3	17.6
17F - 2W, 120.0 - 122.0 cm	118.71	982.8	1.51	22.2	21.1	18.4	26.4	24.7	16.2
17F - 3W, 72.0 - 75.0 cm	119.94	988.0	1.55	24.5	22.5	20.6	27.1	25.6	18.1

Sample U1437B-	Absolute depth (m CSF-B)	Age (ka)	RI-OH	RI-OH SST_{global} (°C)	RI-OH SST_{annual} (°C)	RI-OH SST_{spring} (°C)	RI-OH SST_{summer} (°C)	RI-OH SST_{autumn} (°C)	RI-OH SST_{winter} (°C)
17F - 3W, 30.0 - 33.0 cm	120.43	993.7	1.51	22.4	21.2	18.6	26.5	24.8	16.4
18F - 1W, 139.0 - 141.0 cm	122.24	1019.9	1.55	24.7	22.7	20.8	27.2	25.7	18.3

Chapter 8

Impact of climate change on the magnetic mineral assemblage in marine sediments from Izu rear arc, NW Pacific Ocean, over the last 1 Ma

Myriam Kars[1], Robert J. Musgrave[2,3], Kazuto Kodama[1], Ann-Sophie Jonas[4], Manuela Bordiga[5], Wolfgang Ruebsam[4], Maryline J. Mleneck-Vautravers[6], Thorsten Bauersachs[4]

[1] Center for Advanced Marine Core Research, Kochi University, B200 Monobe, Nankoku 783-0004, Japan

[2] School of Geosciences, University of Sydney, Sydney, NSW2006, New South Wales, Australia

[3] Geological Survey of New South Wales, NSW Department of Industry, Maitland, NSW 2320, New South Wales, Australia

[4] Department of Organic Geochemistry, Institute of Geosciences, Christian-Albrechts-University, Ludewig-Meyn-Straße 10, 24118 Kiel, Germany

[5] Department of Earth Sciences, Uppsala University, Villavägen 16, 752 36 Uppsala, Sweden

[6] Department of Earth Sciences, University of Cambridge, Downing Street, Cambridge CB2 3EQ, United Kingdom

Published in *Palaeogeography, Palaeoclimatology, Palaeoecology* 480 (2017), 53-69, doi:10.1016/j.palaeo.2017.05.016.

Abstract

A rock magnetic study was conducted on upper Pleistocene marine sediments from International Ocean Discovery Program Expedition 350 Site U1437 in order to highlight the paleoenvironmental changes in the NW Pacific Ocean influenced by the East Asian monsoon regime. Remanent magnetization analyses, hysteresis properties, first-order reversal curves and low temperature magnetic measurements were carried out, along with electron microscope observations. The results indicate that coarse-grained (titano)-magnetite is the dominant magnetic phase in the magnetic mineral assemblage. Time-series analysis supports that this

assemblage is modulated by global climate changes over the last 1 Ma. During the interglacial stages, magnetic minerals are more abundant; and are dominated by coarse-grained (titano)-magnetite of both terrigenous (likely from mainland China) and volcanic (Izu arc front, Japan) origin. During the glacial stages, the magnetic mineral content is lower, probably reflecting partial dissolution of (Ti)-magnetite, and the magnetic assemblage is composed of terrigenous coarse-grained (titano)-magnetite and of higher coercivity, presumably finer eolian particles (likely hematite) as a result of the enhancement of the winter monsoon in continental Asia. The magnetic mineral assemblage reflects a superimposition of volcanic and global climate signals. Bulk organic-geochemical analyses for total and organic carbon as well as nitrogen and sulfur contents confirm a climatic signature in the composition of the sediments with more oxygenated water masses being present during glacial periods. Additional X-ray fluorescence measurements on bulk samples indicate various origins of the sediment particles with both proximal and distal sources.

8.1. Introduction

The Pleistocene is characterized by a significant change in climate cyclicity from a 41-ka to a 100-ka periodicity without any known change in the orbital forcing. This is the so-called Mid-Pleistocene Transition (MPT) from 1.25 to 0.70 Ma (e.g., Clark et al., 2006; Lisiecki and Raymo, 2007), during which the Earth's climate shifted gradually toward lower global temperatures and more intense glaciations with increased ice volume after 0.95 Ma (e.g., Pisias and Moore, 1981; Clark et al., 2006; Kitamura and Kawagoe, 2006; Lisiecki and Raymo, 2007). During the Pleistocene, loess deposition was continuous in the central part of China (e.g., Buylaert et al., 2008), providing good terrestrial archives for Quaternary climatic changes. The loess sequence represents alternation of glacial and interglacial periods with more dust deposition during cold and dry stages and increased pedogenesis and weathering during warm and humid stages (paleosol formation) (e.g., Kukla and An, 1989). This reflects changes in the East Asian Monsoon regime with the dominance of winter monsoon during glacials resulting in increased aridity and eolian dust deposition in Central Asia (e.g., Xiao and An, 1999; An, 2000; An et al., 2015). The monsoon is one of the driving forces for paleoenvironment changes in East Asia, which has become a topic of increasing interest with multiple studies on terrestrial, lacustrine and marine materials been performed over the last decades (e.g., An, 2000; and references therein). Climatic cycles recorded by the Chinese loess-paleosol stratigraphy are well correlated with the benthic oxygen isotope record of marine sediments and with magnetic susceptibility variations in marine sediment cores (e.g., An et al., 1991; Bloemendal et al.,

1995). The rock magnetic properties of sediments are potentially a good record of paleoenvironmental changes expressed as the variations in the magnetic mineralogy (concentration, grain size, composition of the magnetic mineral assemblage). Many rock magnetic studies around Asia and the Pacific Ocean successfully documented paleoclimatic and monsoonal changes in marine sediments by recognizing characteristic magnetic signatures in response to climatic variations (e.g., Yamazaki and Ioka, 1997; Kissel et al., 2003; Yamazaki, 2009). Nevertheless, the rock magnetic results may differ from site to site as a result of different geographical locations and varying sediment sources. Site U1437 was drilled in the Izu rear arc (NW Pacific Ocean) during the International Ocean Discovery Program Expedition 350 (Fig. 8.1) (Tamura et al., 2015a; Busby et al., 2017). This study investigates the upper 120 m of deep-sea sediments cored at Site U1437 spanning the last 1 Ma. Site U1437 is close to both the Izu volcanic front and continental Asia, and is under the influence of both the strong westerly jet winds from Asia and the occasional large meander of the Kuroshio Current, one of the most important surface water currents in the NW Pacific Ocean (Qiu, 2001). Thus, Site U1437 is a location where the origin of sediments and magnetic particles is diverse and potentially reflect changes in the Pleistocene climate in this region which is subject to the monsoonal regime (e.g., An, 2000; Tada et al., 2016). In this paper, we report the results of a rock magnetic study conducted to characterize the changes in magnetic properties and mineralogy related to paleoenvironmental changes over the last 1 Ma in the NW Pacific. By combining rock magnetic techniques and geochemical analyses, this study aims to deepen the knowledge on the glacial-interglacial (G-I) cycles and MPT dynamics, and to bring new insights on the impact of the East Asian monsoon on the magnetic mineral assemblage in the Izu rear arc.

8.2. Geological setting

IODP Site U1437 (31°47.39 ′N, 139°01.58 ′E; water depth: 2116 m; bottom-hole depth: 1806.5 m below seafloor) is located in a ~20 km wide volcano-bounded intra-arc basin between two major constructional volcanic ridges: the Manji and Enpo rear arc seamount chains which are two of several Izu seamount chains (Fig. 8.1). Site U1437 is located behind the main chain of active volcanoes (Izu arc front) about 90 km west of the arc front Myojinsho Volcano and Myojin Knoll and 330 km west of the axis of the Izu-Bonin trench.

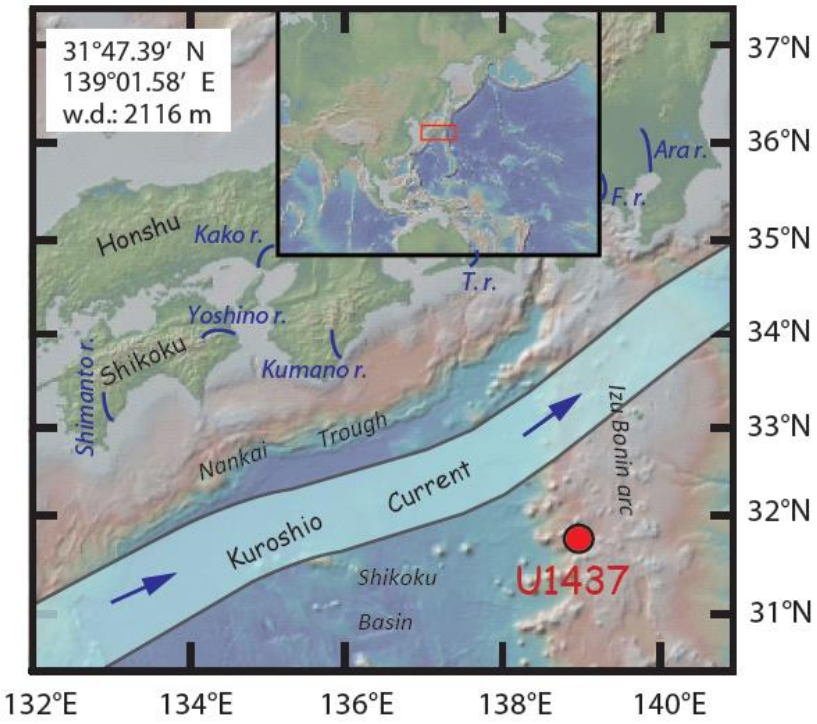

Figure 8.1 | Location map and coordinates of Site U1437 drilled during IODP Expedition 350 (w.d. is water depth). Major rivers in Japan are indicated (T.r.: Tenryu river; F. r.: Fuji river). The map was generated with GeoMapApp (http://www.geomapapp.org) (Ryan et al., 2009).

Although Site U1437 is in a location that should be topographically shielded from more concentrated arc front-derived density currents, arc front-derived sediments may have arrived via both more dilute equivalents of these currents and through direct ash fall (Tamura et al., 2015a). Site U1437 is well located for paleoceanographic studies, as it is close to the large meander path of the Kuroshio Current (KC) (Fig. 8.1). South of Japan, the path of the KC oscillates between a straight path and one that meanders eastwards. The largest amplitudes of the meander (southward) occurred during intervals of decreasing current velocity and volume transport of the KC during El Niño-Southern Oscillation (ENSO) events (e.g., Ito and Horikawa, 2000; Qiu, 2001; Tsujino et al., 2013; Usui et al., 2013). Site U1437 is located slightly south of the northeastward flowing KC, about 400 km east of its exit from the East China Sea as it enters the deep Shikoku Basin. Site U1437 is under the influence of the Antarctic Intermediate Water (AAIW), which is relatively well ventilated (medium to high oxygen content) with low CO_2 and low nutrient (Mleneck-Vautravers, 2018). The AAIW has a stonger influence on the region west of the Izu Rise, which creates a hydrographic divide (Mleneck-Vautravers, 2018).

8.3. Material and methods

A total of 360 deep-sea sediment samples from 0 (Section 1H-1) to 120 m below sea floor (mbsf) (Section 17F-3) of Hole U1437B was collected and studied, of which 143 samples are oriented 7 cm^3 plastic cubes.

The samples are tuffaceous mud and mudstone, belonging to Lithologic Unit I (0-682.12mbsf) (Expedition 350 Scientists, 2014; Tamura et al., 2015b). The tuffaceous mudstones of Unit I contain abundant fine colorless glass shards with rare crystals, plus carbonate materials such as foraminifers (Tamura et al., 2015b).

8.3.1. Rock magnetic measurements

Magnetic measurements were performed at the paleomagnetic laboratory of the Center for Advanced Marine Core Research (CMCR), Kochi University, Japan. Low field-low frequency (0.465 kHz) and low field-high frequency (4.65 kHz) magnetic susceptibility (χ_{lf} and χ_{hf}, respectively) was measured with a MS2 Bartington apparatus (field = 250 μT). Frequency dependence of the magnetic susceptibility additionally was investigated by measuring the susceptibility of cube samples at F_1 = 0.976, F_2 = 3.904 and F_3 = 15.616 kHz with a MFK1-FA Agico Kappabridge apparatus (field = 20 μT).

Natural remanent magnetization (NRM), alternating field (AF) demagnetization up to 60 mT with steps every 5 mT, and anhysteretic remanent magnetization (ARM) were measured with a 2G 760R cryogenic magnetometer in a shielded room (noise level ~10^{-10} Am^2). ARM was imparted in a DC bias field of 50 μT in the presence of an 80 mT peak alternating field. Isothermal remanent magnetization (IRM) was subsequently imparted at 0.1, 0.3, 0.9 and 1.2 T by using a MMPM10 pulse magnetizer before being measured at each step with a Natsuhara Giken spinner magnetometer (noise level ~10^{-8} Am^2). The IRM at 1.2 T is called hereafter SIRM (Saturation IRM). The samples were subsequently remagnetized in a DC reverse field of 0.1 and 0.3 T and measured again, in order to calculate the parameter $S_{-0.3T}$ (=[(IRM$_{-0.3T}$) / SIRM) + 1]/2); Bloemendal et al., 1992), an indication of the relative contribution of high (e.g, hematite, goethite, ferromagnetic iron sulfides) and low (e.g. magnetite, maghemite) coercivity minerals to the remanence. Hard (high-coercivity) IRM defined as HIRM = (SIRM + IRM$_{-0.3T}$)/2, and the L-ratio = (SIRM + IRM$_{-0.3T}$)/(SIRM + IRM$_{-0.1T}$) were also calculated from these measurements. HIRM isolates the contribution of hematite and/or goethite from that of magnetite. The L-ratio is an indicator of how the hardness of hematite affects HIRM and $S_{-0.3T}$ (Liu et al., 2007a).

Hysteresis loops with a maximum applied field of 1 T were measured at room temperature with a Princeton Vibrating Sample Magnetometer (VSM) (noise level ~10^{-7} Am^2). Saturation magnetization (M_s), saturation remanent magnetization (M_{rs}) and coercivity (B_c) were derived from these measurements. Backfield remanence curve for remanent coercivity (B_{cr}) was subsequently measured.

First Order Reversal Curves (FORC) (Pike et al., 1999; Roberts et al., 2000) were also measured for 101 samples spaced every ~0.5-1 m, with a 1 T saturating field at low resolution (Hb: -50 to +50 mT; Hc: 0 to 120 mT; averaging time: 200 ms; field increment: 5 mT; slew rate limit: 1 T/s; number of FORCs: 58). These low-resolution FORC measurements allow a quick overview of the dominant magnetic mineral assemblage of the samples. Nine selected samples were measured at very high resolution (Hb: -15 to +15 mT; Hc: 0 to + 150 mT; averaging time: 100 ms; field increment: 0.5 mT; slew rate limit: 1 T/s; number of FORCs: 383) in order to check the occurrence of biogenic magnetite that cannot be identified with low-resolution measurements (Egli et al., 2010). FORC diagrams were processed by using the software FORCInel (Harrison and Feinberg, 2008).

Low-temperature magnetic measurements (down to 5 K) were made with a Quantum Design Magnetic Properties Measurements System (MPMS) (noise level ~$10^{-10}$$Am^2$) for 38 selected samples covering the entire studied interval. IRM acquisition at room temperature (300 K) was first measured in 20 mT steps up to a maximum field of 5 T. A 300-5-300 K cooling-warming cycle of the IRM was then measured in a zero magnetic field (trapped field <20 μT). After cooling again to 5 K in zero-field conditions, the applied field was increased to 2.5 T to impart a low-temperature saturation IRM (LT-SIRM). The sample was then warmed to room temperature in a zero magnetic field while measuring the magnetization; the resulting LT-SIRM warming curve is referred to as the ZFC curve, for Zero Field Cooled. The sample was subsequently cooled again to 5 K, this time in a continuous 2.5 T magnetic field. The resulting FC (Field Cooled) LT-SIRM was then similarly measured during warming to 300 K.

8.3.2. Bulk-geochemical analyses

Carbonate measurements by coulometry were carried out at the CMCR on 84 selected discrete (not cube) samples on which rock magnetic measurements were formerly done. The samples were previously oven-dried at 50 °C overnight before carbonate measurements. Carbonate content was determined by acidifying 5 mg of dry and powdered bulk sediments with 10% phosphoric acid and by measuring the CO_2 evolved (assuming to be entirely derived from $CaCO_3$) using a UIC Inc. CM5012 CO_2 coulometer.

Bulk-organic geochemical characteristics of the investigated deep-sea sediments were determined at Christian-Albrechts-University. All sediments were oven-dried at 50 °C overnight and ground to a homogeneous powder using agate pestle and mortar. Subsequently, the total carbon (TC), total nitrogen (TN) and total sulfur (TS) contents were determined on ~10 mg of sediment material using a Vario EL III elemental analyzer. About 200 mg of each sediment was analyzed on an ELTRA CS-580A system for its total organic carbon (TOC) content. Prior to this measurement, the powdered samples were treated with 10 % and subsequently 25 % of hydrochloric acid solution (until no reaction) to remove inorganic carbon minerals. The amount of total inorganic carbon (TIC) as well as the $CaCO_3$ content was calculated as follows:

$$TIC\ (wt\%) = TC - TOC \quad (1)$$

$$CaCO_3\ (wt\%) = TIC \times 8.33 \quad (2)$$

where 8.33 is the stoichiometric factor for C in $CaCO_3$.

X-ray fluorescence (XRF) measurements on 20 bulk dry powder samples (every 5 m) were carried out with a Spectris Co. Ltd. XRF-P MagiXPro spectrometer at the CMCR. No pre-treatment (e.g. acid leaching) was performed on the samples prior to measurement. XRF measurements were performed in order to assess the detrital input and the provenance of the magnetic particles. The $CaCO_3$ content (presumably entirely from marine origin) is high (up to 60 wt%; Tamura et al., 2015b) and thus influences the Ca content measured by XRF. In the absence of prior acid leaching procedures, a correction on Ca content measured by XRF ($Ca_{XRFmeasured}$) from coulometry-based Ca content (Ca_{coulo}) has been applied. Hereafter, the XRF results are discussed after Ca correction (Table 8.S3, Figs. 8.11 and 8.S12):

$$Ca_{XRFcorr} = Ca_{XRFmeasured} - Ca_{coulo} \quad (3)$$

8.3.3. Time series analysis

Time series analysis has been applied to datasets of Natural Gamma Ray (NGR) counts (Tamura et al., 2015b), magnetic susceptibility and saturation remanence (M_{rs} measured from the hysteresis analysis, this study), adopted to the age model developed for Site U1437. Prior to the time series analysis, high-resolution data were linearly interpolated to obtain an even-scaled data set. Long-term trends present in the data were removed by low-frequency band-pass filtering.

Even-scaled and detrended data sets were subjected to spectral analysis using the multi-taper method (MTM) (Thomson, 1982) as implemented in the KSpectra toolkit V3.4.1. (Ghil et al.,

2002). MTM was applied with the number of tapers set to 3 and a bandwidth parameter of 2. Confidence levels were calculated using the red-noise modeling method after Mann and Lees (1996). Statistically significant spectral components were extracted from the data series by application of a Taner band-pass filtering.

8.4. Age model

At Site U1437 a robust multiproxy age model was built by combining off- and onshore data derived from magnetostratigraphy, calcareous nannofossil biostratigraphy and stratigraphy from stable oxygen isotope ($\delta^{18}O$) measurements on planktonic foraminiferal shells.

Magnetostratigraphy at Site U1437 was determined on board ship by measurement of remanent magnetization of archive section halves after 30 mT demagnetization, supplemented by similar demagnetization and measurement of discrete samples taken as 7 cm^3 cubes. Within the upper 120 mbsf which is the subject of this study, two magnetostratigraphic datums were identified: the Brunhes/Matuyama (C1n/C1r) boundary at 89.85 mbsf and the top of C1r.1n (Jaramillo Subchron) at 119.35 mbsf (Fig. 8.2; Table 8.S1).

A total of 80 samples have been analyzed for their calcareous nannofossil content in order to identify the bioevents occurring in the studied interval (Fig. 8.2). At least 500 specimens were counted in each sample, and they were identified at species level following the taxonomy reported in Young et al. (2014). Four bioevents were recognized allowing some refinement of the position to which they were originally assigned on the basis of the shipboard data (Table 8.S1 for details). The base (B) of *Emiliania huxleyi*, top (T) of *Pseudoemiliania lacunosa* and top common (Tc) occurrence of *Reticulofenestra asanoi* are assigned within a ~3 m range due to low sampling resolution in the intervals in which they occur (Fig. 8.2; Table 8.S1).

The $\delta^{18}O$ data measured on the shell of the planktonic foraminifera *Neogloboquadrina dutertrei* are from Mleneck-Vautravers (2018), who provided a high-resolution database analyzing 198 samples within the upper 122 mbsf of Site U1437.

The age model for Site U1437 was constructed by inserting magnetostratigraphic datums, bioevents and $\delta^{18}O$ data into AnalySeries software (Paillard et al., 1996) which allows a graphical comparison between the measured planktonic foraminiferal isotope curve and the standard $\delta^{18}O$ curve of LR04 (Lisiecki and Raymo, 2005). The bioevents and magnetostratigraphic datums represent the age control points used as reference for the calibration of the isotope curve. The reference ages for both magnetostratigraphic datums and calcareous nannofossil bioevents are from Gradstein et al. (2012).

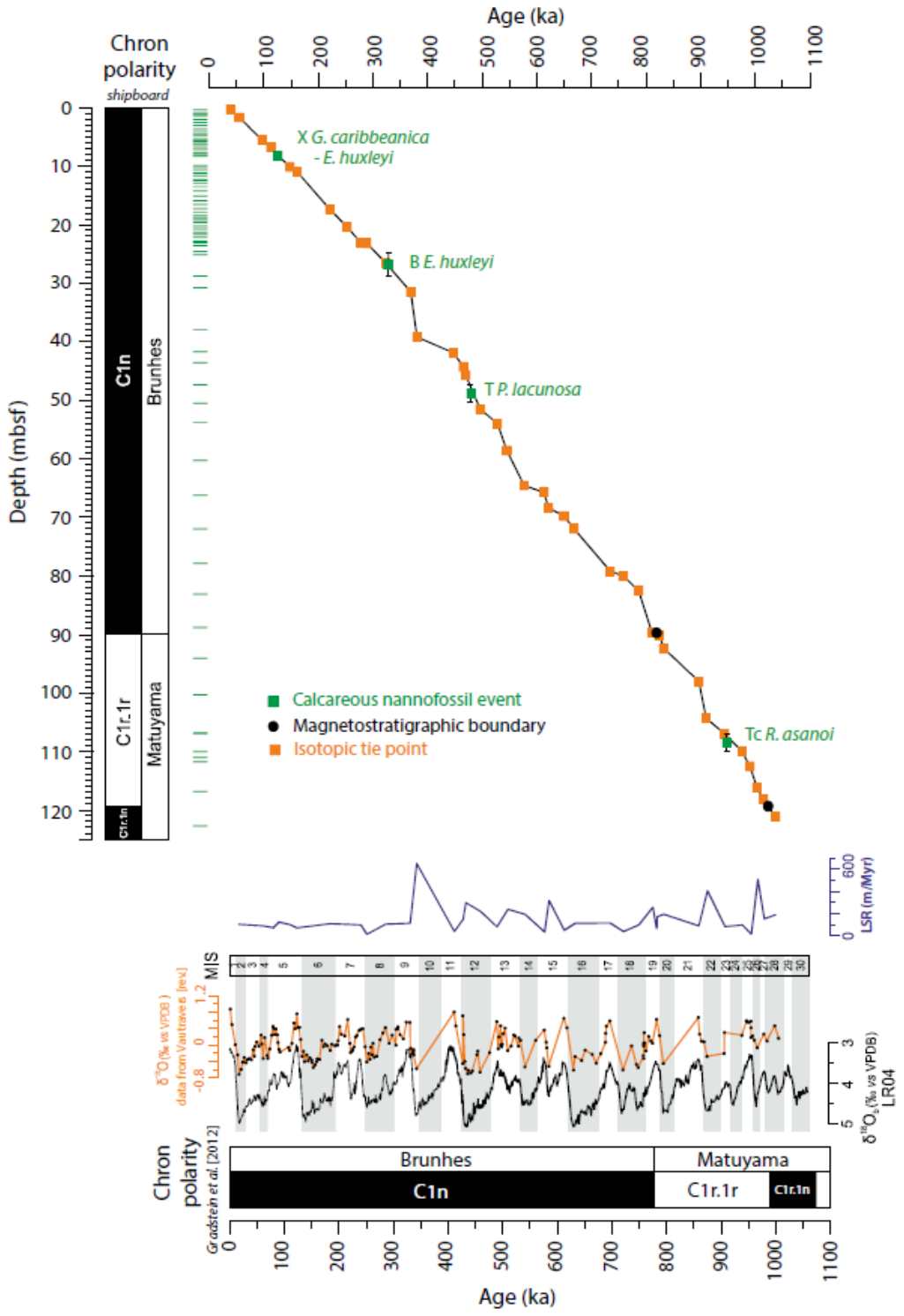

Figure 8.2 | Multiproxy age model at Site U1437, constructed by combining magnetostratigraphic datums (black dots), calcareous nannofossil bioevents (green squares) and stable oxygen isotope ($\delta^{18}O$) data measured on planktonic foraminifera shells (orange squares) from Mleneck-Vautravers (2018). The lower part of the figures shows the isotopic data (orange curve) tuned to the orbitally calibrated LR04 reference stack of Lisiecki and Raymo (2005). The linear sedimentation rate (LSR) curve is expressed in m/Ma (blue curve). Glacial stages are in gray and the marine isotope stages (MIS) are shown. Green bars indicate the location of samples used for calcareous nannofossil analysis.

At Site U1437, the age model was defined by 38 key points identified on the isotope curve together with two magnetostratigraphic datums and the calcareous nannofossil bioevent of

Gephyrocapsa caribbeanica (Fig. 8.2; Table 8.S2). The age of samples between control points was calculated by linear interpolation. The three other bioevents with a larger error in depth were not directly included in the age calculation, but they agree very well with the final age model as their error bars fall on the interpolation line (Fig. 8.2).

The age model for Site U1437 used in this study shows a continuous sedimentary succession spanning marine isotope stage (MIS) 1 to MIS 28, thus the last ~1 Ma. The linear sedimentation rate during a MIS is very variable through the studied sequence, from a minimum of 20 m/Ma to a maximum of 650 m/Ma, with the highest sedimentation rates related to intervals with frequent ash layers representing episodes of more intense volcanic activity at ~350, 870 and 980 ka (Fig. 8.2).When corrected for the occurrence of ash layers, the sedimentation rate varies from ~5 cm/ka (~50 m/Ma in MIS 11) to ~30 cm/ka (~300 m/Ma in MIS 27) with an average of ~11 cm/ka (~110 m/Ma), which is close to the shipboard age model (~120 m/Ma, Tamura et al., 2015b). The mean sampling resolution for the rock magnetic analysis is ~2.6 ka throughout the entire interval.

8.5. Results

8.5.1. Magnetic mineral concentration

NRM, magnetic susceptibility χ_{lf} and SIRM are widely used as first order proxies for magnetic mineral concentration. Measurements on cube samples show that NRM varies downcore with a sawtooth pattern alternating between lower and higher values ranging from ~5.8×10^{-6} to ~2.6×10^{-4} Am^2/kg (Fig. 8.3a). ARM generally mimics the variations of the NRM, and the magnitude of the ARM signal is less than twice that of the NRM (Fig. 8.3a), suggesting a coarse-grained magnetic mineral assemblage of pseudo-single domain (PSD) and multidomain (MD) grains. χ_{lf} and SIRM on cube samples also correlate with the NRM, with values ranging from ~12 to ~153×10^{-8} m^3/kg and ~1.6×10^{-3} to ~2×10^{-2} Am^2/kg, respectively (Fig. 8.3b and c).

The magnetic susceptibility χ_{lf}, measured on all samples, varies from ~0.23 to ~278×10^{-8} m^3/kg (Fig. 8.S1a). However, the magnetic susceptibility depends on many factors, particularly on dilution by the carbonate matrix. Shipboard (Tamura et al., 2015b) and onshore (this study) coulometry measurements show that the carbonate content of the samples can be up to 60 %, indicating that a dilution effect cannot be ruled out a priori. In order to highlight the changes in magnetic mineral concentration, it is thus necessary to determine and correct for the carbonate dilution effect. The corrected magnetic susceptibility χ_{lfcorr} is calculated according to:

$\chi_{lfcorr} = \chi_{lf} / (1 - CaCO_3\,\%)$, where χ_{lf} represents a proxy for the magnetic mineral concentration. It appears that the pattern of the corrected magnetic susceptibility is similar to the non-corrected magnetic susceptibility (Figs. 8.8 and 8.S1a). Therefore, the observed sawtooth variations of the magnetic susceptibility (and of the other rock magnetic parameters) are unlikely due to a dilution effect by the carbonate matrix, but rather due to changes in magnetic concentration and/or magnetic mineralogy.

8.5.2. Magnetic mineralogy

Several analyses were carried out in order to identify the magnetic mineralogy of the samples. The $S_{-0.3T}$ displays high values ranging between 0.94 and 0.98, suggesting a higher contribution of low coercivity minerals such as magnetite to the remanence (Fig. 8.3e). The lower range of $S_{-0.3T}$ values could represent a larger contribution of high coercivity minerals (e.g., hematite or goethite). In order to confirm this, L-ratio and HIRM were investigated. The L-ratio is independent of the HIRM, indicating that changes in HIRM as a function of depth/age are mainly controlled by fluctuations in the overall concentration of high coercivity minerals, rather than by simple changes in the relative proportions of high and low coercivity minerals (Fig. 8.S2).

Non-oriented samples were measured for hysteresis properties in order to characterize their grain size and coercivity. The hysteresis loops (Figs. 8.4a and 8.S3) are open at low applied magnetic field which suggests a mixed magnetic assemblage with grain sizes ranging between single domain (SD) and multidomain (MD) (Tauxe et al., 1996, 2002). The samples are not saturated because of a significant paramagnetic component likely to be due to the presence of clays. Indeed, samples are mudstones with significant clay content as indicated by X-ray diffraction analysis (Musgrave et al., 2019) and relatively high NGR values (Tamura et al., 2015b). After the paramagnetic slope correction (saturation is assumed above 70 % of H_{max} = 1 T), the loops show saturation from ~500 mT. The IRM acquisition curves up to 4 T show that the samples reach saturation at ~600 mT, probably indicating a mixture of both low (dominant) and high coercivity minerals (Fig. 8.S4).

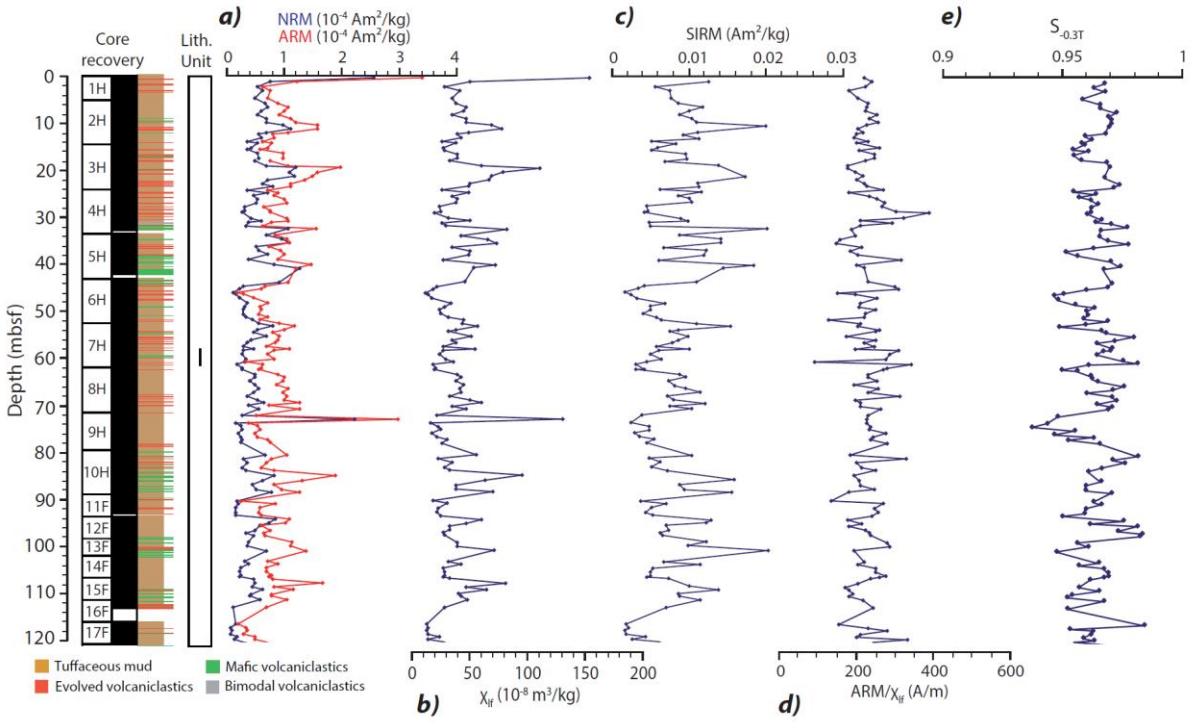

Figure 8.3 | Evolution of a) natural remanent magnetization (NRM) and anhysteretic remanent magnetization (ARM), b) magnetic susceptibility χ_{lf}, c) saturation isothermal remanent magnetization (SIRM), d) ARM/χ_{lf} and e) $S_{-0.3T}$ as a function of depth in meters below sea floor (mbsf) in Hole U1437B for the oriented samples. Core recovery and lithology from Tamura et al. (2015b) are also indicated.

The hysteresis parameters, M_{rs}/M_s, B_c, B_{cr}, fluctuate around mean values of 0.2, 17 mT and 44 mT, respectively (Fig. 8.5). The hysteresis properties are consistent downcore with no major changes. This is supported by FORC diagrams that show mean B_c values ranging between ~15 and 20 mT, indicating the presence of a low coercivity mineral, such as magnetite or titanomagnetite (Roberts et al., 2000), and a long tail toward higher B_c values >100 mT (Figs. 8.4b and 8.S5). The general contours of the FORCs are close to a triangular-like shape suggesting a PSD-MD sized grain population (e.g., Roberts et al., 2000; Muxworthy and Dunlop, 2002). The negative distribution in the lower left corner suggests the presence of fine-grained particles (SD to fine-grained PSD) (Fig. 8.4b).

Low temperature behavior of the remanence confirms the dominant presence of (Ti)-magnetite in the samples by the occurrence of a very well developed Verwey transition at temperature (T_V) of ~110-120 K on the ZFC, FC and RT-SIRM curves (Muxworthy and McClelland, 2000; Figs. 8.4c, d and 8.S6). During the warming of RT-SIRM, the remanence is not fully recovered through the Verwey transition suggesting that (Ti)-magnetite is rather coarse-grained from PSD to MD. Oxidation and maghemitization (e.g., Özdemir and Dunlop, 2010; Chang et al., 2013) are unlikely to occur as the observed Verwey transition occurs in the range of the theoretical value for unoxidized stoichiometric magnetite.

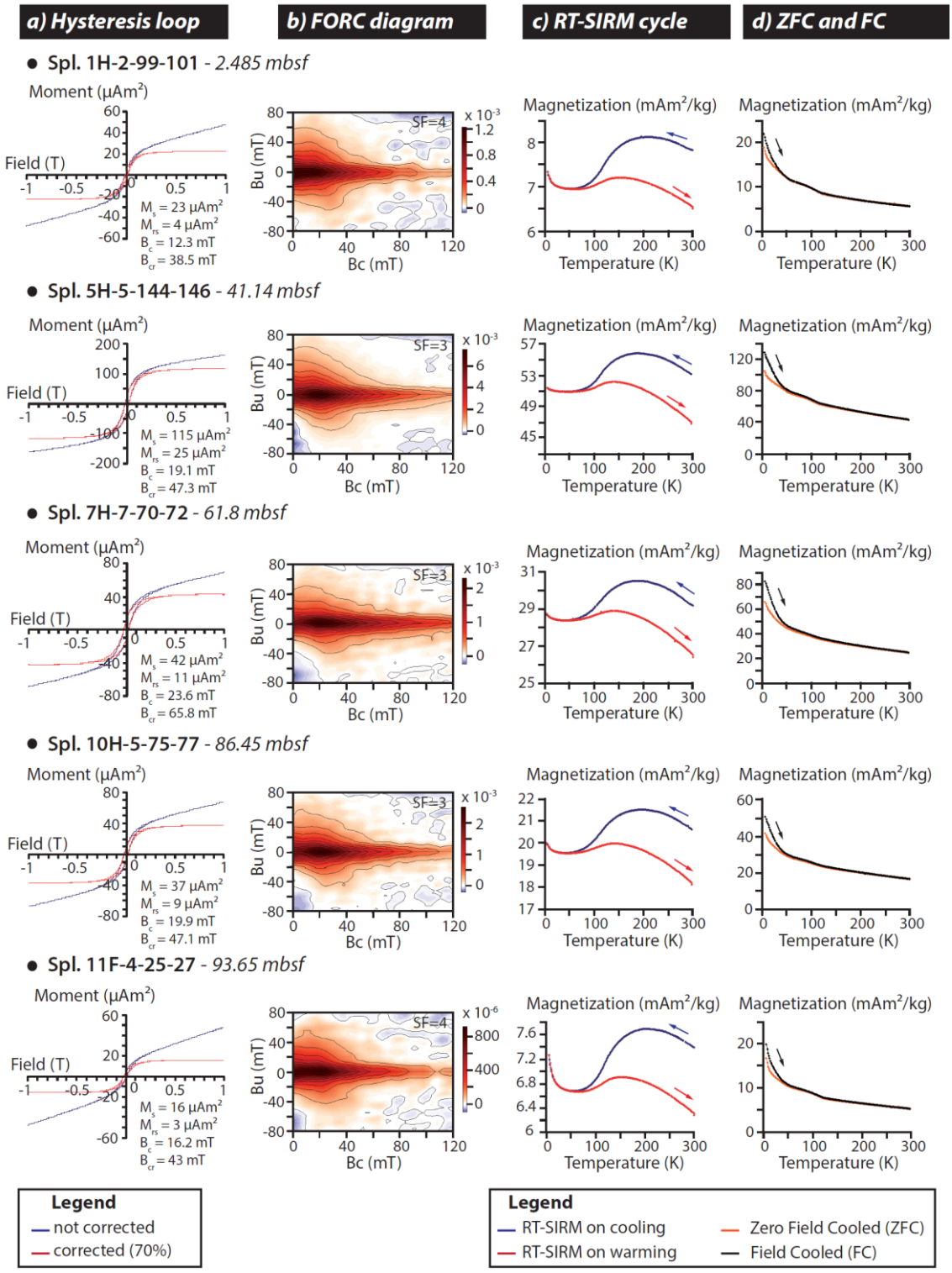

Figure 8.4 | Representative rock magnetic results for a) hysteresis loops before (blue) and after (red) paramagnetic slope correction (saturation is assumed above 70 % of H_{max}=1T), b) FORC diagrams (SF is the smoothing factor), c) RT-SIRM on warming and cooling, and d) ZFC and FC. The rock magnetic measurements indicate (Ti-) magnetite as the dominant magnetic phase.

There is however no strong evidence of the higher coercivity phase likely to be hematite or goethite. The typical increase of RT-SIRM on cooling for goethite is not observed (Dekkers, 1989; Guyodo et al., 2006; Kars et al., 2015). This is not surprising as it has been shown that

very high magnetic fields are sometimes needed to saturate goethite (as well as hematite) at room temperature (Rochette et al., 2005). If hematite occurs in very small size (<0.1 μm), the Morin transition of hematite is lowered from its theoretical temperature at 250 K or is even suppressed (Özdemir et al., 2008). Moreover, hematite (if any) must represent >88 % of the total magnetic assemblage by mass in order to be detected on a FORC diagram (Carvallo et al., 2006).

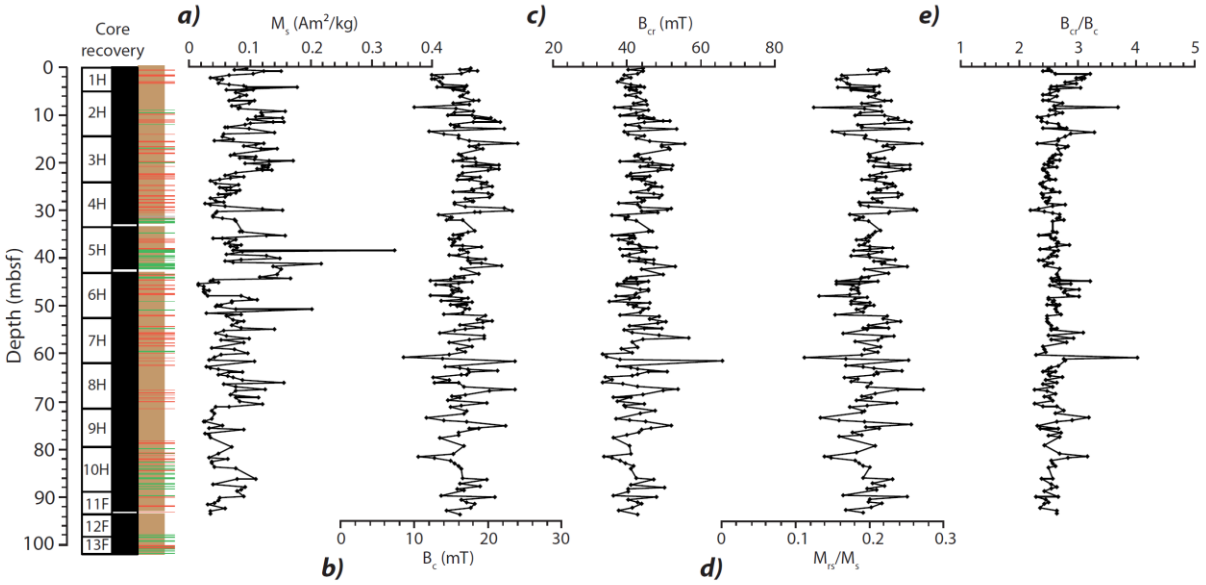

Figure 8.5 | Evolution of the hysteresis properties as a function of depth in Hole U1437B. a) saturation magnetization (M_s), b) coercive field (B_c), c) remanent coercive field (B_{cr}), d) M_{rs}/M_s, e) B_{cr}/B_c. No major changes in the hysteresis properties are observed.

The δ_{FC}/δ_{ZFC} ratio (Moskowitz et al., 1993) is close to 1 suggesting that magnetite is mainly inorganic (detrital). It is however known that biogenic magnetite may be a non-negligible component of the magnetic mineralogy in pelagic sediments in the central (e.g., Yamazaki, 2009), tropical (e.g., Yamazaki and Horiuchi, 2016) and Northwest (e.g., Korff et al., 2016) Pacific Ocean. To test the possibility that biogenic magnetite may be an additional, minor contributor to the magnetic mineralogy, additional high-resolution FORC analyses were conducted. Resulting FORC diagrams (Fig. 8.6 a) reveal the presence of a weak central ridge along the Hc axis representing grains with little or no interaction. This feature is characteristic of biogenic magnetite (magnetofossils) (e.g., Egli et al., 2010). The negative first derivatives of ZFC and FC low temperature warming curves (Fig. 8.6 b) show two shoulders around the temperature of the Verwey transition of magnetite at ~100 K and ~120 K: this feature is most clearly seen in sample U1437B-10H-5, 70-72 cm. Double Verwey peaks of this sort have been reported to result from mixes of biogenic (lower T_V) and detrital (higher T_V) magnetite (Chang

et al., 2016a), although other mechanisms (populations with bimodal Ti contents, for example) are possible.

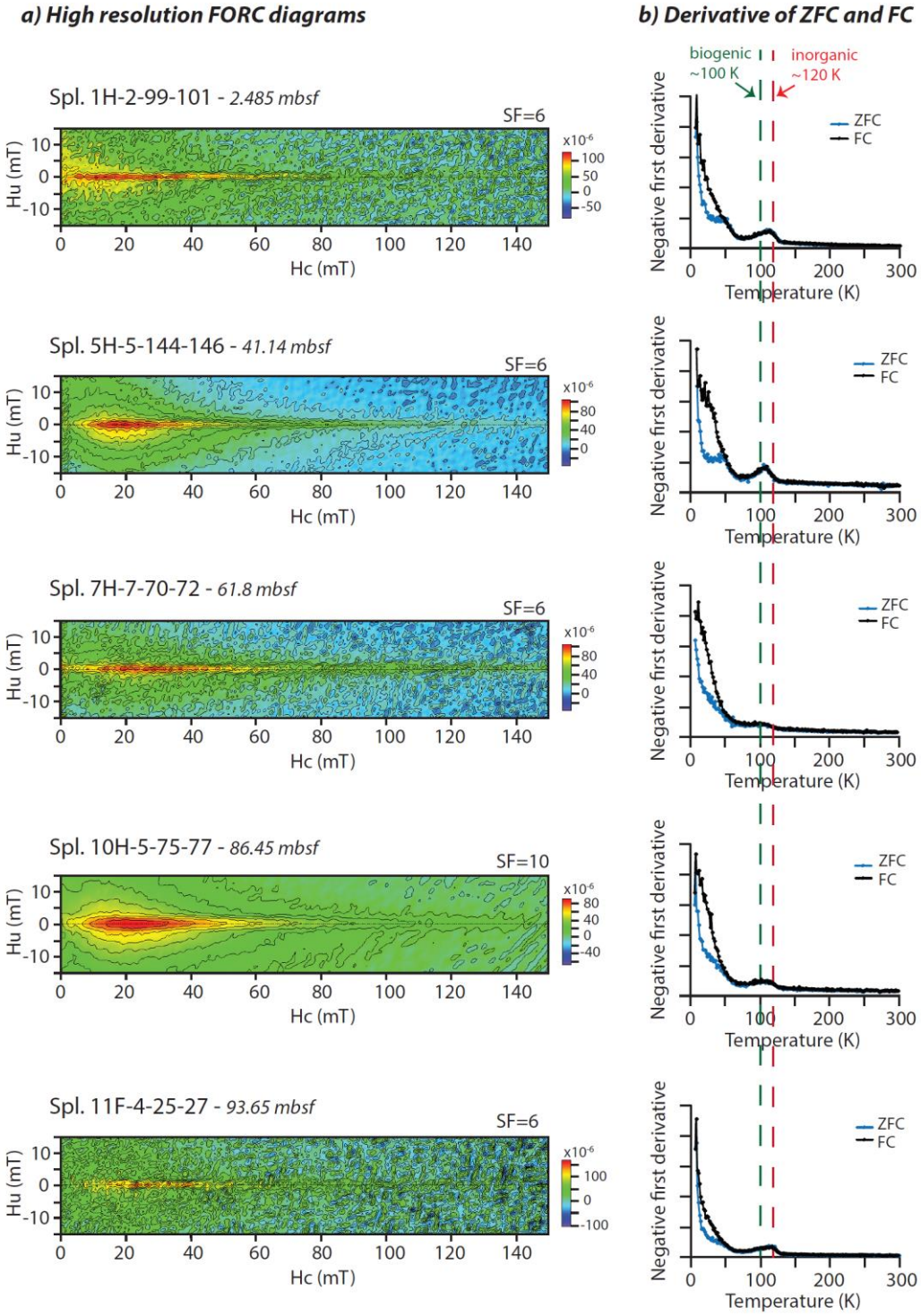

Figure 8.6 | a) High-resolution FORC diagrams for samples presented in Fig. 8.4 showing a central ridge suggesting the presence of magnetofossils (biogenic magnetite), b) negative first derivative of the ZFC and FC curves (shown in Fig. 8.4) showing a double Verwey transition temperature indicating the presence of both biogenic and detrital magnetite.

Definitive identification of biogenic magnetite in magnetosome chains requires magnetic extraction and TEM observations that are beyond the scope of this paper. Although inferred to be present in the studied samples, SD magnetofossils are unlikely to be the dominant magnetic phase. The χ_{ARM}/SIRM ratio (where χ_{ARM} is the susceptibility of ARM) is low (<50 μA/m) supporting the inference from the hysteresis, RT-SIRM cycling and δ_{FC}/δ_{ZFC} ratio studies that relatively coarse-grained, PSD to MD terrigenous magnetic minerals rather than fine-grained biogenic magnetite dominate the magnetic mineralogy (e.g., Yamazaki and Horiuchi, 2016).
In addition to the iron oxides magnetite and hematite, magnetic iron sulfides are a likely contributor to the overall magnetic mineralogy. Musgrave and Kars (2016) reported the occurrence of authigenic greigite in shallow sediments based on rock magnetic analyses, visual description of samples and SEM observations. Greigite lacks a crystallographic transition, and has coercivity in the ferrimagnetic range, making distinction from magnetite on the basis of low-temperature and hysteresis studies difficult (Roberts et al., 2011). Diagenetic greigite likely occurs in superparamagnetic (SP) to SD sizes as a low coercivity phase in the overall magnetic mineral assemblage.

8.5.3. Grain size of the magnetic minerals

Grain size variations can be approximated by the ratio ARM/χ_{lf} by assuming that the magnetic mineralogy is mainly magnetite. Indeed, ARM is sensitive to magnetite or in a broader sense to low coercivity magnetic minerals, because the maximum alternating field applied in the laboratory is limited to 80 mT. ARM/χ_{lf} shows variations from ~90 to ~390 A/m, oscillating around a mean value of ~250 A/m (Fig. 8.3d), and suggests alternations between finer (higher ARM/χ_{lf}) and coarser (lower ARM/χ_{lf}) magnetic assemblage. The hysteresis ratios, M_{rs}/M_s and B_{cr}/B_c, indicate that the magnetic minerals lie in the PSD domain on a Day plot (Fig. 8.S7). This finding is rather common in sediments (e.g., Roberts et al., 2012) and confirms the previous observations that (Ti)-magnetite is overall coarse-grained (probably a mixture of SD, PSD and MD grains) (Dunlop and Özdemir, 2007). SEM observations and EDS analyses conducted on two samples confirm the occurrence of >5 μm Ti-magnetite grains (Fig. 8.S8).
The SIRM difference at 5 K between ZFC and FC measurements could be an indicator of ferrimagnet grains in the size range of nanoparticles. The difference ranges between 10 and 20 % which may suggest a small amount of SP grains, typically with sizes ≪20-30 nm for magnetite. Nevertheless, this difference might be due to other factors, such as the presence of (much coarser) multidomain grains, and the best way to assess the presence of SP particles is to investigate the frequency dependence of the magnetic susceptibility.

χ_{fd} % (= 100 × (χ_{lf} - χ_{hf})/χ_{lf}) varies from 0.2 % to 10 %, suggesting that SP particles may be present (Fig. 8.S1 b) (Bowles et al., 2009). Frequency dependence of magnetic susceptibility at higher frequency, $\chi_{F1 - F3}$ % (= 100 × (χ_{F1} - χ_{F3})/χ_{F1}) presents higher values from 2 % to 25 %, further supporting the presence of SP particles (Fig. 8.S1 b). Altogether, the results above suggest the dominant presence of SD to MD (Ti)-magnetite grains through the studied interval with varying (and less) amount of SP particles.

8.5.4. Time series analysis

The time series analysis of NGR counts, χ_{lf} and M_{rs} confirms the presence of a significant periodicity. In all the datasets, statistically significant spectral peaks exceeding the 90 % confidence level occur at frequencies of ~0.010 and 0.028 cycles/ka as well as in the frequency range from 0.035 to 0.050 cycles/ka. These frequencies can be attributed to short eccentricity (~100 ka), obliquity (~40 ka) and precession (19-23 ka) periods (Fig. 8.7).

8.6. Discussion

Magnetic mineral concentration appears to be the principal control on fluctuations of the magnetic parameters χ_{lf} and M_{rs}. Indices dependent on the magnetic mineralogy do not change greatly through the studied sequence, but rather suggest a relatively uniform magnetic mineralogy composed of low coercivity Ti-magnetite as the dominant magnetic mineral, a component of higher coercivity that could be hematite or goethite, and greigite as an accessory mineral. Grain size variations tracked by ARM/χ_{lf} do occur, but these are not correlated with the magnetic concentration parameters (Fig. 8.3).

Variations in the relative abundance of the different magnetic minerals could be attributed to factors such as different provenance of the magnetic particles, climatically driven environmental changes and/or variations in diagenetic processes. In the following, these aspects are investigated in order to better understand the evolution of the rock magnetic properties and mineralogy in the upper Pleistocene sediments of the Izu rear arc.

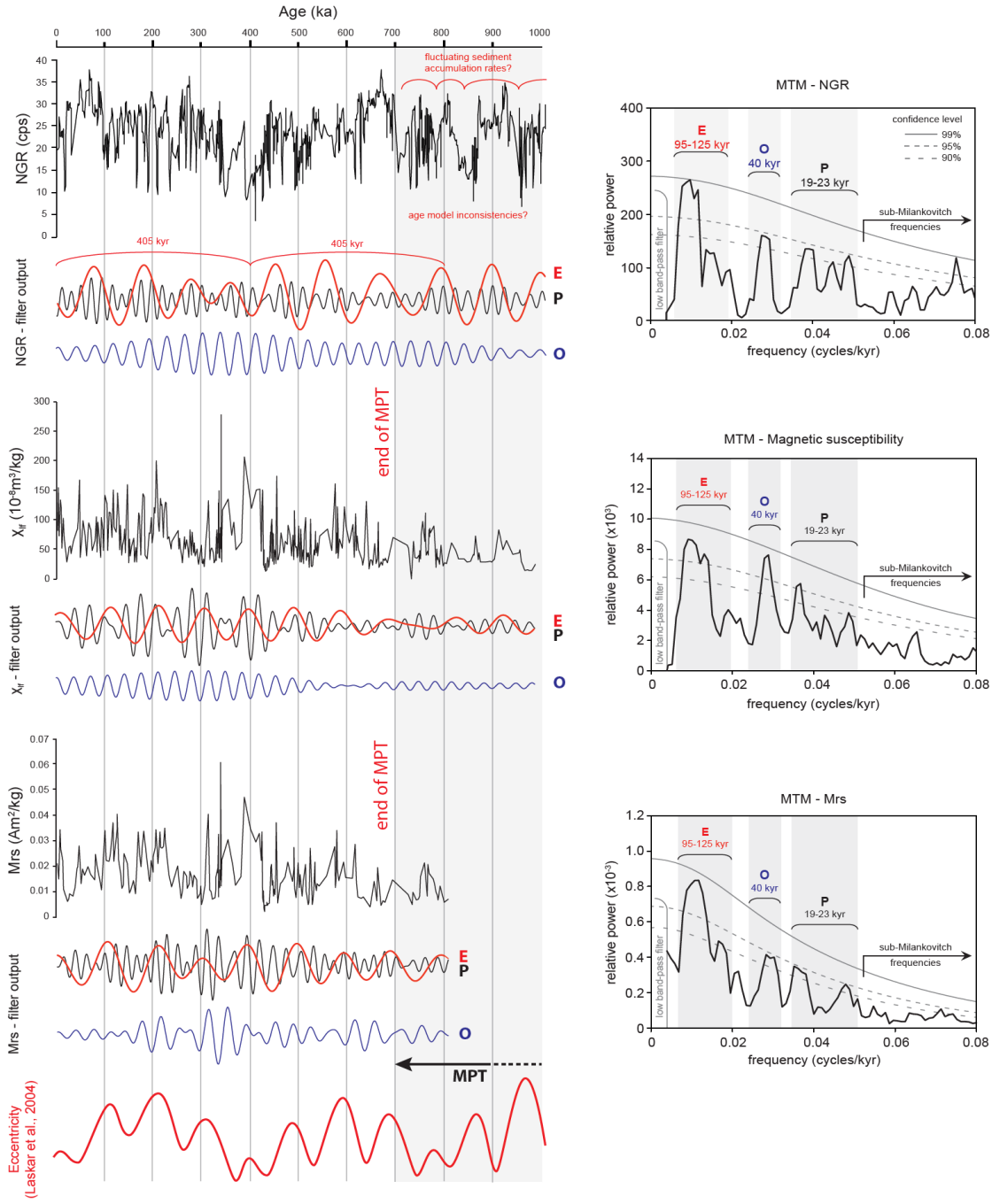

Figure 8.7 | Time series analysis on Natural Gamma Ray (NGR) data averaged every 5 points (from Tamura et al., 2015b), magnetic susceptibility χ_{lf} and saturation remanent magnetization M_{rs} (this study, measured on non-oriented samples). Note the dominance of the 100-ka eccentricity cycle in all data sets. A 180° phase shift is observed between NGR and χ_{lf}. The cyclicity is less obvious during the Mid-Pleistocene Transition (MPT), likely as a result of lower core recovery.

8.6.1. Magnetic signal and global climate change

Global climate change is thought to be driven in part by astronomically forced insolation changes, as a result of variations in Earth's orbital motions. In cyclostratigraphy, variations of magnetic mineral concentrations are used to detect orbitally driven global climate change at

millennial timescales, i.e. the Milankovitch cycles. On Figs. 8.8 and 8.S10, magnetic susceptibility χ_{lf} and SIRM display roughly similar variations with respect to time.

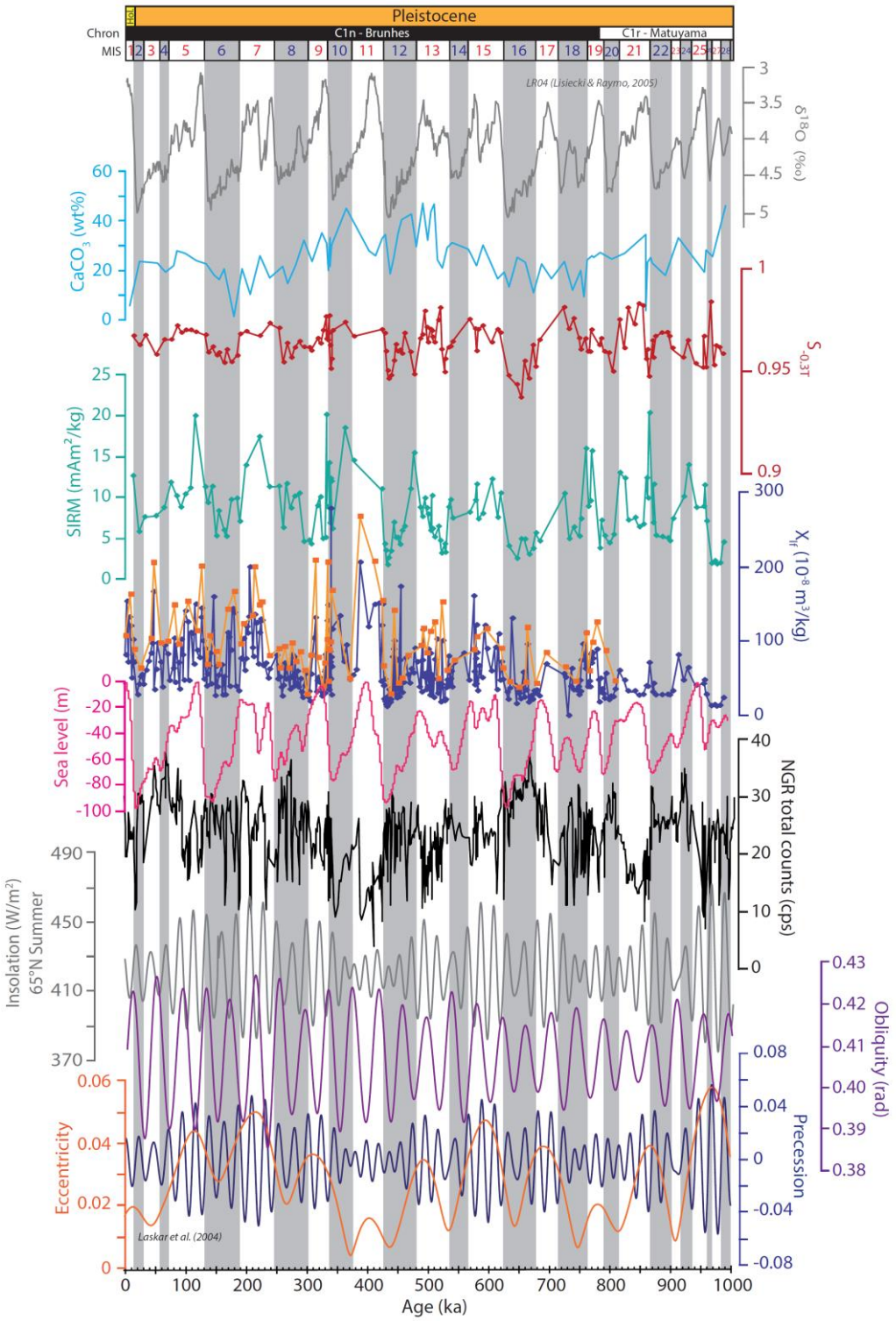

Figure 8.8 | Evolution of selected parameters as a function of time. $\delta^{18}O$ data are from Lisiecki and Raymo (2005) (gray). Carbonate measurements are from Tamura et al. (2015b). $S_{-0.3T}$, SIRM (measured on cube samples) and χ_{lf} (non-corrected values in blue, corrected values by carbonate content in orange) are from this study. Sea level fluctuations are from Rohling et al. (2014). Natural Gamma Ray (NGR) counts are averaged every 5 data points (data from Tamura et al. (2015b)). Orbital parameters (insolation, precession, obliquity and eccentricity) are from Laskar et al. (2004). Marine isotope stages (MIS) and magnetic chrons are indicated and glacial stages are shaded in gray.

Generally, higher SIRM values occur in interglacials and the magnetic susceptibility declines after each interglacial, with the exception of MIS 9. This suggests that there is an increasing proportion of magnetic particles deposited during the interglacials. Furthermore, the magnetic susceptibility variations seem to be correlated with sea level fluctuations over the last 1 Ma (Fig. 8.8). Higher magnetic particle abundances seem to occur during sea level high stands, although the trend is not very clear during the Mid-Pleistocene Transition (i.e. before 700 ka). The magnetic susceptibility appears anticorrelated with the NGR counts, i.e. high susceptibility corresponds to low NGR in the interglacials (Fig. 8.8).

Time series analysis on NGR data confirms a strong orbital forcing that is dominated by short eccentricity periods (Fig. 8.7). Obliquity and precession periods are present as well, whereby amplitudes of the precession are modulated by short eccentricity cycles. Moreover, the excellent match of the short eccentricity cycles extracted from the data with the theoretical astronomical model (Laskar et al., 2004) support the age model developed for Site U1437. However, inconsistencies between the age model and the astronomical model are apparent. Before 700 ka, fluctuations in the sediment accumulation rate may have impacted on the periodicity expressed in the data. Long eccentricity periods (405 ka) might be present as well, but could not be confirmed by time series analysis due to the detrending procedure applied to the data. Moreover, detection of those periods is also prohibited by the short time span of ~1000 ka investigated in this study.

Milankovitch periods are also expressed in the χ_{lf} and M_{rs} data sets. The short eccentricity component (~100 ka) is well expressed in both data. Obliquity and precession are significant in the χ_{lf} data and less marked in M_{rs} data. The anticorrelation of NGR counts and magnetic susceptibility is also evident from time series analysis. Maxima in NGR correspond to minima in χ_{lf} and M_{rs}, indicating a ~180° phase shift between both proxies (Fig. 8.7). Results from time series analysis attest to a strong impact of Milankovitch-driven climate and sea level changes on the mineralogy at the study site.

Although variations in magnetic concentration are the main response to climate cyclicity, the composition of the magnetic assemblage composition varies with time. $S_{-0.3T}$ and HIRM are generally lower in the glacials and L-ratio higher, except for MIS 18 and MIS 10 (Fig. 8.9). As discussed above, the changes in $S_{-0.3T}$ reflect variations in the proportion of higher coercivity magnetic minerals (hematite and goethite) in the ferrimagnetic assemblage. The lower $S_{-0.3T}$ values during the glacials suggest a proportionally increased contribution of higher coercivity minerals to the remanence. HIRM is lower during the glacials because the overall magnetic

mineral concentration is lower. It does not reflect a proportionally lower contribution of higher coercivity minerals, because L-ratio is higher during the glacials.

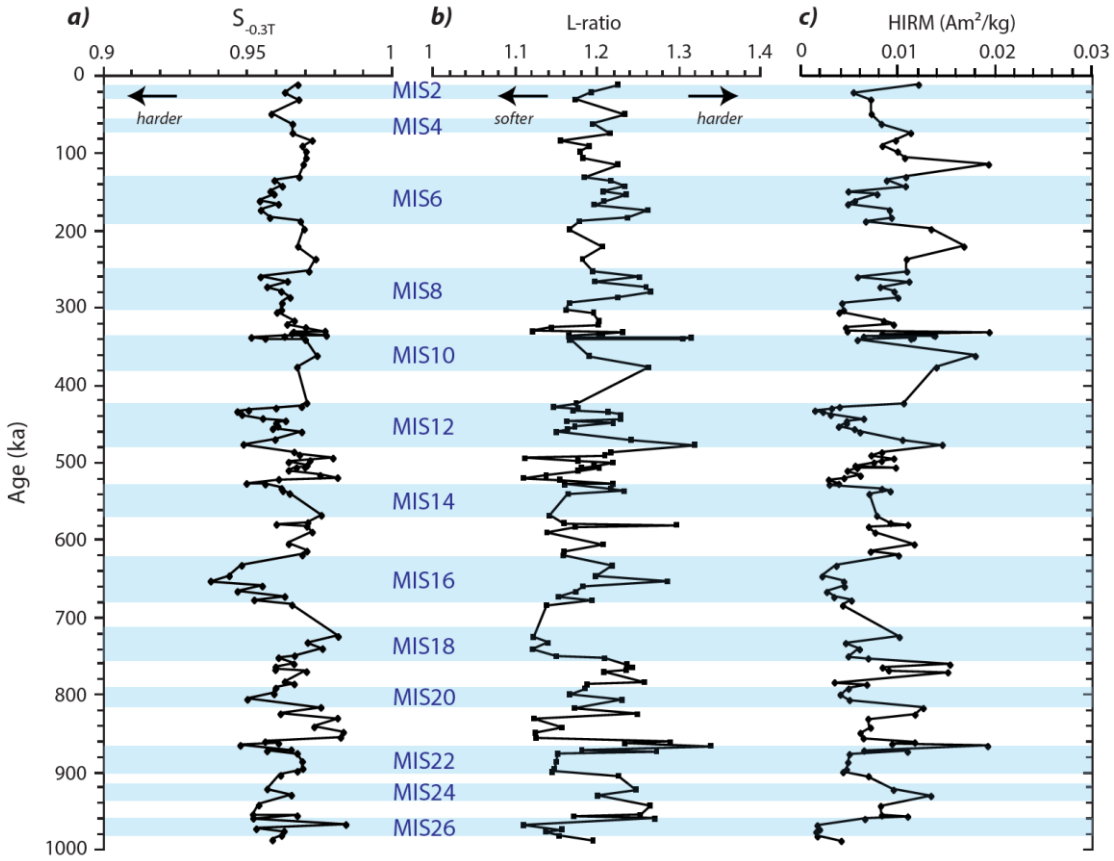

Figure 8.9 | a) $S_{-0.3T}$, b) L-ratio and c) HIRM values as a function of time. Glacial stages are shaded in blue.

To highlight these observations, a detailed and quantitative rock magnetic study was performed on two glacial/interglacial transitions, MIS 6/5 (8.5-16 mbsf; ~95-171 ka) and MIS 16/15 (66-76 mbsf; ~579-663 ka), characterized by marked changes in the rock magnetic parameters especially $S_{-0.3T}$ (Fig. 8.10).

For quantifying the changes in magnetic mineral concentration and for sake of clarity, a simple magnetic mineral assemblage composed only of (Ti)-magnetite grains is considered, as (Ti)-magnetite is the dominant magnetic phase identified in the Izu rear arc sediments. The low-temperature rock magnetic measurements performed on samples covering the transitions MIS 6/5 and MIS 16/15 show that there is an increase of the magnetic mineral content in the interglacials (Fig. 8.10a and b).

The maximum (Ti)-magnetite content c was calculated according to: $c = \text{RT-SIRM}_{300K} / M_{SD}$ where M_{SD} (= 10 Am^2/kg) is the saturation remanence for soft SD magnetite, the highest value for the iron oxides (Maher and Thompson, 1999). PSD-MD and titanium-rich magnetite grains

present lower saturation remanence. Therefore, the concentration discussed in the following is a minimum estimate, the actual concentration is more likely higher.

At the end of the glacials, the minimum magnetite content varies from 0.11 to 0.24 % (0.11 ± 0.15 %) and from 0.01 to 0.15 % (0.08 ± 0.04 %) for MIS 6 and MIS 16, respectively. At the onset of the interglacials, minimum magnetite content varies from 0.18 to 0.47 (0.30 ± 0.09 %) and from 0.16 to 0.40 % (0.21 ± 0.08) for MIS 5 and MIS 15, respectively.

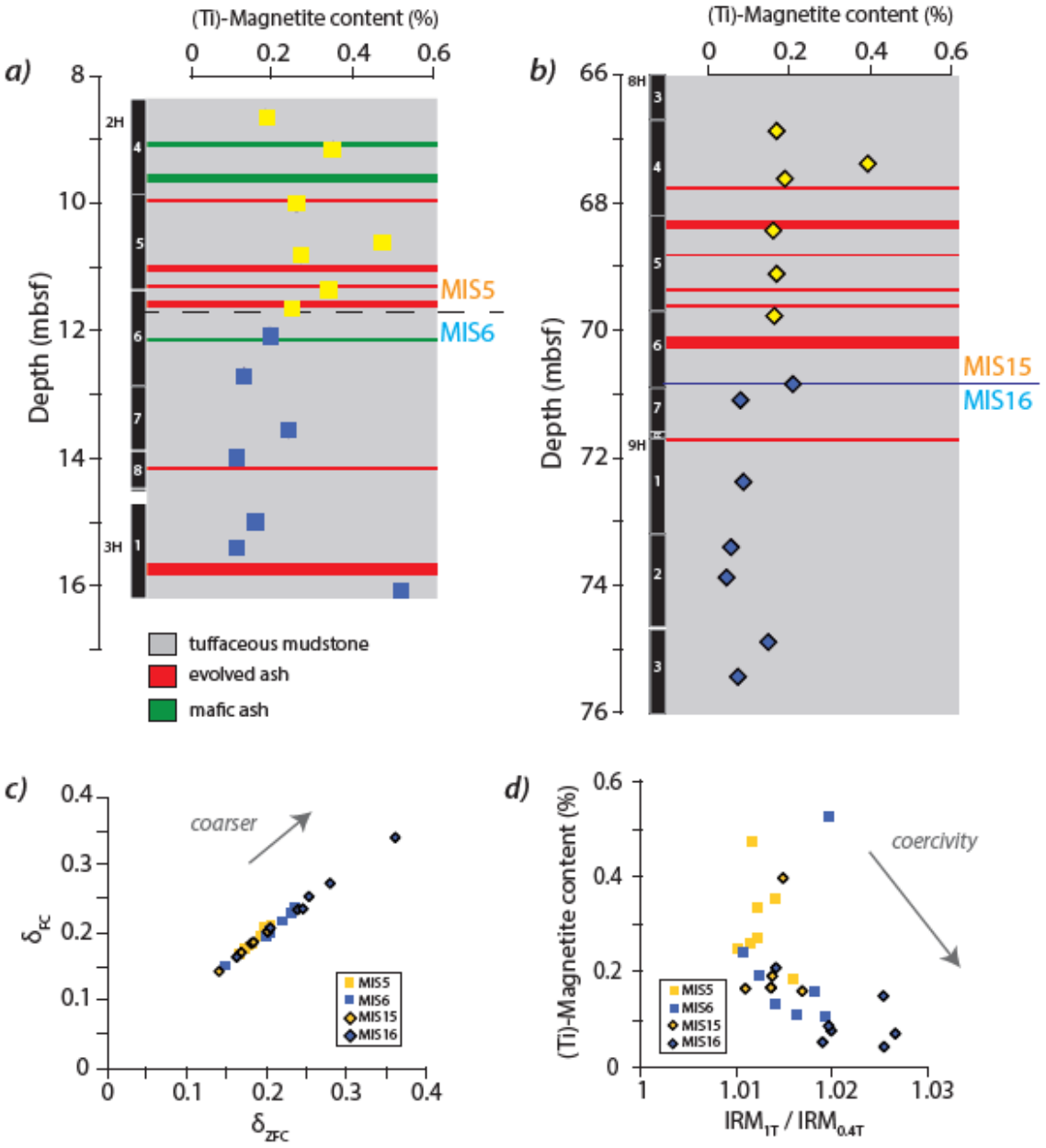

Figure 8.10 | Detailed rock magnetic study for two selected glacial/interglacial transitions. (Ti)-magnetite content as a function of depth for the a) MIS 16/15 and b) MIS 6/5 transitions, c) δ_{FC} *vs.* δ_{ZFC}, and d) (Ti)-magnetite content *vs.* $IRM_{1T}/IRM_{0.4T}$ (proxy for coercivity) measured on the same aliquot for the MIS 16/15 and MIS 6/5 specimens. Squares and diamonds represent the analyzed specimens for the MIS 6/5 and MIS 16/15 transitions, respectively. (Ti-)magnetite content is higher during the interglacials. Particles are coarser and of higher coercivity during the glacials.

These results strongly suggest a higher concentration of magnetic particles during the interglacials especially for the MIS 16/15 transition. A volcanic origin of at least a part of the magnetic particles deposited cannot be excluded, as numerous tephra layers are present in the studied interglacials. When investigating δ_{FC} and δ_{ZFC}, parameters that characterize the amplitude of the Verwey transition of magnetite on FC and ZFC curves (Moskowitz et al., 1993), the samples can be divided into two groups: interglacial *vs.* glacial (Fig. 8.10c). The glacial samples present higher δ_{FC} and δ_{ZFC} values compared to the interglacial samples. This suggests a diagnostic rock magnetic signature between glacial and interglacial stages, which may indicate different origins of the magnetite grains (continental *vs*. volcanic). Magnetic minerals of lower coercivity are more abundant during interglacials whereas during the glacials, magnetic minerals are less abundant and with relatively higher coercivity (Fig. 8.10d). The detailed magnetic measurements at MIS 6/5 and MIS 16/15 transitions (Fig. 8.10) confirm the overall trend observed throughout the studied interval and support a climatically driven change of rock magnetic properties and mineralogy, at least over the last 1 Ma.

Because Site U1437 is located in the NW Pacific Ocean, close to Asia, changes in magnetic mineralogy probably reflect different origins of the magnetic minerals. In fact, the studied area is subject to a monsoonal regime and thus likely records the monsoon changes via eolian dust composition of sediments (Rea, 1994). For the last 0.8 Ma, the magnetic susceptibility record of the Chinese loess correlates with the benthic $\delta^{18}O$ record at orbital scales and is dominated by the 100-ka cycle (eccentricity). The intervals of high magnetic susceptibility correspond to warm humid interglacials and intervals of low susceptibility to cooler dryer glacials (Bloemendal et al., 1995). A similar magnetic susceptibility trend is observed in the Quaternary SW Japanese eolian deposits (Kimura et al., 2001), where dust from Asia formed massive deposits during colder climate intervals (Miyazaki et al., 2016). Very similar findings are observed in this study (Figs. 8.8 and 8.S10). However, as marine and terrestrial environments are subject to different post-depositional and diagenetic processes, no further comparison can be made.

The periodicity of the East Asian summer monsoon (EASM) is controlled by Northern Hemisphere ice volume but not by Northern Hemisphere summer insolation (e.g., Bloemendal et al., 1995; Nie et al., 2008). Increasing Northern Hemisphere high latitude ice cover results in an intensification of the high-pressure cell over the Himalayas during the winter and enhanced Asian winter trade wind circulation, with reduced winter precipitation (e.g., deMenocal and Rind, 1993). During glacial stages, aridity increased in Asia (Hovan et al., 1991; Sun and An, 2005) leading to an increase of eolian dust particles. Such particles could contain fine-grained

high coercivity magnetic minerals such as hematite and goethite that are constituents of Chinese loess/paleosols (Liu et al., 2007b). These particles could be supplied by westerly winds (stronger in the glacials) particularly to sediments of the Pacific Ocean (Yamazaki and Ioka, 1997; Rea et al., 1998) and thus in the Izu arc area. That would explain the lower $S_{-0.3T}$, i.e. increased higher coercivity mineral contribution during the glacials at Site U1437.

The rock magnetic trends during the MPT (>700 ka), especially in $S_{-0.3T}$, seem less pronounced. For instance, MIS 18 and MIS 22 present higher $S_{-0.3T}$ values compared to the previous interglacial stages MIS 19 and MIS 23, respectively (Fig. 8.9). This might be explained by the weakening of the East Asian winter monsoon while global ice volume was increasing (e.g., Heslop et al., 2002), thereby reducing dust particles supply from the mainland of China.

8.6.2. Paleoproductivity and water mass properties

The reduced values of magnetic susceptibility, ARM and SIRM during the glacials, and the matching reduction in $S_{-0.3T}$ that suggest lower concentrations of magnetic minerals, could alternatively be explained by preferential dissolution of magnetite. Recently, Korff et al. (2016) showed a cyclic dissolution of magnetite in Pleistocene sediments of the abyssal NW Pacific Ocean. They suggested that during glacial stages (MIS 22, 12, 10, 8, 6 and 2), magnetite in sediments is removed as a result of changes in redox conditions because of the creep of bottom water sourced from the oxygen-depleted Antarctic Bottom Water (AABW). These new redox conditions would have preserved organic matter and reduced biogenic and detrital magnetite, leading to the decrease of the rock magnetic concentration parameters. The lower $S_{-0.3T}$ during glacial times has been attributed to the fact that hematite is less sensitive to reductive dissolution than magnetite (e.g., Yamazaki et al., 2003). The rock magnetic properties at Site U1437 show the same overall variations as in the NW Pacific sediments studied by Korff et al. (2016).

The bulk organic-geochemical analyses on the MIS 6/5 and MIS 16/15 transitions (Fig. 8.11), where the changes in magnetic mineralogy are well marked and documented, allow of the possible dissolution effect to be more clearly identified.

At Site U1437, the TOC content is generally higher during glacial stages MIS 16 and 6 (average 0.59 and 0.67 wt%, respectively) and lower during the following interglacial periods MIS 15 and 5 (0.46 and 0.43 wt%, respectively) (Fig. 8.11). The elevated TOC contents in sediments deposited during glacial periods, as also observed by Korff et al. (2016), may indicate either a higher primary productivity, a more efficient export flux of organic carbon to abyssal depths, a change to conditions that facilitate the preservation of organic matter or a combination of these factors (e.g., Calvert et al., 1995; Kao et al., 2006b).

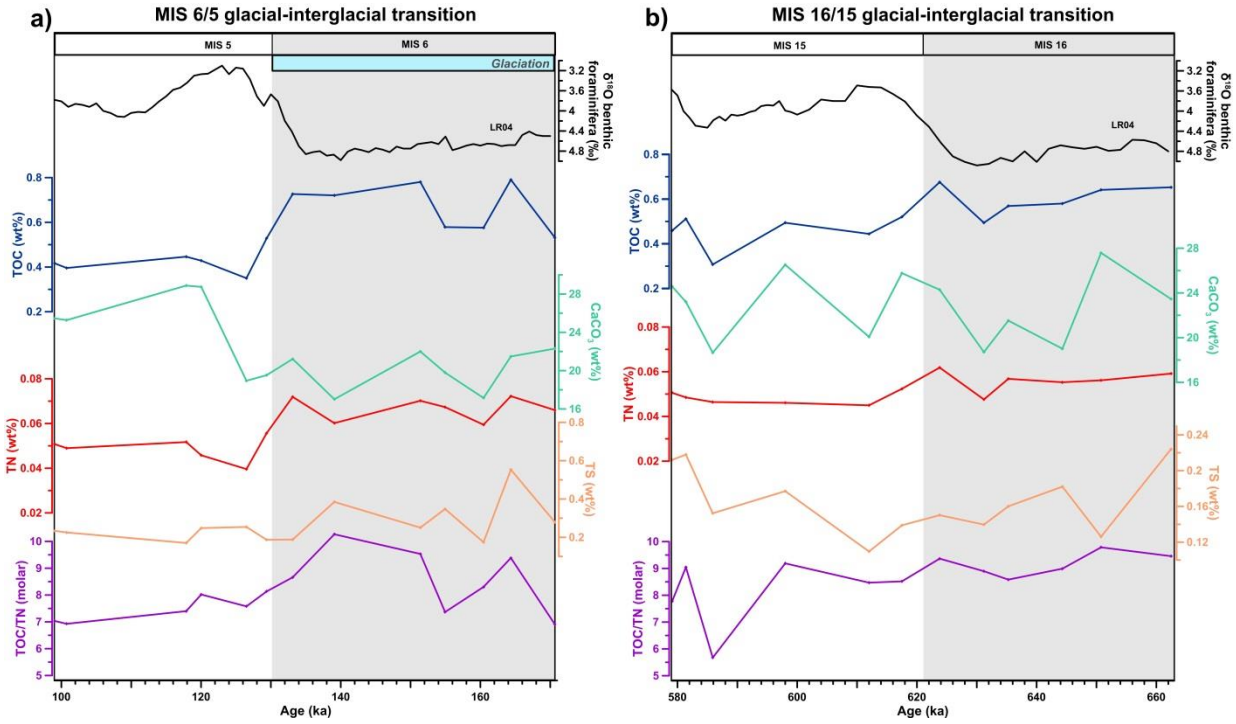

Figure 8.11 | Variations of selected geochemical parameters for MIS 6/5 and MIS 16/15 glacial-interglacial transitions. LR04 $\delta^{18}O$ are reported by Lisiecki and Raymo (2005). TOC: total organic carbon; $CaCO_3$: carbonate content; TN: total nitrogen; TS: total sulfur. TOC/TN ratios are provided on a molar basis.

The more organic matter is produced in and exported from the photic zone to greater depth, the more can be both respirated and buried in sediments. An enhanced primary productivity and higher export flux during glacials may be explained by an increased input of terrigenous dust particles from Asia as reported by Serno et al. (2014). However, several authors argued that primary productivity in the NW Pacific off central Japan (Yasudomi et al., 2014) as well as the export flux of carbon in subarctic regions of the NW Pacific (e.g., Jaccard et al., 2010) were at their maximum during interglacial phases based on radiolarian assemblages, Ba/Al ratios and biogenic opal contents. Furthermore, Korff et al. (2016) found that organic carbon accumulation within sediments in the open central NW Pacific and bioproductivity were decoupled during glacial periods and concluded that elevated sedimentary TOC contents during cold stages were rather a result of an enhanced and accelerated export flux from the surface ocean to greater depth and minimum benthic carbon degradation efficiency instead of being due to higher productivity.

Molar TOC/TN ratios, which allow an identification of sources of organic matter (Meyers, 1994), range from 6.9 to 10.3 during the MIS 6/5 transition and from 5.7 to 9.8 during the MIS 16/15 transition with higher values observed during glacial periods (Fig. 8.11). Organic matter from marine algae typically has TOC/TN ratios ranging from 4 to 10, while terrestrial organic matter has values >20 (Meyers, 1994). As to be expected, the TOC/TN ratios at Site U1437

point to a predominantly marine origin for the organic matter. The slightly higher values of ~10 during MIS 6 are still within the range commonly observed for organic matter of an aquatic source, but may also be associated with an elevated dust supply from arid regions in inner Asia bringing terrestrial organic material to Site U1437, and/or result from more exposed continental shelf areas due to a lower sea level. Another possible explanation for the slightly higher glacial TOC/TN ratios would be aquatic primary production under nitrogen-limited conditions (Healey, 1978). For the MIS 16/15 transition, however, this distinct pattern in TOC/TN is less apparent. A similar observation as for MIS 6/5 at Site U1437 has also been made for the transition from the last deglaciation to the Holocene in the southern Okinawa Trough (Kao et al., 2005). These authors attributed an observed decrease in TOC/TN ratios to enhanced production caused by upwelling induced by the intensification of the Kuroshio Current during the post-glacial period. However, Site U1437 is located in an open oceanographic setting and there is no evidence for increased upwelling during warm periods in the study area. Instead, one could expect upwelling when winter monsoonal winds are stronger, i.e. during glacials as observed in the northeastern South China Sea (Sadatzki et al., 2015).

A number of carbonate preservation proxies (Mleneck-Vautravers, 2018) demonstrate that carbonate dissolution is always higher during the interglacials despite the fact that $CaCO_3$ contents for the two selected G-I transitions (Fig. 8.11) seem to show the opposite. The latter is more likely due to the proximity of Site U1437 to terrigenous sediment sources, elevated fluxes of terrestrial dust from inner Asia may have diluted the $CaCO_3$ content during glacial periods, independently of their preservation status. During glacials, increased fluxes of organic matter to the deep sea may have promoted oxygen consumption in the deeper water masses, which would have affected the magnetic mineral assemblage as discussed below.

Although the rock magnetic properties and TOC content develop in the same way during the glacial periods as described by Korff et al. (2016), the location and oceanographic setting of Site U1437 differ from those of the above study. Indeed, Site U1437 is shallower (2116 mbsl against 4000-5000 mbsl), and presumably affected by AAIW and not by AABW. AAIW formation seems to have been enhanced during glacial periods as a result of reduced formation of the North Atlantic Deep Water (NADW) and cooling of high latitude Southern Hemisphere oceanic areas (Muratli et al., 2010). Thus, the AAIW was well oxygenated during the glacials, while findings by Korff et al. (2016) suggest oxygen-depleted AABW-sourced bottom water during the glaciations to explain rock magnetic observations and magnetite dissolution at their study sites in the Northwest Pacific Ocean. Nevertheless, based on the results presented here, the oxygen-depleted water mass hypothesis cannot be ruled out completely. Because TOC

content is higher during glacial periods, oxygenation might have decreased and reducing biogeochemical reactions might have occurred leading to partial dissolution of (Ti)-magnetite.

8.6.3. Effect of magnetic diagenesis

In anoxic marine sediments, at shallow depth (few cm to few m) detrital iron (oxyhydr)oxide minerals undergo a series of transformations and alterations via a number of geochemical processes to eventually form paramagnetic iron sulfides (pyrite FeS_2) (see review by Roberts, 2015; and references therein). These phenomena, which mainly occur in the sulfate-methane transition zone (SMTZ), are expressed by drastic changes in magnetic properties and mineralogy and may have an impact on the paleomagnetic record (e.g., Karlin, 1990; Leslie et al., 1990a, 1990b). In this study, the first 120 m of Hole U1437B are investigated. This depth interval corresponds to a zone that is subject to early diagenetic processes as a result of microbial activity (Tamura et al., 2015b). Sulfate reduction occurs at Site U1437, as shown by the presence of diagenetic pyrite (Fig. 8.S8; Musgrave and Kars, 2016). Unlike many studies in anoxic environments that show a decrease of the magnetic susceptibility and remanence related to the dissolution of detrital iron oxides (e.g., Kasten et al., 1998; Garming et al., 2005; Riedinger et al., 2005) in the SMTZ, there is no such dramatic change observed in the shallow (27-83 mbsf) SMTZ of Hole U1437B (Figs. 8.3 and 8.S9).

However, this does not mean that diagenesis has had no impact on rock magnetic properties at Site U1437. A recent study by Chang et al. (2016b) on sediments from the NW Pacific Ocean spanning the last 60 ka shows that non-steady-state diagenesis modulated by the Asian monsoon induced changes in the magnetic properties and mineralogy. Site U1437 results resemble findings from Chang et al. (2016b) in the following ways: 1) hysteresis loops (Figs. 8.4 and 8.S3), FORC diagrams (Figs. 8.4 and 8.S5), low temperature magnetic measurements (Figs. 8.4 and 8.S6) are similar in the two studies (see Fig. 8.4 of Chang et al., 2016b); 2) SD to MD (Ti)-magnetite is dominant in both studies; 3) magnetic mineral concentration proxies (e.g., M_s, M_{rs}) seem to anticorrelate with magnetic hardness (B_c) and TOC and TS (Fig. 8.S11). In other words, intervals with higher magnetic mineral content and correspondingly stronger magnetization are dominated by low coercivity minerals and lower TOC and pyrite contents (assuming that TS is an estimate for the iron sulfide content). This latter correlation, however, is not as well marked as in the study of Chang et al. (2016b). This is likely explained by: 1) a lower TOC content at Site U1437 (~0.5 wt% in average *vs*. 0.5-2.1 wt% with an average of ~1.2 wt%), 2) a lower sedimentation rate (~5-30 cm/ka (~12 cm/ka average) at Site U1437 *vs*. ~10-100 cm/ka), 3) different water masses (warm Kuroshio and AAIW *vs*. cold Oyashio and NPIW). Combined,

these factors appear to have led to a reduced influence of fluctuations in diagenesis on the rock magnetic properties of Site U1437. The difference between the present study and that of Chang et al. (2016b) is the implications of the rock magnetic results for the environmental and climatic record. Whereas Chang et al. (2016b) found that diagenesis is weakened during cold Asian monsoon periods (low TOC, low TS) leading to higher magnetized intervals, this study suggests the opposite with higher TOC and lower magnetic mineral concentration during the glacial stages (Figs. 8.8 and 8.11), similar to the findings of Korff et al. (2016). This implies that postdepositional diagenetic processes at the site investigated by Chang et al. (2016b) and Site U1437 are not governed by the same mechanism. However, the time interval spanned by these two studies is different: the last 60 ka (Chang et al., 2016b) *vs*. the last 1000 ka (this study). The time resolution is lower at Site U1437 and it might be possible that at the glacial/interglacial scale, diagenesis appears stronger in the glacials whereas at the stadial scale, diagenesis appears stronger in warmer episodes. Alternatively, the difference between the two studies may simply reflect different terrigenous sources, organic matter supply and water mass properties.

At Site U1437, the dissolution (reduction) of detrital coarse-grained (Ti)-magnetite is apparently limited for at least the first 120 m of Hole U1437B favoring the preservation of the primary magnetization (Musgrave and Kars, 2016). There is no direct evidence from the rock magnetic studies reported in the present study for fine-grained (Ti)-magnetite hosted as inclusion in larger silicate minerals, identified by Chang et al. (2016c) as a possible carrier of primary magnetization in intervals of strong diagenetic alteration. Future magnetic extraction and transmission electron microscope analyses on extracts are needed to carefully check for the presence of inclusions.

Intervals of “ghost polarity” intervals, i.e., normal polarity intervals in the reverse Matuyama Chron, were identified below 90 mbsf in Hole U1437B, and are likely to have resulted from alteration of detrital ferromagnetic iron oxides (Ti-magnetite) into greigite (Musgrave and Kars, 2016). Lesser reducing redox conditions may have occurred at Site U1437 favoring the formation and preservation of at least some greigite (Fe_3S_4) rather than complete reduction into pyrite (Kao et al., 2004). Unlike pyrite that is paramagnetic and does not carry a remanence, greigite is ferrimagnetic and carries a secondary magnetization that can overprint the primary magnetization.

8.6.4. Origin of the magnetic minerals

Hereafter, the XRF data collected in this study are compared to the ones at ODP leg 185 Site 1149 (31°20.5 ´N, 143°21.1 ´E) located about 100 km east of the Izu Bonin trench (Plank

et al., 2000), for which a wealth of information on the origin of sediments and ashes is available. Scudder et al. (2014) proposed four end-member sources that explain the bulk sediment composition: 1) Chinese loess (eolian), 2) rhyolitic ash from the Honshu arc, 3) mafic ash from the Izu-Bonin frontal arc, 4) a second eolian dust component including "Upper Continent Crust". The possible sediment sources at Site U1437 are tentatively discussed based on comparison with those of Site 1149.

SiO_2, the major oxide identified in the studied samples, ranges between ~46 and 72 wt% (Fig. 8.S12): most samples fall close to a mean value of about 61 wt%. The mean SiO_2 content is slightly lower than the SiO_2 content for pelagic clays from Units I and II at Site 1149 (~64 %) (Plank et al., 2007). The SiO_2 content at Site U1437 is also closer to the Chinese loess component (65 %) than to the basaltic component (50 %) described from Site 1149 (Scudder et al., 2014). Al_2O_3 is relatively uniform downcore (~15 wt%) with a minimum value at ~50 mbsf. At the same depth, SiO_2 is at a minimum as well. CaO is relatively high with 30 wt% (Fig. 8.S12). Al_2O_3 values are typical of clay-rich sediments and similar to the Units I and II at Site 1149 (Plank et al., 2007).

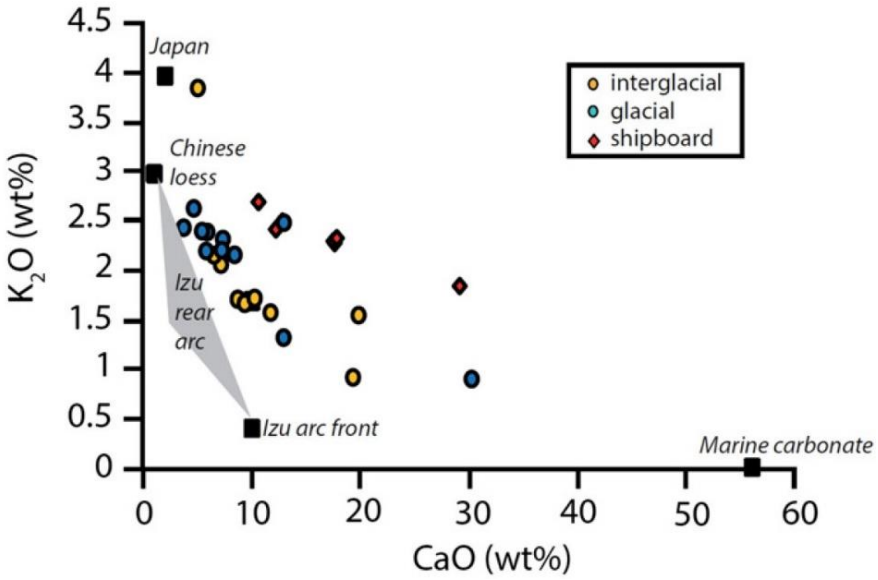

Figure 8.12 | K_2O *vs*. CaO plot (wt%) from XRF measurements. Three possible endmembers are indicated: Japan, Izu arc front and marine carbonate. Average elemental compositions of Izu rear arc (gray zone) and Chinese loess (after acid leaching and loss of ignition) (Chen et al., 2001) are also reported. Note that shipboard data are not corrected for their carbonate content.

The Ti/Al ratio, a proxy for variations in detrital supply, shows a nearly constant value downcore with an average of 0.058, omitting two outliers at 40.5 and 60.4 mbsf that correspond to carbonate-rich and potassium-rich (e.g., ash-bearing) samples, respectively (Fig. 8.S12). This ratio is close to the Ti/Al ratio for Chinese loess (Jahn et al., 2001). Log (Ti/Ca) values vary between -2 and -0.9 showing variable terrigenous input through time. At the resolution of this

study, however, no clear trend of log (Ti/Ca) related to climatic cycles can be established. Onshore XRF studies at much higher resolution are currently ongoing and may help to discriminate a climatic signature in the composition of Site U1437 sediments (E. Bongiolo, J. Gill, S. Straub, *pers. com.* 2016).

The preliminary onboard interpretation suggested that the sedimentation at Site U1437, consisting of hemipelagic clay and carbonate, was punctuated by ash deposition as a result of proximal or distal volcanic events (Tamura et al., 2015b). Onboard portable XRF and ICP-AES (inductively coupled plasma-atomic emission spectroscopy) data showed that the composition of the tuffaceous mudstones is a mixture of at least three end member components: 1) marine carbonate (Morse and Mackenzie, 1990), 2) Izu arc front (e.g., Tamura et al., 2009) and 3) Ryukyu dacite (Scudder et al., 2009), representing a typical volcanic input from the mainland of Japan.

The CaO content varies between ~5 and 31 % and the K_2O content between ~0.6 and 3.6 % in the studied samples (Fig. 8.12). The samples are mainly located in the left side of the plot, suggesting both a terrestrial (e.g., continental Chinese loess) and a volcanic (Izu arc, Japan) origin for the sediments.

This preliminary XRF study and onboard measurements on bulk sediments support mixed origin of the sediments at Site U1437 and therefore also of the magnetic minerals with sources varying between local (e.g., Izu front) and distal (mainland Asia) provenances. Ongoing onshore studies on this topic should help to quantify the contribution of each source in the future.

8.7. Conclusions

The rock magnetic properties and mineralogy of marine sediments recovered during IODP Expedition 350 at Site U1437 in the Izu rear arc are primarily influenced by paleoenvironmental changes over the last 1 Ma. During interglacial periods, an increased terrigenous supply is indicated by higher values of the rock magnetic proxies for magnetic mineral concentration with a magnetic mineralogy dominated by coarse-grained (Ti)-magnetite of detrital and volcanic origin. During glacial periods, the magnetic mineral content is lower and the magnetic mineralogy changes to a magnetic assemblage with a higher contribution of higher coercivity minerals. The latter are likely finer eolian particles of hematite that result from increased aridity in continental Asia. The lower magnetic content in glacial stages likely results from preferential dissolution of (Ti)-magnetite in a less oxygenated water mass and related post-depositional diagenetic processes related to differences in organic matter supply and

sedimentation rates. Therefore, the variations of the mineralogy at Site U1437 are mainly controlled by combined changes in atmospheric and terrigenous inputs, as well as changes in water masses properties (oxygenation) and productivity.

Further mineralogical and geochemical studies are necessary in order to trace for the presence of fine-grained magnetic inclusions in silicate grains and to better characterize the origin of the sediments that are deposited at Site U1437. Improving the age model downcore will be necessary to reliably expand the mineralogical analyses of this study back in time in order to establish rock magnetic trends in sediments older than ~1 Ma and to better constrain changes in the sedimentary regime over the entire MPT.

8.8. Acknowledgements

This research used samples and data provided by the International Ocean Discovery Program (IODP). We would like to thank the IODP staff and shipboard scientists for their help during the sampling party onboard the R/V *JOIDES Resolution* during Expedition 350.

We are thankful to M. Ikehara at Kochi University for providing and supporting instrumental facilities for carbonate measurements, and to E. Kirchhoff at Christian-Albrechts-University for assistance during bulk organic-geochemical analyses.

J. Gill, S. Straub and J. Schindlbeck are thanked for insightful discussions.

We are also grateful to Liao Chang and an anonymous reviewer for their constructive comments that helped to improve the manuscript and to editors Thomas Algeo and Thierry Correge for editorial handlings.

This work was supported by a J-DESC/JAMSTEC IODP Expedition 350 after cruise research fund allocated to M. K. R. M. was supported by funding from the Australian and New Zealand International Ocean Discovery Program Consortium (ANZIC). A.-S. J. was funded through grants BA 3841/6-1 and SCHW 554/27-1 awarded by the German Research Foundation (DFG) to T. B. and L. Schwark, respectively. M. B. is thankful to J. Henderiks and the Paleobiology Program at Uppsala University for providing research and travel funding. M. M-V. received funding for her research through NERC via a post-cruise grant with UK-IODP grant number RG 74950.

This is contribution PMG17-XX from the Center of Advanced Marine Core Research, Kochi University.

8.9. Appendix A. Supplementary data

Supplementary data to this article can be found online at http://dx.doi.org/10.1016/j.palaeo.2017.05.016.

Chapter 8

Supplementary Online Material

Impact of climate change on the magnetic mineral assemblage in marine sediments from Izu rear arc, NW Pacific Ocean, over the last 1 Ma

Myriam Kars[1*], Robert J. Musgrave[2,3], Kazuto Kodama[1], Ann-Sophie Jonas[4], Manuela Bordiga[5], Wolfgang Ruebsam[4], Maryline J. Mleneck-Vautravers[6], and Thorsten Bauersachs[4]

[1] Center for Advanced Marine Core Research, Kochi University, B200 Monobe, Nankoku 783-0004, Japan

[2] School of Geosciences, University of Sydney, Sydney, NSW2006, New South Wales, Australia

[3] Geological Survey of New South Wales, NSW Department of Industry, Maitland, NSW 2320, New South Wales, Australia

[4] Department of Organic Geochemistry, Institute of Geosciences, Christian-Albrechts-University, Ludewig-Meyn-Straße 10, 24118 Kiel, Germany

[5] Department of Earth Sciences, Uppsala University, Villavägen 16, 752 36 Uppsala, Sweden

[6] Department of Earth Sciences, University of Cambridge, Downing Street, Cambridge CB2 3EQ, United Kingdom

In this Supplementary Online Material, we present additional tables and figures showing the age model used in the study, as well as rock magnetic results, SEM observations and geochemical analyses that support the main text.

	This study			Shipboard Scientific Party		Age (ka)
Datum	**Interval (section, cm)**	**Depth interval (mbsf)**	**Average Depth (mbsf)**	**Interval (section, cm)**	**Average Depth (mbsf)**	
X *Gephyrocapsa caribbeanica-Emiliania huxleyi*	2H-3, 120-121		8.065	1H-CC to 2H-CC	9.88	90
B *Emiliania huxleyi*	4H-1, 84-86 to 4H-4, 11-13	25.05-28.82	26.935	2H-CC to 3H-CC	19.51	290
T *Pseudoemiliania lacunosa*	6H-3, 110-112 to 6H-5, 121-123	47.31-50.42	48.865	6H-5, 75-76 to 6H-CC	51.48	440
C1n (base)				11F-1, 65	89.85	781
Tc *Reticulofenestra asanoi*	15F-1, 21-23 to 15F-3, 24-26	107.02-110.05	108.53	15F-3, 80-81 to 15F-CC	111.16	910
C1r.1n (top)				17F-3, 15	119.35	988

Table 8.S1 | Core interval and average depth (in meters below sea floor, mbsf) of the calcareous nannofossil bioevents as identified in this study. The core interval and average depth of bioevents and magnetochron boundaries (underlined) identified by the Shipboard Scientific Party (Tamura et al., 2015a) are reported for comparison. The reference ages for each bioevent and magnetochron are from Gradstein et al. (2012).

Datum Type	Depth (mbsf)	Age (ka)
A	0.025	1
A	1.655	17
A	5.505	61
A	6.845	80
B	8.065	90
A	10.065	110
A	10.965	123
A	17.505	184
A	20.725	216
A	23.01	240
A	23.14	251
A	26.63	285
A	31.61	330

A	39.415	342
A	41.985	411
A	44.345	427
A	45.825	432
A	51.55	458
A	54.02	489
A	58.77	509
A	64.82	541
A	65.93	576
A	68.46	584
A	69.8	612
A	72.02	632
A	79.25	696
A	80.125	720
A	82.78	748
A	89.405	774
C	89.85	781
A	90.02	782
A	92.33	794
A	97.96	858
A	104.42	874
A	107.02	906
A	110.05	938
A	110.26	954
A	116.32	966
A	118.12	978
C	119.35	988
A	121.22	998

Table 8.S2 | Age control points at IODP Site U1437 employed in the age model construction. A: planktonic foraminifera $\delta^{18}O$ event as calibrated through AnalySeries software; B: calcareous nannofossil datum, i.e. cross-over of *Gephyrocapsa caribbeanica* and *Emiliania huxleyi*; C: magnetostratigraphic boundary. Reference ages for nannofossil bioevent and magnetochrons are from Gradstein et al. (2012). $\delta^{18}O$ data are from Mleneck-Vautravers (2018).

Sample name	1H-1-99-101	2H-1-18-20	2H-4-114-116	2H-8-52-54	3H-4-102-104	4H-1-102-104	4H-4-122-124	5H-1-138-140	5H-5-80-82	6H-1-120-122	6H-5-103-105
Raw oxide concentration (wt%)											
SiO2	51.854	54.144	56.357	58.005	50.17	53.833	49.661	52.967	71.252	46.537	46.01
TiO2	0.589	0.616	0.691	0.621	0.568	0.667	0.52	0.609	0.314	0.509	0.565
Al2O3	13.650	13.699	13.781	13.158	12.315	14.433	12.07	13.417	12.675	11.494	12.109
Fe2O3	5.829	5.577	6.204	5.365	4.376	5.425	4.74	5.566	3.056	4.332	4.746
MnO	0.077	0.087	0.13	0.107	0.106	0.085	0.105	0.115	0.088	0.123	0.11
MgO	2.470	2.356	2.232	2.028	1.907	2.484	1.899	2.016	0.874	1.813	2.132
CaO *	7.492	4.968	6.488	4.123	9.752	6.435	7.5	5.505	3.678	10.12	29.857
Na2O	2.689	2.421	2.907	2.876	2.637	2.337	2.432	2.508	4.622	2.303	2.294
K2O	1.482	1.897	1.879	2.348	1.32	2.048	1.347	1.832	2.424	1.042	0.894
P2O5	0.128	0.127	0.137	0.131	0.153	0.124	0.121	0.133	0.063	0.149	0.134
Raw total (wt%)	86.260	85.892	90.806	88.762	83.304	87.871	80.395	84.668	99.046	78.422	98.851
CaCO3 (wt%) (coulometry)	26	26	18	21	32	22	37	28	2	40	4
Normalized oxide concentration (wt%)											
SiO2	60.114	63.037	62.063	65.349	60.225	61.264	61.771	62.558	71.938	59.342	46.545
TiO2	0.683	0.717	0.761	0.700	0.682	0.759	0.647	0.719	0.317	0.649	0.572
Al2O3	15.824	15.949	15.176	14.824	14.783	16.425	15.013	15.847	12.797	14.657	12.250
Fe2O3	6.757	6.493	6.832	6.044	5.253	6.174	5.896	6.574	3.085	5.524	4.801
MnO	0.089	0.101	0.143	0.121	0.127	0.097	0.131	0.136	0.089	0.157	0.111
MgO	2.863	2.743	2.458	2.285	2.289	2.827	2.362	2.381	0.882	2.312	2.157
CaO	8.685	5.784	7.145	4.645	11.707	7.323	9.329	6.502	3.713	12.905	30.204
Na2O	3.117	2.819	3.201	3.240	3.166	2.660	3.025	2.962	4.667	2.937	2.321
K2O	1.718	2.209	2.069	2.645	1.585	2.331	1.675	2.164	2.447	1.329	0.904
P2O5	0.148	0.148	0.151	0.148	0.184	0.141	0.151	0.157	0.064	0.190	0.136
Normalized total (wt%)	100.000	100.000	100.000	100.000	100.000	100.000	100.000	100.000	100.000	100.000	100.000

Continued

Sample name	7H-2-83-85	7H-6-81-83	8H-2-120-122	8H-6-116-118	9H-3-97-99	10H-1-112-114	10H-5-52-54	11F-1-53-55	11F-4-25-27	JA-1 (measured)	JA-1 (reference)
Raw oxide concentration (wt%)											
SiO2	39.752	63.221	59.194	54.116	55.126	55.028	52.498	50.863	53.903	64.983	
TiO2	0.466	0.38	0.571	0.666	0.706	0.651	0.733	0.617	0.695	0.869	
Al2O3	10.133	13.082	13.439	14.586	14.845	13.957	13.78	12.447	14.422	15.412	
Fe2O3	3.868	2.858	4.732	5.462	5.831	6.033	6.96	5.283	6.306	6.951	
MnO	0.147	0.131	0.112	0.108	0.122	0.123	0.139	0.143	0.139	0.157	
MgO	1.613	1.072	1.791	2.427	2.49	2.397	2.428	2.092	2.694	1.525	
CaO *	14	4.653	12.738	7.515	6.508	5.217	20.002	8.664	4.729	5.947	
Na2O	1.769	3.664	3.349	2.503	2.394	2.87	2.757	2.851	2.429	3.852	
K2O	0.669	3.596	2.462	1.941	1.999	2.128	1.574	1.462	2.112	0.778	
P2O5	0.163	0.092	0.128	0.141	0.132	0.132	0.139	0.155	0.123	0.162	
Raw total (wt%)	72.58	92.749	98.516	89.465	90.153	88.536	101.01	84.577	87.552	100.635	
CaCO3 (wt%) (coulometry)	52	14	4	20	19	21	0	29	23		
Normalized oxide concentration (wt%)											
SiO2	54.770	68.164	60.086	60.488	61.147	62.153	51.973	60.138	61.567	64.572	64.413
TiO2	0.642	0.410	0.580	0.744	0.783	0.735	0.726	0.730	0.794	0.863	0.856
Al2O3	13.961	14.105	13.641	16.304	16.466	15.764	13.642	14.717	16.472	15.314	15.325
Fe2O3	5.329	3.081	4.803	6.105	6.468	6.814	6.890	6.246	7.203	6.907	7.119
MnO	0.203	0.141	0.114	0.121	0.135	0.139	0.138	0.169	0.159	0.156	0.158
MgO	2.222	1.156	1.818	2.713	2.762	2.707	2.404	2.473	3.077	1.515	1.581
CaO	19.289	5.017	12.930	8.400	7.219	5.893	19.802	10.244	5.401	5.909	5.739
Na2O	2.437	3.950	3.399	2.798	2.655	3.242	2.729	3.371	2.774	3.828	3.867
K2O	0.922	3.877	2.499	2.170	2.217	2.404	1.558	1.729	2.412	0.773	0.775
P2O5	0.225	0.099	0.130	0.158	0.146	0.149	0.138	0.183	0.140	0.161	0.166
Normalized total (wt%)	100.000	100.000	100.000	100.000	100.000	100.000	100.000	100.000	100.000	99.999	99.999

Table 8.S3 | Normalized XRF measurements for 20 selected samples. XRF measurements on the standard sample JA-1 (far right) were triplicated. Data for JA-1 are average of three measurements. The raw XRF data (top) were obtained at the same time and under the same conditions as the results for JA-1. $CaCO_3$ was estimated using coulometry. Raw CaO* was reduced accordingly ($Ca^* = Ca_{XRFmeasured} - Ca_{coulometry}$)

$CaO^* = CaO_{XRFmeasured} - [CaCO_{3coulometry} \times 56/100]$ where 56/100 is the stoechiometric factor for Ca in $CaCO_3$

The XRF data sum to 100 in order to give results on an anhydrous, carbonate-free basis. Normalized data are used in Figure 8.11 (main text).

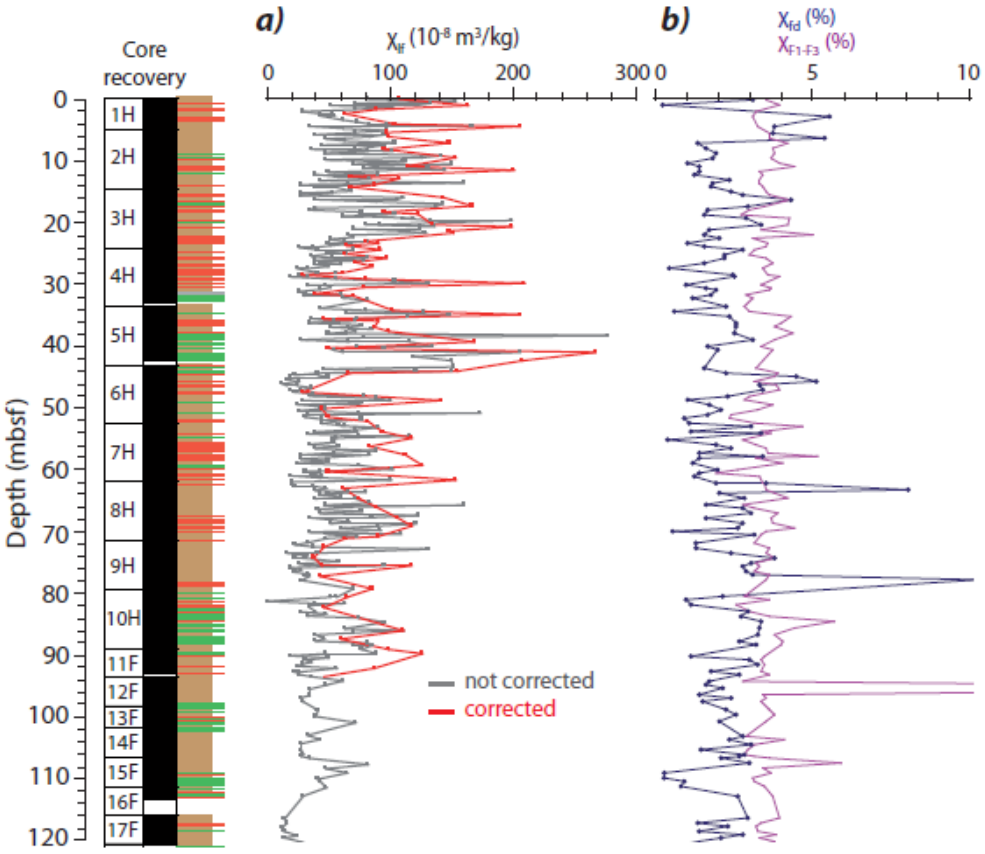

Figure 8.S1 | Evolution as a function of depth of a) the magnetic susceptibility χ_{lf} before (gray) and after (orange) correction by the carbonate content. b) $\chi_{fd\%}$ and $\chi_{F1\text{-}F3}$ used for checking the frequency dependence of the susceptibility (proxies for nanoparticles). Note that the magnetic susceptibility χ_{lf} before and after correction by the carbonate content show the same pattern; then the fluctuations of χ_{lf} are not a result of a dilution effect by the carbonate matrix.

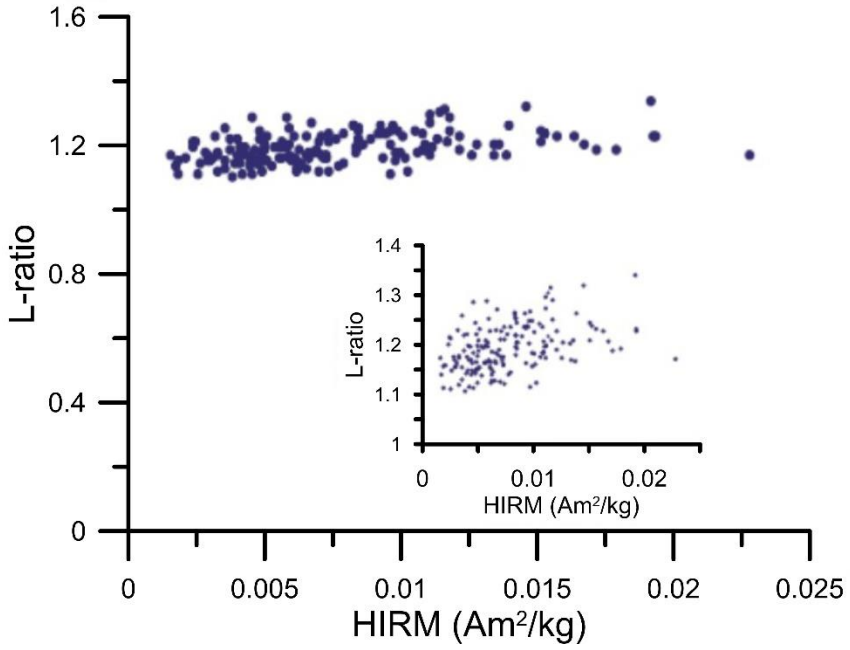

Figure 8.S2 | L-ratio *vs*. HIRM. L-ratio is independent of HIRM, indicating that the HIRM changes as a function of depth/age are mainly controlled by fluctuations in the concentration of high coercivity minerals.

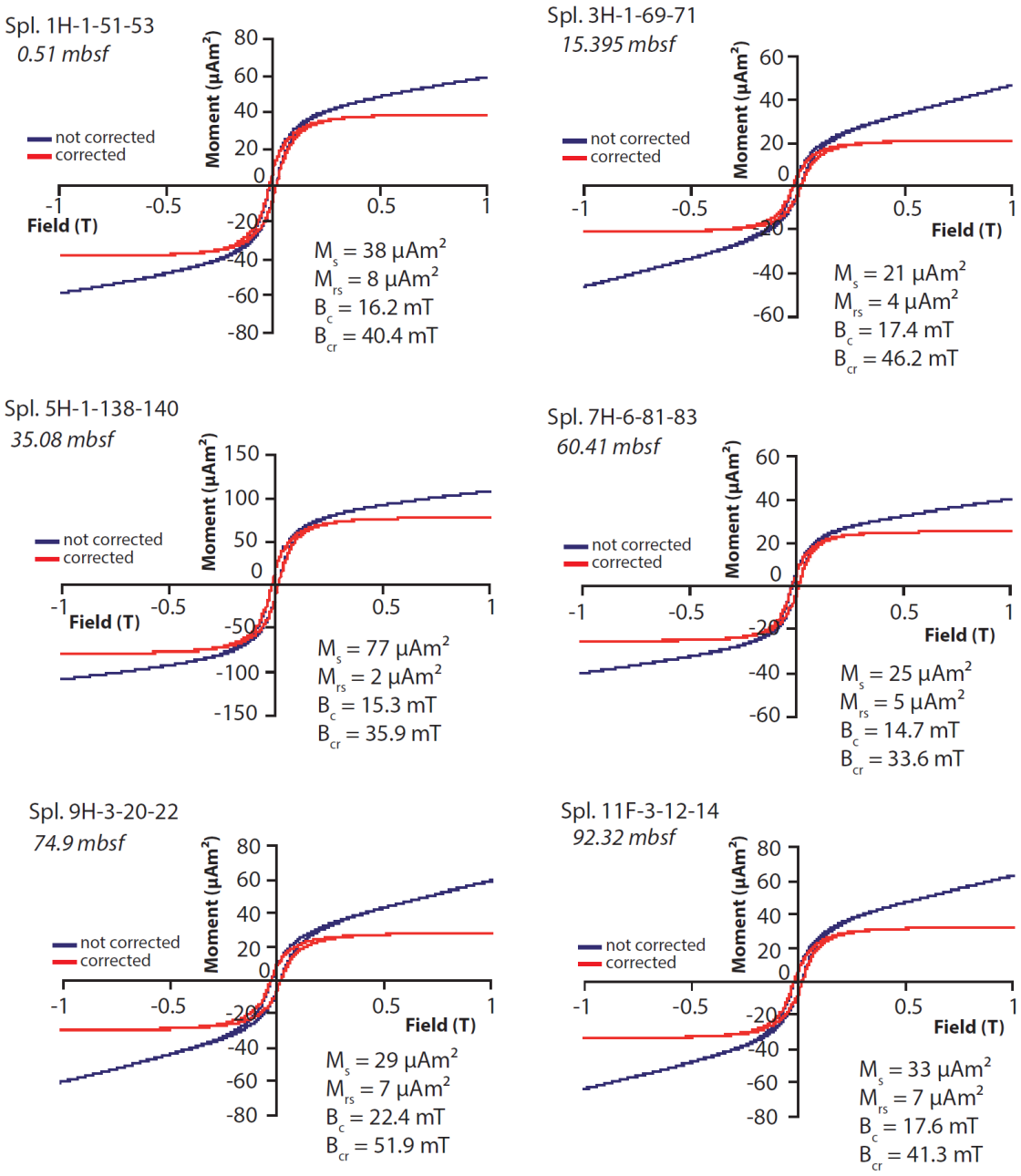

Figure 8.S3 | Examples of hysteresis loops before (blue) and after (red) paramagnetic slope correction (saturation is assumed above 70 % of H_{max} = 1T). Samples show saturation at ~500-600 mT suggesting a dominant low coercivity phase, and probable mixture with a higher coercivity phase.

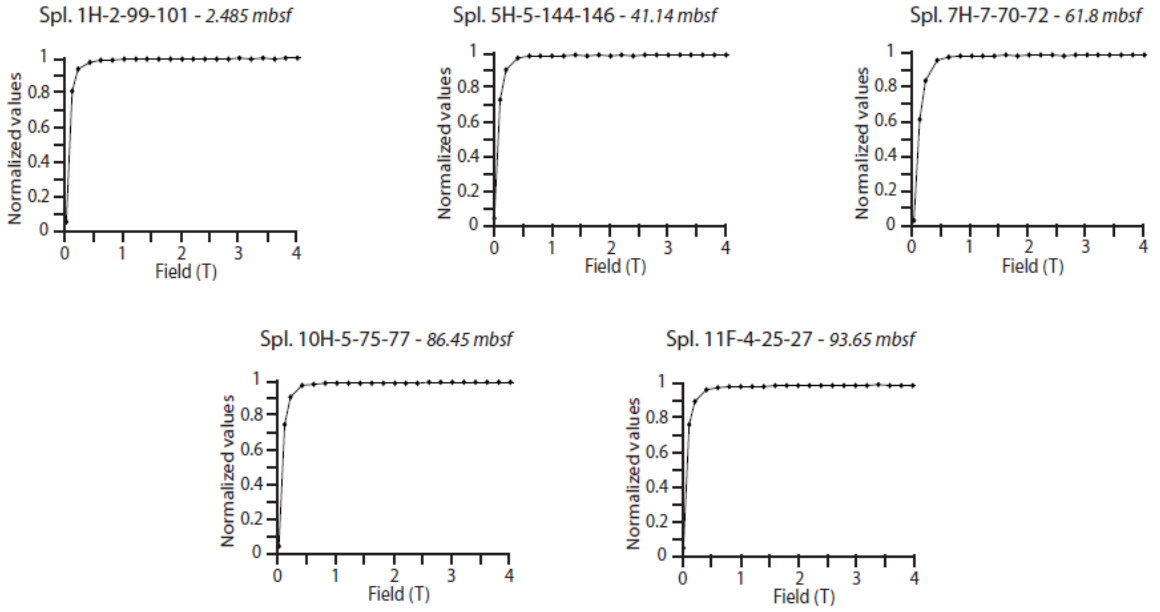

Figure 8.S4 | IRM acquisition curve up to 4 T for samples shown on Figure 8.4. Saturation is reached by ~500 - 600 mT.

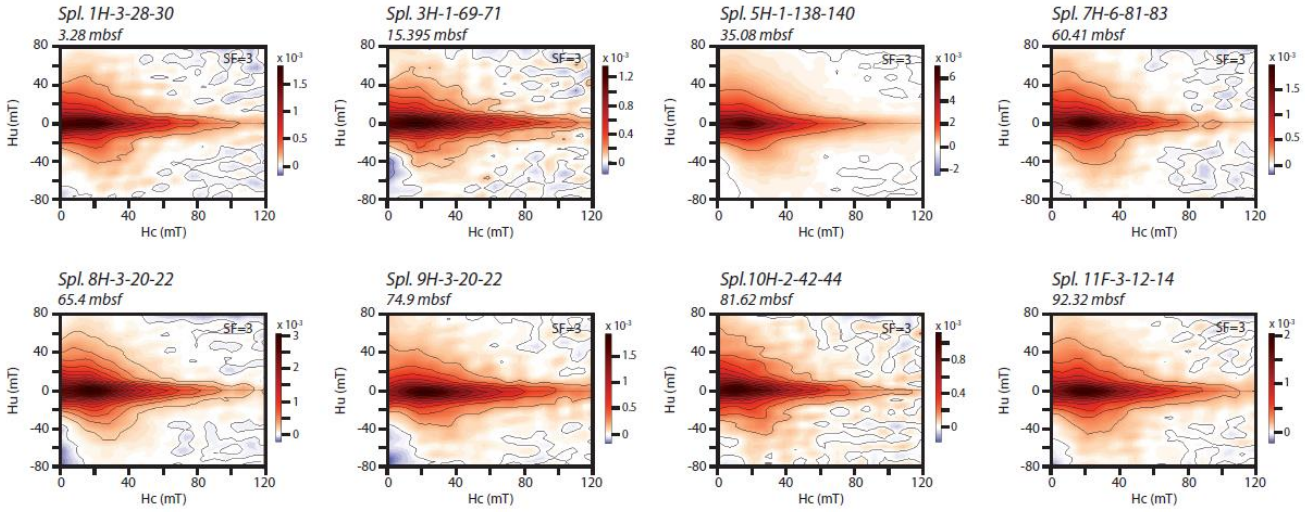

Figure 8.S5 | Examples of FORC diagrams showing typical PSD-sized low coercivity magnetic grains.

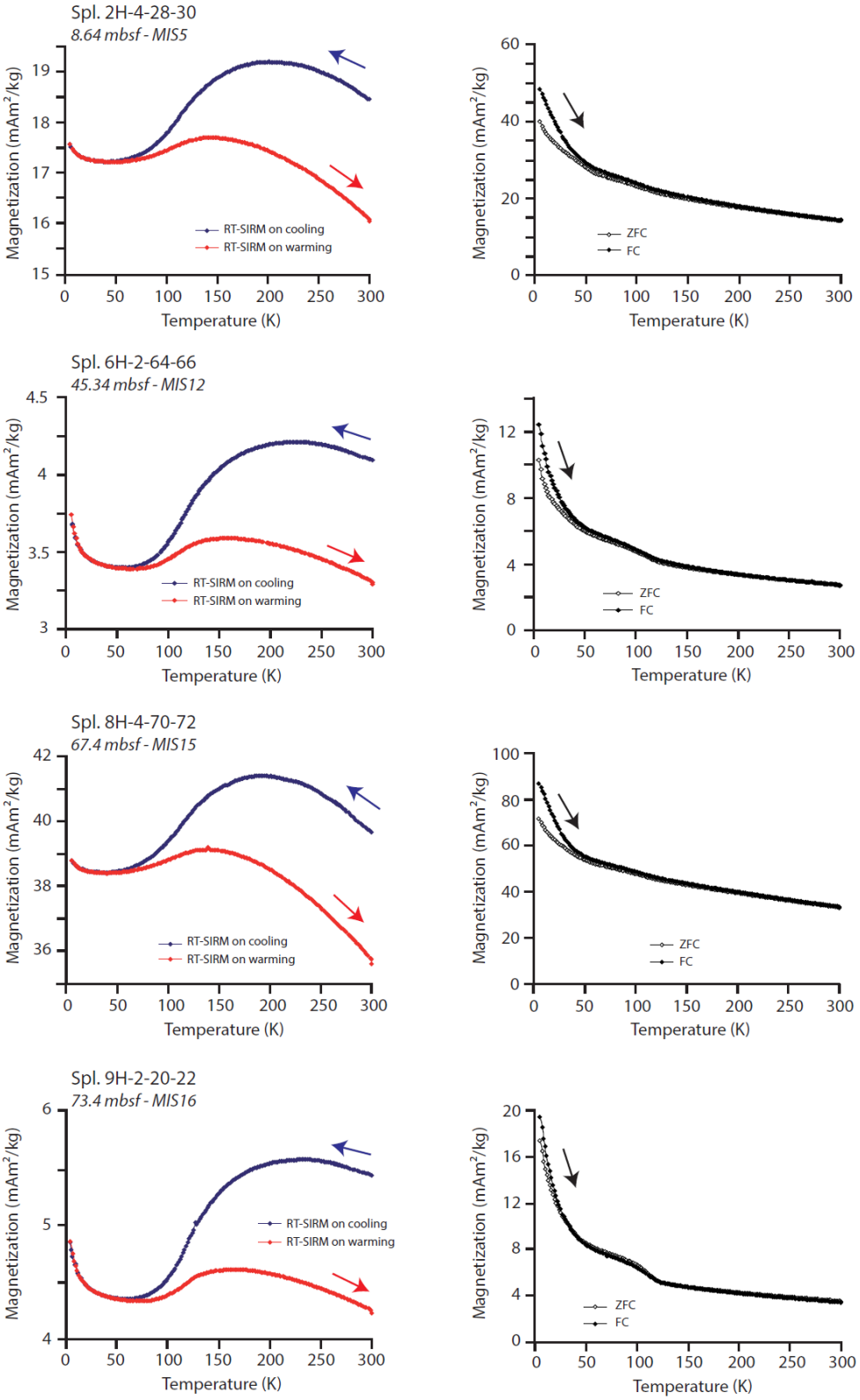

Figure 8.S6 | Examples of SIRM cycles at low temperature (RT-SIRM, ZFC and FC). The Verwey transition of magnetite at ~120 K (e.g., *Muxworthy and McClelland*, 2000) is easily recognized on all curves. The RT-SIRM is not fully recovered when warming back to room temperature suggesting coarse-grained (Ti-)magnetite.

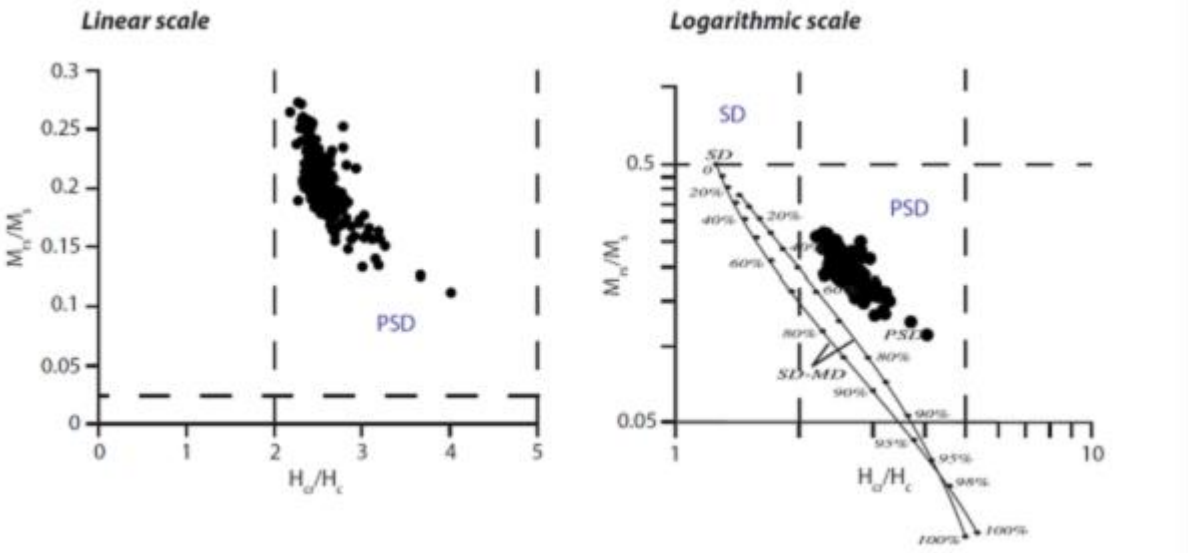

Figure 8.S7 | Day plot (Day et al., 1977). All the samples are in the pseudo-single domain (PSD) field. Mixing curves for SD+MD assemblage from Dunlop (2002) are reported.

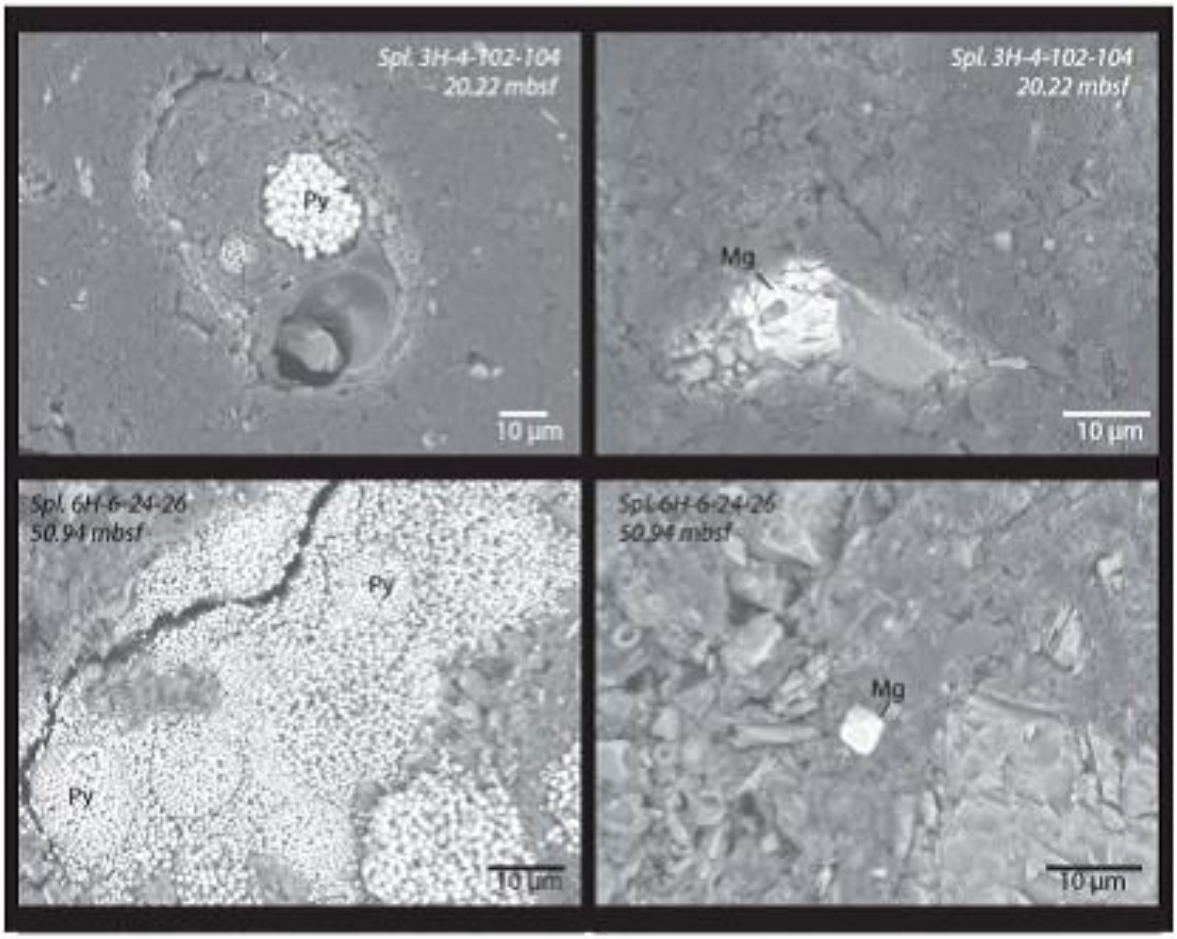

Figure 8.S8 | SEM observations. Scanning Electron Microscope (SEM) observations were carried out on 2 selected samples with a JEOL JSM-6500F microscope equipped with an energy dispersive X-ray spectrometer (EDS) at the CMCR. Py: pyrite, Mg: magnetite/titano-magnetite.

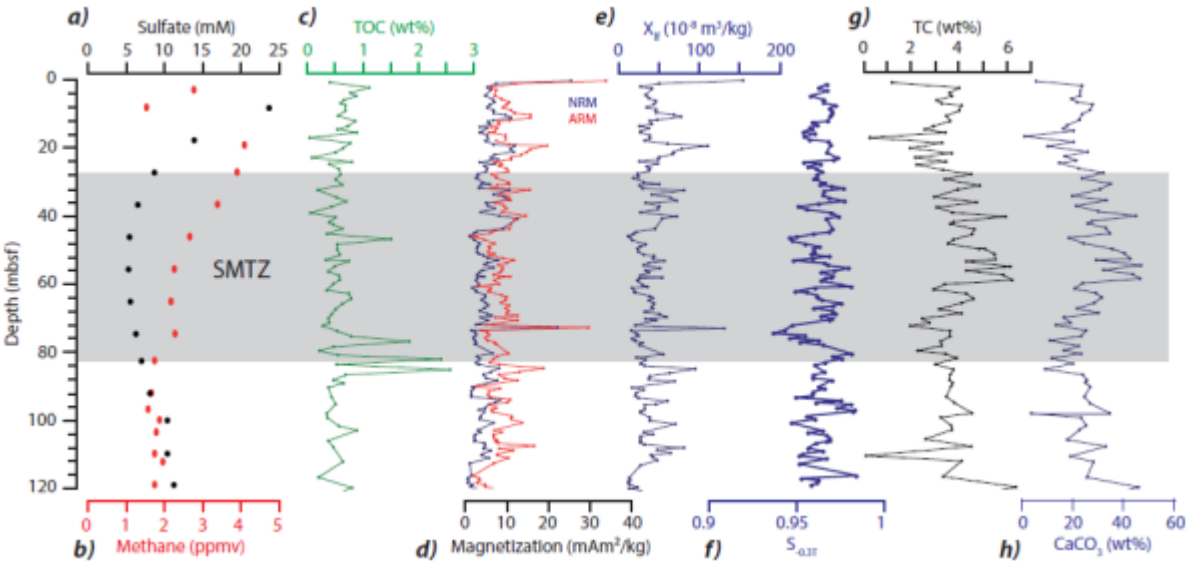

Figure 8.S9 | Evolution of geochemical and selected rock magnetic data in the first 120 meters of Hole U1437B that includes early diagenetic processes. a) sulfate (mM) and b) methane (ppm) content, c) Total Organic Carbon (TOC) defined as TOC = TC - $CaCO_3$, d) remanent magnetization (NRM and ARM), e) magnetic susceptibility χ_{lf} , f) $S_{-0.3T}$, g) Total Carbon (TC) and h) carbonate content $CaCO_3$. The sulfate-methane transition zone (SMTZ) identified onboard (27-83 mbsf) is reported (Tamura et al., 2015a). Data shown in a, b, c, g and h are from (Tamura et al., 2015a), data shown in d, e and f are from this study.

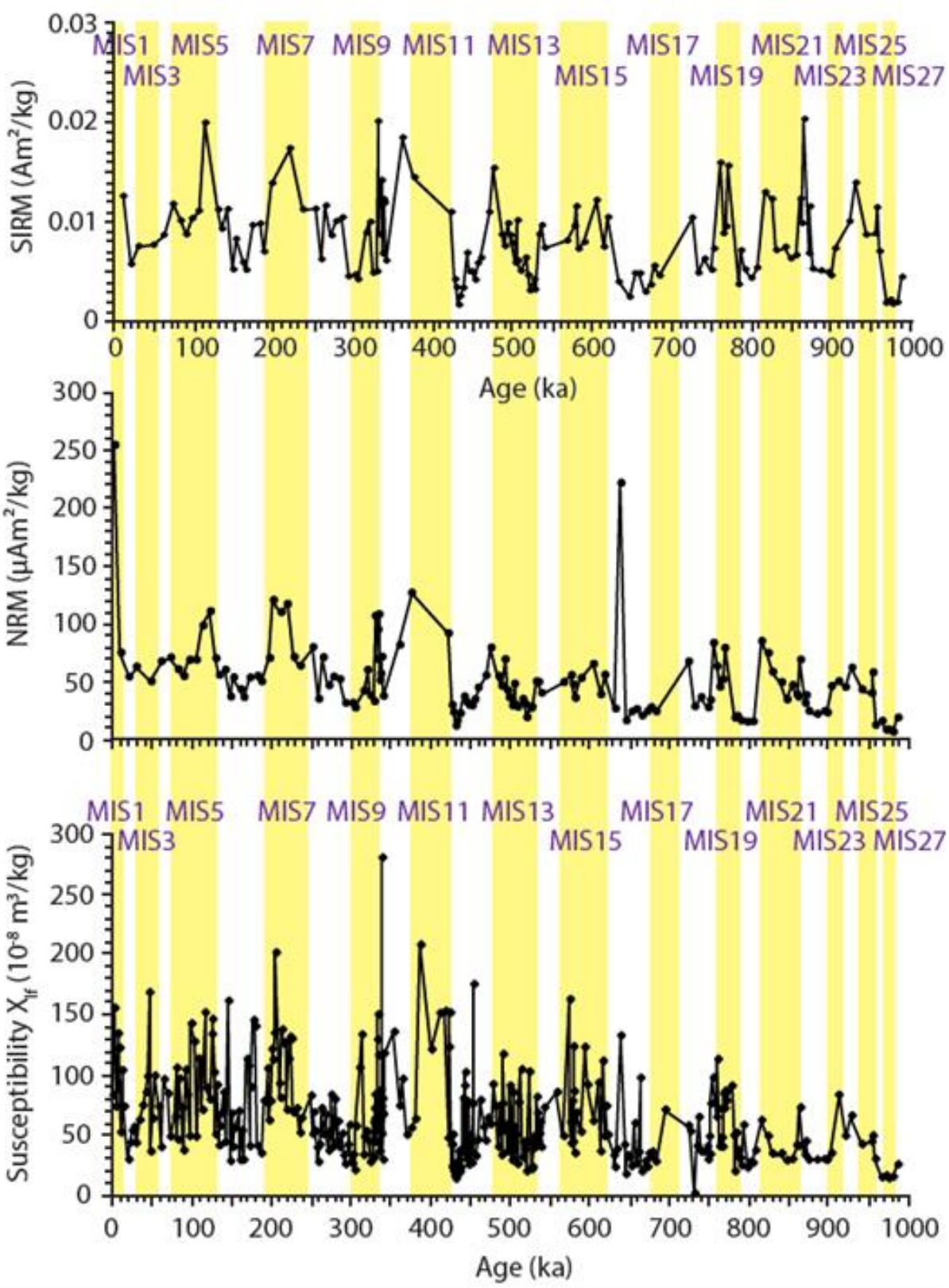

Figure 8.S10 | Evolution of rock magnetic proxies for magnetic mineral concentration (NRM, SIRM and χ_{lf}) as a function of time. Interglacial stages are shaded in yellow. The values for χ_{lf} come from all oriented and non-oriented samples. NRM and SIRM are from cube samples.

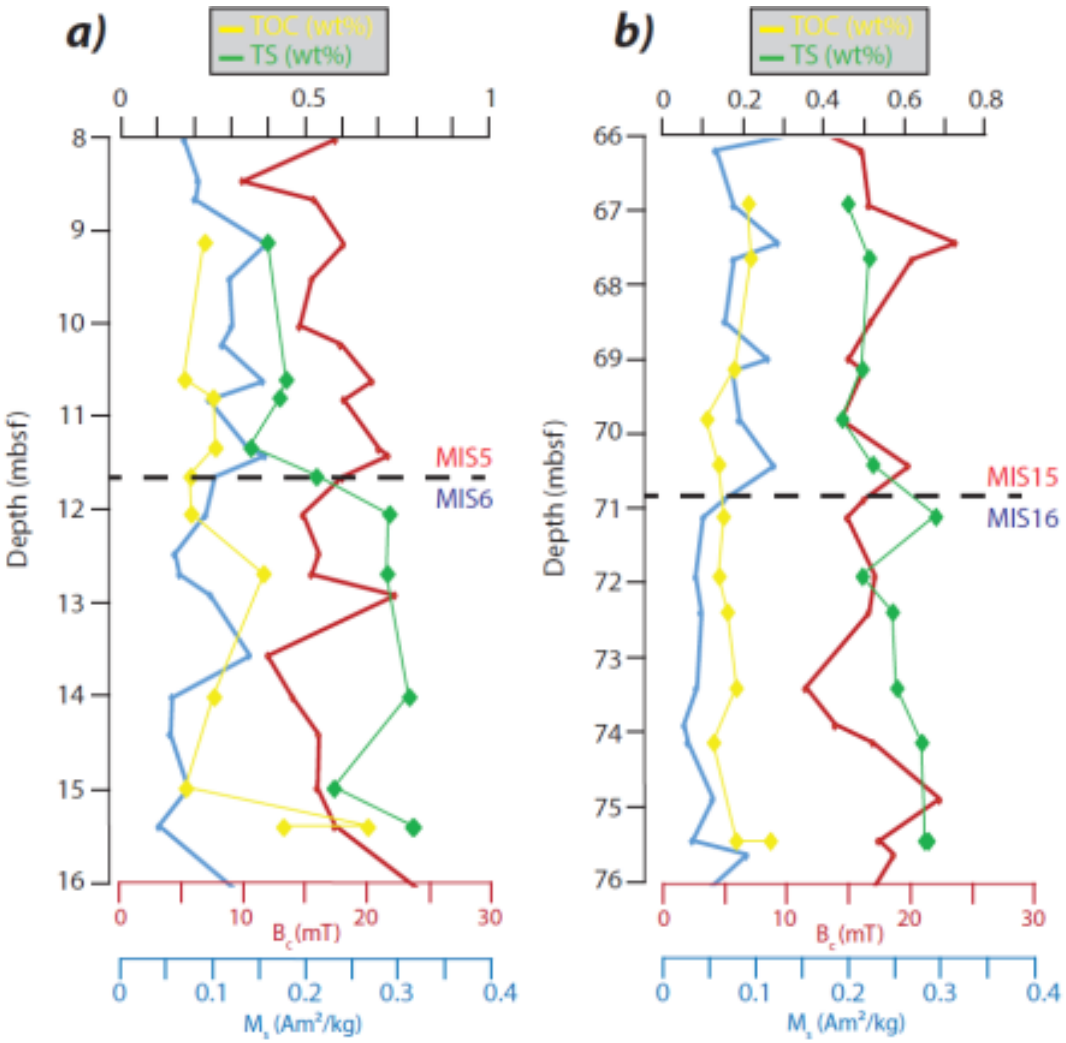

Figure 8.S11 | Comparison of magnetic mineral concentration and hardness proxies (M_s and B_c, respectively) with TOC and TS for two glacial/interglacial transitions (MIS 6/5 and MIS 16/15). Note the increase of TS and the lower M_s value in the glacials.

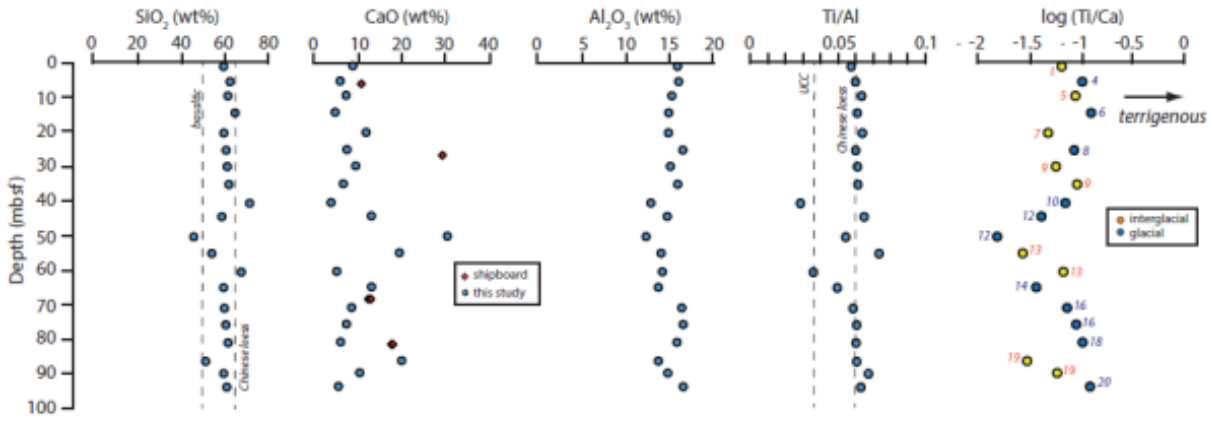

Figure 8.S12 | XRF data. Evolution of SiO_2 (wt%), CaO (wt%), Al_2O_3 (wt%), Ti/Al and log (Ti/Ca). Shipboard data are from Tamura et al. (2015b). MIS stages are reported in italic.

SURVIVAL SUIT

Chapter 9

Summary and outlook to future work

The objective of this thesis was to investigate the paleoclimatic and paleoceanographic evolution of the Northwest Pacific Ocean and adjacent East Asian continent from the late Miocene to the Present. For the paleoceanographic investigations, emphasis was placed on the reconstruction of ocean temperature evolution and inferred latitudinal movements of oceanic fronts, that is the Kuroshio and Oyashio currents and their interfrontal zone. A second focus was set on associated changes in the atmosphere and on land, including past changes in the East Asian monsoon system and the subtropical westerly jet stream.

For this thesis work, samples from two marine sediment successions obtained from IODP Sites C0011 and U1437 spanning the past 8.2 Ma and 4 Ma, respectively, were sampled and studied for their bulk geochemical and lipid biomarker inventory. The following sections will briefly summarize the findings of the preceding chapters and draw main conclusions inferred from the scientific outcomes of this study. Finally, potential future work is suggested which may help to improve, deepen and constrain the findings made in the framework of this thesis.

In a first step to characterize the impact of production season and habitat depth on the lipid paleothermometers used for the ocean temperature reconstructions, a high-resolution study on samples from the past ~145 ka at Site C0011 was carried out. Comparison of the three different paleothermometers $U^{K'}_{37}$, LDI, and TEX^{H}_{86} with *in situ* temperatures showed that while the first two were representative of sea surface temperatures, the latter seemed to more accurately reflect the water temperature evolution close to the depth of the seasonal thermocline. Offsets between the $U^{K'}_{37}$ and LDI resulted from different production seasons of the particular source organisms. This multi-proxy study furthermore shed light on the paleoceanographic and paleoclimate evolution throughout the last two glacial-interglacial cycles. Warm MIS 1, 3, and 5 were characterized by generally higher water temperatures both at the sea surface and subsurface, which was attributed to a fortified northward transport of tropical water masses via the KC. Intercomparison of the different warm MIS with higher Holocene than Eemian temperatures indicated a strong KC and the predominance of its short meander south of Japan during the Holocene, whereas a less strong KC during the Eemian presumably favored the formation of the large meander, with warm KC waters therefore bypassing the study site to the south. Lower glacial water temperatures were interpreted as the southward displacement of

major oceanic fronts, including the KC and the downstream KE, the OC and their interfrontal zone. This enabled the elevated influence of polar waters advected by the OC at Site C0011.

In order to investigate synchronous glacial-interglacial changes in both oceanic and atmospheric circulation, a second study targeted the paleoclimatic and paleoceanographic evolution of the past 1 million years at IODP Site U1437, which is located ~230 km to the southeast of Site C0011 and is occasionally under the influence of the large KC meander. The studied time interval comprised numerous glacial-interglacial cycles and major climate transitions such as the Mid-Pleistocene Transition (1.2-0.7 Ma) and the Mid-Brunhes Event (~430 ka). $U^{K'}_{37}$- and TEX^{H}_{86}-based water temperature records revealed a fortified warm water mass transport via the KC during post-MBE interglacial periods. Slightly colder post-MBE than pre-MBE glacials and hence larger amplitudes in glacial-interglacial temperature variations are in line with previous observations for the glacial-interglacial cycles after the MBE.

The study of sedimentary concentrations of land plant-derived wax lipids as indicators for dust fluxes to the NW Pacific Ocean in the same set of samples enabled the investigation of simultaneous changes in atmospheric and oceanic circulation. Elevated glacial concentrations were interpreted as pulsed dust fluxes from mainland Asia to the downwind regions of the NW Pacific Ocean, predominantly mediated by the WJS. In general, the concentrations of land plant-derived long-chain *n*-alkyl lipids and nonacosan-*10*-ol showed a distinct glacial-interglacial pattern from 1 Ma to ~430 ka with glacial concentrations being up to twenty times higher than during interglacials. The distinct glacial-interglacial variations in dust flux are in line with similar biomarker-based observations made in other regions from the westerly wind belt in both the Northern and Southern Hemisphere. After the MBE at ~430 ka, however, an abrupt cessation in increased glacial wax lipid concentrations in the studied sediments from the NW Pacific Ocean was observed and glacial-interglacial variations in dust fluxes became negligibly small. The cessation of dust fluxes after the MBE was attributed to a displacement of the main path of the WJS to the south of the Himalayan-Tibetan Plateau during peak glacials, thereby bypassing the major dust source areas in the arid Asian interior and hence reducing dust fluxes to the study site. This southward displacement was suggested to result from enhanced glacial Arctic cooling, which has been previously shown to have intensified in the aftermath of the MBE, and was hypothesized to have added to the aridification of central Asia.

While the long-term paleoclimate evolution from the late Miocene to the Present was studied intensively at various sites from the North Pacific Ocean, an unfortunate regional gap still existed in the NW Pacific off Japan. The region south and east of Japan is of major importance for the heat balance of the whole northern Pacific Ocean as it hosts the confluence region of its

two major western boundary currents and hence provides a crucial link between the tropical and Subarctic Pacific. The study of the long-term ocean temperature evolution in the NW Pacific at Sites C0011 and U1437 closed this existing regional gap of paleoclimatic and paleoceanographic reconstruction of the northern Pacific and will help to understand major changes in ocean circulation across the Pacific associated with tectonic reorganization and general global cooling.

At present, Sites C0011 and U1437 are occasionally located beneath the short or large meander path of the KC, respectively. Temperature differences between the two sites throughout the past 4 Ma were interpreted to mostly result from the latitudinal position of the KC and the impact of its warm water masses on the temperature evolution at the two sites. Considering present and past locations of the study sites, the KC may have reached Site U1437 by ~3.3 Ma and sustained higher SSTs between 3.3 to 0.7 Ma at the site compared to C0011 indicated that the KC was predominantly located over Site U1437 throughout this time. It was only after ~0.7 Ma that SSTs at Site C0011 occasionally exceeded those at Site U1437 which presumably reflected the alternating predominance of either the short (Site C0011) or large meander path (Site U1437) south of Japan. Like existing long-term records from the North Pacific Ocean spanning the time interval from the late Miocene to the Present, the ocean temperature records from Sites C0011 and U1437 showed a unidirectional cooling trend. In contrast to most of the other regions of the North Pacific, however, oceanic cooling south of Japan was less pronounced, with a cooling of 1 °C from the late Miocene to the Pliocene and an additional 2-3 °C from the Pliocene to the Present. Similarly, cooling in the equatorial West Pacific Ocean was less severe than in the equatorial East Pacific. As the KC is fed from the WPWP in the tropical West Pacific and advects warm water masses to the region south of Japan, the less pronounced cooling in this region was attributed to a stronger KC that reached its present-day latitude around ~3 Ma.

Several short-lived declines in subsurface temperatures at Site C0011 during the late Miocene were potentially caused by intruding subpolar waters of the OC at intermediate depth. This observation is to date, to the best of our knowledge, unique during this time in the North Pacific. Concomitant variations in the inventory of land plant-derived wax lipids furthermore indicated that the long-term cooling was accompanied by progressive aridification of the Asian continent, presumably resulting from coupled global cooling and tectonic uplift of the HTP. An elevated sampling resolution and potentially additional study sites that can be expected to have experienced similar temperature declines during southward migrations of the OC (e.g., additional samples from Site U1437 from the late Miocene) may help to further constrain the observations made at Site C0011.

Lately, a novel proxy, the RI-OH index, was introduced for the reconstruction of sea surface temperatures. We tested its applicability on geological timescales by generating a RI-OH record for the last 1 Ma at Site U1437. Comparison with existing $U^{K'}_{37}$- and TEX^{H}_{86}-reconstructed temperatures from the same set of samples showed a good fit with all three records reflecting similar temperature variations and the same sawtooth pattern as can be seen in the global benthic oxygen isotope record. Our study provides the longest existing RI-OH-based SST record and documents the general applicability of the RI-OH for paleo-SST reconstructions at least back to the mid-Pleistocene.

In order to investigate the impact of paleoenvironmental changes in the region of the NW Pacific Ocean and the adjacent East Asian continent on the magnetic mineral assemblage and associated magnetic properties throughout the past 1 Ma, a multiproxy-based study was carried out in deep-sea sediments from Site U1437. The study used independent rock magnetic, bulk geochemical and elemental parameters to characterize the magnetic mineral assemblage and paleoenvironmental conditions. Substantial glacial-interglacial differences were revealed with overall higher abundances of magnetic minerals and a dominance of coarse-grained (titano)-magnetite of both terrigenous (presumably from mainland China) and volcanic origin (from the Izu arc front) during interglacial stages. Glacial periods, on the other hand, were characterized by reduced magnetic mineral contents, potentially resulting from the partial dissolution of (titano)-magnetite. Furthermore, it was assumed that a stronger East Asian winter monsoon in continental Asia led to a higher proportion of higher coercivity, fine-grained eolian particles (likely hematite) in the glacial magnetic mineral assemblage. Additional time series analysis on the natural gamma ray, magnetic susceptibility and saturation remanence data sets confirmed the statistically significant presence of Milankovitch periodicities, including eccentricity, obliquity and precessional periods in all records and hence confirmed the impact of astronomically forced climate and sea level changes on the magnetic mineral assemblage at Site U1437.

Altogether, the ocean temperature records from the two study sites in the NW Pacific Ocean showed the same unidirectional cooling trend from the late Miocene and Pliocene to the Present as seen in numerous other paleotemperature records from all over the globe. A less steep decline in temperatures from ~3.3 Ma onwards was attributed to the “arrival” of the KC at its present-day latitude south of Japan. Following the onset and intensification of stable Northern Hemisphere glaciation and the emergence into frequent glacial-interglacial cycles, the paleotemperature records from both sites indicated a concomitant latitudinal migration of

oceanic fronts, with a retreat of the KC to more southerly latitudes and an intrusion of colder OC waters in the subsurface layer during glacial phases. The climate changes across the MBE involved higher glacial-interglacial oceanic temperature variations and a decrease in pulsed glacial dust fluxes from the Asian interior to the NW Pacific Ocean. This was attributed to a displacement of the glacial westerly jet stream to the south of the HTP due to amplified Arctic cooling in the aftermath of the MBE. Following the MBE, increased interglacial magnetic susceptibility pointed towards a strengthening of the EASM and elevated associated precipitation, which is in line with previous findings from the region and indicated a northward movement of the ITCZ in boreal summer during the post-MBE interglacials. This also further supported the findings of a fortified northward transport of warm water masses via the KC during post-MBE interglacial periods.

Future work

In order to further substantiate the observations and interpretations made based on the results from this thesis, proposed future work, which may help to increase our understanding of climate-related paleoenvironmental changes in the NW Pacific Ocean and on the adjacent East Asian continent, may include increasing the sampling resolution prior to 1 Ma at both study sites, but especially at Site U1437, where high sedimentation rates and a detailed age model will allow for a precise and targeted placement of additional samples. An increased sampling resolution and potentially also the addition of further study sites located in the region south of Japan would help to further deepen the investigation of latitudinal movements of the KC and may help to more precisely date its arrival south of Japan, which, based on previous studies and our own findings, may be placed between 5 to 3 Ma (Tsuchi and Shuto, 1984; Shuto, 1990; Gallagher et al., 2009; Tomida and Kitao, 2002; Tomida et al., 2013). One especially interesting interval for high-resolution sampling at Site U1437 would be around ~7 Ma in order to validate the spatial extent of the observed short-lived subsurface cooling events identified at Site C0011. Another future target may involve the study of changes in continental vegetation with respect to C_3 and C_4 plants. One useful means would be compound-specific carbon isotope measurements on wax lipids of land plants. C_3 and C_4 plants are characterized by different carbon isotopic signatures (C_3 plants: 20 to -30 ‰ (average -27 ‰); C_4 plants: -10 to -16 ‰ (average -12 ‰)) (Collister et al., 1994) owing to their photosynthetic pathway, and compound-specific carbon isotope ($\delta^{13}C$) measurements on wax lipids would help to study climate-related changes in the floral community. Previous compound-specific $\delta^{13}C$ measurements in eolian deposits on the CLP indicated multiple expansions of C_4 plants associated with strengthened

EASM circulation from the late Miocene to present (An et al., 2005). A complementary study of carbon isotopic signatures of wax lipids from existing and potentially additional samples from Site U1437 and other sites would enable the determination of floral changes in the dust source regions upwind of the site in relation to previously reported temperature, atmospheric greenhouse gas, and aridity/humidity changes.

A further potential target may be the investigation of changes in paleoprecipitation with respect to the East Asian continent´s and adjacent oceanic regions´ dominant moisture sources (e.g., the East Asian and Indian summer monsoons, and moisture advected by the WJS). This may allow to identify changes in the relative contributions and hence strengths of the different moisture sources in relation to the climatic evolution (e.g., long-term global cooling, glacial-interglacial climate variability) and topographic changes (e.g., uplift of the HTP). For the characterization of changes in the hydrological cycle, the stable hydrogen isotopic signature (δD, deuterium/hydrogen ratio) of land plant-derived wax lipids provides an efficient tracer, since rainwater is the main source of hydrogen for land plants (Eglinton and Eglinton, 2008). Thereby, a good correlation of the δD imprint of long-chain *n*-alkanes with the δD signature of the moisture source enables the reconstruction of (paleo-) precipitation patterns (Sachse et al., 2012). Hence, the determination of δD signatures of specific land plant-derived *n*-alkanes extracted from existing and potentially additional samples from Site U1437 and other sites would allow to draw conclusions about changes in the region´s atmospheric circulation in the geological past with respect to its major hydrological features.

A more precise sediment source allocation, especially in terms of dust source regions on the (East) Asian continent, may help to validate the proposed changes in the glacial WJS path across the MBE. Such a discrimination between dust transported by the WJS *vs*. the EAWM could be carried out by a detailed provenance analysis and hence dust source allocation using complementary magnetic, minor and trace elemental (e.g., REE), as well as isotopic data (e.g., Nd, Sr, Pb, Hf) of existing and additional samples from the past 1 Ma at Site U1437. First attempts at low resolution were undertaken by Gill et al. (2018) for selected glacial and interglacial phases and enabled a distinction between a “foreign component” sourced from the CLP and a “local component” derived from the Izu arc, whose abundances varied significantly over glacial and interglacial stages.

With the work carried out in the frame of this thesis, we accomplished to close the previously existing regional gap of long-term paleoclimate evolution in the NW Pacific Ocean, a region that is crucial for the heat balance of the whole Pacific Ocean as it hosts the confluence region of the two major western boundary currents of the North Pacific. An integration of the results

from this thesis in modelling studies will thus help to more precisely predict the future behavior of the Pacific Ocean and adjacent East Asian continent under a warming climate and rising greenhouse gas levels.

Expeditions 333 and 350 were two out of several expeditions that were carried out within the frame of the International Ocean Discovery Program in the Northwest Pacific, tropical Pacific and northern Indian Ocean during the past decade. The integration of our data and a compilation of newly generated records for ocean temperature evolution and reconstructions of changes in the East Asian and Indian (paleo-)monsoon system would help to create a more complete picture of past and ongoing changes in the Pacific and the Asian continent both in terms of oceanic and atmospheric circulation.

350 U1437D 26R7
W10 12 cm

Appendix

Appendix Chapter 10

Magnetic mineral diagenesis in a high temperature and deep methanic zone in Izu rear arc marine sediments, Northwest Pacific Ocean

Myriam Kars[1], Robert J. Musgrave[2,3,4], Tatsuhiko Hoshino[5,6], Ann-Sophie Jonas[7], Thorsten Bauersachs[7], Fumio Inagaki[6,8], and Kazuto Kodama[1,9]

[1] Center for Advanced Marine Core Research, Kochi University, B200 Monobe, Nankoku 783-0004, Japan

[2] School of Geosciences, University of Sydney, Sydney, NSW2006, New South Wales, Australia

[3] Geological Survey of New South Wales, NSW Department of Industry, Maitland, NSW 2320, New South Wales, Australia

[4] PALM Laboratory, Centre for Frontier Geoscience, Newcastle Institute for Energy and Resources, The University of Newcastle, Newcastle, New South Wales, Australia

[5] Geomicrobiology Group, Kochi Institute for Core Sample Research, Japan Agency for Marine-Earth Science and Technology, Nankoku, Japan,

[6] Research and Development Center for Submarine Resources, Japan Agency for Marine-Earth Science and Technology, Nankoku, Japan,

[7] Department of Organic Geochemistry, Institute of Geosciences, Christian-Albrechts-University, Ludewig-Meyn-Straße 10, 24118 Kiel, Germany

[8] Research and Development Center for Ocean Drilling Science, Japan Agency for Marine-Earth Science and Technology, Yokohama, Japan

[9] Research Center for Knowledge Science in Cultural Heritage, Doshisha University, Kyoto, Japan

Published in *Journal of Geophysical Research: Solid Earth* 123 (2018), Special Section: Magnetism in the Geosciences - Advances and Perspectives, 8331-8348, doi:10.1029/2018JB015861.

Abstract

Magnetic mineral diagenesis is an important process in sediments that is responsible for the partial or total destruction of records of Earth's magnetic field variations and also plays an important part in iron and sulfur cycling. A rock magnetic study has been carried out at International Ocean Discovery Program Expedition 350 Site U1437 in the Izu Bonin rear arc to investigate magnetic mineral diagenesis in deeply buried sediments from ~775 to ~1,002 m below sea floor (mbsf) with burial temperatures ranging from ~67 to 85 °C. Nonsteady state geochemical environments occur within an unusual deep methanic zone (below 850 mbsf) because of a release of sulfate below the shallow sulfate reduction zone. A drastic decline in magnetic susceptibility and remanence is observed at ~850 mbsf due to a decrease in ferrimagnetic iron oxide contents. Reduction of (titano)-magnetite and pyritization occur at this inferred deep sulfate-methane transition zone. Below ~850 mbsf, lower magnetic mineral contents coincide with further methane release. Geochemical analyses support a change in redox conditions and secondary precipitation of iron sulfides and carbonates in the methane-rich zone. Magnetic mineral alteration is enhanced in zones where methane accumulates underneath low porosity intervals that act as seals. Although geochemical processes due to methane occurrence are likely dominant, more than one mechanism, possibly involving microbial activity, is probably responsible for the observed magnetic mineral assemblage changes.

Key points

- Dissolution of magnetic iron oxides is observed in an unusual deep methanic zone
- Magnetic mineral alteration is enhanced in methane-rich intervals below lower porosity seal-like sediments
- Geochemical reactions involving methane, and possible microbial processes, are likely responsible for the observed diagenetic alteration

10.1. Introduction

Magnetic mineral diagenesis in marine sediments is an important process that affects the original magnetic properties of sediments and occurs as soon as burial begins. A succession of contrasting redox and pressure-temperature conditions has led to the definition of diagenetic zones (e.g., Canfield and Thamdrup, 2009; Jørgensen and Kasten, 2006) with respective formation and transformation (alteration) of magnetic minerals from the shallow subsurface to greater depth (e.g., Roberts, 2015; Rowan et al., 2009).

During diagenesis, detrital iron (oxyhydr)oxide minerals (e.g., (titano)-magnetite, hematite, and goethite) undergo a series of transformations and alterations via a variety of biogeochemical processes (Roberts, 2015). Two main biogeochemical processes occur within anoxic sediment, at depths of a few centimeters to tens of meters, to transform iron (oxyhydr)oxides into iron sulfides (Berner, 1984; Canfield and Berner, 1987; Roberts and Weaver, 2005). Dissolved hydrogen sulfide, produced by sulfate consumption during organoclastic sulfate reduction (Berner, 1981) and anaerobic oxidation of methane (AOM; Knittel and Boetius, 2009; Treude et al., 2005), will react with dissolved Fe^{2+} (originating from reductive dissolution of both detrital and authigenic Fe-bearing oxides) within a specific interval called the sulfate-methane transition (SMT) zone. Transformation of ferrimagnetic iron (oxyhydr)oxides into paramagnetic pyrite at the SMT means that this zone is usually characterized by a decrease in magnetic susceptibility, which has been observed, for example, in sediments of the Argentine Basin (Garming et al., 2005; Riedinger et al., 2005) and the Zambezi deep-sea fan (März et al., 2008). More importantly, dissolution and alteration of the magnetic mineral assemblage, due to changes in redox conditions, for instance, also have a profound impact on the paleomagnetic record in sediments (Karlin, 1990; Leslie et al., 1990a, b; Passier et al., 1998).

In marine sedimentary sequences, steady-state conditions are often interrupted because of, for example, temporarily variable organic matter input and changes in sedimentation rate (Roberts, 2015). In depositional environments characterized by nonsteady state situations, specific environmental conditions (such as limited sulfide concentrations or low organic carbon contents) may favor preservation of pyrite (FeS_2) precursors such as ferrimagnetic greigite (Fe_3S_4), leading to arrest of the pyritization process. A combination of limited microbial production of dissolved sulfide (from organic matter decomposition) and high concentrations of reactive iron generally favors greigite formation (Kao et al., 2004). If authigenic ferrimagnetic iron sulfide minerals are preserved, they can potentially carry a stable remanence (when growing through their blocking volume) that is responsible for recording a secondary magnetization (Roberts and Weaver, 2005; Sagnotti et al., 2005).

While iron sulfide formation in the sulfidic zone and SMT is reasonably well understood, the mechanisms responsible for the formation, preservation, and transformation of iron sulfides in the methanic zone underneath the SMT are poorly resolved. Below the SMT, ferrimagnetic greigite can precipitate at an active sulfidization front (formed with opposing gradients of downward dissolved sulfide and upward dissolved iron). This generates a magnetic susceptibility peak, as reported, for instance, in Quaternary marine sediments of the Amazon Fan (Kasten et al., 1998) and the Black Sea (Holmkvist et al., 2011; Neretin et al., 2004). Greigite formation in methane-rich environments at a later diagenetic stage and often hundreds to thousands of years after host sediment deposition has been documented previously (Florindo and Sagnotti, 1995; Kars and Kodama, 2015; Larrasoaña et al., 2007; Rowan and Roberts, 2005), and many formation pathways, such as greigite formation on pyrite surfaces, within sheet silicates or on siderite, have been proposed (Jiang et al., 2001; Roberts, 2015; Roberts and Weaver, 2005). Pyrrhotite ($Fe_{1-x}S$, x = 0-0.125) is also known to form in methane-rich sediments if sulfate-bearing fluids enter sediments after deposition (e.g., Dinarès-Turell and Dekkers, 1999) or in the presence of gas hydrates in accretionary prisms (e.g., Horng, 2018) along with greigite (Housen and Musgrave, 1996; Larrasoaña et al., 2007).

Site U1437 (supporting information Figure 10.S1), NW Pacific Ocean, drilled during International Ocean Discovery Program (IODP) Expedition 350 (Tamura et al., 2015a), records the longest continuous (~1,300 m) magnetic polarity stratigraphy in the history of scientific ocean drilling (Musgrave and Kars, 2016). However, interpretation of this record is not straightforward due to numerous overprints including authigenic growth of magnetic iron sulfides and diagenetic magnetic mineral alteration (Musgrave and Kars, 2016). In addition, Kars et al. (2017) showed that rock magnetic properties in the Upper Pleistocene sediments are modulated by glacial-interglacial cycles and that the magnetic mineral assemblages reflect a superimposition of volcanic and monsoonal signals. In this paper, magnetic mineral diagenesis is investigated over the depth interval between about 775 and 1,002 m below sea floor (mbsf) in Hole U1437D. This interval corresponds to a deep methanic zone within which methane concentrations increase significantly below 850 mbsf (Tamura et al., 2015a). The SMT at this site is unusually deep (i.e., deeper than the first tens of meters) because of the unusual sulfate profile at this site, which returns to near-seawater values at about 270 mbsf and remains elevated to at least 700 mbsf, the deepest sulfate measurement (Text 10.S1 and Figure 10.S2). Present-day burial temperatures range from 67 to 85 °C in the studied stratigraphic interval (geothermal gradient: 83 °C/km; Tamura et al., 2015a). Rock magnetic measurements and complementary microbiological and geochemical analyses were carried out to characterize the magnetic

mineral assemblage and the environment in which it is embedded. Iron reduction and iron oxide dissolution coupled to high methane abundances are evident at Site U1437. Possible mechanisms responsible for the postdepositional magnetic mineral assemblage changes are discussed.

10.2. Materials and Methods

IODP Expedition 350 drilled a 1,806.5-m-thick sediment sequence from Site U1437 in the Izu Bonin rear arc in April and May 2014 from R/V *JOIDES Resolution*. The site (31° 47.39´ N, 139° 01.58´ E; water depth: 2,116 m) is located within a ~20-km-wide volcano-bounded intra-arc basin between two major constructional volcanic ridges: the Manji and Enpo rear arc seamount chains, which are two of several seamount chains in this region (Figure 10.S1). It is located at the rear of the main chain of active volcanoes (Izu arc front) about 90 km west of the arc front Myojinsho Volcano and Myojin Knoll and 330 km west of the axis of the Izu-Bonin trench (Tamura et al., 2015a).

10.2.1. Studied samples

One hundred fourteen saw-cut cubic samples (2×2 cm) of hemipelagic sediments were collected from Hole U1437D in Sections 350-U1437D-37R-6 (~775 mbsf) to 350-U1437D-62R-3 (~1,002 mbsf). All samples are derived from Lithologic Unit III (726.5-1,017.88 mbsf), which is dominated by tuffaceous mudstones intercalated with ash layers (evolved tuff; Busby et al., 2017; Tamura et al., 2015a). The tuffaceous mudstone samples span an age of ~4.5-6 Ma (Miocene-Pliocene transition) according to the shipboard age model (Tamura et al., 2015a).

10.2.2. Rock magnetic measurements

Magnetic measurements were performed at the paleomagnetic laboratory of the Center for Advanced Marine Core Research, Kochi University, Japan. Low-field, low-frequency (0.465 kHz) and low-field, high-frequency (4.65 kHz) magnetic susceptibilities (χ_{lf} and χ_{hf}, respectively) were measured with a MS2B Bartington Instruments magnetic susceptibility meter (field = 250 μT). The natural remanent magnetization (NRM) and an anhysteretic remanent magnetization (ARM) were measured with a 2-G Enterprises 760R cryogenic magnetometer in a shielded room. ARM was imparted in a direct current bias field of 50 μT in the presence of an 80-mT peak alternating field.

A saturation isothermal remanent magnetization (SIRM) was subsequently imparted on 0.5×0.5 cm discrete samples (cut from the 2×2 cm samples) in the +*z* direction at 1.2 T by using a MMPM10 impulse magnetizer before being measured at each step with a Natsuhara Giken spinner magnetometer. The samples were subsequently remagnetized in the -*z* direction with a direct current field of 0.3 T and measured again, to calculate the $S_{-0.3T}$ parameter (=[(-IRM$_{-0.3T}$)/SIRM)+1]/2; Bloemendal et al., 1992), which provides an indication of the relative proportion of high coercivity minerals (e.g., hematite, goethite, and ferrimagnetic iron sulfides) in a mixture with soft ferrimagnetic minerals (e.g., magnetite and maghemite).

Hysteresis loops with a maximum applied field (H_{max}) of 1 T were measured on dry sediment powder sister samples at room temperature (RT) with a Princeton Measurements Corporation vibrating sample magnetometer. Magnetization at saturation (M_s), saturation remanent magnetization (M_{rs}), and coercivity (B_c) were measured. χ_{hfield}, which is the susceptibility at high fields, is derived from the hysteresis loop slope correction. Here saturation is assumed above 70 % of H_{max}, although this may underestimate M_{rs}/M_s as discussed by Roberts et al. (2018) and references therein. Coercivity of remanence (B_{cr}) was subsequently measured by backfield demagnetization of M_{rs}. First-order reversal curves (FORCs; Pike et al., 1999) were measured for 27 samples selected at ~10-m stratigraphic intervals, with a 1.2-T saturating field (averaging time: 100 ms; field increment: 4 mT; number of FORCs: 91). FORC diagrams were processed using the FORCinel software (Harrison and Feinberg, 2008).

Low-temperature magnetic measurements (from 300 to 5 K) were made with a Quantum Design SQUID magnetic properties measurements system (MPMS) for 17 selected samples. The samples each have ~120-mg mass and had been dried, ground lightly to a fine powder, and sealed in a gelatin capsule before being measured. A RT-SIRM was acquired at 2.5 T. A 300-5-300-K cooling-warming cycle of the RT-SIRM was then measured in a zero magnetic field (trapped field inside the MPMS <20 μT). A low temperature SIRM (LT-SIRM) was imparted at 5 K at 2.5 T. Samples were then warmed to RT in a zero magnetic field and measured (termed ZFC for zero-field-cooled). Samples were subsequently cooled to 5 K in a 2.5-T magnetic field, and the LT-SIRM was measured during warming to 300 K (termed FC for field-cooled).

Thermomagnetic experiments in vacuum were measured on eight selected specimens with a Natsuhara Giken NMB-89 magnetic balance from RT to 700 °C (with a heating rate of 10 °C/min in a 0.3-T field). Repeated heating-cooling cycles with increased final temperatures in the range 250-370 °C were made on three specimens to check for the presence of pyrrhotite.

10.2.3. Geochemical Analyses

10.2.3.1. X-ray Fluorescence

Cores 350-U1437D-42R to 50R (815-892.5 mbsf) were scanned for elemental analysis with an ITRAX micro-Xray fluorescence (XRF) scanner at Kochi Core Center, Japan. These cores were selected to investigate changes in elemental composition related to the transition from low to elevated methane contents. XRF spectra were measured every 2 cm (exposure time: 10 s) with an X-ray beam generated with a 3 kW Mo target (run at 30 kV and 55 mA).

10.2.3.2. Carbon, Nitrogen, and Sulfur

Bulk geochemical sediment parameters were determined at Christian-Albrechts-University, Germany. Twenty sediments were oven-dried at 50 °C and ground to a homogeneous powder using agate pestle and mortar. Subsequently, the total carbon (TC), total nitrogen (TN), and total sulfur (TS) contents were determined on ~10 mg of sediment using a Vario EL III elemental analyzer. About 200 mg of each sediment sample were analyzed for the total organic carbon (TOC) content on an ELTRA CS-580A system. Prior to the TOC measurement, the powdered samples were each treated with 10 % and subsequently 25 % of hydrochloric acid (HCl) solution until no reaction to remove inorganic carbon. The amount of total inorganic carbon (TIC) as well as calcium carbonate ($CaCO_3$) was calculated as follows:

$$\text{TIC (wt\%)} = \text{TC} - \text{TOC, and}$$

$$CaCO_3\ \text{(wt\%)} = \text{TIC} \times 8.33, \text{ respectively,}$$

where 8.33 is the stoichiometric factor for C in $CaCO_3$.

10.2.4. DNA-Based Microbial Community Analysis

All the deep-frozen sediment samples (n = 14) used in this study were provided by Kochi Institute for Core Sample Research, JAMSTEC. The depth interval studied for a complete borehole profile of the microbial community at Site U1437 ranged from 97.3 to 1,655 mbsf. DNA was extracted from 5 g of each sediment sample using a DNeasy PowerMax Soil Kit (Qiagen, Tokyo, Japan) according to the manufacturer's instructions, except that zirconium beads instead of garnet beads were used to enhance disruption efficiency of microbial cells. The obtained DNA was further concentrated and purified by ethanol precipitation. Using the concentrated DNA, the 16S ribosomal RNA (rRNA) gene was quantified by microfluidic digital polymerase chain reaction (PCR) using domain specific primers as described by Hoshino et al. (2017). To determine the microbial community composition within the sediments, the V3-V4

hypervariable region of the 16S rRNA gene was amplified and sequenced followed by quality filtering and taxonomic identification according to Hoshino et al. (2017). Sample preparation before PCR amplification was performed in a clean laboratory to avoid contamination of DNA. All sequence data obtained in this study were submitted to the DNA Data Bank of Japan database under accession number DRA006351.

10.3. Results

10.3.1. Magnetic Mineral Contents

NRM, ARM, χ_{lf}, and SIRM are widely used as first-order proxies for magnetic mineral concentration. In the studied interval, they have similar down-core variations (Figure 10.1). ARM is between 2 and 10 times higher than NRM, except for three NRM spikes below 950 mbsf which are not matched in ARM. From ~775 to ~846 mbsf, the four indices have their highest values (Figure 10.1; Table 10.S1). No core material was recovered between 846 and 855 mbsf, but below this gap, the four parameters suddenly decrease by one to two orders of magnitude. They remain at this low level down to 1,002 mbsf, except for a small local maximum at 936-949 mbsf. χ_{hfield}, which is a proxy for the dia/paramagnetic component of magnetic susceptibility, has a similar pattern to the magnetic concentration-dependent parameters and decreases by a factor of 2 below ~846 mbsf (Figure 10.1). Based on these observations, four magnetic zones are defined as a function of depth. Zone 1 (775-846 mbsf) and zone 3 (936-949 mbsf) correspond to intervals with higher values of the aforementioned rock magnetic parameters, while zone 2 (855-936 mbsf) and zone 4 (949-1,002 mbsf) correspond to intervals with lower values of concentration-dependent rock magnetic parameters.

The lower concentration of magnetic minerals in zones 2 and 4 may be due partially to dilution caused by an increased proportion of carbonate matrix. The ferrimagnetic mineral concentration, however, can only be diluted by a factor of 2.5 at maximum (dilution factor = (100-0)/(100-60) where 0 and 60 are the minimum and maximum contents (wt%) of $CaCO_3$ in the studied samples, respectively, Figure 10.S2). Hence, carbonate dilution alone cannot explain the one to two order of magnitude decrease in NRM, χ_{lf}, and SIRM between zones 1 and 2, but it might explain the χ_{hfield} drop. Therefore, changes in the above rock magnetic parameters are considered to mainly reflect variations in magnetic mineralogy as expressed in a significant decline in the concentration of magnetic minerals between 846 and 855 mbsf (transition to zone 2).

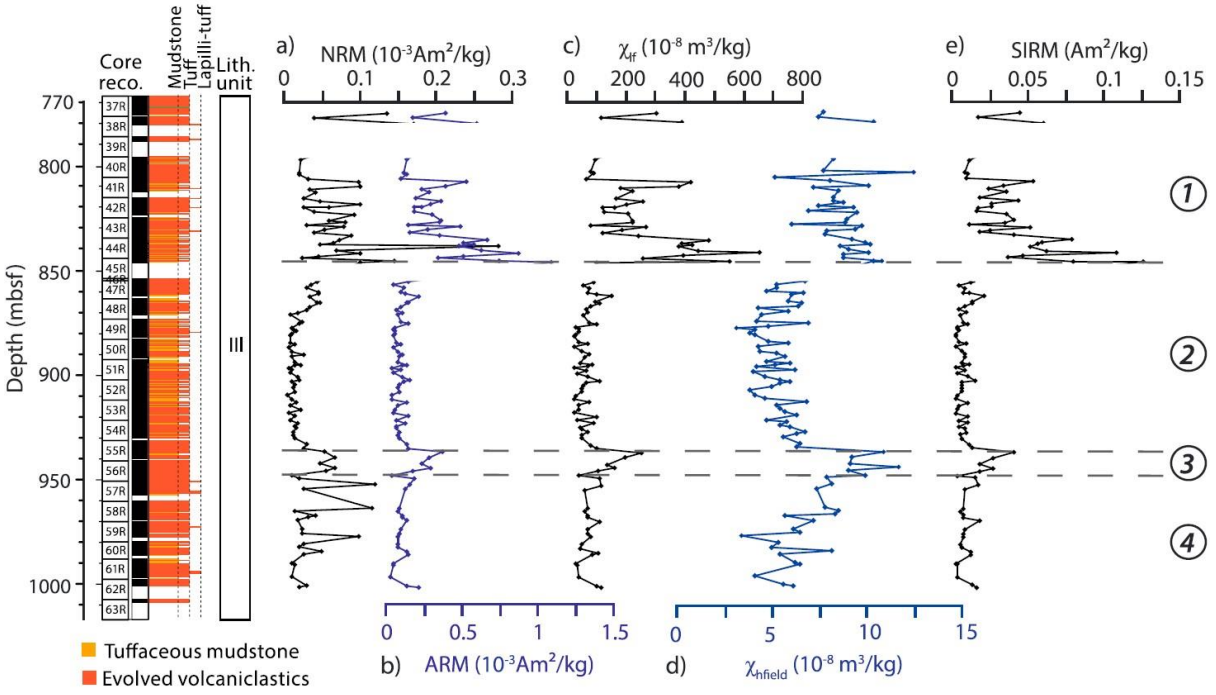

Figure 10.1 | Down-core variations of rock magnetic parameters in Hole U1437D. (a) Natural remanent magnetization (NRM), (b) anhysteretic remanent magnetization (ARM), (c) low-frequency magnetic susceptibility χ_{lf}, (d) high-field magnetic susceptibility χ_{hfield}, and (e) saturation isothermal remanent magnetization (SIRM) as a function of depth. Four magnetic zones are identified based on changes in the rock magnetic properties. Zones 1 and 3 correspond to higher rock magnetic parameter values; zones 2 and 4 correspond to lower values. Core recovery and lithology are indicated (from Tamura et al., 2015a). Evolved volcaniclastics are unaltered volcanic grains and clasts inferred to be intermediate and silicic in composition compared to basalt and basaltic andesite. mbsf = meters below sea floor.

10.3.2. Grain Size of the Magnetic Minerals

A slight increase in ARM/χ_{lf}, which is used as an indicator for the relative proportion of fine-grained to coarse-grained magnetite, between 870 and 950 mbsf, points toward finer magnetite grains (Figure 10.S4). ARM/SIRM is a more appropriate parameter when paramagnetism is dominant (Lu and Banerjee, 1994) and indicates a similar trend, which is supported by hysteresis loops (Figure 10.S5) and χ_{hfield} variations (Figure 10.1). ARM/SIRM is slightly higher in zone 2 (from ~870 mbsf) compared to adjacent zones, which may indicate that the magnetic grain size is finer in this interval (Figure 10.S4). However, ARM/χ_{lf} and ARM/SIRM are only valid as grain size indicators if one ferrimagnetic mineral dominates the magnetic mineral assemblage. Similarly, χ_{fd} (%)(=100×(χ_{lf}-χ_{hf})/χ_{lf}), which indicates the presence of superparamagnetic (SP) particles, is generally low (<3%) and does not vary significantly down-core, apart from local peaks that may indicate higher proportions of finer particles (Figure 10.S4).

Hysteresis ratios for the studied samples, M_{rs}/M_s versus B_{cr}/B_c, fall within the range expected for the vortex state (Roberts et al., 2017) in a Day et al. (1977) diagram, as expected for bulk

sediment analyses (Figure 10.S6; Roberts et al., 2012). More likely, such results reflect an assemblage of grains with sizes ranging from the single domain (SD) to multidomain (MD) states (Roberts et al., 2017). The complex mineralogy of the studied samples (see below) prevents reliable interpretation of ARM/χ_{lf} and ARM/SIRM and use of the Day diagram (Figure 10.S6) in terms of grain size (Roberts et al., 2018).

10.3.3. Magnetic Mineralogy

10.3.3.1. Coercivity

$S_{-0.3T}$ is slightly lower (~0.98-0.99) in zones 2 and 4 (Figure 10.2), which indicates a higher proportion of higher coercivity magnetic minerals. These may include hematite, which was inferred in the shallower part of Site U1437 (Kars et al., 2017), goethite, dissolution-resistant titano-hematite, or ferrimagnetic iron sulfides such as greigite and pyrrhotite that can have coercivities up to hundreds of milliteslas (Peters and Dekkers, 2003; Roberts et al., 2011). Mean B_c and B_{cr} values are 10.6 ± 1 and 27.6 ± 1.3 mT, respectively, which indicate a dominant low coercivity magnetic phase (Table 10.S1). B_c and B_{cr} are lower at the top of zone 2 and increase slightly down-core below 870 mbsf (Figure 10.2). The upper part of zone 2 (~855-869 mbsf) corresponds to a transition zone with lower ARM/SIRM, B_c, B_{cr}, and higher $S_{-0.3T}$; while the lower part of zone 2 (~869-936 mbsf) has higher ARM/SIRM, B_c, B_{cr}, and lower $S_{-0.3T}$.

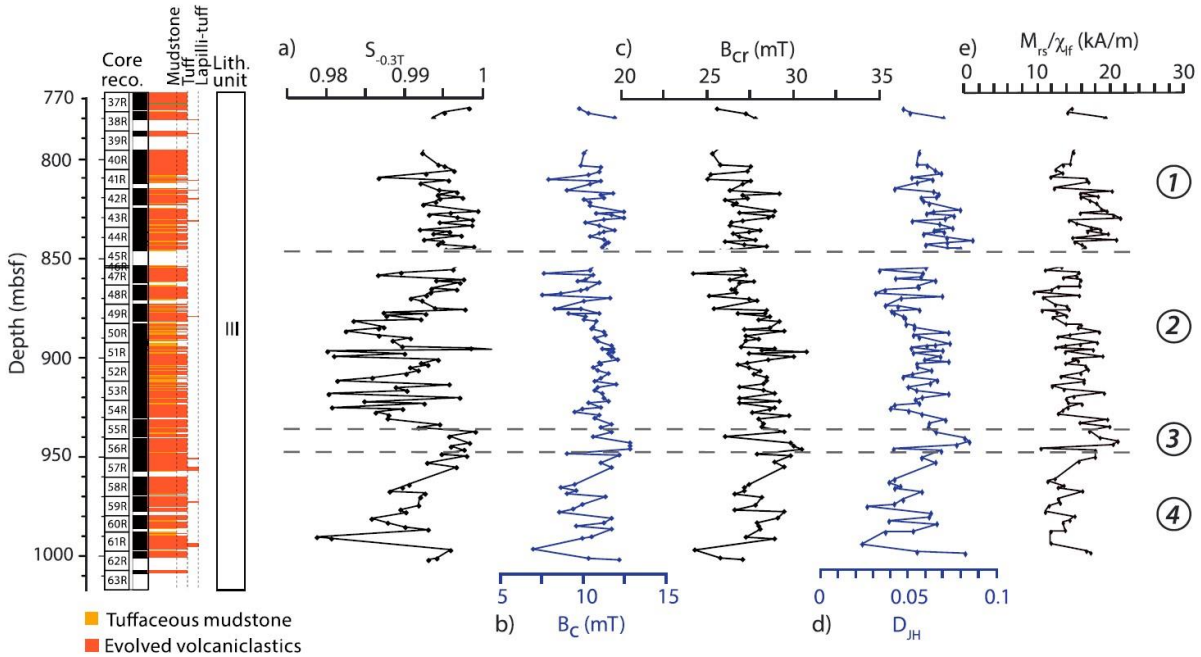

Figure 10.2 | Down-core variations of coercivity proxies in the studied interval at Site U1437. (a) $S_{-0.3T}$, (b) B_c, (c) B_{cr}, (d) D_{JH}, and (e) M_{rs}/χ_{lf}. The magnetic zones (1 to 4) are indicated. Note the $S_{-0.3T}$ decrease in zones 2 and 4 and higher D_{JH} values in zones 1 and 3. The upper part of zone 2 has lower coercivity values and represents a transition zone. Core recovery and lithology are indicated (from Tamura et al., 2015a). mbsf = meters below sea floor.

FORC diagrams indicate a mean coercivity of ~15-20 mT (Figure 10.S5) with a tail up to ~80-100 mT in each magnetic zone. The peak coercivity occurs at slightly higher values in samples from zone 2 compared to samples from zone 1. The closed contour lines and the triangular shape at low B_c values indicate the presence of vortex state (titano)-magnetite (Muxworthy and Dunlop, 2002; Roberts et al., 2000, 2017). FORC diagrams for samples from zones 1 and 3 have tighter distributions around the B_u = 0 axis; that is, they have less magnetostatic interactions than samples from zones 2 and 4. The optimum smoothing factor used to process FORCs generally requires greater smoothing for samples from zones 2 and 4 because of their relatively weaker magnetizations.

In methane-rich environments, particularly in gas hydrate-bearing marine sediments, M_{rs}/χ_{lf} (Larrasoaña et al., 2007) and D_{JH} (=(M_{rs}/M_s)/(B_{cr}/B_c)) (Housen and Musgrave, 1996) are used to identify high coercivity (SD) ferrimagnetic iron sulfides (greigite and pyrrhotite). In zones 1 and 3, these parameters have higher values compared to zones 2 and 4 (Figure 10.2). In zone 2, D_{JH} and M_{rs}/χ_{lf} decrease downhole in the transition zone and increase below. These higher values may suggest an increase in the proportion of ferrimagnetic minerals, likely greigite which forms during diagenesis (Larrasoaña et al., 2007; Musgrave and Kars, 2016). The lower values would reflect conversion of greigite into pyrite (pyritization) in the transition zone and zone 4. The elevated D_{JH} values may also reflect an increased SD relative to MD magnetite content. This is supported by ARM/χ_{lf} and ARM/SIRM, which both have higher values (= finer grain size) in the interval with high D_{JH}.

10.3.3.2. Low Temperature Magnetic Measurements

Low temperature magnetic measurements have characteristic magnetic signatures with respect to the magnetic zones (Figure 10.3). The RT-SIRM is one order of magnitude higher in samples from zones 1 and 3 compared to samples from zones 2 and 4 (Table 10.S2), which is consistent with a higher magnetic mineral content. All analyzed samples, regardless of the magnetic zone, undergo a RT-SIRM decrease on cooling at ~110-120 K, at around the Verwey transition temperature (T_V = 120 K) of magnetite (e.g., Muxworthy and McClelland, 2000; Özdemir et al., 2002; Verwey, 1939), which indicates the presence of this mineral in the samples. A lower T_V (~100-110 K) indicates that magnetite grains are nonstoichiometric (Ti substitution; Moskowitz et al., 1998), biogenic (Chang et al., 2016a), or slightly oxidized (Özdemir et al., 1993; Özdemir and Dunlop, 2010).

Remanence did not fully recover during warming back to RT, which may indicate a MD grain size in magnetite (Özdemir et al., 2002). Below 50 K, the remanence increases down to 5 K,

which probably provides evidence of a paramagnetic contribution due to the presence of clays or other paramagnetic minerals (e.g., iron sulfides and Fe-Mn carbonates; Aubourg and Pozzi, 2010; Kars et al., 2011).

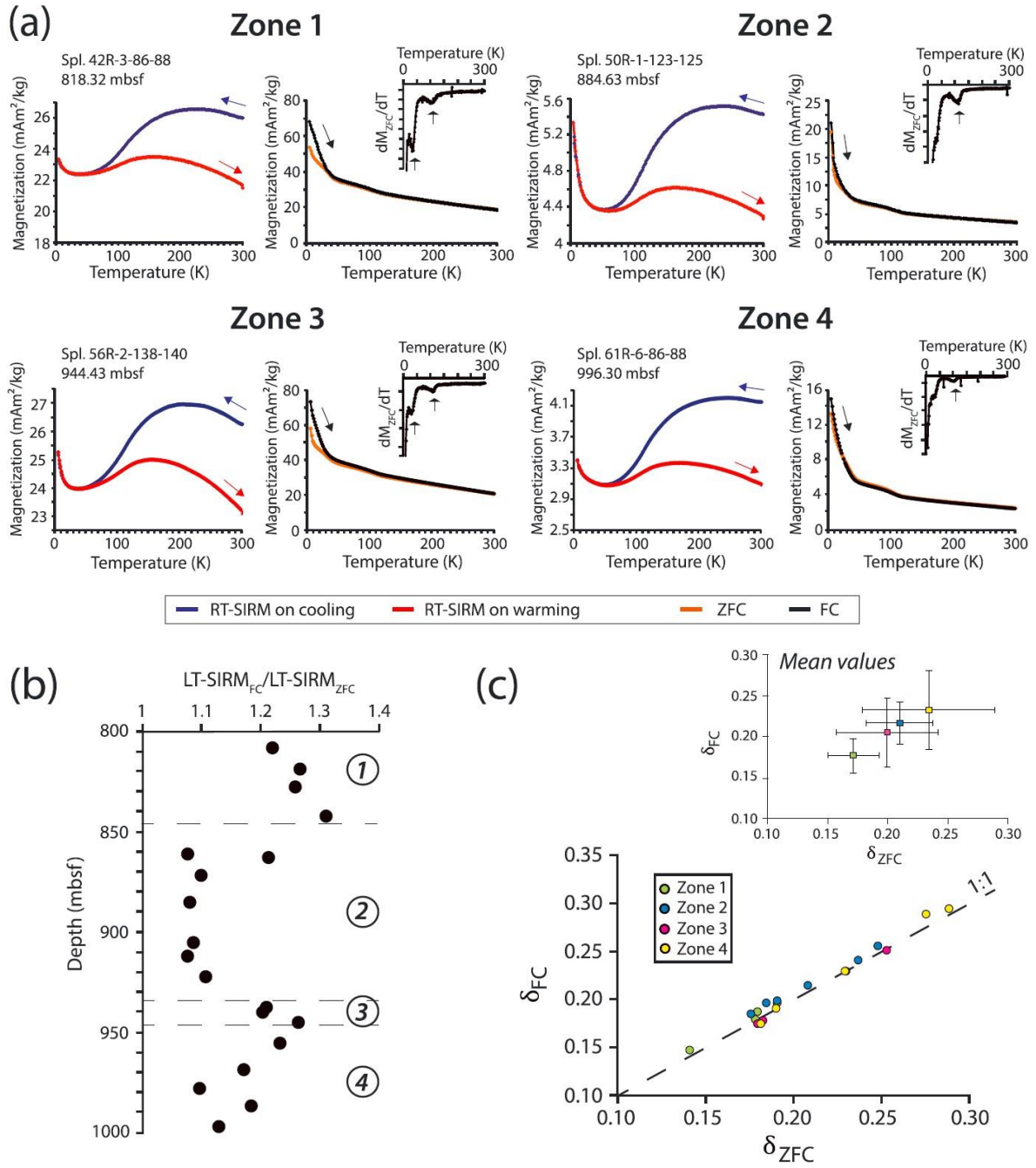

Figure 10.3 | Low temperature magnetic measurements for representative samples from the different magnetic zones. (a) RT-SIRM cycle, ZFC, and FC curves. RT-SIRM cycling indicates an incompletely recovered Verwey transition at ~110-120 K, which suggests the presence of coarse-grained (titano)-magnetite. LT-SIRM results have an additional magnetic phase with a transition at ~32-34 K (first derivative of ZFC in inset) for samples from zones 1 and 3; (b) $LT\text{-}SIRM_{FC}$ / $LT\text{-}SIRM_{ZFC}$ as a function of depth (note the higher values for zones 1 and 3); (c) δ_{FC} versus δ_{ZFC} with a 1:1 distribution. mbsf = meters below sea floor; RT-SIRM = room temperature saturation isothermal remanent magnetization; LT-SIRM = low temperature saturation isothermal remanent magnetization; ZFC = zero-field-cooled; FC = field-cooled.

By contrast, LT-SIRM behavior varies between the magnetic zones. The loss of remanence for the ZFC curve at 30 K for zones 2 and 4 is twice the decrease for zones 1 and 3 (40-62 % *vs*. 20-27 %, respectively), which suggests a higher proportion of SP particles that undergo blocking to the stable SD state in samples from zones 2 and 4 (Passier and Dekkers, 2002) (Figure 10.3b, Table 10.S2). Both ZFC and FC curves for all analyzed samples have a clear break-in-slope at ~110 K, which is revealed as a peak in the first derivative of the curves (inset in Figure 10.3a) and indicates the occurrence of (titano)-magnetite. The derivative does not reveal, however, clear evidence of the two peaks that are indicative of a mixture of biogenic (~100 K) and detrital (inorganic) magnetite (~120 K; Chang et al., 2016a) as found at the top of Hole U1437B (Kars et al., 2017). SD biogenic magnetite (due to magnetofossils) is not identified, which probably indicates dissolution of fine-grained particles. In contrast to samples from zones 1 and 3, which have divergent ZFC and FC curves at low temperatures (<50 K), samples from zones 2 and 4 have nearly superimposed ZFC and FC curves. ZFC derivative curves for samples from zones 1 and 3 additionally have a second break-in-slope at ~32 K. This break-in-slope represents an additional magnetic phase that is not visible in RT-SIRM cycling. This is likely because the magnetic minerals responsible are SP-stable SD or paramagnetic at RT and do not acquire a remanence. During cooling, some minerals that are paramagnetic at RT become magnetic when they pass through their Néel temperature (T_N; Dunlop and Özdemir, 1997). By applying a strong magnetic field below T_N, the Néel transition of these minerals is emphasized in the ZFC and FC curves. There are three known candidates with a magnetic transition temperature between 30 and 40 K: siderite ($FeCO_3$) with T_N ~38 K (Frederichs et al., 2003; Housen et al., 1996), rhodochrosite ($MnCO_3$) with T_N ~32 K (Frederichs et al., 2003; Kosterov et al., 2006), which both have a spin-canted remanence below T_N (Frederichs et al., 2003), and monoclinic pyrrhotite (Fe_7S_8) with the Besnus transition at ~32-34 K (Besnus and Meyer, 1964; Dekkers et al., 1989; Rochette et al., 1990; Volk et al., 2016). The inflection is observed at ~32 K, so monoclinic pyrrhotite or rhodochrosite are most likely. However, low-temperature magnetic measurements are not diagnostic of the presence of authigenic greigite and magnetic hexagonal pyrrhotite. Greigite lacks any low-temperature magnetic transition and exhibits only a negligible difference between FC and ZFC curves (Chang et al., 2009; Roberts et al., 2011). Authigenic hexagonal pyrrhotite that forms in gas hydrate/methane seepage environments and that is magnetic at RT (Horng, 2018) also lacks a low-temperature magnetic transition (Horng and Roberts, 2018).

The thermomagnetic curves (Figure 10.S7a) do not contain any clear break-in-slope at ~320-350 °C; only a slight change is observed for zones 1 and 3 that might indicate ferrimagnetic

iron sulfides. The repeated heating-cooling cycles with increased final temperature in the 300-370 °C temperature range (Figure 10.S7b) are reversible and do not support unambiguously the occurrence of monoclinic pyrrhotite in the samples (Dekkers, 1989). It is, thus, likely that the observed additional phase in zones 1 and 3 at low temperature is rhodochrosite which may occur in solid solution $(Fe,Mn)CO_3$ with siderite.

The parameters δ_{FC} and δ_{ZFC} represent the amount of remanence lost during warming through T_V for FC and ZFC curves, respectively, and are calculated according to the formula of Moskowitz et al. (1993): $\delta = M_{80K}\text{-}M_{150K})/M_{80K}$, where M is the magnetic moment at a given temperature. The ratio δ_{FC}:δ_{ZFC} is close to 1:1 for samples through all four zones (Figure 10.3c). This distribution could reflect a difference in concentration and/or grain size distribution of (titano)-magnetite particles (Moskowitz et al., 1993). Higher δ_{FC} and δ_{ZFC} in zones 2 and 4, compared to zones 1 and 3 (inset Figure 10.3c), may indicate a higher proportion of SP-stable SD particles, which are evident in these zones from the pronounced LT-SIRM decrease between 5 and 30 K.

Our rock magnetic results are supported by scanning electron microscope observations of (titano)-magnetite in the MD size range (tens of micrometers) in zone 1 (Figure 10.S8). No coarse-grained (titano)-magnetite was observed in zone 2, but small numbers of fine-grained iron oxides are present. In addition, framboidal pyrite (~10-µm diameter) and aggregates of pyrite grains are observed in samples from zone 1, whereas submicron euhedral iron sulfide grains with no clear clustering are more common in zone 2 (Figure 10.S8). These observations, however, were made on only three samples and may not be representative for the entire sample set. Yet pyrite is clearly visible on cut core surfaces at Site U1437, associated with burrows in greenish clay-rich layers that probably contain glauconite (Musgrave and Kars, 2016; Tamura et al., 2015a).

10.3.4. Bulk Solid Phase Analysis

10.3.4.1. XRF Profiles

XRF scans on cores for the depth interval between 815 and 892.5 mbsf, which spans parts of zones 1 and 2 (Figure 10.S9), indicate a downward decrease of the major elements Fe and Ti, which correlate positively (R^2~0.86). Mn/Fe and Mn/Ti have largely similar trends. They increase downward in zone 2 by a factor of 2 due to the decrease in Fe and Ti contents (Mn is relatively constant), as confirmed by the magnetic susceptibility and magnetization decrease (Figures 10.1a, 1c, and 1e). S and S/Cl (proxy for pyrite authigenesis) do not vary significantly between zones 1 and 2 over the scanned depth interval. This, and higher Fe/S in

zone 1, indicates that iron oxides are more susceptible to diagenetic redox changes than iron sulfides in zone 2. V/Al has higher values in zone 1 and together with a higher sulfur content may indicate more reducing (euxinic) depositional conditions in zone 1 compared to zone 2 (Algeo and Maynard, 2004; Tribovillard et al., 2006). This may suggest that rock magnetic property and mineralogy variations are due to postdepositional changes.

10.3.4.2. C, N, and S Elemental Analysis

TC is mainly dominated by TIC. Higher TC and $CaCO_3$ values occur in zone 2 and in the lower part of zone 4, in intervals of lower magnetic susceptibility and remanence (Figure 10.4, Table 10.S3). TS is generally below 0.2 wt%, except for one sample at ~922 mbsf (Figure 10.4, Table 10.S3). Zones 2 and 4 have higher TS and $CaCO_3$ concentrations, unlike the higher magnetization zones 1 and 3. TOC varies between 0.18 and 0.55 wt% (Figure 10.4, Table 10.S3), and TN is generally low (<0.05 wt%; Table 10.S3). No specific trend with respect to the magnetic zones is recognizable for TOC and TN.

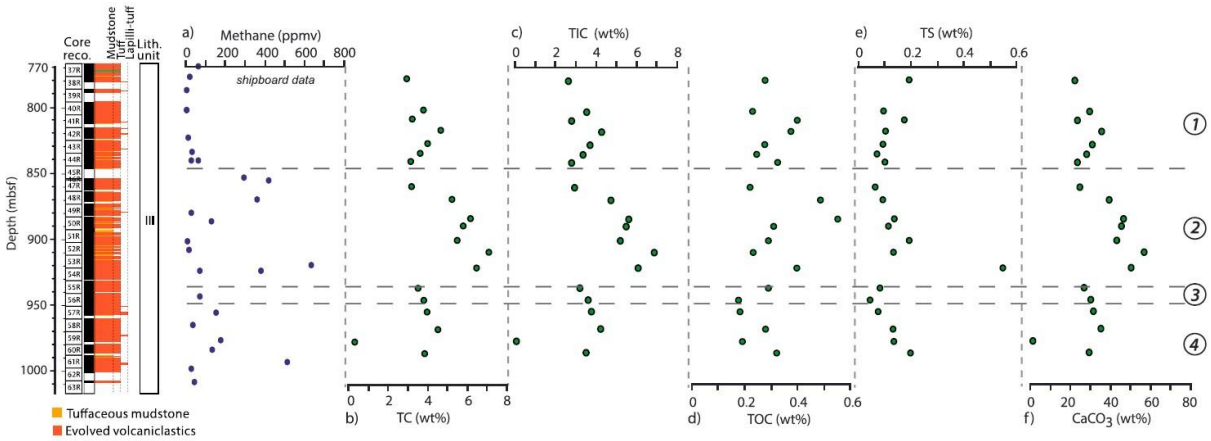

Figure 10.4 | Down-core variations of (a) methane (shipboard data), (b) total carbon (TC), (c) total inorganic carbon (TIC), (d) total organic carbon (TOC), (e) total sulfur (TS), and (f) $CaCO_3$ in the 770-1,010-mbsf depth interval. Note the increase in $CaCO_3$ content in zone 2, which may have altered the magnetic mineral concentration by dilution. Reported shipboard data, core recovery, and lithology are from Tamura et al. (2015a). The magnetic zones identified in this study are indicated. mbsf = meters below sea floor.

10.3.5. Microbiological Analyses

Microbiological analyses indicate relatively small numbers of archaea and bacteria (<0.2×10^3 and <$0.2\text{-}12 \times 10^3$ copies per gram sediment, respectively) in deep-sea sediments from Site U1437 (Figure 10.S10) with <2 and ~50-170 copies per gram sediment, respectively, for the 775-1,002-mbsf depth interval. Due to the low biomass volume in the sediments, potential contaminants are overrepresented in the obtained sequence libraries (Salter et al., 2014) and may originate from the chemicals used for DNA extraction and PCR.

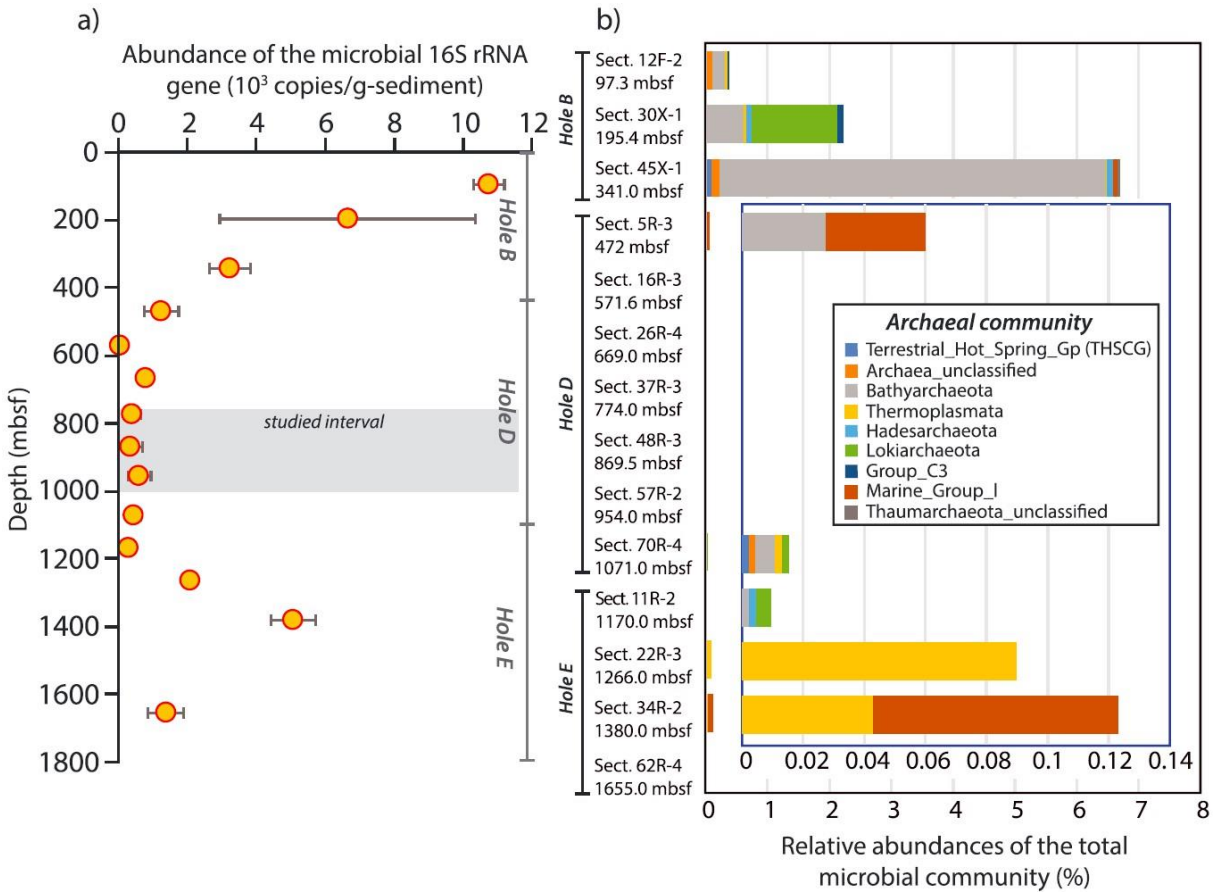

Figure 10.5 | Microbiological analyses for Site U1437. (a) Depth profile of 16S rRNA gene abundance determined by digital polymerase chain reaction and (b) archaeal community composition at class level. The inset is a zoom-in view of low relative 16S rRNA abundance for samples at depths between 472 and 1,380 mbsf, which includes the target stratigraphic interval of this study (~775-1,002 mbsf). mbsf = meters below sea floor; rRNA = ribosomal RNA.

We exclude those potential contaminants from analysis by subtracting sequences found in negative control experiments from the sequence libraries constructed from the sediment samples. Microfluidic digital PCR provides an accurate number of the 16S rRNA gene sequences in the sediment samples (Hoshino and Inagaki, 2012). At 97.3 mbsf, the abundance of microbial 16S rRNA genes is 1.08×10^{4} copies per gram sediment, which generally decreases with depth to 3.11×10^{1} copies per gram sediment at 571 mbsf (Figure 10.5a). The abundance of 16S rRNA genes remains as low as 10^{2} copies per gram sediment in the interval between 669 and 1,071 mbsf and then increases again below 1,071 mbsf before peaking at 1,380 mbsf.

10.4. Discussion

The most drastic magnetic property and mineralogy changes in the studied stratigraphic interval at Site U1437 occur when passing from zone 1 to zone 2. Lack of core recovery in the ~9-m interval from ~846 to 855 mbsf could be the result of lithological factors such as a higher porosity interval or the presence of a fault. No magnetic chrons and subchrons are missing, which suggests a continuous record (Musgrave and Kars, 2016). It is, therefore, unlikely that the changes in magnetic properties between zones 1 and 2 are due to a nonidentified sedimentary hiatus. This is supported by downhole logging results which do not change at that depth (Tamura et al., 2015a). Unlike the top of Hole U1437B (0-120 mbsf) where the magnetic mineral assemblage reflects interglacial/glacial climatic cycles for the last 1 Myr (Kars et al., 2017), no such correlation is observed in the studied interval (4.5-6 Ma) that spans the Miocene-Pliocene transition that occurs at ~890 mbsf within zone 2. It is, nevertheless, possible that variations in (titano)-magnetite minerals in the studied samples (e.g., $S_{-0.3T}$) are partially due to variations in terrigenous sediment supply. Iron oxides would have been preserved as inclusions within sheet silicates and would not have been affected by diagenesis (Chang et al., 2016b; Shi et al., 2017). That may explain why Musgrave and Kars (2016) were able to establish a reliable magnetostratigraphy in the studied interval. Elemental composition variations are more likely associated with redox conditions rather than with detrital provenance. The lithostratigraphy in the studied interval of Hole U1437D is homogenous, with no evidence of change in source provenance (Tamura et al., 2015a). Changes in redox conditions are likely associated with a stronger release of methane below ~850 mbsf (Figure 10.S2), either by local methanogenesis or transport (migration) into zone 2. Hence, magnetic property and mineralogy changes, especially from zone 1 to zone 2, are interpreted to be related mainly to postdepositional diagenetic processes.

10.4.1. Dissolution and Authigenic Magnetic Mineral Formation

Rock magnetic results indicate that vortex state to MD (titano)-magnetite is the dominant magnetic phase throughout the deep methanic zone and more generally at Site U1437 (Kars et al., 2017; Musgrave and Kars, 2016). Greigite has been identified in a series of intervals representing repeated phases of nonsteady state diagenesis in the sediment sequence above the deep methanic zone (Musgrave et al., 2017), but its presence within the deep methanic zone is difficult to assess based solely on the magnetic data presented here. Similarly, the presence of pyrrhotite is not confirmed unambiguously.

The lower $S_{-0.3T}$ values in zones 2 and 4 may be explained by a higher contribution to the remanence of higher coercivity minerals compared to the adjacent zones 1 and 3 (Figure 10.2a). This is likely to be the result of preferential dissolution of detrital (titano)-magnetite in these zones, possibly combined with preferential survival of detrital hematite (Kars et al., 2017) and local authigenesis of SD greigite (Musgrave et al., 2017). It has previously been reported that hematite is more resistant to dissolution than (titano)-magnetite (e.g., Emiroglu et al., 2004; Liu et al., 2004; Yamazaki et al., 2003). The decrease in (titano)-magnetite contents, with preferential dissolution of fine over coarse grains (Figure 10.3c), is supported by a lower Fe content (Figure 10.S9) and lower magnetic susceptibility and remanence in zone 2 (Figure 10.1). If (titano)-magnetite is assumed to be the main magnetic remanence carrier, the maximum (titano)-magnetite concentration c decreased by one order of magnitude from ~600 ppmv (zone 1) to ~60 ppmv (zone 2) with c = RT-SIRM$_{300K}$/M_{rs} (M_{rs} = 10 Am^2/kg for MD magnetite; Maher and Thompson, 1999; Table 10.S2). Zones 2 and 4 are also characterized by a higher proportion of SP particles (Figure 10.3b), which might correspond to the newly formed SP greigite (Musgrave et al., 2017; Rowan et al., 2009).

Higher values of D_{JH} and M_{rs}/χ_{lf} in zones 1 and 3 (Figure 10.2) seem to indicate the presence of SD greigite, which forms at shallower depth during diagenesis and is preserved during burial in a restricted sulfate reduction environment, likely in association with pyrite (Ebert et al., 2018; Musgrave and Kars, 2016; Musgrave et al., 2017), or that forms during methane diagenesis (e.g., Horng, 2018; Larrasoaña et al., 2007). Authigenic SD greigite has been recognized as responsible for remagnetized intervals at Site U1437 and is identified in sediments as deep as ~632 mbsf where pyritization has not yet been completed (Musgrave and Kars, 2016). D_{JH} and M_{rs}/χ_{lf} decrease in the transition zone (before partly recovering from ~870 mbsf) and zone 4, so authigenic SD greigite is likely to have transformed into pyrite in both zones. Pyrite is ubiquitous at Site U1437 and is identified throughout the entire sequence, where it is observed on core surfaces and thin sections (Figure 10.S8; Musgrave and Kars, 2016). The magnetic mineral assemblage is dominated by coarse-grained, vortex state- MD (titano)-magnetite, so it is probable that the decrease in D_{JH} also partially reflects dissolution of fine-grained (titano)-magnetite (Musgrave and Kars, 2016) in the transition zone and zone 4. Increased D_{JH} (and M_{rs}/χ_{lf}) in zone 2 (~896-936 mbsf), along with higher ARM/SIRM values may indicate a new generation of greigite (SP/SD grains) as a result of continued exposure to high methane contents.

The interpreted changes in magnetic mineralogy are sketched in Figure 10.6. The magnetic mineral assemblage of zone 1 is referred to as “above”, in contrast to the “below” magnetic

mineral assemblage of zone 2. The terms “above” and “below” are defined with respect to the ~9-m-thick interval between zones 1 and 2 where no core was recovered (i.e., ~846-855 mbsf). Zone 1 is magnetically dominated by coarse-grained (vortex state-MD) (titano)-magnetite, possible detrital fine-grained hematite, authigenic SD greigite, and possible authigenic pyrrhotite (“above” assemblage). Zone 2 is composed of finer-grained (titano)-magnetite, surviving hematite, and possible SP greigite (“below” assemblage). In the transition zone at the top of zone 2, greigite has been entirely converted into pyrite, while deeper in zone 2, a new population of SP greigite may have been formed. Zone 3 has the same magnetic mineral assemblage as zone 1 and can be considered as a relict of the “above” assemblage despite some degree of alteration. Zone 4 has the same characteristics as zone 2. Pore water data are lacking in the studied interval, so part of the interpretation remains unconfirmed.

10.4.2. Role of Methane and Porosity

The studied interval is characterized by a stronger release of methane below 855 mbsf, in a zone where the most significant magnetic mineralogy changes are observed. Whether methane is produced *in situ* (by methanogenesis) or transported upward from deeper sources, or both, cannot be determined unambiguously based on our data set.

Zone 1 has the lowest methane concentrations (<80 ppmv) with a small increase near its base likely from upward diffusion from the top of zone 2 (Figure 10.6). Porosity throughout zone 1 declines systematically from 52 % near the top to 22 % near its base, consistent with compaction due to increasing burial. Methane suddenly appears in comparatively high concentrations in the transition zone (up to 400 ppmv), which is characterized by locally increased porosity (up to 50 %). The porosity increase is due to the presence of more abundant ash and lapilli tuffs (Tamura et al., 2015a). Methane accumulates in the transition zone because the base of zone 1 acts as a seal due to its lower porosity (~20 %) and presumed lower permeability (mostly clay-rich sediments). Zone 2 (below the transition zone) has both high (650 ppmv) and low (~10 ppmv) methane concentrations. Porosity generally decreases throughout zone 2 but some intervals with higher values occur. Some methane could be trapped below the low porosity seal-like intervals of zone 2, because high methane contents occur in places where porosity is higher. Methane would be expected to migrate upward through these porous zones and accumulate in the transition zone below the seal at the base of zone 1. In zone 3, only one methane gas analysis has been performed (the obtained value of ~80 ppmv is a low concentration), but this zone has higher porosity values than those in zone 2. The lack of low porosity intervals (i.e., seals) in zone 3 does not allow gas to be trapped. Therefore, methane has likely migrated upward into

zone 2 and has accumulated below 900 mbsf where low porosity intervals are present. This may partly explain the highest methane count at 920 mbsf (638 ppmv).

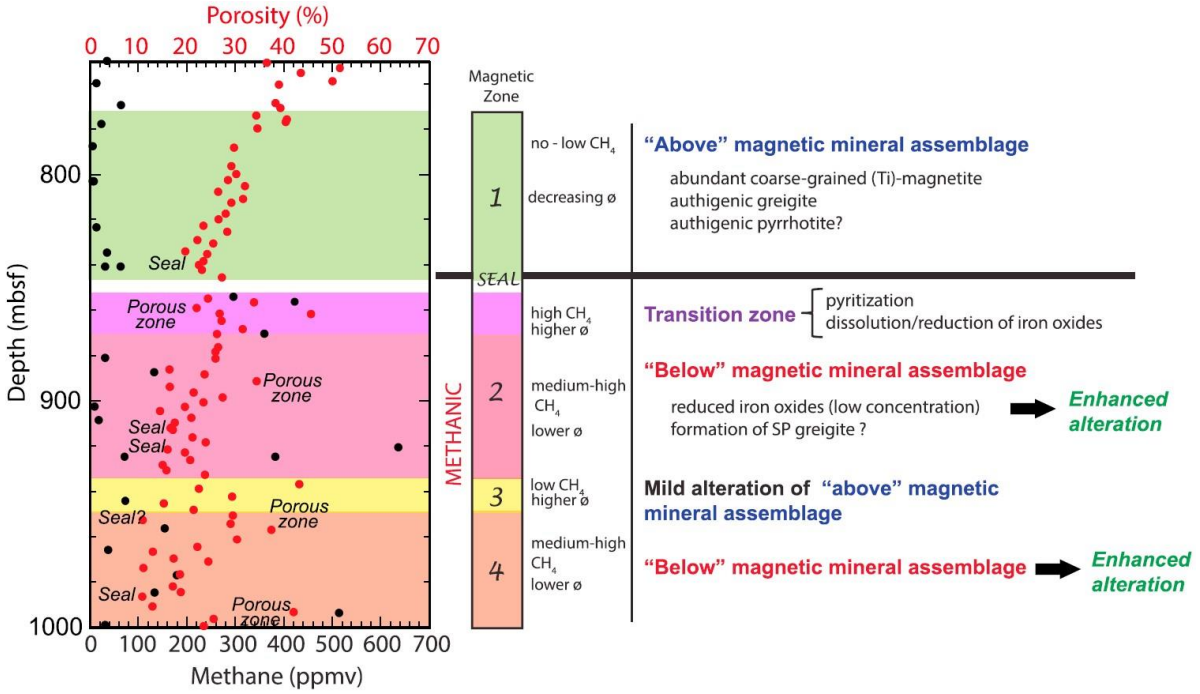

Figure 10.6 | Down-core variations of methane (CH_4) and porosity (ϕ) in the studied stratigraphic interval (data from Tamura et al., 2015a) with corresponding magnetic zones and magnetic mineral assemblages. mbsf = meters below sea floor; SP = superparamagnetic.

Hydrocarbon gas is not accumulating in zone 3, so one can expect less magnetic mineral reduction in that interval, which seems to be the case (with similar magnetic mineral assemblage and magnetic properties to zone 1). Zone 4 again has generally decreasing porosity with depth, with mixed low and high values similar to those of zone 2. Methane in zone 4 also occurs in low and high concentrations. The highest methane value (~515 ppmv) occurs in a porous interval around 994 mbsf near the base of the zone and immediately below a low porosity interval at ~985 mbsf.

Higher methane contents below ~855 mbsf are associated with enhanced alteration of the above magnetic mineral assemblage, which is converted into the below magnetic mineral assemblage. By contrast, lower methane contents favor preservation of the above magnetic mineral assemblage. Rock magnetic properties and the reduction (dissolution) of iron oxides may be explained by the presence of methane and the associated processes discussed below.

10.4.3. Possible Mechanisms Responsible for Magnetic Mineral Alteration

Possible mechanisms to explain the observed rock magnetic properties, and the formation and alteration of magnetic minerals, are given below. The discussed mechanisms are not exclusive, and other processes may have occurred.

10.4.3.1. Microbially Driven AOM

After an initial phase of sulfate reduction that drives the sulfate decline from the seafloor to a minimum at about 50 mbsf, the sulfate content at Site U1437 increases again down-core to return to sea-water compositions at about 460 mbsf, below which it slowly decreases again (Figure 10.S2). Sulfate concentrations are still high at ~700 mbsf. Whether sulfate remains high or decreases drastically, especially from ~850 mbsf when methane suddenly appears in zone 2, cannot be determined because of the lack of pore water analyses below 700 mbsf. A high sulfate content above ~850 mbsf would have prevented methanogenesis by inhibiting the activity of methanogenic archaea (e.g., Treude et al., 2014), perhaps restricting methanogenesis to the deep methanic interval observed here. Methane production by microbial activity could have been enhanced by deeper fluid circulation as observed in mud volcanoes where clay mineral dehydration (>60 °C) leads to the stimulation of methanogenesis (Ijiri et al., 2018).

In a shallow SMT, that is, within the first few meters below the sediment-water interface, methane is consumed mainly by anaerobic oxidation (e.g., Treude et al., 2005). TOC is low in the studied sediments (<0.4%, Figure 10.4), so AOM ($CH_4 + SO_4^{2-} \rightarrow HS^- + HCO_3^- + H_2O$) is likely favored over organoclastic sulfate reduction, as is the case in gas hydrate environments (e.g., Pohlman et al., 2013). In this simplest case where one assumes an AOM reaction in the transition zone, sulfate would decrease inversely proportionally to methane from the interval below. Hydrogen sulfide produced by AOM at this deep SMT would react with dissolved iron (from the reduction of iron oxides) to form iron sulfides, such as observed in this study. Another argument in favor of AOM is the simultaneous precipitation of authigenic carbonate minerals (such as aragonite; Bohrmann et al., 1998; Peckmann et al., 2001; Sivan et al., 2007).

Alternatively, AOM can occur without the participation of sulfate (Beal et al., 2009; Riedinger et al., 2014; Roberts, 2015; Segarra et al., 2013). Iron reduction (release of Fe^{2+}) in the methanic zone concurrent with significant methane concentrations, as is the case for Site U1437 (Figure 10.S2), could indicate a sulfate-independent Fe-AOM reaction (as opposed to the sulfate-mediated AOM reaction at shallow SMTs; Riedinger et al., 2014). An Fe-AOM reaction could explain the lower magnetic mineral content and susceptibility by dissolution of Fe^{3+}-bearing

magnetic minerals. In the studied interval, carbonate concentrations increase by a factor of 1.5-2 in zone 2, in which we expect AOM to have occurred (Figure 10.4).

In shallow environments, AOM and Fe-AOM are performed by anaerobic methanotrophic archaea with or without participation of sulfate-reducing bacteria (Boetius et al., 2000; Milucka et al., 2012). The present-day temperature in the studied interval ranges from 67 to 85 °C, and it is not known whether microorganisms involved in shallower biogeochemical processes are metabolically active under these more extreme environmental conditions. The steep decrease of 16S rRNA (Figure 10.5) may be due to high burial temperature, which damages constituents (e.g., DNA or amino acids) of microbial cells. In energy-limited environments such as the deep subseafloor (limited availability of nutrients and/or electron acceptors), it is difficult to repair damaged cell material because the energetic cost of repair increases as a function of depth/temperature (Inagaki et al., 2015), which may explain the low abundance of 16S rRNA in deeper portions of the investigated sediment sequence. In addition, microbial cell abundances decline with depth because microbes in subseafloor sediments are generally also fewer in number (Kallmeyer et al., 2012).

Although the mechanism of AOM coupled with metal oxide reduction (Fe-AOM or Mn-AOM; Riedinger et al., 2014) is not yet fully understood and the microorganisms involved in this process are largely unknown (Ettwig et al., 2016), identified methane oxidizers are similar to those employing sulfate-dependent AOM, which all belong to the class *Methanomicrobia*. In this study, *Methanomicrobia*-related 16S rRNA sequences were not found throughout the sedimentary sequence, perhaps partly because of the low concentrations of DNA-extractable microbial cells.

10.4.3.2. Iron Reduction by Methanogens

Methanogens, such as those belonging to the genus *Methanosarcina*, are able to cease methane production and reduce iron oxides in sediments with high methane concentrations by using iron oxides as substrates (Sivan et al., 2016). At Site U1437, iron oxide reduction in zones 2 and 4, where methane accumulates, could be alternatively explained by this process. Instead of producing methane, methanogens here may reduce iron oxides and release Fe^{2+} in pore water. Increased dissolved iron in pore water is supported by Fe decrease in the solid phase (Figure 10.S9). High dissolved iron and methane contents would coexist in the methanic zone. *Methanosarcina*-related 16S rRNA sequences, however, are not identified in the samples analyzed in this study, likely due to the low concentration of extractable DNA (see section 10.4.3.1.). Alternatively, it is also plausible that the process of iron oxide reduction is more

widespread but not recognized yet in archaea of the deep biosphere such as those found in our study.

10.4.3.3. Thermal Degradation of Organic Matter: Catagenesis

The present-day burial temperature of the deep methanic zone (~67-85 °C) corresponds to the beginning of the oil window in petroleum systems where low concentration of light hydrocarbons (e.g., thermogenic methane and ethane) may be produced from sedimentary organic matter decomposition during burial (Tissot et al., 1987). Methane is the only hydrocarbon gas detected in Hole U1437D, and its measured concentration does not exceed 640 ppmv (Figure 10.S2). From Figure 10.4, it can be concluded that TOC and methane contents do not correlate well, which may suggest that methane is not produced *in situ* but that it formed in a deeper part of the sediment column (i.e., in the gas window, >90 °C) and that it was transported upward via faults or porous zones. Co-occurrence of thermogenic and biogenic methane is, however, not excluded at Site U1437.

Low sediment magnetic susceptibility and magnetization associated with higher and heavier hydrocarbon gas contents have been identified previously in Nankai Trough sediments at Ocean Drilling Program (ODP) Leg 131 Site 808 where the burial temperature is around 75 °C (Lu and Banerjee, 1994). These authors proposed that organic matter is mature in the low magnetic intensity zones and that its thermal decomposition was responsible for magnetic mineral transformation (magnetite dissolution). CO_2 production by catagenesis results in reduction of Fe^{3+}, which causes dissolution of (titano)-magnetite, similar to the organoclastic reduction at shallower depths. At ODP Site 808, (titano)-magnetite dissolution in the low intensity zones corresponds to intervals where $CaCO_3$ and TS are higher (Lu and Banerjee, 1994). Calcite is precipitated as CO_2 is released in pore water and reacts with available Ca^{2+}. The higher TS content has been attributed to organic matter decomposition and subsequent formation of pyrite in the low intensity zones (Lu and Banerjee, 1994). We observe similar relationships at Site U1437, with iron reduction associated with Fe^{3+}-bearing magnetic mineral dissolution, precipitation of carbonate ($CaCO_3$), and slightly higher TS values in low magnetization zones (zones 2 and 4; Figure 10.4).

Site 1174, which was drilled during ODP Leg 190, is located ~2 km away from Site 808 and has a pore-water profile, organic matter, and geochemical data as well as magnetic zones similar to those observed at Site 808 (Moore et al., 2001). Light hydrocarbons (e.g., propane) are found in sediments at ~400-700 mbsf where, unlike Site 808, maturity is not high enough to generate such hydrocarbons, which indicates that the propane migrated into overlying sediments (Moore

et al., 2001). Burial temperatures at Sites 808 and 1174 are generally higher than those at Site U1437 (~120 and ~180 °C/km, respectively, versus 83 °C/km). Despite the high thermal gradients, an overlap between active catagenesis and living systems has been found in Nankai Trough at Site 1174 (Horsfield et al., 2006). Abiotic thermal degradation reactions are ongoing in the same part of the sediment column where a deep biosphere exists even if TOC is low (average of 0.4 wt%; Horsfield et al., 2006).

10.4.3.4. Alteration of Volcanic Ash

The studied interval contains numerous evolved ash layers (tuffs) with compositions ranging from basaltic andesite to dacite (SiO_2 <70 %; Tamura et al., 2015a). Florindo et al. (2003) showed that dissolution of silicic volcanic ashes leads to high pore-water silica concentrations based on a survey of widely distributed ODP sites. Magnetite is unstable in environments with elevated pore-water Si concentration and is dissolved rapidly to produce Fe-bearing smectite (Florindo et al., 2003). Magnetite dissolution by this process would cause lower magnetization and lower susceptibility. At Site U1437, no diatoms or siliceous plankton are observed below 483 mbsf (Tamura et al., 2015a). If pore waters in the studied interval once contained high dissolved Si contents from the dissolution of originally deposited siliceous organisms and volcanic ashes, the lower magnetic mineral concentration and magnetic susceptibility observed in zone 2 might also be explained by (titano)-magnetite dissolution to produce Fe-rich clays. This may be supported by the observation that Lithologic Unit III in Hole U1437D contains alteration features with greenish layers rich in chlorite or mixed-layer chlorite-smectite (Tamura et al., 2015a).

10.5. Conclusions

Rock magnetic properties and mineralogy of deeply buried sediments at Site U1437 are used to define four successive magnetic zones associated with distinct methane concentrations. Zone 1 in the methane-poor interval is characterized by higher contents of coarse-grained (titano)-magnetite with high coercivity minerals and greigite. The upper part of zone 2 is a transition zone sharing similarities with zone 1. In contrast with zone 1, zone 2 in the methane-rich interval has lower proportions of magnetic particles because these minerals have undergone reduction/dissolution, as well as some degree of dilution due to secondary $CaCO_3$ precipitation. Zone 3 contains a remnant of the magnetic mineral assemblage present in zone 1, where active alteration is ongoing. Zone 4 has similar geochemical and magnetic properties as zone 2.

Dissolution of (titano)-magnetite grains is enhanced in intervals where methane has accumulated below overlying low porosity sediments that act as seals. This scheme occurs repeatedly in the studied interval, where seals are recognized at the bottom of zone 1, at the transition zone, and at zone 3. Within the limits of the currently available data and constrained by the lack of pore water data in the studied interval between 775 and 1,002 mbsf, it is not possible to be conclusive about the mechanism(s) responsible for magnetic mineral alteration in the deep methanic zone. Although geochemical processes due to methane occurrence are more likely, it is highly probable that more than one mechanism, possibly involving microbial activity, is responsible for the observed changes in the studied magnetic mineral assemblages. Further studies of deep methanic zones, where nonsteady state diagenetic conditions and elevated temperatures prevail, should be conducted to improve our knowledge of the mechanisms responsible for magnetic mineral formation and preservation, especially of iron sulfides. This, in turn, could help to reconstruct past methane-rich environments and potentially also methane fluxes.

10.6. Acknowledgments

This research used samples and data provided by the International Ocean Discovery Program (IODP). We thank IODP staff and shipboard scientists of Expedition 350 for their help during the sampling party onboard the R/V *JOIDES Resolution*. We are grateful to M. Murayama at Kochi University for supporting ITRAX measurements and S. Yagyu for performing the measurements. We thank Andrew P. Roberts and Jaume Dinarès-Turell for helpful constructive reviews that improved the manuscript and Editor Michael Walter for editorial handling. This work was supported by a J-DESC/JAMSTEC IODP Expedition 350 after cruise research fund allocated to M. K.. R. J. M. was supported by funding from the Australian and New Zealand International Ocean Discovery Program Consortium (ANZIC). A.-S. J. was funded through grants BA 3841/6-1 and SCHW 554/27-1 awarded by the German Research Foundation (DFG) to T. B. and L. Schwark, respectively. This work was partially supported by the Japan Society for the Promotion of Science Grant-in-Aid for Science Research (grants 26251041 to F. I. and 17H03956 to T. H.). Shipboard data and Expedition 350 Proceedings are available from http://publications.iodp.org/proceedings/350/350title.html. Additional data relevant to this study are provided in the supporting information. The authors declare no conflicts of interest.

Supporting Information for

Magnetic Mineral Diagenesis in a High Temperature and Deep Methanic Zone in Izu Rear Arc Marine Sediments, NW Pacific Ocean

Myriam Kars[1], Robert J. Musgrave[2,3,4], Tatsuhiko Hoshino[5,6], Ann-Sophie Jonas[7], Thorsten Bauersachs[7], Fumio Inagaki[6,8], and Kazuto Kodama[1,9]

[1] Center for Advanced Marine Core Research, Kochi University, B200 Monobe, Nankoku 783-0004, Japan

[2] School of Geosciences, University of Sydney, Sydney, NSW2006, New South Wales, Australia

[3] Geological Survey of New South Wales, NSW Department of Industry, Maitland, NSW 2320, New South Wales, Australia

[4] PALM Laboratory, Centre for Frontier Geoscience, Newcastle Institute for Energy and Resources, The University of Newcastle, Newcastle, New South Wales, Australia

[5] Geomicrobiology Group, Kochi Institute for Core Sample Research, Japan Agency for Marine-Earth Science and Technology, Nankoku, Japan,

[6] Research and Development Center for Submarine Resources, Japan Agency for Marine-Earth Science and Technology, Nankoku, Japan,

[7] Department of Organic Geochemistry, Institute of Geosciences, Christian-Albrechts-University, Ludewig-Meyn-Straße 10, 24118 Kiel, Germany

[8] Research and Development Center for Ocean Drilling Science, Japan Agency for Marine-Earth Science and Technology, Yokohama, Japan

[9] Research Center for Knowledge Science in Cultural Heritage, Doshisha University, Kyoto, Japan

Contents of this file

Text 10.S1
Figures 10.S1 to 10.S10
Tables 10.S1 to 10.S3

Additional Supporting Information

Caption for Dataset 10.S1

Introduction

The supporting information contains a brief presentation of selected shipboard data necessary for the comprehension of this study. All shipboard data and Proceedings of IODP Expedition 350 are available from http://publications.iodp.org/proceedings/350/350title.html. The additional figures and tables show rock magnetic, geochemical and microbiological results discussed in the main text. Methods used to acquire these data are described in the "Materials and Methods" section of the manuscript.

Text 10.S1. Shipboard data

The reader is referred to Tamura et al. (2015a) for a full and detailed description of the shipboard results.

a) Pore water profile

Pore water profiles at Site U1437 are affected by three different processes: biological activity, lateral fluid transport and diagenesis (e.g. hydration of volcanic ash, formation of hydrous alteration products) (Tamura et al., 2015a). The sulfate content decreases from ~24 mM at the surface to ~5 mM at ~50 mbsf (Figure 10.S2). This coincides with an increase in alkalinity which is consistent with sulfate reduction by bacteria as organic matter is degraded (organoclastic reduction). Below this zone, the sulfate content progressively increases downward to near sea-water composition (28.6 mM) at ~460 mbsf. From there, the sulfate gradually slowly decreases with depth (27.1 mM at 693.4 mbsf). The last pore water analysis is at 693 mbsf (i.e. above the interval studied in this manuscript), because of indurated sediments that for the remainder of the sequence do not allow obtaining pore water by squeezing. The increase of sulfate below the sulfate reduction zone (27-83 mbsf) is considered to result from seawater infiltration and upward diffusion of sulfate-rich fluids (for instance, from the alteration of the basaltic basement) (Tamura et al., 2015a).

Fe concentrations are higher (>4 µM) near the surface (<150 mbsf) especially in the interval of sulfate depletion (Figure 10.S2). From ~150 mbsf, Fe concentrations are low ranging from seawater composition (0.5 µM) to 2 µM, save for a local maximum at ~500 mbsf. Below 550 mbsf, Fe concentrations are again close to seawater composition. Mn concentrations are relatively constant (~5 µM) at depths above 420 mbsf (Figure 10.S2). Below 420 mbsf, Mn concentrations increase to reach a maximum of 35 µM in the last pore water analysis.

b) Methane content

Methane is the only hydrocarbon gas detected in Hole U1437D (Tamura et al., 2015a). The methane content gradually increases with depth and remains below 10 ppmv for depths <750 mbsf (Figure 10.S2). The depth interval between ~750-1459 mbsf (Holes U1437D and U1437E) shows significant variation in methane concentrations ranging from exceptionally low 2.6 to 638 ppmv. From 750 to ~850 mbsf, the methane content increases to 65 ppmv. From 850 mbsf, methane drastically increases to reach a maximum value of 638 ppmv at 920 mbsf.

c) Carbonate and organic carbon content

Most of the carbon present in the investigated sediments is of inorganic nature. $CaCO_3$ concentrations vary in the tuffaceous mudstones and reach up to ~60 wt% (Figure 10.S2). High $CaCO_3$ content is also observed at depths above 170 mbsf (~26 ± 9 wt% with a maximum value of 47 wt%) and at ~912 mbsf (~57 wt%) (Figure 10.S2). The total organic carbon (TOC) content is relatively low throughout the stratigraphic sequence with an average of 0.45 ± 0.52 wt%. It is generally higher (0.59 ± 0.4 wt%) in the shallow intervals (<230 mbsf). TOC/total nitrogen (TN) ratios range from 0 to 213 (average of 18.5 ± 26.4) and suggest a mixed input of both marine-derived and terrestrial-derived organic matter.

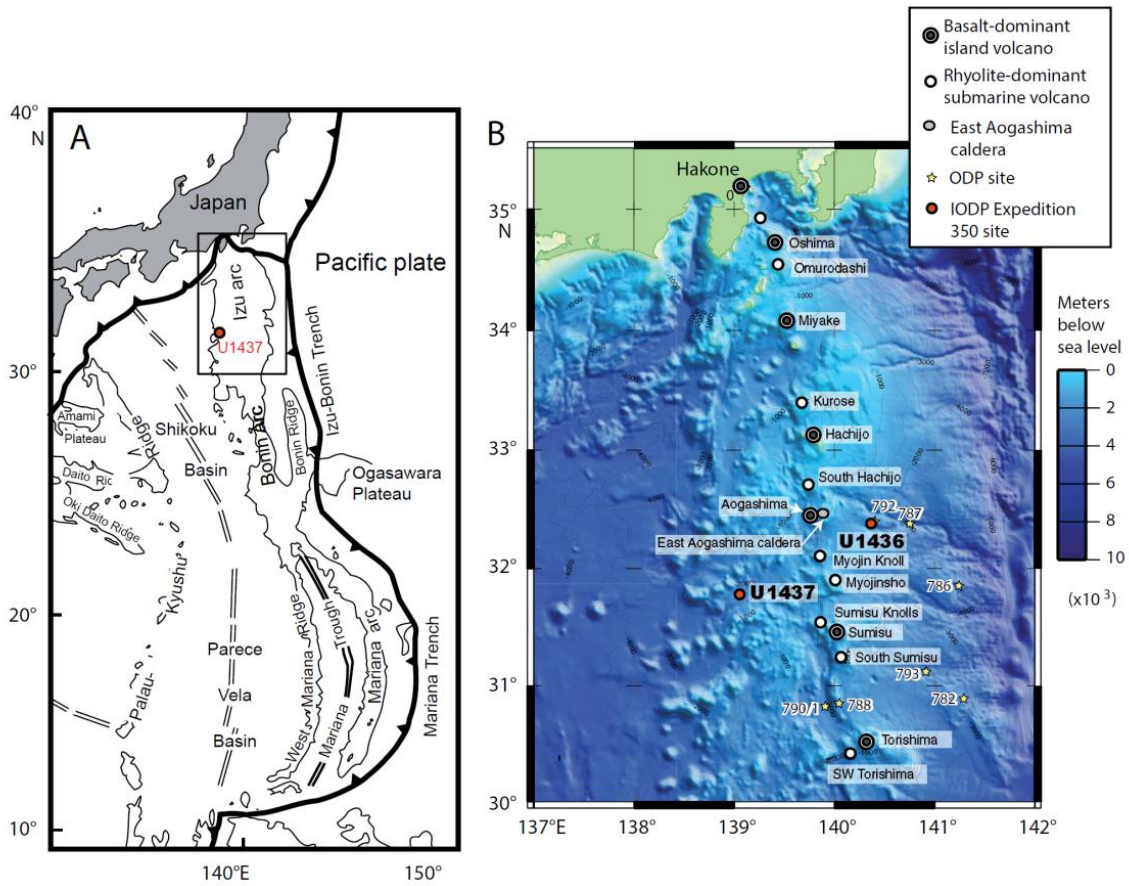

Figure 10.S1 | Location map of IODP Expedition 350 Site U1437 (modified from Tamura et al., 2015a).

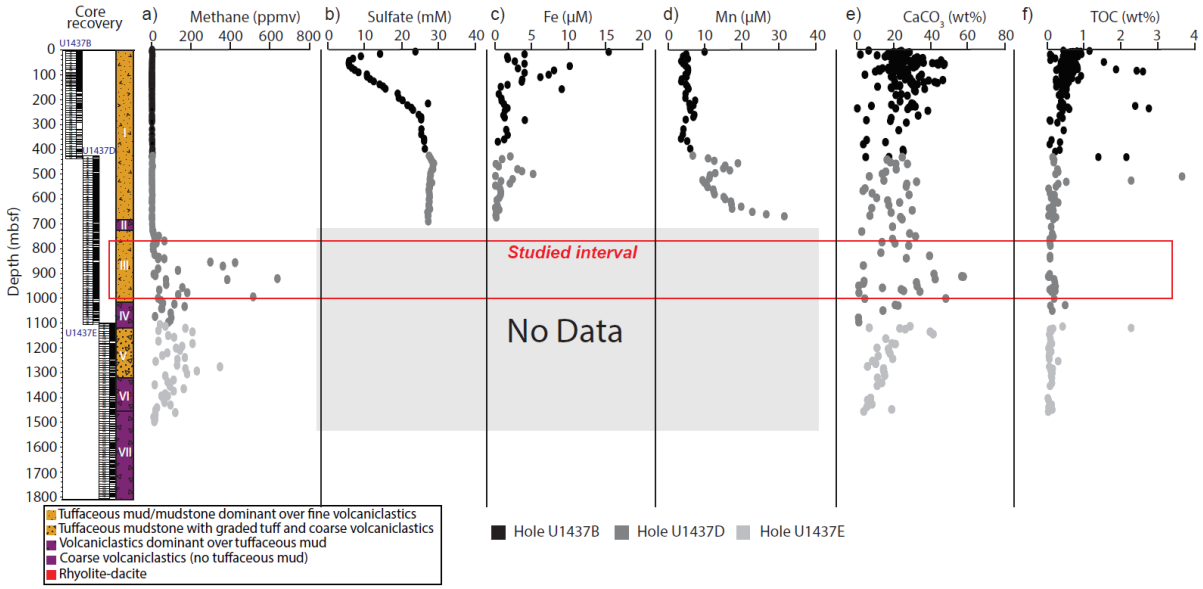

Figure 10.S2 | Selected shipboard gas and geochemical data for Site U1437 (Tamura et al., 2015a). a) Methane, b) sulfate, c) dissolved iron (Fe), d) dissolved manganese (Mn), e) calcium carbonate ($CaCO_3$), f) total organic carbon (TOC). The red box indicates the depth interval studied in this manuscript. The gray zone is the interval in which no pore water could be obtained.

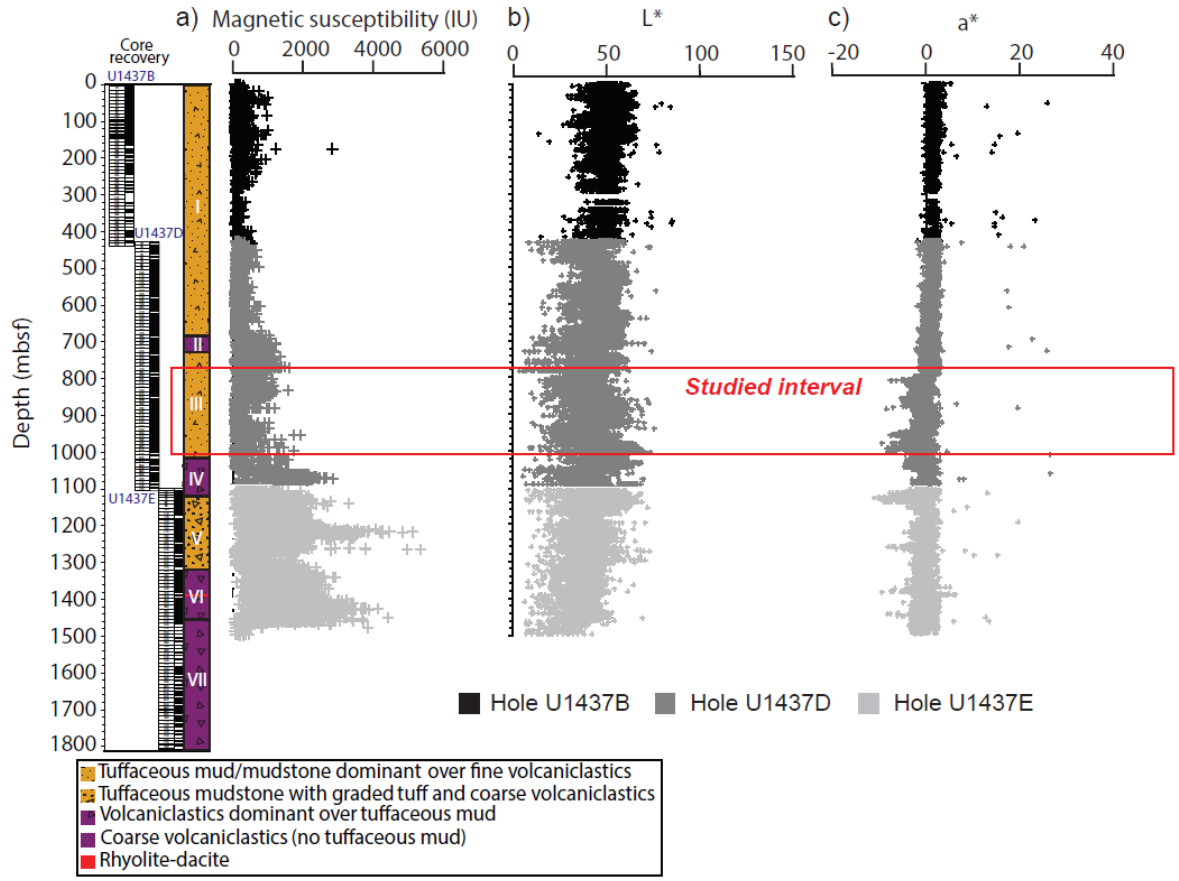

Figure 10.S3 | Selected shipboard physical properties data for Site U1437 (Tamura et al., 2015a). a) Magnetic susceptibility (Instrumental Unit, IU), b) colorimetric parameter L*, c) colorimetric parameter a*. The red box indicates the depth interval studied in this manuscript.

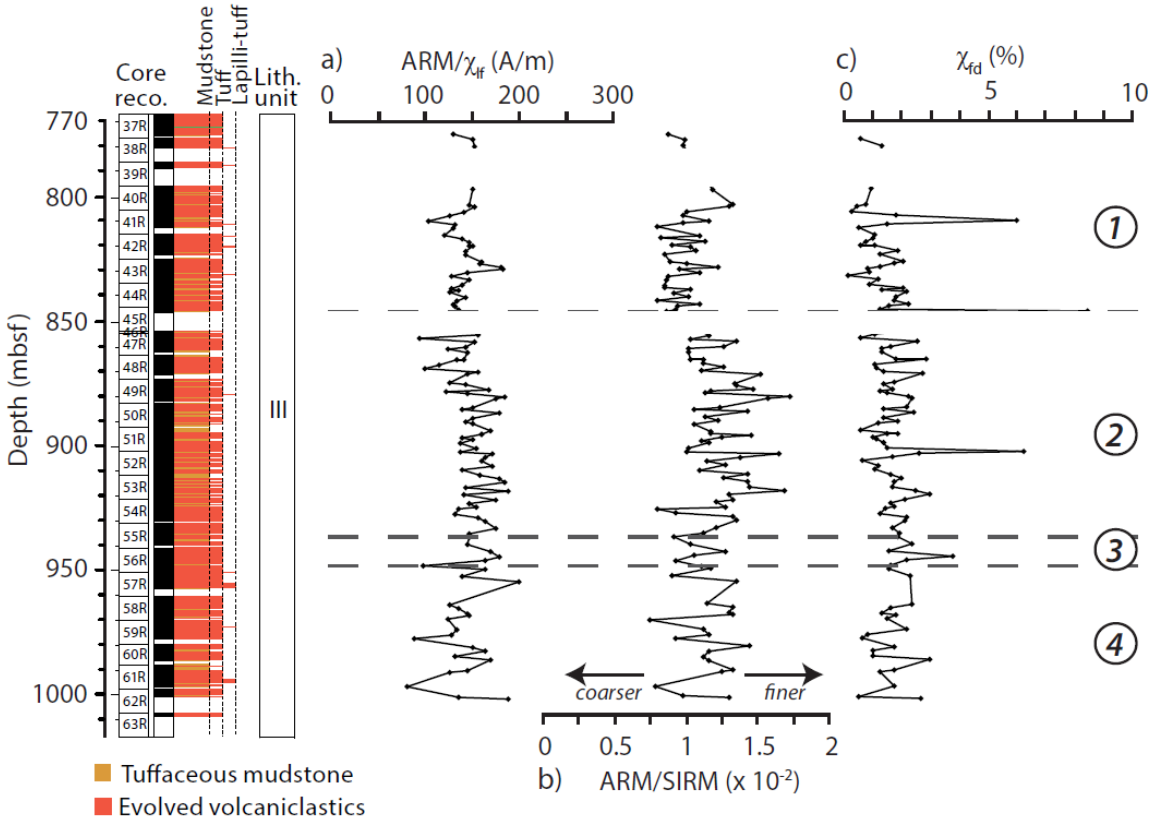

Figure 10.S4 | Down-core variations of magnetic grain size proxies in the studied interval. a) ARM/χ_{lf}, b) ARM/SIRM and c) χ_{fd} (%). The magnetic zones (1 to 4) are indicated. Note the slight increase of ARM/SIRM in zone 2. Core recovery and lithology are indicated (from Tamura et al., 2015a).

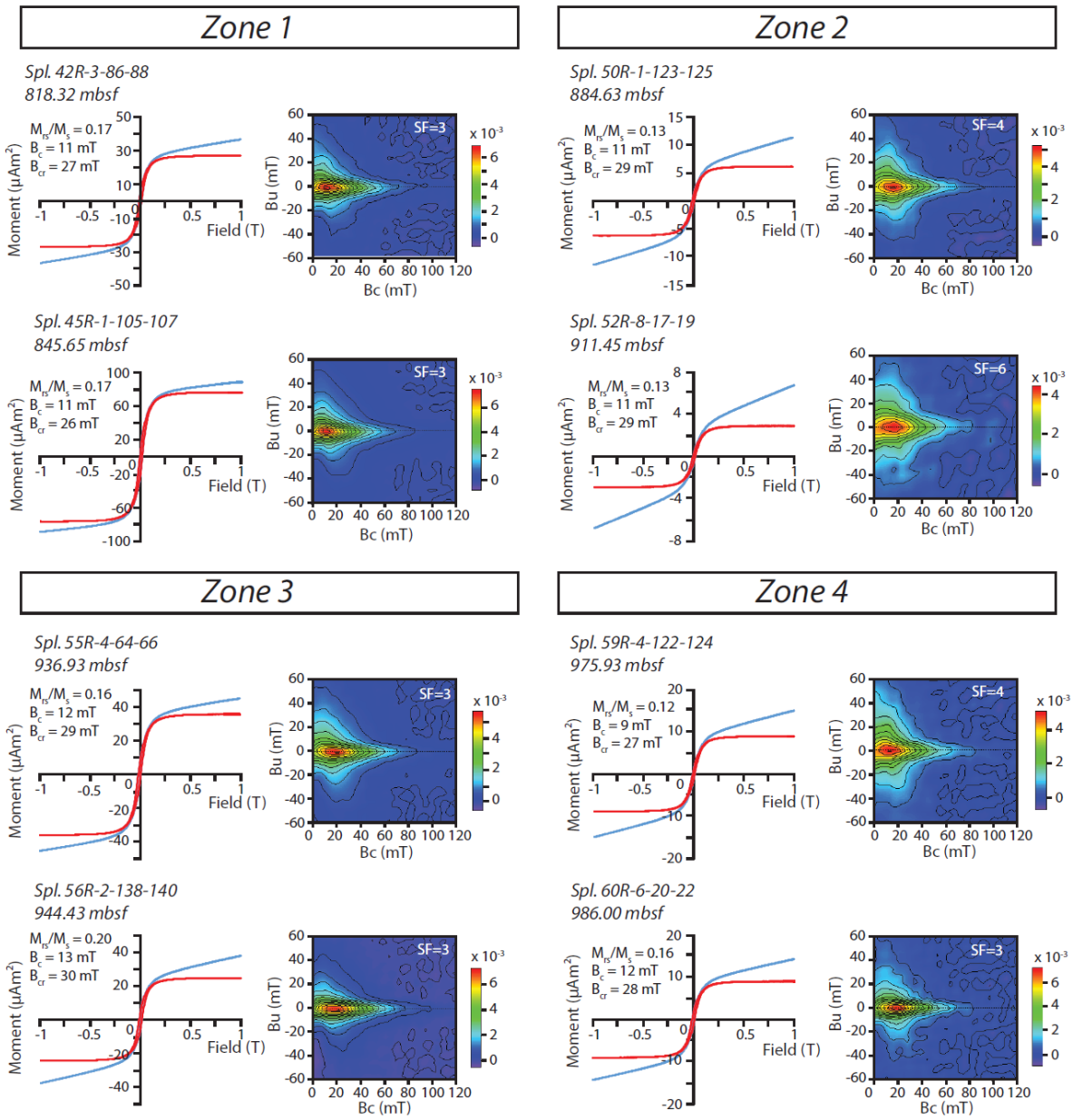

.

Figure 10.S5 | Selected hysteresis loops (not corrected in blue and high-field slope-corrected in red) and FORC diagrams for representative samples from the different magnetic zones. The magnetic mineralogy inferred from the FORC diagrams is vortex state low coercivity (titano)-magnetite.

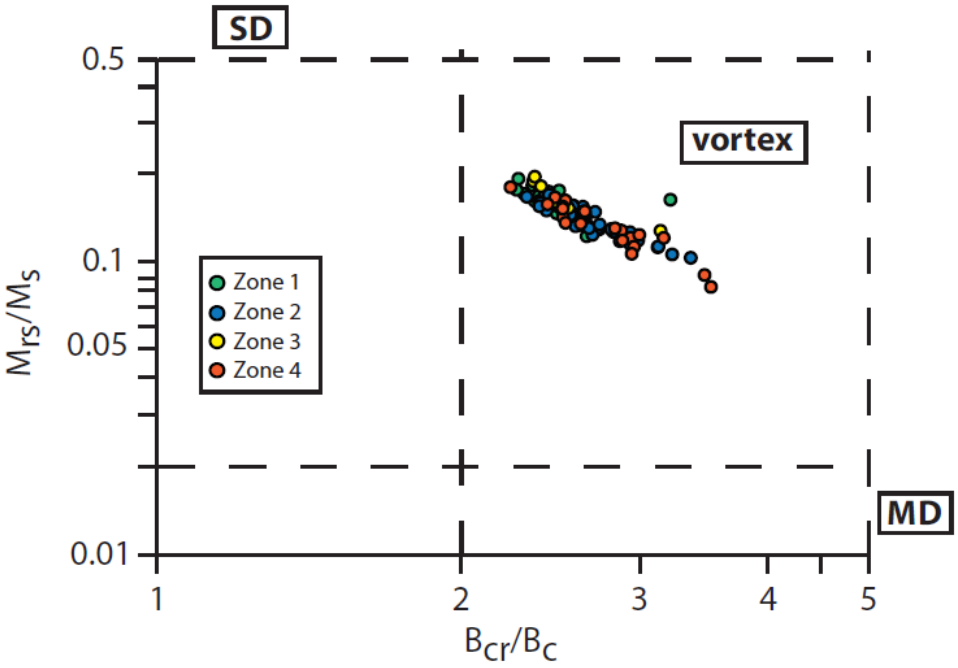

Figure 10.S6 | Day diagram (Day et al., 1977) showing the magnetic state of samples.

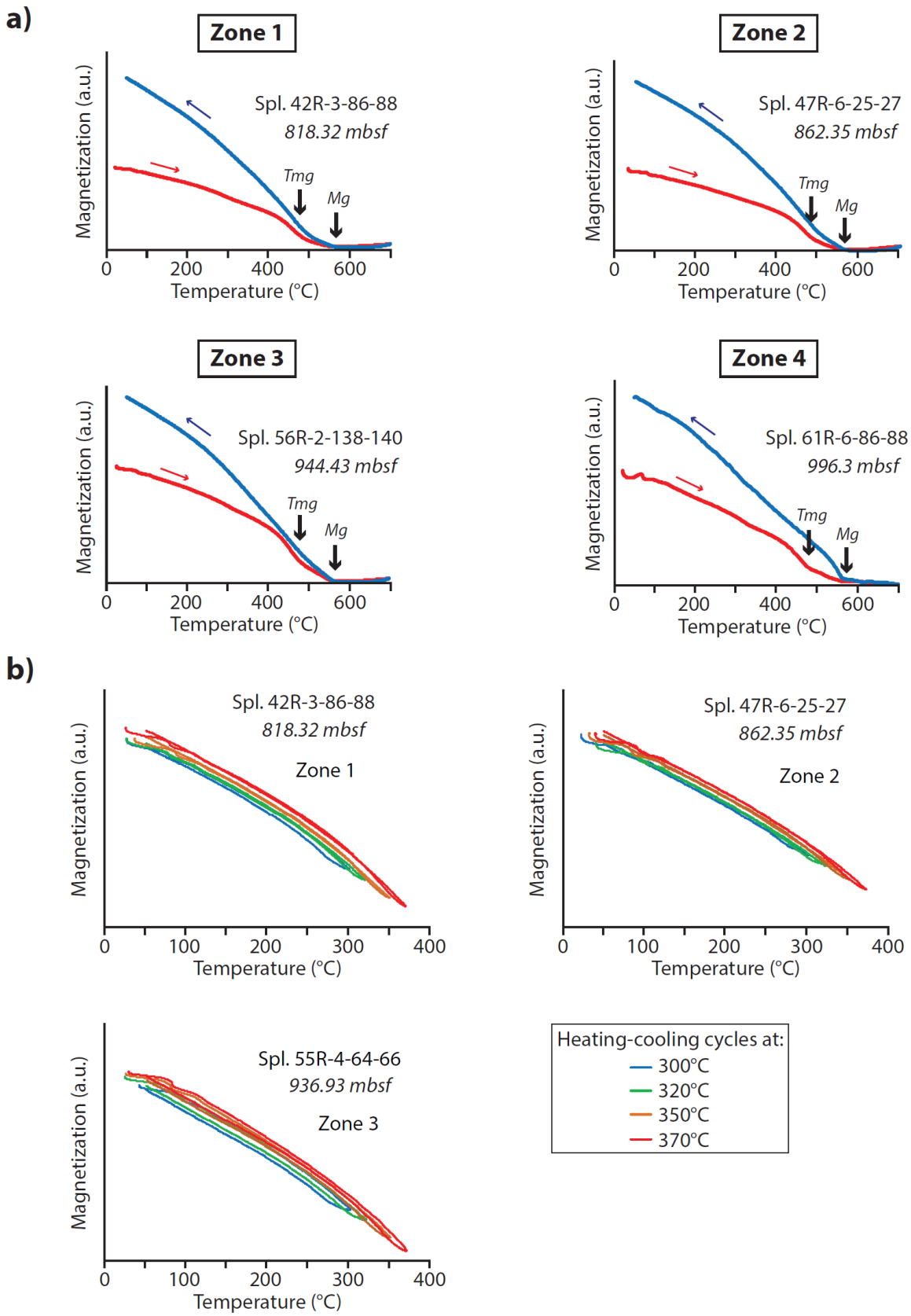

Figure 10.S7 | a) Thermomagnetic curves for representative samples from the four magnetic zones. Tmg: titanomagnetite, Mg: magnetite; b) repeated heating-cooling cycles in the range 300-370 °C for three samples showing reversible cycles.

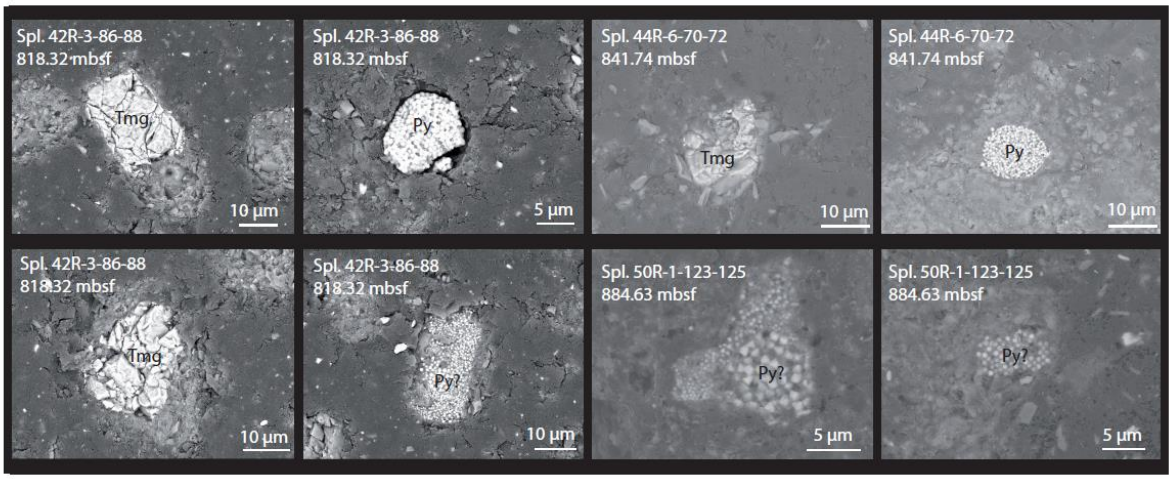

Figure 10.S8 | Scanning electron microscope (SEM) observations of samples from zones 1 and 2 showing the occurrence of coarse-grained titanomagnetite (Tmg), pyrite (Py) and small iron sulfide grains.

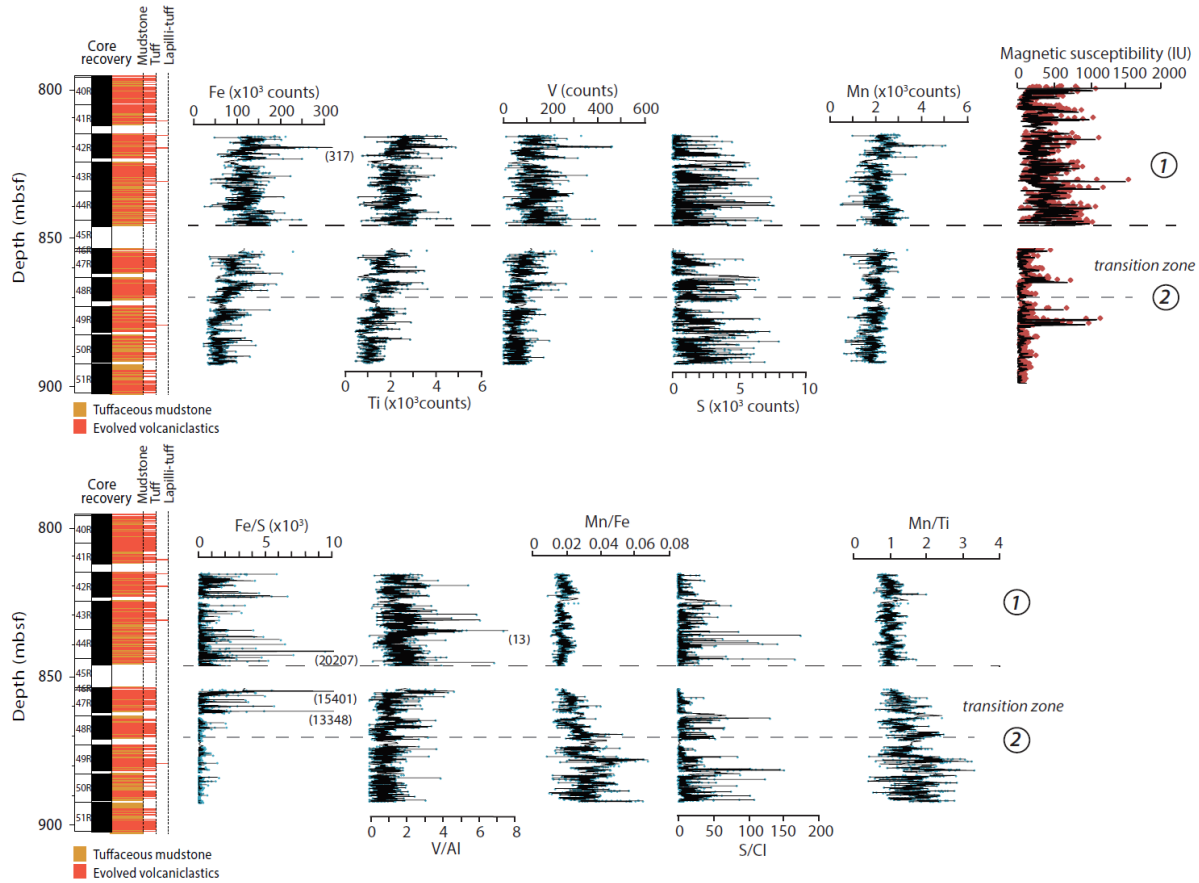

Figure 10.S9 | Down-core variations of shipboard magnetic susceptibility (Tamura et al., 2015a) and selected elements and element ratios for 820-870 mbsf depth interval which covers zone 1 and the top of zone 2. Fe/S spikes are due to localized low concentration of S. The upper part of zone 2 (~855-863 mbsf) compares better to zone 1 and is called transition zone. Black lines are 10-pt average curves. Core recovery and lithology are indicated (from Tamura et al., 2015a).

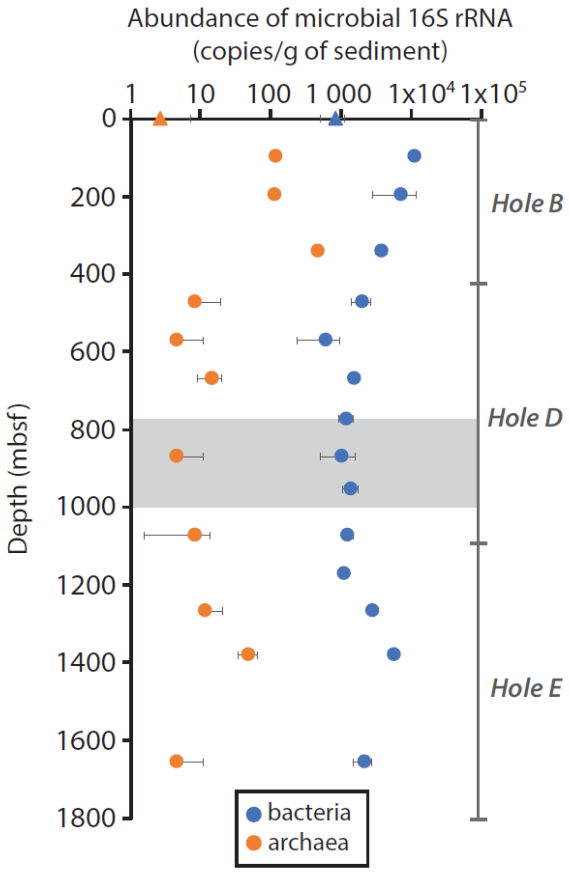

Figure 10.S10 | Abundance of archaea and bacteria in subsurface sediments at Site U1437. Average and standard deviation are indicated. The depth interval in gray corresponds to the interval studied in the main text (775-1002 mbsf).

Magnetic Zone	NRM (μAm²/kg)	ARM (μAm²/kg)	χ_{lf} (x 10^{-8} m^3/kg)	M_s (mAm²/kg)	M_{rs} (mAm²/kg)	B_c (mT)	B_{cr} (mT)	N
1	71 ± 53	384 ± 229	258 ± 149	284 ± 170	47 ± 31	11 ± 1	27 ± 1	35
2	18 ± 12	94 ± 39	63 ± 27	64 ± 28	9 ± 5	11 ± 1	28 ± 1	53
3	50 ± 21	232 ± 115	149 ± 74	164 ± 98	28 ± 15	12 ± 2	29 ± 2	6
4	37 ± 34	109 ± 49	76 ± 28	81 ± 34	11 ± 5	11 ± 1	28 ± 1	20

Table 10.S1 | Average and standard deviation of selected rock magnetic properties for the different magnetic zones. Zone 1 = 775-846 mbsf, zone 2 = 855-936 mbsf, zone 3 = 936-949 mbsf, zone 4 = 949-1002 mbsf. N is the total number of samples analyzed per magnetic zone.

Magnetic zone	RT-SIRM (mAm²/kg)	ZFC LT-SIRM (mAm²/kg)	FC LT-SIRM (mAm²/kg)	δ_{ZFC}	δ_{FC}	N
1	57 ± 42	110 ± 70	140 ± 93	0.17 ± 0.02	0.18 ± 0.02	4
2	8 ± 5	24 ± 9	26 ± 12	0.21 ± 0.03	0.22 ± 0.03	7
3	33 ± 9	70 ± 19	86 ± 22	0.20 ± 0.04	0.20 ± 0.04	3
4	9 ± 3	24 ± 8	27 ± 8	0.23 ± 0.05	0.23 ± 0.05	5

Table 10.S2 | Mean RT-SIRM and LT-SIRM for samples measured at low temperature. RT-SIRM: room temperature saturation isothermal remanent magnetization; LT-SIRM: low temperature saturation isothermal remanent magnetization: ZFC: zero field cooled; FC: field cooled. N is the total number of samples analyzed per magnetic zone.

Depth (mbsf)	TC (wt%)	TIC (wt%)	TOC (wt%)	TS (wt%)	TN (wt%)	$CaCO_3$ (wt%)
779.62	2.91	2.64	0.28	0.19	0.03	21.95
803.14	3.75	3.53	0.23	0.09	0.03	29.37
809.88	3.19	2.79	0.40	0.17	0.03	23.26
818.32	4.63	4.25	0.37	0.10	0.03	35.42
828.26	3.96	3.69	0.28	0.09	0.03	30.73
835.61	3.59	3.35	0.24	0.07	0.02	27.88
841.74	3.12	2.79	0.32	0.10	0.04	23.25
860.59	3.16	2.94	0.22	0.06	0.02	24.47
870.20	5.19	4.70	0.49	0.09	0.03	39.19
884.63	6.12	5.57	0.55	0.14	0.05	46.40
890.14	5.76	5.45	0.31	0.11	0.03	45.37
900.97	5.45	5.16	0.29	0.19	0.03	43.00
909.90	7.04	6.81	0.23	0.13	0.03	56.74
921.70	6.43	6.03	0.40	0.54	0.03	50.22
936.93	3.48	3.19	0.29	0.08	0.02	26.61
945.98	3.77	3.60	0.18	0.04	0.02	29.96
954.76	3.94	3.76	0.18	0.07	0.02	31.29
967.96	4.48	4.21	0.28	0.13	0.03	35.03
977.31	0.3	0.11	0.19	0.13	0.02	0.89
986.00	3.82	3.50	0.32	0.20	0.04	29.12

Table 10.S3 | Bulk-geochemical parameters of samples shown on Figure 10.4. TC: total carbon, TIC: total inorganic carbon, TOC: total organic carbon, TS: total sulfur, TN: total nitrogen, $CaCO_3$: calcium carbonate.

Dataset 10.S1 | Rock magnetic parameters shown on Figures 10.1 and 10.2. χ_{lf} (x 10^{-8} m^3/kg), NRM (Am^2/kg), ARM (Am^2/kg), SIRM (Am^2/kg), $S_{-0.3T}$, χ_{hfield} (x 10^{-8} m^3/kg), M_s (Am^2/kg), M_{rs} (Am^2/kg), B_c (T), B_{cr} (T), D_{JH}, M_{rs}/χ_{lf} (kA/m).

Sample	Top depth CSF-A (m)	Bottom depth CSF-A (m)	Top depth CSF-B (m)	Bottom depth CSF-B (m)	χ_{lf} x 10^{-8} m^3/kg	NRM Am^2/kg	ARM Am^2/kg	SIRM Am^2/kg	$S_{-0.3T}$	χ_{hfield} x 10^{-8} m^3/kg	M_s Am^2/kg	M_{rs} Am^2/kg	B_c T	B_{cr} T	D_{JH}	M_{rs}/χ_{lf} kA/m
350-U1437D - 37R - 6W, 75.0 - 77.0 cm	774.91	774.93	774.91	774.93	305.13	1.36E-04	3.95E-04	4.52E-02	1.00	7.72	0.36	0.04	9.67E-03	2.56E-02	0.047	118.00
350-U1437D - 38R - 1W, 52.0 - 54.0 cm	777.12	777.14	777.12	777.14	115.00	3.89E-05	1.74E-04	1.76E-02	1.00	7.45	0.12	0.02	1.03E-02	2.72E-02	0.051	104.25
350-U1437D - 38R - 3W, 29.0 - 31.0 cm	779.62	779.64	779.62	779.64	389.43	1.71E-04	5.93E-04	6.03E-02	0.99	10.34	0.46	0.08	1.18E-02	2.77E-02	0.070	117.41
350-U1437D - 40R - 1W, 135.0 - 137.0 cm	797.35	797.37	797.35	797.37	94.16	2.18E-05	1.41E-04	1.19E-02	0.99	8.28	0.10	0.01	9.97E-03	2.53E-02	0.056	104.41
350-U1437D - 40R - 5W, 128.0 - 130.0 cm	803.14	803.16	803.14	803.16	79.51	1.94E-05	1.17E-04	8.78E-03	0.99	7.71	0.08	0.01	9.78E-03	2.58E-02	0.055	99.54
350-U1437D - 40R - 6W, 62.0 - 64.0 cm	803.87	803.89	803.87	803.89	88.79	2.01E-05	1.36E-04	1.04E-02	1.00	12.43	0.08	0.01	1.10E-02	2.75E-02	0.061	88.71
350-U1437D - 41R - 1W, 44.0 - 46.0 cm	806.24	806.26	806.24	806.26	67.65	3.15E-05	9.53E-05	9.44E-03	1.00	5.20	0.05	0.01	1.09E-02	2.73E-02	0.065	76.07
350-U1437D - 41R - 2W, 75.0 - 77.0 cm	807.74	807.76	807.74	807.76	418.22	9.87E-05	5.25E-04	5.35E-02	0.99	8.07	0.33	0.06	1.02E-02	2.52E-02	0.069	79.32
350-U1437D - 41R - 4W, 20.0 - 22.0 cm	809.88	809.90	809.88	809.90	379.78	1.01E-04	3.91E-04	3.38E-02	0.99	10.06	0.27	0.04	7.83E-03	2.50E-02	0.052	70.97
350-U1437D - 41R - 5W, 11.0 - 13.0 cm	811.01	811.03	811.01	811.03	180.50	3.25E-05	2.40E-04	2.46E-02	1.00	7.22	0.19	0.03	1.10E-02	2.75E-02	0.064	104.39
350-U1437D - 41R - 6W, 51.0 - 53.0 cm	812.44	812.46	812.44	812.46	220.86	4.04E-05	2.89E-04	3.64E-02	0.99	8.54	0.26	0.04	1.03E-02	2.70E-02	0.055	118.27
350-U1437D - 42R - 1W, 22.0 - 24.0 cm	815.72	815.74	815.72	815.74	166.22	2.61E-05	2.01E-04	1.84E-02	0.99	8.27	0.16	0.02	8.96E-03	2.63E-02	0.042	99.03
350-U1437D - 42R - 2W, 19.0 - 21.0 cm	816.97	816.99	816.97	816.99	257.89	4.66E-05	3.59E-04	4.36E-02	1.00	8.22	0.33	0.05	1.18E-02	2.92E-02	0.064	126.26
350-U1437D - 42R - 3W, 86.0 - 88.0 cm	818.32	818.34	818.32	818.34	203.14	1.01E-04	2.97E-04	2.60E-02	0.99	8.79	0.19	0.03	1.10E-02	2.71E-02	0.067	95.39
350-U1437D - 42R - 4W, 94.0 - 96.0 cm	819.71	819.73	819.71	819.73	162.66	5.79E-05	2.40E-04	2.67E-02	1.00	7.47	0.18	0.03	1.12E-02	2.74E-02	0.066	113.62
350-U1437D - 42R - 5W, 8.0 - 10.0 cm	820.18	820.20	820.18	820.20	122.74	2.61E-05	1.84E-04	1.79E-02	0.99	9.33	0.13	0.02	9.95E-03	2.60E-02	0.057	106.11
350-U1437D - 42R - 6W, 31.0 - 33.0 cm	821.86	821.88	821.86	821.88	127.42	3.89E-05	1.82E-04	1.70E-02	0.99	6.89	0.14	0.02	1.04E-02	2.67E-02	0.059	113.67
350-U1437D - 42R - 7W, 75.0 - 77.0 cm	823.18	823.20	823.18	823.20	209.96	9.14E-05	3.03E-04	3.56E-02	0.99	9.48	0.24	0.04	1.03E-02	2.65E-02	0.062	113.90
350-U1437D - 43R - 1W, 112.0 - 114.0 cm	826.32	826.34	826.29	826.31	224.21	5.86E-05	3.61E-04	4.06E-02	1.00	8.95	0.23	0.04	1.24E-02	2.89E-02	0.079	100.75
350-U1437D - 43R - 2W, 65.0 - 67.0 cm	827.22	827.24	827.17	827.19	222.81	7.99E-05	3.53E-04	3.52E-02	1.00	8.88	0.27	0.04	1.07E-02	2.68E-02	0.064	120.46
350-U1437D - 43R - 3W. 61.0 - 63.0 cm	828.26	828.28	828.18	828.20	79.92	2.88E-05	1.44E-04	1.18E-02	0.99	6.06	0.08	0.01	1.17E-02	2.88E-02	0.060	105.98
350-U1437D - 43R - 4W, 33.0 - 35.0 cm	829.43	829.45	829.32	829.34	269.91	7.87E-05	4.93E-04	5.20E-02	1.00	9.77	0.32	0.05	1.24E-02	2.85E-02	0.076	117.04
350-U1437D - 43R - 5W, 62.0 - 64.0 cm	830.77	830.79	830.63	830.65	187.90	5.36E-05	2.71E-04	2.49E-02	1.00	9.36	0.23	0.04	1.12E-02	2.70E-02	0.071	124.31
350-U1437D - 43R - 6W, 40.0 - 42.0 cm	831.99	832.01	831.81	831.83	123.53	3.99E-05	1.59E-04	1.81E-02	0.99	7.89	0.13	0.02	1.00E-02	2.64E-02	0.052	104.00
350-U1437D - 43R - 7W, 72.0 - 74.0 cm	833.47	833.49	833.25	833.27	242.63	8.85E-05	3.58E-04	4.13E-02	1.00	7.79	0.23	0.04	1.09E-02	2.63E-02	0.068	93.91

Sample	Top depth CSF-A (m)	Bottom depth CSF-A (m)	Top depth CSF-B (m)	Bottom depth CSF-B (m)	χ_{lf} x 10^{-8} m^3/kg	NRM Am^2/kg	ARM Am^2/kg	SIRM Am^2/kg	$S_{-0.3T}$	χ_{hfield} x 10^{-8} m^3/kg	M_s Am^2/kg	M_{rs} Am^2/kg	B_c T	B_{cr} T	D_{JH}	M_{rs}/χ_{lf} kA/m
350-U1437D - 44R - 1W, 71.0 - 73.0 cm	835.61	835.63	835.59	835.61	478.93	7.20E-05	6.71E-04	7.85E-02	0.99	9.24	0.46	0.08	1.18E-02	2.80E-02	0.075	96.79
350-U1437D - 44R - 2W, 92.0 - 94.0 cm	836.84	836.86	836.79	836.81	392.34	6.39E-05	5.06E-04	5.97E-02	1.00	9.88	0.46	0.07	1.12E-02	2.74E-02	0.065	117.29
350-U1437D - 44R - 3W, 63.0 - 65.0 cm	837.68	837.70	837.61	837.63	426.15	4.72E-05	5.82E-04	5.67E-02	0.99	10.18	0.42	0.07	1.09E-02	2.65E-02	0.070	98.68
350-U1437D - 44R - 4W, 39.0 - 41.0 cm	838.69	838.71	838.59	838.61	379.56	2.83E-04	4.80E-04	5.21E-02	1.00	8.56	0.49	0.07	1.04E-02	2.68E-02	0.059	129.26
350-U1437D - 44R - 5W, 111.0 - 113.0 cm	840.68	840.70	840.52	840.54	443.28	6.92E-05	6.32E-04	6.24E-02	0.99	9.05	0.37	0.07	1.12E-02	2.78E-02	0.072	82.78
350-U1437D - 44R - 6W, 70.0 - 72.0 cm	841.74	841.76	841.55	841.57	652.79	9.91E-05	8.73E-04	1.09E-01	0.99	10.09	0.69	0.14	1.15E-02	2.60E-02	0.086	105.99
350-U1437D - 44R - 7W, 106.0 - 108.0 cm	843.00	843.02	842.78	842.80	393.58	4.61E-05	5.12E-04	4.67E-02	0.99	8.73	0.34	0.06	1.13E-02	2.71E-02	0.072	86.68
350-U1437D - 44R - 8W, 82.0 - 84.0 cm	844.19	844.21	843.94	843.96	259.68	2.45E-05	3.45E-04	3.66E-02	1.00	8.74	0.27	0.04	1.11E-02	2.84E-02	0.060	104.69
350-U1437D - 45R - 1W, 105.0 - 107.0 cm	845.65	845.67	845.65	845.67	551.74	1.44E-04	7.45E-04	8.03E-02	1.00	10.78	0.53	0.09	1.11E-02	2.64E-02	0.072	96.24
350-U1437D - 45R - 2W, 20.0 - 22.0 cm	846.14	846.16	846.14	846.16	100.24	9.93E-05	1.08E-03	1.26E-01	1.00	10.36	0.75	0.14	1.14E-02	2.57E-02	0.080	751.63
350-U1437D - 47R - 1W, 40.0 - 42.0 cm	855.70	855.72	855.70	855.72	93.33	4.29E-05	1.46E-04	1.25E-02	1.00	6.77	0.08	0.01	1.04E-02	2.71E-02	0.060	84.50
350-U1437D - 47R - 2W, 62.0 - 64.0 cm	857.24	857.26	857.24	857.26	56.46	3.46E-05	5.38E-05	5.24E-03	0.99	5.31	0.06	0.01	7.53E-03	2.42E-02	0.034	102.28
350-U1437D - 47R - 3W, 38.0 - 40.0 cm	858.48	858.50	858.48	858.50	74.17	3.02E-05	1.14E-04	8.44E-03	0.99	5.30	0.08	0.01	1.05E-02	2.72E-02	0.058	103.82
350-U1437D - 47R - 4W, 105.0 - 107.0 cm	860.59	860.61	860.59	860.61	71.36	4.56E-05	1.03E-04	8.15E-03	1.00	4.70	0.07	0.01	1.01E-02	2.63E-02	0.057	102.77
350-U1437D - 47R - 5W, 20.0 - 22.0 cm	861.16	861.18	861.16	861.18	99.57	4.60E-05	1.23E-04	1.21E-02	0.99	6.69	0.11	0.01	9.59E-03	2.77E-02	0.043	109.53
350-U1437D - 47R - 6W, 25.0 - 27.0 cm	862.35	862.37	862.35	862.37	151.52	3.34E-05	2.20E-04	2.16E-02	1.00	6.08	0.15	0.02	1.09E-02	2.69E-02	0.065	98.69
350-U1437D - 48R - 1W, 130.0 - 132.0 cm	865.3	865.32	865.30	865.32	95.80	4.35E-05	1.36E-04	1.33E-02	0.99	5.92	0.10	0.02	1.02E-02	2.66E-02	0.055	108.64
350-U1437D - 48R - 2W, 34.0 - 36.0 cm	865.73	865.75	865.73	865.75	111.21	4.62E-05	1.50E-04	1.34E-02	1.00	6.58	0.09	0.01	9.81E-03	2.64E-02	0.056	85.13
350-U1437D - 48R - 3W, 42.0 - 44.0 cm	867.27	867.29	867.27	867.29	82.11	3.32E-05	9.52E-05	8.53E-03	0.99	6.44	0.09	0.01	8.59E-03	2.67E-02	0.037	104.11
350-U1437D - 48R - 4W, 32.0 - 34.0 cm	868.67	868.69	868.67	868.69	66.25	2.98E-05	6.67E-05	5.27E-03	0.99	4.30	0.06	0.01	7.49E-03	2.51E-02	0.031	90.34
350-U1437D - 48R - 5W, 53.0 - 55.0 cm	870.20	870.22	870.20	870.22	71.78	1.68E-05	1.12E-04	1.01E-02	0.99	5.90	0.07	0.01	1.16E-02	2.74E-02	0.069	95.48
350-U1437D - 48R - 6W, 64.0 - 66.0 cm	871.23	871.25	871.23	871.25	56.15	7.68E-06	8.21E-05	5.38E-03	0.99	4.44	0.05	0.01	9.93E-03	2.79E-02	0.046	83.47
350-U1437D - 49R - 1W, 127.0 - 129.0 cm	874.97	874.99	874.97	874.99	77.80	2.33E-05	9.84E-05	7.36E-03	0.99	4.17	0.08	0.01	8.18E-03	2.54E-02	0.037	108.11
350-U1437D - 49R - 2W, 52.0 - 54.0 cm	875.66	875.68	875.66	875.68	103.31	1.92E-05	1.49E-04	1.09E-02	1.00	6.90	0.11	0.01	9.75E-03	2.84E-02	0.044	108.91
350-U1437D - 49R - 3W, 96.0 - 98.0 cm	877.29	877.31	877.29	877.31	32.30	8.87E-06	5.41E-05	3.68E-03	0.99	4.84	0.03	0.00	1.09E-02	2.83E-02	0.056	98.02
350-U1437D - 49R - 4W, 46.0 - 48.0 cm	877.95	877.97	877.95	877.97	39.59	1.19E-05	4.86E-05	4.12E-03	0.99	3.12	0.03	0.00	9.03E-03	2.68E-02	0.041	88.09
350-U1437D - 49R - 5W, 10.0 - 12.0 cm	878.96	878.98	878.96	878.98	41.54	1.60E-05	6.01E-05	5.32E-03	0.99	4.08	0.04	0.01	1.00E-02	2.86E-02	0.042	105.39

Sample	Top depth CSF-A (m)	Bottom depth CSF-A (m)	Top depth CSF-B (m)	Bottom depth CSF-B (m)	χ_{lf} x 10^{-8} m^3/kg	NRM Am^2/kg	ARM Am^2/kg	SIRM Am^2/kg	$S_{-0.3T}$	χ_{hfield} x 10^{-8} m^3/kg	M_s Am^2/kg	M_{rs} Am^2/kg	B_c T	B_{cr} T	D_{JH}	M_{rs}/χ_{lf} kA/m
350-U1437D - 49R - 6W, 62.0 - 64.0 cm	880.61	880.63	880.61	880.63	31.07	1.01E-05	5.77E-05	3.34E-03	0.99	3.83	0.03	0.00	1.00E-02	2.79E-02	0.047	105.87
350-U1437D - 49R - 7W, 13.0 - 15.0 cm	881.44	881.46	881.44	881.46	27.51	7.43E-06	4.85E-05	3.08E-03	0.98	4.13	0.03	0.00	1.07E-02	2.92E-02	0.048	91.72
350-U1437D - 50R - 1W, 123.0 - 125.0 cm	884.63	884.65	884.63	884.65	42.70	8.62E-06	6.42E-05	5.16E-03	0.99	4.78	0.04	0.01	1.06E-02	2.86E-02	0.049	105.30
350-U1437D - 50R - 2W, 30.0 - 32.0 cm	885.20	885.22	885.20	885.22	71.91	1.32E-05	1.01E-04	9.60E-03	0.99	5.84	0.08	0.01	1.05E-02	2.71E-02	0.053	115.38
350-U1437D - 50R - 3W, 39.0 - 41.0 cm	886.65	886.67	886.65	886.67	27.28	5.80E-06	4.87E-05	3.40E-03	0.98	4.26	0.03	0.00	1.12E-02	2.95E-02	0.053	110.62
350-U1437D - 50R - 4W, 109.0 - 111.0 cm	888.81	888.83	888.81	888.83	49.65	9.99E-06	7.46E-05	6.56E-03	0.99	4.42	0.05	0.01	1.13E-02	2.72E-02	0.073	105.09
350-U1437D - 50R - 5W, 110.0 - 112.0 cm	890.14	890.16	890.14	890.16	73.88	2.50E-05	1.06E-04	8.67E-03	0.99	5.27	0.08	0.01	1.06E-02	2.80E-02	0.053	103.54
350-U1437D - 50R - 6W, 100.0 - 102.0 cm	891.28	891.30	891.28	891.30	60.49	9.40E-06	9.10E-05	8.57E-03	0.99	5.72	0.05	0.01	1.08E-02	2.72E-02	0.056	89.72
350-U1437D - 51R - 1W, 112.0 - 114.0 cm	894.22	894.24	894.18	894.20	43.85	1.31E-05	7.46E-05	6.38E-03	0.99	4.76	0.05	0.01	1.17E-02	2.69E-02	0.074	106.84
350-U1437D - 51R - 2W, 77.0 - 79.0 cm	895.16	895.18	895.09	895.11	87.09	2.22E-05	1.39E-04	1.19E-02	1.00	5.94	0.09	0.01	1.18E-02	2.89E-02	0.065	98.75
350-U1437D - 51R - 3W, 35.0 - 37.0 cm	895.69	895.71	895.60	895.62	68.80	1.42E-05	1.11E-04	7.60E-03	1.00	5.15	0.06	0.01	1.11E-02	2.81E-02	0.060	90.11
350-U1437D - 51R - 4W, 14.0 - 16.0 cm	896.70	896.72	896.58	896.59	25.81	6.58E-06	3.60E-05	2.87E-03	0.98	4.17	0.02	0.00	1.17E-02	3.07E-02	0.052	91.91
350-U1437D - 51R - 5W, 28.0 - 30.0 cm	897.83	897.85	897.67	897.69	65.13	1.02E-05	9.84E-05	8.82E-03	0.99	6.24	0.07	0.01	1.14E-02	2.74E-02	0.069	105.77
350-U1437D - 51R - 6W, 14.0 - 16.0 cm	899.05	899.07	898.84	898.86	33.61	7.02E-06	4.62E-05	3.97E-03	0.98	4.03	0.03	0.00	1.16E-02	3.00E-02	0.053	100.69
350-U1437D - 51R - 7W. 78.0 - 80.0 cm	900.97	900.99	900.70	900.72	70.36	1.83E-05	1.09E-04	1.06E-02	0.99	4.68	0.08	0.01	1.20E-02	2.85E-02	0.068	116.27
350-U1437D - 51R - 9W, 27.0 - 29.0 cm	902.52	902.54	902.19	902.21	112.52	2.00E-05	1.54E-04	1.52E-02	0.99	5.43	0.11	0.02	1.09E-02	2.74E-02	0.059	99.63
350-U1437D - 52R - 1W, 68.0 - 70.0 cm	903.48	903.5	903.48	903.5	65.78	9.09E-06	1.13E-04	6.81E-03	0.99	5.92	0.06	0.01	1.10E-02	2.68E-02	0.073	87.88
350-U1437D - 52R - 2W, 115.0 - 117.0 cm	904.70	904.72	904.70	904.72	53.86	1.40E-05	8.85E-05	6.40E-03	0.99	5.48	0.05	0.01	1.05E-02	2.74E-02	0.055	96.48
350-U1437D - 52R - 4W, 32.0 - 34.0 cm	906.20	906.22	906.20	906.22	48.47	1.09E-05	7.78E-05	6.73E-03	0.99	5.04	0.06	0.01	1.08E-02	2.81E-02	0.055	115.49
350-U1437D - 52R - 5W, 57.0 - 59.0 cm	907.95	907.97	907.95	907.97	49.73	1.32E-05	8.52E-05	6.68E-03	0.99	3.89	0.06	0.01	1.15E-02	2.76E-02	0.063	110.91
350-U1437D - 52R - 6W, 100.0 - 102.0 cm	909.90	909.92	909.90	909.92	28.67	4.86E-06	4.02E-05	3.66E-03	0.99	4.10	0.03	0.00	1.10E-02	2.84E-02	0.052	117.93
350-U1437D - 52R - 8W, 17.0 - 19.0 cm	911.45	911.47	911.45	911.47	26.55	9.14E-06	4.21E-05	2.93E-03	0.98	4.65	0.03	0.00	1.06E-02	2.85E-02	0.047	104.69
350-U1437D - 53R - 1W, 69.0 - 71.0 cm	913.19	913.21	913.17	913.19	74.77	1.60E-05	1.35E-04	1.06E-02	1.00	6.83	0.08	0.01	1.19E-02	2.83E-02	0.066	103.63
350-U1437D - 53R - 2W, 97.0 - 99.0 cm	914.62	914.64	914.55	914.57	41.13	8.38E-06	7.59E-05	5.30E-03	0.99	5.23	0.04	0.01	1.08E-02	2.69E-02	0.062	105.05
350-U1437D - 53R - 3W, 137.0 - 139.0 cm	916.45	916.47	916.31	916.33	42.47	2.16E-05	6.08E-05	4.21E-03	0.99	5.48	0.04	0.01	1.06E-02	2.82E-02	0.050	90.31
350-U1437D - 53R - 5W, 17.0 - 19.0 cm	918.08	918.10	917.89	917.91	26.85	6.01E-06	5.06E-05	2.99E-03	0.98	5.69	0.03	0.00	1.11E-02	2.89E-02	0.055	95.39

Sample	Top depth CSF-A (m)	Bottom depth CSF-A (m)	Top depth CSF-B (m)	Bottom depth CSF-B (m)	χ_{lf} x 10^{-8} m^3/kg	NRM Am^2/kg	ARM Am^2/kg	SIRM Am^2/kg	$S_{-0.3T}$	χ_{hfield} x 10^{-8} m^3/kg	M_s Am^2/kg	M_{rs} Am^2/kg	B_c T	B_{cr} T	D_{JH}	M_{rs}/χ_{lf} kA/m
350-U1437D - 53R - 6W, 49.0 - 51.0 cm	919.91	919.93	919.65	919.67	102.39	1.30E-05	1.44E-04	1.11E-02	1.00	6.28	0.11	0.02	1.12E-02	2.69E-02	0.073	108.92
350-U1437D - 53R - 7W, 92.0 - 94.0 cm	921.7	921.72	921.38	921.40	36.99	8.27E-06	6.48E-05	4.86E-03	0.98	4.75	0.04	0.01	1.14E-02	2.91E-02	0.058	101.35
350-U1437D - 54R - 1W, 67.0 - 69.0 cm	922.87	922.89	922.87	922.89	90.14	1.73E-05	1.32E-04	1.10E-02	0.99	5.75	0.09	0.01	1.03E-02	2.69E-02	0.054	98.51
350-U1437D - 54R - 2W, 109.0 - 111.0 cm	924.79	924.81	924.79	924.81	44.49	1.36E-05	6.86E-05	5.35E-03	0.98	5.41	0.04	0.01	1.10E-02	2.89E-02	0.056	95.72
350-U1437D - 54R - 3W, 60.0 - 62.0 cm	925.59	925.61	925.59	925.61	51.72	1.51E-05	7.05E-05	8.78E-03	0.99	6.00	0.07	0.01	9.89E-03	2.86E-02	0.042	131.20
350-U1437D - 54R - 4W, 108.0 - 110.0 cm	927.36	927.38	927.36	927.38	69.20	1.19E-05	9.14E-05	9.82E-03	0.99	6.80	0.08	0.01	9.44E-03	2.76E-02	0.040	121.38
350-U1437D - 54R - 5W, 96.0 - 98.0 cm	928.66	928.68	928.66	928.68	49.38	1.26E-05	7.69E-05	5.80E-03	0.99	6.29	0.05	0.01	1.09E-02	2.97E-02	0.050	98.30
350-U1437D - 54R - 7W, 3.0 - 5.0 cm	930.32	930.34	930.32	930.34	52.73	1.32E-05	8.70E-05	6.44E-03	0.99	5.61	0.04	0.01	1.06E-02	2.80E-02	0.058	84.46
350-U1437D - 55R - 1W, 137.0 - 139.0 cm	933.27	933.29	933.27	933.29	80.72	3.00E-05	1.41E-04	1.17E-02	0.99	6.48	0.09	0.02	1.17E-02	2.83E-02	0.071	113.18
350-U1437D - 55R - 3W, 7.0 - 9.0 cm	934.91	934.93	934.91	934.93	100.88	2.56E-05	1.48E-04	1.32E-02	0.99	6.28	0.10	0.02	1.10E-02	2.81E-02	0.062	99.63
350-U1437D - 55R - 4W, 64.0 - 66.0 cm	936.93	936.95	936.93	936.95	253.80	5.34E-05	3.72E-04	4.06E-02	1.00	10.84	0.32	0.05	1.16E-02	2.94E-02	0.061	127.56
350-U1437D - 55R - 6W, 22.0 - 24.0 cm	939.35	939.37	939.35	939.37	198.38	6.58E-05	2.87E-04	2.77E-02	1.00	9.20	0.21	0.03	1.05E-02	2.60E-02	0.066	105.12
350-U1437D - 56R - 1W, 96.0 - 98.0 cm	942.56	942.58	942.53	942.55	136.42	4.79E-05	2.32E-04	1.81E-02	1.00	9.14	0.13	0.03	1.27E-02	2.98E-02	0.082	96.44
350-U1437D - 56R - 2W, 138.0 - 140.0 cm	944.43	944.45	944.35	944.37	161.74	6.73E-05	2.91E-04	2.75E-02	1.00	11.62	0.17	0.03	1.28E-02	3.00E-02	0.085	105.26
350-U1437D - 56R - 3W, 145.0 - 147.0 cm	945.98	946.00	945.86	945.88	105.44	5.51E-05	1.73E-04	1.87E-02	1.00	9.01	0.12	0.02	1.28E-02	3.04E-02	0.077	110.05
350-U1437D - 56R - 5W, 64.0 - 66.0 cm	948.17	948.19	947.99	948.01	39.42	9.21E-06	3.90E-05	3.52E-03	0.99	9.94	0.03	0.00	8.91E-03	2.78E-02	0.042	80.42
350-U1437D - 56R - 6W, 30.0 - 32.0 cm	949.12	949.14	948.92	948.94	113.47	1.97E-05	1.86E-04	1.59E-02	1.00	7.88	0.12	0.02	1.21E-02	2.99E-02	0.069	105.86
350-U1437D - 57R - 1W, 122.0 - 124.0 cm	952.52	952.54	952.52	952.54	116.61	1.19E-04	1.62E-04	1.79E-02	0.99	8.13	0.14	0.02	1.10E-02	2.88E-02	0.058	117.86
350-U1437D - 57R - 3W, 106.0 - 108.0 cm	954.76	954.78	954.76	954.78	61.97	2.56E-05	1.24E-04	9.15E-03	1.00	7.41	0.06	0.01	1.17E-02	2.94E-02	0.065	94.72
350-U1437D - 58R - 3W, 6.0 - 8.0 cm	963.52	963.54	963.52	963.54	73.37	1.15E-04	9.24E-05	8.03E-03	0.99	7.78	0.07	0.01	9.38E-03	2.74E-02	0.042	100.44
350-U1437D - 58R - 4W, 7.0 - 9.0 cm	964.94	964.96	964.94	964.96	60.50	1.39E-05	8.18E-05	6.16E-03	0.99	8.55	0.06	0.01	8.61E-03	2.71E-02	0.039	92.48
350-U1437D - 58R - 5W, 73.0 - 75.0 cm	966.95	966.97	966.95	966.97	72.85	4.11E-05	1.06E-04	8.09E-03	0.99	8.34	0.08	0.01	9.48E-03	2.71E-02	0.046	104.33
350-U1437D - 58R - 7W, 5.0 - 7.0 cm	967.96	967.98	967.96	967.98	70.58	3.07E-05	1.03E-04	7.78E-03	0.99	5.66	0.07	0.01	8.92E-03	2.66E-02	0.042	101.63
350-U1437D - 58R - 8W, 46.0 - 48.0 cm	969.76	969.78	969.76	969.78	109.20	1.77E-05	1.36E-04	1.81E-02	0.99	7.17	0.12	0.02	1.12E-02	2.82E-02	0.058	111.56
350-U1437D - 59R - 3W, 69.0 - 71.0 cm	973.9	973.92	973.90	973.92	72.31	2.28E-05	9.69E-05	8.64E-03	0.99	6.16	0.07	0.01	9.87E-03	2.78E-02	0.047	96.74
350-U1437D - 59R - 4W, 122.0 - 124.0 cm	975.93	975.95	975.93	975.95	69.25	2.31E-05	8.92E-05	7.65E-03	0.99	6.51	0.08	0.01	9.28E-03	2.66E-02	0.042	108.64
350-U1437D - 59R - 5W, 123.0 - 125.0 cm	977.31	977.33	977.31	977.33	82.91	9.71E-05	7.35E-05	7.94E-03	0.99	3.41	0.10	0.01	8.52E-03	2.94E-02	0.027	125.90

Sample	Top depth CSF-A (m)	Bottom depth CSF-A (m)	Top depth CSF-B (m)	Bottom depth CSF-B (m)	χ_{lf} x 10^{-8} m^3/kg	NRM Am^2/kg	ARM Am^2/kg	SIRM Am^2/kg	$S_{-0.3T}$	χ_{hfield} x 10^{-8} m^3/kg	M_s Am^2/kg	M_{rs} Am^2/kg	B_c T	B_{cr} T	D_{JH}	M_{rs}/χ_{lf} kA/m
350-U1437D - 60R - 1W, 16.0 - 18.0 cm	980.56	980.58	980.56	980.58	53.06	2.51E-05	7.98E-05	5.52E-03	0.99	5.35	0.04	0.01	1.16E-02	2.90E-02	0.063	70.22
350-U1437D - 60R - 3W, 18.0 - 20.0 cm	982.55	982.57	982.55	982.57	45.24	2.03E-05	7.46E-05	6.45E-03	0.99	4.96	0.04	0.01	1.12E-02	2.79E-02	0.062	97.44
350-U1437D - 60R - 4W, 113.0 - 115.0 cm	984.69	984.71	984.69	984.71	104.89	4.91E-05	1.38E-04	1.23E-02	0.99	8.13	0.13	0.02	9.51E-03	2.80E-02	0.039	125.44
350-U1437D - 60R - 6W, 20.0 - 22.0 cm	986.00	986.02	986.00	986.02	87.84	2.48E-05	1.50E-04	1.29E-02	0.99	5.47	0.07	0.01	1.16E-02	2.80E-02	0.066	84.13
350-U1437D - 61R - 1W, 118.0 - 120.0 cm	989.78	989.80	989.78	989.80	31.00	9.97E-06	4.48E-05	3.38E-03	0.98	6.22	0.03	0.00	1.05E-02	2.73E-02	0.053	100.15
350-U1437D - 61R - 2W, 33.0 - 35.0 cm	990.43	990.45	990.43	990.45	35.28	1.42E-05	4.43E-05	3.53E-03	0.98	6.48	0.04	0.00	9.86E-03	2.89E-02	0.037	108.87
350-U1437D - 61R - 6W, 86.0 - 88.0 cm	996.30	996.32	996.30	996.32	39.98	1.01E-05	3.26E-05	4.12E-03	1.00	4.09	0.06	0.00	6.94E-03	2.43E-02	0.024	141.74
350-U1437D - 62R - 2W, 97.0 - 99.0 cm	1000.41	1000.43	1000.41	1000.43	101.63	3.03E-05	1.38E-04	1.41E-02	0.99	5.64	0.12	0.02	1.02E-02	2.58E-02	0.055	120.47
350-U1437D - 62R - 3W, 38.0 - 40.0 cm	1001.22	1001.24	1001.22	1001.24	116.64	1.94E-05	2.20E-04	1.69E-02	0.99	6.17	0.11	0.02	1.21E-02	2.70E-02	0.082	94.20

Marine

References

Abell, J. T., G. Winckler, R. F. Anderson, and T. D. Herbert (2021), Poleward and weakened westerlies during Pliocene warmth. *Nature* 589, 70-75.

Algeo, T. J., and J. B. Maynard (2004), Trace-element behavior and redox facies in core shales of Upper Pennsylvanian Kansas-type cyclothems. *Chem. Geol.* 206 (3-4), 289-318.

An, Z., G. J. Kukla, S. C. Porter, and J. Xiao (1991), Magnetic susceptibility evidence of monsoon variation on the Loess Plateau of central China during the last 130,000 years. *Quat. Res.* 36 (1), 29-36.

An, Z. (2000), The history and variability of the East Asian paleomonsoon climate. *Quat. Sci. Rev.* 19, 171-187.

An, Z., J. E. Kutzbach, W. L. Prell, and S. C. Porter (2001), Evolution of Asian monsoons and phased uplift of the Himalaya-Tibetan plateau since Late Miocene times. *Nature* 411, 62-66.

An, Z., Y. Huang, W. Liu, Z. Guo, S. Clemens, L. Li, W. Prell, Y. Ning, Y. Cai, W. Zhou, B. Lin, Q. Zhang, Y. Cao, X. Qiang, H. Chang, and Z. Wu (2005), Multiple expansions of C_4 plant biomass in East Asia since 7 Ma coupled with strengthened monsoon circulation. *Geology* 33 (9), 705-708.

An, Z., G. Wu, J. Li, Y. Sun, Y. Liu, W. Zhou, Y. Cai, A. Duan, L. Li, J. Mao, H. Cheng, Z. Shi, L. Tan, H. Yan, H. Ao, H. Chang, and J. Feng (2015), Global monsoon dynamics and climate change. *Annu. Rev. Earth Planet. Sci.* 43 (1), 29-77.

Andersen, K. K., N. Azuma, J.-M. Barnola, M. Bigler, P. Biscaye, N. Caillon, J. Chappellaz, H. B. Clausen, D. Dahl-Jensen, H. Fischer, J. Flückiger, D. Fritzsche, Y. Fujii, K. Goto-Azuma, K. Grønvold, N. S. Gundestrup, M. Hansson, C. Huber, C. S. Hvidberg, S. J. Johnsen, U. Jonsell, J. Jouzel, S. Kipfstuhl, A. Landais, M. Leuenberger, R. Lorrain, V. Masson-Delmotte, H. Miller, H. Motoyama, H. Narita, T. Popp, S. O. Rasmussen, D. Raynaud, R. Rothlisberger, U. Ruth, D. Samyn, J. Schwader, H. Shoji, M.-L. Siggard-Andersen, J. P. Steffensen, T. Stocker, A. E. Sveinbjörnsdóttir, A. Svenson, M. Takata, J.-L. Tison, Th. Thorsteinsson, O. Watanabe, F. Wilhelms, and J. W. C. White (2004), High-resolution record of Northern Hemisphere climate extending into the last interglacial period. *Nature* 431, 147-151.

Aubourg, C., and J. P. Pozzi (2010), Toward a new < 250 °C pyrrhotite-magnetite geothermometer for claystones. *Earth Planet. Sci. Lett.* 294 (1-2), 47-57.

Barkley, R. A. (1970), The Kuroshio Current. *Sci. J.* 6, 54-60.

Barth, A. M., P. U. Clark, N. S. Bill, F. He, and N. G. Pisias (2018), Climate evolution across the Mid-Brunhes Transition. *Clim. Past* 14, 2071-2087.

Bartoli, G., B. Hönisch, and R. E. Zeebe (2011), Atmospheric CO_2 decline during the Pliocene intensification of northern hemisphere glaciations. *Paleoceanography* 26, PA4213.

Beal, E. J., C. H. House, and V. J. Orphan (2009), Manganese- and iron-dependent marine methane oxidation. *Science* 325, 184-187.

Becker, K. W., J. S. Lipp, G. J. M. Versteegh, L. Wörmer, and K.-U. Hinrichs (2015), Rapid and simultaneous analysis of three molecular sea surface temperature proxies and application to sediments from the Sea of Marmara. *Org. Geochem.* 85, 42-53.

Beerling, D. J., and D. L. Royer (2011), Convergent Cenozoic CO_2 history. *Nat. Geosci.* 4, 418-420.

Beny, F., S. Toucanne, C. Skonieczny, G. Bayon, and M. Ziegler (2018), Geochemical provenance of sediments from the northern East China Sea document a gradual migration of the Asian Monsoon belt over the past 400,000 years. *Quat. Sci. Rev.* 190, 161-175.

Berner, R. A. (1981), A new geochemical classification of sedimentary environments. *J. Sed. Petrol.* 51, 359-365.

Berner, R. A. (1984), Sedimentary pyrite formation: An update. *Geochim. Cosmochim. Acta* 48 (4), 605-615.

Berger, A., and M. F. Loutre (1991), Insolation values for the climate of the last 10 million years. *Quat. Sci. Rev.* 10, 297-317.

Besnus, M. J., and A. J. P. Meyer (1964), Nouvelles données expérimentales sur le magnétisme de la pyrrhotine naturelle. In: *Proceedings of the International Conference on Magnetism*. Institute of Physics, Nottingham, London, United Kingdom, Vol. 20, pp. 507-511.

Bloemendal, J., J. W. King, F. R. Hall, and S.-J. Doh (1992), Rock magnetism of Late Neogene and Pleistocene deep-sea sediments: relationship to sediment sources, diagenetic processes and sediment lithology. *J. Geophys. Res.* 97 (B4), 4361-4375.

Bloemendal, J., X. M. Liu, and T. C. Rolph (1995), Correlation of the magnetic susceptibility stratigraphy of Chinese loess and the marine oxygen isotope record: chronological and palaeoclimatic implications. *Earth Planet. Sci. Lett.* 131, 371-380.

Boetius, A., K. Ravenschlag, C. J. Schubert, D. Rickert, F. Widdel, A. Gieseke, R. Amann, B. Barker Jørgensen, U. Witte, and O. Pfannkuche (2000), A marine microbial consortium apparently mediating anaerobic oxidation of methane. *Nature* 407 (6804), 623-626.

Bohrmann, G., J. Greinert, E. Suess, and M. Torres (1998), Authigenic carbonates from the Cascadia subduction zone and their relation to gas hydrate stability. *Geology* 26 (7), 647-650.

Bowles, J., M. Jackson, A. Chen, and P. Solheid (2009), Interpretation of low temperature data part 1: superparamagnetism and paramagnetism. *IRM Q.* 9 (3), 1-5.

Brassell, S. C., G. Eglinton, I. T. Marlowe, U. Pflaumann, and M. Sarnthein (1986), Molecular stratigraphy: A new tool for climatic assessment. *Nature* 320, 129-133.

Brassell, S. C., M. Dumitrescu, and ODP Leg 198 Shipboard Science Party (2004), Recognition of alkenones in a lower Aptian porcellanite from the west-central Pacific. *Org. Geochem.* 35, 181-188.

Brassell, S. C. (2014), Climatic influences on the Paleogene evolution of alkenones. *Paleoceanography* 29, 255-272.

Bray, E. E., and E. D. Evans (1961), Distribution of *n*-paraffins as a clue to recognition of source beds. *Geochim. Cosmochim. Acta* 22, 2-15.

Brierley, C. M., Fedorov, A. V., Z. Liu, T. D. Herbert, K. T. Lawrence, and J. P. LaRiviere (2009), Greatly expanded tropical warm pool and weakened Hadley circulation in the early Pliocene. *Science* 323, 1714-1718.

Brochier-Armanet, C., B. Boussau, S. Gribaldo, and P. Forterre (2008), Mesophilic archaea: proposal for a third archaeal phylum, the Thaumarchaeota. *Nat. Rev. Microbiol.* 6 (3), 245-252.

Busby, C. J., Y. Tamura, P. Blum, G. Guèrin, G. D. M. Andrews, A. K. Barker, J. L. R. Berger, E. M. Bongiolo, M. Bordiga, S. M. DeBari, J. B. Gill, C. Hamelin, J. Jia, E. H. John, A.-S. Jonas, M. Jutzeler, M. Kars, Z. A. Kita, K. Konrad, S. H. Mahony, M. Martini, T. Miyazaki, R. J. Musgrave, D. B. Nascimento, A. R. L. Nichols, J. M. Ribeiro, T. Sato, J. C. Schindlbeck, A. K. Schmitt, S. M. Straub, M. J. Mleneck-Vautravers, and A. Y. Yang (2017), The missing half of the subduction factory: shipboard results from the Izu rear arc, IODP Expedition 350. *Int. Geol. Rev.* 59 (13), 1677-1708.

Bush, R. T., and F. A. McInerney (2013), Leaf wax *n*-alkane distributions in and across modern plants. Implications for paleoecology and chemotaxonomy. *Geochim. Cosmochim. Acta* 117, 161-179.

Buylaert, J. P., A. S. Murray, D. Vandenberghe, M. Vriend, F. De Corte, and P. Van den Haute (2008), Optical dating of Chinese loess using sand-sized quartz: establishing a time frame for Late Pleistocene climate changes in the western part of the Chinese Loess Plateau. *Quat. Geochronol.* 3, 99-113.

Calvert, S. E., T. F. Pedersen, P. D. Aaidu, and U. Vonstackelberg (1995), On the organic-carbon maximum on the continental-slope of the eastern Arabian Sea. *J. Mar. Res.* 53, 269-296.

Calvo, E., C. Pelejero, G. A. Logan, and P. De Deckker (2004), Dust-induced changes in phytoplankton composition in the Tasman Sea during the last four glacial cycles. *Paleoceanography* 19, PA2020.

Canfield, D. E., and R. A. Berner (1987), Dissolution and pyritization of magnetite in anoxic marine sediments. *Geochim. Cosmochim. Acta* 51 (3), 645-659.

Canfield, D. E., and B. Thamdrup (2009), Towards a consistent classification scheme for geochemical environments, or, why we wish the term ‘suboxic’ would go away. *Geobiology* 7 (4), 385-392.

Carvallo, C., A. R. Muxworthy, and D. J. Dunlop (2006), First-order reversal curve (FORC) diagrams of magnetic mixtures: micromagnetic models and measurements. *Phys. Earth Planet. Inter.* 154, 308-322.

Castañeda, I. S., S. Mulitza, E. Schefuß, R. A. Lopes dos Santos, J. S. Sinninghe Damsté, and S. Schouten (2009), Wet phases in the Sahara/Sahel region and human migration patterns in North Africa. *Proc. Natl. Acad. Sci. USA* 106 (48), 20159-20163.

Castañeda, I. S., E. Schefuß, J. Pätzold, J. S. Sinninghe Damsté, S. Weldeab, and S. Schouten (2010), Millennial-scale sea surface temperature changes in the Mediterranean (Nile River Delta region) over the last 27,000 years. *Paleoceanography* 25, PA1208.

Cerling, T. E., J. M. Harris, B. J. MacFadden, M. G. Leakey, J. Quade, V. Eisenmann, and J. R. Ehleringer (1997), Global vegetation change through the Miocene/Pliocene boundary. *Nature* 389, 153-158.

Chang, L., A. P. Roberts, C. J. Rowan, Y. Tang, P. Pruner, Q. Chen, and C.-S. Horng (2009), Low-temperature magnetic properties of greigite (Fe_3S_4). *Geochem. Geophys. Geosyst.* 10, Q01Y04.

Chang, L., M. Winklhofer, A. P. Roberts, D. Heslop, F. Florindo, M. J. Dekkers, W. Krijgsman, K. Kodama, and Y. Yamamoto (2013), Low-temperature magnetic properties of pelagic carbonates: oxidation of biogenic magnetite and identification of magnetosome chains. *J. Geophys. Res. Solid Earth* 118, 6049-6065.

Chang, L., D. Heslop, A. P. Roberts, D. Rey, and K. J. Mohamed (2016a), Discrimination of biogenic and detrital magnetite through a double Verwey transition temperature. *J. Geophys. Res. Solid Earth* 121, 3-14.

Chang, L., C. T. Bolton, M. J. Dekkers, A. Hayashida, D. Heslop, W. Krijgsman, K. Kodama, G. A. Paterson, A. P. Roberts, E. J. Rohling, Y. Yamamoto, and X. Zhao (2016b), Asian monsoon modulation of nonsteady state diagenesis in hemipelagic marine sediments offshore of Japan. *Geochem. Geophys. Geosyst.* 17, 4383-4398.

Chang, L., A. P. Roberts, D. Heslop, A. Hayashida, J. Li, X. Zhao, W. Tian, and Q. Huang (2016c), Widespread occurrence of silicate-hosted magnetic mineral inclusions in marine sediments and their contribution to paleomagnetic recording. *J. Geophys. Res. Solid Earth* 121, 8415-8431.

Chen, J., Z. An, L. Liu, J. Ji, J. Yang, and Y. Chen (2001), Variations in chemical compositions of the eolian dust in Chinese Loess Plateau over the past 2.5 Ma and chemical weathering in the Asian inland. *Sci. China Ser. D. Earth Sci.* 44 (5),403-413.

Chen, R., J. Shen, C. Li, E. Zhang, W. Sun, and M. Ji (2015), Mid- to late-Holocene East Asian summer monsoon variability recorded in lacustrine sediments from Jingpo Lake, Northeastern China. *The Holocene* 25 (3), 454-468.

Chen, S., Y. Wang, H, Cheng, R. L. Edwards, X. Wang, X. Kong, and D. Liu (2016), Strong coupling of Asian monsoon and Antarctic climates on sub-orbital timescales. *Sci. Rep.* 6, 32995.

Chen, G., P. Zhang, and J. Lu (2020), Sensitivity of the latitude of the westerly jet stream to climate forcing. *Geophys. Res. Lett.* 47, e2019GL086563.

Chern, C.-S. and J. Wang (1994), Influence of the seasonal thermocline on the intrusion of Kuroshio across the continental shelf northeast of Taiwan. *J. Oceanogr.* 50, 691-711.

Chinzei, K., K. Fujioka, H. Kitazato, I. Koizumi, T. Oba, M. Oda, H. Okada, T. Sakai, and Y. Tanimura (1987), Postglacial environmental change of the Pacific Ocean off the coasts of central Japan. *Mar. Micropaleontol.* 11, 273-291.

Chiyonobu, S., Y. Mori, and M. Oda (2012), Reconstruction of paleoceanographic conditions in the northwestern Pacific Ocean over the last 500 kyr based on calcareous nannofossil and planktic foraminiferal assemblages. *Mar. Micropaleontol.* 96-97, 29-37.

Clark, P. U., D. Archer, D. Pollard, J. D. Blum, J. A. Rial, V. Brovkin, A. C. Mix, N. G. Pisias, and M. Roy (2006), The Middle Pleistocene transition: characteristics, mechanisms, and implications for long-term changes in atmospheric pCO_2. *Quat. Sci. Rev. 25,* 3150-3184.

Clift, P. D., A. Holbourn, C. France-Lanord, and H. Zheng (2020), Evolution of the Asian monsoon. *EOS* 101, https://doi.org/10.1029/2020EO146198.

COHMAP Members (1988), Climatic changes of the last 18,000 years: observations and model simulations. *Science* 241, 1043-1052.

Collister J. W., G. Rieley, B. Stern, G. Eglinton, and B. Fry (1994), Compound-specific $\delta^{13}C$ analyses of leaf lipids from plants with differing carbon dioxide metabolisms. *Org. Geochem.* 21, 619-627.

Conte, M. H., A. Thompson, G. Eglinton, and J. C. Green (1995), Lipid biomarker diversity in the coccolithophorid *Emiliania huxleyi* (Prymnesiophyceae) and the related species *Gephyrocapsa oceanica*. *J. Phycol.* 31, 272-282.

Conte, M. H., M.-A. Sicre, C. Rühlemann, J. C. Weber, S. Schulte, D. Schulz-Bull, and T. Blanz (2006), Global temperature calibration of the alkenone unsaturation index ($U^{K'}_{37}$) in surface waters and comparison with surface sediments. *Geochem. Geophys. Geosyst.* 7 (2), Q02005.

Coumou, D., G. Di Capua, S. Vavrus, L. Wang, and S. Wang (2018), The influence of Arctic amplification on mid-latitude summer circulation. *Nat. Comm.* 9, 2959.

Cronin, T.M., G.S. Dwyer, E.K. Caverly, J. Farmer, L.H. DeNinno, J. Rodriguez-Lazaro, and L. Gemery (2017), Enhanced Arctic Amplification began at the Mid-Brunhes Event ~400,000 years ago. *Sci. Rep.* 7, 14475.

Dai, A., D. Luo, M. Song, and J. Liu (2019), Arctic amplification is caused by sea-ice loss under increasing CO_2. *Nat. Comm.* 10, 121.

Dansgaard, W., H. B. Clausen, N. Gundestrup, C. U. Hammer, S. F. Johnsen, P. M. Kristinsdottir, and N. Reeh (1982), A new Greenland deep ice core. *Science* 218, 1273-1277.

Dansgaard, W., J. W. C. White, and S. J. Johnsen (1989), The abrupt termination of the Younger Dryas climate event. *Nature* 339, 532-534.

Davtian, N., G. Ménot, Y. Fagault, and E. Bard (2019), Western Mediterranean Sea paleothermometry over the last glacial cycle based on the novel RI-OH index. *Paleoceanography and Paleoclimatology* 34, 616-634.

Davtian, N., E. Bard, S. Darfeuil, G. Ménot, and F. Rostek (2021), The novel hydroxylated tetraether index RI-OH´ as a sea surface temperature proxy for the 160-45 ka BP period off the Iberian margin. *Paleoceanography and Paleoclimatology* 36, e2020PA004077.

Day, R., M. Fuller, and V. Schmidt (1977), Hysteresis properties of titanomagnetites: grain-size and compositional dependence, *Phys. Earth Planet. Int.* 13, 260-267.

De Bar, M. W., D. J. C Dorhout, E. C. Hopmans, S. W. Rampen, J. S. Sinninghe Damsté, and S. Schouten (2016), Constraints on the application of long chain diol proxies in the Iberian Atlantic margin. *Org. Geochem.* 101, 184-195.

De Bar, M. W., S. W. Rampen, E. C. Hopmans, J. S. Sinninghe Damsté, and S. Schouten (2019), Constraining the applicability of organic paleotemperature proxies for the last 90 Myrs, *Org. Geochem.* 128, 122-136.

Dekens, P. S., A. C. Ravelo, and M. D. McCarthy (2007), Warm upwelling regions in the Pliocene warm period. *Paleoceanography* 22, PA3211.

Dekkers, M. J. (1989), Magnetic properties of natural goethite II. TRM behaviour during thermal and alternating field demagnetization and low-temperature treatment. *Geophys. J. Int.* 97, 341-355.

Dekkers, M. J., J. L. Mattéi, G. Fillion, and P. Rochette (1989), Grain-size dependence of magnetic behavior of pyrrhotite during its low temperature transition at 34 K. *Geophys. Res. Lett.* 16 (8), 855-858.

De la Torre, J. R., C. B. Walker, A. E. Ingalls, M. Könneke, and D. A. Stahl (2008), Cultivation of a thermophilic ammonia oxidizing archaeon synthesizing crenarchaeol. *Environ. Microbiol.* 10, 810-818.

DeLong, E. F. (1992), Archaea in coastal marine environments. *Proc. Natl. Acad. Sci. USA* 89, 5685-5689.

DeLong, E. F., L. L. King, R. Massana, H. Cittone, A. Murray, C. Schleper, and S. G. Wakeham (1998), Dibiphytanyl ether lipids in nonthermophilic crenarchaeotes. *Appl. Environ. Microbiol.* 64, 1133-1138.

DeMenocal, P. B., and D. Rind (1993), Sensitivity of Asian and African climate to variations in seasonal insolation, glacial ice cover, sea-surface temperature and Asian orography. *J. Geophys. Res.* 98, 7265-7297.

De Rosa, M., and A. Gambacorta (1988), The lipids of archaeabacteria. *Progr. Lipid Res.* 27, 153-175.

Diefendorf A. F., K. H. Freeman, S. L. Wing, and H. V. Graham (2011), Production of n-alkyl lipids in living plants and implications for the geologic past. *Geochim. Cosmochim. Acta* 75, 7472-7485.

Diefendorf, A. F., A. B. Leslie, and S. L. Wing (2015), Leaf wax composition and carbon isotopes vary among major conifer groups. *Geochim. Cosmochim. Acta* 170, 145-156.

Dinarès-Turell, J., and M. J. Dekkers (1999), Diagenesis and remanence acquisition in the Lower Pliocene Trubi marls at Punta di Maiata (southern Sicily): Palaeomagnetic and rock magnetic observations. In: Tarling, D. H. and P. Turner (Eds.), *Palaeomagnetism and diagenesis in sediments, Special Publications.* Geological Society, London, Vol. 151, pp. 53-69.

Ding, Z., T. Liu, Z. Yu, Z. Guo, and R. Zhu (1995), Ice-volume forcing of East Asian winter monsoon variations in the past 800,000 years. *Quat. Res.* 44, 149-159.

Ding Z. L., E. Derbyshire, S. L. Yang, Z. W. Yu, S. F. Xiong, and T. S. Liu (2002), Stacked 2.6-Ma grain size record from the Chinese loess based on five sections and correlation with the deep-sea $\delta^{18}O$ record. *Paleoceanography* 17 (3), 1033.

Dunlop, D., and O. Özdemir (1997), Rock magnetism: Fundamentals and frontiers. Cambridge University Press, New York, p. 573.

Dunlop, D. J. (2002), Theory and Application of the Day plot (M_{rs}/M_s versus H_{cr}/H_c). 1. Theoretical curves and tests using titanomagnetite data. *J. Geophys. Res.* 107 (B3), 2056.

Dunlop, D., and O. Özdemir (2007), Magnetizations in Rocks and Minerals. In: Kono, M. (Ed.), *Treatise on Geophysics: Geomagnetism*. Elsevier, Amsterdam, the Netherlands, Vol. 5, pp. 277-336.

Duplessy, J. C., G. Delibrias, J. L. Turon, C. Pujol, and J. Duprat (1981), Deglacial warming of the northeastern Atlantic Ocean: Correlation with the paleoclimatic evolution of the European continent. *Palaeogeogr., Palaeoclimatol., Palaeoecol.* 35, 121-144.

Ebert, Y., R. Shaar, S. Emmanuel, N. Nowaczyk, and M. Stein (2018), Overwriting of sedimentary magnetism by bacterially mediated mineral alteration. *Geology* 46 (4), 291-294.

Egli, R., A. P. Chen, M. Winklhofer, K. P. Kodama, and C. S. Horng (2010), Detection of noninteracting single domain particles using first-order reversal curve diagrams. *Geochem. Geophys. Geosyst.* 11, Q01Z11.

Eglinton, T. I., and G. Eglinton (2008), Molecular proxies for paleoclimatology, *Earth Planet. Sci. Lett.* 275, 1-16.

Ehleringer, J. R., T. E. Cerling, and B. R. Helliker (1997), C_4 photosynthesis, atmospheric CO_2, and climate. *Oecologica* 112, 285-299.

Elling, F. J., M. Könneke, J. S. Lipp, K. W. Becker, E. J. Gagen, and K.-U. Hinrichs (2014), Effects of growth phase on the membrane lipid composition of the thaumarchaeon *Nitrosopumilus maritimus* and their implications for archaeal lipid distributions in the marine environment. *Geochim. Cosmochim. Acta* 141, 579-597.

Elling, F. J., M. Könneke, M. Mußmann, A. Greve, and K.-U. Hinrichs (2015), Influence of temperature, pH, and salinity on membrane lipid composition and TEX_{86} of marine planktonic thaumarchaeal isolates. *Geochim. Cosmochim. Acta* 171, 238-255.

Emiroglu, S., D. Rey, and N. Petersen (2004), Magnetic properties of sediment in the Ria de Arousa (Spain): Dissolution of iron oxides and formation of iron sulphides. *Phys. Chem. Earth* 29 (13-14), 947-959.

Erez, J., and B. Luz (1983), Experimental paleotemperature equation for planktonic foraminifera. *Geochim. Cosmochim. Acta* 47, 1025-1031.

Ettwig, K. F., B. Zhu, D. Speth, J. T. Keltjens, M. S. Jetten, and B. Kartal (2016), Archaea catalyze iron-dependent anaerobic oxidation of methane. *Proc. Natl. Acad. Sci. USA* 113 (45), 12792-12796.

Expedition 322 Scientists (2010), Site C0011. In: Saito, S., M. B. Underwood, Y. Kubo, and the Expedition 322 Scientists, *Proceedings of the Integrated Ocean Drillingy Program., Expedition 322*. Tokyo (Integrated Ocean Drilling Program Management International, Inc.).

Expedition 333 Scientists (2012), Site C0011. In: Henry, P., T. Kanamatsu, K. Moe, and the Expedition 333 Scientists, *Proceedings of the Integrated Ocean Drilling Program., Expedition 333*. Tokyo (Integrated Ocean Drilling Program Management International, Inc.).

Expedition 350 Scientists (2014), Izu-Bonin-Mariana rear arc: the missing half of the subduction factory. International Ocean Discovery Program Expedition 350 Preliminary Report, http://dx.doi.org/10.14379/iodp.pr.350.2014.

Fang, X., Z. An, S. C. Clemens, J. Zan, Z. Shi, S. Yang, and W. Han (2020), The 3.6-Ma aridity and westerlies history over midlatitude Asia linked with global climate cooling. *Proc. Natl. Acad. Sci. USA* 117 (40), 24729-24734.

Fietz, S., C. Huguet, J. Bendle, M. Escala, C. Gallacher, L. Herfort, R. Jamieson, A. Martínez-Garcia, E. L. McClymont, V. L. Peck, F. G. Prahl, S. Rossi, G. Rueda, A. Sanson-Barrera, and A. Rosell-Melé, A. (2012), Co-variation of crenarchaeol and branched GDGTs in globally-distributed marine and freshwater sedimentary archives. *Global and Planetary Change* 92, 275-285.

Fietz, S., C. Huguet, G. Rueda, B. Hambach, and A. Rosell-Melé (2013), Hydroxylated isoprenoidal GDGTs in the Nordic Seas. *Mar. Chem.* 152, 1-10.

Florindo, F., and L. Sagnotti (1995), Palaeomagnetism and rock magnetism at the upper Pliocene Valle Ricca (Rome, Italy) section. *Geophys. J. Int.* 123 (2), 340-354.

Florindo, F., A. P. Roberts, and M. R. Palmer (2003), Magnetite dissolution in siliceous sediments. *Geochem. Geophys. Geosyst.* 4 (7), 1053.

Frederichs, T., T. von Dobeneck, U. Bleil, and M. J. Dekkers (2003), Towards the identification of siderite, rhodochrosite, and vivianite in sediments by their low-temperature magnetic properties. *Phys. Chem. Earth* 28 (16-19), 669-679.

Gagosian, R. B., and E. T. Peltzer (1986), The importance of atmospheric input of terrestrial organic material to deep-sea sediments. *Adv. in Org. Geochem.* 10, 661-669.

Gallagher, S. J., M. W. Wallace, C. L. Li, B. Kinna, J. T. Bye, K. Akimoto, and M. Torii (2009), Neogene history of the West Pacific warm pool, Kuroshio and Leeuwin Currents. *Paleoceanography* 24 (1), PA1206.

Gallagher, S. J., A. Kitamura, Y. Iryu, T. Itaki, I. Koizumi, and P. W. Hoiles (2015), The Pliocene to recent history of the Kuroshio and Tsushima Currents: a multi-proxy approach. *Prog. Earth Planet. Sci.* 2, 17.

Garming, J. F. L., U. Bleil, and N. Riedinger (2005), Alteration of magnetic mineralogy at the sulfate-methane transition: analysis of sediments from the Argentine continental slope. *Phys. Earth Planet. Inter*. 151, 290-308.

Garrison, V.H., E.A. Shinn, W.T. Foreman, D.W. Griffin, C.W. Holmes, C.A. Kellogg, M.S. Majewski, L.L. Richardson, K.B. Ritchie, and G.W. Smith (2003), African and Asian dust: from desert soils to coral reefs. *BioScience* 53 (5), 469-480.

Ghil, M., R. M. Allen, M. D. Dettinger, K. Ide, D. Kondrashov, M. E. Mann, A. Robertson, A. Saunders, Y. Tian, F. Varadi, and P. Yiou (2002), Advanced spectral methods for climatic time series. *Rev. Geophys.* 40, 1-41.

Gill, J. B., E. M. Bongiolo, T. Miyazaki, C. Hamelin, M. Jutzeler, S. M. DeBari, A.-S. Jonas, B. S. Vaglarov, L. S. Nascimento, and M. Yakavonis (2018), Tuffaceous Mud is a Volumetrically Important Volcaniclastic Facies of Submarine Arc Volcanism and Record of Climate Change. *Geochem. Geophys. Geosyst.* 19, 1217-1243.

Gladenkov, A. Y., A. E. Oleinik, L. Marinchovich Jr., and K. B. Barinov (2002), A refined age for the earliest opening of Bering Strait. *Palaeogeogr., Palaeoclimatol., Palaeoecol.* 183, 321-328.

Gong, C., and D. J. Hollander (1999), Evidence for differential degradation of alkenones under contrasting bottom water oxygen conditions: Implications for paleotemperature reconstruction. *Geochim. Cosmochim. Acta* 63, 405-411.

Gorbarenko, S. A., N. Harada, M. I. Malakhov, Y. P. Vasilenko, A. A. Bosin, and E. L. Goldberg (2010), Orbital and millennial-scale environmental and sedimentological changes in the Okhotsk Sea during the last 350 kyr. *Glob. Planet. Change* 72, 79-85.

Gowik, U., and P. Westhoff (2011), The path from C_3 to C_4 photosynthesis. *Plant Physiol.* 155, 56-63.

Gradstein, F. M., J. G. Ogg, M. Schmitz, and G. Ogg (2012), The Geologic Time Scale 2012. Elsevier, Amsterdam, The Netherlands, pp. 1176.

Grauel, A.-L., A. Leider, M.-L. S. Goudeau, I. A. Müller, S. M. Bernasconi, K.-U. Hinrichs, G. J. de Lange, K. A. F. Zonneveld, and G. J. M. Versteegh (2013), What do SST proxies really tell us? A high-resolution multiproxy ($U^{K'}_{37}$, TEX^{H}_{86} and foraminifera $\delta^{18}O$) study in the Gulf of Taranto, central Mediterranean Sea. *Quat. Sci. Rev.* 73, 115-131.

Grootes, P. M., M. Stuiver, J. W. C. White, S. Johnsen, and J. Jouzel (1993), Comparison of oxygen isotope records from the GISP2 and GRIP Greenland ice cores. *Nature* 366, 552-554.

Grousset, F. E., P. Ginoux, A. Bory, and P. E. Biscaye (2003), Case study of a Chinese dust plume reaching the French Alps. *Geophys. Res. Lett.* 30 (6), 1277.

Guo, Z. T., B. Sun, Z. S. Zhang, S. Z. Peng, G. Q. Xiao, J Y. Ge, Q. Z. Hao, Y. S. Qiao, M. Y. Liang, J. F. Liu, Q. Z. Lin, and J. J. Wei (2008), A major reorganization of Asian climate by the early Miocene. *Clim. Past.* 4, 153-174.

Guyodo, Y., T. M. La Para, A. J. Anschutz, R. L. Penn, S. K. Banerjee, C. E. Geiss, and W. Zanner (2006), Rock magnetic, chemical and bacterial community analysis of a modern soil from Nebraska. *Earth Planet. Sci. Lett.* 251, 168-178.

Hao, Q., L. Wang, F. Oldfield, S. Peng, L. Qin, Y. Song, B. Xu, Y. Qiao, J. Bloemendal, and Z. Guo (2012), Delayed build-up of Arctic ice sheets during 400,000-year minima in insolation variability. *Nature* 490, 393-396.

Harada, N., N. Ahagin, M. Uchida, and M. Murayama (2004), Northward and southward migrations of frontal zones during the past 40 kyr in the Kuroshio-Oyashio transition area. *Geochem. Geophys. Geosyst.* 5, Q09004.

Harada, N., M. Sato, O. Seki, A. Timmermann, H. Moossen, J. Bendle, Y. Nakamura, K. Kimoto, Y. Okazaki, K. Nagashima, S. A. Gorbarenko, A. Ijiri, T. Nakatsuka, L. Menviel, M. O. Chikamoto, A. Abe-Ouchi, and S. Schouten (2012), Sea surface temperature changes in the Okhotsk Sea and adjacent North Pacific during the last glacial maximum and deglaciation. *Deep-Sea Res. II* 61-64, 93-105.

Harrison, R. J., and J. M. Feinberg (2008), FORCInel: an improved algorithm for calculating first order reversal curve distributions using locally weighted regression smoothing. *Geochem. Geophys. Geosyst.* 9 (5), Q05016.

Hayashida, A., H. Kamata, and T. Danhara (1996), Correlation of widespread tephra deposits based on paleomagnetic directions: link between a volcanic field and sedimentary sequences in Japan. *Quat. Int.* 34-36, 89-98.

Healey, F. P. (1978), Physiological indicators of nutrient deficiency in algae. *Mitt. Int. Ver. Theor. Angew. Limnol*. 21, 34-41.

Heinrich, H. (1988), Origin and consequences of cyclic ice rafting in the Northeast Atlantic Ocean during the past 130,000 years. *Quat. Res.* 29, 142-152.

Henry, P., T. Kanamatsu, and K. T. Moe (2010), NanTroSEIZE Stage 2: subduction inputs 2 and heat flow. Integrated Ocean Drilling Program Expedition 333 Scientific Prospectus, doi:10.2204/iodp.sp.333.2010.

Herbert, T. D. (2003), Alkenone paleotemperature determinations. In: Holland, H. D. and K. K. Turekian (Eds.), *Treatise on Geochemistry*. Elsevier, Amsterdam, The Netherlands, Vol. 6, pp. 391-432.

Herbert, T. D., K. T. Lawrence, A. Tzanova, L. Cleaveland Peterson, R. Caballero-Gill, and C. S. Kelly (2016), Late Miocene cooling and the rise of modern ecosystems. *Nat. Geosci.* 9, 843-847.

Herfort, L., S. Schouten, B. Abbas, M. J. W. Veldhuis, M. J. L. Coolen, C. Wuchter, J. P. Boon, G. J. Herndl, and J. S. Sinninghe Damsté (2007), Variations in spatial and temporal distribution of Archaea in the North Sea in relation to environmental variables. *FEMS Microbiol. Ecol.* 62, 242-257.

Herndl, G. J., T. Reinthaler, E. Teira H. van Aken, C. Veth, A. Pernthaler, and J. Pernthaler (2005), Contribution of Archaea to total prokaryotic production in the deep Atlantic Ocean. *Appl. Environ. Microbiol.* 71, 2303-2309.

Herzschuh, U., X. Cao, T. Laepple, A. Dallmeyer, R. J. Telford, J. Ni, F. Chen, Z. Kong, G. Liu, K.-B. Liu, X. Liu, M. Stebich, L. Tang, F. Tian, Y. Wang, J. Wischnewski, Q. Xu, S. Yan, Y. Yang, G. Yu, Y. Zhang, Y. Zhao, and Z. Zheng (2019), Position and orientation of the westerly jet determined Holocene rainfall patterns in China. *Nat. Comm.* 10, 2376.

Heslop, D., M. J. Dekkers, and C. G. Langereis (2002), Timing and structure of the mid-Pleistocene transition: records from the loess deposits of northern China. *Palaeogeogr. Palaeoclimatol. Palaeoecol.* 185, 133-143.

Heyng, A. M., C. Mayr, A. Lücke, R. Moschen, H. Wissel, B. Striewski, and T. Bauersachs (2015), Middle and Late Holocene paleotemperatures reconstructed from oxygen isotopes and GDGTs of sediments from Lake Pupuke, New Zealand. *Quatern. Int.* 374, 3-14.

Hoefs, M. J. L., G. J. M. Versteegh, W. I. C. Rijpstra, J. W. de Leeuw, and J. S. Sinninghe Damsté (1998), Postdepositional oxic degradation of alkenones: Implications for the measurement of palaeo sea surface temperatures. *Paleoceanography* 13, 42-49.

Hönisch, B., N. G. Hemming, D. Archer, M. Siddal, and J. F. McManus (2009), Atmospheric carbon dioxide concentration across the Mid-Pleistocene Transition. *Science* 324, 1551-1554.

Holmkvist, L., A. Jr. Kamyshny, C. Vogt, K. Vamvakopoulos, T. G. Ferdelman, and B. B. Jørgensen (2011), Sulfate reduction below the sulfate-methane transition in Black Sea sediments. *Deep-Sea Res. I* 58 (5), 493-504.

Hopmans, E. C., S. Schouten, R. D. Pancost, M. T. J. van der Meer, and J. S. Sinninghe Damsté (2000), Analysis of intact tetraether lipids in archaeal cell material and sediments by high performance liquid chromatography/atmospheric pressure chemical ionization mass spectrometry. *Rapid Commun. Mass Spectro.* 14, 585-589.

Hopmans, E. C., J. W. H. Weijers, E. Schefuß, L. Herfort, J. S. Sinninghe Damsté, and S. Schouten (2004), A novel proxy for terrestrial organic matter in sediments based on branched and isoprenoid tetraether lipids. *Earth Planet. Sci. Lett.* 224, 107-116.

Horng, C.-S. (2018), Unusual magnetic properties of sedimentary pyrrhotite in methane seepage sediments: Comparison with metamorphic pyrrhotite and sedimentary greigite. *J. Geophys. Res.: Sol. Earth* 123, 4601-4617.

Horng, C.-S., and A. P. Roberts (2018), The low-temperature Besnus magnetic transition: Signals due to monoclinic and hexagonal pyrrhotite. *Geochem. Geophys. Geosyst.* 19 (9), 3364-3375.

Horsfield, B., H. J. Schenk, K. Zink, R. Ondrak, V. Dieckmann, J. Kallmeyer, K. Mangelsdorf, R. di Primio, H. Wilkes, R. J. Parkes, J. Fry, and B. Cragg (2006), Living microbial ecosystems within the active zone of catagenesis: Implications for feeding the deep biosphere. *Earth Planet. Sci. Lett.* 246 (1-2), 55-69.

Hoshino, T., and F. Inagaki (2012), Molecular quantification of environmental DNA using microfluidics and digital PCR. *System. Appl. Microbiol.* 35 (6), 390-395.

Hoshino, T., T. Toki, A. Ijiri, Y. Morono, H. Machiyama, J. Ashi, K. Okamura, and F. Inagaki (2017), *Atribacteria* from the subseafloor sedimentary biosphere disperse to the hydrosphere through submarine mud volcanoes. *Front. Microbiol.* 8, 1135.

Housen, B. A., S. K. Banerjee, and B. M. Moskowitz (1996), Low-temperature magnetic properties of siderite and magnetite in marine sediments. *Geophys. Res. Lett.* 23 (20), 2843-2846.

Housen, B. A., and R. J. Musgrave (1996), Rock-magnetic signature of gas hydrates in accretionary prism sediments. *Earth Planet. Sci. Lett.* 139 (3-4), 509-519.

Hovan, S. A., D. K. Rea, N. G. Pisias (1991), Late Pleistocene continental climate and oceanic variability recorded in Northwest Pacific sediments. *Paleoceanography* 6, 349-370.

Hu, B., Z. Yang, M. Zhao, Y. Saito, D. Fan, and L. Wang (2012), Grain size records reveal past variability of the East Asian winter monsoon since the middle Holocene in the central Yellow Sea mud area, China. *Earth Sci. China* 55 (10), 1656-1668.

Hu, A., Z. Yang, C.-P. Yu, and N. Jiao (2013), Dynamics of autotrophic marine planktonic Thaumarchaeota in the East China Sea. *PLoS ONE* 8 (4)*:* e61087.

Huguet, C., J. E. Cartes, J. S. Sinninghe Damsté, and S. Schouten (2006), Marine crenarchaeotal membrane lipids in decapods: Implications for the TEX_{86} paleothermometer. *Geochem. Geophys. Geosyst.* 7 (11), Q11010, doi:10.1029/2006GC001305.

Huguet, C., A. Schimmelmann, R. Thunell, L. J. Lourens, J. S. Sinninghe Damsté, and S. Schouten (2007), A study of the TEX_{86} paleothermometer in the water column and sediments of the Santa Barbara Basin, California. *Paleoceanography* 22, PA3203.

Huguet, C., J.-H. Kim, G. J. de Lange, J. S. Sinninghe Damsté, and S. Schouten (2009), Effects of long term oxic degradation on the $U^{K'}_{37}$, TEX_{86} and BIT organic proxies. *Org. Geochem.* 40, 1188-1194.

Huguet, C., S. Fietz, and A. Rosell-Melé (2013), Global distribution patterns of hydroxyl glycerol dialkyl glycerol tetraethers. *Org. Geochem.* 57, 107-118.

Hurley, S. J., F. J. Elling, M. Könneke, C. Buchwald, S. D. Wankel, A. E. Santoro, J. S. Lipp, K.-U. Hinrichs, and A. Pearson (2016), Influence of ammonia oxidation rate on thaumarchaeal lipid composition and the TEX_{86} temperature proxy. *Proc. Natl. Acad. Sci. USA* 113 (28), 7762-7767.

Ijiri, A., F. Inagaki, Y. Kubo, R. R. Adhikari, S. Hattori, T. Hoshino, H. Imachi, S. Kawagucci, Y. Morono, Y. Ohtomo, S. Ono, S. Sakai, K. Takai, T. Toki, D. T. Wang, M. Y. Yoshinaga, G. L. Arnold, J. Ashi, D. H. Case, T. Feseker, K.-U. Hinrichs, Y. Ikegawa, M. Ikehara, J. Kallmeyer, H. Kumagai, M. A. Lever, S. Morita, K. Nakamura, Y. Nakamura, M. Nishizawa, V. J. Orphan, H. Røy, F. Schmidt, A. Tani, W. Tanikawa, T. Terada, H. Tomaru, T. Tsuji, I. Tsunogai, Y. T. Yamaguchi, and N. Yoshida (2018), Deep-biosphere methane production stimulated by geofluids in the Nankai accretionary complex. *Sci. Adv.* 4 (6), 1-15.

Ike, T., G. F. Moore, S. Kuramoto, J.-O. Park, Y. Kaneda, and A. Taira (2008), Tectonics and sedimentation around Kashinosaki Knoll: a subducting basement high in the eastern Nankai Trough. *Isl. Arc.* 17 (3), 358-375.

Inagaki, F., K.-U. Hinrichs, Y. Kubo, M. W. Bowles, V. B. Heuer, W.-L. Hong, T. Hoshino, A. Ijiri, H. Imachi, M. Ito, M. Kaneko, M. A. Lever, Y.-S. Lin, B. A. Methé, S. Morita, Y. Morono, W. Tanikawa, M. Bihan, S. A. Bowden, M. Elvert, C. Glombitza, D. Gross, G. J. Harrington, T. Hori, K. Li, D. Limmer, C.-H. Liu, M. Murayama, N. Ohkouchi, S. Ono, Y.-S. Park, S. C. Phillips, X. Prieto-Mollar, M. Purkey, N. Riedinger, Y. Sanada, J. Sauvage, G. Snyder, R. Susilawati, Y. Takano, E. Tasumi, T. Terada, H. Tomaru, E. Trembath-Reichert, D. T. Wang, and Y. Yamada (2015), Exploring deep microbial life in coal-bearing sediment down to ~2.5 km below the ocean floor. *Science* 349 (6246), 420-424.

Inglis, G. N., and J. E. Tierney (2020), The TEX_{86} paleotemperature proxy. In: Lyons, T., A. Turchyn, and C. Reinhard (Eds.), *Cambridge Element: Elements in Geochemical Tracers in Earth System Science*. Cambridge University Press, Cambridge, United Kingdom.

Isoguchi, O., and Kawamura, H. (2006), Oyashio seasonal intensification and its effect on subsurface temperature variation off the Sanriku coast. *J. Geophys. Res.* 111, C10006.

Isono, D., M. Yamamoto, T. Irino, T. Oba, M. Murayama, T. Nakamura, and H. Kawahata (2009), The 1500-year climate oscillation in the midlatitude North Pacific during the Holocene. *Geology* 37 (7), 591-594.

Ito, M., and K. Horikawa (2000), Millennial- to decadal-scale fluctuation in the paleo-Kuroshio current documented in the Middle Pleistocene shelf succession on the Boso Peninsula, Japan. *Sediment. Geol.* 137 (1-2), 1-8.

Itoh, S., and I. Yasuda (2009), Characteristics of mesoscale eddies in the Kuroshio-Oyashio extension region detected from the distribution of the sea surface height anomaly. *J. Phys. Oceanogr.* 40, 1018-1034.

Jaccard, S. L., E. D. Galbraith, D. M. Sigman, and G. H. Haug (2010), A pervasive link between Antarctic ice core and subarctic Pacific sediment records over the past 800 kyrs. *Quat. Sci. Rev.* 29, 206-212.

Jahn, B. M., S. Gallet, and J. M. Han (2001), Geochemistry of the Xining, Xifeng and Jixian sections, Loess Plateau of China: eolian dust provenance and paleosol evolution during the last 140 ka. *Chem. Geol.* 178 (1-4), 71-94.

Jansen, J. H. F., A. Kuijpers, and S. R. Troelstra (1986), A Mid-Brunhes Climatic Event: long term changes in global atmosphere and ocean circulation. *Science* 232, 619-622.

Japan Oceanographic Data Center: http://www.jodc.go.jp/jdoss_stat/stat-infor-sca_e.htm.

Jetter, R., L. Kunst, and A. L. Samuels (2006), Composition of plant cuticular waxes. In: Riederer, M., and C. Muller (Eds.), *Annual plant reviews, Vol. 23, Biology of the plant cuticle*. Blackwell Publishing, Oxford, United Kingdom.

Jian, Z., P. Wang, Y. Saito, J. Wang, U. Pflaumann, T. Oba, and X. Cheng (2000) Holocene variability of the Kuroshio Current in the Okinawa Trough, northwestern Pacific Ocean. *Earth Planet. Sc. Lett.* 184, 305-319.

Jiang, W.-T., C.-S. Horng, A. P. Roberts, and D. R. Peacor (2001), Contradictory magnetic polarities in sediments and variable timing of neoformation of authigenic greigite. *Earth Planet. Sci. Lett.* 193, 1-12.

Jo, K.-N., K. S. Woo, S. Yi, D. Y. Yang, H. S. Lim, Y. Wang, H. Cheng, and R. L. Edwards (2014), Mid-latitude interhemispheric hydrologic seesaw over the past 550,000 years. *Nature* 508, 378-382.

Jonas, A.-S., L. Schwark, and T. Bauersachs (2017), Late Quaternary water temperature variations of the Northwest Pacific based on the lipid paleothermometers TEX^{H}_{86}, $U^{K'}_{37}$ and LDI. *Deep-Sea Res. I* 125, 81-93.

Jørgensen, B. B., and S. Kasten (2006), Sulfur cycling and methane oxidation. In: H. D. Schulz, and M. Zabel (Eds.), *Marine geochemistry*. Springer, Berlin, Heidelberg, Germany, pp. 271-309.

Jouzel, J., V. Masson-Delmotte, O. Cattani, G. Dreyfus, S. Falourd, G. Hoffmann, B. Minster, J. Nouet, J. M. Bamola, J. Chappellaz, H. Fischer, J. C. Gallet, S. Johnsen, M. Leuenberger, L. Loulergue, D. Lüthi, H. Oerter, F. Parrenin, G. Raisbeck, D. Raynaud, A. Schilt, J. Schwander, E. Selmo, R. Souchez, R. Spahni, B. Stauffer, J. P. Steffensen, B. Stenni, T. F. Stocker, J. L. Tison, M. Werner, and E. W. Wolff (2007), Orbital and millennial Antarctic climate variability over the past 800,000 years. *Science* 317, 793-796.

Kagimoto, T., and T. Yamagata (1997), Seasonal transport variations of the Kuroshio: An OGCM simulation. *J. Phys. Oceanogr.* 27, 403-418.

Kallmeyer, J., R. Pockalny, R. R. Adhikari, D. C. Smith, and S. D'Hondt (2012), Global distribution of microbial abundance and biomass in subseafloor sediment. *Proc. Natl. Acad. Sci. USA* 109 (40), 16213-16216.

Kao, S. J., C. S. Horng, A. P. Roberts, and K. K. Liu (2004), Carbon-sulfur-iron relationships in sedimentary rocks from southwestern Taiwan: influence of geochemical environment on greigite and pyrrhotite formation. *Chem. Geol.* 203, 153-168.

Kao, S. J., C. S. Horng, S. C. Hsu, K. Y. Wei, J. Chen, and Y. S. Lin (2005), Enhanced deepwater circulation and shift of sedimentary organic matter oxidation pathway in the Okinawa Trough since the Holocene. *Geophys. Res. Lett.* 32, L15609.

Kao, S. J., C.-R. Wu, Y.C. Hsin, and M. Dai (2006a), Effects of sea level change on the upstream Kuroshio Current through the Okinawa Trough. *Geophys. Res. Lett.* 33, L16604.

Kao, S. J., A. P. Roberts, S. C. Hsu, Y. P. Chang, W. B. Lyons, and M. T. Chen (2006b), Monsoon forcing, hydrodynamics of the Kuroshio Current, and tectonic effects on sedimentary organic carbon and sulfur cycling in the Okinawa Trough since 90 ka. *Geophys. Res. Lett.* 33, L05610.

Karlin, R. (1990), Magnetite diagenesis in marine sediments from the Oregon continental margin. *J. Geophys. Res.* 95, 4405-4419.

Karner, M. B., E. F. DeLong, and D. M. Karl (2001), Archaeal dominance in the mesopelagic zone of the Pacific Ocean. *Nature* 409, 507-510.

Kars, M., C. Aubourg, J.-P. Pozzi (2011), Low temperature magnetic behaviour near 35 K in unmetamorphosed claystones. *Geophys. J. Internat.* 186 (3), 1029-1035.

Kars, M., C. Lerouge, S. Grangeon, C. Aubourg, C. Tournassat, B. Madé, and F. Claret (2015), Identification of nanocrystalline goethite in reduced clay formations. Application to the Callovian-Oxfordian formation of Bure (France). *Am. Mineral.* 100 (7), 1544-1554.

Kars, M., and K. Kodama (2015), Authigenesis of magnetic minerals in gas hydrate-bearing sediments in the Nankai Trough, offshore Japan. *Geochem. Geophys. Geosyst.* 16, 947-961.

Kars, M., R. J. Musgrave, K. Kodama, A.-S. Jonas, M. Bordiga, W. Ruebsam, M. J. Mleneck-Vautravers, and T. Bauersachs (2017), Impact of climate change on the magnetic mineral assemblage in marine sediments from the Izu rear arc, NW Pacific Ocean, over the last 1 Myr. *Palaeogeogr., Palaeoclimatol., Palaeoecol.* 480, 53-69.

Kasten, S., T. Freudenthal, F. X. Gingele, and H. D. Schulz (1998), Simultaneous formation of iron-rich layers at different redox boundaries in sediments of the Amazon deep-sea fan. *Geochim. Cosmochim. Acta* 62, 2253-2264.

Kawabe, M. (1985), Sea level variations at the Izu Islands and typical stable paths of the Kuroshio. *J. Oceanogr. Soc. Japan* 41, 307-326.

Kawabe, M. (1995), Variations of Current Path, Velocity, and Volume Transport of the Kuroshio in Relation with the Large Meander. *J. Phys. Oceanogr.* 25, 3103-3117.

Kawabe, M. (2005), Variations of the Kuroshio in the Southern Region of Japan: Conditions for Large Meander of the Kuroshio. *J. Oceanogr.* 61, 529-537.

Kawahata, H., and H. Ohshima (2002), Small latitudinal shift in the Kuroshio Extension (Central Pacific) during glacial times: evidence from pollen transport. *Quat. Sci. Rev.* 21 (14), 1705-1717.

Kawamura, K. (1995), Land-derived lipid class compounds in the deep-sea sediments and marine aerosols from North Pacific. In: Nozaki, Y., and H. Sakai (Eds.), *Biogeochemical Processes and Ocean Flux in the Western Pacific*. Terra Scientific Publishing Company, Tokyo, Japan, pp. 31-51.

Kawamura, K., Y. Ishimura, and K. Yamazaki (2003), Four years´ observations of terrestrial lipid class compounds in marine aerosols from the western North Pacific. *Glob. Biogeochem. Cycl.* 17(1), 1003.

Kemp, A. E. S., I. Grigorov, R. B. Pearce, and A. C. Naveira Garabato (2010), Migration of the Antarctic Polar Front through the mid-Pleistocene transition: evidence and climatic implications. *Quat. Sci. Rev.* 29, 1993-2009.

Killops, S. D., and V. J. Killops (2005), An Introduction to Organic Geochemistry, 2nd edition. Blackwell Publishing Ltd., Malden, MA, USA.

Kim, J.-H., N. Rimbu, S. J. Lorenz, G. Lohmann, S.-I. Nam, S. Schouten, C. Rühlemann, and R. R. Schneider (2004), North Pacific and North Atlantic sea-surface temperature variability during the Holocene. *Quat. Sci. Rev.* 23, 2141-2154.

Kim, J.-H., J. van der Meer, S. Schouten, P. Helmke, V. Willmott, F. Sangiorgi, N. Koc, E. C. Hopmans, and J. S. Sinninghe Damsté (2010), New indices and calibrations derived from the distribution of crenarchaeal isoprenoid tetraether lipids: Implications for past sea surface temperature reconstructions. *Geochim. Cosmochim. Acta* 74, 4639-4654.

Kim, J.-H., O. E. Romero, G. Lohmann, B. Donner, T. Laepple, E. Haam, and J. S. Sinninghe Damsté (2012), Pronounced subsurface cooling of North Atlantic waters off Northwest Africa during Dansgaard-Oeschger interstadials. *Earth Planet. Sci. Lett.* 339-340, 95-102.

Kim, J.-H., S. Schouten, M. Rodrigo-Gámiz, S. Rampen, G. Marino, C. Huguet, P. Helmke, R. Buscail, E. C. Hopmans, J. Pross, F. Sangiorgi, J. B. M. Middelburg, and J. Sinninghe-Damsté (2015), Influence of deep-water derived isoprenoid tetraether lipids on the TEX^{H}_{86} paleothermometer in the Mediterranean Sea. *Geochim. Cosmochim. Acta* 150, 125-141.

Kim, J.-H., L. Villanueva, C. Zell, and J. S. Sinninghe Damsté (2016), Biological source and provenance of deep-water derived isoprenoid tetraether lipids along the Portuguese continental margin. *Geochim. Cosmochim. Acta* 172, 177-204.

Kimura, J.-I., Y. Okada, K. Nakayama, and S. Okada (2001), Variations of magnetic susceptibility and fine quartz accumulation rate in Daisen loam over the past 200 000 years: interaction between winter and summer monsoons in south-west Japan. *Isl. Arc* 10, 85-97.

Kimura, J.-I., R. J. Stern, and T. Yoshida (2005), Reinitiation of subduction and magmatic responses in SW Japan during Neogene time. *Geol. Soc. Am. Bull.* 117(7-8), 969-986.

Kissel, C., C. Laj, S. Clemens, and P. Solheid (2003), Magnetic signature of environmental changes in the last 1.2 Myr at ODP Site 1146, South China Sea. *Mar. Geol.* 201, 119-132.

Kitamura, A., and T. Kawagoe (2006), Eustatic sea-level change at the Mid Pleistocene climate transition: new evidence from the shallow marine sediment record of Japan. *Quat. Sci. Rev.* 25, 323-335.

Knittel, K., and A. Boetius (2009), Anaerobic oxidation of methane: Progress with an unknown process. *Annual Rev. Microbiol.* 63 (1), 311-334.

Koga, Y., T. Kyuragi, M. Nishihara, and N. Sone (1998), Did archaeal and bacterial cells arise independently from noncellular precursors? A hypothesis stating that the advent of membrane phospholipid with enantiomeric glycerophosphate backbones caused the separation of the two lines of descent. *J. Mol. Evol.* 46, 54-63.

Koizumi, I. (2008), Diatom-derived SSTs (*Td´* ratio) indicate warm seas off Japan during the middle Holocene (8.2-3.3 kyr BP). *Mar. Micropal.* 69, 263-281.

Koizumi, I., and T. Sakamoto (2010), Synchronous *Td´*-derived SSTs (°C) off Japan with climatic events in the northern hemisphere. *J. Geogr.* 119, 489-509 (in Japanese with English abstract).

Koizumi, I., and H. Yamamoto (2010), Paleoceanographic evolution of North Pacific surface water off Japan during the past 150,000 years. *Mar. Micropaleontol.* 74, 108-118.

Korff, L., T. von Dobeneck, T. Frederichs, S. Kasten, G. Kuhn, R. Gersonde, and B. Diekmann (2016), Cyclic magnetite dissolution in Pleistocene sediments of the abyssal northwest Pacific Ocean: evidence for glacial oxygen depletion and carbon trapping. *Paleoceanography* 31, PA002882.

Kosterov, A., T. Frederichs, and T. von Dobeneck (2006), Low-temperature magnetic properties of rhodochrosite ($MnCO_3$). *Phys. Earth Planet. Interiors* 154 (3-4), 234-242.

Kotthoff, U., J. Groeneveld, J. L. Ash, A. S. Fanget, N. Q. Krupinski, O. Peyron, A. Stepanova, A., J. Warnock, N. A. G. M. Van Helmond, B. H. Passey, O. R. Clausen, O. Bennike, E. Andrén, W. Granoszewski, T. Andrén, H. L. Filipsson, M. S. Seidenkrantz, C. P. Slomp, and T. Bauersachs (2017), Reconstructing Holocene temperature and salinity variations in the western Baltic Sea region: A multi-proxy comparison from the Little Belt (IODP Expedition 347, Site M0059). *Biogeosciences* 14, 5607-5632.

Kremer, A., R. Stein, K. Fahl, Z. Ji, Z. Yang, S. Wiers, J. Matthiessen, M. Forwick, L. Löwemark, M. O´Regan, J. Chen, and I. Snowball (2018), Changes in sea ice cover and ice sheet extent at the Yermak Plateau during the last 160 ka – Reconstructions from biomarker records. *Quat. Sci. Rev.* 182, 93-108.

Kucera, M., M. Weinelt, T. Kiefer, U. Pflaumann, A. Hayes, M. Weinelt, M-T. Chen, A. C. Mix, T. T. Barrows, E. Cortijo, J. Duprat, S. Juggins, and C. Waelbroeck (2005), Reconstruction of sea-surface temperatures from assemblages of planktonic foraminifera: multi-technique approach based on geographically constrained calibration data sets and its application to glacial Atlantic and Pacific Oceans. *Quat. Sci. Rev.* 24, 951-998.

Kuhnt, W., A. Holbourn, R. Hall, M. Zuvera, M., and R. Kase (2004), Neogene history of the Indonesian throughflow. In: Clift, P., W. Kuhnt, P. Wang, and D. Hayes (Eds.), *Continent-Ocean Interactions Within East Asian Marginal Seas.* In: *Geophysical Monograph Series.* American Geophysical Union, Washington, DC, USA, Vol. 149, pp. 299-320.

Kukla, G., and Z. An (1989), Loess stratigraphy in Central China. *Palaeogeogr. Palaeoclimatol. Palaeoecol.* 72, 203-225.

Labe, Z., Y. Peings, and G. Magnusdottir (2020), Warm Arctic, cold Siberia pattern: role of full Arctic Amplification versus sea-ice loss alone. *Geophys. Res. Lett.* 47, e2020GL088583.

LaRiviere, J. P., A. C. Ravelo, A. Crimmins, P. S. Dekens. H. L. Ford, M. Lyle, and M. W. Wara (2012), Late Miocene decoupling of oceanic warmth and atmospheric carbon dioxide forcing. *Nature* 486, 97-100.

Larrasoaña, J. C., A. P. Roberts, R. J. Musgrave, E. Gràcia, E. Piñero, M. Vega, and F. Martínez-Ruiz (2007), Diagenetic formation of greigite and pyrrhotite in marine sedimentary systems containing gas hydrates. *Earth Planet. Sci. Lett.* 261 (3-4), 350-366.

Laskar, J., P. Robutel, F. Joutel, M. Gastineau, A. C. M. Correia, and B. Levrard (2004), A long-term numerical solution for the insolation quantities of the Earth. *Astron. Astrophys.* 428, 261-285.

Lattaud, J., J.-H. Kim, C. de Jonge, C. Zell, J. S. Sinninghe Damsté, and S. Schouten (2017), The C_{32} alkane-1,15-diol as a tracer for riverine input in coastal seas. *Geochim. Cosmochim. Acta* 202, 146-158.

Lattaud, J., L. Lo, J.-J. Huang, Y.-M. Chou, S. A. Gorbarenko, J. S. Sinninghe Damsté, and S. Schouten (2018), A comparison of late Quaternary organic proxy-based paleotemperature records of the central Sea of Okhotsk. *Paleoceanography and Paleoclimatology* 33 (7), 732-744.

Lattaud, J., S. Balzano, M. T. J. van der Meer, L. Villanueva, E. C. Hopmans, J. S. Sinninghe Damsté, and S. Schouten (2021), Sources and seasonality of long-chain diols in a temperate lake (Lake Geneva). *Org. Geochem.* 156, 104223.

Lawrence, K. T., Z. Liu, and T. D. Herbert (2006), Evolution of the Eastern tropical Pacific through Plio-Pleistocene glaciation. *Science* 312, 79-83.

Leider, A., K.-U. Hinrichs, G. Mollenhauer, and G. J. M. Versteegh (2010), Core-top calibration of the lipid-bases $U^{K'}_{37}$ and TEX_{86} temperature proxies on the southern Italian shelf (SW Adriatic Sea, Gulf of Taranto). *Earth Planet. Sci. Lett.* 300, 112-124.

Leslie, B. W., D. E. Hammond, W. M. Berelson, and S. P. Lund (1990a), Diagenesis in anoxic sediments from the California continental borderland and its influence on iron, sulfur, and magnetite behavior. *J. Geophys. Res.* 95, 4453-4470.

Leslie, B. W., S. P. Lund, and D. E. Hammond (1990b), Rock magnetic evidence for the dissolution and authigenic growth of magnetic minerals within anoxic marine sediments of the California continental borderland. *J. Geophys. Res.* 95, 4437-4452.

Levitan, M. A., T. G. Kuzmina, V. L. Luksha, I. A. Roshchina, K. V. Syromyatnikow, L. Max, D. Nuernberg, J.-R. Riethdorf, and R. Tiedemann (2013), Late Pleistocene sedimentation history of the Shirshov Ridge, Bering Sea. *Geochem. Int.* 51 (3), 173-204.

Li, T., Z. Liu, M. A. Hall, S. Berne, Y. Saito, S. Cang, and Z. Cheng (2001), Heinrich event imprints in the Okinawa Trough: evidence from oxygen isotope and planktonic foraminifera. *Palaeogeogr., Palaeoclimatol., Palaeoecol.* 176, 133-146.

Li, L., Q. Li, J. Tian, P. Wang, H. Wang, and Z. Liu (2011), A 4-Ma record of thermal evolution in the tropical western Pacific and its implications on climate change. *Earth Planet. Sci. Lett.* 309, 10-20.

Li, M., L. Hinnov, and L. R. Kump (2019), Acycle: Time-series analysis software for paleoclimate research and education. *Computers & Geosciences* 127, 12-22.

Licht, A., M. van Cappelle, H. A. Abels, J.-B. Ladant, J. Trabucho-Alexandre, C. France-Lanord, Y. Donnadieu, J. Vandenberghe, T. Rigaudier, C. Lécuyer, D. Terry Jr., R. Adriaens, A. Boura, Z. Guo, Aung Naing Soe, J. Quade, G. Dupont-Nivet, and J.-J. Jaeger (2014), Asian monsoons in a late Eocene greenhouse world. *Nature* 513, 501-506.

Lincoln, S. A., B. Wai, J. M. Eppley, M. J. Church, R. E. Summons, and E. F. DeLong (2014), Planktonic Euryarchaeota are a significant source of archaeal tetraether lipids in the ocean. *Proc. Natl. Acad. Sci. USA*, 111 (27), 9858-9863.

Lisiecki, L. E., and M. E. Raymo (2005), A Pliocene-Pleistocene stack of 57 globally distributed benthic $\delta^{18}O$ records. *Paleoceanography* 20, PA1003.

Lisiecki, L. E., and M. E. Raymo (2007), Plio-Pleistocene climate evolution: trends and transitions in glacial cycle dynamics. *Quat. Sci. Rev.* 26, 56-69.

Liu, Z., and T. D. Herbert (2004), High-latitude influence on the eastern equatorial Pacific climate in the early Pleistocene epoch. *Nature* 427, 720-723.

Liu, J., R. Zhu, A. P. Roberts, S. Li, and J. H. Chang (2004), High-resolution analysis of early diagenetic effects on magnetic minerals in post-middle-Holocene continental shelf sediments from the Korea Strait. *J. Geophys. Res.* 109, B03103.

Liu, Q., A. P. Roberts, J. Torrent, C.-S. Horng, and J. C. Larrasoaña (2007a), What do the HIRM and S-ratio really measure in environmental magnetism? *Geochem. Geophys. Geosyst.* 8 (9), Q09011.

Liu, Q., C. Deng, J. Torrent, and R. Zhu (2007b), Review of recent developments in mineral magnetism of the Chinese loess. *Quat. Sci. Rev.* 26, 368-385.

Liu, X.-L., J. S. Lipp, J. H. Simpson, Y.-S. Lin, R. E. Summons, and K.-U. Hinrichs (2012), Mono- and dihydroxyl glycerol dibiphytanyl glycerol tetraethers in marine sediments: identification of both core and intact polar lipid forms. *Geochim. Cosmochim. Acta* 89, 102-115.

Liu, J., D. Wu, G. Liu, R. Mao, S. Chen, M. Ji, P. Fu, Y. Sun, Y. Pan, H. Jin, Y. Zhou, and X. Wan (2020), Impact of Arctic amplification on declining spring dust events in East Asia. *Clim. Dyn.* 54, 1913-1935.

Lo, L., S. Belt, J. Lattaud, T. Friedrich, C. Zeeden, S. Schouten et al. (2018), Precession and atmospheric CO_2 modulated variability of sea ice in the central Okhotsk Sea since 130,000 years ago. *Earth Planet. Sci. Lett.* 488, 36-45.

Lopes dos Santos, R. A., M. Prange, I. S. Castañeda, E. Schefuß, S. Mulitza, M. Schulz, E. M. Niedermeyer, J. S. Sinninghe Damsté, and S. Schouten (2010), Glacial-interglacial variability in Atlantic meridional overturning circulation and thermocline adjustments in the tropical North Atlantic. *Earth Planet. Sci. Lett*. 300, 407-414.

Lopes dos Santos, R. A., M. I. Spooner, T. T. Sparrows, P. De Deckker, J. S. Sinninghe Damsté, and S. Schouten (2013), Comparison of organic ($U^{K'}_{37}$, TEX^{H}_{86}, LDI) and faunal proxies (foraminiferal assemblages) for reconstruction of late Quaternary sea surface temperature variability from offshore southeastern Australia. *Paleoceanography* 28, 377-387.

Lorius, C., L. Merlivat, J. Jouzel, and M. Pourchet (1979), A 30,000-yr isotope climatic record from Antarctic ice. *Nature* 280, 644-648.

Lu, R., and S. K. Banerjee (1994), Magnetite dissolution in deep sediments and its hydrologic implication: A detailed study of sediments from site 808, leg 131. *J. Geophys. Res.* 99 (B5), 9051-9059.

Lu, H., X. Wang, X. Wang, X. Chang, H. Zhang, Z. Xu, W. Zhang, H. Wei, X. Zhang, S. Yi, W. Zhang, H. Feng, Y. Wang, Y. Wang, and Z. Han (2019), Formation and evolution of Gobi Desert in central and eastern Asia. *Earth-Sci. Rev.* 194, 251-263.

Lü, X., X.-L. Liu, F. J. Elling, H. Yang, S. Xie, J. Song, X. Lie, H. Yuan, N. Li, and K.-U. Hinrichs (2015), Hydroxylated isoprenoid GDGTs in Chinese coastal seas and their potential as a paleotemperature proxy for mid-to-low latitude marginal seas. *Org. Geochem.* 89-90, 31-43.

Lü, X., J. Chen, T. Han, H. Yang, W. Wu, W. Ding, and K.-U. Hinrichs (2019), Origin of hydroxyl GDGTs and regular isoprenoid GDGTs in suspended particulate matter of Yangtze River Estuary. *Org. Geochem.* 128, 78-85.

Lüthi, D., M. Le Floch, B. Bereiter, T. Blunier, J. M. Bamola, U. Siegenthaler, D. Raynaud, J. Jouzel, H. Fischer, K. Kawamura, and T. F. Stocker (2008), High-resolution carbon dioxide concentration record 650,000-800,000 years before present. *Nature* 453, 379-382.

Lyle, M., J. Barron, T. J. Bralower, M. Huber, A. Olivarez Lyle, A. C. Ravelo, D. K. Rea, and P. A. Wilson (2008), Pacific Ocean and Cenozoic evolution of climate. *Rev. Geophys.* 46, RG2002.

Ma, C., S. Coffinet, J. S. Lipp, K.-U. Hinrichs, and C. Zhang (2020), Marine Group II Euryarchaeota contribute to the Archaeal Lipid Pool in Northwestern Pacific Ocean surface waters. *Front. Microbiol.*, 11, 1034.

Maher, B. A., and R. Thompson (1999), Quaternary Climates, Environments and Magnetism. Cambridge University Press, Cambridge, United Kingdom, pp. 1-48.

Maier-Reimer, E., U. Mikolajewicz, and T. Crowley (1990), Ocean general circulation model sensitivity experiment with an open Central American Isthmus. *Paleoceanography* 5 (3), 349-366.

Mann, M. E., and J. M. Less (1996), Robust estimation of background noise and signal detection in climatic series. *Climat. Change* 33, 409-445.

Marlowe, I. T., S. C. Brassell, G. Eglinton, and J. C. Green J. C. (1984), Long-chain unsaturated ketones and esters in living algae and marine sediments. *Org. Geochem*. 6, 135-141.

Marlowe, I. T., S. C. Brassell, G. Eglinton, and J. C. Green (1990), Long-chain alkenones and alkyl alkenoates and the fossil record of marine sediments. *Chem. Geol.* 88, 349-375.

Martínez-Garcia, A., A. Rosell-Melé, E. L. McClymont, R. Gersonde, and G. H. Haug (2010), Subpolar link to the emergence of the modern equatorial Pacific cold tongue. *Science* 328, 1550-1553.

Martínez-Garcia, A., A. Rosell-Melé, S. L. Jaccard, W. Geibert, D. M. Sigman, and G. H. Haug (2011), Southern Ocean dust-climate coupling over the past four million years. *Nature* 476, 312-315.

Martiny, A. C., M. W. Lomas, W. Fu, P. W. Boyd, Y. L. Chen, G. A. Cutter, M. J. Ellwood, K. Furuya, F. Hashihama, J. Kanda, D. M. Karl, T. Kodama, Q. P. Li, J. Ma, T. Moutin, E. M. S. Woodward, and J. K. Moore (2019), Biogeochemical controls of surface ocean phosphate. *Sci. Adv.* 5, eaax0341.

März, C., J. Hoffman, U. Bleil, G. J. de Lange, and S. Kasten (2008), Diagenetic changes of magnetic and geochemical signals by anaerobic methane oxidation in sediments of the Zambezi deep-sea fan (SW Indian Ocean). *Mar. Geol.* 255 (3-4), 118-130.

Maslin, M. A., X. S. Li, M.-F. Loutre, and A. Berger (1998), The contribution of orbital forcing to the progressive intensification of northern hemisphere glaciation. *Quat. Sci. Rev.* 17, 411-426.

Masson-Delmotte, V., M. Kageyama, P. Braconnot, S. Charbit, G. Krinner, C. Ritz, E. Guilyardi, J. Jouzel, A. Abe-Ouchi, M. Crucifix, R. M. Gladstone, C. D. Hewitt, A. Kitoh, A. N. LeGrande, O. Marti, U. Merkel, T. Motoi, R. Ohgaito, B. Otto-Bliesner, W. R. Peltier, I. Ross, P. J. Valdes, G. Vettoretti, S. L. Weber, F. Wolk, and Y. Yu (2006), Past and future polar amplification of climate change: climate model intercomparisons and ice-core constraints. *Clim. Dyn.* 26, 513-529.

Matas, A. J., M. J. Sanz, and A. Heredia (2003), Studies on the structure of the plant wax nonacosan-10-ol, the main component of epicuticular wax conifers. *Int. J. Biol. Macromol.* 33, 31-35.

Matsuzaki, K. M., H. Nishi, N. Suzuki, G. Cortese, F. Eynaud, R. Takashima, Y. Kawate, and T. Sakai (2014), Paleoceanographic history of the Northwest Pacific Ocean over the past 740 kyr, discerned from radiolarian fauna. *Palaeogeogr., Palaeoclimatol., Palaeoecol.* 396, 26-40.

Meng, X., L. Liu, X. Miao, W. Zhao, E. Zhang, and J. Ji (2021), Significant influence of Northern Hemisphere high latitude climate on appeared precession rhythm of East Asian summer monsoon after Mid-Brunhes Transition interglacials recorded in Chinese loess. *Catena* 197, 105002.

Meyers, P. A. (1994), Preservation of elemental and isotopic source identification of sedimentary organic matter. *Chem. Geol.* 114, 289-302.

Meyers, P. A. (2003), Applications of organic geochemistry to paleolimnological reconstructions: a summary of examples from the Laurentian Great Lakes. *Org. Geochem.* 34, 261-289.

Middelburg, J. J. (2019), Marine Carbon Biogeochemistry – A primer for Earth system scientists. *Springer Briefs in Earth System Sciences*, Springer Nature Switzerland AG, Switzerland, https://doi.org/10.1007/978-3-030-10822-9_4.

Miller, G. H., R. B. Alley, J. Brigham-Grette, J. J. Fitzpatrick, L. Polyak, M. C. Serreze, and J. W. C. White (2010), Arctic amplification: can the past constrain the future? *Quat. Sci. Rev.* 29 (15-16), 1779-1790.

Milucka, J., T. Ferdelman, L. Polerecky, D. Franzke, G. Wegener, M. Schmid, I. Lieberwirth, M. Wagner, F. Widdel, M. M. M. Kuypers (2012), Zero-valent sulphur is a key intermediate in marine methane oxidation. *Nature* 491 (7425), 541-546.

Minoshima, K., H. Kawahata, and K. Ikehara (2007), Changes in biological production in the mixed water region (MWR) of the northwestern Pacific during the last 27 kyr. *Palaeogeogr., Palaeoclimatol., Palaeoecol.* 254, 430-437.

Miyazaki, T., J.-I. Kimura, and M. Katakuse (2016), Geochemical records from loess deposits in Japan over the last 210 kyr: lithogenic source changes and paleoclimatic indications. *Geochem. Geophys. Geosyst.* 17, 2745-2761.

Mleneck-Vautravers, M. J. (2018), Quantitative planktonic foraminifers taphonomy and palaeoceanographic implications over the last 1 My from IODP Sites U1436 and U1437. Cogent Geoscience 4 (1), 1447263.

Moore T. C., L. H. Burckle, K. Geitzenauer, B. Luz, A. Molina-Cruz, J. H. Robertson, H. Sachs, C. Sancetta, J. Thiede, P. Thompson, and C. Wenkam (1980), The reconstruction of sea surface temperatures in the Pacific Ocean of 18,000 BP. *Mar. Micropaleontol.*5, 215-247.

Moore, G. F., A. Taira, A. Klaus, K. Becker, L. Becker, B. Boeckel, B. A. Cragg, P. A. Dean, C. L. Fergusson, P. Henry, S. Hirano, T. Hisamitsu, S. Hunze, M. Kastner, A. J. Maltman, J. K. Morgan, Y. Murakami, D. M. Saffer, M. Sánchez-Gómez, E. J. Screaton, D. C. Smith, A. J. Spivack, J. Steurer, H. J. Tobin, K. Ujiie, M. B. Underwood, and M. Wilson (2001), Proceedings of the Ocean Drilling Program, Initial Reports (Vol. 190). College Station, TX: Ocean Drilling Program. https://doi.org/10.2973/odp.proc.ir.190.2001.

Morse, J. W., and F. T. Mackenzie (1990), Developments in Sedimentology. In: Morse, J. W., and F. T. Mackenzie (Eds.), *Geochemistry of Sedimentary Carbonates*. Elsevier, Amsterdam, The Netherlands, Vol. 48, pp. vii-x, 1-707, http://dx.doi.org/10.1016/S0070-4571(08)70329-7.

Moskowitz, B., R. B. Frenkel, and D. A. Bazylinski (1993), Rock magnetic criteria for the detection of biogenic magnetite. *Earth Planet. Sci. Lett.* 120, 283-300.

Moskowitz, B. M., M. Jackson, and C. Kissel (1998), Low-temperature magnetic behavior of titanomagnetites. *Earth Planet. Sci. Lett.* 157, 141-149.

Müller, P. J., G. Kirst, G. Ruhland, I. von Storch, and A. Rosell-Melé (1998), Calibration of the alkenone paleotemperature index ($U^{K'}_{37}$) based on core tops from the eastern South Atlantic and the global ocean (60 °N-60 °S). *Geochim. Cosmochim. Acta* 62, 1757-1772.

Muratli, J. M., Z. Chase, A. C. Mix, and J. McManus (2010), Increased glacial-age ventilation of the Chilean margin by Antarctic Intermediate Water. *Nat. Geosci.* 3, 23-26.

Musgrave, R. J., and M. Kars (2016), Recognizing magnetostratigraphy in overprinted and altered marine sediments: Challenges and solutions from IODP Site U1437. *Geochem. Geophys. Geosyst.* 17, 3190-3206.

Musgrave, R. J., M. Kars, and M. E. Vega (2017), Deep magnetic diagenesis in sediments: Progressive and punctuated processes. Paper presented at *AGU Fall Meeting 2017*, New Orleans, Louisiana, USA.

Musgrave, R. J., M. Kars, and M. E. Vega (2019), Progressive and punctuated magnetic mineral diagenesis: The rock magnetic record of multiple fluid inputs and progressive pyritization in a volcano-bounded basin, IODP Site U1437, Izu Rear Arc. *J. Geophys. Res.: Sol. Earth* 124 (6), 5357-5378.

Muxworthy, A. R., and E. McClelland (2000), Review of the low-temperature magnetic properties of magnetite from a rock magnetic perspective. *Geophys. J. Int.* 140, 101-114.

Muxworthy, A. R., and D. J. Dunlop (2002), First-Order Reversal Curve (FORC) diagrams for pseudosingle- domain magnetites at high temperature. *Earth Planet. Sci. Lett.* 203, 369-382.

Naafs, B. D. A., J. Hefter, and R. Stein (2012a), Application of the long chain diol index (LDI) paleothermometer to the early Pleistocene (MIS 96). *Org. Geochem.* 49, 83-85.

Naafs, B. D. A., J. Hefter, G. Acton, G. H. Haug, A. Martínez-Garcia, R. Pancost, and R. Stein (2012b), Strengthening of North American dust sources during the late Pliocene (2.7 Ma). *Earth Planet. Sci. Lett.* 317-318, 8-19.

Nagahashi, Y., and Y. Satoguchi, (2007), Stratigraphy of the Pliocene to lower Pleistocene marine formations in Japan on the basis of tephra beds correlation. *Quat. Res. (Daiyonki Kenkyu)* 46 (3), 205-213.

Nagashima, K., R. Tada, H. Matsui, T. Irino, A. Tani, and S. Toyoda (2007), Orbital- and millennial-scale variations in Asian dust transport path to the Japan Sea. *Palaeogeogr., Palaeoclimatol., Palaeoecol.* 247, 144-161.

Nagashima, K., R. Tada, A. Tani, Y. Sun, Y. Isozaki, S. Toyoda, and H. Hasegawa (2011), Millennial-scale oscillations of the westerly jet path during the last glacial period. *J. Asian Earth Sci.* 40, 1214-1220.

Nakagawa, T., H. Kitagawa, Y. Yasuda, P. E. Tarasov, K. Nishida, K. Gotanda, Y. Sawai, and Yangtze Civilization Program Members (2003), Asynchronous climate changes in the North Atlantic and Japan during the last termination. *Science* 299, 688-691.

Nakamura, H., A. Nishina, and S. Minobe (2012), Response of storm tracks to bimodal Kuroshio path states south of Japan. *J. Clim.* 25, 7772-7779.

Nakamura, H., K. Sawada, H. Araie, I. Suzuki, and Y. Shiraiwa (2015), *n*-Nonacosadienes from the marine haptophytes *Emiliania huxleyi* and *Gephyrocapsa oceanica*. *Phytochem.* 111, 107-113.

Nakanishi, T., M. Yamamoto, T. Irino, and R. Tada (2012a), Distribution of glycerol dialkyl glycerol tetraethers, alkenones and polyunsaturated fatty acids in suspended particulate organic matter in the East China Sea. *J. Oceanogr.* 68, 959-970.

Nakanishi, T., M. Yamamoto, R. Tada, and H. Oda (2012b), Centennial-scale winter monsoon variability in the northern East China Sea during the Holocene. *J. Quaternary Sci.* 27 (9), 956-963.

Neretin, L. N., M. E. Böttcher, B. B. Jørgensen, I. I. Volkov, H. Lüschen, and K. Hilgenfeldt (2004), Pyritization processes and greigite formation in the advancing sulfidization front in the Upper Pleistocene sediments of the Black Sea. *Geochim. Cosmochim. Acta* 68 (9), 2081-2093.

Nie, J., J. W. King, and X. Fang (2008), Correlation between the magnetic susceptibility record of the Chinese Aeolian sequences and the marine benthic oxygen isotope record. *Geochem. Geophys. Geosyst.* 9 (12), Q12026.

Nie, J., A. Pullen, C. N. Garzione, W. Peng, and Z. Wang (2018), Pre-Quaternary decoupling between Asian aridification and high dust accumulation rates. *Sci. Adv.* 4, eaao6977.

Nürnberg, D., J. Blima, and C. Hemleben (1996), Assessing the reliability of magnesium in foraminiferal calcite as a proxy for water mass temperatures. *Geochim. Cosmochim. Acta* 60, 803-814.

Oba, T., and M. Murayama (2004), Sea-surface temperature and salinity changes in the northwest Pacific since the Last Glacial Maximum. *J. Quat. Sci.* 19 (4), 335-346.

Oba, T., T. Irino, M. Yamamoto, M. Murayama, A. Takamura, and K. Aoki (2006), Paleoceanographic change off central Japan since the last 144,000 years based on high-resolution oxygen and carbon isotope records. *Global Planet. Change* 53, 5-20.

O'Brien, C. L., G. L. Foster, M. A. Martínez-Boti, R. Abell, J. W. B. Rae, and R. D. Pancost (2014), High sea surface temperatures in tropical warm pools during the Pliocene. *Nat. Geosci.* 7, 606-611.

O'Brien, C. L., S. A. Robinson, R. D. Pancost, J. S. Sinninghe Damsté, S. Schouten, D. J. Lunt, H. Alsenz, A. Bornemann, C. Bottini, S. C. Brassell, A. Farnsworth, A. Forster, B. T. Huber, G. N. Inglis, H. C. Jenkyns, C. Linnert, K. Littler, P. Markwick, A. McAnena, J. Mutterlose, B. D. A. Naafs, W. Püttmann, A. Sluijs, N. A. G. M. van Helmond, J. Vellekoop, T. Wagner, and N. E. Wrobel (2017), Cretaceous sea-surface temperature evolution: Constraints from TEX_{86} and planktonic foraminiferal oxygen isotopes. *Earth-Sci. Rev.* 172, 224-247.

Ogi, M., Y. Tachibana, and K. Yamazaki (2004), The connectivity of the Winter North Atlantic Oscillation (NAO) and the summer Okhotsk High. *J. Meteorol. Soc. Jpn*. 82 (3), 905-913.

Okino, K., Y. Shimakawa, and S. Nagaoka (1994), Evolution of the Shikoku Basin. *J. Geomag. Geoelectr.* 46, 463-479.

Özdemir, Ö., D. J. Dunlop, and B. M. Moskowitz (1993), The effect of oxidation on the Verwey transition in magnetite. *Geophys. Res. Lett.* 20 (16), 1671-1674.

Özdemir, Ö., D. J. Dunlop, and B. M. Moskowitz (2002), Changes in remanence, coercivity and domain state at low temperature in magnetite. *Earth Planet. Sci. Lett.* 194, 343-358.

Özdemir, Ö., D. J. Dunlop, and T. S. Berquó (2008), Morin transition in hematite: size dependence and thermal hysteresis. *Geochem. Geophys. Geosyst.* 9 (10), Q10Z01.

Özdemir, Ö., and D. J. Dunlop (2010), Hallmarks of maghemitization in low-temperature remanence cycling of partially oxidized magnetite nanoparticles. *J. Geophys. Res.* 115, B02101.

Pagani, M., M. A. Arthur, and K. H. Freeman (1999), Miocene evolution of atmospheric carbon dioxide. *Paleoceanography* 14 (3), 273-292.

Paillard, D., L. Labeyrie, and P. Yiou (1996), Macintosh program performs time-series analysis. *EOS Trans. Am. Geophys. Union* 77 (39), 379.

Passey, B. H., L. K. Ayliffe, A. Kaakinen, Z. Zhang, J. T. Eronen, Y. Zhu, L. Zhou, T. E. Cerling, and M. Fortelius (2009), Strengthened East Asian summer monsoons during a period of high-latitude warmth? Isotopic evidence from Mio-Pliocene fossil mammals and soil carbonates from northern China. *Earth Planet. Sci. Lett.* 277, 443-452.

Passier, H. F., M. J. Dekkers, and G. J. de Lange (1998), Sediment chemistry and magnetic properties in an anomalously reducing core from the eastern Mediterranean Sea. *Chem. Geol.* 152 (3-4), 287-306.

Passier, H. F., and M. J. Dekkers (2002), Iron oxide formation in the active oxidation front above sapropel S1 in the eastern Mediterranean Sea as derived from low-temperature magnetism. *Geophys. J. Internat.* 150 (1), 230-240.

Pearson, A., Y. Pi, W. Zhao, W. Li, Y. Li, W. Inskeep, A. Perevalova, C. Romanek, S. Li, and C. L. Zhang (2008), Factors controlling the distribution of archaeal tetraethers in terrestrial hot springs. *Appl. Environ. Microbiol.* 74, 3523-3532.

Peckmann, J., A. Reimer, U. Luth, C. Luth, B. T. Hansen, C. Heinicke, J. Hoefs, and J. Reitner (2001), Methane-derived carbonates and authigenic pyrite from the northwestern Black Sea. *Mar. Geol.* 177 (1-2), 129-150.

Peng, T., J. Liu, C. Song, B. Guo, J. Liu, Z. Zhao, and J. Zhang (2016), An integrated biomarker perspective on Neogene-Quaternary climatic evolution in NE Tibetan Plateau: Implications for Asian aridification. *Quat. Internat.* 399, 174-182.

Peters, C., and M. J. Dekkers (2003), Selected room temperature magnetic parameters as a function of mineralogy, concentration and grain size. *Phys. Chem. Earth* 28 (16-19), 659-667.

Peterse, F., J.-H. Kim, S. Schouten, D. Klitgaard Kristensen, N. Koç, and J. S. Sinninghe Damsté (2009), Constraints on the application of the MBT/CBT paleothermometer in high latitude environments (Svalbard, Norway). *Org. Geochem.* 40, 692-699.

Peterse, F., J. van der Meer, S. Schouten, J. W. H. Weijers, N. Fierer, R. B. Jackson, J.-H. Kim, J. S. Sinninghe Damsté (2012), Revised calibration of the MBT-CBT paleotemperature proxy based on branched tetraether membrane lipids in surface soils. *Geochim. Cosmochim. Acta* 96, 215-229.

Pfadenhauer J. S., and F. A. Klötzli (2020), Vegetation of the Boreal (Cold-Temperate) Zone. In: Global Vegetation. Springer, Cham. https://doi.org/10.1007/978-3-030-49860-3_13.

Pike, C. R., A. P. Roberts, and K. L. Verosub (1999), Characterizing interactions in fine magnetic particle systems using first order reversal curves. *J. Appl. Phys.* 85 (9), 6660-6667.

Pisias, N. G., and T. C. Moore Jr. (1981), The evolution of the Pleistocene climate: a time series approach. *Earth Planet. Sci. Lett.* 52, 450-458.

Pitcher, A., E. C. Hopmans, A. C. Mosier, A.C., S.-J. Park, S.-K. Rhee, C. A. Francis, S. Schouten, and J. S. Sinninghe Damsté (2011), Core and intact polar glycerol dibiphytanyl glycerol tetraether lipids of ammonia-oxidizing archaea enriched from marine and estuarine sediments. *Appl. Environ. Microbiol.* 77 (10), 3468-3477.

Plank, T., J. N. Ludden, C. Escutia, L. Abrams, J. C. Alt, R. N. Armstrong, S. Barr, A. Bartolini, G. Cairns, M. R. Fisk, G. Guèrin, S. A. Haveman, T. Hirono, J. Honnorez, K. A. Kelley, R. L. Larson, F. M. Lozar, R. W. Murray, T. K. Pletsch, R. A. Pockalny, O. Rouxel, A. Schmidt, D. C. Smith, A. J. Spivack, H. Staudigel, M. B. Steiner, and R. B. Valentine (2000), Proceedings of the Ocean Drilling Program, Initial Reports, 185. Ocean Drilling Program, College Station, TX, USA.

Plank, T., K. A. Kelley, R. W. Murray, and L. Q. Stern (2007), Chemical composition of sediments subducting at the Izu-Bonin trench. *Geochem. Geophys. Geosyst.* 8, Q04I16.

Pohlman, J. W., M. Riedel, J. M. Bauer, E. A. Canuel, C. K. Paull, L. Lapham, K. S. Grabowski, R. B. Coffin, and G. D. Spence (2013), Anaerobic methane oxidation in low-organic content methane seep sediments. *Geochim. Cosmochim. Acta* 108, 184-201.

Polyak, L., K. M. Best, K. A. Crawford, E. A. Council, and G. St-Onge (2013), Quaternary history of sea ice in the western Arctic Ocean based on foraminifera. *Quat. Sci. Rev.* 79, 145-156.

Prahl, F. G., and S. G. Wakeham (1987), Calibration of unsaturation patterns in long-chain ketone compositions for paleotemperature assessment. *Nature* 330, 367-369.

Pujos-Lamy, A. (1977), Essai d'établissement d'une biostratigraphie du nannoplancton calcaire dans le Pléistocène de l'Atlantique Nord-oriental. *Boreas* 6, 323-331.

Qiu, B. (2001), Kuroshio and Oyashio Currents. *In: Thorpe, S.A., Turekian, K.K. (Eds.), Encyclopedia of Ocean Sciences. Academic Press, Oxford, UK*, pp. 1413-1425.

Qiu, B. (2002), Large-scale variability in the midlatitude subtropical and subpolar North Pacific Ocean: observations and causes. *J. Phys. Oceanogr.* 32, 353-375.

Qiu, B., S. Chen, and P. Hacker (2004), Synoptic-scale air-sea flux forcing in the western North Pacific: observations and their impact on SST and the mixed layer. *J. Phys. Oceanogr.* 34, 2148-2159.

Raffi, I., J. Backman, E. Fornaciari, H. Pälike, D. Rio, L. Lourens, and F. Hilgen (2006), A review of calcareous nannofossil astrobiology encompassing the past 25 million years. *Quat. Sci. Rev.* 25, 3113-3137.

Rampen, S. W., S. Schouten, S. G. Wakeham, and J. S. Sinninghe Damsté (2007), Seasonal and spatial variation in the sources and fluxes of long chain diols and mid-chain hydroxy methyl alkanoates in the Arabian Sea. *Org. Geochem.* 38, 165-179.

Rampen, S. W., S. Schouten, and J. S. Sinninghe Damsté (2011), Occurrence of long chain 1,14 diols in *Apedinella radians*. *Org. Geochem.* 42, 572-574.

Rampen, S. W., V. Willmott, J.-H. Kim, E. Uliana, G. Mollenhauer, E. Schefuß, J. S. Sinninghe Damsté, and S. Schouten (2012), Long chain 1,13- and 1,15-diols as a potential proxy for palaeotemperature reconstruction. *Geochim. Cosmochim. Acta* 84, 204-216.

Rampen, S. W., M. Datema, M. Rodrigo-Gámiz, S. Schouten, G.-J. Reichert, and J. S. Sinninghe Damsté (2014), Sources and proxy potential of long chain alkyl diols in lacustrine environments. *Geochim. Cosmochim. Acta* 144, 59-71.

Rashid, H., R. Hesse, and D. J. W. Piper (2003), Evidence for an additional Heinrich event between H5 and H6 in the Labrador Sea. *Paleoceanography* 18 (4), 1077.

Rasmussen, T.L., D. W. Oppo, E. Thomsen, and S. J. Lehman (2003), Deep sea records from the southeast Labrador Sea: Ocean circulation changes and ice-rafting events during the last 160,000 years. *Paleoceanography* 18 (1), 1018.

Rea, D. K., and M. Leinen (1988), Asian aridity and the zonal westerlies: Late Pleistocene and Holocene record of eolian deposition in the northwest Pacific Ocean. *Palaeogeogr. Palaeoclimatol. Palaeoecol.* 66, 1-8.

Rea, D. K. (1994), The paleoclimatic record provided by eolian deposition in the deep sea: the geologic history of wind. *Rev. Geophys.* 32 (2), 159-195.

Rea, D. K., H. Snoeckx, and L. H. Joseph (1998), Late Cenozoic eolian deposition in the North Pacific: Asian drying, Tibetan uplift, and cooling of the Northern hemisphere. *Paleoceanography* 13 (3), 215-224.

Reiche, S., Rampen, S. W., Dorhout, D. J. C., Sinninghe Damsté, J. S., Schouten, S. (2018), The impact of oxygen exposure on long-chain alkyl diols and the long-chain diol index (LDI)- a long-term incubation study. *Org. Geochem.* 124, 238-246.

Riedinger, N., K. Pfeifer, S. Kasten, L. F. L. Garming, C. Vogt, and C. Hensen (2005), Diagenetic alteration of magnetic signals by anaerobic oxidation of methane related to a change in sedimentation rate. *Geochim. Cosmochim. Acta* 69, 4117-4126.

Riedinger, N., M. J. Formolo, T. W. Lyons, S. Henkel, A. Beck, and S. Kasten (2014), An inorganic geochemical argument for coupled anaerobic oxidation of methane and iron reduction in marine sediments. *Geobiology* 12 (2), 172-181.

Roberts, A. P., C. R. Pike, and K. L. Verosub (2000), First-order reversal curve diagrams: a new tool for characterizing the magnetic properties of natural samples. *J. Geophys. Res.: Sol. Earth* 105 (B12), 28461-28475.

Roberts, A. P., and R. Weaver (2005), Multiple mechanisms of remagnetization involving sedimentary greigite (Fe_3S_4). *Earth Planet. Sci. Lett.* 231 (3- 4), 263-277.

Roberts, A. P., L. Chang, C. J. Rowan, C.-S. Horng, and F. Florindo (2011), Magnetic properties of sedimentary greigite (Fe_3S_4): an update. *Rev. Geophys.* 49, RG1002.

Roberts, A. P., L. Chang, D. Heslop, F. Florindo, and J. C. Larrasoaña (2012), Searching for single domain magnetite in the "pseudo-single-domain" sedimentary haystack: implications of biogenic magnetite preservation for sediment magnetism and relative paleointensity determinations. *J. Geophys. Res.* 117, B08104.

Roberts, A. P. (2015), Magnetic mineral diagenesis. *Earth-Sci. Rev.* 151, 1-47.

Roberts, A. P., T. P. Almeida, N. S. Church, R. J. Harrison, D. Heslop, Y. Li, J. Li, A. R. Muxworthy, W. Williams, and X. Zhao (2017), Resolving the origin of pseudo-single domain magnetic behavior. *J. Geophys. Res.: Sol. Earth* 122, 9534-9558.

Roberts, A. P., L. Tauxe, D. Heslop, X. Zhao, and Z. Jiang (2018), A critical appraisal of the "Day" diagram. *J. Geophys. Res.: Sol. Earth* 123, 2618-2644.

Robinson, S. A., M. Ruhl, D. L. Astley, B. D. A. Naafs, A. J. Farnsworth, P. R. Bown, H. C. Jenkyns, D. J. Lunt, C. O´Brien, R. D. Pancost, and P. J. Markwick (2017), Early Jurassic North Atlantic sea-surface temperatures from TEX_{86} paleothermometry. *Sedimentology* 64, 215-230.

Rochette, P., G. Fillion, J.-L. Mattéi, and M. J. Dekkers (1990), Magnetic transition at 30-34 Kelvin in pyrrhotite: Insight into a widespread occurrence of this mineral in rocks. *Earth Planet. Sci. Lett.* 98 (3-4), 319-328.

Rochette, P., P. E. Mathé, L. Esteban, H. Rakoto, J.-L. Bouchez, Q. Liu, and J. Torrent (2005), Non-saturation of the defect moment of goethite and fine-grained hematite up to 57 T. *Geophys. Res. Lett.* 32, L22309.

Rodrigo-Gámiz, M., F. Martinez-Ruiz, S. W. Rampen, S. Schouten, and J. S. Sinninghe Damsté (2014), Sea surface temperature variations in the western Mediterranean Sea over the last 20 kyr: a dual-organic proxy ($U^{K'}_{37}$ and LDI) approach. *Paleoceanography* 29, 87-98.

Rodrigo-Gámiz, M., S. W. Rampen, H. de Haas, M. Baas, S. Schouten, and J. S. Sinninghe Damsté (2015), Constraints on the applicability of the organic temperature proxies $U^{K'}_{37}$, TEX_{86} and LDI in the subpolar region around Island. *Biogeosciences* 12, 6573-6590.

Rodrigo-Gámiz, M., S. W. Rampen, S. Schouten, J. S. Sinninghe Damsté (2016), The impact of oxic degradation on long chain alkyl diol distributions in Arabian Sea surface sediments. *Org. Geochem.* 100, 1-9.

Rohling, E. J., G. L. Foster, K. M. Grant, G. Marino, A. P. Roberts, M. E. Tamisiea, and F. Williams (2014), Sea-level and deep-sea-temperature variability over the past 5.3 million years. *Nature* 508, 477-482.

Rommerskirchen, F., G. Eglinton, L. Dupont, U. Günther, C. Wenzel, and J. Rullkötter (2003), A north to south transect of Holocene southeast Atlantic continental margin sediments: Relationship between aerosol transport and compound—specific $\delta^{13}C$ land plant biomarker and pollen records. *Geochem. Geophys. Geosyst.* 4 (12), 1101.

Rommerskirchen, F., A. Plader, G. Eglinton, Y. Chikaraishi, and J. Rullkötter (2006) Chemotaxonomic significance of distribution and stable carbon isotopic composition of long-chain alkanes and alkan-1-ols in C_4 grass waxes. *Org. Geochem.* 37, 1303-1332.

Rommerskirchen, F., T. Condon, G. Mollenhauer, I. Dupont, and E. Schefuß (2011), Miocene to Pliocene development of surface and subsurface temperatures in the Benguela Current system. *Paleoceanography* 26, PA3216.

Rosell-Melé, A., and F. G. Prahl (2013), Seasonality of $U^{K'}_{37}$ temperature estimates as inferred from sediment trap data. *Quat. Sci. Rev.* 72, 128-136.

Rouselle, G., C. Beltran, M.-A. Sicre, I. Raffi, and M. De Rafélis (2013), Changes in sea-surface conditions in the Equatorial Pacific during the middle Miocene-Pliocene as inferred from coccolith geochemistry. *Earth Planet. Sci. Lett.* 361, 412-421.

Rowan, C. J., and A. P. Roberts (2005), Tectonic and geochronological implications of variably timed magnetizations carried by authigenic greigite in marine sediments from New Zealand. *Geology* 33 (7), 553-556.

Rowan, C. J., A. P. Roberts, and T. Broadbent (2009), Reductive diagenesis, magnetite dissolution, greigite growth and paleomagnetic smoothing in marine sediments: A new view. *Earth Planet. Sci. Lett.* 277 (1-2), 223-235.

Ruddiman, W. F., and A. McIntyre (1981), The North Atlantic Ocean during the last Deglaciation. *Palaeogeogr., Palaeoclimatol., Palaeoecol.* 35, 145-214.

Ruebsam, W., M. Reolid, N. Sabatino, D. Masetti, and L. Schwark (2020), Molecular paleothermometry of the early Toarcian climate perturbation. *Global Planet. Change* 195, 103351.

Ryan, W. B. F., S. M. Carbotte, J. O. Coplan, S. O'Hara, A. Melkonian, R. Arko, R. A. Weissel, V. Ferrini, A. Goodwillie, F. Nitsche, J. Bonczkowski, and R. Zemsky (2009), Global multi-resolution topography synthesis. *Geochem. Geophys. Geosyst.* 10, Q03014.

Sachse D., I. Billault, G. J. Bowen, Y. Chikaraishi, T. E. Dawson, S. J. Feakins, K. H. Freeman, C. R. Magill, F. A. McInerney, M. T. J. van der Meer, P. Polissar, R. J. Robins, J. P. Sachs, H. L. Schmidt, A. L. Sessions, J. W. C. White, J. B. West, and A. Kahmen (2012), Molecular paleohydrology: interpreting the hydrogen-isotopic composition of lipid biomarkers from photosynthesizing organisms. *Annu. Rev. Earth Planet. Sci.* 40, 221-249.

Sadatzki, H., M. Sarnthein, and N. Andersen (2015), Changes in monsoon-driven upwelling in the South China Sea over glacial Terminations I and II: a multi-proxy record. *Int. J. Earth Sci.* 105 (4), 1273-1285.

Sagawa, T., K. Toyoda, and T. Oba (2006), Sea surface temperature record off central Japan since the Last Glacial Maximum using planktonic foraminiferal Mg/Ca thermometry. *J. Quaternary Sci.* 21, 63-73.

Sagnotti, L., A. P. Roberts, R. Weaver, K. L. Verosub, F. Florindo, C. R. Pike, T. Clayton, and G. S. Wilson (2005), Apparent magnetic polarity reversals due to remagnetization resulting from late diagenetic growth of greigite from siderite. *Geophys. J. Internat.* 160 (1), 89-100.

Sakurai, Y. (2007), An overview of the Oyashio ecosystem. *Deep-Sea Res. II* 54, 2526-2542.

Salter, S. J., M. J. Cox, E. M. Turek, S. T. Calus, W. O. Cookson, M. F. Moffatt, P. Turner, J. Parkhill, N. J. Loman, and A. W. Walker (2014), Reagent and laboratory contamination can critically impact sequence-based microbiome analyses. *BMC Biology* 12 (1), 87.

Sampe, T., and S.-P. Xie (2010), Large-scale dynamics of the Meiyu-Baiu rainband: environmental forcing by the Westerly Jet. *J. Climate* 23, 113-134.

Sassen, K. (2002), Indirect climate forcing over the western US from Asian dust storms. *Geophys. Res. Lett.* 29 (10), 1465.

Sato, K., M. Oda, S. Chiyonobu, K. Kimoto, H. Domitsu, and J. C. Ingle Jr. (2008), Establishment of the western Pacific warm pool during the Pliocene: evidence from planktic foraminifera, oxygen isotopes, and Mg/Ca ratios. *Palaeogeogr., Palaeoclimatol., Palaeoecol.* 265, 140-147.

Satoguchi, Y., Y. Higuchi, and K. Kurokawa (2005), Correlation of the Ohta tephra bed in the Tokai group with a tephra in the Miura group, central Japan. *Chishitsugaku Zasshi* 111 (2), 74-86.

Sawada, K., N. Handa, Y. Shiraiwa, A. Danbara, and S. Montani (1996), Long-chain alkenones and alkyl alkenoates in the coastal and pelagic sediments of the northwest North Pacific, with special reference to the reconstruction of *Emiliania huxleyi* and *Gephyrocapsa oceanica* ratios. *Org. Geochem.* 24, 751-764.

Sawada, K., N. Handa, and T. Nakatsuka (1998), Production and transport of long-chain alkenones and alkyl alkenoates in a sea water column in the northwestern Pacific off central Japan. *Mar. Chem.* 59, 219-234.

Sawada, K., and N. Handa (1998), Variability of the path of the Kuroshio ocean current over the past 25,000 years. *Nature* 392, 592-595.

Schefuß, E., S. Schouten, J. H. F. Jansen, and J. S. Sinninghe Damsté (2003a), African vegetation controlled by tropical sea surface temperatures in the mid-Pleistocene period. *Nature* 422, 418-421.

Schefuß, E., V. Rathmeyer, J.-B. W. Stuut, J. H. F. Jansen, and J. S. Sinninghe Damsté (2003b), Carbon isotope analyses of *n*-alkanes in dust from the lower atmosphere over the central eastern Atlantic. *Geochim. Cosmochim. Acta* 67, 1757-1767.

Schiemann, R., D. Lüthi, and C. Schär (2009), Seasonality and interannual variability of the westerly jet in the Tibetan Plateau region. *J. Clim.* 22, 2940-2957.

Schouten, S., E. C. Hopmans, E. Schefuß, and J. S. Sinninghe Damsté (2002), Distributional variations in marine crenarchaeotal membrane lipids: A new tool for reconstructing ancient sea water temperatures? *Earth Planet. Sci. Lett.* 204, 265-274.

Schouten, S., E. C. Hopmans, and J. S. Sinninghe Damsté (2004), The effect of maturity and depositional redox conditions on archaeal tetraether lipid palaeothermometry. *Org. Geochem.* 35, 567-71.

Schouten, S., E. C. Hopmans, and J. S. Sinninghe Damsté, (2013), The organic geochemistry of glycerol dialkyl glycerol tetraether lipids: A review. *Org. Geochem.* 54, 19-61.

Schulz, H.-M., A. Schöner, and K.-C. Emeis (2000), Long-chain alkenone patterns in the Baltic Sea – an ocean-freshwater transition. *Geochim. Cosmochim. Acta* 64, 469-477.

Schwark L., K. Zink and J. Lechterbeck (2002), Reconstruction of postglacial to early Holocene vegetation history in terrestrial Central Europe via cuticular lipid biomarkers and pollen records from lake sediments. *Geology* 30, 463-466.

Scudder, R. P., R. W. Murray, and T. Plank (2009), Dispersed ash in deeply buried sediment from the northwest Pacific Ocean: an example from the Izu-Bonin arc (ODP Site 1149). *Earth Planet. Sci. Lett.* 284 (3-4), 639-648.

Scudder, R. P., R. W. Murray, J. C. Schindlbeck, S. Kutterolf, F. Hauff, and C. C. McKinley, (2014), Regional-scale input of dispersed and discrete volcanic ash to the Izu-Bonin and Mariana subduction zones. *Geochem. Geophys. Geosyst.* 15, 4369-4379.

Segarra, K. E. A., C. Comerford, J. Slaughter, and S. B. Joye (2013), Impact of electron acceptor availability on the anaerobic oxidation of methane in coastal freshwater and brackish wetland sediments. *Geochim. Cosmochim. Acta* 115, 15-30.

Seibold, E., and W. H. Berger (1996), The Sea Floor – An Introduction to Marine Geology. 3rd Edition, Springer-Verlag, Berlin, Heidelberg, Germany.

Seki, O., G. L. Foster, D. L. Schmidt, A. Mackensen, K. Kawamura, and R. D. Pancost (2010), Alkenone and boron-based Pliocene pCO_2 records. *Earth Planet. Sci. Lett.* 292, 201-211.

Seki, O., D. N. Schmidt, S. Schouten, E. C. Hopmans, J. S. Sinninghe Damsté, and R. D. Pancost (2012), Paleoceanographic changes in the Eastern Equatorial Pacific over the last 10 Myr. *Paleoceanography* 27, PA3224.

Serno, S., G. Winckler, R. F. Anderson, C. T. Hayes, D. McGee, B. Machalett, H. Ren, S. M. Straub, R. Gersonde, and G. M. Haug (2014), Eolian dust input to the Subarctic North Pacific. *Earth Planet. Sci. Lett.* 387, 252-263.

Shen, X., S. Wan, C. Colin, R. Tada, X. Shi, W. Pei, Y. Tan, X. Jiang, and A. Li (2018), Increased seasonality and aridity drove the C_4 plant expansion in Central Asia since the Miocene-Pliocene boundary. *Earth-Planet. Sci. Lett.* 502, 74-83.

Shi, X., Wu, Y., Zou, J., Liu, Y., Ge, S., Zhao, M., Liu, J., Zhu, A., Meng, X., Yao, Z., and Han, Y. (2014), Multiproxy reconstruction for Kuroshio responses to northern hemispheric oceanic climate and the Asian Monsoon since Marine Isotope Stage 5.1 (88 ka). *Clim. Past* 10, 1735-1750.

Shi, M., H. Wu, A. P. Roberts, S. Zhang, X. Zhao, H. Li, X. Su, T. Yang, L. Chang, P. Hu, X. Zhao, and H. Wang (2017), Tectonic, climatic, and diagenetic control of magnetic properties of sediments from Kumano Basin, Nankai margin, southwestern Japan. *Mar. Geol.* 391, 1-12.

Shimizu, Y., I. Yasuda, and S.-I. Ito (2001), Distribution and circulation of the coastal Oyashio-Intrusion. *J. Phys. Oceanogr.* 31, 1561-1578.

Shuto, T. (1990), Origin of a subtropical fauna in the middle latitude as exemplified by the Kakegawa fauna. *Bull. Mar. Sci.* 47 (1), 10-22.

Sikes, E. L., and J. K. Volkman (1993), Calibration of alkenone unsaturation ratios ($U^{K'}_{37}$) for paleotemperature estimation in cold polar waters. *Geochim. Cosmochim. Acta* 57, 1883-1889.

Simoneit, B. R. T. (2004), Biomarkers (molecular fossils) as geochemical indicators of life. *Adv. Space Res.* 33 (8), 1255-1261.

Sinninghe Damsté, J. S., E. C. Hopmans, S. Schouten, A. C. T. van Duin, and J. A. J. Geenevasen (2002), Crenarchaeol: the characteristic core glycerol dibiphytanyl glycerol tetraether membrane lipid of cosmopolitan pelagic crenarchaeota. *J. Lipid Res.* 43, 1641-1651.

Sinninghe Damsté, J. S., W. I. C. Rijpstra, B. Abba, G. Muyzer, and S. Schouten (2003), A diatomaceous origin for long-chain diols and mid-chain hydroxy methyl alkanoates widely occurring in Quaternary marine sediments: Indicators for high nutrient conditions. *Geochim. Cosmochim. Acta* 67 (7), 1339-1348.

Sinninghe Damsté, J. S., J. Ossebaar, B. Abbas, S. Schouten, and D. Verschuren (2009), Fluxes and distribution of tetraether lipids in an equatorial African lake: constraints on the application of the TEX_{86} palaeothermometer and branched tetraether lipids in lacustrine settings. *Geochim. Cosmochim. Acta* 73, 4232-4249.

Sivan, O., D. P. Schrag, and R. W. Murray (2007), Rates of methanogenesis and methanotrophy in deep-sea sediments. *Geobiology* 5 (2), 141-151.

Sivan, O., S. S. Shusta, and D. L. Valentine (2016), Methanogens rapidly transition from methane production to iron reduction. *Geobiology* 14, 190-203.

Stolpnikova, E., N. Kovaleva, and I. Kovalev (2020), *n*-Alkane distribution – a paleovegetation change indicator during the period from late glacial to late Holocene on Russian Plain (Bryansk Region). *Geosciences* 10, 86.

Stults, D. Z., F. Wagner-Cremer, and B. J. Axsmith (2011), Atmospheric paleo-CO_2 estimates based on *Taxodium distichum* (Cupressaceae) fossils from the Miocene and Pliocene of Eastern North America. *Palaeogeogr., Palaeoclimatol., Palaeoecol.* 309, 327-332.

Sun, Y., and Z. An (2005), Late Pliocene-Pleistocene changes in mass accumulation rates of eolian deposits on the central Chinese Loess Plateau. *J. Geophys. Res.* 110, D23101.

Sun, J., Z. Zhang, and L. Zhang (2009), New evidence on the age of the Taklimakan Desert. *Geology* 37 (2), 159-162.

Sun, Y., S. C. Clemens, C. Morrill, X. Lin, X. Wang, and Z. An (2011), Influence of Atlantic Meridional Overturning Circulation on the East Asian winter monsoon. *Nat. Geosci.* 5, 46-49.

Tada, R., H. Zheng, and P. D. Clift (2016), Evolution and variability of the Asian monsoon and its potential linkage with uplift of the Himalaya and Tibetan Plateau. *Progr. Earth Planet. Sci.* 3, 4.

Taira, A. (2001), Tectonic evolution of the Japanese island arc system. *Annu. Rev. Earth Planet. Sci.* 29, 109-134.

Tamura, Y., J. B. Gill, D. Tollstrup, H. Kawabata, H. Shukuno, Q. Chang, T. Miyazaki, T. Takahashi, Y. Hirahara, S. Kodaira, O. Ishizuka, T. Suzuki, Y. Kido, R. S. Fiske, and Y. Tatsumi (2009), Silicic magmas in the Izu-Bonin oceanic arc and implications for crustal evolution. *J. Petrol.* 50 (4), 685-723.

Tamura, Y., C. J. Busby, P. Blum, and the Expedition 350 Scientists (2015a), Proceedings of the International Ocean Discovery Program., Expedition 350: Izu-Bonin-Mariana Rear Arc. International Ocean Discovery Program, College Station, TX, USA, http://dx.doi.org/10.14379/iodp.proc.350.2015.

Tamura, Y., C. J. Busby, P. Blum, G. Guèrin, G. D. M. Andrews, A. K. Barker, J. L. R. Berger, E. M. Bongiolo, M. Bordiga, S. M. DeBari, J. B. Gill, C. Hamelin, J. Jia, E. H. John, A.-S. Jonas, M. Jutzeler, M. A. C. Kars, Z. A. Kita, K. Konrad, S. H. Mahoney, M. Martini, T. Miyazaki, R. J. Musgrave, D. B. Nascimento, A. R. L. Nichols, J. M. Ribeiro, T. Sato, J. C. Schindlbeck, A. K. Schmitt, S. M. Straub, M. J. Vautravers, and Y. Yang (2015b), Site U1437. In: Tamura, Y., C. J. Busby, P. Blum, and the Expedition 350 Scientists (Eds.), *Proceedings of the International Ocean Discovery Program, Expedition 350: Izu-Bonin-Mariana Rear Arc*. International Ocean Discovery Program, College Station, TX.

Tao, S. Y., and L. X. Chen (1957), The atmospheric structure over the Asian continent in summer. *Bull. Meteorol.* 28, 234-236.

Tatebe, H., and I. Yasuda (2001), Seasonal axis migration of the upstream Kuroshio Extension associated with standing oscillations. *J. Geophys. Res.* 106 (C8), 16685-16692.

Tauxe, L., T. A. T. Mullender, and T. Pick (1996), Potbellies, wasp-waists, and superparamagnetism in magnetic hysteresis. *J. Geophys. Res.* 101 (B1), 571-583.

Tauxe, L., H. N. Bertram, and C. Seberino (2002), Physical interpretation of hysteresis loops: micromagnetic modeling of fine particle magnetite. *Geochem. Geophys. Geosyst.* 3 (10), 1055.

Ternois, Y., K. Kawamura, N. Ohkouchi, and L. Keigwin (2000), Alkenone sea surface temperature in the Okhotsk Sea for the last 15 kyr. *Geochem. Journal* 34, 283-293.

Thierstein, H. R., K. R. Geitzenauer, B. Molfino, and N. J. Shackleton (1977), Global synchroneity of late Quaternary coccolith datum levels: validation by oxygen isotopes. *Geology* 5, 400-404.

Thompson, P. R., and N. J. Shackleton (1980), North Pacific palaeoceanography: late Quaternary coiling variations of planktonic foraminifer *Neogloboquadrina pachyderma*. *Nature* 287, 829-833.

Thompson, P. R. (1981), Planktonic foraminifera in the western North Pacific during the past 150000 years: comparison of modern and fossil assemblages. *Palaeogeogr., Palaeoclimatol., Palaeoecol.* 35, 241-279.

Thomson, D. J. (1982), Spectrum estimation and harmonic analysis. *Proc. IEEE* 70, 1055-1096.

Tipple, B. J., and M. Pagani (2013), Environmental control on eastern broadleaf forest species' leaf wax distributions and D/H ratios. *Geochim. Cosmochim. Acta* 111, 64e77.

Tissot, B., R. Pelet, and P. Ungerer (1987), Thermal history of sedimentary basins, maturation indexes, and kinetics of oil and gas generation. *AAPG Bulletin* 71, 1445-1466.

Tomida, S., and F. Kitao (2002), Occurrence of *Hartungia* (Gastropoda: Janthinidae) from the Tonohama Group, Kochi Prefecture, Japan. *Bulletin Mizunami Fossil Museum* 29, 157-160.

Tomida, S., H. Akazaki H, and T. Kawano (2013), A janthinid gastropod from late Neogene Miyazaki group of Southwestern Japan, and a status of *Hartungia*. *Bulletin of the Mizunami Fossil Museum* 39, 59-63.

Treude, T., J. Niggemann, J. Kallmeyer, P. Wintersteller, C. J. Schubert, A. Boetius, and B. B. Jørgensen (2005), Anaerobic oxidation of methane in the sulfate-methane transition along the Chilean continental margin. *Geochim. Cosmochim. Acta* 69 (11), 2767-2779.

Treude, T., S. Krause, J. Maltby, A. W. Dale, R. Coffin, and L. J. Hamdan (2014), Sulfate reduction and methane oxidation activity below the sulfate-methane transition zone in Alaskan Beaufort Sea continental margin sediments: Implications for deep sulfur cycling. *Geochim. Cosmochim. Acta* 144, 217-237.

Tribovillard, N., T. J. Algeo, T. Lyons, and A. Riboulleau (2006), Trace metals as paleoredox and paleoproductivity proxies: An update. *Chem. Geol.* 232 (1-2), 12-32.

Tsuchi, R., and T. Shuto (1984), Western Pacific Molluscan bio-events and their relationship to Neogene Datum planes. In: Ikebe, N., and R. Tsuchi (Eds.), *Pacific Neogene datum planes.* University of Tokyo Press, Tokyo, Japan, pp. 75-81.

Tsujino, H., S. Nishikawa, K. Sakamoto, N. Usui, H. Nakano, and G. Yamanaka (2013), Effects of large-scale wind on the Kuroshio path south of Japan in a 60-year historical OGCM simulation. *Clim. Dyn.* 41, 2287-2318.

Tsukada, M. (1983), Vegetation and Climate during the Last Glacial Maximum in Japan, *Quat. Res.* 19, 212-235.

Uno, I., K. Eguchi, K. Yumimoto, T. Takemura, A. Shimizu, M. Uematsu, Z. Liu, Z. Wang, Y. Hara, and N. Sugimoto (2009), Asian dust transported one full circuit around the globe. *Nat. Geosci.* 2, 557-560.

Usui, N., H. Tsujino, H. Nakano, and S. Matsumoto (2013), Long-term variability of the Kuroshio path south of Japan. *J. Oceanogr.* 69 (6), 647-670.

Vaks, A., O.S. Gutareva, S. F. M. Breitenbach, E. Avirmed, A. J. Mason, A. L. Thomas, A. V. Osinzev, A. M. Kononov, and G. M. Henderson (2013), Speleothems reveal 500,000-year history of Siberian Permafrost. *Science* 340, 183-186.

Versteegh, G. J. M., H.-J. Bosch, and J. W. de Leeuw (1997), Potential palaeoenvironmental information of C_{24} to C_{36} mid-chain diols, keto-ols and mid-chain hydroxyl fatty acids; a critical review. *Org. Geochem*. 27, 1-13.

Versteegh, G. J. M., R. Riegman, J. W. de Leeuw, and J. H. F. Jansen (2001), $U^{K'}_{37}$ values for *Isochrysis galbana* as a function of culture temperature, light intensity and nutrient concentrations. *Org. Geochem.* 32, 785-794.

Verwey, E. J. W. (1939), Electronic conduction of magnetite (Fe_3O_4) and its transition point at low temperatures. *Nature* 144 (3642), 327-328.

Vogts, A., H. Moossen, F. Rommerskirchen, and J. Rullkötter (2009), Distribution patterns and stable carbon isotopic composition of alkanes and alkan-1-ols from plant waxes of African rain forest and savanna C_3 species. *Org. Geochem.* 40, 1037e1054.

Vogts, A., E. Schefuß, T. Badewien, and J. Rullkötter (2012), *n*-Alkane parameters from a deep-sea sediment transect off southwest Africa reflect continental vegetation and climate conditions. *Org. Geochem.* 47, 109e119.

Volk, M., S. Gilder, and J. Feinberg (2016), Low-temperature magnetic properties of monoclinic pyrrhotite with particular relevance to the Besnus transition. *Geophys. J. Internat.* 207 (3), 1783-1795.

Volkman, J. K., G. Eglinton, E. D. S. Corner, and J. R. Sargent (1980a), Novel unsaturated straight-chain C_{37}-C_{39} methyl and ethyl ketones in marine sediments and a coccolithophore *Emiliania huxleyi*. *Phys. Chem. Earth* 12, 219-227.

Volkman, J. K., G. Eglinton, E. D. S. Corner, and T. E. V. Forsberg (1980b), Long-chain alkenes and alkenones in the marine coccolithophorid *Emiliania huxleyi*. *Phytochemistry* 19, 2619-2622.

Volkman, J. K., S. M. Barrett, G. A. Dunstan, and S. W. Jeffrey (1992), C_{30}-C_{32} alkyl diols and unsaturated alcohols in microalgae of the class Eustigmatophyceae. *Org. Geochem.* 18, 131-138.

Volkman, J. K., S. M. Barrett, S. I. Blackburn, and Elisabeth L. Sikes (1995), Alkenones in *Gephyrocapsa oceanica*: Implications for studies of paleoclimate. *Geochim. Cosmochim Acta* 59 (3), 513-520.

Wang, Y. J., H. Cheng, R. L. Edwards, Z. S. An, J. Y. Wu, C.-C. Shen, and J. A. Dorale (2001), A high-resolution absolute-dated late Pleistocene monsoon record from Hulu cave, China. *Science* 294, 2345-2348.

Wang, Y., H. Cheng, R. L. Edwards, X. Kong, X. Shao, S. Chen, J. Wu, Y. Jiang, X. Weng, and Z. An (2008), Millennial- and orbital-scale changes in the East Asian monsoon over the past 224,000 years. *Nature* 451, 1090-1093.

Wang, P., S. C. Clemens, R. Tada, and R. W. Murray (2019a), Blowing in the monsoon wind. *Oceanography* 32 (1), 48-59.

Wang, H., H. Lu, L. Zhao, H. Zhang, F. Lei, and Y. Wang (2019b), Asian monsoon rainfall variation during the Pliocene forced by global temperature change. *Nat. Comm.* 10, 5272.

Wang, Y., H. Lu, K. Wang, Y. Wang, Y. Li, S. Clemens, H. Lv, Z. Huang, H. Wang, X. Hu, F. Lu, and H. Zhang (2020), Combined high- and low-latitude forcing of East Asian monsoon precipitation variability in the Pliocene warm period. *Sci. Adv.* 6, eabc2414.

Wara, M. W., A. C. Ravelo, and M. L. Delaney (2005), Permanent El Niño-like conditions during the Pliocene warm period. *Science* 309, 758-761.

Wei, W., R. Zhang, M. Wen, and S. Yang (2017), Relationship between Asian westerly jet stream and summer rainfall in central Asia and North China: Roles of the Indian monsoon, and the South Asia High. *J. Clim.* 30 (2), 537-552.

Weijers, J. W. H., S. Schouten, O. C. Spaargaren, and J. S. Sinninghe Damsté (2006a), Occurrence and distribution of tetraether membrane in soils: Implications for the use of the BIT index and the TEX_{86} SST proxy. *Org. Geochem.* 37, 1680-1693.

Weijers, J. W. H., S. Schouten, J. A. J. Geenevasen, O. R. P. David, J. Coleman, R. D. Pancost, and J. S. Sinninghe Damsté (2006b), Membrane lipids of mesophilic anaerobic bacteria thriving in peats have typical archaeal traits. *Environ. Microbiol.* 8, 648-657.

Weijers, J.W.H., S. Schouten, J. C. van Den Donker, E. C. Hopmans, and J. S. Sinninghe Damsté (2007), Environmental controls on bacterial tetraether membrane lipid distribution in soils. *Geochim. Cosmochim. Acta* 71, 703-713.

Wu, B., and J. Wang (2002), Winter Arctic Oscillation, Siberian High and East Asian Winter Monsoon. *Geophys. Res. Lett.* 29 (19), 1897.

Wu, Y., R. Zhang, Z. Han, and Z. Zeng (2010), Relationship between East Asian Monsoon and dust weather frequency over Beijing. *Adv. Atmos. Sci.* 27 (6), 1389-1398.

Wu, B., X. Lin, and B. Qiu (2018), Meridional shift of the Oyashio Extension front in the past 36 years. *Geophys. Res. Lett.* 45, https://doi.org/10.1029/2018GL078433.

Wu, J., R. Stein, K. Fahl, N. Syring, S.-I. Nam, J. Hefter, G. Mollenhauer, and W. Geibert (2020), Deglacial to Holocene variability in surface water characteristics and major floods in the Beaufort Sea. *Comm. Earth & Environment* 1, 27.

Wuchter, C., S. Schouten, S. G. Wakeham, and J. S. Sinninghe Damsté (2005), Temporal and spatial variation in tetraether membrane lipids of marine Crenarchaeota in particulate organic matter: Implications for TEX_{86} paleothermometry. *Paleoceanography* 20, PA3031.

Xiao, J., and Z. An (1999), Three large shifts in East Asian monsoon circulation indicated by loess-paleosol sequences in China and late Cenozoic deposits in Japan. *Palaeogeogr., Palaeoclimatol., Palaeoecol.* 154, 179-189.

Xin, S., J. Shen, W. Zhang, W. Sun, and X. Xiao (2020), East Asian winter monsoon variability since the late Pliocene based on a pollen record from Lake Xingkai, northeast Asia. *Quat. Res.* 93, 40-59.

Xu, Z., T. Li, P. D. Clift, D. Lim, S. Wan, H. Chen, Z. Tang, F. Jiang, and Z. Xiong (2015), Quantitative estimates of Asian dust input to the western Philippine Sea in the mid-late Quaternary and its potential significance for paleoenvironment. *Geochem. Geophys. Geosyst*. 16, 3182-3196.

Yamamoto, M., K. Ficken, M. Baas, H. J. Bosch, and J. W. de Leeuw (1996), Molecular palaeontology of the earliest Danian at Geulhemmerberg (the Netherlands). *Geol. Mijnbouw* 75, 255-267.

Yamamoto H., M. Yamauchi, T. Kanamatsu, and T. Mishima (2004), The ocean environment in the eastern area off Honshu from the 20,000 years B.P to the Present. *JAMSTECR* 49, 1-14 (in Japanese with English abstract).

Yamamoto, M., A. Shimamoto, T. Fukuhara, Y. Tanaka, and J. Ishizaka (2012), Glycerol dialkyl glycerol tetraethers and TEX_{86} index in sinking particles in the western North Pacific. *Org. Geochem.* 53, 52-62.

Yamamoto, M., M. Kishizaki, T. Oba, and H. Kawahata (2013), Intense winter cooling of the surface water in the northern Okinawa Trough during the last glacial period. *J. Asian Earth Sci.* 69, 86-92.

Yamazaki, T., and N. Ioka (1997), Environmental rock-magnetism of pelagic clay: implications for Asian eolian input to the North Pacific since the Pliocene. *Paleoceanography* 12 (1), 111-124.

Yamazaki, T., A. L. Abdeldayem, and K. Ikehara (2003), Rock-magnetic changes with reduction diagenesis in Japan Sea sediments and preservation of geomagnetic secular variation in inclination during the last 30,000 years. *Earth, Planets Space* 55 (6), 327-340.

Yamazaki, T. (2009), Environmental magnetism of Pleistocene sediments in the North Pacific and Ontong-Java Plateau: Temporal variations of detrital and biogenic components. *Geochem. Geophys. Geosyst.* 10, Q07Z04.

Yamazaki, T., M. Takahashi, Y. Iryu, T. Sato, M. Oda, H. Takayanagi, S. Chiyonobu, A. Nishimura, T. Nakazawa, and T. Ooka (2010), Philippine Sea Plate motion since the Eocene estimated from paleomagnetism of seafloor drill cores and gravity cores. *Earth Planets* Space 62, 495-502.

Yamazaki, T., and K. Horiuchi (2016), Precessional control on ocean productivity in the Western Pacific Warm Pool for the last 400 kyr: insight from biogenic magnetite. *Geochem. Geophys. Geosyst.* 17, 4399-4412.

Yancheva, G., N. R. Nowaczyk, J. Mingram, P. Dulski, G. Schettler, J. F. W. Negendank, J. Liu, D. M. Sigman, L. C. Peterson, and G. H. Haug (2007), Influence of the intertropical convergence zone on the East Asian monsoon. *Nature* 445, 74-77.

Yang, S-K., Y. Nagata, K. Taira, and M. Kawabe (1993), Southward intrusion of the Intermediate Oyashio Water along the east coast of the Boso Peninsula, Japan II. Intrusion events into Sagami Bay. *J. Oceanogr. Soc. Jpn.* 49, 173-191.

Yang, Y., C. Gao, X. Dang, Y. Ruan, X. Lü, S. Xie, X. Li, Y. Yao, and H. Yang (2017), Assessing hydroxylated isoprenoid GDGTs as a paleothermometer for the tropical South China Sea. *Org. Geochem.* 115, 156-165.

Yasuda, I., J. H. Yoon, and N. Suginohara (1985), Dynamics of the Kuroshio large meander-Barotropic model. *J. Oceanogr. Soc. Jpn.* 41, 259-273.

Yasuda, I., K. Okuda, and Y. Shimizu (1996), Distribution and Modification of the North Pacific Intermediate Water in the Kuroshio-Oyashio Interfrontal Zone. *J. Phys. Oceanogr.* 26, 448-465.

Yasuda, I. (2003), Hydrographic Structure and Variability in the Kuroshio-Oyashio Transition Area. *J. Oceanogr.* 59, 389-402.

Yasudomi Y., I. Motoyama, T. Oba, and R. Anma (2014), Environmental fluctuations in the northwestern Pacific Ocean during the last interglacial period: evidence from radiolarian assemblages. *Mar. Micropaleontol.* 108, 1-12.

Yatsu, A., Chiba, S., Yamanaka, Y., Ito, S.-I., Shimizu, Y., Kaeriyama, M., and Watanabe, Y. (2013), Climate forcing and the Kuroshio/Oyashio ecosystem. *ICES J. Mar. Sci.* 70 (5), 922-933.

Yin, Q. Z., and A. Berger (2010), Insolation and CO_2 contribution to the interglacial climate before and after the Mid-Brunhes Event. *Nat. Geosci.* 3, 243-246.

Yin, Q. (2013), Insolation-induced mid-Brunhes transition in Southern Ocean ventilation and deep-ocean temperature. *Nature* 494, 222-225.

Young, J. R., P. R. Bown, and J. A. Lees (2014), Nannotax3 Website, International Nannoplankton Association. (2014, April 21). http://ina.tmsoc.org/Nannotax3.

Yu, Y., O. V. Kalashnikova, M. J. Garay, and M. Notaro (2019), Climatology of Asian dust activation and transport potential based in MISR satellite observations and trajectory analysis. *Atmos. Chem. Phys.* 19, 363-378.

Zachos, J., Pagani, M., Sloan, L., Thomas, E., and K. Billups (2001), Trends, rhythms, and aberrations in global climate 65 Ma to present. *Science* 292, 686-693.

Zhang, R., A. Sumi, and M. Kimoto (1996), Impact of El Niño on the East Asian Monsoon: A diagnostic study of the ´86/87 and ´91/92 events. *J. Meteorol. Soc. Japan* 74, 49-62.

Zhang, C., Y. Wang, T. Deng, X. Wang, D. Biasatti, Y. Xu, and Q. Li (2009), C_4 expansion in the central Inner Mongolia during the latest Miocene and early Pliocene. *Earth Plant. Sci. Lett.* 287, 311-319.

Zhang, J., Y. Bai, S. Xu, F. Lei, and G. Jia (2013a), Alkenone and tetraether lipids reflect different seasonal seawater temperatures in the coastal northern South China Sea. *Org. Geochem.* 58, 115-120.

Zhang, Y. G., M. Pagani, Z. Liu, S. M. Bohaty, and R. DeConto (2013b), A 40-million-year history of atmospheric CO_2. *Phil. Trans. R. Soc. A.* 371, 20130096.

Zhang, Y. G., M. Pagani, and Z. Liu (2014), A 12-Million-Year Temperature History of the tropical Pacific Ocean. *Science* 344, 84-87.

Zhang, R., Z. Zhang, and D. Jiang (2018), Global cooling contributed to the establishment of a modern-like East Asian monsoon climate by the early Miocene. *Geophys. Res. Lett.* 45, 11941-11948.

Zhao, C., Y. P. Chang, M.-T. Chen, and Z. Liu (2013), Possible reverse trend in Asian summer monsoon strength during the late Holocene. *J. Asian Earth Sci.* 69, 102-112.

Zheng, H., X. Wei, R. Tada, P. D. Clift, B. Wang, F. Jourdan, P. Wang, P., and M. He (2015), Late Oligocene-early Miocene birth of the Taklimakan Desert. *Proc. Natl. Acad. Sci. USA* 112 (25), 7662-7667.

Zheng, H., C. McA Powell, D. K. Rea, J. Wang, and P. Wang (2016), Late Miocene and mid-Pliocene enhancement of the East Asian monsoon as viewed from the land and sea. *Glob. Planet. Change* 41 (3-4), 147-155.

Zhou, W. (2017), Impact of Arctic amplification on East Asian winter climate. *Atmos. Ocean. Sci. Lett*. 10, 385-388.

Zhou, P., Z. Shi, X. Li, and W. Zhou (2020), Response of westerly jet over the northern hemisphere to astronomical insolation during the Holocene. *Front. Earth Sci.* 8, 282.

Zhu, C., S. G. Wakeham, F. J. Elling, A. Basse, G. Mollenhauer, G. J. M. Versteegh, M. Könneke, and K.-U. Hinrichs (2016), Stratification of archaeal membrane lipids in the ocean and implications for adaption and chemotaxonomy of planktonic archaea. *Environ. Microbiol.* 18 (12), 4324-4336.

Photos separating individual chapters were taken by me whilst onboard R/V *JOIDES Resolution* and are hence my personal property.

Personal contribution to multiple-author publications

This PhD thesis comprises three publications (Chapters 4, 8 and 10) and three manuscripts in review (Chapter 5) or in preparation for publication (Chapters 6 and 7). All these publications and manuscripts were prepared in cooperation with several other co-authors. My personal contribution to these publications and manuscripts was as follows:

Chapter 4: All deep-sea sediment samples were obtained during Integrated Ocean Drilling Program Expedition 333 to the Nankai Trough area south of Japan in December 2010 and January 2011, in which Dr. T. Bauersachs participated. A.-S. Jonas performed preparation of samples for further analytical processing, bulk geochemical analyses and lipid extractions. Calculations were performed by A.-S. Jonas. Data interpretation, synthesis of results and preparation of the manuscript was done by A.-S. Jonas under supervision of Dr. T. Bauersachs and Prof. Dr. L. Schwark.

Chapter 5: All deep-sea sediment samples were obtained during International Ocean Discovery Program Expedition 350 to the Izu-Bonin rear arc area south of Japan in April and May 2014, in which A.-S. Jonas participated. A.-S. Jonas performed preparation of samples for further analytical processing and lipid extractions. Calculations were performed by A.-S. Jonas. M. Kars performed XRF scanning at Kochi Core Center, Japan. W. Ruebsam performed spectral analysis. Data interpretation, synthesis of results and preparation of the manuscript was done by A.-S. Jonas under supervision of Prof. Dr. L. Schwark.

Chapter 6: All deep-sea sediment samples were obtained during International Ocean Discovery Program Expedition 350 to the Izu-Bonin rear arc area south of Japan in April and May 2014, in which A.-S. Jonas participated. A.-S. Jonas performed preparation of samples for further analytical processing and lipid extractions. Calculations were done by A.-S. Jonas. Data interpretation, synthesis of results and preparation of the manuscript was done by A.-S. Jonas under supervision of Prof. Dr. L. Schwark and Dr. T. Bauersachs.

Chapter 7: All deep-sea sediment samples were obtained during International Ocean Discovery Program Expedition 350 to the Izu-Bonin rear arc area south of Japan in April and May 2014, in which A.-S. Jonas participated. A.-S. Jonas performed preparation of samples for further analytical processing and lipid extractions. Calculations were done by A.-S. Jonas. Data interpretation, synthesis of results and preparation of the manuscript was done by A.-S. Jonas under supervision of Dr. T. Bauersachs and Prof. Dr. L. Schwark.

Chapter 8: All deep-sea sediment samples were obtained during International Ocean Discovery Program Expedition 350 to the Izu-Bonin rear arc area south of Japan in April and May 2014, in which A.-S. Jonas and M. Kars participated. A.-S. Jonas performed bulk geochemical (TOC, TC, TN, and TS) analysis on 25 samples of the whole sample set, wrote the method section on bulk geochemical analysis and wrote the discussion section "*6.2. Paleoproductivity and water mass properties"* together with M. Kars.

Appendix Chapter 10: All deep-sea sediment samples were obtained during International Ocean Discovery Program Expedition 350 to the Izu-Bonin rear arc area south of Japan in April and May 2014, in which A.-S. Jonas and M. Kars participated. A.-S. Jonas performed bulk geochemical (TOC, TC, TN, and TS) analysis on 20 samples of the whole sample set.

List of publications

Peer-reviewed research articles

Jonas, A.-S., L. Schwark, and T. Bauersachs (2017), Late Quaternary water temperature variations of the Northwest Pacific based on the lipid paleothermometers TEX^{H}_{86}, $U^{K'}_{37}$ and LDI. Published in *Deep-Sea Research Part I* 125, 81-93, https://doi.org/10.1016/j.dsr.2017.04.018.

Kars, M., R. J. Musgrave, K. Kodama, **A.-S. Jonas**, M. Bordiga, W. Ruebsam, M. J. Mleneck-Vautravers, and T. Bauersachs (2017), Impact of climate change on the magnetic mineral assemblage in marine sediments from Izu rear arc, NW Pacific Ocean, over the last 1 Ma. Published in *Palaeogeography, Palaeoclimatology, Palaeoecology* 480, 53-69, doi:10.1016/j.palaeo.2017.05.016.

Busby, C. J., Y. Tamura, P. Blum, G. Guèrin, G. D. M. Andrews, A. K. Barker, J. L. R. Berger, E. M. Bongiolo, M. Bordiga, S. M. DeBari, J. B. Gill, C. Hamelin, J. Jia, E. H. John, **A.-S. Jonas**, M. Jutzeler, M. Kars, Z. A. Kita, K. Konrad, S. H. Mahony, M. Martini, T. Miyazaki, R. J. Musgrave, D. B. Nascimento, A. R. L. Nichols, J. M. Ribeiro, T. Sato, J. C. Schindlbeck, A. K. Schmitt, S. M. Straub, M. J. Mleneck-Vautravers, and A. Y. Yang (2017), The missing half of the subduction factory: shipboard results from the Izu rear arc, IODP Expedition 350. Published in *International Geology Review* 59 (13), 1677-1708, doi:10.1080/00206814.2017.1292469.

Kars, M., R. J. Musgrave, T. Hoshino, **A.-S. Jonas**, T. Bauersachs, F. Inagaki, and K. Kodama (2018), Magnetic mineral diagenesis in a high temperature and deep methanic zone in Izu rear arc marine sediments, Northwest Pacific Ocean. Published in *Journal of Geophysical Research: Solid Earth* 123, 8331-8348. https://doi.org/10.1029/2018JB015861.

Gill, J. B., E. M. Bongiolo, T. Miyazaki, C. Hamelin, M. Jutzeler, S. M. DeBari, **A.-S. Jonas**, B. S. Vaglarov, L. S. Nascimento, and M. Yakavonis (2018), Tuffaceous Mud is a Volumetrically Important Volcaniclastic Facies of Submarine Arc Volcanism and Record of Climate Change. Published in *Geochemistry, Geophysics, Geosystems* 19, 1217-1243, https://doi.org/10.1002/2017GC007300.

Expedition reports

Tamura, Y., C. J. Busby, P. Blum, and the **Expedition 350 Scientists** (2015a), *Proceedings of the International Ocean Discovery Program, Expedition 350: Izu-Bonin-Mariana Rear Arc*. International Ocean Discovery Program, College Station, TX. http://dx.doi.org/10.14379/iodp.proc.350.2015.

Tamura, Y., C. J. Busby, P. Blum, G. Guèrin, G. D. M. Andrews, A. K. Barker, J. L. R. Berger, E. M. Bongiolo, M. Bordiga, S. M. DeBari, J. B. Gill, C. Hamelin, J. Jia, E. H. John, **A.-S. Jonas**, M. Jutzeler, M. A. C. Kars, Z. A. Kita, K. Konrad, S. H. Mahoney, M. Martini, T. Miyazaki, R. J. Musgrave, D. B. Nascimento, A. R. L. Nichols, J. M. Ribeiro, T. Sato, J. C. Schindlbeck, A. K. Schmitt, S. M. Straub, M. J. Vautravers, and Y. Yang (2015b), Site U1437. In: Tamura, Y., C. J. Busby, P. Blum, and the Expedition 350 Scientists (Eds.), *Proceedings of the International Ocean Discovery Program, Expedition 350: Izu-Bonin- Mariana Rear Arc*. International Ocean Discovery Program, College Station, TX.

Poster presentations at scientific conferences

Jonas, A.-S., L. Schwark, and T. Bauersachs (2018), Variation in the flow path of the Kuroshio Current and its impact on NW Pacific paleoclimate evolution. *Institutskolloquium Institut für Geowissenschaften der Uni Kiel,* Kiel, Germany.

Jonas, A.-S., L. Schwark, L., and T. Bauersachs (2017), Mid-Pleistocene to Holocene evolution of the Kuroshio Current, Northwest Pacific Ocean. *28th International Meeting on Organic Geochemistry*, Florence, Italy.

Jonas, A.-S., L. Schwark, and T. Bauersachs (2017), Variation in the flow path of the Kuroshio Current and its impact on NW Pacific paleoclimate evolution. *IODP/ ICDP Kolloquium 2017*, Braunschweig, Germany.

Jonas, A.-S., L. Schwark, and T. Bauersachs (2016), Late Pliocene to Holocene spatio-temporal variation in the flow path of the Kuroshio Current. *IODP Expedition 350 Postcruise Meeting*, Marrakesh, Morroco.

Jonas, A.-S., L. Schwark, and T. Bauersachs (2016), Late Pliocene to Holocene spatio-temporal variation in the flow path of the Kuroshio Current (NW Pacific). *IODP/ICDP Kolloquium 2016*, Heidelberg, Germany.

Oral presentations at scientific conferences

Jonas, A.-S., M. Kars, T. Bauersachs, W. Rübsam, and L. Schwark (2019), Decoupling of NW Pacific from global climate evolution linked to the Mid-Pleistocene Transition and Mid-Brunhes Event. *29th International Meeting on Organic Geochemistry*, Gothenburg, Sweden.

Jonas, A.-S., T. Bauersachs, and L. Schwark (2015), 730 ka records of paleoceanographic and climate evolution of the Northwest Pacific Ocean. *27th International Meeting on Organic Geochemistry*, Prague, Czech Republic.

Jonas, A.-S., J. C. Schindlbeck, C. Busby, Y. Tamura, and Expedition 350 Scientists (2015), IODP Expedition 350 - Izu-Bonin-Mariana Rear Arc: The missing half of the subduction factory. *IODP/ICDP Kolloquium 2015*, Bonn, Germany.

Acknowledgements

First of all, I would like to thank Prof. Dr. Lorenz Schwark for giving me the opportunity to work on this thesis, for sharing his knowledge, providing a plenty of thought-provoking impulses and for his patience as the births of my daughters took precedence over my PhD thesis for some time.

I am grateful to Dr. Thorsten Bauersachs for his co-mentorship, for letting me work on this topic and his samples from IODP Expedition 333 in the first place, his guidance in HPLC/MS measurements and analysis, presentation practice and fruitful discussions.

I would also like to thank Prof. Dr. Denise K. Kulhanek for serving as the second referee for this thesis as well as Prof. Dr. Martin Frank and Prof. Dr. Julia Gottschalk as part of the examination board.

Furthermore, I would like to thank all my colleagues from the Organic Geochemistry Department for their support in the laboratory, discussing results and also on a personal basis, especially Nicole Häuser, Vanessa Grote, Petra Fiedler, Marieke Muijsers, Eyke Kirchhof and Dr. Wolfgang Rübsam.

Also, I would like to thank all scientists and crew from IODP Expedition 350, who made the stay on the ship so enjoyable. Special thanks to Dr. Myriam Kars, Dr. Robert “Bob” Musgrave, and Dr. James “Jim” Gill for your support, fruitful discussions and your interest in my work.

Last but not least, I am most thankful to my family for their continuous support, motivation and encouragement over the last years. I owe many thanks to my parents and my sister Katharina for looking after Luise and Linnéa so that I had time to work on my thesis.

And most importantly: thank you Cris, Luise and Linnéa, I am so happy to have you! Luise and Linnéa, you always know how to put a smile on my face. Cris, I could not have finished this thesis without your love, endless support and continuous encouragement.

Affidavit

Hiermit erkläre ich, dass ich die vorliegende Arbeit mit dem Titel „Paleoceanographic and paleoclimate evolution of the Northwest Pacific Ocean from the late Miocene to present“ selbstständig, ohne unzulässige Hilfe Dritter und ohne Benutzung anderer als der angegebenen Quellen und Hilfsmittel angefertigt habe. Die Arbeit entstand unter Einhaltung der Regeln guter wissenschaftlicher Praxis der Deutschen Forschungsgemeinschaft. Ferner erkläre ich, dass ich diese Dissertation weder in ihrer Gesamtheit noch in Teilen zu einem früheren Zeitpunkt an der Christian-Albrechts-Universität zu Kiel oder einer anderen wissenschaftlichen Hochschule im In- und Ausland im Rahmen eines Prüfungsverfahrens vorgelegt habe. Mir wurde kein akademischer Grad entzogen.

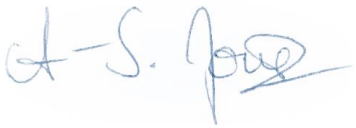

Kiel, den 30. September 2021 Ann-Sophie Jonas